

Quantum Critical Matter:
Quantum Phase Transitions with Multiple Dynamics and
Weyl Superconductors

Inaugural-Dissertation

zur

Erlangung des Doktorgrades

der Mathematisch-Naturwissenschaftlichen Fakultät

der Universität zu Köln

vorgelegt von

Tobias Meng

aus Mainz

Köln 2012

Berichterstatter: Prof. Dr. Achim Rosch
Prof. Dr. Simon Trebst
Prof. Dr. Jörg Schmalian

Tag der mündlichen Prüfung: 19. Juni 2012

Für meinen kleinen Bruder, als Anzahlung auf das Fliegeauto.

Abstract

In this PhD thesis, the physics of quantum critical matter and exotic quantum state close to quantum phase transitions is investigated. We will focus on three different examples that highlight some of the interesting phenomena related to quantum phase transitions. Firstly, we discuss the physics of quantum phase transitions in quantum wires as a function of an external gate voltage when new subbands are activated. We find that at these transitions, strong correlations lead to the formation of an impenetrable gas of polarons, and identify criteria for possible instabilities in the spin- and charge sectors of the model. Our analysis is based on the combination of exact resummations, renormalization group techniques and Luttinger liquid approaches.

Secondly, we turn to the physics of multiple divergent time scales close to a quantum critical point. Using an appropriately generalized renormalization group approach, we identify that the presence of multiple dynamics at a quantum phase transition can lead to the emergence of new critical scaling exponents and thus to the breakdown of the usual scaling schemes. We calculate the critical behavior of various thermodynamic properties and detail how unusual physics can arise. It is hoped that these results might be helpful for the interpretation of experimental scaling puzzles close to quantum critical points.

Thirdly, we turn to the physics of topological transitions, and more precisely the physics of Weyl superconductors. The latter are the superconducting variant of the topologically non-trivial Weyl semimetals, and emerge at the quantum phase transition between a topological superconductor and a normal insulator upon perturbing the transition with a time reversal symmetry breaking perturbation, such as magnetism. We characterize the topological properties of Weyl superconductors and establish a topological phase diagram for a particular realization in heterostructures. We discuss the physics of vortices in Weyl superconductors, and establish under which conditions they can trap zero energy Majorana modes. Our discussion ends with some remarks on possible experimental signatures.

Kurzzusammenfassung

Diese Dissertation befasst sich mit quantenkritischen Materialien und insbesondere mit ungewöhnlichen Quantenzuständen an Quantenphasenübergängen. Die Diskussion erfolgt an Hand von drei spezifischen Beispielen für ungewöhnliche Physik an und nahe von quantenkritischen Punkten. Teil eins der Dissertation beschäftigt sich mit dem Verhalten von Quantendrähten nahe Lifshitz-Übergängen, an denen als Funktion eines Elektrodenpotentials Unterbänder aktiviert werden. Wir finden, dass sich dort ein stark-korreliertes Gas von Polaronen ausbildet und identifizieren Kriterien für Instabilitäten dieses ungewöhnlichen Zustands. Unsere Analyse basiert auf einer Kombination von exakten Resummierungen, Renormierungsgruppenanalysen und Luttinger Flüssigkeit Berechnungen.

In Teil zwei betrachten wir die Physik von multiplen divergenten Zeitskalen an Quantenphasenübergängen. Mittels einer verallgemeinerten Renormierungsgruppenanalyse zeigen wir, dass die Existenz verschiedener Dynamiken an einem Quantenphasenübergang neue Skalen-Exponenten hervorbringen kann, so dass die üblichen kritischen Skalentheorien nicht mehr gültig sind. Wir berechnen das quantenkritische Verhalten verschiedener thermodynamischer Größen und analysieren detailliert die Mechanismen die zu den ungewöhnlichen Exponenten führen. Wir hoffen, dass unsere Ergebnisse für manche der Experimente die anscheinend im Widerspruch zu den üblichen kritischen Skalentheorien stehen relevant sein könnten.

Als letztes Beispiel betrachten wir in Teil drei die Physik von Weyl Supraleitern. Diese sind die supraleitenden Verwandten von topologischen Weyl Halbmetallen und entstehen wenn der Quantenphasenübergang zwischen einem topologischen Supraleiter und einem normalen Isolator mit einer Zeitumkehrinvarianz brechenden Störung betrachtet wird. Spezifisch diskutieren wir das topologische Phasendiagramm von Weyl Supraleitern in Heterostrukturen und analysieren die Physik von Vortices in Weyl Supraleitern, die unter bestimmten Umständen auch Majorana Null-Moden beherbergen können. Wir schließen das Kapitel mit einer Diskussion von experimentellen Signaturen von Weyl Supraleitern.

Contents

| | | |
|----------|---|-----------|
| 1 | Introduction | 1 |
| I | Quantum phase transitions in quantum wires | 3 |
| 2 | Quantum phase transitions in quantum wires | 5 |
| 2.1 | Why one-dimensional physics are special | 6 |
| 2.1.1 | Mermin-Wagner theorem and phase transitions in 1d | 7 |
| 2.1.2 | Luttinger liquid theory and bosonization | 8 |
| 2.2 | Limits of the Luttinger liquid theory | 10 |
| 2.3 | From 2DEGs to quantum wires: a mean-field analysis | 11 |
| 2.4 | A short discussion of the Wigner crystal regime | 17 |
| 3 | Quantum wire close to the Lifshitz transition | 23 |
| 3.1 | Microscopic derivation of the effective model | 23 |
| 3.1.1 | First subband | 25 |
| 3.1.2 | Second subband (for $\mu_2 < 0$) | 27 |
| 3.1.3 | Coupling between the subbands | 29 |
| 3.1.4 | Values of the coupling strengths | 30 |
| 3.2 | Introductory remarks on the perturbative analysis | 31 |
| 3.2.1 | Multiple divergencies of the perturbation theory | 31 |
| 3.2.2 | The quantum critical perspective on the multiple divergencies | 33 |
| 3.3 | Vertex correction to 1 loop order | 34 |
| 3.4 | Perturbative regime at large negative μ_2 | 36 |
| 3.5 | Quantum phase transition at $\mu_2 = 0$ | 38 |
| 3.5.1 | Leading renormalizations: resummation of the square-root divergencies | 38 |
| 3.5.2 | Sub-leading renormalizations: Lifshitz transition of polarons | 40 |
| 3.5.3 | Universality class of the quantum phase transition | 41 |
| 3.6 | Comparison to an ϵ -renormalization | 41 |
| 4 | Quantum wire above the Lifshitz transition | 45 |
| 4.1 | Small positive chemical potential: $0 < \mu_2 < E_p$ | 45 |
| 4.2 | Coupled Luttinger liquids for $\mu_2 > E_p$ | 46 |
| 4.2.1 | Bosonization | 47 |
| 4.2.2 | A first bosonized form of the two-subband Hamiltonian | 49 |
| 4.2.3 | Polaron effect | 52 |
| 4.3 | Transformation to polarons | 54 |

| | | |
|--|--|------------|
| 4.3.1 | Final form of the Hamiltonian | 55 |
| 4.4 | Renormalization group analysis | 55 |
| 4.5 | Summary: Lifshitz transition in quantum wires | 58 |
| 4.5.1 | Global summary: quantum phase transitions in quantum wires | 60 |
| II Quantum phase transitions with multiple dynamics | | 61 |
| 5 Quantum criticality and multiple dynamics | | 63 |
| 5.1 | Quantum criticality and scaling hypothesis | 65 |
| 5.1.1 | Universal physics close to phase transitions | 66 |
| 5.1.2 | Thermodynamics and phase diagram | 67 |
| 5.2 | Theory of a QCP with single dynamics | 70 |
| 5.2.1 | Quantum and classical fluctuations | 70 |
| 5.2.2 | Dimensional reduction | 73 |
| 5.3 | Case study above the quantum critical point | 75 |
| 5.3.1 | Summary: critical dimensions | 78 |
| 5.4 | Finite temperature renormalization group | 79 |
| 5.5 | Scaling with multiple dynamics | 82 |
| 5.5.1 | Scaling form and thermodynamics | 84 |
| 5.6 | Multiple dynamics renormalization group | 87 |
| 5.7 | Pomeranchuk instability | 88 |
| 6 Emergent unusual exponents | | 91 |
| 6.1 | Generalized Pomeranchuk model | 91 |
| 6.2 | Extended quantum to classical crossover | 92 |
| 6.3 | Renormalization group equations up to $\xi_T^{\leq -1}$ | 94 |
| 6.4 | Analysis of the RG equations | 96 |
| 6.4.1 | Zero temperature, finite mass | 97 |
| 6.4.2 | Zero mass, finite temperature | 98 |
| 6.5 | Scaling with the multiple dynamics and diagonalized RG equations | 102 |
| 6.6 | Solution to the RG equations at arbitrary r and T | 103 |
| 6.7 | Thermodynamics | 105 |
| 6.7.1 | Coupling exponents | 107 |
| 6.7.2 | Scaling of thermodynamic observables | 108 |
| 6.8 | Summary | 113 |
| III Weyl superconductors | | 119 |
| 7 Introduction to Weyl semimetals | | 121 |
| 7.1 | Topology and solid state physics | 122 |
| 7.1.1 | A very short introduction to topology | 123 |
| 7.1.2 | Topology in physics | 124 |
| 7.1.3 | Topological insulators | 128 |
| 7.2 | Dirac, Weyl and Majorana | 132 |
| 7.2.1 | The Dirac equation | 132 |
| 7.2.2 | Weyl fermions: special massless Dirac fermions | 134 |

| | | |
|-----------|---|------------|
| 7.2.3 | Majorana fermions: particles being their own antiparticles | 134 |
| 7.3 | Weyl fermions and Weyl nodes | 136 |
| 7.3.1 | Weyl fermions at band touchings: Weyl nodes | 136 |
| 7.3.2 | The Nielsen-Ninomiya fermion doubling theorem | 138 |
| 7.3.3 | Topological character of Weyl nodes | 139 |
| 7.3.4 | Weyl nodes with and without symmetries | 141 |
| 7.4 | Weyl semimetal as perturbed TI/NI transition | 142 |
| 7.4.1 | Transition between topological and normal insulators | 143 |
| 7.4.2 | Weyl semimetals in heterostructures | 144 |
| 8 | Weyl superconductors | 149 |
| 8.1 | Weyl superconductors in heterostructures | 149 |
| 8.1.1 | Physical model and Hamiltonian | 149 |
| 8.1.2 | Existence of Bogoliubov Weyl nodes | 152 |
| 8.1.3 | Time reversal and inversion symmetry | 154 |
| 8.1.4 | Bogoliubov Weyl nodes vs. normal Weyl nodes | 155 |
| 8.1.5 | Surface states | 156 |
| 8.1.6 | Accessible phases of a Weyl superconductor heterostructure | 157 |
| 8.2 | Vortices in Weyl superconductors | 160 |
| 8.2.1 | Model of a vortex | 161 |
| 8.2.2 | Vortex along the superlattice axis | 161 |
| 8.2.3 | Stability of the Majorana zero modes | 163 |
| 8.2.4 | Vortex perpendicular to the superlattice axis | 164 |
| 8.2.5 | Vortex along some general direction and vortices in time reversal and inversion symmetry broken Weyl superconductors | 166 |
| 8.2.6 | Vortices in time reversal symmetric Weyl superconductors | 167 |
| 8.3 | Experimental realization and signatures | 167 |
| 8.3.1 | Anomalous thermal Hall effect | 168 |
| 8.3.2 | Unidirectional electrical transport | 170 |
| 8.4 | Conclusions | 171 |
| IV | Appendices | 173 |
| A | Introduction to the standard renormalization group | 175 |
| A.1 | Kadanoff spin block renormalization group | 175 |
| A.2 | Renormalization group equations | 177 |
| A.3 | RG fixed points | 178 |
| B | Quantum phase transitions in quantum wires | 181 |
| B.1 | Derivation of the Wigner crystal action | 181 |
| B.2 | 2-particle Green's function in the second band | 185 |
| B.2.1 | Resummation of the interacting two-particle Green's function | 187 |
| B.3 | Bubbles in the first band | 188 |
| B.3.1 | Bubbles involving both bands, $\mu_2 < 0$ | 188 |
| B.3.2 | Both particles in the first subband | 189 |
| B.4 | RG in the limit of large negative μ_2 | 190 |
| B.5 | RG at $\mu_2 = 0$ | 191 |

| | | |
|----------|--|------------|
| B.5.1 | Intermediate stationary point | 192 |
| B.5.2 | Contribution of the stationary point to the total flow | 193 |
| B.5.3 | Full initial flow | 193 |
| B.6 | Analytical evaluation of the coupling strengths | 194 |
| B.7 | Canonical transformation to polarons | 195 |
| B.8 | Second bosonization and final form of the Hamiltonian | 197 |
| B.8.1 | Diagonalization of the remaining quadratic Hamiltonian | 200 |
| B.8.2 | Comment on the singularity encountered without polaronic degrees of freedom | 202 |
| B.9 | Derivation of the RG equations | 203 |
| B.10 | Complete 1 st order RG equations | 204 |
| B.11 | Limiting cases | 206 |
| B.11.1 | Pair tunneling of parallel spins: $g_{t\parallel}$ | 206 |
| B.11.2 | Pair tunneling of opposite spins without spin flip: $g_{t\perp(2)}$ | 207 |
| B.11.3 | Pair tunneling of opposite spins without spin flip: $g_{t\perp(1)}$ | 207 |
| B.11.4 | The spin exchange interaction with spin flip: u_s^\perp | 207 |
| B.11.5 | Intraband coupling with spin flip in the first band: $g_{1\perp(1)}$ | 208 |
| B.11.6 | Intraband coupling with spin flip in the second band: $g_{2\perp(1)}$ | 208 |
| B.12 | Solution of the leading order RG equations | 208 |
| C | Quantum phase transitions with multiple dynamics | 211 |
| C.1 | Evaluation of the one-loop diagrams | 211 |
| C.1.1 | Mass correction | 212 |
| C.1.2 | Analysis at zero temperature | 212 |
| C.1.3 | Analysis at finite temperature, case $y = 1$ | 215 |
| C.1.4 | Correction to the interaction | 219 |
| C.2 | Single dynamics RG | 220 |
| C.3 | Integrating out the non-zero Matsubara modes | 221 |
| C.4 | Full RG equations for single dynamics for $r = 0$ | 223 |
| C.5 | RG equations for the generalized Pomeranchuk model | 227 |
| C.6 | The RG equations with kinetic coefficients | 229 |
| C.6.1 | Additional mixed diagrams | 231 |
| C.7 | Integration of the generalized RG equations | 232 |
| C.7.1 | Zero temperature flow | 232 |
| C.7.2 | Finite temperature flow: $\frac{1}{\nu_{\text{WF}}} < z_{<}$ | 234 |
| C.7.3 | Finite temperature flow: $\frac{1}{\nu_{\text{WF}}} > z_{<}$ | 235 |
| C.7.4 | General expression of the correlation length | 235 |
| C.8 | RG equation for the free energy | 237 |
| C.9 | Calculation of $\mathcal{F}_{<}$ via RG | 240 |
| C.10 | The thermal expansion via RG trajectories | 242 |
| C.10.1 | Contribution of the mode with the smaller dynamical exponent | 242 |
| C.10.2 | Contribution of the mode with the larger dynamical exponent | 247 |
| D | Weyl superconductors | 253 |
| D.1 | Derivation of the Weyl superconductor Hamiltonian | 253 |
| D.2 | Stability of Weyl nodes against superconductivity | 255 |
| D.3 | Bogoliubov Weyl nodes as 1/2 of regular Weyl nodes | 257 |

| | | |
|-------|---|-----|
| D.4 | A Weyl superconductor with a surface at $y = 0$ | 258 |
| D.5 | A reminder on vortices in superconductors | 260 |
| D.6 | Symmetries of the Hamiltonian for magnetic fields $\parallel \hat{z}$ | 263 |
| D.6.1 | Superconducting particle-hole symmetry | 263 |
| D.6.2 | Charge conjugation symmetry | 263 |
| D.7 | Vortices along \hat{z} in Weyl superconductors | 265 |
| D.7.1 | Expression of the zero energy Majorana bound state | 266 |

Chapter 1

Introduction

One of the greatest motivations to study solid state systems is, besides the beauty of their properties, the fact that they never stop to surprise us with novel and unexpected behavior. Given the enormous complexity of the world surrounding us, it is (not) astonishing that depending on the perspective only the simple Hydrogen atom can be fully and exactly understood (if anything at all). On the other hand, generations of physicists have succeeded in developing effective descriptions valid within some well-defined limits and assumptions. These theories are precise enough to predict fascinating properties which can be verified by experiments (such as the existence of topological insulators, just to name a prominent recent example).¹⁻⁵ One tantalizing question is thus how these theories describing different limiting cases can be connected to draw a global and comprehensive picture of material properties.

An important manifestation of this question arises at so-called phase transitions when materials change their macroscopic behavior in an important way, such as the transition between magnetic and non-magnetic iron. While the different phases can in many cases be described by well-defined limiting theories, the nature of the material at the transition remains in general unclear. Excitingly, such “critical” materials are not just a mixture of the two limiting phases, but have new and distinct properties including for instance divergences in physical quantities.^{6,7} To put it in an ancient Greek way, the whole is again greater than the sum of its parts. The attempt to understanding phase transitions has not only succeeded in explaining a large number of experimental observations, but has also been fruitful for the progress of physics in general (for instance by its contributions to the renormalization group approach).⁷⁻⁹ Despite this great success, critical materials are still far from being generally understood. This open question has seen renewed interest with the advent of quantum phase transitions, which mark phase transitions driven by quantum fluctuations rather than thermal motion.^{7,9-11} While these quantum critical points strictly speaking only exist as a theoretical construction at zero temperature, they can be related to new and unexpected physics even at finite and experimentally accessible temperatures. As an example, the usually very successful description of physics in terms of Landau quasiparticles is not applicable any more. Therefore, new theories describing the physics at and close to the transitions have to be developed, and no general solution to this problem has been established so far.¹²

In this thesis devoted to quantum critical matter, i.e. physical systems at and close to quantum phase transitions, we want to discuss how the existence of a nearby quantum critical point allows for novel physics to arise, and how the usual description of

material properties can break down in quantum critical matter. To this end, we study three examples of quantum critical matter. At first, we discuss a very concrete manifestation of quantum critical physics, namely the activation of conductance channels in one-dimensional quantum wires defined in GaAs-heterostructures. We show how the usual description of these systems in terms of coupled Luttinger liquids breaks down due to the presence of interactions. We identify the strongly correlated state of the system at the transition from one to two conductance channels, and discuss under which conditions this state becomes unstable. This is achieved by a combination of different approaches, each appropriate to a precise way on which the transition is approached. However, a global picture of these transitions is still missing, and further work is needed to unify the different limiting cases.

In a second part, we turn to the description of quantum critical points in terms of universal low energy theories depending only on a small set of critical exponents. While many experimental observations could have been explained by these theories, experiments sometimes also seem to be beyond their scope. We discuss that the usual scaling can indeed break down if different parts of a system become critical at the same time, and extend the theory of scaling to the scenario of multiple dynamics. More precisely, we analyze quantum critical points characterized by a single divergent length scale ξ and two divergent time scales $\tau_i = \xi^{z_i}$, and find that they can be described by a new, emergent length scale and a related emergent dynamical exponent. These considerations might be relevant in the context of experimental scaling puzzles close to quantum critical points.

Last but not least, we turn to the physics of Weyl superconductors, an unusual state of matter that can be understood in the framework of quantum critical systems. More precisely, Weyl superconductors have topologically trivial and non-trivial subsystems in different part of the momentum space. We find that these are separated by Bogoliubov Weyl nodes which correspond to quantum critical points of $p_x + ip_y$ -superconductors when the system is considered in terms of layers of constant momentum p_z in the reciprocal space. Weyl superconductors are shown to exhibit unusual phenomena such as Fermi arcs, i.e. open Fermi lines in their surface Brillouin zones. We derive a topological phase diagram of Weyl superconductors in heterostructures of standard superconductors and topological insulators, and discuss that vortices in Weyl superconductors can, under certain circumstances, trap zero energy Majorana modes that could in principle be used for quantum computation. The exotic quantum critical state of Weyl superconductors is however also interesting for its own sake, and has fascinating experimental implications, some of which are discussed at the end of this third part.

Part I

Quantum phase transitions in quantum wires

Chapter 2

Quantum phase transitions in quantum wires

Throughout the last century, the progress in consumer electronics has been one of the driving forces of condensed matter physics. Numerous groundbreaking developments in the field have shaped today's world, and have been awarded with several Nobel prizes (like the transistor, optoelectronics or integration of circuits, to name just a few). The technical advances also gave rise to the so-called digital revolution marking the beginning of the information age.

One of the main answers to the increasing demand of computational power is the integration and miniaturization of electronic components. By now, the mass production of semiconductor structures with an average half-pitch of 32 nm has become industrial standard. Such small devices are often fabricated starting from a two-dimensional electron gas (2DEG), which can be realized in semiconductor heterostructures, e.g. GaAs/GaAlAs devices (see Fig. 2.1a) or metal-oxide-semiconductor (MOS) sandwiches. The electronic structures may then be defined by, for instance, etching them into the sample, somewhat analogously to drawing on a paper. A commercially important but scientifically not always intended consequence of the chemical definition of nanocircuits is that the samples can not easily be changed after their production. A higher in-situ tunability can be achieved by using electrostatic gates which deplete certain areas of the 2DEG, see Fig. 2.1b. As an alternative to the chemical or electrostatic shaping of a 2DEG, conducting nanostructures can also be realized using molecules, e.g. carbon nanotubes connecting different parts of the circuit, giving rise to the field of molecular electronics.

Within such nanoscopic structures, currents are transported in wires thin enough for quantum mechanics to play an important role. Quantum wires, as such wires are consequently dubbed, are most prominently characterized by a strong confinement of the electrons which behave as particles in quantum wells along both transversal directions, while they move more or less freely along the third axis. Far beyond their usage in electronic circuits, quantum wires are also of fundamental scientific interest. From a condensed matter physicist's perspective, quantum wires are ideal playgrounds to study one-dimensional physics such as conductance quantization (shown in Fig. 2.2 adapted from Ref. [14]), Luttinger liquid physics or spintronics. Recently, it has also been realized that quantum wires can be in a topologically non-trivial state, which has generated a lot of scientific interest.¹⁵ After some more general introductory remark on one-dimensional systems, we will however turn to yet another fascinating facet of quantum wire physics,

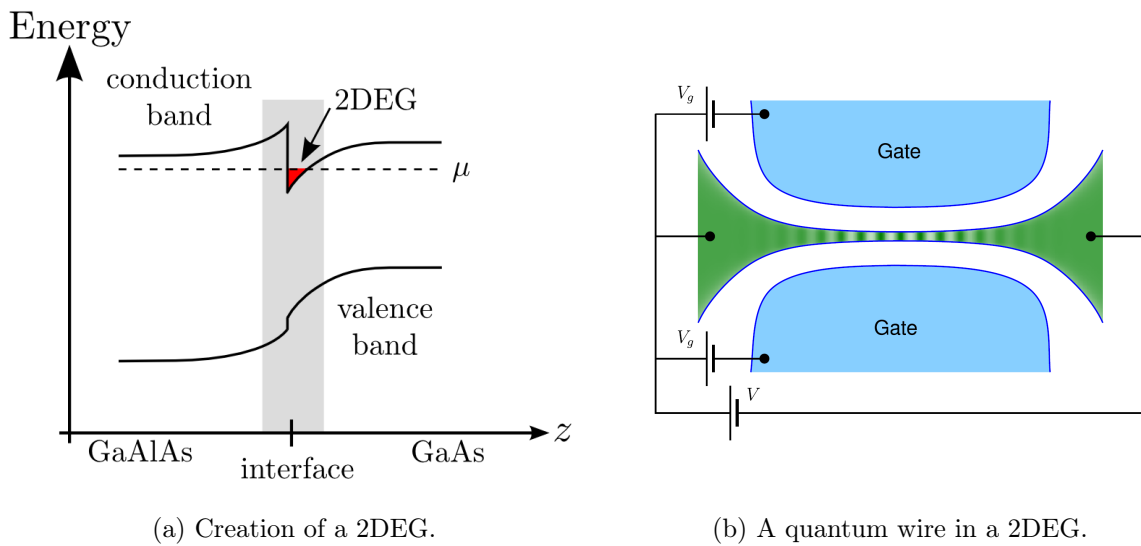


Figure 2.1: Subfigure (a) schematically shows the creation of a 2-dimensional electron gas (2DEG) at the interface of a GaAs/GaAlAs heterostructure due to the alignment of the chemical potentials in the sample, leading to a curved bandstructure. The spatial direction perpendicular to the interface is denoted by z , μ is the chemical potential. Subfigure (b) depicts the definition of a quantum wire in a 2DEG using electrostatic gates which confine the electrons to a quasi one-dimensional area (figure taken from Ref. [13]). The gates are located on the top of the sample, i.e. at some distance above the 2DEG.

namely quantum phase transitions in one dimension. At first, the precise model of an interacting quantum wire that we will be working with shall be defined. After deriving a mean-field phase diagram, we will turn to the limit of strong interactions to give a first flavor of the precise Lifshitz transition that we are concerned with. The subsequent chapters will then analyze the latter for weaker interaction strengths.

Publication of the project on quantum phase transitions in quantum wires

Some of the results deriving from the subsequent considerations have been published in Ref. [16], and the next two chapters will partially follow along the lines of thought of this publication. The latter covers large parts of chapters 2 and 3, while the discussion of two subbands of finite filling in terms of coupled Luttinger liquids contained in chapter 4 has not been published. I would like to seize the opportunity to again thank my colleagues who have been involved in this project for our fruitful collaboration.

2.1 Why one-dimensional physics are special

One-dimensional (1D) systems of interacting particles are in many respects different from their higher dimensional analogs. As an example, the Mermin-Wagner theorem states that continuous symmetries can not be broken at finite temperatures in systems with less than two dimensions. One-dimensional systems do thus “not exhibit true long-range order”. In addition, the famous Fermi liquid theory emerging as a low-energy description of a large number of higher dimensional systems fails in one dimension. As we will

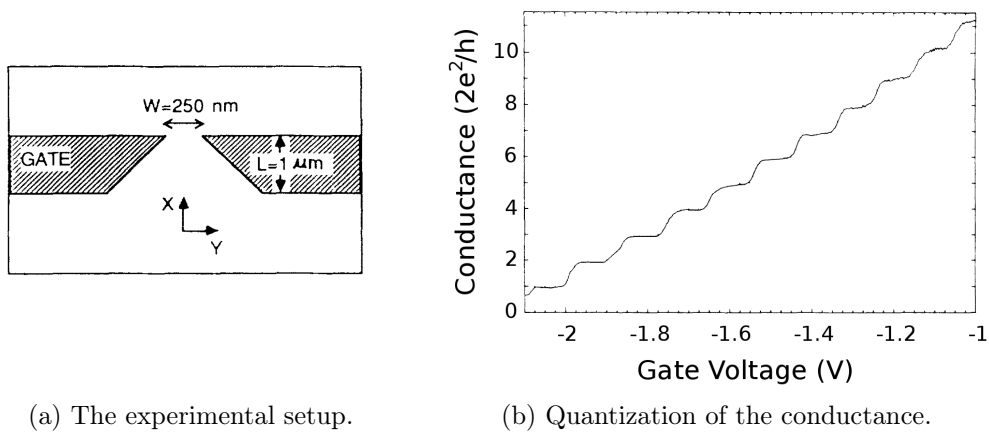


Figure 2.2: Experimental data on the quantization of the conductance in quantum point contact (equivalent to a short quantum wire), adapted from Ref. [14]. The sample is a GaAs/GaAlAs heterostructure, the setup is shown in subfigure (a). The conductance in subfigure (b) is measured as a function of a gate voltage which controls the width of the quantum point contact and thus the number of accessible channels.

furthermore see, Bosons and Fermions are in a way equivalent in 1D. All of these points make one-dimensional systems special and fascinating, and have driven a big amount of research in the last decades. New theoretical tools, such as the Luttinger liquid description, have been developed in order to tackle such systems, and a vast amount of experimental realizations of (effectively) one-dimensional systems has been found, examples of which include spin chain compounds, carbon nanotubes, edge states in topological systems, and cold atom realizations.

2.1.1 Mermin-Wagner theorem and phase transitions in one dimension

Interacting systems have in general the tendency to form ordered states. The order and composition of the building blocks of these states are such that the system optimizes the interaction energy, and the global state of the system can be controlled by changing the interaction strength. This leads to the concept of spontaneous symmetry breaking. In a ferromagnet, for instance, each magnetic moment may in principle point in any direction, and the Hamiltonian is invariant under global rotations. Nevertheless, the magnetic moments will in general spontaneously and arbitrarily choose one specific direction and collectively align, i.e. order, along the latter. This so-called spontaneous symmetry breaking is driven by the ferromagnetic interaction of the spins. In terms of the free energy, the gain in the spin-spin interaction energy outweighs the loss in entropy of an ordered state with respect to the disordered state, where each magnetic moment could point an arbitrary direction.

The tendency to form ordered states depends however crucially on the dimensionality of the system. The smaller the number of space dimensions, the less important is the gain in energy with respect to the loss in entropy. As an example, consider a system of N^d Ising spins (where d is the number of space dimensions) that are ferromagnetically coupled to their nearest neighbors. The relevant excitations around the ferromagnetic state are domain walls (i.e. $d - 1$ -dimensional hyperplanes). These are associated with an energy

cost of $E \sim J N^{d-1}$. A domain wall can however be placed at any position in the system, which leads to an entropy of $S \sim k_B T \ln(N)$. In the thermodynamic limit $N \rightarrow \infty$, an ordered state is thus excluded at any finite temperature T for dimensions $d \leq 1$ because domain walls proliferate due to the associated gain of free energy $F = E - TS$. In short, a classical lattice of Ising spins with nearest neighbor interactions does thus not exhibit an ordered state in one dimension, while it does so in two dimensions (which has been discussed in detail by Ising for the one-dimensional case and by Onsager in the two-dimensional case).^{17,18} On more general grounds, it has been shown by Mermin and Wagner that the spontaneous breaking of continuous symmetries does not occur at finite temperatures in systems with two or less dimensions.^{19,20} In more mathematical terms, the Goldstone bosons related to a spontaneous symmetry breaking would have a low-energy divergent correlation function, which is in disagreement with the hypothesis of a stable, ordered state.²¹ Note that this does in general not exclude an ordered phase at zero temperature or other types of (quantum) phase transitions. For one-dimensional quantum systems, which at zero temperature correspond to a classical system of $D = d + z = 1 + z$ dimensions (where d is the spatial dimension and z the dynamical exponent), continuous symmetry breaking is however generically excluded if the low energy excitations have a linear dispersion characterized by the dynamical exponent $z = 1$, which is for example the usual situation in one-dimensional electronic bands.

Despite the fact that true long-range order is generally forbidden in one dimensional systems, the latter often exhibit Kosterlitz-Thouless (or Berezinsky-Kosterlitz-Thouless) type transitions. At these transitions, the system changes from an entirely disordered phase with correlations that decay exponentially in the distance to a quasi long-range ordered phase with correlation functions decaying as a power law in distance. Kosterlitz-Thouless transitions can also be interpreted as phase transitions of infinite order. A second example of quantum phase transitions in quantum wires are the so-called Lifshitz-transitions, at which the topology of the Fermi surface changes. This includes in particular the appearance of additional Fermi points, as happens when new bands are activated in a quantum wire. In the following, we will precisely discuss the physics of Lifshitz transitions in interacting quantum wires.

2.1.2 Luttinger liquid theory and bosonization

Interacting fermions can often be conveniently described by a Fermi liquid description. The latter is based on the picture of emergent low energy degrees of freedom forming well-defined quasiparticles with effective parameters set by the, generally strong, interactions in the system. These quasiparticles may themselves still be interacting, but should of course be stable against spontaneous instabilities. While Fermi liquid theory has been of great success in two and three dimensions, it generically fails in one-dimensional systems. From a technical perspective, the break-down of Fermi liquid theory in one dimension can be understood as a divergence of the electronic susceptibilities $\chi(q, \omega)$ given the particle-particle and particle-hole bubbles. These bubbles also constitute the lowest order renormalization of the interactions in the system. Their divergence thus signals an instability and consequently the break-down of the electronic quasiparticle picture. Further details can be found in textbook, see for instance Ref. [22].

In 1950, Tomonaga proposed a different picture for one-dimensional systems, today known as the Tomonaga-Luttinger or Luttinger liquid.²²⁻²⁶ It is based on the picture

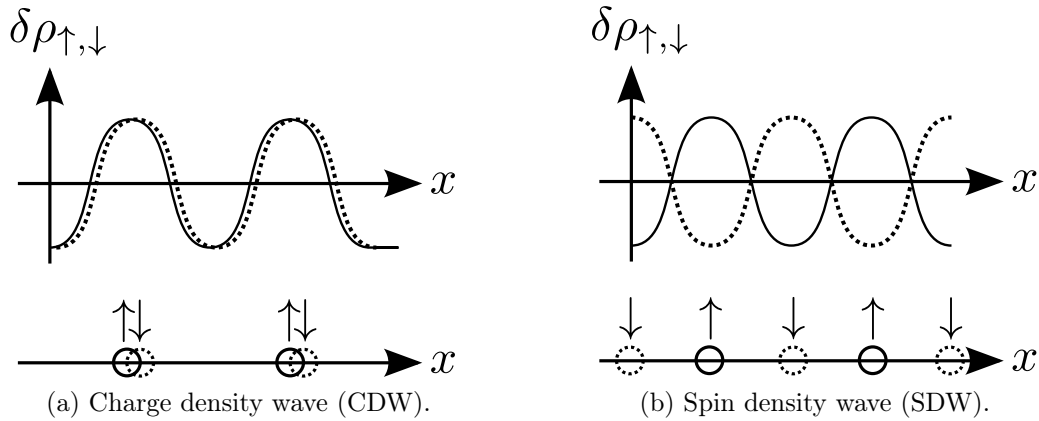


Figure 2.3: Density waves in a one-dimensional system. The upper panels show the spatial density modulations of spin up particles (solid lines) and spin down particles (dashed lines), relative to the uniform average densities. The lower panels depict spin up and spin down particles in real space. Subfigure (a) depicts a charge density wave (CDW), where the charge density is modulated while the spin density vanishes everywhere. Subfigure (b) shows a spin-density wave of uniform charge density but modulated spin densities. Figure adapted from Ref. [22].

that the relevant low-energy degrees of freedom in one-dimensional systems are collective density waves rather than single-particle excitations. To understand this, consider a chain of one-dimensional particles with repulsive interactions. When energy and momentum are transferred to one of these particles, i.e. whenever a single particle excitation is created in the system, the corresponding particle will start to move. Different from higher dimensional systems, it can however not avoid crashing into the surrounding particles, similarly to a Newton's cradle. By virtue of these collisions, energy and momentum are transferred to neighboring particles, until the initial single-particle excitation has finally decayed into a collective density wave of all particles in the system. Importantly, this picture is independent of the statistics of the underlying particles. It turns out that the relevant low-energy degrees of freedom of a one-dimensional system are collective, bosonic density waves and not single-particle excitations, and that it does in this respect not matter whether the system is microscopically composed of fermions or bosons. As depicted in Fig. 2.3, these waves correspond to modulations of the charge or spin densities. Importantly, the spin and charge densities can vary independently. This leads to the important concept of spin-charge separation, stating that the spin and charge degrees of freedom are decoupled in one dimension. This is yet another important difference to quasiparticle excitations in higher dimensions.

When working with one-dimensional systems, the main task is thus often to distill the density wave Hamiltonian from the initial degrees of freedom. To this end, one commonly uses the technique of bosonization, which relates single particle creation and annihilation operators to non-local, string like operators corresponding to the relevant density waves. Since bosonization simply extracts the bosonic collective density wave excitations from the single-particle picture, it may be applied to both bosonic and fermionic systems. The equivalence between bosonic and fermionic formulations of a one-dimensional theory also allows to voluntarily switch between bosonic and fermionic descriptions. This often turns out to greatly simplify the calculations. Besides bosonization, this can be achieved by, for

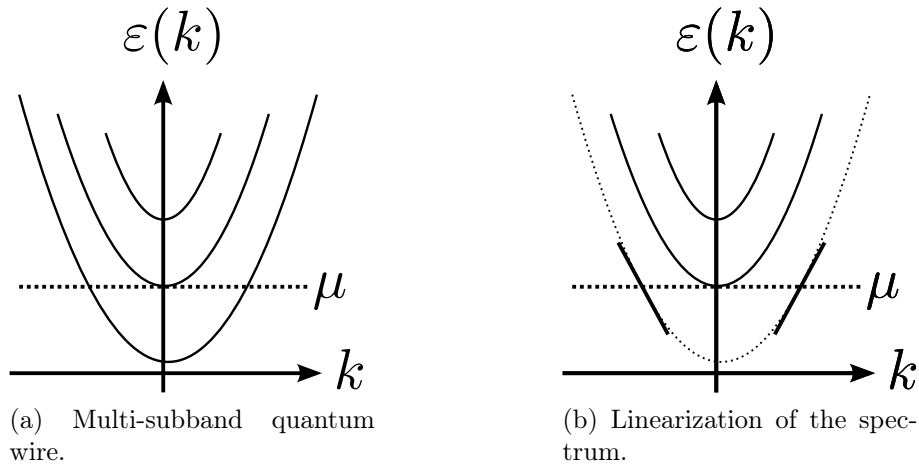


Figure 2.4: Schematic representation of the dispersion $\varepsilon(k)$ in a multi-subband quantum wire as a function of the linear momentum k . Each subband corresponds to a quadratic dispersion. For filled bands, the dispersion can be linearized around the chemical potential μ . This is however not possible if the chemical potential is at the bottom of one of the bands, or even below the band bottom.

instance, fermionization or Jordan-Wigner transformations. Pedagogical introductions to all of these techniques can be found in Refs. [22,27–29].

2.2 Limits of the Luttinger liquid theory: Lifshitz transitions in quantum wires

Within the framework of Luttinger liquid theory, a large amount of one-dimensional physics, even including interacting systems, could have been brought to more or less exact solutions. This again relies on the picture of density waves as relevant low energy degrees of freedom. Since the density operator of particles described by operators c is already quadratic in these fields, $\rho_c \sim c^\dagger c$, a standard quartic interaction term is only quadratic in the densities, and thus allows for exact solutions by mere diagonalization in terms of the correct degrees of freedom.²² If however the picture of collective density waves is not valid anymore, the situation is much less clear. As an example, the standard technique of bosonization is generally based on the linearization of the dispersion around the Fermi level. This is however not possible at the Lifshitz transitions corresponding to the activation of subbands of a quantum wire. If the chemical potential is exactly at the bottom of one of the bands, the latter can clearly not be linearized, see Fig. 2.4. In addition, the newly activated subband is only very dilutely populated, and its physics corresponds to scattering between isolated particles rather than modulations of a more or less homogenous density. Similar considerations hold true if the chemical potential is close to the band edge on the energy scales of temperature or interactions.

In the next two chapters, we thus intend to shed some more light on the non-Luttinger liquid behavior of quantum wires close to quantum phase transitions. In doing so, we first distinguish two limiting cases. Firstly, the system can be dominated by its repulsive Coulomb interactions, in which case the formation of a Wigner crystal is expected.¹³ In this case, the simplest possible quantum phase transition corresponds to a zigzag-

deformation of the Wigner crystal as a function of the electronic density (or confinement). The effect of interactions on this transition is the subject of Sec. 2.3. Secondly, if the kinetic energy dominates over the interaction energy, i.e. when the picture of a multi subband quantum wire is applicable, we discuss how interactions affect the Lifshitz transition corresponding to the activation of further subbands. More precisely, we will be interested in the case that the chemical potential is close to the bottom of the second band, see Fig. 2.4. The second subband is then just about to get filled or "activated".

The activation of the second subband has been approached from different perspectives with different conclusions.^{30–36} For spinless (spin-polarized) electrons, it was shown that the transition at weak interactions corresponds to a Lifshitz transition of polarons, i.e. electrons dressed with a screening cloud.^{13,37,38} For stronger interactions, the transition was identified as an Ising transition, which translates to Wigner crystal physics.³⁸ In the case of spinful electrons, two publications are most relevant for our subsequent discussions. Firstly, Varma and Zawadowski have analyzed the physics of two coupled, one-dimensional bands of different fillings.³⁰ In the limit that the corresponding Fermi velocities are largely different, this regime corresponds to having the chemical potential just slightly above the bottom of the second band (i.e. just a little bit higher than depicted in Fig. 2.4), and can thus be understood as approaching the activation of the second band "from above". They found that the system may exhibit several kinds of instabilities, depending on the values of the various interaction strengths. This regime will be investigated in chapter 4. In a second work, Balents and Fisher have tackled the transition for a two-chain Hubbard system using an ϵ -expansion of the quadratic dispersion of the band bottom, $E(k) \sim k^2 \rightarrow k^{1+\epsilon}$.³³ They also found potential instabilities, including a possible superconducting instability.

Nevertheless, a full picture of the transition is still to be drawn. In particular, we would like to quantify the presence or absence of instabilities for the experimentally (and, to some extent, also commercially) important quantum wires made from interacting two-dimensional electron gases in GaAs/GaAlAs structures. We will therefore first derive the corresponding model from a microscopic Hamiltonian in the next section, before analyzing it for strong and weak interactions, two limits demanding for different approaches. In particular, Sec. 2.4 will be concerned with the limit of strong interactions. The limit of weak interactions will finally be the subject of the remainder of the next two chapters.

2.3 From two-dimensional electron gases to quantum wires: a mean field analysis

In order to derive an effective model for a quantum wire electrostatically defined in a 2DEG (as shown in Fig. 2.1b), we first identify the tuning parameters of the system, which can naturally be expressed in terms of characteristic length scales. From the comparison of these length scales, different regimes will be identified and the mean field phase diagram shown in Fig. 2.5 shall be derived.

Length scales in the system

The quantum wire under consideration is described by a model Hamiltonian for a two-dimensional electron gas interacting by Coulomb repulsion, plus a confining potential

defining the quantum wire. The Coulomb interaction is generally screened by the nearby gates necessary to define the wire. The corresponding model can be decomposed into kinetic energy T , the screened Coulomb potential V_{int} and the confinement V_{conf} ,

$$H_{2\text{DEG}} = T + V_{\text{int}} + V_{\text{conf}} . \quad (2.1)$$

Working in units of $\hbar = 1$, $k_B = 1$, $4\pi\epsilon_0 = 1$, the kinetic energy T of the electron gas is simply given by

$$T = \sum_i \frac{\vec{p}_i^2}{2m} , \quad (2.2)$$

where \vec{p}_i is the first quantized momentum operator of the i^{th} electron and m the effective electron mass in the material. The screening of the Coulomb interaction happens by virtue of mirror charges in the metallic gates. Assuming that these gates are at some distance d from the 2DEG, the total interaction reads

$$V_{\text{int}} = \frac{1}{2} \sum_{i \neq j} U(|\vec{r}_i - \vec{r}_j|) , \quad (2.3)$$

with the interaction between the particles i and j at sites \vec{r}_i and \vec{r}_j being

$$U(|\vec{r}|) = \frac{e^2}{\epsilon_r} \left[\frac{1}{|\vec{r}|} - \frac{1}{\sqrt{r^2 + (2d)^2}} \right] \quad (2.4)$$

(where e is the electron charge and ϵ_r is the material-dependent relative permittivity or dielectric constant). The confining potential defining the quantum wire is approximated as parabolic and assumed to be characterized by a frequency Ω . It thus reads

$$V_{\text{conf}} = \frac{1}{2} m \Omega^2 \sum_i y_i^2 , \quad (2.5)$$

with y_i being the y-coordinate of the i^{th} electron.

The four terms of the Hamiltonian (kinetic energy, bare interaction, screening term, and confinement) set four characteristic length scales. The average kinetic energy is related to the electron density, and the corresponding length scale is the mean particle spacing $1/n$, with n being the number of electrons per unit length in the wire (or n^2 being the number of electrons per unit area if the confining potential is weak). The interaction between the electrons depends on material properties through the dielectric constant ϵ_r and the sample dependent effective mass, which define the Bohr's radius $a_B = \epsilon/(e^2m)$ (note that we use the convention $\hbar = 1$ throughout the whole text). The screening of the interaction is characterized by the distance d between the gates and the electron gas, which sets the screening length of the system. Last but not least, the confining potential relates to an oscillator length $x_0 = 1/\sqrt{m\Omega}$. The ratios of these four characteristic length scales govern the physics of the system, and all of them are experimentally tunable (a_B and d may be varied by using different samples, whereas $1/n$ and x_0 can even be changed in-situ by adjusting gate voltages). A summary of the length scales, along with typical experimental values taken from Ref. [13], is given in Tab. 2.1. The remainder will be devoted to GaAs structures, such that in particular the Bohr's radius is assumed to be much smaller than the screening length, $a_B \ll d$.

| | length scale | typical experimental value for GaAs |
|-------|--------------------------------------|-------------------------------------|
| $1/n$ | mean particle spacing | in-situ tunable |
| a_B | material dependent Bohr's radius | 10 nm |
| d | screening length/distance to gates | 100 nm |
| x_0 | oscillator length of the confinement | width of the wire (in-situ tunable) |

Table 2.1: Characteristic length scales of a quantum wire in a 2-dimensional electron gas. The typical experimental values concern GaAs structures and are taken from Ref. [13].

Mean field phase diagram

Depending on the ratio of the four characteristic length scales (and associated energy scales), the quantum wire can exhibit different phases. The principal distinction is to be made between an interaction dominated regime and a single-particle regime. If V_{conf} dominates over the kinetic energy T , the quantum wire is in a Wigner crystal state with essentially localized electrons. If on the other hand the dominant scale is set by the kinetic energy T , the wire is described by multiple subbands of interacting, wavelike electrons. The interplay of the respective dominant energy scale with the confining potential V_{conf} finally triggers a quantum phase transition from the truly one-dimensional to a quasi one-dimensional system, which is at the heart of the following discussions. We will now analyze the different regimes in a mean-field approach that minimizes the dominant term in the Hamiltonian, and will finally be able to draw a mean field phase diagram in Fig. 2.5. The physics associated with the spins of the electrons turn out to be decoupled from their charge degree of freedom and will be discussed subsequently.

Screened and unscreened interaction energy scale At first, it is instructive to analyze the behavior of the average interaction energy for different electron fillings. For an average electron density n per unit length, the typical interaction energy scale is of the order

$$\bar{U} \sim \frac{e^2}{\epsilon_r} n \left[1 - \frac{1}{\sqrt{1 + (2nd)^2}} \right]. \quad (2.6)$$

In case the inverse particle density is higher than the screening length, $nd \gg 1$, the electrons interact by an essentially unscreened repulsion. If however the inter particle spacing becomes of the order of, or larger than, the screening length, the image charges in the nearby gates screen the Coulomb interaction. An expansion to leading order in the respective small parameter $(nd)^{\pm 1}$ yields the characteristic energy scale as

$$\bar{U} \sim \begin{cases} (e^2/\epsilon_r) n & , nd \gg 1 \\ (e^2/\epsilon_r) 2n^3 d^2 & , nd \ll 1 \end{cases}. \quad (2.7)$$

Note that the mirror charges in the gates thus ensure that the interaction potential falls off as a dipole field for large inter particle distances. As will be discussed in chapter 3, local interactions different from the mean field considered here will become important in the low density limit $nd \ll 1$ for spinful fermions.

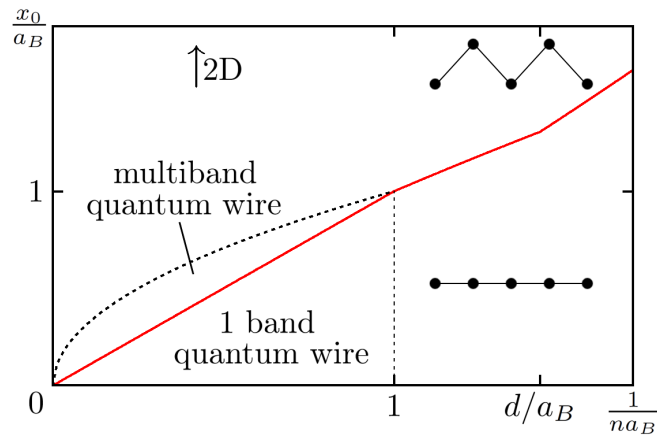


Figure 2.5: Mean-field phase diagram of the Hamiltonian (2.1) as a function of the inverse one-dimensional electron density n^{-1} and the oscillator length $x_0 = 1/\sqrt{m\Omega}$, both measured in units of the Bohr radius $a_B = \epsilon/(e^2m)$. As x_0 increases, a transition occurs at the (red) solid line from a one-dimensional to a quasi-one-dimensional state. At low densities $1/(na_B) \gg 1$, this transition corresponds to the deformation of a one-dimensional Wigner crystal into a zigzag configuration. At high densities, $1/(na_B) \ll 1$, the transition is triggered by the filling of a second subband. The (curved) thick dotted line indicates where the interaction energy equals the subband separation so that the band picture ceases to be well-defined, the vertical dashed line denotes the limit between the Wigner crystal and multi-subband quantum wire regimes. For large x_0 , the two-dimensional limit is approached. For a derivation of the various lines and regimes, see the main text. Figure taken from Ref. [16].

Single-particle limit: multi-subband quantum wire The characteristic energy scale of single particle physics is the Fermi energy E_F ,

$$E_F \sim \frac{n^2}{2m}, \quad (2.8)$$

and is of the order of the average kinetic energy of the system. The system is thus governed by its single particle sector if the mean field interaction energy is smaller than the Fermi energy (we however note that local interactions not considered yet will turn out to be important in this case, see chapter 3). Comparing the expressions (2.7) and (2.8), we find that this happens both at high and very low densities, namely if

$$n a_B > 1 \quad \text{or} \quad n a_B < \left(\frac{a_B}{d}\right)^2 \ll 1. \quad (2.9)$$

In these cases, it is appropriate to first choose the eigenbasis of the single-particle part of the Hamiltonian consisting of $T + V_{\text{conf}}$, see Eqs. (2.2) and (2.3), and to analyze interactions as a secondary effect in that basis. The single-particle eigenbasis is given by product-states of traveling waves along the wire and the oscillator eigenfunctions in the transverse directions. The system is, quantum-mechanically speaking, strictly one-dimensional (1D) as long as only the lowest oscillator level is occupied. The quantum wire is on the other hand considered to be “quasi-1D” if several subbands are occupied, i.e. if the transversal part of the wave function is not uniquely defined anymore. By comparing the Fermi energy $E_F = n^2/(2m)$ with the typical confining energy Ω (note that we work in units of $\hbar = 1$), one obtains the condition

$$x_0 < \frac{1}{n}, \quad (2.10)$$

that is shown as a solid line in Fig. 2.5. The transition from a single- to a two-subband quantum wire, which shall be analyzed in the following, happens if the chemical potential reaches the bottom of the second band corresponding to the second transversal wave function. The transition occurs if the chemical potential is of the order of the energetic separation of the transversal wave functions, $E_F = n^2/(2m) \stackrel{!}{\sim} \Omega$. The second subband is thus filled if $n x_0 \gtrsim 1$. Upon further increasing the density n or relaxing the confining potential, i.e. increasing the oscillator length x_0 , more and more subbands are populated.

The oscillator levels are however only well defined as long as the oscillator frequency Ω is larger than the typical Coulomb energy $U(1/n)$ and the temperature (the latter is here however considered to be negligibly small). In the multiband quantum wire regime, where the electrons are so dense that interaction can safely be approximated by the unscreened limit, this translates to the condition

$$x_0 < \sqrt{a_B/n}, \quad (2.11)$$

shown as a dotted line in Fig. 2.5. For even larger oscillator length x_0 one crosses over from the quasi-1D case to a two-dimensional regime where the subbands are washed out.

Interaction dominated regime: Wigner crystal For moderate but not too small densities, $1 \gg n a_B \gg (a_B/d)^2$, interactions dominate over the kinetic energy of the particles. The electrons in the quantum wire will then localize on distinct sites in

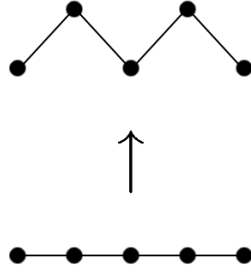


Figure 2.6: Transition from a one-dimensional to a quasi-one-dimensional state. At strong coupling, $na_B \ll 1$, the transition corresponds to the deformation of a 1D Wigner crystal to a zigzag configuration. Figure taken from Ref. [16].

order to minimize the dominant interaction energy, resulting in a Wigner crystal state of electrons.^{39,40} As a function of oscillator length x_0 , there is a competition between the interaction and the confining potential. If the confining potential is deep, transverse excitations are very costly, and the Wigner crystal has linear order. As the potential gets increasingly shallow, the Wigner crystal exhibits a transition from linear to zigzag order, see Fig. 2.6. Upon further decreasing the confinement, additional transitions to multi-row configurations occur. In the limit of infinitely shallow confinement, the full two-dimensional behavior is recovered.^{13,37,41–44}

The deformation of the Wigner crystal from a linear to a zigzag structure occurs if the gain in Coulomb repulsion due to a larger inter particle spacing outweighs the energy cost of pushing the electrons perpendicularly to the wire and thus away from the minimum of the confining potential. Comparing the energy gain in Coulomb interaction for a small dilatation δy with the energy cost in confining energy,

$$U(1/n) - U\left(\sqrt{1/n^2 + 4\delta y^2}\right) \sim \frac{1}{2} m \Omega^2 \delta y^2, \quad (2.12)$$

one arrives at the stability criterion for the one-dimensional Wigner crystal state. At intermediate densities, $1 > na_B > a_B/d$, where the interaction is still approximately unscreened, the crystal is stable for

$$x_0 < \left(\frac{a_B}{n^3}\right)^{1/4}, \quad (2.13)$$

indicated by the solid line in Fig. 2.5. At low densities, $n < 1/d$, the mirror charges in the gates becomes important. Equation (2.12) then has to be evaluated using the screened limit of the interaction, which yields the stability criterion

$$x_0 < \sqrt{\frac{1}{nd}} \left(\frac{a_B}{n^3}\right)^{1/4}, \quad (2.14)$$

and thus a modified transition line between the linear and the zigzag crystal. At even lower densities, $n < a_B/d^2$, the effective interaction between electrons in the crystal is of dipole type due to the mirror charges induced in the gate electrodes, $U \sim d^2 n^3$ (see Eq. (2.7)). These dipole interactions are not sufficient to sustain long range (quasi-)order anymore, and the Wigner crystal melts again. This is however not shown in Fig. 2.5.

2.4 A short discussion of the Wigner crystal regime

If the physics is dominated by the interactions between electrons in the wire, a Wigner crystal forms. As discussed in the last section, the latter exhibits a transition from a one-dimensional arrangement to a zigzag crystal when the oscillator length x_0 is increased, i.e. when the confinement is weakened. In the next section, we want to analyze if, and possibly how, interactions affect this transition.

Effective model for the charge sector The effective model for the Wigner crystal is derived based on the physical picture of quasi-long range ordered electrons oscillating around their equilibrium positions $(x_j^0, y_j^0)^T = (j a, 0)^T$ with $j \in \mathbb{Z}$. The spacing between the different sites is given by the inverse average density $a = n^{-1}$. The low energy physics are then described by the phonons corresponding to the displacements of the electrons around their equilibrium positions, and their interactions. We thus derive the model of the Wigner crystal as usual for phonons by expanding the full Hamiltonian in Eq. (2.1) in the dimensionless displacements

$$\begin{pmatrix} u_{xj} \\ u_{yj} \end{pmatrix} = \begin{pmatrix} \frac{x_j - x_j^0}{a}, \frac{y_j - y_j^0}{a} \end{pmatrix}^T. \quad (2.15)$$

Next, we extract the physically most important phonon modes from the full spectrum. Firstly, we have to take into account the Goldstone mode associated with the spontaneous breaking of translational symmetry in the crystal, which corresponds to the uniform displacement of all electrons along the axis of the wire,

$$\vec{u}_0^{\parallel}(x_j) \approx u_0^{\parallel}(1, 0)^T. \quad (2.16)$$

Being a Goldstone mode, u_0^{\parallel} is certainly gapless, but should also be harmless. The next important mode is the out-of-phase displacement perpendicular to the wire axis,

$$\vec{u}_\pi^\perp(x_j) \approx u_\pi^\perp(0, (-1)^j)^T. \quad (2.17)$$

This mode describes a the zigzag type motion of the electrons in the Wigner crystal. We therefore expect it to become gapless at the zigzag quantum phase transition. For completeness, we also keep track of the modes

$$\vec{u}_\pi^{\parallel}(x_j) \approx u_\pi^{\parallel}((-1)^j, 0)^T, \quad (2.18)$$

which corresponds to the longitudinal out-of-phase mode, and

$$\vec{u}_0^\perp(x_j) \approx u_0^\perp(0, 1)^T, \quad (2.19)$$

the transversal in-phase mode. Although we expect these modes to have large gaps, we want to be sure that interactions do not lead to a substantial softening for either of them. In case there was such a softening, the system might for instance exhibit a Peierls transition (if the u_π^{\parallel} -mode becomes gapless).²² The detailed derivation of the phonon action also yields the interactions between the different modes, and can be found in appendix B.1.

We find that indeed, the mode u_π^{\parallel} and u_0^\perp have large gaps Δ_π^{\parallel} and Δ_0^\perp determined by the Coulomb interaction and the confining potential, respectively. At the zigzag

transition, which is due to the competition of Coulomb repulsion and confinement, these two gaps are of the same order. The low energy physics, on the other hand, is governed by the Lagrangian density $\mathcal{L} = \mathcal{L}_0^\parallel + \mathcal{L}_\pi^\perp + \mathcal{L}_{\text{int}}$ with

$$\mathcal{L}_{\parallel 0} = \frac{m}{2n} \left[(\partial_\tau u_0^\parallel)^2 + v_{\parallel 0}^2 (\partial_x u_0^\parallel)^2 \right], \quad (2.20a)$$

$$\mathcal{L}_{\perp \pi} = \frac{m}{2n} \left[(\partial_\tau u_\pi^\perp)^2 + v_{\perp \pi}^2 (\partial_x u_\pi^\perp)^2 + r (u_\pi^\perp)^2 + s (u_\pi^\perp)^4 \right], \quad (2.20b)$$

$$\mathcal{L}_{\text{int}} = \lambda (\partial_x u_0^\parallel) u_\pi^{\perp 2}, \quad (2.20c)$$

where τ is the imaginary time and where, in the limit $d^{-1} \ll n \ll a_B^{-1}$, the longitudinal velocity $v_{\parallel 0}$ evaluates to $v_{\parallel 0}^2 = 2n/(m^2 a_B)$, the transversal velocity is $v_{\perp \pi}^2 = n/(m^2 a_B)$, the control parameter is $r = (2/m) (x_0^{-4} - x_{0c}^{-4})$ with $x_{0c} = (a_B/(2n^3))^{1/4}$, and $s = 6n^3/(m^2 a_B)$. The interaction between the modes finally evaluates to $\lambda = 6n/(a_B m)$ (see appendix B.1.)

As expected, the mode u_0^\parallel is a gapless Goldstone mode, while the mode u_π^\perp drives a quantum phase transition as the parameter r is tuned. At the transition, where the Coulomb interaction is of the order of the confinement energy, the latter mode is gapless, while it has a gap of order \sqrt{r} away from the transition. At low densities (or strong confinement), corresponding $r > 0$ and thus the disordered phase, it has a vanishing expectation value, such that the Wigner crystal exhibits a truly linear (quasi-)order without zigzag deformation, see Fig. 2.6. For high fillings (or weak confinement), where $r < 0$, the mode u_π^\perp however acquires a finite expectation value $\langle u_\pi^\perp \rangle$, and the Wigner crystal is in a zigzag arrangement.

At criticality, $r = 0$, the Lagrangian $\mathcal{L}_{\perp \pi}$ corresponds to a critical one-dimensional Ising model (note that $s > 0$ ensure the stability of the latter). A finite expectation value of the related field u_π^\perp describes a finite dilatation of the Wigner crystal perpendicular to the wire axis in the plane of the two-dimensional electron gas, which corresponds to a finite magnetization of chain of Ising spins.¹⁶ The zigzag transition is thus in the Ising universality class if the coupling of $\mathcal{L}_{\perp \pi}$ to all other modes are irrelevant. If the Wigner crystal was pinned and the positions of particles along the wire were fixed, the transition would break the reflection symmetry in the confining plane. However, the presence of the mode u_0^\parallel , i.e., the fact that the crystal may deform in the longitudinal direction, makes the zigzag order non-local.⁴⁵ The critical properties of the u_π^\perp mode can be further analyzed by mapping them on a fermionic degree of freedom Ψ . This mapping is most conveniently done by interpreting u_π^\perp as a critical, one-dimensional Ising chain, which in turn can be mapped to a fermionic quantum wire by a Jordan-Wigner type transformation. This yields the Lagrangian density⁴⁶

$$\mathcal{L}_{\perp \pi}^{\text{ferm}} = \Psi^\dagger \partial_\tau \Psi + \frac{v_{\perp \pi}}{2} (\Psi \partial_x \Psi + \text{h.c.}) + r \Psi^\dagger \Psi. \quad (2.21)$$

The longitudinal plasmon u_0^\parallel couples to the most relevant operator $(u_\pi^\perp)^2 \sim \Psi^\dagger \Psi$ of the Ising model so that the interaction term (2.20c) can be rewritten in the fermionic formulation as

$$\mathcal{L}_{\text{int}}^{\text{ferm}} = \lambda (\partial_x u_0^\parallel) \Psi^\dagger \Psi, \quad (2.22)$$

where, for simplicity of notation, we suppressed in Eqs. (2.21) and (2.22) renormalizations of coupling constants due to the change to a fermionic description.

The model $\mathcal{L}_{\parallel 0} + \mathcal{L}_{\perp\pi}^{\text{ferm}} + \mathcal{L}_{\text{int}}^{\text{ferm}}$ and its critical properties were analyzed and discussed in Ref. [38]. It was found that the critical renormalization group flow of the model parameters depends on the ratio of velocities, $v_{\perp\pi}/v_{\parallel 0}$. If $v_{\perp\pi} < v_{\parallel 0}$, which is the case for quantum wires (see above), the interaction λ is marginally irrelevant and decreases with decreasing energy. At the same time, the ratio of velocities $v_{\perp\pi}/v_{\parallel 0}$ approaches one. The critical fixed point is, thus, characterized by an enhanced SU(2) symmetry. However, a peculiarity of the RG flow is that the velocity $v_{\parallel 0}$ itself vanishes in the low-energy limit resulting, e.g., in a diverging specific heat coefficient at the critical point. In the opposite limit, $v_{\perp\pi} > v_{\parallel 0}$, run-away RG flow was found, but this case is not relevant for our quantum wire model. In the following, we address the question whether these critical properties are modified in the presence of a coupling to the spin degrees of freedom (note that Ref. [38] considered spinless or spin-polarized electrons).

Coupling to the spin sector So far, the spins of the electrons have been neglected. For a linear Wigner crystal, the spin is more or less independent of the charge and can be described by an anti-ferromagnetic Heisenberg model with nearest-neighbor interactions. In the zigzag Wigner crystal, next-nearest neighbor interactions as well as ring exchange processes become important and lead to rich spin physics.^{47,48} Similar situations have been discussed in the context of spin liquids, which may occur in ladder-type structures due to ring-exchange interactions.⁴⁹ However, these additional interactions are only important once the lateral extent of the crystal is sufficiently large. Close to the transition, they are negligible, and the spin interactions are given by the Heisenberg Hamiltonian,

$$\mathcal{H}_s = \sum_j J_j \vec{S}_j \cdot \vec{S}_{j+1}, \quad (2.23)$$

where the coupling constant J_j is exponentially small in $1/(na_B)$.⁵⁰

Since the spin-spin interaction is exponentially dependent on the inter particle distance, the phononic motion of electrons immediately affects the spin-spin exchange coupling, giving rise to a spin-charge coupling. In the picture of a phononic motion of a Wigner crystal, we can expand the exchange couplings in the small displacements. Since the exchange is exponentially suppressed in the inter particle distance, we can reasonably approximate the interaction J_j between the electrons at sites j and $j+1$ to only depend on the positions of these two electrons, $J_j = J(\vec{r}_j, \vec{r}_{j+1}) \simeq J(|\vec{r}_{j+1} - \vec{r}_j|)$, and not on the position of the surrounding ones.⁵¹ The perturbative expansion then yields

$$J_j \simeq J(a) + aJ'(a) \left(u_{x_{j+1}} - u_{x_j} + \frac{1}{2}(u_{y_{j+1}} - u_{y_j})^2 \right).$$

Note that the expansion of the coupling J in the longitudinal fluctuations u_{x_j} starts in linear order, yielding

$$\mathcal{H}_{sc}^{\parallel} = -g_{\parallel} \sum_j (u_{x_{j+1}} - u_{x_j}) \vec{S}_j \cdot \vec{S}_{j+1}, \quad (2.24)$$

with $g_{\parallel} = -aJ'(a)$. By contrast, due to the inversion symmetry of the one-dimensional Wigner crystal with respect to the wire axis, the expansion in the transverse fluctuations

u_{yj} begins only in second order, i.e.

$$\mathcal{H}_{sc}^{\perp} = -g_{\perp} \sum_j (u_{yj+1} - u_{yj})^2 \vec{S}_j \cdot \vec{S}_{j+1}, \quad (2.25)$$

with $g_{\perp} = -aJ'(a)/2$.

The linear coupling to the longitudinal mode (2.24) is familiar from the spin-Peierls problem.²² In particular, the mode u_{π}^{\parallel} with momentum $q \approx \pi$, $u_{xj} \approx u_{\pi}^{\parallel}(-1)^j$, couples to the staggered part of $\vec{S}_j \cdot \vec{S}_{j+1}$,

$$\mathcal{H}_{sc}^{\parallel} \approx -2g_{\parallel} \sum_j u_{\pi}^{\parallel}(-1)^j \vec{S}_j \cdot \vec{S}_{j+1}. \quad (2.26)$$

If the u_{π}^{\parallel} mode was sufficiently soft, this term would lead to a spin-Peierls transition. The crystal would distort such that the mode u_{π}^{\parallel} assumes a non-vanishing expectation value giving rise to an alternation of weak and strong bonds, $J \pm \delta J$, and the system could gain magnetic energy by forming singlets on the strong bonds.⁵² In our case, however, the magnetic energy is exponentially small such that it never can compete with the charge gap of the u_{π}^{\parallel} mode, that is on the order of $(n/m)\sqrt{n/a_B}$, see appendix B.1. We can thus conclude that the interaction (2.24) of the spin degrees of freedom with the longitudinal modes does not influence the critical properties of the charge sector.

To conclude, we turn to the coupling of the spins to the transverse modes. The most singular contribution is attributed to the critical u_{π}^{\perp} mode. Substituting $u_{yj} = u_{\pi}^{\perp}(-1)^j$, we obtain

$$\mathcal{H}_{sc}^{\perp} \approx -4g_{\perp} \sum_j (u_{\pi}^{\perp})^2 \vec{S}_j \cdot \vec{S}_{j+1}. \quad (2.27)$$

It turns out, however, that this interaction is also irrelevant as far as the critical properties of the Ising transition are concerned. This conclusion follows from a straightforward power counting analysis of the Ising operator, $(u_{\pi}^{\perp})^2 \sim \Psi^{\dagger}\Psi$, and the non-staggered spin-spin operator, $\vec{S}_j \cdot \vec{S}_{j+1}$, with respect to the antiferromagnetic Heisenberg fixed point.¹⁶

Summary and conclusions Our analysis of the transition from a strictly one-dimensional Wigner crystal to a zigzag structure confirms earlier work on this subject and substantiates some of the assumptions already used in the field by a proper derivation (like the effective decoupling of spin and charge). The transition happens in the charge sector, and can be described as a simple softening of a transversal phonon mode. Except for the uniform longitudinal translation of the entire Wigner crystal (the Goldstone mode corresponding to the spontaneous breaking of translational symmetry in the crystal), all other modes are gapped and do not enter the low-energy description. The charge sector can thus be mapped on a model of longitudinal plasmons coupled to a transverse field Ising model. This situation has already been analyzed by Sitte et al. in Ref. [38], where it was found that the coupling between plasmons and Ising fields is marginally irrelevant, but lead to interesting logarithmic corrections. The transition is therefore in the Ising universality class (with logarithmic corrections).

The spin sector of the quantum wire can be described by a Heisenberg chain with nearest neighbor interactions. Although the exchange couplings depend exponentially

on the positions of the electrons, the magneto-elastic couplings, g_{\parallel} and g_{\perp} are irrelevant under RG and therefore do not modify the transition to the zigzag Wigner crystal. In conclusion, the zigzag transition happens only in the charge sector and is in the Ising universality class, whereas the essentially decoupled spin sector acts as a spectator.

Chapter 3

Two-subband quantum wire close to the Lifshitz transition

At large densities, $na_B > 1$, i.e. on the lefthand side in Fig. 2.5, the average kinetic energy dominates over the mean field interaction. If additionally the transversal confinement is sufficiently strong, the electrons in the quantum wire are well described by one-dimensional plane waves traveling along the wire, while their interactions can be treated perturbatively. This leads to the physical picture of a multi-subband quantum wire in which each of the bands corresponds to one of the quantized levels in the transversal direction, see Fig. 3.1a.

The analysis of the multiband wire close to the activation of the second subband, see Fig. 3.1b, is complicated by the fact that the interacting system has multiple dynamical scales.^{53,54} Whereas the first subband can be understood as Luttinger liquid with dynamical exponent $z = 1$, the spectrum of the second subband is characterized by $z = 2$. The multiple scales lead to the appearance of two different types of infra-red divergences in perturbation theory. The linear spectrum of the first subband, $z = 1$, yields logarithmic divergences, while the quadratic spectrum of the second subband, $z = 2$, yields square-root singularities. In order to understand the interplay between these two types of divergences, we first derive an effective multi-subband quantum wire Hamiltonian starting from the microscopic picture of a confined two-dimensional electron gas. In Sec. 3.4, we discuss the case that only the lowest subband is occupied. In Secs. 3.5 and 3.6 we then turn to the behavior of the system close to the Lifshitz transition. The regime of a partially occupied second band will finally be the subject of chapter 4. The various regimes are indicated in Fig. 3.1b.

3.1 Microscopic derivation of the effective model

The effective model is based on the single-particle Hamiltonian (2.1), deriving from the kinetic energy and the confining potential, $T + V_{\text{conf}}$. The wave functions are product states of harmonic oscillator levels in transversal direction and plane waves in longitudinal direction, with each transversal oscillator state defining one of the energy subbands. The subband picture is applicable as long as the spacing between subbands is much bigger than interaction energy and temperature. Otherwise, thermal excitations or scattering events will result in an important mixing of the bands, which then cease to be well-defined. For the low temperature scenario considered here, the band picture thus holds

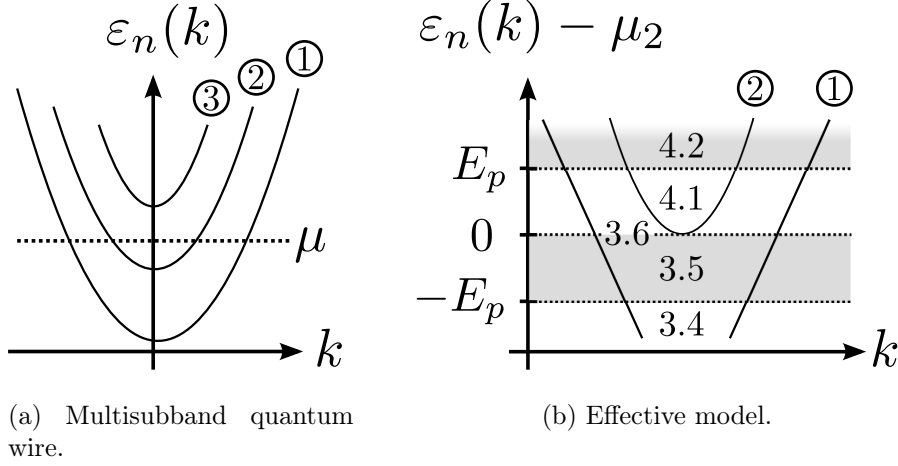


Figure 3.1: Subfigure (a) depicts the energy spectrum of a multisubband quantum wire as a function of the longitudinal momentum k . The subbands are labeled by the index $n = 1, 2, 3, \dots$. Subfigure (b) shows the energy spectrum as a function of k for a two subband quantum wire with a lower subband 1 and a higher subband 2. We consider the quantum phase transition when the chemical potential reaches the bottom of the second subband, $\mu_2 = 0$. Depending on the position of chemical potential μ_2 , we apply different approaches in sections 3.4, 3.5, 3.6, 4.1, and 4.2 as indicated in the figure. The energy scale E_p is defined in Eq. (3.22). Figure adapted from Ref. [16].

as long as the mean interaction energy \bar{U} in Eq. (2.7) is much smaller than the spacing of the harmonic oscillator levels Ω . The one-dimensional multiband picture is thus valid as long as

$$\frac{x_0}{a_B} \stackrel{!}{\lesssim} (na_B)^{-1/2}. \quad (3.1)$$

We start deriving the effective model by using the full wave functions of the single-particle basis. For an electron of momentum k in the n^{th} subband, the corresponding product state of the n^{th} harmonic oscillator wave function in transversal direction $\phi_n(y)$ and the plane wave of momentum k in longitudinal direction reads

$$\Psi_{n,k}(x, y) = \phi_n(y) e^{ikx}, \quad (3.2)$$

with

$$\phi_n(y) = \sqrt{\frac{1}{2^n n!}} \left(\frac{m\Omega}{\pi} \right)^{1/4} e^{-\frac{1}{2}m\Omega y^2} H_n(\sqrt{m\Omega}y) \quad (3.3)$$

(where H_n is the n^{th} Hermite polynomial). Using this basis, the full Hamiltonian (2.1) can be rewritten in second quantized form as

$$\mathcal{H} = \sum_{n,k,\sigma} \left(\frac{k^2}{2m} - \mu_n \right) c_{nk\sigma}^\dagger c_{nk\sigma} + \frac{1}{2} \sum_{\substack{n_1, n_2, n_3, n_4 \\ k, k', q; \sigma, \sigma'}} U_{n_1 n_2 n_3 n_4}(q) c_{n_1 k + q \sigma}^\dagger c_{n_2 k' - q \sigma'}^\dagger c_{n_3 k' \sigma'} c_{n_4 k \sigma}, \quad (3.4)$$

where the electron operators $c_{nk\sigma}$ destroy an electron with subband index n (i.e., the quantum number of the harmonic oscillator defined by V_{conf}), momentum k in \hat{x} -direction along the wire, and spin $\sigma = \uparrow, \downarrow$. Two consecutive chemical potentials differ by the oscillator frequency, $\mu_n - \mu_{n+1} = \Omega$.

The electrons interact with an interaction amplitude U that depends on the transferred (longitudinal) momentum q and the subband indices n_i . Its value is given by matrix elements of the screened Coulomb interaction in the basis of the wavefunctions (3.2),

$$U_{n_1 n_2 n_3 n_4}(q) = \langle n_1 k + q, n_2 k' - q | U | n_3 k, n_4 k' \rangle = \int \frac{dq_y}{2\pi} U(q, q_y) \Gamma_{n_1 n_2 n_3 n_4}(q_y), \quad (3.5)$$

where the Fourier transform of the interaction is given by

$$U(q, q_y) = \int d^2r e^{-i\vec{r}\cdot\vec{q}} U(\vec{r}) = \frac{e^2}{\epsilon} \frac{2\pi}{\sqrt{q^2 + q_y^2}} \left(1 - e^{-2d\sqrt{q^2 + q_y^2}} \right) \quad (3.6)$$

and the matrix elements read

$$\Gamma_{n_1 n_2 n_3 n_4}(q_y) = \int dy_1 dy_2 e^{iq_y(y_1 - y_2)} \phi_{n_1}^*(y_1) \phi_{n_2}^*(y_2) \phi_{n_3}(y_2) \phi_{n_4}(y_1) \quad (3.7)$$

with the n^{th} one-dimensional oscillator wavefunctions $\phi_n(y)$. Restricting ourselves to the low-energy properties of the system, only interaction matrix elements $U_{n_1 n_2 n_3 n_4}$ where the indices n_i are pair-wise equal will appear. The remainder is devoted to the situation where the first subband is filled, $\mu_1 > 0$, and the density of electrons in the second subband is dilute, $|\mu_2| \ll \mu_1$, i.e., the second subband is close to the quantum phase transition occurring at $\mu_2 = 0$. Fig. 3.2 depicts this situation in the band structure picture. The Hamiltonian (3.4) can thus be reduced to a two-band setting described by

$$\mathcal{H} = \mathcal{H}_1 + \mathcal{H}_2 + \mathcal{H}_{12}, \quad (3.8)$$

where \mathcal{H}_i represent the two (interacting) subbands, $i = 1, 2$, and \mathcal{H}_{12} captures the inter-subband interactions. In the following, we discuss the different parts of the two-subband Hamiltonian (3.8) separately and without inter band coupling before turning to the analysis of the full Hamiltonian.

3.1.1 First subband

The first subband describes a one-dimensional electronic system of finite filling. If the coupling between the bands is initially neglected, this subband can be described by a standard Luttinger liquid. Although in principle all interactions up to spin-flip terms can be dealt with exactly by virtue of bosonization, see Sec. 4.2.1, we stick to fermionic degrees of freedom for now. This mainly has the advantage of symmetrizing the theory with respect to the second band, which can not be dealt with as a Luttinger liquid, see next section. We do, however, linearize the spectrum around the Fermi level, and distinguish the modes at the two Fermi points in right- and left-movers, denoted by R and L , respectively. These effective low energy degrees of freedom are related to the initial electrons by

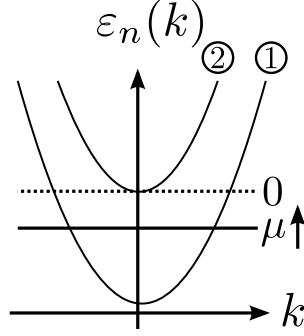


Figure 3.2: Transition from a one-dimensional to a quasi-one-dimensional state. At weak coupling, $na_B \gg 1$, the transition is triggered by filling a second subband upon tuning the chemical potential μ_2 through zero. Figure adapted from Ref. [16].

$$c_{1\sigma}(x) = e^{ik_{F1}x} R_{1\sigma}(x) + e^{-ik_{F1}x} L_{1\sigma}(x), \quad (3.9)$$

where σ denotes the spin and k_{F1} is the Fermi momentum in the first band. For further details on the linearization procedure, see Sec. 4.2.1. The low-energy degrees of freedom L and R are of course interacting. Chiral interactions, which only renormalize the Fermi velocity, are considered to be already contained in v_{F1} . The remaining interactions correspond to forward and backward scattering of a right-mover with a left-mover. In terms of the microscopic interaction amplitudes, they correspond to $U_{1111}(0)$ and $U_{1111}(2k_{F1})$, respectively, but can be written as a spin-density interaction g_{1s} and a charge-density interaction g_{1c} ,

$$g_{1c} = U_{1111}(0) - \frac{U_{1111}(2k_{F1})}{2}, \quad g_{1s} = 2U_{1111}(2k_{F1}). \quad (3.10)$$

Their magnitude is evaluated and discussed in Sec. 3.1.4 and appendix B.6. Most importantly, we note that for a quantum wire defined in a two-dimensional GaAs/GaAlAs electron gas, the spin interaction is much weaker than the charge interaction,

$$\frac{g_{1s}}{g_{1c}} \sim \frac{1}{\ln(d/x_0)} \ll 1. \quad (3.11)$$

Together with the linearized kinetic energy characterized by the Fermi velocity v_{F1} , the full Hamiltonian reads

$$\mathcal{H}_1 = \int dx \left[-iv_{F1} \sum_{\sigma} \left(R_{1\sigma}^{\dagger} \partial_x R_{1\sigma} - L_{1\sigma}^{\dagger} \partial_x L_{1\sigma} \right) + g_{1c} \rho_{1R} \rho_{1L} - g_{1s} \vec{S}_{1R} \cdot \vec{S}_{1L} \right] \quad (3.12)$$

where the spin and charge densities of the fields $r = L, R$ take the usual forms

$$\rho_{1r} = \sum_{\sigma} r_{1\sigma}^{\dagger} r_{1\sigma}, \quad \vec{S}_{1r} = \frac{1}{2} \sum_{\sigma, \sigma'} r_{1\sigma}^{\dagger} \vec{\sigma}_{\sigma, \sigma'} r_{1\sigma'}, \quad (3.13)$$

with σ_i denoting the Pauli matrices. As usual for standard Luttinger liquids, the charge mode is gapless whereas the fate of the spin mode depends on the sign of g_{1s} . If g_{1s} were negative, the spin mode would acquire a gap.²² In the present case, however, g_{1s} is positive, see Eq. (3.10). The spin sector of the isolated first subband is thus gapless.

$$\mathcal{D}_2(k, \omega) = \begin{array}{c} \longrightarrow \\ \longrightarrow \end{array} + \begin{array}{c} \diagup \quad \diagdown \\ \bullet \\ \diagdown \quad \diagup \\ V \end{array} + \begin{array}{c} \diagup \quad \diagdown \quad \diagup \quad \diagdown \\ \bullet \quad \bullet \\ \diagdown \quad \diagup \quad \diagdown \quad \diagup \\ V \quad V \end{array} + \begin{array}{c} \diagup \quad \diagdown \quad \diagup \quad \diagdown \quad \diagup \quad \diagdown \\ \bullet \quad \bullet \quad \bullet \\ \diagdown \quad \diagup \quad \diagdown \quad \diagup \quad \diagdown \quad \diagup \\ V \quad V \quad V \end{array} + \dots$$

Figure 3.3: The full two-particle Green's function $\mathcal{D}_2(k, \omega)$ corresponds to the resummation of all ladder diagrams, i.e. particle-particle bubbles in the first band.

3.1.2 Second subband (for $\mu_2 < 0$)

We now turn to the second subband, and specialize to the case $\mu_2 \leq 0$. The second subband is then only very dilutely occupied by thermal or virtual excitations living at the band bottom. It can thus not be described by a Luttinger liquid, and neither is it possible to distinguish between right- and left-movers. We model the second subband by the explicitly quadratic dispersion,

$$\epsilon_2(k) = \frac{k^2}{2m} - \mu_2, \quad (3.14)$$

where m_2 is the effective band mass. The leading interaction in the second band is given by the local interaction V between spin up and spin down particles. Pauli principle ensures that all other interaction are necessarily “non-local” (i.e. involve gradient terms), which renders them irrelevant in the renormalization group (RG) sense. The second band can thus be modeled by the Hamiltonian

$$\mathcal{H}_2 = \int dx \left[\sum_{\sigma} c_{2\sigma}^{\dagger}(x) \left(-\frac{\partial_x^2}{2m} - \mu_2 \right) c_{2\sigma}(x) + V c_{2\uparrow}^{\dagger}(x) c_{2\downarrow}^{\dagger}(x) c_{2\downarrow}(x) c_{2\uparrow}(x) \right]. \quad (3.15)$$

Since all particles live at the band bottom, the interaction V can not lead to a momentum transfer and is thus given by

$$V = U_{2222}(0), \quad (3.16)$$

in terms of the microscopic Coulomb repulsion. It is evaluated in Sec. 3.1.4 and appendix B.6.

Impenetrable electron gas close to $\mu_2 = 0$

Because the second subband is essentially empty, the list of possible scattering processes is particularly short. In the low temperature limit considered here, the ground state of the band is entirely empty. The only possible scattering events thus result from virtually exciting two particles to the band bottom, which may then scatter off each other. Hole-type excitations, on the other hand, are totally forbidden.

The effect of interactions can thus be described by virtue of the full two-particle Green's function, which corresponds to the resummation of all ladder-type diagrams, see Fig. 3.3. We derive the latter by first calculating the bare retarded two-particle Green's functions

$$\mathcal{D}_2^0(x - x', t - t') = -i\theta(t - t') \langle [c_{2\uparrow}(x, t) c_{2\downarrow}(x, t), c_{2\downarrow}^{\dagger}(x', t') c_{2\uparrow}^{\dagger}(x', t')] \rangle_0. \quad (3.17)$$

This calculation amounts to the solution of a non-interacting two-particle problem and can thus be performed without difficulty. The explicit calculation may be found in appendix B.2, and yields for the momentum k and frequency ω dependent retarded two-particle Green's function

$$\mathcal{D}_2^0(k, \omega) = -i \frac{\sqrt{m}}{\sqrt{\omega - \frac{k^2}{4m} + 2\mu_2 + i0^+}} = -i \frac{\sqrt{m}}{\sqrt{\epsilon + i0^+}}, \quad (3.18)$$

where we introduced the distance to the two-particle mass shell $\epsilon = \omega - \frac{k^2}{4m} + 2\mu_2$.

The effect of repeated two-particle scattering, see Fig. 3.3, can be captured in its totality using the full two-particle Green's function. As shown in appendix B.2, the latter is obtained from the bare two-particle Green's function as the solution of the Dyson equation

$$\mathcal{D}_2^{-1}(k, \omega) = \mathcal{D}_2^0(k, \omega) - V. \quad (3.19)$$

and is thus found to be

$$\mathcal{D}_2(k, \omega) = \frac{\mathcal{D}_2^0(k, \omega)}{1 - \mathcal{D}_2^0(k, \omega) V}. \quad (3.20)$$

For large negative μ_2 , where any excitation of the second band is punished by the large chemical potential, the effect of interactions is weak. Close to the band bottom, i.e. for $\epsilon \rightarrow 0$, the full Green's function is however dominated by strong correlations, since

$$\mathcal{D}_2^0(k, \omega)^{-1} \ll V \quad \text{if} \quad \epsilon \ll mV^2. \quad (3.21)$$

This defines an energy scale E_p beyond which the repeated scattering in the second band leads to substantial renormalizations,

$$E_p = mV^2. \quad (3.22)$$

In the interaction dominated regime $-E_p < \mu_2 < 0$, it is instructive to express the two-particle Green's function in terms of the \mathcal{T} -matrix, which characterizes the transition rate from an initial to a final state. One may also think of the \mathcal{T} -matrix as a black box containing the entire information about scattering events, which now govern the physics. It allows to rewrite the full two-particle Green's function as

$$\mathcal{D}_2(k, \omega) = \mathcal{D}_2^0(k, \omega) + \mathcal{D}_2^0(k, \omega) \mathcal{T}(k, \omega) \mathcal{D}_2^0(k, \omega), \quad (3.23)$$

and is thus given by

$$\mathcal{T}(k, \omega) = \frac{V}{1 - V \mathcal{D}_2^0(k, \omega)}. \quad (3.24)$$

In the on-shell limit $\epsilon \rightarrow 0$, which corresponds to the low energy physics at the transition $\mu_2 \rightarrow 0^-$, the effect of scattering is to leading order described by

$$\mathcal{T}(k, \omega) \xrightarrow{\epsilon \rightarrow 0} -\mathcal{D}_2^0(k, \omega)^{-1} . \quad (3.25)$$

Remarkably, the same limit would have been obtained for infinitely repulsive interactions $V \rightarrow \infty$. Close to its activation, i.e. for $-E_p < \mu_2 < 0$ with E_p defined in Eq. (3.22) the second subband is thus effectively described by a so-called ‘‘impenetrable electron gas’’, irrespective of the precise value of V .^{55–58} As a consequence, the two-particle wavefunction has not only nodes for electrons with the same spin as required by the Pauli principle, but also for electrons with opposite spin polarizations. The formation of an impenetrable electron gas at the transition can physically be understood as a signature of the van Hove singularity of the one-dimensional density of states, which has a square-root divergence at the band bottom. Since the dimensionless parameter characterizing the interactions is (density of states \times interaction), the divergent density of states naturally boosts the effect of interactions. This in turn explains the effectively infinite repulsion at the band bottom.

Second band at $\mu_2 > 0$

We close this section by shortly commenting on $\mu_2 > 0$, i.e. the case of a filled second subband. Just like the first subband, the second subband can be described as a Luttinger liquid, provided that the dimensionless interaction strength at the Fermi level is perturbative (if the chemical potential is close to the bottom of the second band, the formation of polarons needs to be taken into account, see Sec. 4.2.3). This translates to the condition

$$1 \gg \nu_{F2} V \sim \sqrt{\frac{m}{E_{F2}}} V \quad , \quad \text{and thus} \quad E_{F2} \gg mV^2 = E_p \quad , \quad (3.26)$$

where ν_{F2} is the density of states at the Fermi level of the second subband and where E_p is the same scale as for negative μ_2 , see Eq. (3.22). The presence of strong correlations in the second subband is thus quantified by the condition

$$-E_p < \mu_2 < E_p . \quad (3.27)$$

In this range, the physics of the second subband are governed by the physics of a (nearly) impenetrable electron gas. Since furthermore no interaction of the coupled two-band system is stronger than V , see Eq. (3.30), we expect this criterion to persist even if the coupling to the first band is turned on. We will analyze the physics of $\mu_2 > 0$ later on in chapter 4.

3.1.3 Coupling between the subbands

The interactions between the subbands can be divided into three types. There is a repulsive density-density interaction of electrons between the subbands with amplitude $u_c > 0$, and a spin density-density interaction that is generically ferromagnetic, $u_s > 0$. In addition, pair tunneling processes between the two subbands, see Fig. 3.4, correspond to a hopping amplitude u_t . Note that single particle tunneling between the bands is quadratic in creation and annihilation operators, and is therefore considered to be already taken

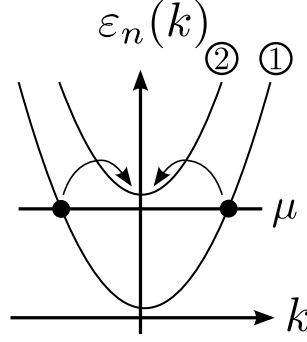


Figure 3.4: Pair-tunneling process between the two subbands.

into account by an appropriate initial diagonalization of the Hamiltonian. The interband interaction Hamiltonian \mathcal{H}_{12} reads

$$\begin{aligned} \mathcal{H}_{12} = & \int dx \left[u_c \rho_2 (\rho_{1R} + \rho_{1L}) - u_s \vec{S}_2 (\vec{S}_{1R} + \vec{S}_{1L}) \right] \\ & + u_t \int dx \sum_{\sigma} \left(c_{2\sigma}^{\dagger} c_{2\bar{\sigma}}^{\dagger} L_{1\bar{\sigma}} R_{1\sigma} + \text{h.c.} \right) \end{aligned} \quad (3.28)$$

with $\bar{\sigma} = -\sigma$. Here $\rho_2 = \sum_{\sigma} c_{2\sigma}^{\dagger} c_{2\sigma}$ and $\vec{S}_2 = \frac{1}{2} \sum_{\sigma, \sigma'} c_{2\sigma}^{\dagger} \vec{\sigma}_{\sigma, \sigma'} c_{2\sigma'}$, analogous to Eq. (3.13). The values for the couplings in terms of the interaction function U , Eq. (3.5), are given by

$$u_c = U_{1221}(0) - \frac{1}{2} U_{1212}(k_{F1}), \quad u_s = 2U_{1212}(k_{F1}), \quad (3.29a)$$

$$u_t = U_{1122}(k_{F1}), \quad (3.29b)$$

and are detailed in the next section and appendix B.6. As in Eq. (3.15), we neglected in Eq. (3.28) interaction processes involving additional spatial gradient terms. In particular, we disregarded tunneling of electron pairs with the same spin polarization. Due to the gradients, these interactions would however again be irrelevant in the renormalization group sense.

3.1.4 Values of the coupling strengths

The magnitude of the coupling constants follows from the microscopic model (2.1) as the matrix elements of the interaction, calculated for the wavefunctions of the first and second subband. They are explicitly evaluated in appendix B.6. Close to the activation of the second subband, the effective interaction constants take the values

$$g_{1s}, u_s, u_t \sim \frac{1}{\nu_1 n a_B}, \quad (3.30a)$$

$$g_{1c}, V, u_c \sim \frac{1}{\nu_1 n a_B} \ln \frac{d}{x_0}, \quad (3.30b)$$

We note that when the Wigner crystal regime is approached, $n a_B \rightarrow 1$, the dimensionless couplings $\nu_1 U_{n_1 n_2 n_3 n_4}$, with ν_1 being the Fermi level density of states in the first subband,

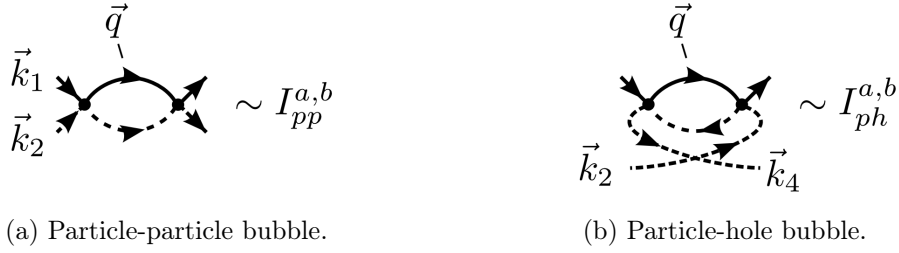


Figure 3.5: 1 loop diagrams renormalizing the various interaction strengths. Subfigure (a) shows a particle-particle bubble involving a particle of type a (solid lines) and a particle of type b (dashed line). Subfigure (b) shows the corresponding particle-hole diagram. The momentum vectors are understood to comprise both the one-dimensional momentum and the Matsubara frequency, e.g. $\vec{q} = (q, \omega_n)$. Incoming momenta are labeled as \vec{k}_1 and \vec{k}_2 , outgoing momenta are \vec{k}_3 (not shown here) and \vec{k}_4 .

become of order one (apart from the logarithmic enhancement⁵⁹), as expected. In the multiband quantum wire regime, however, the interactions are small and can be treated perturbatively. Concerning the different strengths of the various interactions, we note in particular that the pair tunneling u_t is logarithmically smaller than the intraband interactions $V \sim g_{1c}$, which will be important later on.

3.2 Introductory remarks on the perturbative analysis

In the subsequent sections, we analyze the behavior of the two-band quantum wire for negative chemical potentials $\mu_2 < 0$. Dwelling on the discussion of Sec. 3.1.2, we have to distinguish between the regime at large negative chemical potential, $\mu_2 < -E_p$, and the physics close to the activation of the second subband, $-E_p < \mu_2 < 0$, where the scale $E_p \sim mV^2$ characterizes the presence or absence of strong correlations due to the second subband. These two cases will be discussed in sections 3.4 and 3.5, respectively.

3.2.1 Multiple divergencies of the perturbation theory

In both regimes, we will base our analysis on a perturbative treatment of the interactions. To one-loop order, the vertex renormalizations are given by particle-particle and particle-hole diagrams as depicted in Fig. 3.5. At zero temperature, the perturbation theory is particularly simple since the second subband has an empty ground state. We thus only need to calculate the standard particle-particle and particle-hole bubbles of the Luttinger liquid type first band and the particle-particle bubble of the second band. It is thus useful to first recall the expression of a generic particle-particle and particle-hole bubble.

A particle-particle bubble involving a particle of type a and a particle of type b , see Fig. 3.5a), is given by the expression

$$\begin{aligned}
 I_{pp}^{a,b} &= \frac{1}{\beta L} \sum_{\omega_n, q} G_a(i\omega_n, q) G_b(i\omega_{n_1} + i\omega_{n_2} - i\omega_n, k_1 + k_2 - q) \\
 &= \frac{1}{L} \sum_q \frac{n_F(-\epsilon_b(k_1 + k_2 - q)) - n_F(\epsilon_a(q))}{\epsilon_a(q) + \epsilon_b(k_1 + k_2 - q) - (\omega_{n_1} + \omega_{n_2})},
 \end{aligned} \tag{3.31}$$

where β is the inverse temperature, L the length of the system, $\omega_{n_1} + \omega_{n_2}$ is the total incoming Matsubara frequency, $k_1 + k_2$ is the total incoming momentum, ω_n and q characterize the internal Matsubara frequency and momentum of the bubble, and n_F is the Fermi-Dirac distribution. The step from the first to the second line in Eq. (3.31) is done by the standard trick of rewriting the sum over Matsubara frequencies as a contour integral close to the imaginary axis, which is then deformed into a contour integral enclosing the entire complex plane except for the imaginary axis, combined with the use of the residue theorem. The calculation is in fact analogous to the derivation of the two-particle Green's function in appendix B.2. The Green's functions in Eq. (3.31) are given by

$$G_i(i\omega_n, q) = \frac{1}{i\omega_n - \epsilon_i(q)}, \quad (3.32)$$

with $\epsilon_i(q)$ being the dispersion of the particle i . The corresponding particle hole-bubble, see Fig. 3.5b, reads

$$\begin{aligned} I_{ph}^{a,b} &= \frac{1}{\beta L} \sum_{\omega_n, q} G_a(i\omega_n, q) G_b(i\omega_{n_2} - i\omega_{n_4} + i\omega_n, k_2 - k_4 + q) \\ &= \frac{1}{L} \sum_q \frac{n_F(\epsilon_a(q)) - n_F(\epsilon_b(k_2 - k_4 + q))}{\epsilon_a(q) - \epsilon_b(k_2 - k_4 + q) - (\omega_{n_2} - \omega_{n_4})}. \end{aligned} \quad (3.33)$$

Note that the Fermi functions ensure that diagrams involving holes in the second band vanish at zero temperature, as had been explained on physical grounds. In the important on-shell limit for incoming and outgoing particles, one explicitly finds a very useful symmetry between the particle-particle and particle-hole diagrams if at least one of the two particles lives in the first (Luttinger liquid type) subband, namely

$$I_{pp}^{a,b} \Big|_{\substack{\omega_1 + \omega_2 \rightarrow 0 \\ k_1 + k_2 \rightarrow 0}} = - I_{ph}^{a,b} \Big|_{\substack{\omega_2 - \omega_4 \rightarrow 0 \\ k_2 - k_4 \rightarrow 0}}. \quad (3.34)$$

This symmetry is inherited from the symmetry of particles and holes in a Luttinger liquid due to the linear dispersion, and will lead to the cancellation of several terms in our later analysis. The evaluation of these integrals depends on the exact choice of a and b as right- or left-moving particles in the first subband, or particles in the second subband. In the on-shell limit, however, they are proportional to

$$I_{pp}^{a,b} \sim I_{ph}^{a,b} \sim \int dq \frac{1}{\epsilon_a(q) \pm \epsilon_b(q)} \sim \int dq \frac{1}{q} \sim \ln(q) \sim \ln(\omega_n) \quad (3.35)$$

if at least one of the particles a and b lives in the first subband, whereas one has

$$I_{pp}^{2,2} \sim \int dq \frac{1}{\epsilon_2(q) + \epsilon_2(q)} \sim \int dq \frac{1}{q^2} \sim \frac{1}{q} \sim \frac{1}{\sqrt{\omega_n}}, \quad (3.36)$$

if both particles live in the second subband. As has been detailed in appendix B.2 the particle-particle bubble in the second band in fact coincides with the expression of the two-particle Green's function,

$$I_{pp}^{2,2} \sim \mathcal{D}_2^0. \quad (3.37)$$

More details on the evaluation of the particle-particle and particle-hole bubbles as well as the symmetry $I_{pp} \sim -I_{ph}$ for particles in the first band may be found in appendix B.3.

The different dynamics of the two subbands thus lead to distinct types of divergences, namely logarithmic and square-root singularities. The type of divergence depends on the intermediate state. Diagrams involving only particles in the first subband, which have a linear dispersion and a constant density of state, yield the usual, logarithmically divergent Luttinger liquid corrections. If the diagrams involves both a particle in the lower and the upper subband, the logarithmic divergence is cut off by the corresponding energy cost of μ_2 , see appendix B.3. If however a diagram only involves particles in the second subband, a square root divergence is obtained, which again is cut off for finite μ_2 . In the next sections, we will base our discussion on the fundamental difference between the logarithmic divergencies of the Luttinger liquid like first band and the (possibly cut off) square root divergencies of the second band.

At large negative μ_2 , see Sec. 3.4, only processes in the first subband are divergent, whereas all other diagrams are regularized by the finite value of μ_2 . The Luttinger liquid type divergencies can then simply be summed up with a standard renormalization group (RG) procedure. Upon approaching the Lifshitz transition for $\mu_2 \rightarrow 0$, see Sec. 3.5, the diagrams involving the second subband begin to substantially renormalize the model for $-E_p < \mu_2$, see Sec. 3.1.2. More importantly, these diagrams even yield the leading singularities of the theory, since they diverge with a square root instead of a logarithm. It is thus appropriate to first sum up these most divergent diagrams, which however is a simple task since it only amounts to summing up repeated two-particle scattering in the second subband, see Fig. 3.3. This resummation will yield effective interaction constants for the Luttinger liquid, who's logarithmic divergencies are then taken care of by a secondary RG flow.

3.2.2 The quantum critical perspective on the multiple divergencies

The multiple divergences can also be understood from a quantum critical perspective. At the quantum critical point $\mu_2 = 0$, the two subbands correspond to two gapless and coupled degrees of freedom with multiple dynamics. As a Luttinger liquid, the first subband is in a way equivalent to a classical, two-dimensional system right at the critical temperature of a phase transition to some ordered state.²² Its quantum theory supports gapless and linearly dispersing excitations, which live at their upper critical dimension (this follows from simple power counting of the action corresponding to the Hamiltonian (3.12)). The second subband is approaching criticality for $\mu_2 \rightarrow 0$. Exactly at the quantum critical point $\mu_2 = 0$ and neglecting couplings between the bands, the interaction u within the second subband can be analyzed by a perturbative renormalization group approach. The engineering dimension of the interaction is $[u]_{\text{engin.}} = 4 - d - z = 2 - d$, with a dynamical exponent $z = 2$ and the spatial dimension being $d = 1$. As discussed in Ref. [60], the interaction is RG irrelevant above $d = 2$, while it goes to a Wilson-Fisher type fixed point value corresponding to a spinless Fermi gas in dimensions $d < 2$. In this sense, the second band is below its upper critical dimension if the chemical potential is exactly at the band bottom, i.e. for $\mu_2 = 0$. One can thus expect the second band to have more singular fluctuations than the Luttinger liquid type band (which is at its upper critical dimension). Nevertheless, the first subband can still importantly influence the

critical physics as it is exactly at its upper critical dimension. If the chemical potential lies within the second band, $\mu_2 > 0$, the latter band should not be interpreted as a critical system below its upper critical dimension anymore, but should be viewed as a Luttinger liquid, and fluctuations of both bands should in this sense be treated on equal footing.

Compared to other problems involving multiple dynamics and quantum criticality,⁵³ the present problem of a Lifshitz transition in a quantum wire is somewhat simpler for mainly two reasons. Firstly, if the system is not too close to criticality, only the quantum fluctuations stemming from standard Luttinger liquid(s) need to be taken into account. Only upon approaching the Lifshitz transition very closely, i.e. for $|\mu_2| \leq E_p$ with E_p defined in Eq. (3.5), low energy fluctuations of different dynamics coexist. Secondly, we do not have to treat the multiple dynamics by a simultaneous RG for both bands, which would technically be non-trivial (but possible, see part II). On the contrary, we are able to first solve the more singular problem of square-root divergent corrections from the second subband exactly, because it is a simple two-particle problem (see Sec. 3.1.2). The remaining less singular problem of log-divergent terms stemming from the first subband can then be treated by a perturbative RG as a secondary step, in accordance with the lower relevance of these fluctuations with respect to the square-root divergent ones.

3.3 Vertex correction to 1 loop order

In order to capture the effect of interactions on the activation of the second band at $\mu_2 = 0$, we proceed with a perturbative expansion to one loop order in the coupling constants. We assume that self-energy corrections, which are essentially proportional to the fillings and thus not singular, have already been taken care of by an appropriate redefinition of the chemical potentials. The problem then boils down to the calculation of 1 loop vertex correction. We recall that these are potentially divergent, see Sec. 3.2.

For negative μ_2 , when the second subband is essentially empty, the various 1 loop diagrams can easily be calculated, and the details of the calculation may be found in appendices B.2 and B.3. For the first, Luttinger liquid type band, the 1 loop corrections are given by spin scattering processes within the first band, which are proportional to g_{1s}^2 , and virtual tunneling to the second band and back, which yields terms proportional to u_t^2 . We note that the charge interaction g_{1c} does not renormalize itself to 1 loop order because of a cancellation of particle-particle and particle-hole type diagrams. The corresponding diagrams are shown in Fig. 3.6. This is the usual behavior of a Luttinger liquid.²² Collecting all prefactors for the different bubbles, we find that

$$\delta g_{1c} = \frac{1}{2} u_t^2 \mathcal{D}_2^{(0)}(0, \omega), \quad (3.38a)$$

$$\delta g_{1s} = -\frac{g_{1s}^2}{2\pi v_{F1}} \ln \frac{E_0}{|\omega|} + 2u_t^2 \mathcal{D}_2^{(0)}(0, \omega), \quad (3.38b)$$

where we made use of the fact that a particle-particle bubble in the second band can be written as the bare two-particle Green's function $\mathcal{D}_2^{(0)}$, see appendix B.2. Note that we here choose to evaluate all diagrams in the limit of vanishing incoming momentum, $k = 0$, and small incoming frequency ω .

The interaction of the second, quadratically dispersing band is to 1 loop order renormalized by two kinds of processes depicted in Fig. 3.7. Firstly, two particles propagating



Figure 3.6: 1 loop diagrams renormalizing the couplings g_{1c} and g_{1s} in the first band. Solid lines indicate particles in the first subband, dashed lined are for particles in the second subband. The spins are indicated by the arrows.

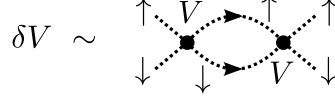


Figure 3.7: 1 loop diagram renormalizing the interaction V in the second subband. The dashed lines depict propagation in the second subband, and arrows indicate the spins.

in the second band may repeatedly scatter off each other (to one loop order twice), giving rise to a term proportional to V^2 . Secondly, the pair tunneling allows for the two particles to virtually hop to the first band and back, which yields a renormalization proportional to u_t^2 . The total renormalization is thus given by

$$\delta V = V^2 \mathcal{D}_2^{(0)}(0, \omega) - \frac{u_t^2}{\pi v_{F1}} \ln \frac{E_0}{|\omega|}. \quad (3.39)$$

Finally, also the interband interaction experiences renormalizations. We again find that the particle-particle and particle-hole bubbles for the interband charge interaction u_c cancel, such that it is only renormalized by the pair tunneling. On the contrary, the spin-spin interaction u_s is able to renormalize itself, yielding a term proportional to u_s^2 . The pair tunneling, finally, is renormalized by three kinds of processes. Firstly, two particles in the first subband may first scatter off each other whilst propagating in the first subband and then tunnel, yielding renormalizations proportional to $g_{1c}u_t$ and $g_{1s}u_t$. Secondly, the particles may also first tunnel and then scatter, which gives a term proportional to u_tV . Finally, there is also a particle-hole type diagram involving an interband charge interaction, which is proportional to u_cu_t . The corresponding diagrams can be found in Fig. 3.8. In total, we find that the interband interactions are renormalized as

$$\delta u_c = \frac{u_t^2}{2\pi v_{F1}} \ln \frac{E_0}{|\omega + \mu_2|}, \quad (3.40a)$$

$$\delta u_s = -\frac{u_s^2}{2\pi v_{F1}} \ln \frac{E_0}{|\omega + \mu_2|}, \quad (3.40b)$$

$$\delta u_t = V u_t \mathcal{D}_2^{(0)}(0, \omega) - \frac{(g_{1c} + \frac{3}{4}g_{1s})u_t}{2\pi v_{F1}} \ln \frac{E_0}{|\omega|} + \frac{2u_t u_c}{\pi v_{F1}} \ln \frac{E_0}{|\omega + \mu_2|}. \quad (3.40c)$$

In the following, we want to resum the divergent classes of diagrams as explained in Sec. 3.2, starting with the case of large negative potential $\mu_2 < -E_p$.

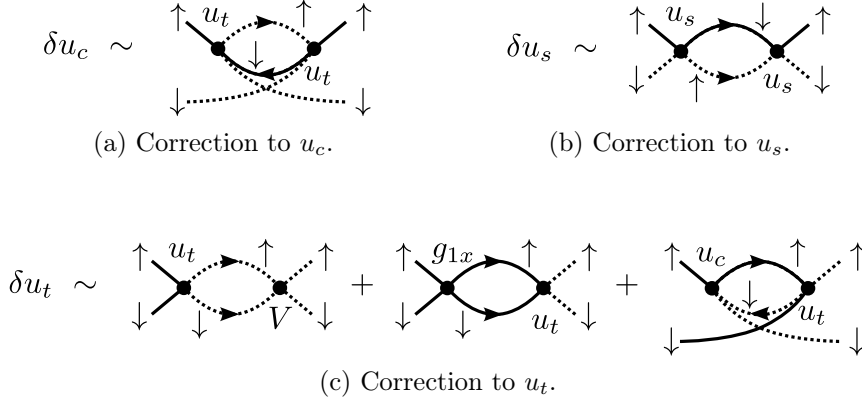


Figure 3.8: 1 loop diagrams renormalizing the couplings interband couplings u_c , u_s and u_t in the first band. Solid lines indicate particles in the first subband, dashed lined are for particles in the second subband. The spins are indicated by the arrows.

3.4 Perturbative regime at large negative μ_2 : dilute weakly interacting Fermi gas in the second subband

If the chemical potential of the second subband is largely negative, we expect the latter not to lead to singular renormalizations. Any process involving particles in the second band is punished by a large energy cost of order $|\mu_2|$. Upon approaching the quantum phase transition at $\mu_2 = 0$, interaction processes in the second subband get increasingly important. Because of the square-root divergent density of states at the bottom of the second band, they finally even dominate over the logarithmically divergent diagrams involving particles in the Luttinger liquid type, first band. Indeed, the 1 loop corrections involving the second subband become of order 1 and thus non-perturbative if $\mu_2 \sim \mathcal{O}(\max\{mu_t^4/g_{1c}^2, mu_t^4/g_{1s}^2, mV^2\})$. Since however no interaction is stronger than V , see Eq. (3.30), we find that renormalizations due to the second subband are perturbative as long as

$$\mu_2 < -E_p \quad \text{with} \quad E_p = mV^2, \quad (3.41)$$

as foreseen in Sec. 3.1.2. For this regime, only diagrams exclusively involving particles in the first subband are divergent, which off course correspond to the usual renormalization of the interactions in an isolated Luttinger liquid. The corresponding logarithmic divergencies can be summed up by a conventional perturbative renormalization group (RG) approach. As shown in appendix B.3, the diagrams correspond to integrals

$$I_{pp}^{a,b}, I_{ph}^{a,b} = \int_0^{E_0/v_{F1}} dq \dots, \quad (3.42)$$

such that the RG step correspond to integrating out a small shell around the high energy cutoff E_0 ,

$$\delta I_{pp}^{a,b}, \delta I_{ph}^{a,b} = \int_{E_0/v_{F1}}^{(E_0/v_{F1})/b} dq \dots \quad (3.43)$$

with $b > 1$. The RG equations are given by the logarithmic derivatives $\partial\delta I/\partial\ln b$, and thus simply correspond to the prefactors of the divergent logarithms in Sec. 3.3. They read

$$\frac{\partial g_{1s}}{\partial\ln b} = -\frac{g_{1s}^2}{2\pi v_{F1}}, \quad (3.44a)$$

$$\frac{\partial V}{\partial\ln b} = -\frac{u_t^2}{\pi v_{F1}}, \quad (3.44b)$$

$$\frac{\partial u_t}{\partial\ln b} = -\frac{(g_{1c} + 3g_{1s}/4)u_t}{2\pi v_{F1}}. \quad (3.44c)$$

These RG equations can now simply be integrated, which is detailed in appendix B.4. At first, we find that the ferromagnetic spin interaction g_{1s} flows logarithmically to weak coupling. We also note that an antiferromagnetic spin coupling would have led to a runaway flow and the formation of a gap in the spin sector. This of course reproduces the expected behavior of a Luttinger liquid.²² The pair tunneling has a negative scaling dimension which asymptotically approaches $-g_{1c}/(2\pi v_{F1})$ since g_{1s} flows to weak coupling. It thus flows to zero as a power law, $u_t(b) \sim b^{-g_{1c}/(2\pi v_{F1})}$. The running u_t renormalizes the coupling in the second subband, V . Since the pair tunneling does however vanish as a power law, and thus relatively quickly, the flow of V is short and only yields a finite renormalization. We find that at the end of the day, the second band is subject to an effective interaction

$$V_{\text{eff}} = V - \frac{u_t^2}{g_{1c}} \phi\left(\frac{g_{1s}}{g_{1c}}\right), \quad (3.45)$$

where the function ϕ has the limits $\phi(0) = 1$ and $\phi(x) \approx 4/x$ for $x \rightarrow \infty$, see appendix B.4. Using the initial values of the interaction constants, Eq. (3.30), one obtains $(V_{\text{eff}} - V)/V \sim 1/(\ln d/x_0)^2$, such that the correction is logarithmically small. The effective interaction V_{eff} thus remains repulsive and perturbative for $\mu_2 < -E_p$. If however the effective coupling was positive, which implies the condition

$$\frac{u_t^2}{Vg_{1c}} \stackrel{!}{\gtrsim} \mathcal{O}(1), \quad (3.46)$$

the formation of a two-particle bound state in the second band would have been energetically favorable, leading to the opening of a charge gap. This condition is however *not* fulfilled in our case.

In conclusion, find that in the limit of large negative chemical potential μ_2 , the two-subband quantum wire can be viewed as a regular Luttinger liquid with ferromagnetic spin coupling. Consequently, both the spin and the charge sector of the Luttinger liquid remain gapless. The second subband corresponds to an exponentially dilute, thermally occupied electron gas. This electron gas is subject to weak, repulsive interaction and effectively decoupled from the Luttinger liquid, since u_t flows to zero. Confirming earlier discussions, we found that this picture breaks down for $\mu_2 > -E_p$ with $E_p = mV^2$, when the correlation of the second subband become non-perturbative. This regime will be discussed in the next section.

3.5 Quantum phase transition at $\mu_2 = 0$

Close to the activation of the second band, when $-E_p < \mu_2 \leq 0$ (see Eq. (3.41)), correlations in the second subband are strong and in fact even yield the dominant renormalizations of the coupling constants. Technically, this is due to the square-root divergence of diagrams living in this second subband, while all other diagrams only exhibit logarithmic singularities, see Sec. 3.2. Physically, the second subband should govern the physics if the chemical potential is close to its band edge since its density of states has a square root divergence (which then in turn gives rise to the square root divergent diagrams), in contrast to the Luttinger liquid type first band exhibiting a constant density of state.

Since the square-root divergent renormalizations of the second subband largely outweigh the logarithmically divergent corrections stemming from the first subband, the regime $-E_p < \mu_2 \leq 0$ can be analyzed in a two-step procedure. More concretely, we will first resum the leading square root singularities of the second subband. The less singular logarithmic corrections will then be treated as a subleading effect in a secondary resummation.

3.5.1 Leading renormalizations: resummation of the square-root divergencies

The square-root divergencies in the 1 loop renormalizations of Sec. 3.3 are due to scattering processes of two particles in the second subband, where the large density of states at the band bottom leads to very strong correlation effects. For $-E_p < \mu_2 \leq 0$, this leads to singular vertex corrections. We thus have to first resum the class of diagrams corresponding to repeated two-particle scattering events in the second subband, see Fig. 3.3. All other diagrams can be treated in a secondary step since they correspond to subleading renormalizations. These latter diagrams would necessarily involve a tunneling to the first band, where the density of states is constant, which would render the corresponding diagram less divergent.

The resummation of these diagrams is however particularly simple. The second subband is essentially empty for $\mu_2 \leq 0$, such that hole-type excitations are forbidden. The resummation of the leading scattering events within the second subband thus amounts to replacing the bare two-particle Green's function $\mathcal{D}_2^0(0, \omega)$ by the full two-particle Green's function $\mathcal{D}_2(0, \omega)$, which has been calculated in Sec. 3.1.2. Close to the bottom of the second band, i.e. for $\varepsilon \rightarrow 0$ (we recall that $\varepsilon = \omega - k^2/(4m) + 2\mu_2$ is the distance to the two-particle mass shell, see Sec. 3.1.2), the two-particle Green's function takes the form

$$\mathcal{D}_2(k, \omega) \stackrel{k, \omega \rightarrow 0}{\approx} -\frac{1}{V} - \frac{1}{V^2 \mathcal{D}_2^{(0)}(k, \omega)}, \quad (3.47)$$

where

$$\mathcal{D}_2^0(k, \omega) = -\frac{i}{2} \sqrt{\frac{m}{\varepsilon + i0}}. \quad (3.48)$$

As discussed in Sec. 3.1.2), the form of the two-particle Green's function indicates that the strong correlations at the band bottom, $\mu_2 \approx 0$, lead to the formation of an impenetrable electron gas.

The resummation of the square root divergencies leads to new effective values for the different coupling constants. By replacing $\mathcal{D}_2^0(0, \omega) \rightarrow \mathcal{D}_2(0, \omega)$ in the 1 loop corrections derived in Sec. 3.3, we obtain the effective coupling constants

$$V^{\text{eff}} = V + V^2 \mathcal{D}_2(0, \omega) , \quad (3.49a)$$

$$u_t^{\text{eff}} = u_t + V u_t \mathcal{D}_2(0, \omega) , \quad (3.49b)$$

$$g_{1c}^{\text{eff}} = g_{1c} + \frac{1}{2} u_t^2 \mathcal{D}_2(0, \omega) , \quad (3.49c)$$

$$g_{1s}^{\text{eff}} = g_{1s} + 2u_t^2 \mathcal{D}_2(0, \omega) . \quad (3.49d)$$

Firstly, we find that the interaction within the second subband takes the universal form

$$V^{\text{eff}} \stackrel{\omega \rightarrow 0}{\approx} -\frac{1}{\mathcal{D}_2^0(k, \omega)} \sim \sqrt{\varepsilon} , \quad (3.50)$$

which is characteristic of an impenetrable electron gas. The relevant dimensionless interaction strength, given by (density of states $\times V^{\text{eff}}$), thus approaches a constant (we recall that the density of states diverges as a square root). This of course signals the formation of an impenetrable electron gas in the second subband. The pair tunneling, on the other hand, is suppressed due to the formation of this impenetrable electron gas,

$$u_t^{\text{eff}} \stackrel{\omega \rightarrow 0}{\approx} -\frac{u_t}{V^2} \frac{1}{\mathcal{D}_2^0(0, \omega)} \stackrel{\omega \rightarrow 0}{\rightarrow} 0 . \quad (3.51)$$

We note that in contrast to the coupling V , the relevant dimensionless interaction for the pair tunneling between the two bands is formed by multiplying u_t^{eff} with a mixed density of states of both bands, which certainly is less singular than a square root. On physical grounds, this simply means that the formation of the impenetrable electron gas in the second subband suppresses the local pair tunneling term u_t acting on electrons at the same position. Finally, interactions in the first subband obtain a finite renormalization, which reads

$$g_{1c}^{\text{eff}} = g_{1c} - C_c \frac{u_t^2}{V} , \quad (3.52a)$$

$$g_{1s}^{\text{eff}} = g_{1s} - C_s \frac{u_t^2}{V} , \quad (3.52b)$$

$$C_c = \frac{1}{2}, \quad C_s = 2 . \quad (3.52c)$$

We can understand the attractive character of this correction by recalling that it derives from the local pair tunneling term. The latter likes electrons to be at the same position, since they can then gain kinetic energy by virtually hopping to the second band and back. The intermediate state is however punished by the potential energy cost V in the second band. In total, this process thus yields an attractive correction of the form u_t^2/V to the intraband interactions, similar to an antiferromagnetic nearest neighbor spin exchange coupling deriving from a tight-binding chain.

3.5.2 Sub-leading renormalizations: Lifshitz transition of polarons

Having resummed the leading square-root interaction exactly, we can next analyze the effect of the logarithmic renormalizations due to interaction processes involving the first, Luttinger liquid type band. We resum these divergencies by a renormalization group (RG) analysis similar to the regime $\mu_2 < -E_p$, see Sec. 3.4. Except for the effective bare values resulting from the resummation of the leading singularities, the resulting RG equations are very similar. In particular, we note that the pair tunneling is suppressed by the strong correlations in the second band, $u_t^{\text{eff}} \rightarrow 0$ in the limit $\omega \rightarrow 0$, see above. The RG equations thus read

$$\frac{\partial g_{1s}^{\text{eff}}}{\partial \ln b} = -\frac{(g_{1s}^{\text{eff}})^2}{2\pi v_{F1}}, \quad (3.53a)$$

$$\frac{\partial u_s}{\partial \ln b} = -\frac{u_s^2}{2\pi v_{F1}}. \quad (3.53b)$$

These two independent RG equations can easily be integrated similarly to the case of large negative μ_2 , see appendix B.4. We thus find a logarithmic flow for both of them. For the interband spin interaction u_s , which has a positive bare value, this flow is to weak coupling. For the intraband coupling g_{1s} however, the flow might be either to weak coupling for $g_{1s} > 0$, or to strong coupling for negative $g_{1s} < 0$, which would lead to the opening of a spin gap in the first subband. The fate of the system thus depends on the strength of the finite shift of g_{1s} due to the pair tunneling. Using the effective coupling constants (3.52) obtained after the resummation of repeated two-particle scattering in the second subband as initial conditions for the secondary RG flow, we find that the spin gap would only open if

$$\frac{u_t^2}{V g_{1s}} \stackrel{!}{\geq} \frac{1}{2}. \quad (3.54)$$

For a quantum wire defined in a two-dimensional electron gas, however, the pair tunneling is logarithmically suppressed with respect to the intraband interaction V , see Eq. (3.30). We can therefore conclude that the effective interactions flow to weak coupling. Since $g_{1c}/g_{1s} \sim \ln(d/x_0)$, we also note that we obtain a similar but logarithmically weaker (i.e. easier to fulfill) criterion for the opening of a gap than in the case $\mu_2 < -E_p$, see Eqs. (3.46) and (3.30).

Since it is governed by essentially the same equation, the intraband spin interaction u_s seemingly also flows to weak coupling. However, its RG equation (3.53b) is only valid for scales larger than the chemical potential μ_2 , since the latter cuts off the logarithmic divergence of the correction to u_s , see Eq. (3.40b). For u_s , the RG flow must thus be stopped at this scale. This yields the frequency dependent effective interaction

$$u_s(\omega) = \frac{u_s}{1 + \frac{u_s}{2\pi v_{F1}} \ln \frac{E_p}{\max\{\omega, |\mu_2|\}}}, \quad (3.55)$$

where E_p denotes the high-energy cutoff (for the integration of the RG equation, see again appendix B.4). We can thus conclude that for $-E_p < \mu_2 \leq 0$, the two subband quantum

wire can be understood as a Luttinger liquid in the first band and an impenetrable gas in the second band. The latter is exponentially dilute in $-\mu_2$. These two bands are coupled by a logarithmically suppressed spin-spin interaction u_s and a charge density interaction u_c (note that the latter only received perturbative corrections). The interband couplings will eventually lead to a polaron effect, see Ref. [61]. Close to the transition, the particles in the second subband are much slower than the density waves in the Luttinger liquid type first subband, such that the latter can adiabatically follow the prior ones. The true degrees of freedom in the second band are thus polarons, i.e. electrons dressed with density waves. The polaron effect will be further discussed in the regime $\mu_2 > +E_p$, see Sec. 4.3. Physically, the density wave excitations in the first subband move with a relatively large velocity v_{F1} , while the particles in the second subband, living at the band bottom, are slow. The fast density wave can thus adiabatically rearrange in order to optimize the interband spin and charge interaction u_s and u_c , such that the second band is actually occupied by polarons, i.e. electrons surrounded by a cloud of density waves. The polaron effect does however not show up to 1 loop order. It will, though, lead to logarithmically singular 2 loop corrections to the residue Z of the fermionic single-particle Green function in the second subband.¹⁶

3.5.3 Universality class of the quantum phase transition

After all, we can identify the quantum phase transition occurring at $\mu_2 = 0$ as a Lifshitz transition corresponding to the filling of an empty subband as a function of the chemical potential μ_2 . The electrons that fill this empty subband are, however, strongly interacting and characterized by unitary scattering. Furthermore, each of these electrons is screened by charge and spin density wave excitations of the Luttinger liquid in the filled first subband. As a result, the quantum phase transition is a Lifshitz transition of impenetrable polarons.

3.6 Comparison to an ϵ -renormalization of the $z_2 = 2$ singularities

The two subband Hamiltonian, Eq. (3.8), has previously been considered by Balents and Fisher in Ref. [33] in the context of the two-chain Hubbard model. In order to deal with the logarithmic and square-root singularities encountered in perturbation theory, see section 3.3, they considered a generalized dispersion for the electrons in the second subband, $\varepsilon(k) = |k|^{1+\epsilon}v^{1-\epsilon}/(2m)^\epsilon$, where v is an artificial parameter with the dimension of velocity. The physical quadratic dispersion of the Hamiltonian (3.15) is recovered for $\epsilon = 1$ whereas $\epsilon = 0$ corresponds to a linear spectrum. Treating ϵ as a small parameter, the square-root singularities are regularized to logarithmic ones and RG equations for the Hamiltonian close to criticality, $\mu_2 \approx 0$, can be derived (note that the ϵ -expansion is thus another way to get around the problem of multiple dynamic exponents). Simply translating the results of Balents and Fisher to our notation, the RG equations in lowest

order in ϵ read³³

$$\frac{\partial g_{1c}}{\partial \ln b} = -\frac{u_t^2}{4\pi v}, \quad (3.56a)$$

$$\frac{\partial g_{1s}}{\partial \ln b} = -\frac{g_{1s}^2}{2\pi v_{F1}} - \frac{u_t^2}{\pi v}, \quad (3.56b)$$

$$\frac{\partial V}{\partial \ln b} = \epsilon V - \frac{V^2}{2\pi v} - \frac{u_t^2}{\pi v_{F1}}, \quad (3.56c)$$

$$\frac{\partial u_c}{\partial \ln b} = \frac{u_t^2}{2\pi(v_{F1} + v)}, \quad (3.56d)$$

$$\frac{\partial u_s}{\partial \ln b} = -\frac{u_s^2}{2\pi(v_{F1} + v)}, \quad (3.56e)$$

$$\frac{\partial u_t}{\partial \ln b} = \left(\frac{\epsilon}{2} - \frac{V}{2\pi v} + \frac{2u_c}{\pi(v_{F1} + v)} - \frac{g_{1c} + \frac{3}{4}g_{1s}}{2\pi v_{F1}} \right) u_t. \quad (3.56f)$$

These equations have been derived perturbatively under the assumption that all dimensionless coupling constants are much smaller than ϵ . Therefore, the initial flow is given by the terms proportional to ϵ , which appear in the equations for intra-subband interaction in the second subband, V , and the pair tunneling, u_t . In other words, these two couplings initially have relatively large scaling dimensions of ϵ and $\epsilon/2$, respectively, and consequently increase rapidly according to the very initial RG equations,

$$\frac{\partial V}{\partial \ln b} \approx \epsilon V, \quad (3.57a)$$

$$\frac{\partial u_t}{\partial \ln b} \approx \frac{\epsilon}{2} u_t. \quad (3.57b)$$

In particular, we find that the intraband coupling V even grows much faster than the tunnel coupling. When V becomes of the order of $V/(2\pi v) \approx \epsilon/2$, the flow of u_t stops, since it is then described by the RG equation

$$\frac{\partial u_t}{\partial \ln b} \approx \left(\frac{\epsilon}{2} - \frac{V}{2\pi v} \right) u_t \approx 0. \quad (3.58)$$

After reaching this stationary point, where the initial flow has already largely increased u_t by a factor of $\sqrt{\pi v \epsilon / (2V)}$, see appendix B.5, the pair tunneling decreases again and finally flows to weak coupling. At the stationary point, however, it causes important renormalizations for some of the other couplings. It is instructive to note that the intermediate approximate fixed point close to $V \approx \epsilon/2$ actually yields the biggest part of the renormalizations corresponding to the resummation of repeated scattering events in the second subband. In an RG language, this intermediate stationary point corresponds to an RG scale b_{\max} , and the flow of the interaction V and the pair tunneling u_t close to b_{\max} can be approximated as

$$V(b \approx b_{\max}) \approx 2\pi v \left[\frac{\epsilon}{2} + \frac{\epsilon^2}{4} \ln(b/b_{\max}) \right], \quad (3.59)$$

$$u_t(b \approx b_{\max}) \approx u_t(b_{\max}) e^{-\epsilon^2/8 \ln^2(b/b_{\max})}. \quad (3.60)$$

where the pair tunneling at the stationary point reads $u_t(b_{\max}) \approx u_t \sqrt{\pi v \epsilon / (2V)}$, see appendix B.5. These expressions can now be plugged into the approximate RG equations of g_{1c} and g_{1s} close to this approximate fixed point, which read

$$\frac{\partial g_{1x}}{\partial \ln b} = -C_x \frac{u_t^2}{2\pi v}, \quad (3.61)$$

where $C_c = 1/2$ and $C_s = 2$ like in Eq. (3.52). Integrating these equations yields the asymptotic values

$$g_{1x}^{\text{eff}} = g_{1x} - C_x \frac{\sqrt{\pi}}{4} \frac{u_t^2}{V}. \quad (3.62)$$

The stationary point of the RG flow thus already accounts for a reduction of the coupling constant with a prefactor $\sqrt{\pi}/4$ as compared to the full reduction obtained in section 3.5. The latter can be reproduced by approximating the full initial RG flow by an effective set of equations proportional to ϵ , V and u_t (note that all other terms only involve the perturbatively small bare coupling constants). In addition, we note that u_t is generally much smaller than V , except for the very initial RG flow. Since the latter is however governed by ϵ anyway, we can approximate the initial flow of the RG equations (3.56) as

$$\frac{\partial g_{1c}}{\partial \ln b} = -\frac{u_t^2}{4\pi v}, \quad (3.63a)$$

$$\frac{\partial g_{1s}}{\partial \ln b} = -\frac{u_t^2}{\pi v}, \quad (3.63b)$$

$$\frac{\partial V}{\partial \ln b} = \epsilon V - \frac{V^2}{2\pi v}, \quad (3.63c)$$

$$\frac{\partial u_c}{\partial \ln b} = \frac{u_t^2}{2\pi(v_{F1} + v)}, \quad (3.63d)$$

$$\frac{\partial u_t}{\partial \ln b} = \left(\frac{\epsilon}{2} - \frac{V}{2\pi v} \right) u_t. \quad (3.63e)$$

The flow described by these equations indeed corresponds to the resummation of the leading square-root divergencies of the theory. The dimensionless intraband interaction V flows to a finite value, $V/(2\pi v) \rightarrow \epsilon$, which corresponds to the impenetrable electron gas. The interband pair tunneling u_t asymptotically flows to zero, since the strong interaction V in the second band suppresses local tunneling, see Sec. 3.5. On the way to the impenetrable electron fixed point $V/(2\pi v) = \epsilon$, $u_t = 0$, the pair tunneling however leads to a renormalization of the intraband couplings in the first band, g_{1c} and g_{1s} , and the interband charge coupling u_c , mostly due to the intermediate stationary point. As shown in appendix B.5, we can simply integrate these RG equations. In particular, we find that the pair tunneling asymptotically yields a finite renormalization for the intraband couplings g_{1s} and g_{1c} ,

$$g_{1x}^{\text{eff}} = g_{1x} - C_x \frac{u_t^2}{V}. \quad (3.64)$$

where $C_c = 1/2$ and $C_s = 2$. This exactly reproduces the results of Sec. 3.5, see Eq. (3.52), and of course leads to the same instability criterion

$$\frac{u_t^2}{Vg_{1s}} \stackrel{!}{\gtrsim} \mathcal{O}(1). \quad (3.65)$$

that had already been established in Eq. (3.54). The remaining flow of the theory after reaching the impenetrable electron gas fixed point is given by the RG equations

$$\frac{\partial g_{1s}^{\text{eff}}}{\partial \ln b} = -\frac{(g_{1s}^{\text{eff}})^2}{2\pi v_{F1}}, \quad (3.66a)$$

$$\frac{\partial u_s}{\partial \ln b} = -\frac{u_s^2}{2\pi(v_{F1} + v)}, \quad (3.66b)$$

which again exactly reproduces the secondary flow of Sec. 3.5. In summary, we thus find that also the ϵ expansion of Ref. [33] arrives at the same conclusion concerning the stability of the Luttinger liquid as in the previous section, see the criterion of Eq. (3.54). The main difference between our analysis and the results of Ref. [33] arises from the evaluation of this criterion. There, a two-chain Hubbard ladder was considered, in which case all interactions are of the same order, namely on the order of the Hubbard interaction U . Thus, for Hubbard initial conditions the criterion (3.54) can be fulfilled, and a spin gap is to be expected in agreement with Ref. [33]. For the quantum wire with screened Coulomb interaction, however, the system remains gapless.

To conclude, we note that it is not by accident that the analysis of Balents and Fisher correctly describes the physics of impenetrable particles established in our RPA-type analysis. The prior can actually be interpreted as a renormalization group (RG) analysis in the presence of multiple dynamic, as will be considered in part II. The role of the kinetic coefficients used in part II is in Ref. [33] played by the mass of the particles the second band. As mentioned in Sec. 3.2.2, the Luttinger liquid band can be understood as being at its upper critical dimension, while the quadratic band is below its upper critical dimension. At zero temperature, the RG is thus dominated by processes involving only the second subband, i.e. precisely the ones taken into account by our RPA analysis. The condition $\epsilon \ll 1$ finally simply encodes that the perturbative RG approach used by Balents and Fisher is only valid as long as the Wilson-Fisher fixed point interaction (the interaction in the second subband) is small. As it turns out, this technical limitation does not prevent the ϵ -expansion used by Balents and Fisher to obtain the correct result.

Chapter 4

Two-subband quantum wire above the Lifshitz transition

The square-root singularities of the perturbation theory at $\mu_2 = 0$ can also be regularized by considering a finite positive chemical potential larger than the strong-coupling scale defined in Eq. (3.22), $\mu_2 > E_p$. The ground state then contains a finite density of particles in both subbands. At low temperatures, we can interpret the two-subband Hamiltonian in terms of interacting Tomonaga-Luttinger liquids. We will start by defining the precise model and then proceed by a bosonized analysis. The latter takes into account some more non-perturbative effects than earlier, fermionic studies.³⁰ This does, however, not lead to substantially different results. Before turning to the regime of coupled Luttinger liquids, we shortly comment on the regime of very small but finite chemical potential in the second subband, $0 < \mu_2 < E_p$.

4.1 Small positive chemical potential: $0 < \mu_2 < E_p$

If the chemical potential in the second subband is positive but small, $0 < \mu_2 < E_p$, the physics in this band is still strongly influenced by the physics of impenetrable electrons that emerges for $\mu_2 < 0$, and which controls the quantum phase transition at $\mu_2 = 0$, see Sec. 3.1.2. However, a description in terms of two-particle scattering as given in Sec. 3.5 is clearly insufficient, since the second subband is now populated by a finite density of strongly interacting particles. One may however strongly speculate that the regime $0 < \mu_2 < E_p$ still shares certain similarities with the impenetrable electron gas. In particular, the charge sector might correspond to a spinless Fermi gas, as in the case of an impenetrable electron gas.⁵⁵

If the charge sector is sufficiently close to an impenetrable electron gas state, the physics of the system might be similar to the behavior of a two-subband system of *spinless* fermions. There, one generically finds an instability for small but finite μ_2 because pair-tunneling becomes relevant and leads to the opening of a gap.³⁷ The main reason is that, for the spinless case, the intra-subband interaction of the weakly populated second subband is of order $\mathcal{O}(v_{F2}^2)$ due to the Pauli principle, whereas pair-tunneling is only suppressed by a factor v_{F2} . The (almost local) repulsive interaction in the second subband can not suppress the (almost local) tunneling anymore, and the latter turns marginally relevant. The flow of the pair-tunneling to strong coupling signals the appearance of a gap due to a locking of the relative charge mode. Importantly, for spinless fermions there

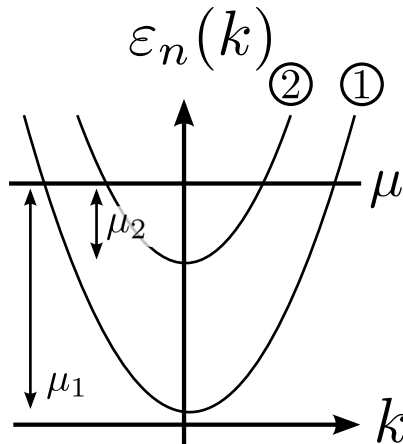


Figure 4.1: The system we investigate: two filled, one-dimensional bands with different respective chemical potentials $\mu_1 \gg \mu_2$.

does not exist any energy scale E_p that limits the range of validity of the perturbative RG. It is not unlikely that a similar kind of relevant pair-tunneling mechanism might be at work in the spinful case as well in the regime $0 < \mu_2 < E_p$ where the physics is already influenced by the impenetrable electron gas fixed-point, maybe giving rise to a gap in the charge sector. Interesting physics could however also occur in the spin sector, which might in some regime correspond to mobile Kondo impurities coupled to a one-dimensional band of spinful fermions. As has been argued by Lamacraft, the latter system may exhibit a two-channel Kondo effect.⁶²

4.2 Analysis of the regime $\mu_2 > E_p$ in terms of coupled Luttinger liquids

In the next sections, we will tackle the regime $\mu_2 > E_p$ by linearizing the dispersions of both bands and modeling them by coupled, interacting Luttinger liquids. We derive this effective model starting from the full quadratic dispersions resulting from the confined two-dimensional electron gas as described in Sec. 3.1, and then distill the effective Luttinger liquid Hamiltonians by bosonization of the fermionic bands. Compared to the previous analysis by Varma and Zawadowski,³⁰ our bosonized approach has the advantage of taking into account density-density interactions in an exact manner, such that only spin-flip and pair tunneling terms need to be treated by a perturbative renormalization group (RG) approach.

The system before bosonization Before turning to the bosonized analysis, we shortly recall the microscopic model Hamiltonian that derives from a confined two-dimensional electron gas, see Eq. (3.4). As discussed, we specialize to the case that the lowest two subbands are activated and partially filled, while all other bands are largely gapped and will consequently be neglected. The interacting fermionic Hamiltonian thus reads

$$\mathcal{H} = \sum_{n,k,\sigma} \left(\frac{k^2}{2m} - \mu_n \right) c_{nk\sigma}^\dagger c_{nk\sigma} + \frac{1}{2} \sum_{\substack{n_1, n_2, n_3, n_4 \\ k, k', q; \sigma, \sigma'}} U_{n_1 n_2 n_3 n_4}(q) c_{n_1 k + q \sigma}^\dagger c_{n_2 k' - q \sigma'}^\dagger c_{n_3 k' \sigma'} c_{n_4 k \sigma}, \quad (4.1)$$

where $n = 1, 2$ labels the lowest two subbands and $c_{nk\sigma}$ annihilates an electron in band n of momentum k and spin σ , while m_n is the effective mass in band n . The free part of the Hamiltonian,

$$\mathcal{H}_0 = H_1^0 + H_2^0 = \sum_{n=1,2} \sum_{k,\sigma} \varepsilon_n(k) c_{nk\sigma}^\dagger c_{nk\sigma} \quad (4.2)$$

$$\varepsilon_n(k) = \left(\frac{k^2}{2m} - \mu_n \right) \quad (4.3)$$

comprises two quadratically dispersing bands of finite filling, $\mu_1, \mu_2 > 0$, while the interaction $U_{n_1 n_2 n_3 n_4}(q)$ microscopically derives from the screened Coulomb repulsion in the two-dimensional electron gas. More precisely, and $U_{n_1 n_2 n_3 n_4}(q)$ denotes the interaction matrix element for electrons from subbands n_i interacting with a momentum transfer q .

4.2.1 Bosonization

As usual, the presence of the interaction $U_{n_1 n_2 n_3 n_4}(q)$ prohibits an exact solution of the full problem (simply because the latter is quartic in the electronic operators). In one dimension, however, the problem can be largely simplified by the Luttinger liquid approach. As discussed in Sec. 2.1, the latter is based on the insight that for bands of finite filling, the relevant degrees of freedom are collective density waves of the entire system rather than excitations of individual particles. These waves may independently modulate the spin and/or charge densities, such that spin and charge degrees of freedom are in principle independent of each other. The extraction of the relevant low energy degrees of freedom, namely the spin and charge density waves (naturally described by bosonic fields) from the underlying fermionic theory is achieved by virtue of the technique of bosonization. In this section, we will proceed along these lines (and with the conventions of Ref. [22]) in order to derive the bosonized version of the Hamiltonian (4.1), which then reduces to two coupled Luttinger liquids. Interactions of density-density type will naturally be quadratic in the new degrees of freedom (which precisely describe density waves). This will allow us to treat these density-density interactions in an exact manner.

As a first step towards the derivation of the bosonized Hamiltonian, we linearize the dispersions of the two bands around the Fermi level. This is always possible, provided that temperature and interactions are small compared to the respective Fermi energies (which sets the characteristic scale for the curvature of the bands). Due to the formation of polarons, the bosonized approach breaks down for $\mu_2 < E_p$ (see Sec. 4.2.3). For $\mu_2 > E_p$, however, the linearization can safely be done, as illustrated in figure 4.2. In the vicinity of the Fermi points, the dispersions $\varepsilon_n(k)$ defined in Eq. (4.3) can be written as

$$\varepsilon_n(k) \stackrel{|k| \approx k_{F_n}}{=} \sum_{k \approx -k_{F_n}} v_{F_n}(k + k_{F_n}) + \sum_{k \approx k_{F_n}} v_{F_n}(k - k_{F_n}), \quad (4.4)$$

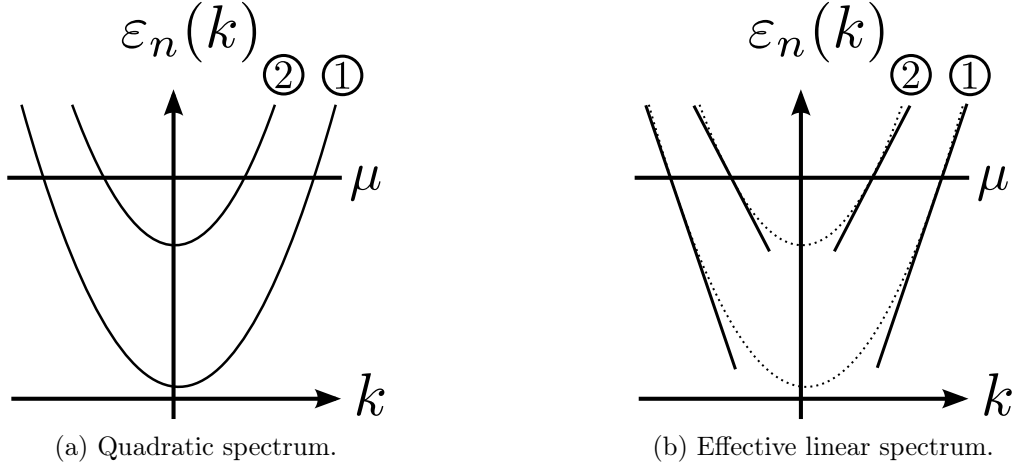


Figure 4.2: Linearization and decomposition of the fermionic spectrum into right and left movers.

where we introduced the Fermi velocities $v_{F_n} = k_{F_n}/m_n$. Since only the physics close to the Fermi points is relevant, it is useful to also decompose the creation and annihilation operators into the Fourier modes close to each of the Fermi points. To be explicit, the operator $c_{n\sigma}(x)$ annihilating an electron in the band n at a position x is decomposed as

$$\begin{aligned}
 c_{n\sigma}(x) &= \frac{1}{\sqrt{L}} \sum_k e^{ikx} c_{nk\sigma} = \frac{1}{\sqrt{L}} \sum_{k < 0} e^{ikx} c_{n,k,\sigma} + \frac{1}{\sqrt{L}} \sum_{k > 0} e^{ikx} c_{n,k,\sigma} \\
 &= e^{-ik_F x} \frac{1}{\sqrt{L}} \sum_{k < k_F} e^{ikx} c_{n,-k_F+k,\sigma} + e^{ik_F x} \frac{1}{\sqrt{L}} \sum_{k > -k_F} e^{ikx} c_{n,k_F+k,\sigma} .
 \end{aligned} \tag{4.5}$$

Here, L denotes the length of the quantum wire. Alluding to their respective direction of motion set by the velocity $\partial\epsilon/\partial k$, the modes close to $-k_F$ are conventionally called left movers, while the modes close to $+k_F$ are named right movers. In order to obtain a more simple theory, the linear dispersions can be continued up to infinite momenta. The right- and left-moving particles then correspond to the new operators

$$c_{nsL}(x) = e^{-ik_F x} \frac{1}{\sqrt{L}} \sum_k e^{ikx} c_{n,-k_F+k,\sigma} \quad \text{and} \quad c_{nsR}(x) = e^{ik_F x} \frac{1}{\sqrt{L}} \sum_k e^{ikx} c_{n,k_F+k,\sigma} . \tag{4.6}$$

Note that we have switched the notation of the spin index from σ to s for later convenience. As a next step, we extract the collective density wave excitations from the individual fermionic particles. Because of their very nature as density waves, these excitations are intrinsically non-local. The local operators $c_{nsj}(x)$, $j = L, R$ for right- and left-movers thus correspond to non-local string operators in terms of the new bosonic fields $\theta_{ns}(x, \tau)$ and $\Phi_{ns}(x, \tau)$ describing the density waves. Using furthermore the so-called Klein fields F_{nsj} , one can express the fermionic operators as

$$c_{nsR}(x, \tau) = F_{nsR} \frac{1}{\sqrt{2\pi\alpha_n}} e^{-i(\Phi_{ns}(x,\tau) - \theta_{ns}(x,\tau))} , \tag{4.7}$$

$$c_{nsL}(x, \tau) = F_{nsL} \frac{1}{\sqrt{2\pi\alpha_n}} e^{i(\Phi_{ns}(x,\tau) + \theta_{ns}(x,\tau))} , \tag{4.8}$$

where α_n is a short distance cut-off (e.g. interatomic distance). As advertised, the new fields $\theta_{ns}(x, \tau)$ and $\Phi_{ns}(x, \tau)$ can be related to the spin and charge densities of band n . In the limit of large system size $L \rightarrow \infty$, they can be expressed in terms of the density ρ_{nsj} of spin $s = \uparrow, \downarrow$ electrons moving in the direction $j = L, R$ in the band $n = 1, 2$ as

$$\frac{\partial}{\partial x} \Phi_{ns}(x, \tau) = -\pi(\rho_{nsR}(x, \tau) + \rho_{nsL}(x, \tau)) , \quad (4.9)$$

$$\frac{\partial}{\partial x} \theta_{ns}(x, \tau) = \pi(\rho_{nsR}(x, \tau) - \rho_{nsL}(x, \tau)) . \quad (4.10)$$

By inspection, we conclude that Φ_{ns} is linked to the total (charge) density of electrons of spin s charge density in the lead n , whereas θ_{ns} relates to the spin s current in this lead. In addition, the new bosonic fields describing position and motion of the electronic densities form a canonical basis of the system similar to momentum and position variables. As can be checked by a straight-forward calculation, they obey the commutation relation

$$[\Phi_{ns}(x_1), \theta_{n's'}(x_2)] = \delta_{n,n'} \delta_{s,s'} i \frac{\pi}{2} \text{sgn}(x_2 - x_1) . \quad (4.11)$$

In the continuum limit $L \rightarrow \infty$ and then $\alpha_n \rightarrow 0$, this yields

$$[\Phi_{ns}(x_1), \nabla \theta_{n's'}(x_2)] = \delta_{n,n'} \delta_{s,s'} i \pi \delta(x_2 - x_1) , \quad (4.12)$$

which is indeed the canonical bosonic commutation relation. Further details of these calculations may be found in Ref. [22].

4.2.2 A first bosonized form of the two-subband Hamiltonian

Whilst bosonizing the Hamiltonian (4.1), we find it useful to first redefine the bosonic fields such that they explicitly and separately describe spin and charge degrees of freedom in each of the bands. This is achieved by the fields

$$\Phi_{n\rho}(x, \tau) = \frac{1}{\sqrt{2}}(\Phi_{n\uparrow}(x, \tau) + \Phi_{n\downarrow}(x, \tau)) \sim \text{integrated charge density in the lead } n, \quad (4.13a)$$

$$\Phi_{n\sigma}(x, \tau) = \frac{1}{\sqrt{2}}(\Phi_{n\uparrow}(x, \tau) - \Phi_{n\downarrow}(x, \tau)) \sim \text{integrated spin density in the lead } n, \quad (4.13b)$$

$$\theta_{n\rho}(x, \tau) = \frac{1}{\sqrt{2}}(\theta_{n\uparrow}(x, \tau) + \theta_{n\downarrow}(x, \tau)) \sim \text{integrated charge current in the lead } n, \quad (4.13c)$$

$$\theta_{n\sigma}(x, \tau) = \frac{1}{\sqrt{2}}(\theta_{n\uparrow}(x, \tau) - \theta_{n\downarrow}(x, \tau)) \sim \text{integrated spin current in the lead } n, \quad (4.13d)$$

which again obey canonical commutation relations. Before coupling the two bands, we first bosonize the interactions within each of the bands using the new degrees of freedom in Eq. (4.13) and plugging them into the definition of the right- and left-moving fields, see Eq. (4.6). Per band, the general interaction $U_{n_1 n_2 n_3 n_4}(q)$ yields three relevant types

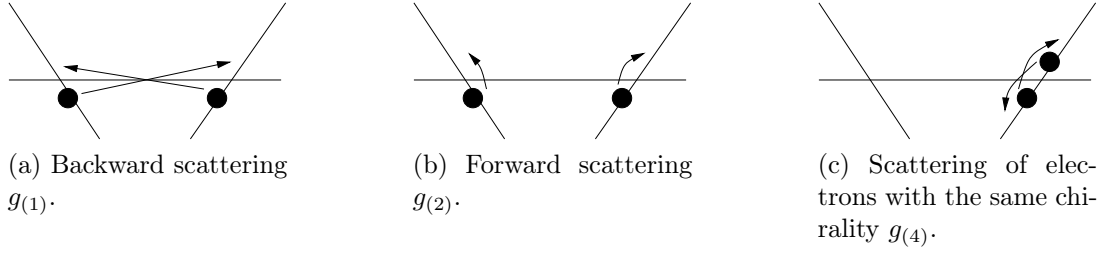


Figure 4.3: The different intraband scattering processes taken into account.

of scattering processes for the right- and left-moving fields depicted in Fig. 4.3. These processes correspond to backward scattering, dispersion and forward scattering. We note that spin umklapp scattering events are forbidden by the global momentum conservation since we do not consider half-filled bands. Different to the last chapter, we denote the interaction constants in standard notation for Luttinger liquids.²² They read

$$g_{n(1)} \quad \text{for backward scattering in subband } n \text{ (opposite chiralities),} \quad (4.14)$$

$$g_{n(2)} \quad \text{for forward scattering in subband } n \text{ (opposite chiralities),} \quad (4.15)$$

$$g_{n(4)} \quad \text{for scattering of electrons in subband } n \text{ with the same chirality.} \quad (4.16)$$

Furthermore, we distinguish scattering events involving two electrons of parallel and antiparallel spin by introducing $g_{n\parallel(j)}$ and $g_{n\perp(j)}$, respectively. We can then combine $g_{n\parallel(1)}$ and $g_{n\parallel(2)}$ into a new coupling constant

$$g_{n\parallel} = g_{n\parallel(2)} - g_{n\parallel(1)} \quad (4.17)$$

because they correspond to the same scattering process. These coupling constants are related to the ones considered before (see Eq. (3.12)) by

$$g_{n\parallel} = g_{nc} - g_{ns}/4, \quad (4.18a)$$

$$g_{n\perp(1)} = g_{ns}/2, \quad (4.18b)$$

$$g_{n\perp(2)} = g_{nc} + g_{ns}/4, \quad (4.18c)$$

where the interactions in the second band read

$$g_{2c} = U_{2222}(0) - \frac{U_{2222}(2k_{F2})}{2} \approx \frac{V}{2}, \quad g_{2s} = 2U_{2222}(2k_{F2}) \approx 2V, \quad (4.19)$$

and where the approximate values of these new coupling constants in terms of the interaction V in the first band are correct up to logarithmic corrections, and become better the smaller k_{F2} is. Note that the process g_{n4} had been dropped in chapter 2. Although it is in principle equally unimportant than before (since it does not lead to singular corrections), we can take it into account exactly, and thus do so. The Luttinger liquid Hamiltonians are obtained following the standard procedure of bosonization (see again Ref. [22]). We note that Eqs. (4.18) imply

$$g_{n\parallel} = g_{n\perp(2)} - g_{n\perp(1)}, \quad (4.20)$$

which has to be fulfilled in a spin-rotation invariant system. All intraband interactions, except for spin-flip terms, can be written as density-density interactions and are thus quadratic in the new fields. Collecting all of these terms, one obtains the so-called Luttinger parameters $K_{\mu,i}$ and the effective propagation velocities of the bosonic excitations $u_{\mu,i}$ defined by

$$u_{\rho,n} = v_{F_n} \sqrt{\left(1 + \frac{g_{n\parallel(4)} + g_{n\perp(4)}}{2\pi v_{F_n}}\right)^2 - \left(\frac{g_{n\parallel} + g_{n\perp(2)}}{2\pi v_{F_n}}\right)^2}, \quad (4.21)$$

$$K_{\rho,n} = \sqrt{\frac{1 + \frac{g_{n\parallel(4)} + g_{n\perp(4)}}{2\pi v_{F_n}} - \frac{g_{n\parallel} + g_{n\perp(2)}}{2\pi v_{F_n}}}{1 + \frac{g_{n\parallel(4)} + g_{n\perp(4)}}{2\pi v_{F_n}} + \frac{g_{n\parallel} + g_{n\perp(2)}}{2\pi v_{F_n}}}}, \quad (4.22)$$

$$u_{\sigma,n} = v_{F_n} \sqrt{\left(1 + \frac{g_{n\parallel(4)} - g_{n\perp(4)}}{2\pi v_{F_n}}\right)^2 - \left(\frac{g_{n\parallel} - g_{n\perp(2)}}{2\pi v_{F_n}}\right)^2}, \quad (4.23)$$

$$K_{\sigma,n} = \sqrt{\frac{1 + \frac{g_{n\parallel(4)} - g_{n\perp(4)}}{2\pi v_{F_n}} - \frac{g_{n\parallel} - g_{n\perp(2)}}{2\pi v_{F_n}}}{1 + \frac{g_{n\parallel(4)} - g_{n\perp(4)}}{2\pi v_{F_n}} + \frac{g_{n\parallel} - g_{n\perp(2)}}{2\pi v_{F_n}}}}. \quad (4.24)$$

The two bands are then described by

$$\mathcal{H} = \sum_{n=1,2} (\mathcal{H}_{\rho,n}^0 + \mathcal{H}_{\sigma,n}^0 + \mathcal{H}_{\sigma,n}^1) + \mathcal{H}_{12}, \quad (4.25)$$

$$\mathcal{H}_{\rho,n}^0 = \frac{1}{2\pi} \int dx \left(u_{\rho,n} K_{\rho,n} \left(\frac{\partial}{\partial x} \theta_{\rho,n} \right)^2 + \frac{u_{\rho,n}}{K_{\rho,n}} \left(\frac{\partial}{\partial x} \Phi_{\rho,n} \right)^2 \right), \quad (4.26)$$

$$\mathcal{H}_{\sigma,n}^0 = \frac{1}{2\pi} \int dx \left(u_{\sigma,n} K_{\sigma,n} \left(\frac{\partial}{\partial x} \theta_{\sigma,n} \right)^2 + \frac{u_{\sigma,n}}{K_{\sigma,n}} \left(\frac{\partial}{\partial x} \Phi_{\sigma,n} \right)^2 \right), \quad (4.27)$$

$$\mathcal{H}_{\sigma,n}^1 = \frac{g_{1,n\perp}}{(2\pi\alpha_j)^2} \int dx \left(F_{\uparrow,L,n}^\dagger F_{\downarrow,R,n}^\dagger F_{\downarrow,L,n} F_{\uparrow,R,n} e^{-i\sqrt{8}\Phi_{\sigma,n}} + \text{h.c.} \right). \quad (4.28)$$

We finally consider the interaction between the subbands. Besides a charge density interaction and spin density interaction, we also take into account pair tunneling terms. This way, the interband interactions can be written as

$$\mathcal{H}_{12} = \mathcal{H}_{12c}^0 + \mathcal{H}_{12s}^0 + \mathcal{H}_{12s}^1 + \mathcal{H}_{12t}, \quad (4.29)$$

where the interactions in terms of the bosonic fields are given by

$$\mathcal{H}_{12c}^0 = \frac{1}{2\pi} \frac{4u_c}{\pi} \int dx \left(\frac{\partial}{\partial x} \Phi_{\rho,1} \right) \left(\frac{\partial}{\partial x} \Phi_{\rho,2} \right), \quad (4.30)$$

$$\mathcal{H}_{12s}^0 = -\frac{1}{2\pi} \frac{u_s}{\pi} \int dx \left(\frac{\partial}{\partial x} \Phi_{\sigma,1} \right) \left(\frac{\partial}{\partial x} \Phi_{\sigma,2} \right), \quad (4.31)$$

$$\begin{aligned} \mathcal{H}_{12s}^1 = & -\frac{u_s}{2} \frac{1}{(2\pi)^2 \alpha_1 \alpha_2} \int dx \left\{ \left(F_{\uparrow,R,1}^\dagger F_{\downarrow,R,1}^\dagger e^{i\sqrt{2}(\Phi_{\sigma,1} - \theta_{\sigma,1})} + F_{\uparrow,L,1}^\dagger F_{\downarrow,L,1}^\dagger e^{-i\sqrt{2}(\Phi_{\sigma,1} + \theta_{\sigma,1})} \right) \right. \\ & \left. \times \left(F_{\downarrow,R,2}^\dagger F_{\uparrow,R,2}^\dagger e^{-i\sqrt{2}(\Phi_{\sigma,2} - \theta_{\sigma,2})} + F_{\downarrow,L,2}^\dagger F_{\uparrow,L,2}^\dagger e^{i\sqrt{2}(\Phi_{\sigma,2} + \theta_{\sigma,2})} \right) + \text{h.c.} \right\}, \quad (4.32) \end{aligned}$$

and \mathcal{H}_{12t} denotes the pair tunneling, detailed in appendix B.8. Besides the tunneling amplitudes for opposite spins with and without spin-flip, $g_{t\perp(1)}$ and $g_{t\perp(2)}$, the tunneling Hamiltonian \mathcal{H}_{12t} now also contains a tunnel coupling for pairs of equal spin, $g_{t\parallel}$. Different to chapter 2, where the low energy excitations only lived around a single momentum $k \approx 0$, the presence of two distinct Fermi points now allows a local pair tunneling term of particles with equal spin but opposite chirality. Spin-rotation invariance however ensures that there are only two independent tunneling amplitudes, as $g_{t\parallel} = g_{t\perp(2)} - g_{t\perp(1)}$. We note that the Hamiltonian remains almost spin-charge separated despite the presence of the various interactions. Only the tunneling spoils the spin-charge separation because it transfers both the charge and the spin of the electron from one band to the other, see Sec. B.8.

4.2.3 Polaron effect

The bosonized Hamiltonian (4.25) still contains quadratic terms that stem from the spin and charge density interactions between the two subbands. These terms can of course be taken into account exactly by an appropriate basis transformation. Only the terms $\mathcal{H}_{\sigma,n}^1$, \mathcal{H}_{12s}^1 and the pair tunneling have to be treated perturbatively, and have a form commonly referred to as ‘‘cosine-terms’’ (an evident notion if the Klein factors are dropped and the exponentials regrouped). The quadratic part of the Hamiltonian

$$\mathcal{H}^0 = \sum_n (\mathcal{H}_{\rho,n}^0 + \mathcal{H}_{\sigma,n}^0) + \mathcal{H}_{12c}^0 + \mathcal{H}_{12s}^0, \quad (4.33)$$

can be diagonalized by a unitary basis transformation. This diagonalization can most conveniently be performed by first transforming the fields to

$$\theta_{\mu,n} \rightarrow \theta'_{\mu,n} = \sqrt{u_{\mu,n} K_{\mu,n}} \theta_{\mu,n}, \quad (4.34a)$$

$$\Phi_{\mu,n} \rightarrow \Phi'_{\mu,n} = 1/(\sqrt{u_{\mu,n} K_{\mu,n}}) \Phi_{\mu,n} \quad (4.34b)$$

$$(4.34c)$$

(with $\mu = \rho, \sigma$, note that this transformation conserves the canonical commutation relations for the fields $\theta'_{\mu,n}$ and $\Phi'_{\mu,n}$). Next, we rewrite the Hamiltonian in terms of 2×2 -matrices, one matrix describing the θ -sector, and one matrix for the Φ -sector, while the 2×2 -structure comprises the two bands. The transformation (4.34) then reduces the θ -sector of the Hamiltonian to an identity matrix. The Φ -sector can now be diagonalized by a straightforward diagonalization. Of course, the θ -fields have to be transformed accordingly in order to preserve the canonical commutation relations, which however does not affect the Hamiltonian any further because the θ -sector is an identity. The final new eigenfields are (again using $\mu = \rho, \sigma$)

$$\Phi_\mu^+ = \sqrt{\frac{u_\mu^+ K_\mu^+}{1 + a_\mu^2}} \left(\frac{1}{\sqrt{u_{\mu,1} K_{\mu,1}}} \Phi_{\mu,1} + \frac{a_\mu}{\sqrt{u_{\mu,2} K_{\mu,2}}} \Phi_{\mu,2} \right), \quad (4.35)$$

$$\Phi_\mu^- = \sqrt{\frac{u_\mu^- K_\mu^-}{1 + a_\mu^2}} \left(\frac{a_\mu}{\sqrt{u_{\mu,1} K_{\mu,1}}} \Phi_{\mu,1} - \frac{1}{\sqrt{u_{\mu,2} K_{\mu,2}}} \Phi_{\mu,2} \right), \quad (4.36)$$

$$\theta_\mu^+ = \sqrt{\frac{1}{u_\mu^+ K_\mu^+ (1 + a_\mu^2)}} \left(\sqrt{u_{\mu,1} K_{\mu,1}} \theta_{\mu,1} + a_\mu \sqrt{u_{\mu,2} K_{\mu,2}} \theta_{\mu,2} \right), \quad (4.37)$$

$$\theta_\mu^- = \sqrt{\frac{1}{u_\mu^- K_\mu^- (1 + a_\mu^2)}} \left(a_\mu \sqrt{u_{\mu,1} K_{\mu,1}} \theta_{\mu,1} - \sqrt{u_{\mu,2} K_{\mu,2}} \theta_{\mu,2} \right). \quad (4.38)$$

The new velocities and Luttinger parameters are

$$u_\mu^\pm = \sqrt{\frac{u_{\mu,1}^2 + u_{\mu,2}^2}{2} \pm \sqrt{\left(\frac{u_{\mu,1}^2 - u_{\mu,2}^2}{2}\right)^2 + \left(\frac{V_\mu}{2\pi}\right)^2 u_{\mu,1} u_{\mu,2} K_{\mu,1} K_{\mu,2}}}, \quad (4.39)$$

$$K_\mu^\pm = 1, \quad (4.40)$$

and the basis transformation introduces factors of

$$a_\mu = \frac{\frac{V_\mu}{\pi} \sqrt{\frac{K_{\mu,1} K_{\mu,2}}{u_{\mu,1} u_{\mu,2}}}}{\sqrt{\left(\frac{u_{\mu,1}}{u_{\mu,2}} - \frac{u_{\mu,2}}{u_{\mu,1}}\right)^2 + \left(\frac{V_\mu}{\pi}\right)^2 \frac{K_{\mu,1} K_{\mu,2}}{u_{\mu,1} u_{\mu,2}} + \frac{u_{\mu,1}}{u_{\mu,2}} - \frac{u_{\mu,2}}{u_{\mu,1}}}}, \quad (4.41)$$

and where V_μ denotes the corresponding coupling constant,

$$V_\sigma = -u_s, \quad V_\rho = 4u_c. \quad (4.42)$$

By virtue of this transformation, all density-density interactions of the system, including both intra- and inter-band interactions, are taken into account exactly in the quadratic part of the Hamiltonian, which takes the diagonal form

$$\begin{aligned} \mathcal{H}_{\text{diag}} = & \frac{1}{2\pi} \int dx \left(u_\rho^+ K_\rho^+ \left(\frac{\partial}{\partial x} \theta_\rho^+ \right)^2 + \frac{u_\rho^+}{K_\rho^+} \left(\frac{\partial}{\partial x} \Phi_\rho^+ \right)^2 + u_\rho^- K_\rho^- \left(\frac{\partial}{\partial x} \theta_\rho^- \right)^2 + \frac{u_\rho^-}{K_\rho^-} \left(\frac{\partial}{\partial x} \Phi_\rho^- \right)^2 \right), \\ & (4.43) \\ & + \frac{1}{2\pi} \int dx \left(u_\sigma^+ K_\sigma^+ \left(\frac{\partial}{\partial x} \theta_\sigma^+ \right)^2 + \frac{u_\sigma^+}{K_\sigma^+} \left(\frac{\partial}{\partial x} \Phi_\sigma^+ \right)^2 + u_\sigma^- K_\sigma^- \left(\frac{\partial}{\partial x} \theta_\sigma^- \right)^2 + \frac{u_\sigma^-}{K_\sigma^-} \left(\frac{\partial}{\partial x} \Phi_\sigma^- \right)^2 \right). \end{aligned}$$

Unfortunately, this transformation is not well-defined in the limit $v_{F2} \ll v_{F1}$. The velocities u_ρ^- and u_σ^- tend to 0 upon approaching the Lifshitz transition from above, and vanish before the transition is reached if the spin and charge velocities in the second band are smaller than

$$u_{\sigma,2}^c = \left(\frac{u_s}{2\pi} \right)^2 \frac{K_{\sigma,1} K_{\sigma,2}}{u_{\sigma,1}}, \quad (4.44a)$$

$$u_{\rho,2}^c = \left(\frac{4u_c}{2\pi} \right)^2 \frac{K_{\rho,1} K_{\rho,2}}{u_{\rho,1}}. \quad (4.44b)$$

On physical grounds, the appearance of this singularity is not too surprising, keeping in mind the discussion of Sec. 3.5. The two subbands have very different Fermi velocities, $v_{F1} \gg v_{F2}$, which allows for the fast density waves in the lower subband to adiabatically screen the slow excitations in the upper band. This upper subband is thus filled with a Luttinger liquid of polarons rather than regular electrons. The fact that we have so far used the wrong degrees of freedom is mathematically reflected in the above singularity. In the next section, we show how the latter can be avoided by transforming to the correct degrees of freedom which take the polaron effect into account.

4.3 Transformation to polarons

The transformation to polaronic degrees of freedom has already been used in Ref. [61] in order to describe two subbands interacting only via charge density interaction. We will now generalize this transformation to our case of multiple interband interactions and spinful electrons. Since we want to capture the formation of polarons in the second subband due to its coupling to density waves, our starting point is a Hamiltonian that already described the first band in the correct basis, namely as a Luttinger liquid, while the second band is still expressed in terms of fermionic degrees of freedom. It reads

$$\mathcal{H} = \mathcal{H}_1 + \mathcal{H}_2 + \mathcal{H}_{12,marg} + \mathcal{H}'_{12} , \quad (4.45)$$

where, as explained, the first band is described by the standard Luttinger liquid Hamiltonian,

$$\begin{aligned} \mathcal{H}_1 = & \frac{1}{2\pi} \int dx \left(u_\rho^{(1)} K_\rho^{(1)} (\partial_x \theta_\rho^{(1)}(x))^2 + \frac{u_\rho^{(1)}}{K_\rho^{(1)}} (\partial_x \phi_\rho^{(1)}(x))^2 \right) \\ & + \frac{1}{2\pi} \int dx \left(u_\sigma^{(1)} K_\sigma^{(1)} (\partial_x \theta_\sigma^{(1)}(x))^2 + \frac{u_\sigma^{(1)}}{K_\sigma^{(1)}} (\partial_x \phi_\sigma^{(1)}(x))^2 \right) \\ & + \mathcal{H}_1^{\text{spin-flip}} , \end{aligned} \quad (4.46)$$

where $\mathcal{H}_1^{\text{spin-flip}}$ denotes spin-flip terms within the first band. The density-density part of the interband interaction is denoted by

$$\mathcal{H}_{12,marg} = u_c \int dx \left(-\frac{\sqrt{2}}{\pi} \right) (\partial_x \phi_\rho^{(1)}) (\rho_{2\uparrow} + \rho_{2\downarrow}) - \frac{u_s}{2} \int dx \left(-\frac{\sqrt{2}}{\pi} \right) (\partial_x \phi_\sigma^{(1)}) (\rho_{2\uparrow} - \rho_{2\downarrow}) , \quad (4.47)$$

while all other interband interactions are comprised in \mathcal{H}'_{12} . A more explicit form of the Hamiltonian is found in appendix B.7. The transformation to polarons is now achieved by shifting the fields in the lower subband as

$$\phi_\rho^{(1)'}(x) = \phi_\rho^{(1)} + \sqrt{2} \frac{K_\rho^{(1)}}{u_\rho^{(1)}} u_c \int_x^\infty dx' (\rho_{2\uparrow}(x') + \rho_{2\downarrow}(x')) , \quad (4.48)$$

$$\theta_\rho^{(1)'}(x) = \theta_\rho^{(1)}(x) , \quad (4.49)$$

$$\phi_\sigma^{(1)'}(x) = \phi_\sigma^{(1)}(x) - \sqrt{2} \frac{K_\sigma^{(1)}}{u_\sigma^{(1)}} \frac{u_s}{4} \int_x^\infty dx' (\rho_{2\uparrow}(x') - \rho_{2\downarrow}(x')) , \quad (4.50)$$

$$\theta_\sigma^{(1)'}(x) = \theta_\sigma^{(1)}(x) . \quad (4.51)$$

In order to preserve the canonical commutation relations with the second subband, its fermionic operators also have to be shifted as

$$c'_{2\uparrow}(x) = e^{i\frac{1}{\pi}(\gamma_\rho\theta_\rho(x)+\gamma_\sigma\theta_\sigma(x))} c_{2\uparrow}(x) , \quad (4.52)$$

$$c'_{2\downarrow}(x) = e^{i\frac{1}{\pi}(\gamma_\rho\theta_\rho(x)-\gamma_\sigma\theta_\sigma(x))} c_{2\downarrow}(x) , \quad (4.53)$$

with

$$\gamma_\rho = -\sqrt{2} \frac{K_\rho^{(1)}}{u_\rho^{(1)}} u_c \quad \text{and} \quad \gamma_\sigma = \sqrt{2} \frac{K_\sigma^{(1)}}{u_\sigma^{(1)}} \frac{u_s}{4} . \quad (4.54)$$

This transformation eliminates $\mathcal{H}_{12,marg}$ at the expense of introducing a residual interaction. The residual interaction contains a quadratic term that stems from the shift of the operators $c_{2\sigma}$ and some new terms which are cubic in the operators and quadratic in u_c and u_s , and thus irrelevant in the RG sense. A more explicit version of the polaron transformation can be found in appendix B.7.

4.3.1 Final form of the Hamiltonian

Having switched to the correct degrees of freedom leads us to the final form of the Hamiltonian. We proceed by bosonizing the second subband (which now contains polarons). This is done in complete analogy to the first band's bosonization, see Sec. 4.2.1. In addition, we focus on the most relevant interactions, and thus only contain terms that couple right-movers to left-movers. As shown in appendix B.8.1, we can then diagonalize the remaining quadratic part of the residual interaction and obtain the final Hamiltonian. Thanks to the framework of bosonization, the latter contains all density-density interactions between the two bands in an exact manner. In addition, it describes the system in terms of coupled, polaronic Luttinger liquids. The only remaining couplings that could not have been taken into account exactly correspond to ‘‘cosine-terms’’ in the Luttinger liquid language, and correspond to spin-flip interactions within each band and between the bands (and the irrelevant, higher order terms of the residual interactions). As discussed in appendix B.8.2, these new degrees of freedom do indeed not exhibit a singularity anymore. For the sake of readability, the full Hamiltonian is only shown in appendix B.8.1.

4.4 Renormalization group analysis

Having derived the Luttinger liquid Hamiltonian, we can finally analyze the effect of the remaining non-diagonal couplings by means of a renormalization group (RG) approach.

We base the RG on the renormalization of the free energy, which is defined as

$$F = -T \ln(Z) \quad \text{with} \quad Z = \int d\Phi d\theta e^{-\mathcal{S}}, \quad (4.55)$$

where T is the temperature of the system. The partition function is expanded perturbatively as

$$Z = \int d\Phi d\theta e^{-\mathcal{S}} \quad (4.56)$$

$$\approx \int d\Phi d\theta e^{-\mathcal{S}_0} (1 - \mathcal{S}_{int}), \quad (4.57)$$

where we have split the action into the diagonal part \mathcal{S}_0 and all other, cosine-type terms, \mathcal{S}_{int} . The RG equations for the coupling constants are now derived by subsequently integrating out high energy shells. The re-exponentiation of the average $\langle \mathcal{S}_{int} \rangle_{\mathcal{S}_0}$ then yields the renormalization of the different coupling constants. This procedure is further detailed in appendix B.9. This treatment is, admittedly, not complete. Our bosonized formulation does take into account all density-density interactions in a non-perturbative way, and their effects are contained in the Luttinger liquid parameters and effective velocities. In order to capture the renormalization of these parameters, we would have to extend the RG analysis to second order. Even more so, the bosonized first order perturbation theory can only capture the self-renormalization of the remaining cosine-type interactions (i.e. $\partial X / \partial \ln b \sim X$), and thus even misses further diagrams of the second order renormalization in fermionic language. However, already the first order renormalization of the cosine-type terms, which will be studied in the following, shows that we obtain results similar to the ones derived by a purely fermionic treatment in Ref. [30], and that we in particular do not obtain any instabilities for the case of a quantum wire defined in a two-dimensional electron gas. Since already the first order RG equations are more than lengthy and tedious, and since we would not obtain new results, we refrain from going to second order in perturbation theory.

Our results for the full RG equations to first order perturbation theory are detailed in appendix B.10. These equations are in perfect agreement with the results of Varma and Zawadowski, see Ref. [30], as we show in appendix B.11. In order to make contact to our calculations in the previous chapter, we want to analyze the leading terms in the RG equations for low filling of the second subband, $v_{F_2} \ll v_{F_1}$. In this limit, the leading terms in the RG analysis are enhanced by a factor of v_{F_1}/v_{F_2} with respect to all other terms. Using the identifications (see Eq. (4.18))

$$g_{n\perp(1)} = g_{ns}/2, \quad (4.58)$$

$$g_{n\perp(2)} = g_{nc} + g_{ns}/4, \quad (4.59)$$

and the fact that spin-rotation invariance implies $g_{t\parallel} = g_{t\perp(2)} - g_{t\perp(1)}$ (which also remains true under RG and allows us to drop the RG equation for $g_{t\parallel}$, see Eq. (B.104)), we can extract the leading order RG terms from appendix B.11. We stress that we use the equations derived by Varma and Zawadowski in Ref. [30] rather than the bosonized equations, since the latter has to miss some terms of the full second order perturbation theory in fermionic language, see the discussion at the beginning of this section and appendix B.11. In the limit $v_{F_2} \ll v_{F_1}$, we find

$$\frac{dg_{1s}}{d \ln b} = -\frac{2}{\pi v_{F_2}} g_{t\perp(2)} g_{t\perp(1)} , \quad (4.60a)$$

$$\frac{dg_{2s}}{d \ln b} = -\frac{1}{2\pi v_{F_2}} g_{2s}^2 , \quad (4.60b)$$

$$\frac{dg_{t\perp(1)}}{d \ln b} = -\frac{1}{2\pi v_{F_2}} (g_{2c} + g_{2s}/4) g_{t\perp(1)} - \frac{1}{4\pi v_{F_2}} g_{2s} g_{t\perp(2)} , \quad (4.60c)$$

$$\frac{dg_{t\perp(2)}}{d \ln b} = -\frac{1}{2\pi v_{F_2}} (g_{2c} + g_{2s}/4) g_{t\perp(2)} - \frac{1}{4\pi v_{F_2}} g_{2s} g_{t\perp(1)} . \quad (4.60d)$$

The perturbative treatment is controlled as long as all terms on the right hand side of Eqs. (4.60) are smaller than the coupling constants they renormalize. For the parameters of our model, Eqs. (3.30), the largest term is $\sim g_{2s}^2/v_{F_2}$ in Eq. (4.60b). Thus, we obtain the condition $g_{2s}/v_{F_2} \ll 1$ or, equivalently, $\mu_2 \gg E_p$ with the strong-coupling energy scale $E_p = mV^2$ of Eq. (3.22), which is precisely the regime we are working in.

The solution of these RG equations is detailed in appendix B.12. We find that the flow for $E_{F_1} \gg \mu_2 \gg E_p$ shares similarities with the one obtained at large negative chemical potential $|\mu_2| \gg E_p$ in section 3.4 and the one for $-E_p < \mu_2 < 0$ in section 3.5, but with the role of the two subbands partially reversed. Now, the interaction of the second subband decouples, while the tunneling is still reduced by the interactions in the second subband. All of these couplings are thus driven to weak coupling. While the interaction g_{2s} only has a logarithmic flow, the tunnel couplings $g_{t\perp(1)}$ and $g_{t\perp(2)}$ decrease as power laws (with logarithmic corrections). The flow of g_{1s} , determined by the tunneling, is thus rather short and only yields a finite renormalization of the coupling constant. To logarithmic accuracy, the effective coupling is obtained in appendix B.12 as

$$g_{1s}^{\text{eff}} \approx g_{1s} - 2 \frac{g_{t\perp(1)} g_{t\perp(2)}}{g_{2c}} . \quad (4.61)$$

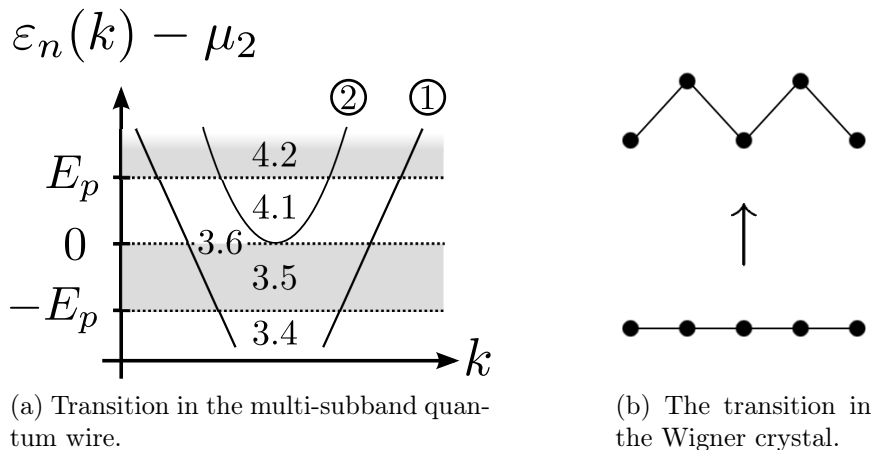
Using the identification $g_{t\perp(1)} = g_{t\perp(2)} = u_t$ valid for $\mu_2 \rightarrow 0$ and $g_{2c} = V/2$, see Eq. (4.19), we obtain

$$g_{1s}^{\text{eff}} \approx g_{1s} - 4 \frac{u_t^2}{V} . \quad (4.62)$$

As in chapter 2, the value of g_{1s}^{eff} determines the fate of the subsequent flow governed by terms that are not enhanced by a factor of v_{F_1}/v_{F_2} . While for positive g_{1s}^{eff} , the flow is towards weak coupling, one obtains a run-away flow for negative g_{1s}^{eff} . This signals the opening of a gap in the spin sector of the first band. The coupling changes sign if

$$u_t^2/(V g_{1s}) > \mathcal{O}(1) , \quad (4.63)$$

so that we again reproduce the instability criterion (3.54). In principle, the corrections to the RG flow due to terms that are not enhanced by $v_{F_2}^{-1}$ could induce other instabilities. The pair-tunneling, that is irrelevant during the initial flow (4.60), also renormalizes the charge coupling g_{2c} and could drive it attractive (as can be found by inspection of Ref. [30]). This renormalization however is always weaker than the one obtained for g_{1s} by a factor of v_{F_2}/v_{F_1} . Since both interactions are initially of the same order, $g_{2c}, g_{2s} \sim \mathcal{O}(V)$, the interaction g_{2c} is much more stable against a run-away flow than g_{1s} . Thus, we conclude that in the regime $\mu_2 > E_p$ the ground state of two Luttinger liquids in the two subbands is stable.



(a) Transition in the multi-subband quantum wire.

(b) The transition in the Wigner crystal.

Figure 4.4: Subfigure (a): different regimes of the multi-subband quantum wire close to the activation of the second subband, $\mu_2 = 0$. The figures indicates which sections treats what regime. Subfigure (b) depicts the corresponding transition in the Wigner crystal regime, which is discussed in Sec. 2.4.

4.5 Summary: Lifshitz transition in quantum wires

Within the last two chapters, we have analyzed the behavior of a quantum wire close to the Lifshitz transition $\mu_2 = 0$ where its second subband gets activated. The problem is in principle complicated by the presence of multiple dynamical scales, characterized by dynamical exponents $z = 1$ and $z = 2$ for the two subbands at and below the transition, $\mu_2 \leq 0$, and largely different Fermi velocities $v_{F2} \ll v_{F1}$ above the transition. The different dynamics however allowed us to distinguish between the leading and subleading interaction effects, and eventually lead to a consistent picture of the transition. As the key result, we found one single criterion for possible instabilities in all regimes indicate in Fig. 4.4a. From there, we could conclude that a quantum wire defined in a two-dimensional GaAs/GaAlAs-electron gas is subject to strong correlation effects (such as the formation of a gas of impenetrable polarons at the bottom of the second band), but does not exhibit an instability at the transition point, $\mu_2 = 0$. Hubbard-like systems, on the other hand, may exhibit instabilities (as was found in Ref. [33]). Only the limit of small, positive chemical potential in the second subband was outside the scope of our analysis.

As mentioned, our calculations made massive use of the fact that the two bands are governed by very different dynamics. Close to the transition, the first subband is a standard Luttinger liquid, while the second band is characterized by a quadratic dispersion. The van Hove singularity at the bottom of the second band renders scattering events there particularly important. In the limit $\mu_2 \rightarrow 0^-$, the second subband is however only very weakly populated. Its physics can thus be described by an effective two-particle problem, which is exactly solvable. Interaction effects due to the first, Luttinger liquid type band, could finally be viewed as a secondary effect. The exact solvability of the leading interactions effects constitutes the main difference to other quantum phase transitions involving multiple dynamics, such as Pomeranchuk instabilities in metals, see part II. There, all interaction effects have to be treated perturbatively and simultaneously, which demands for elaborate RG schemes.⁵³

Summing up the main steps of our analysis, we have first addressed the limit of

largely negative μ_2 , where the second subband is essentially empty. In this case, the large chemical potential μ_2 punished all scattering events involving (virtually excited) particles in the second subband. The corresponding perturbation theory is thus non-divergent. The system can thus be understood as essentially comprising only the first band. Close to the transition, however, fluctuations involving the second subband even yield the dominant renormalizations of the theory. Besides the quantum critical argument, this may also be understood by remembering the divergent density of states at the bottom of the second subband, which boosts interaction effects there.

For $\mu_2 \rightarrow 0^-$, i.e. close to the transition but with a yet unfilled second subband, we found that the latter can be viewed as an effectively infinitely repulsive, dilute gas of particles. This regime is consequently dubbed an “impenetrable gas” in the literature. The strong repulsion leads to a suppression of the pair tunneling between the two bands, which in leading approximation is local and thus wants to put two particles on the same spot. The effectively perturbatively small tunneling does however yield a finite and attractive renormalization of the interactions in the first subband, which can be understood similarly to tight-binding spin exchange terms. In case two particles in the first subband get close to each other, they may gain kinetic energy by virtually hopping to the second band and back (with an amplitude u_t). The intermediate state is however punished by the interaction V in the second subband. This gives rise to an attractive correction (remember that the tunneling is local and thus wants to particles to get close to each other), which reads

$$\delta g_{1x} = -\frac{u_t^2}{V} \quad \Rightarrow \quad g_{1x}^{\text{eff}} = g_{1x} - \frac{u_t^2}{V}, \quad (4.64)$$

where g_{1x} is a short-hand notation for the interactions in the first subband. Only if this finite shift is strong enough to drive one of the interactions in the first subband attractive, instabilities occur. These happen first in the spin sector of the first subband, but the flow to strong coupling of g_{1s} should trigger further instabilities, such as effective pair formation in the second subband.³³ While for Hubbard systems, where all interactions are of the order of the Hubbard- U , instabilities should generically occur, quantum wires do not exhibit instabilities, since the pair tunneling is too small there.

Although no instabilities are associated with the activation of the second band in a quantum wire in GaAs/GaAlAs-heterostructures, we find that the interactions between the bands lead to the emergence of new effective degrees of freedom close to the transition. This again relies on the largely different dynamics of the two sub bands. While the particles in the second subband are close to the band bottom and thus slow, density waves in the first subband propagate with a characteristic velocity of order v_{F1} , the Fermi velocity in the Luttinger liquid type band. Since the latter is rather large, the density waves can adiabatically rearrange in order to optimize the density-density type interactions between the bands. The transition should thus be thought of as the filling of a second band with strongly correlated polarons, i.e. electrons with a screening cloud of density waves. This became particularly apparent for the regime of two partially filled subbands (i.e. at a finite $\mu_2 > 0$), where the system can be described in terms of two coupled Luttinger liquids. The theory is in fact only well-defined if the latter are constructed from polarons. The use of the “wrong”, fermionic particles leads to an unphysical singularity (this is not surprising since density-density interactions are treated exactly in the Luttinger liquid language). We finally note that while the crossover from

an essentially empty and weakly correlated second band at large negative μ_2 to the strongly correlated state of impenetrable electrons for $\mu_2 \rightarrow 0^-$ could be fully understood in terms of a resummation of ladder diagrams yielding a smoothly behaving dressed two-particle Green's function. A similar treatment was not possible for small positive chemical potentials $\mu_2 \rightarrow 0^+$. It would certainly be desirable to discuss this regime in future work.

4.5.1 Global summary: quantum phase transitions in quantum wires

In conclusion, we have studied a quantum wire defined in a two-dimensional electron gas made from GaAs/GaAlAs. In the regime of weak interactions in the two-dimensional electron gas, the quantum wire can be described as a multi-subband system, see Fig. 4.4. The activation of the latter's second subband as a function of increasing chemical potential corresponds to a Lifshitz transition of strongly correlated polarons. In the case of a quantum wire made from GaAs/GaAlAs two-dimensional electron gas, this transition is however not associated with any instabilities. Far below the transition, the system can be viewed as a single Luttinger liquid, and as two coupled Luttinger liquids far above the transition. These results are to be contrasted with the case of strong interactions in the two-dimensional electron gas, where a Wigner crystal forms. The latter exhibits a transition from a linear to a zigzag arrangement as a function of filling (or confinement), see Fig. 4.4b. This transition has been shown to happen in the charge sector only, while the spin sector essentially acts as a spectator and can be modeled as a Heisenberg chain with nearest neighbor exchange. Interactions between charge and spin degrees of freedom were irrelevant in an RG sense. The zigzag transition in a quantum wire made from a two-dimensional electron gas could thus be understood as being in the Ising universality class.

Both transitions correspond to a transition from a truly one-dimensional to a quasi one-dimensional situation, and should thus be connected in some way. Since the two transitions are in different universality classes, there must be a multi-critical point separating the strongly interacting Wigner crystal regime from the weakly interacting multi-subband quantum wire scenario. It would be desirable to extend the present analysis to intermediate interaction strengths in order to describe the multi-critical point as well, which would allow to finally redraw the mean-field phase diagram shown in Fig. 2.5 in a more thorough way.

Part II

Quantum phase transitions with multiple dynamics

Chapter 5

Quantum criticality and multiple dynamics

One of the most interesting features of materials is their ability to change their properties. We do in fact encounter and use such changes naturally in our every day life, with examples ranging from boiling water to driving a car (in both cases, the transition from a liquid to a gas is used). Since it is often precisely this ability to change that allows for applications, the understanding of qualitative transitions in materials, so-called phase transitions, has for a long time been one of the focuses of physics. The most commonly known phase transitions are the ones between a solid and a liquid (melting or freezing) and between a liquid and a gas (evaporation or condensation). There are, however, many conceptually similar but less “every-day life” examples of phase transitions in nature, including for instance the demagnetization of a (former) magnet under heating.

In physics, two main classes of phase transitions are distinguished.^{6,7,9} During a first order transition, a material absorbs or loses a finite amount of energy, the so-called latent heat. When melting ice, for instance, a continuously heated ice-water-mixture remains at precisely 0°C until all the ice has melted, and only then continues to warm up. This is different for second order or continuous phase transitions, which are characterized by a divergence of the typical length and time scales of the system, but where no latent heat is involved. These divergences of characteristic scales give in general rise to much richer physics than first order transitions. Common to both cases is however that a phase transition is driven by the change of some parameter of the system (such as the temperature of the ice). This allows for a second important classification of phase transitions. If a transition happens at finite temperatures, it is called a classical phase transition, while it is called a quantum phase transition if it occurs at zero temperature. Different to classical phase transitions which can also be driven by a change of the temperature, quantum phase transitions are necessarily driven by the tuning of some other parameter such as pressure, magnetic field, or doping. As a unifying feature, a phase transition of any kind can be understood as the transition between two differently ordered states, or the transition between an ordered and a disordered state. The presence of an order is technically measured by so-called order parameters which are non-zero only in the respective ordered state. For the case of a magnet, the order parameter is given by the magnetization. Often, the order spontaneously chooses one of many possible realizations (as an example, the magnetization of an isotropic magnet could in principle point in any direction, but spontaneously picks an arbitrary one). This phenomenon is known as

spontaneous symmetry breaking, and generally occurs at a second order phase transition. Although some of the concepts we alluded to here will be explained in more detail later on, we refer the reader to the standard textbooks on statistical physics and reviews for more extensive introductions to the field of phase transitions.^{6,7,9}

The study of phase transitions, and in the last decades especially quantum phase transitions, is an active field of condensed matter physics. The framework of (quantum) phase transitions has been used to discuss, for instance, the phenomenology of heavy fermion materials or high temperature superconductors.^{63–67} These systems, and quantum critical systems in general, sometimes exhibit several quantum critical points, partially with competing order parameters. One interesting question in the field of quantum criticality is thus how different low energy fluctuations close to a quantum critical point coexist and interact. It is not surprising that the most standard approach to quantum critical systems based on a single divergent time scale τ and a single divergent length scale ξ can not always describe the asymptotic scaling behavior close to a realistic quantum critical point. As a concrete example, the heavy fermion compound $\text{CeCu}_{6-x}\text{Au}_x$ can not be consistently explained by the usual scaling predictions.⁶⁸ Similarly, the itinerant magnet system YbRh_2Si_2 has been reported to have a quantum critical point with two distinct divergent time scales.⁶⁹ Different to the standard scaling approach, a thorough analysis of similar systems should from the very beginning take into account the coexistence of multiple dynamics. As a first step into this direction, the coexistence of multiple dynamics at the d -wave Pomeranchuk instability of a two-dimensional metal has been studied in Refs. [53,54,70]. In Ref. [53], it has been found that the coexistence of multiple dynamics gives rise to an unusual extended quantum to classical crossover regime in which thermal and quantum fluctuations coexist and interact. This in turn leads to logarithmic corrections to the scaling of thermodynamic observables,⁵³ and to non-Fermi liquid self-energy corrections and logarithmically singular renormalization of the quasiparticle residue of electronic degrees of freedom (see Ref. [54] and references therein). The coexistence of multiple degrees of freedom close to a (quantum) phase transition has also been studied in the context of competing orders, such as superconductivity and ferromagnetism in UGe_2 and other materials (see for instance Ref. [71] and references therein). These competing orders are in general also characterized by multiple dynamics. Their interplay has been argued to result in interesting quantum critical physics, such as the possible promotion of second order transitions to first order transitions due to the interactions between the different order parameters.⁷² Yet another example of multiple dynamics close to a quantum critical point can be found in two-dimensional metals close to a density-wave instability. A recently developed two-patch theory describes these systems with an anisotropic energy-momentum relation, $E \sim k_x \sim k_y^2$.^{73,74} Last but not least, similar physics have also been of interest in the context of dynamic critical phenomena close to classical phase transitions.^{75–77}

In the next two chapters, we will show how quantum critical systems with coexisting multiple dynamics can be described by virtue of a generalized renormalization group approach. The latter is able to tackle interacting systems of arbitrary dynamics and spatial dimensionality, and allows to calculate the scaling properties of thermodynamic observables at zero and finite temperature outside the ordered phase. As a main result, we find that the coexistence of multiple dynamics can lead to the break-down of the usual scaling and thus constitutes a novel, and potentially rather generic, mechanism for the generation of unusual scaling exponents close to a quantum critical point. We

organize our discussion as follows. First, we will introduce the basic concepts of scaling and universality close to a quantum critical point, and discuss more standard field theoretical approaches to quantum critical scaling relying on single dynamics. We will then show how the coexistence of multiple dynamics spoils the usual scaling of the free energy and thermodynamic observables in general, before turning to a concrete model. Studying a generalized Pomeranchuk instability in a metal, we demonstrate how and under which conditions unusual scaling exponents emerge and affect physical observables in this concrete example. It is hoped that the novel mechanism for unusual scaling given by coexisting multiple dynamics might be helpful in the context of experimental scaling puzzles close to quantum critical points.

5.1 Quantum criticality and scaling hypothesis

As mentioned in the last paragraph, a second order phase transition is characterized by a divergent characteristic time scale τ and a divergent length scale ξ . These scales are, more precisely, the correlation time and correlation length of the critical fluctuations of the system. Since the characteristic time scale vanishes, the typical energy \hbar/τ of quantum fluctuations around an ordered state as depicted in Fig. 5.2 goes to zero if a second order phase transition is approached. While finite temperature phase transitions, i.e. classical ones, can be tuned by either varying the temperature T or some other control parameter such as pressure or doping, quantum phase transitions are always due to the change of a control parameter g at zero temperature. If the latter has a critical value g_c , the correlation time and length typically behave as

$$\xi \sim |r|^{-\nu} \quad \text{and} \quad \tau \sim |r|^{-\nu z} , \quad (5.1)$$

where $r = g - g_c$, and where ν is known as the correlation length exponent, while z is called the dynamical exponent. The scaling hypothesis now states that close enough to the quantum critical point, a thermodynamic observable f depends only on the ratios of the experimental length scale x and time scale t to the characteristic scales, as well as the various ratios between different characteristic scales.⁷⁸ One of these characteristic scales is always given by the temperature T which close to a quantum critical point behaves like an inverse time. The thermodynamic observable f can thus be expressed close to a quantum critical point as

$$f(x, t, r, T) = \tilde{f}_r(x/\xi, t/\tau, T\tau) . \quad (5.2)$$

Similar scaling laws arise not only close to quantum phase transitions but also close to classical ones and had first been identified by Widom in 1965.⁷⁹ They imply that observing the system at different scales $x \rightarrow x/b$, $t \rightarrow t/b^z$ is like observing the system at some other value of the tuning parameter, $r \rightarrow r b^{1/\nu}$, and a different temperature, $T \rightarrow T b^z$, up to a scaling factor with an exponent D_f corresponding in general to the physical dimension plus an anomalous dimension of the observable itself,

$$f(x, t, r, T) = b^{D_f} f(x b^{-1}, t b^{-z}, r b^{1/\nu}, T b^z) . \quad (5.3)$$

From the scaling relation (5.3), one can also deduce that thermodynamic observables are described by power laws if the system is close to the quantum critical point. Setting $b = r^{-\nu}$, we obtain

$$f(x, t, r, T) \rightarrow r^{-\nu D_f} f(0, 0, 1, 0) \quad \text{for } r \rightarrow 0 \quad \text{and} \quad T \rightarrow 0. \quad (5.4)$$

The critical physics is thus controlled by a small set of numbers, namely the experimentally important parameters close to the transition (here x , t , r and T) and the set of critical exponents (here z , ν and D_f). If a critical system depends not only on a single, but rather on a small number of control parameters r_i , each of the parameters is generally associated with its own scaling exponent ν_i . This leads to the scaling form

$$f(x, t, r_1, \dots, r_N, T) = b^{D_f} f(x b^{-1}, t b^{-z}, r_1 b^{1/\nu_1}, \dots, r_N b^{1/\nu_N}, T b^z). \quad (5.5)$$

Put differently, thermodynamic observables close to a phase transition are in fact only functions of the dimensionless ratios of the different length scales $\xi_T = T^{-1/z}$ and $\xi_{r_i} = r_i^{-\nu_i}$ one can form from the temperature and each of the quantum tuning parameters using the associated critical exponents.

To conclude, we note that since observing the system at different scales $x \rightarrow x/b$, $t \rightarrow t/b^z$ is like observing it at some other values of the tuning parameters r_i and the temperature T (if the system is close enough to the critical point), the physics have to be self-similar on all scales. This implies a number of relations between the different scaling exponents z and ν_i . Similar fixed relations of scaling exponents also exist between different physical observables. Historically, these relations have been dubbed the hyperscaling relations. For a general introduction to the theory of scaling close to phase transitions see for instance Ref. [78].

5.1.1 Universal physics close to phase transitions

The concept of scaling close to a phase transition is intimately related to the observation that many seemingly very different critical systems are described by identical critical theories. As we have already noticed, there is only a small number of physically relevant scales deriving from the control parameters and the temperature, and set by virtue of the critical exponents. This means that most of the microscopic information on critical systems is actually not important for their critical properties. As an example, the correlation length $\xi \sim r^{-\nu}$ is usually the only relevant length scale at zero temperature close to a phase transition driven by a control parameter r . Details such as precise value of microscopic lattice constants in the system do however often not influence the critical scaling laws. Quite generally, this implies that a big number of seemingly very different physical systems have the same critical behavior, provided that they differ only in properties that are irrelevant for the critical scaling. This concept has been named universality, and allows to classify critical systems into so-called universality classes (all systems with the same universal lowest energy physics at a phase transition constitute a universality class). Technically, the concept of universality is best understood in the framework of the renormalization group, see appendix A. Universality is, of course, a property that only emerges on long time and length scales, or equivalently low energies. When one zooms sufficiently into a critical system, the microscopic details such as the lattice structure and inter-particle interactions will eventually be visible and important. Finally, let us notice that not necessarily the entire system needs to be universal. If only a subset of a complex physical system performs a phase transition (e.g. a magnetic transition that leaves the lattice properties unchanged), only the part of the free energy and other thermodynamic observables describing the critical subset follows the discussed universal scaling laws.

One therefore commonly needs to subtract non-universal contributions from a physical measurement in order to obtain the critical scaling properties.

5.1.2 Thermodynamics and phase diagram

In experiments, where often macroscopic samples are used, the observed physical responses correspond to thermodynamic properties of the respective systems. This means that they should not be understood as individual responses of single quasiparticles, but rather as collective properties of all low-energy excitations of the system. As a matter of fact, thermodynamic measurements usually involve particle numbers of the order of Avogadro's number, $N_A \approx 6 \cdot 10^{23}$. Their collective behavior can be characterized by thermodynamic quantities such as the global thermal expansion α , i.e. the relative volume change of the entire sample if the temperature is changed

$$\alpha = \frac{1}{V} \frac{\partial V}{\partial T} . \quad (5.6)$$

Thermodynamic observables can alternatively also be defined as derivatives of the free energy F with respect to the temperature T and the (quantum) tuning parameters r_i . Experimentally most relevant are second order derivatives. For pressure induced quantum criticality, where the pressure p is the only quantum tuning parameter, $r = p$, one can define three second order derivatives. The second order derivative with respect to the temperature

$$c_p = -\frac{T}{V} \frac{\partial^2 F}{\partial T^2} = \frac{T}{V} \frac{\partial S}{\partial T} \Big|_{p=\text{const.}} \quad (5.7)$$

defines the specific heat of the system (S denotes the entropy). The mixed derivative,

$$\alpha = \frac{1}{V} \frac{\partial^2 F}{\partial T \partial p} = \frac{1}{V} \frac{\partial V}{\partial T} \Big|_{p=\text{const.}} \quad (5.8)$$

sets the above mentioned thermal expansion. The second order derivative with respect to $r = p$,

$$\kappa = -\frac{1}{V} \frac{\partial^2 F}{\partial p^2} = \frac{1}{V} \frac{\partial V}{\partial p} \Big|_{T=\text{const.}} \quad (5.9)$$

finally defines the compressibility of the system. More generally, a second order derivative $\partial_{r_i}^2 F$ defines the susceptibility χ_{r_i} of the system with respect to the tuning parameter r_i .

The scaling of these thermodynamic observables can be obtained from the scaling form of the critical part of the free energy discussed in the last section. We found that the critical part of the free energy per volume, i.e. the critical part of the free energy density $\mathcal{F} = F_{\text{cr}}/V$, has a scaling behavior given by

$$\mathcal{F} = b^{-(d+z)} f(b^{1/\nu_1} r_1, \dots, b^{1/\nu_N} r_N, b^z T) , \quad (5.10)$$

where ν_i is the scaling exponent of the quantum tuning parameter r_i . For a system with just a single tuning parameter, e.g. pressure p , the free energy density assumes the simple scaling form

$$\mathcal{F} = b^{-(d+z)} f(b^{1/\nu} r, b^z T) . \quad (5.11)$$

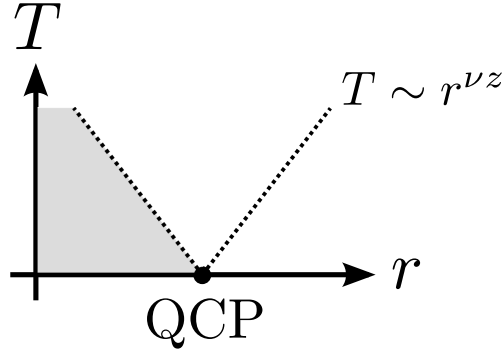


Figure 5.1: Generic phase diagram for a system with a single dynamical exponent z and a correlation length exponent ν as a function of temperature T and the quantum critical tuning parameter r driving a quantum phase transition at $r = 0$. This gives rise to a quantum critical point (QCP) at $r = 0$, $T = 0$. Crossovers occur at $T \sim |r|^{\nu z}$, where the dominant type of fluctuations changes from thermal to quantum. This modifies the scaling behavior of physical observables. At low temperatures, an ordered phase appears for negative r , the details and extension of which however depends on further details of the system.

Each of the two relevant scaling fields r and T gives rise to a length scale. The quantum tuning parameter defines the length $\xi_r = |r|^{-\nu}$, while the temperature yields $\xi_T = T^{-1/z}$. These scales can be interpreted as the typical lengths on which correlations of the system are destroyed by either quantum fluctuations (when considering ξ_r) or thermal fluctuations (for ξ_T). The overall correlation length of the system, i.e. the length scale beyond which correlations are destroyed, thus corresponds to the minimum of these two lengths,

$$\xi = \min \{ \xi_r, \xi_T \} . \quad (5.12)$$

This naturally defines two regimes. For $\xi_r < \xi_T$, or equivalently $T < |r|^{\nu z}$, the system is dominated by quantum fluctuations, while thermal fluctuations dominate for $\xi_T < \xi_r$ ($T > |r|^{\nu z}$). These regimes are shown in the generic phase diagram of Fig. 5.1 based on our simple scaling analysis, and the borders between them define crossovers between different scaling behaviors of physical observables, see below. For negative $r < 0$, the formation of an ordered phase is expected. This will generically happen in the low temperature regime because the high temperature regime is characterized by thermal fluctuations of energies larger than typical quantum energy scales. Consequently, any quantum order is destroyed there. The precise form of the low temperature regime for $r < 0$, and especially the extension of the ordered phase, however depends on the details of the model and the spatial dimensionality of the system.

Low temperature regime $T < |r|^{\nu z}$

In the low temperature regime $T < |r|^{\nu z}$, the system is characterized by the length scale $\xi_r = |r|^{-\nu}$. The free energy density should thus dominantly scale as $\mathcal{F} \sim \xi_r^{-(d+z)}$, which corresponds to the choice $b = |r|^{-\nu}$ for the scaling form (5.11). The critical part of the thermodynamics then follow from the scaling form

$$\mathcal{F} = |r|^{\nu(d+z)} f(\pm 1, |r|^{-\nu z} T) . \quad (5.13)$$

Since the free energy is well-defined at zero temperature for finite $|r|$, the limit $T \rightarrow 0^+$ of the scaling function should go to some finite value $f(\pm 1, 0) = \text{const.} > 0$. We can thus expand the scaling form of the free energy for $T \rightarrow 0^+$. The first order derivative with respect to temperature corresponds to the entropy. According to the third law of thermodynamics, the latter has to vanish in the limit $T \rightarrow 0^+$. The expansion of the scaling form thus starts with an exponent larger than one. It can generally be written as

$$f(\pm 1, |r|^{-\nu z} T) \approx f(\pm 1, 0) + C_{\text{LT}} (|r|^{-\nu z} T)^{y_0+1} \quad (5.14)$$

with positive constants y_0 and C_{LT} . Since thermodynamics are only well-defined for positive temperatures, the scaling function $f(\pm 1, x)$ does not need to be analytic for $x \rightarrow 0$, and the exponent y_0 is thus generally not an integer. In addition, we note that the constants y_0 and C_{LT} do not need to be identical in the ordered and disordered phase, i.e. for $r < 0$ and $r > 0$. One can now easily evaluate the critical parts of different thermodynamic quantities as

$$c_r = -T \frac{\partial^2 \mathcal{F}}{\partial T^2} \sim |r|^{\nu(d-y_0z)} T^{y_0} , \quad (5.15a)$$

$$\alpha = \frac{\partial^2 \mathcal{F}}{\partial T \partial r} \sim |r|^{\nu(d-y_0z)-1} T^{y_0} , \quad (5.15b)$$

$$\kappa = \frac{\partial^2 \mathcal{F}}{\partial r^2} \sim |r|^{\nu(d+z)-2} . \quad (5.15c)$$

Quantum critical regime $T > r^{\nu z}$

In the regime $T > |r|^{\nu z}$, thermal fluctuations dominate over quantum fluctuations. It is commonly referred to as quantum critical regime. There, the critical part of the free energy density dominantly scale as $\mathcal{F} \sim \xi_T^{-(d+z)}$, corresponding to $b = T^{-1/z}$ in Eq. (5.11). We can thus write \mathcal{F} as

$$\mathcal{F} = T^{(d+z)/z} f(T^{-1/(\nu z)} r, 1) . \quad (5.16)$$

Again, the free energy should be well-defined in the limit $r \rightarrow 0$ at finite temperature T , implying that $f(0, 1) = \text{const.} > 0$. Since there is no phase transition in the quantum critical region at $r = 0$ for finite temperatures, the scaling form is assumed to be an analytic function of r (as we will see in Sec. 6.7.2, this does in fact not always need to be true). Taylor expansion then yields the leading behavior as

$$f(T^{-1/(\nu z)} r, 1) \approx f(0, 1) + C_{\text{QC}}^{(1)} T^{-1/(\nu z)} r + C_{\text{QC}}^{(2)} T^{-2/(\nu z)} r^2 , \quad (5.17)$$

where $C_{\text{QC}}^{(i)} > 0$ are some constants. From there, we can again obtain the scaling behavior of the critical part of thermodynamic quantities as

$$c_r = -T \frac{\partial^2 \mathcal{F}}{\partial T^2} \sim T^{d/z} , \quad (5.18a)$$

$$\alpha = \frac{\partial^2 \mathcal{F}}{\partial T \partial r} \sim T^{(d-1/\nu)/z} , \quad (5.18b)$$

$$\kappa = \frac{\partial^2 \mathcal{F}}{\partial r^2} \sim T^{(d+z-2/\nu)/z} . \quad (5.18c)$$

5.2 Theoretical description of quantum criticality with single dynamics

Before turning to quantum critical systems involving multiple dynamics, we find it useful to review the more standard case of single dynamics quantum criticality. To make the matter particularly simple, let us consider a system that has a quantum critical point (QCP) as a function of some physical tuning parameter r . In an experiment, this tuning parameter might be pressure, magnetic field, doping, and so on. For simplicity, we however focus on the case that the system has only a single tuning parameter, such that the phase diagram can be fully specified as a function of r and the temperature T (which naturally is the second and by assumption last relevant scaling parameter). We choose the tuning parameter to be $r = 0$ at the phase transition. At zero temperature, negative $r < 0$ corresponds to the ordered phase, while positive $r > 0$ characterizes the disordered state (the finite temperature phase diagram depends on the details of the model). The system is furthermore assumed to exhibit universal physics, and the characteristic exponents related to the two scaling fields are the correlation length exponent ν (which defines the length scale $\xi_\nu = r^{-\nu}$) and the dynamical exponent z (which sets the thermal length $T^{-1/z}$). In the following, we want to review how this set of four numbers (r , T , ν , and z) technically enters and controls the theoretical description close to a quantum critical point.

5.2.1 Quantum and classical fluctuations

Phase transitions can generally be understood as the destruction of some ordered state. The phase transition itself is driven by fluctuations, i.e. (initially) small perturbations of the ordered state, see Fig. 5.2a and 5.2b. Deep in the ordered state, the creation of fluctuations is punished by a large energy cost deriving from the same energy scale that stabilizes the order itself (a ferromagnetic exchange coupling in Fig. 5.2). Fluctuations can nevertheless exist, either as virtual excitations (also known as quantum fluctuations), or due to the thermal energy of a finite temperature system. Close to a second order phase transition, where the energy cost of fluctuations goes to zero, the definition of an ordered state naturally breaks down if the fluctuations do not constitute small perturbations anymore, but rather determine the (now “chaotic”) state of the system, see Fig. 5.2c.

Phase transitions at zero temperature, i.e. transitions driven by quantum fluctuations, are known as quantum phase transitions. The ordered state can however persist up to some critical temperature, and the corresponding generic phase diagrams are depicted in Fig. 5.3 (taken from Ref. [9]). An experimental example of the quantum critical phase diagram in the Ising ferromagnet LiHoF_4 as a function of a transversal magnetic field H is shown in Fig. 5.4.⁸⁰ The quantum fluctuations destabilizing the ordered state comprise all sorts of virtual excitations from the many-particle ground state to excited states. Their characteristic energy scale is related to the distance to the quantum critical point (note that the system becomes gapless at the phase transition). In terms of the universal exponents, the characteristic energy scale of quantum fluctuations reads

$$E_q \sim |r|^{\nu z} \quad (5.19)$$

(we recall that $r^{-\nu}$ corresponds to the characteristic length scale related to the distance to the quantum critical point r , while $(r^{-\nu})^{-z}$ translates this length scale into a temperature,

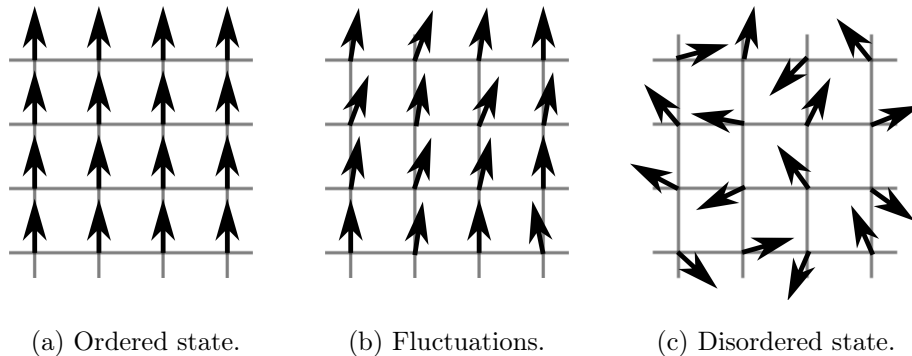


Figure 5.2: Sketch of the transition from an ordered state (subfigure 5.2a) to a disordered state (subfigure 5.2c) in a two-dimensional ferromagnetic spin lattice. Intermediate states between the ordered and disordered limits can be understood as small modulations of the ordered state due to quantum and thermal fluctuations, see subfigure 5.2b.

i.e. energy, see Sec. 5.1). This scale is to be compared to the characteristic energy scale of thermal fluctuations, which is of course given by the temperature itself,

$$E_c \sim T . \quad (5.20)$$

Since thermal fluctuations are the ones driving classical phase transitions, they are also known as classical fluctuations. Close to a phase transition, the system is dominated by these thermal (or classical) fluctuations if $E_c \gg E_q$, while quantum fluctuations dominate in the opposite case. This implies in particular that every finite temperature phase transition is dominated by classical fluctuations. Upon approaching the transition, i.e. for $r \rightarrow 0$, the quantum energy scale E_q is always smaller than the classical energy scale E_c in the regime

$$|r(T)| \lesssim T^{1/(\nu z)} , \quad (5.21)$$

i.e. close enough to the finite temperature phase transition (note that the critical value of r generally shifts away from its zero temperature value for finite temperatures). Therefore, only phase transitions at zero temperature are truly driven by quantum fluctuations. At very high temperatures (i.e. higher energies), non-universal physics start playing an important role, and the behavior changes from universal scaling to system-specific dependencies.

Coming back to the phase diagrams of Fig. 5.3, the order is mainly destroyed by quantum fluctuations for $r > 0$, while it is destroyed by thermal fluctuations for $r < 0$ (there, the quantum energy scale *stabilizes* the order).⁹ In the intermediate region directly above the quantum critical point, the so-called quantum critical region, fluctuations of both types are important. For $T > |r|^{\nu z}$, thermal fluctuations have a higher energy than quantum fluctuations, such that a finite distance to the quantum critical point $|r| > 0$ is washed out. Thermal fluctuations are simply too strong for the system “to be able to tell” whether it is at $r = 0$ or not. Consequently, the system can be described in terms of thermal excitations of the quantum critical ground state at $r = 0$, $T = 0$. Just as the latter, which marks the transition between different quantum states, the entire quantum critical region is prominently characterized by the absence of conventional quasiparticles.

In the following sections, we will analyze in detail how the quantum and classical

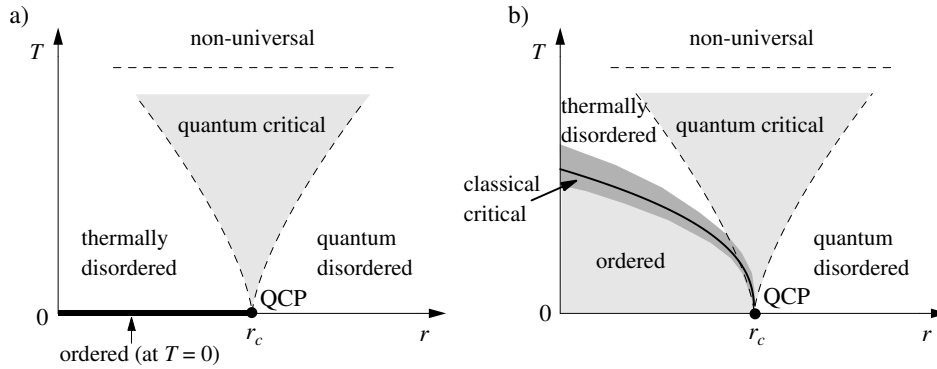


Figure 5.3: Generic phase diagrams close to a quantum critical point (QCP) as a function of a quantum tuning parameter r with critical value r_c and temperature T . Subfigure a) shows a system with order only at zero temperature, while subfigure b) depicts order at finite temperature. In the latter case, the finite temperature phase transition is driven by thermal fluctuations, and the region sufficiently close to the phase transition is described by a classical critical theory. Figure taken from a review by M. Vojta, see Ref. [9].

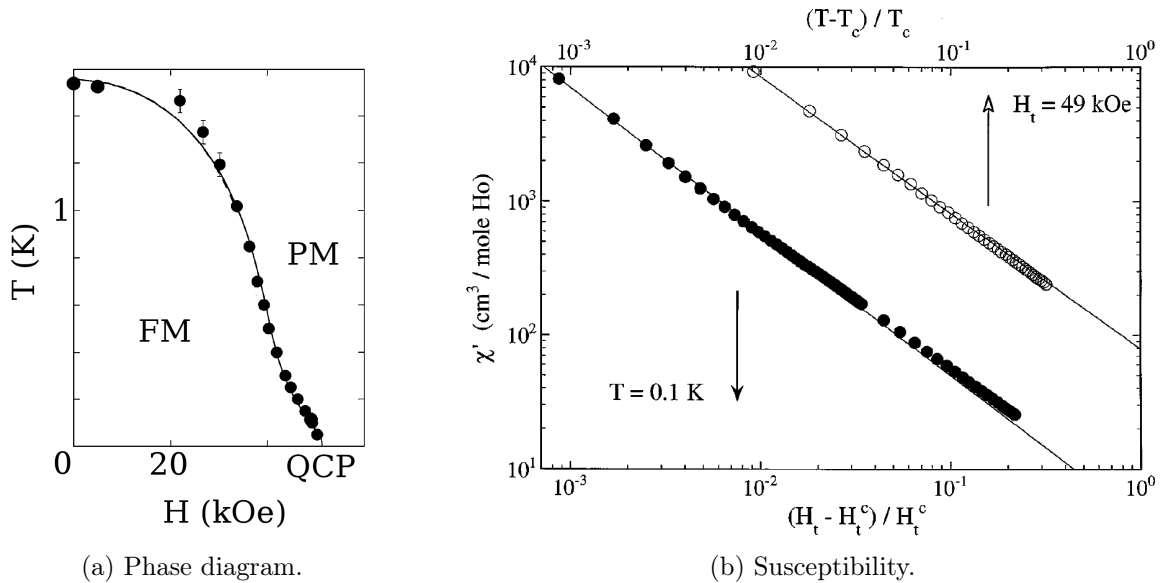


Figure 5.4: Experimental measurement of a quantum critical point in the Ising ferromagnet LiHoF_4 . The data has been recorded by Bitko et al., and the plots are adapted from Ref. [80]. It shows the transition from a ferromagnetic state (FM) to a paramagnetic state (PM) as a function of a transversal magnetic field H . Subfigure (a) depicts the measured phase diagram (the dots show experimental data points, the solid line is a mean field theoretical prediction). Subfigure (b) shows the power law divergence of the magnetic susceptibility χ close to the quantum critical point (once as a function of the reduced temperature for at $H = 49$ kOe upon approaching the quantum critical point from above, open circles, once as a function of reduced magnetic field for $T = 0.1$ K).

fluctuations technically enter the description of a phase transition in terms of a quantum field theory, and how this quantum theory “turns classical” at finite temperatures.

Quantum theory of a phase transition

Disregarding any microscopic physical model, we assume that the phase transition under discussion can be described by a bosonic Ψ^4 theory, which usually derives from a decoupling of a complicated microscopic theory into the relevant interaction channels. For now, we want to keep the theory as general as possible, and thus work in a spatial dimension d . The dynamical exponent z , which translates the temperature T to a length scale, is microscopically defined by the dispersion relation relating energies to inverse lengths. In our theory, we thus use a general dispersion

$$\omega \sim k^z , \quad (5.22)$$

where ω denotes energies (frequencies) and k is a momentum. The correlation length exponent, on the other hand, relates momenta (inverse lengths) to the tuning parameter r as

$$r \sim k^{1/\nu} . \quad (5.23)$$

The latter characterizes the distance to the quantum critical point, and sets the characteristic energy scale for quantum fluctuations above the ordered state (as explained in the last section). The effective bosonic Ψ^4 theory describing the quantum phase transition should thus have a gap $\Delta \sim r^{\nu z}$. Based on these requirements, we can write down a general propagator in terms of momenta $k = |\vec{k}|$ and Matsubara frequencies ω_n as

$$g(\omega_n, \vec{k})^{-1} = r + k^{1/\nu_0} + \frac{|\omega_n|^y}{k^{yz-1/\nu_0}} , \quad (5.24)$$

where $k = |\vec{k}|$ (note that we have implicitly assumed rotational invariance for simplicity) and y is some exponent, which is for now left undefined. We note that the dynamical exponent z and the correlation length exponent ν_0 as they are defined here constitute *bare* values, and will in general be renormalized by interactions. The precise form of the propagator is inspired by our later analysis. Its details do however not affect the qualitative discussion of this section. The resulting Ψ^4 theory then reads

$$\mathcal{S} = \int d^d x \int_0^\beta d\tau \Psi(\vec{x}, \tau) \frac{g^{-1}}{2} \Psi(\vec{x}, \tau) + u \int d^d x \int_0^\beta d\tau \Psi(\vec{x}, \tau) \Psi(\vec{x}, \tau) \Psi(\vec{x}, \tau) \Psi(\vec{x}, \tau) , \quad (5.25)$$

where $\Psi(\vec{x}, \tau)$ is a real bosonic field, τ denotes imaginary time, β is the inverse temperature, u accounts for interaction effects, and the double Fourier transform of the inverse bare propagator is $g(\vec{x}, \tau)^{-1}$.

5.2.2 Dimensional reduction

Let us now show how a quantum theory turns classical at finite temperatures upon approaching the phase transition. For simplicity, we perform this analysis above the quantum critical point, where $r \rightarrow 0$. The only relevant length scale is then set by the temperature as

$$\xi_T = T^{-1/z} , \quad (5.26)$$

whose inverse ξ_T^{-1} defines a characteristic thermal momentum scale. For momenta higher than this scale, $k \gg \xi_T^{-1}$, the quantum fluctuations have an energy $\omega \sim k^z \gg T$, and do thus effectively not know about the finite temperature yet. Fluctuations with momenta smaller than ξ_T^{-1} , on the other hand, do feel the effect of finite temperatures and “turn classical”. On a technical level, the thermal momentum defines whether the spacing between Matsubara modes is important or not. For momenta larger than ξ_T^{-1} , this spacing is negligibly small. Consequently, one can approximate ω_n by a continuous variable ω just like in the zero temperature case, and the theory behaves as a $d + z$ -dimensional quantum theory at zero temperature. For momenta smaller than ξ_T^{-1} , on the contrary, the finite Matsubara spacing is relevant. Moreover, as $\omega_n \sim nT \gg k^z$, the propagator can be approximated by the dynamical term only for non-zero Matsubara frequencies:

$$g(\omega_n, \vec{k})^{-1} \approx \begin{cases} k^{1/\nu_0} + \frac{|\omega_n|^y}{k^{yz-1/\nu_0}} & , k^z \gg T \\ \frac{|2\pi nT|^y}{k^{yz-1/\nu_0}} & , k^z \ll T \text{ and } \omega_n \neq 0 \\ k^{1/\nu_0} & , k^z \ll T \text{ and } \omega_n = 0 \end{cases} . \quad (5.27)$$

This approximate form of the propagator suggests that the very low energy physics at finite temperatures might be dominated by the Matsubara zero mode only, as all other modes are effectively gapped by the temperature. This statement can be substantiated by an analysis along the lines of Ref. [81]. In order to derive the effective lowest-energy theory, one first deals with the momenta $k \gg \xi_T^{-1}$ by a zero temperature one-loop renormalization group (RG) analysis that stops when the flowing thermal scale ξ_T^{-1} equals the cutoff. The effective values r^* for the mass and u^* for the interaction obtained at the end of this RG flow define an effective theory for momenta $k \leq \xi_T^{-1}$,

$$\begin{aligned} \mathcal{S}_{eff} = & \sum_{k \leq \xi_T^{-1}} \sum_{\omega_n} \Psi(-\vec{k}, -\omega_n) \frac{1}{2} \left[r^* + k^{1/\nu_0} + \frac{|\omega_n|^y}{k^{yz-1/\nu_0}} \right] \Psi(\vec{k}, \omega_n) \\ & + u^* \int d^d x \int_0^\beta d\tau \Psi(\vec{x}, \tau) \Psi(\vec{x}, \tau) \Psi(\vec{x}, \tau) \Psi(\vec{x}, \tau) . \end{aligned} \quad (5.28)$$

Note that to one-loop order, the correlation length exponent appearing in the propagator does not change even when the system goes to a Wilson-Fisher fixed point. Assuming that the non-zero Matsubara modes are now effectively gapped, it is admissible to integrate them out perturbatively to one-loop order (an assumption that needs to be checked in the end). This yields a new effective theory for the Matsubara-zero mode only, with an effective mass r_0^* and an interaction u_0^* that account for all physics stemming from momenta higher than ξ_T^{-1} and the effects of all non-zero Matsubara modes,

$$\begin{aligned} \mathcal{S}_{eff}^0 = & \sum_{k \leq \xi_T^{-1}} \Psi(-\vec{k}, 0) \frac{r_0^* + k^{1/\nu_0}}{2} \Psi(\vec{k}, 0) \\ & + \frac{u_0^*}{\beta V} \sum_{k_i \leq \xi_T^{-1}} \Psi(\vec{k}_1, 0) \Psi(\vec{k}_2, 0) \Psi(\vec{k}_3, 0) \Psi(\vec{k}_4, 0) \delta_{\vec{k}_1 + \vec{k}_2, \vec{k}_3 + \vec{k}_4} \end{aligned} \quad (5.29)$$

(with β being the inverse temperature and V the d -dimensional volume). The assumption that the non-zero Matsubara modes can be integrated out perturbatively with respect to the Matsubara zero mode basically implies that the effective mass r_0^* should not be larger than the minimal gap of the non-zero Matsubara modes,

$$r_0^* < \frac{|\omega_n|^y}{\xi_T^{-(yz-1/\nu_0)}} \sim \frac{T^y}{T^{(yz-1/0)/z}} = T^{1/(\nu_0 z)}. \quad (5.30)$$

This inequality corresponds to (the one-loop version of) the comparison of the characteristic energy scales E_q and E_c of quantum and classical fluctuations, see Eq. (5.21). If it holds, the system can indeed be described by an effective classical theory for the Matsubara-zero mode only, i.e. a d -dimensional field theory without quantum dynamics (albeit with non-trivially renormalized parameters r_0^* and u_0^*).

In conclusion, our analysis along the lines of Ref. [81] shows that the action (5.25) close to the quantum critical point $r \rightarrow 0$ behaves like a $d + z$ -dimensional quantum theory at zero temperature for high momenta $k \gg \xi_T^{-1}$, while it may effectively appear as a d -dimensional classical theory at finite temperature for momenta $k \ll \xi_T^{-1}$. This phenomenon is known as dimensional reduction or quantum to classical crossover. We note that the concept of dimensional reduction also has an intuitive interpretation in a language inspired by quantum field theory, see for instance Eq. (5.25). There, the time coordinate acts like an additional space coordinate of finite extent $L_\tau = \beta^{1/z} = T^{-1/z}$. When distances smaller than this extent, i.e. momenta higher than $k \gtrsim T^{1/z}$, are considered, the theory looks like a field theory in $d + z$ dimensions. Only for larger distances, i.e. lower momenta, the system realizes about its finite temperature.

5.3 Case study above the quantum critical point

The following section will illustrate the concept of dimensional reduction with a concrete example. We stick to our model system with a single quantum tuning parameter r driving a quantum phase transition at $r = 0$, and analyze the system at finite temperature T . In order to observe dimensional reduction, we require the system to be in a regime ultimately dominated by thermal fluctuations. This can most easily be guaranteed by setting $r = 0$, i.e. by placing the system at some finite temperature directly above the quantum critical point, see Fig. 5.5. Concretely, the system is modeled by the action

$$\mathcal{S} = \int d^d x \int d\tau \Psi(\vec{x}, \tau) \frac{g^{-1}}{2} \Psi(\vec{x}, \tau) + u \int d^d x \int d\tau \Psi(\vec{x}, \tau) \Psi(\vec{x}, \tau) \Psi(\vec{x}, \tau) \Psi(\vec{x}, \tau), \quad (5.31)$$

with the Fourier transformed inverse Green's function

$$g(\omega_n, \vec{k})^{-1} = r + k^{1/\nu_0} + \frac{|\omega_n|}{k^{z-1/\nu_0}}. \quad (5.32)$$

As before, ν_0 is the bare value of the correlation length exponent. We do not specify the latter in this section in order to keep the discussion as general as possible, but we note that it usually takes the value $\nu_0 = 1/2$ in ϕ^4 -theories. The analysis will now be performed according to Ref. [81] in the two steps advertised in the last section. First, we will integrate out all high energy fluctuations with momenta larger than the thermal

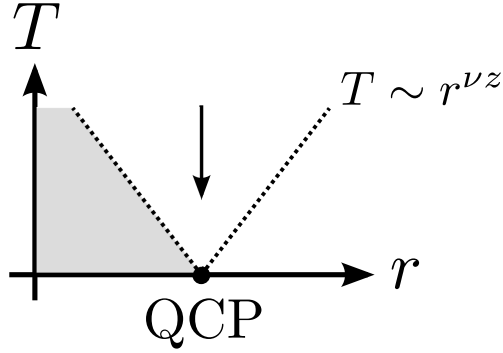


Figure 5.5: Generic phase diagram for a system with a single dynamical exponent z and a correlation length exponent ν as a function of temperature T and the quantum critical tuning parameter r driving a quantum phase transition at $r = 0$. This gives rise to a quantum critical point (QCP) at $r = 0$, $T = 0$. The arrow indicates how the QCP is approached at $r = 0$ upon lowering the temperature, as considered in Sec. 5.3.

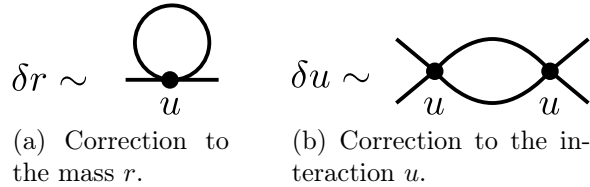


Figure 5.6: One-loop corrections to the mass r and the interaction u .

momentum ξ_T^{-1} . This can be done by virtue of a zero temperature renormalization group (RG) analysis since the high momentum modes do not feel the finite temperature, see Sec. 5.2.2. Subsequently, the finite temperature fluctuations of the non-zero Matsubara modes can (hopefully) be integrated out perturbatively.

Initial RG flow

The first step corresponds to integrating out high energy shells by a standard, zero temperature RG up to the inverse thermal length $\xi_T^{-1} = T^{1/z}$. The RG equations to one loop order correspond to the engineering dimension plus the diagrams shown in Fig. 5.6 and evaluated in appendix C.1. They are derived by subsequently integrating out high energy/momentum shells by reduction of the initial high momentum cutoff $\Lambda \rightarrow \Lambda/b$ with $b > 1$ (energies have a cut-off Λ^z). The full set of zero temperature RG equations reads

$$\frac{\partial r}{\partial \ln(b)} = \frac{1}{\nu_0} r(b) - K_{d,z,1,\nu} \Lambda^{d+z-2/\nu_0} u(b) r(b) , \quad (5.33a)$$

$$\frac{\partial u}{\partial \ln(b)} = \left(\frac{2}{\nu_0} - d - z \right) u(b) - 3 K_{d,z,1,\nu_0} \Lambda^{d+z-2/\nu_0} u^2(b) , \quad (5.33b)$$

$$\frac{\partial T}{\partial \ln(b)} = z T(b) , \quad (5.33c)$$

where K_{d,z,y,ν_0} is a constant of order one, see appendix C.1. The engineering dimensions of the mass and the interaction follow from simple power counting of the action (5.31),

while the temperature has to scale as a frequency (we recall that $\omega_n = 2\pi nT$), and therefore has engineering dimension z . These RG equations can simply be integrated, and two scenarios have to be distinguished.

A system above its upper critical dimension The upper critical dimension D_c^+ is defined as the quantum dimension $D = d + z$ below which fluctuations importantly affect the state of the system, while they can be neglected for systems above the upper critical dimension. In an RG language, a system is above its upper critical dimension if the interaction is irrelevant in the RG sense. The system is then said to approach a Gaussian, i.e. non-interacting fixed point. This happens if the engineering dimension of the interaction is negative. The upper critical dimension of the action (5.31) is thus given by

$$D_c^+ = \frac{2}{\nu_0} . \quad (5.34)$$

In a usual Ψ^4 theory, where $\nu_0 = 1/2$, the upper critical dimension is $D_c^+ = 4$. If the system is above its upper critical dimension, i.e. if $d + z > D_c^+$, the interaction has a negative scaling dimension and thus rapidly flows to weak coupling,

$$u(b) \rightarrow 0 , \quad (5.35)$$

while the mass remains at its initial value,

$$r(b) = 0 , \quad (5.36)$$

since its RG equation (5.33a) is proportional to $r(b)$ and the system is analyzed for bare $r(b=1) = r = 0$. As discussed in appendix C.1, finite shifts due to non-divergent corrections can simply be absorbed into a redefinition of the starting value of r . The full discussion of the RG equations is given in appendix C.2. Below the thermal scale, the non-zero Matsubara modes can simply be integrated out since they have an effective gap of order $T^{1/(\nu_0 z)}$. The residual interaction u^* is essentially equal to the bare interaction u and leads to a small mass for the Matsubara zero mode (we recall that the system is by construction close to an attractive Gaussian fixed point, such that interactions only lead to (in this case dangerously) irrelevant corrections, also to the interaction itself, but that e.g. no interacting fixed point is approached).

A system below its upper critical dimension If the system is below its upper critical dimension,

$$d + z < D_c^+ = \frac{2}{\nu_0} , \quad (5.37)$$

the initial RG flow changes dramatically. Instead of flowing to a non-interacting fixed point, the interaction goes to a finite and constant value. This interacting fixed point is known as the Wilson-Fisher fixed point and generically occurs for theories below the upper critical dimension. As shown in appendix C.2, the Wilson-Fisher fixed point interaction reads

$$u(b) \rightarrow u_{\text{WF}} = \frac{\frac{2}{\nu_0} - d - z}{3 K_{d,z,1,\nu_0} \Lambda^{d+z-2/\nu_0}} = \text{const.} \quad (5.38)$$

The Wilson-Fisher fixed point in fact defines a universal value of the interaction, since it is always the combination $\Lambda^{d+z-2/\nu_0} u(b)$ that shows up in the RG equations (5.33). The dependence on the cutoff Λ therefore drops out of the RG flow (and also out of physical observables). Last but not least, the mass still does not flow since we consider the theory directly above the quantum critical point, $r = 0$.

Integrating out non-zero Matsubara modes After the initial zero temperature RG, we obtain an effective theory

$$\begin{aligned} \mathcal{S}_{eff} = & \sum_{k \leq \xi_T^{-1}} \sum_{\omega_n} \Psi(-\vec{k}, -\omega_n) \frac{1}{2} \left[r^* + k^{1/\nu_0} + \frac{|\omega_n|^y}{k^{yz-1/\nu_0}} \right] \Psi(\vec{k}, \omega_n) \\ & + u^* \int d^d x \int d\tau \Psi(\vec{x}, \tau) \Psi(\vec{x}, \tau) \Psi(\vec{x}, \tau) \Psi(\vec{x}, \tau) . \end{aligned} \quad (5.39)$$

with a reduced cutoff, $|\vec{k}| < T^{1/z}$, an effective mass $r^* = 0$ and an effective interaction strength $u^* = u_{WF} (T/\Lambda)^{2/\nu_0-d-z}$ for a system below the upper critical dimension or an essentially unchanged $u^* \approx u$ if the system is above its upper critical dimension (see again appendix C.3 for details of the calculation). Next, we try to integrate out the non-zero Matsubara modes, which is detailed in appendix C.3. We however find that this is only possible if

$$d > \frac{1}{\nu_0} , \quad (5.40)$$

because the mass correction

$$\delta r \sim \int d^d k \frac{1}{k^{1/\nu_0}} \quad (5.41)$$

is singular otherwise. The coupling to the non-zero Matsubara modes then generates a Matsubara zero mode mass r_0^* . For a system below its upper critical dimension, it is given by

$$r_0^* = \frac{u_{WF}}{\Lambda^{2/\nu_0-d-z}} T^{1/(\nu_0 z)} \sim \left(\frac{2}{\nu_0} - d - z \right) T^{1/(\nu_0 z)} , \quad (5.42)$$

and an even smaller mass for a system above its upper critical dimension. The effective mass r_0^* is indeed smaller than the mass of the other modes, given by $T^{1/(\nu_0 z)}$, at least if the system is not far below its upper critical dimension. This is different if the spatial dimension is small, namely if

$$d < \frac{1}{\nu_0} , \quad (5.43)$$

in which case the integration over the non-zero Matsubara modes is singular. The model can then not be understood as an effectively classical, d -dimensional system.

5.3.1 Summary: critical dimensions

As a main result of our case study, we found that the character of a given system close to a quantum phase transition crucially depends on its dimensionality. More precisely,

we found that both the quantum and classical fluctuations only affect the system if the latter is below a respective critical dimension, while the fluctuations can be integrated out perturbatively above the respective critical dimension.

Critical dimension of quantum fluctuations

As discussed in Sec. 5.2.2, the effective dimension of a quantum theory is given by $D = d + z$, where d is the number of space dimensions and z is the dynamical exponent. Quantum fluctuations are only important if this effective dimension is smaller than the so-called *upper critical dimension* D_c^+ of the system,

$$D_c^+ = \frac{2}{\nu_0} , \quad (5.44)$$

such that quantum fluctuations matter for

$$d + z < D_c^+ . \quad (5.45)$$

In this case, the engineering dimension of the interaction, $[u]_{\text{engin}} = 2/\nu_0 - d - z$ is positive and the interaction is relevant. The theory then flows to an interacting Wilson-Fisher fixed point set by quantum fluctuations. If however $d + z > D_c^+$, the theory flows to a non-interacting Gaussian fixed point.

Critical dimension of classical fluctuations

If the system is at a finite temperature and close to the quantum critical point such that $r^{\nu z} \ll T$, thermal fluctuations ultimately dominate over quantum fluctuations. If the spatial dimension is larger than the *classical critical dimension*,

$$d \stackrel{!}{>} d_c = \frac{1}{\nu_0} . \quad (5.46)$$

the system can be described by a classical, d -dimensional theory. The latter emerges from the full quantum theory by perturbatively integrating out the non-zero Matsubara modes. For smaller dimensions, however, thermal fluctuations of these modes yield singular corrections to the mass. To one loop order, they are given by a Hartree-like term (5.41) that diverges for $d - 1/\nu_0 \leq 0$. In this case, it would be desirable to have a new tool at hand that allows for a controlled resummation of the divergent thermal fluctuations. This will be the subject of the next section.

5.4 Finite temperature renormalization group

The divergencies stemming from thermal fluctuations can be summed up by virtue of a finite temperature renormalization group (RG) approach. Just as more standard RG schemes, the latter consists of subsequently integrating out high-energy shells, now however not only taking into account the logarithmic derivative of zero temperature diagrams, but also of the finite temperature corrections to the latter. As detailed in appendix C.1.3, these yield an additional term to the RG equation for the mass r that is only activated for RG scales below the thermal scale $b_T = \Lambda/\xi_T^{-1}$. As we will show now, this corresponds

to the RG version of integrating out finite temperature corrections of the non-zero Matsubara modes subsequently to the initial zero temperature RG. This analysis will be performed for the more interesting case of a system below its upper critical dimension. The finite temperature RG equations for the action (5.31) read to one-loop order

$$\frac{\partial r}{\partial \ln(b)} = \frac{1}{\nu_0} r(b) - K_{d,z,y=1,\nu_0} \Lambda^{d+z-2/\nu_0} u(b) r(b) + \frac{24 \Omega_d}{(2\pi)^{(d+1)}} \pi u(b) T(b) \Lambda^{d-1/\nu_0} \Theta(b - b_T) , \quad (5.47a)$$

$$\frac{\partial u}{\partial \ln(b)} = \left(\frac{2}{\nu_0} - d - z \right) u(b) - 3 K_{d,z,1,\nu_0} \Lambda^{d+z-2/\nu_0} u^2(b) , \quad (5.47b)$$

$$\frac{\partial T}{\partial \ln(b)} = z T(b) , \quad (5.47c)$$

where the constant $K_{d,z,y=1,\nu_0}$ is of order one, see Eq. (C.78), and Ω_d is the d -dimensional solid angle. The details of the calculation are given in appendix C.4. If we consider the system directly above the quantum critical point, $r = 0$, the RG flow can be divided into two stages.

Flow towards the Wilson-Fisher fixed point

If the RG flow has not yet reached the thermal scale $b_T = \Lambda/T^{1/z}$, the mass does not flow since $\partial_b r(b) \sim r(b) = 0$. The quantum fluctuations then only drive a flow of the interaction, which quickly goes to a Wilson-Fisher fixed point,

$$u(b) = u_{\text{WF}} \frac{1}{1 + (b_{\text{WF}}/b)^{2\nu_0-d-z}} , \quad (5.48a)$$

$$u_{\text{WF}} = \frac{\frac{2}{\nu_0} - d - z}{3 K_{d,z,1,\nu_0} \Lambda^{d+z-2/\nu_0}} , \quad (5.48b)$$

$$b_{\text{WF}} = \left(\frac{u_{\text{WF}}}{u} - 1 \right)^{1/(2\nu_0-d-z)} , \quad (5.48c)$$

where u is the bare value of the interaction. Note that the Wilson-Fisher scale b_{WF} is much smaller than the thermal scale b_T if the system is close enough to the quantum critical point. See again appendix C.4 for details. Importantly, the one-loop approximation is only appropriate if the Wilson-Fisher fixed point interaction is still comparably weak, which implies

$$\frac{2}{\nu_0} - d - z \ll 1 . \quad (5.49)$$

Wilson-Fisher flow

After having reached the Wilson-Fisher fixed point, $u(b)$ can be replaced by u_{WF} . The RG equations then take the effective form

$$\frac{\partial r}{\partial \ln(b)} = \frac{1}{\nu_{\text{WF}}} r(b) + \kappa_{d,z,1,\nu_0} \frac{\frac{2}{\nu_0} - d - z}{\Lambda^{d+z-2/\nu_0}} T(b) \Lambda^{d-1/\nu_0} \Theta(b - b_T) , \quad (5.50)$$

with the Wilson-Fisher fixed point value of ν_{WF} being

$$\frac{1}{\nu_{\text{WF}}} = \frac{1}{\nu_0} - \frac{\frac{2}{\nu_0} - d - z}{3} \quad (5.51)$$

and where the flowing interaction and temperature obey

$$u(b) = u_{\text{WF}} \quad \text{and} \quad T(b) = T b^z . \quad (5.52)$$

The bare value T of the temperature equals the physical temperature, and the new constant $\kappa_{d,z,1,\nu_0}$ is of order one and given in Eq. (C.85). Details can be found in appendix C.4.

Comparison between finite temperature RG and dimensional reduction

The results obtained by integrating out non-zero Matsubara modes and the ones obtained by the finite temperature RG can best be compared via their predictions for physical quantities, and most conveniently the respective predictions for the correlation length. We want to base our comparison on the upper critical dimension and classical critical dimensions defined in Sec. 5.3.1. To this end, we denote the distance to the respective critical dimension as

$$\Delta_q = \frac{2}{\nu_0} - d - z \quad \text{and} \quad \Delta_c = \frac{1}{\nu_0} - d , \quad (5.53)$$

such that the system is below the quantum or classical critical dimension if $\Delta_q > 0$ or $\Delta_c > 0$, respectively. These definitions can now be used to define the correlation length in a transparent way. Integrating out the non-zero Matsubara modes, we have obtained a theory for the Matsubara zero mode only characterized by an effective inverse propagator

$$g^*(\omega_n = 0, \vec{k})^{-1} = r_0^* + k^{1/\nu_0} . \quad (5.54)$$

Fourier transformation along with the definition of r_0^* in Eq. (5.42) then yields a correlation length of

$$\xi \sim (r_0^*)^{-\nu_0} \sim \Delta_q^{-\nu_0} T^{-1/z} , \quad (5.55)$$

where numerical prefactors of order one have been dropped. This result is however only valid as long as thermal fluctuations do not lead to singular corrections, i.e. for $\Delta_c < 0$. The finite temperature RG, on the other hand, can be fully integrated for any choice of d and z , yielding a flowing mass $r(b)$. This flow has to be stopped at the scale b^* when $r(b^*) = \Lambda^{1/\nu_0}$, since all fluctuations are fully gapped beyond this scale. The correlation length can then be obtained as $\xi^{-1/\nu_0} = r(b^*) b^{*-1/\nu_0}$. As detailed in appendix C.4, we find that it evaluates to

$$\xi \sim \left(\frac{|\frac{2}{3}\Delta_q - \Delta_c|}{\Delta_q} \right)^{\frac{1}{\max\{1/\nu_{\text{WF}}, z\}}} T^{-1/z} , \quad (5.56)$$

where again numerical prefactors of order one have been dropped. If $(2/3)\Delta_q = \Delta_c$ there are logarithmic corrections to this expression. It nicely demonstrates the interplay

of thermal and quantum fluctuations. When thermal fluctuations are the most singular ones, i.e. when the second term on the right hand side of Eq. (5.50) is asymptotically more important than the first term, the mass flows with a scaling dimension of z , $\partial_b r(b) \sim T(b) \sim b^z$. In the opposite case, i.e. if thermal fluctuations are not singular (or at least less singular than quantum fluctuations, $\Delta_c < (2/3)\Delta_q$), the flow of the mass has a scaling dimension of $1/\nu_{\text{WF}}$ stemming from the first term on the right hand side of Eq. (5.50). The exponent controlling the RG flow is reflected in the prefactor of the correlation length, while the critical scaling of the latter always goes as $T^{-1/z}$. This was to be expected, since the temperature is by construction the only relevant energy scale (we recall that we chose $r \rightarrow 0$), and the thermal length is thus the only relevant length scale. (we recall that $\Delta_q \ll 1$ for the one-loop approximation to hold).

In summary, a quantum critical system well above its classical critical dimension can at finite temperatures T consistently be understood by a classical d -dimensional theory, with all relevant physics stemming from the Matsubara zero mode. When the system however approaches its classical critical dimension, $\Delta_c \rightarrow 0$, or is even below the latter, both quantum and thermal fluctuations of all Matsubara modes are important, and the prefactor of the correlation length is modified.

5.5 Scaling with multiple dynamics

So far, the concept of universality has made the quantum critical world beautifully simple. Especially if there is only a single quantum tuning parameter, the system could more or less be fully understood in terms of quantum and thermal fluctuations, and the scaling behavior of thermodynamic observables was entirely determined by the two length scales $\xi_T = T^{-1/z}$ and $\xi_r = r^{-\nu}$ set by the quantum critical tuning parameter r and the temperature T . Although this simple concept has explained a large number of experimental observations, more complicated situations can be encountered. In particular, different low energy fluctuations with distinct characteristic time and length scales may coexist and interact. One such example are itinerant magnets, and more precisely the heavy fermion compound YbRh_2Si_2 . This material has been reported to exhibit a quantum critical point at which two distinct energy scales vanish.⁶⁹ Since in itinerant magnets the the dynamics of the electrons close to a quantum critical point are typically faster than the ones of the magnetic fluctuations, the correlation length ξ of the system should be translated into two typical time scales τ_{el} and τ_{m} for electronic and magnetic fluctuations that obey $\tau_{\text{el}} \ll \tau_{\text{m}}$. This implies that the quantum critical point is characterized by two different dynamical exponents for electronic and magnetic fluctuations,

$$\tau_{\text{el}} \sim \xi^{z_{\text{el}}} \quad \text{and} \quad \tau_{\text{m}} \sim \xi^{z_{\text{m}}} \quad (5.57)$$

with $z_{\text{m}} > z_{\text{el}}$. A finite temperature can thus be translated into two thermal length scales $\xi_{T,\text{el}} \sim T^{-1/z_{\text{el}}}$ and $\xi_{T,\text{m}} \sim T^{-1/z_{\text{m}}}$. More generally, if a system has N_q quantum tuning parameters and N_c critical modes, one should generally expect up to $(N_q + 1) \cdot N_c$ different characteristic length scales, since each of the N_c modes might come with its own exponents $\nu_{i,j}$ and z_i ($i = 1, \dots, N_c$, $j = 1, \dots, N_q$) translating the different quantum tuning parameters and the temperature into different length scales. Already from this first estimate, it becomes clear that the physics close to a quantum critical point that is *not* characterized by a single divergent time scale and a single divergent length scale is in

general very complicated. In particular, the usual scaling can not be expected to hold in general. Of course, not every system involving multiple degrees of freedoms needs to be that complex. Most importantly, the quantum critical physics should be well-described by the usual scaling approach if only one of the many degrees of freedom becomes critical at the same time.

In order to observe unusual scaling, different possibilities can be distinguished. When the experimentally probably unrealistic fine tuning of two independent quantum critical points is not considered, one could envision a simultaneous quantum critical point of two sufficiently coupled degrees of freedom, where the instability of the one induces a similar instability of the other. This might be the case for metallic ferromagnets and the itinerant magnet system YbRh_2Si_2 discussed above.⁶⁸ As has been discussed by Belitz et al., the critical behavior of metallic ferromagnets is importantly modified by the presence of multiple dynamics, which in particular leads to logarithmic scaling corrections.^{82,83} Somewhat related situations have also been discussed in the context of dynamical phenomena close to classical phase transitions, where the coupling of dynamical processes can also give rise to a modification of dynamical scaling exponents.^{75–77,84} Alternatively, fluctuations corresponding to different types of order might coexist at a phase transition. These different fluctuations are in general also characterized by several dynamical exponents. The competition between the different orders has been argued to possibly drive second order phase transitions to first order, such that again the presence of multiple dynamics crucially influence the quantum critical physics.⁷² Alternatively, one could also have two modes that are bound to be critical at the same time by symmetry or other constraints. One such example is a Pomeranchuk instability in a two-dimensional metal, see Sec. 5.7. The latter corresponds to a d -wave deformation of the Fermi surface, and is theoretically described by two bosonic modes corresponding to the two independent entries of the quadrupolar tensor order parameter (a 2×2 matrix). One of the two modes is subject to Landau damping, which generates different dynamical exponents. Nevertheless, the two modes describe the same d -wave deformation, and thus have to be critical at the same time.⁷⁰ Finally, in the context of non-Fermi liquid systems in dimensions $d > 1$, Metlitski et al. have recently studied two-dimensional Fermi surfaces coupled to gapless gauge bosons, motivated for example by the problem of spin-density wave instabilities in two-dimensional metals.^{73,74} These systems have been described by a two-patch theory, in which momenta and energies scale in an anisotropic way, $E \sim k_x \sim k_y^2$. While this theory is thus yet another example of quantum critical points involving multiple dynamics, it however turns out to rely only on a single dynamical exponent $z = 3$ for the rescaling of energies.

In the remainder, we want to discuss the probably most simple generalization of the standard scaling scheme, namely a simultaneous quantum critical point of two modes with different dynamical exponents $z_<$ and $z_>$ (with $z_>$ larger than $z_<$) as a function of a single tuning parameter r . In addition, we assume the system to be characterized by a single length scale at zero temperature (i.e. there is only a single exponent ν for both modes). At first, we present generalized quantum critical scaling forms for the free energy which take into account the existence of multiple dynamics. These considerations should in principle be applicable to a large class of systems. Being the most simple toy model, we will then specialize to purely bosonic quantum critical systems. More complicated situations, such as mixed Bose-Fermi systems could be envisioned for future work.

5.5.1 Scaling form and thermodynamics

The scaling hypothesis for a standard quantum critical point involving only a single dynamic was based on the comparison of the different important length scales close to criticality. In our simplest generalization, we assume to have three length scales, set by the scaling fields (the quantum tuning parameter r and the temperature T) and the scaling exponents ($z_<$, $z_>$ and ν) as

$$\xi_T^< = (\eta_< T)^{-1/z_<} \quad , \quad \xi_T^> = (\eta_> T)^{-1/z_>} \quad , \quad \xi_r = r^{-\nu} \quad , \quad (5.58)$$

where the so-called kinetic coefficients η_i are constants that appropriately absorb physical dimensions (and scaling dimensions).⁵³ In this scenario, we can distinguish three possible generalizations of the usual scaling laws.

Scenario 1: one mode dominates

Firstly, the physics might for some reason be entirely dominated by one of the two dynamics, say for instance $z_<$. In this case, one is back to the standard situation discussed in the last section. The phase diagram has a crossover at $T \sim r^{\nu z_<}$, and the scaling of physical observables follows expressions (5.15) and (5.18) with $z \rightarrow z_<$. This scenario is depicted in Fig. 5.7c.

Scenario 2: both modes are independently important

Secondly, a given physical quantity could be dominated by either the one or the other mode. Which mode is dominant might not only depend on the given physical observable, but also on the region of the phase diagram one is interested in. Nevertheless, one could then for each observable (and region of the phase diagram) apply the old scaling laws under replacing either $z \rightarrow z_<$ or $z \rightarrow z_>$. The phase diagram should then exhibit two crossover lines $T \sim r^{\nu z_i}$. Each of these two crossovers would mark a change in the scaling behavior for some, but not all, physical observables, see Fig. 5.7b.

Scenario 3: something new happens

Thirdly, and this is the most interesting case, something new might happen. The co-existence of two thermal length scales could result in the appearance of new exponents somehow mixing these two scales. Alternatively, entirely new scaling laws could be generated. This third scenario is what we shall be concerned with in the following.

Scaling expectation: coupling exponents

We can gain a little more intuition on quantum critical systems with multiple dynamics by considering the generalized scaling of the free energy. Each of the two modes should yield a contribution to the critical part of the free energy density \mathcal{F}_i with respective dominant scaling $r^{\nu(d+z_i)}$ at low temperatures, where there is by assumption only one relevant length scale $\xi_r = r^{-\nu}$. Because of the coupling between the modes, the contribution of each mode should however also know about the thermal length defined with the respective other dynamical exponent. The critical part of the free energy density is thus assumed to have the overall scaling form

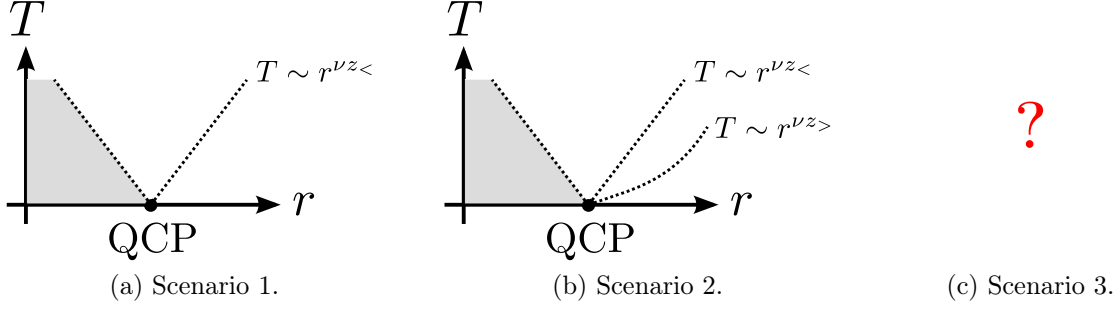


Figure 5.7: Different scenarios for scaling with multiple dynamics. If a system is characterized by two dynamical exponents $z_<$ and $z_>$ (with $z_< < z_>$) and a single correlation length exponent ν , three scaling scenarios can be distinguished. Subfigure (a) depicts the scenario that only one dynamical exponent matters, while subfigure (b) corresponds to the case that both $z_<$ and $z_>$ are important, but do not mix. As a third option, unusual scaling laws might occur.

$$\begin{aligned} \mathcal{F} &= \mathcal{F}_< + \mathcal{F}_> \\ &= b_1^{-(d+z_<)} f_<(b_1^{1/\nu} r, b_1^{z_<} t_<, b_1^{z_>} t_>) + b_2^{-(d+z_<)} f_>(b_2^{1/\nu} r, b_2^{z_<} t_<, b_2^{z_>} t_>) . \end{aligned} \quad (5.59)$$

In the above equation, we have introduced the reduced temperature scaling fields

$$t_i = \eta_i T , \quad (5.60)$$

which have the dimension of a length to the power of minus z_i , and with $i = <, >$. Note that the two contributions $\mathcal{F}_<$ and $\mathcal{F}_>$ can be evaluated at different scales $b_1 \neq b_2$ provided that the free energy decomposes into two summands (since a rescaling in one term mathematically leaves the other term unchanged). The decomposition of the free energy in two summands is however an assumption (which turns out to be valid for the model studied in the next chapter). Consequently, the scaling of the free energy density is asymptotically given by

$$\mathcal{F} = |r|^{\nu(d+z_<)} f_<(\pm 1, 0, 0) + |r|^{\nu(d+z_>)} f_>(\pm 1, 0, 0) \quad (5.61)$$

at low enough temperatures (i.e. for $T \ll |r|^{\nu z_<}, |r|^{\nu z_>}$), and hence dominated by the mode with the smaller dynamical exponent,

$$\mathcal{F} \approx |r|^{\nu(d+z_<)} f_<(\pm 1, 0, 0) , \quad (5.62)$$

since it is the more singular one (note that the limits $\lim_{T \rightarrow 0} f_i(r, t_<, t_>)$ are assumed to be well-behaved and to go to some constants). From an RG perspective, the quantum dimension $D_< = d + z_<$ of this mode is smallest, and its fluctuations are thus the most dominant ones at zero temperature.

At finite temperatures above the quantum critical point, $r \rightarrow 0$, the situation is less obvious. The scaling form of the free energy then yields

$$\mathcal{F} = t_<^{(d+z_<)/z_<} f_<(t_<^{-1/(\nu z_<)} r, 1, t_> t_<^{-z_>/z_<}) + t_>^{(d+z_>)/z_>} f_>(t_>^{-1/(\nu z_>)} r, t_< t_>^{-z_</z_>}, 1) , \quad (5.63)$$

where each of the two parts of the free energy has been evaluated at the respective thermal length. Upon approaching the quantum critical point, i.e. for $T \rightarrow 0$, the scaling function $f_>$ approaches the value $f_>(0, 0, 1)$. The limit of taking the second argument to zero should be well-behaved, just like in the zero temperature case. The scaling function $f_<$, however, will in general exhibit a singular scaling behavior for $T \rightarrow 0$, since its third argument diverges. Because we are close to a quantum critical point, where the physics are supposed to have power law scaling behavior, we furthermore assume that the function $f_<$ behaves as

$$f_<(0, 1, x_3) \sim x_3^{\psi_0} , \quad (5.64)$$

where we have introduced the *coupling exponent* ψ_0 . When calculating thermodynamics, it will furthermore be important to consider derivatives of the free energy with respect to temperature and quantum critical tuning parameter. It is thus useful to generally define the *coupling exponent of order n* as the leading behavior of the n^{th} derivative of $f_<$ with respect to the first argument,

$$f_<^{(n,0,0)}(0, 1, x_3) \sim x_3^{\psi_n} . \quad (5.65)$$

Thermodynamic quantities will primarily be sensitive to the biggest of the two terms in the right-hand side of Eq. (5.63) (or the derivatives thereof). Which term dominates which quantity however depends on the value of the respective coupling exponent, that can be positive, negative or vanish. If the critical behavior of a given thermodynamic quantity depends on both dynamical exponents $z_<$ and $z_>$, we speak of *coupled multiple dynamic scaling* (which corresponds to scenario 3), while *decoupled multiple dynamic scaling* corresponds to scaling laws depending on a single dynamical exponents only (corresponding to scenarios 1 and 2). For each order n the scaling might independently be coupled or decoupled. The case $\psi_n = 0$ corresponds to trivially decoupled multiple dynamic scaling. In order to observe coupled multiple dynamic scaling for a quantity involving n derivatives with respect to r , two conditions need to be fulfilled.

1. The respective scaling exponent needs to be non-trivial, $\psi_n \neq 0$.
2. The scaling must be dominated by $\mathcal{F}_<$ or its derivatives (since $\mathcal{F}_>$ does asymptotically not depend on $z_<$).

As we shall see later on, already the first condition is non-trivial, which might be one reason why the usual, single dynamics scaling approach works so well (although even for $\psi_n = 0$, different physical quantities are in general dominated by different dynamical exponents, see below). We also want to stress that our scaling analysis relies on the assumption that the scaling form of the free energy of the mode with the larger dynamical exponent $z_>$ and its derivatives, i.e. the functions $f_>^{(n,0,0)}$, go to some finite and constant value upon approaching the quantum critical point. As we shall see in the next chapter, this does not always need to be true, which is yet another way of obtaining unusual scaling. Let us now consider the experimentally most relevant second order derivatives of the free energy with respect to the quantum critical tuning parameter r and the temperature T . Based on the scaling form given in Eq. (5.63), their asymptotic scaling behavior directly above to the quantum critical point is given in table 5.1. Depending on the value of the respective coupling exponent ψ_n , decoupled or coupled multiple dynamic scaling can be obtained.

| Observable | Decoupled, dominated by $z_>$ | Decoupled, dominated by $z_<$ | Coupled | Condition |
|--------------------------------|----------------------------------|----------------------------------|--|--------------------------------|
| $F \sim$ | $T^{\frac{d+z_>}{z_>}}$ | not possible | $T^{\frac{d+z_<}{z_<} + \psi_0 \frac{z_<-z_>}{z_<}}$ | $\psi_0 > \frac{d}{z_>}$ |
| $T\partial_T^2 F \sim$ | $T^{\frac{d}{z_>} - 1}$ | not possible | $T^{\frac{d}{z_<} - 1 + \psi_0 \frac{z_<-z_>}{z_<}}$ | $\psi_0 > \frac{d}{z_>}$ |
| $\partial_T \partial_r F \sim$ | $T^{\frac{d-1/\nu}{z_>}}$ | $T^{\frac{d-1/\nu}{z_<}}$ | $T^{\frac{d-1/\nu}{z_<} + \psi_1 \frac{z_<-z_>}{z_<}}$ | $\psi_1 > \frac{d-1/\nu}{z_>}$ |
| $\partial_r^2 F \sim$ | $T^{\frac{d+z_>-2/\nu}{z_>}}$ | $T^{\frac{d+z_<-2/\nu}{z_<}}$ | $T^{\frac{d+z_<-2/\nu}{z_<} + \psi_2 \frac{z_<-z_>}{z_<}}$ | $\psi_2 > \frac{d-2/\nu}{z_>}$ |
| $\partial_r^n F \sim$ | $T^{\frac{d+z_>-n/\nu}{z_>}}$ | $T^{\frac{d+z_<-n/\nu}{z_<}}$ | $T^{\frac{d+z_<-n/\nu}{z_<} + \psi_n \frac{z_<-z_>}{z_<}}$ | $\psi_n > \frac{d-n/\nu}{z_>}$ |

Table 5.1: Scaling laws of some derivatives of the free energy F for finite temperatures T above the quantum critical point, $r \rightarrow 0$, including the most relevant second order derivatives. The exponents are based on a simple scaling analysis for multiple dynamics, see main text. For pressure induced criticality, the second order derivatives correspond to the specific heat c_r , the thermal expansion α and the compressibility κ , see Sec. 5.1.2. For a given derivative, decoupled multiple dynamic scaling depending only on $z_>$ is obtained if the condition in the last row is *not* fulfilled. If the condition is fulfilled, but $\psi_n = 0$, decoupled multiple dynamic scaling depending only on $z_<$ is found. Only if the condition is met *and* $\psi_n \neq 0$, coupled multiple dynamic scaling is obtained. In this case, unusual scaling laws emerge.

Finally, we note that if *decoupled* multiple dynamic scaling is obtained, physical quantities involving few derivatives with respect to r are at finite temperature generally dominated by the mode with the larger dynamical exponent $z_>$. This can be explained by the larger phase space dimension $d + z_>$ of the fluctuations of this mode with respect to the second mode. Especially, the specific heat $c_r \sim T\partial_T^2 F$ and the free energy F itself are always dominated by the $z_>$ mode. The naive phase space picture does however not hold for higher order derivatives with respect to r . These quantities are naturally more sensitive to the fluctuations associated with the quantum tuning parameter r , i.e. quantum fluctuations, and thus dominantly influenced by the mode with the smaller dynamical exponent $z_<$. More precisely, we find that for decoupled multiple dynamic scaling, the thermodynamic scaling is dominated by the mode with the larger dynamical exponent $z_>$ for derivatives of order $n < d\nu$, while the mode with the smaller dynamical exponent $z_<$ dominates for $n > d\nu$.

5.6 Multiple dynamics renormalization group

In systems with single dynamics, we have seen that a finite temperature renormalization group (RG) approach was able to describe the relevant physics even if the system is below the classical critical dimension. It would of course be desirable to apply a similar analysis to systems with multiple dynamics. However, the renormalization group approach is based on the rescaling of momenta and energies with a fixed and unique prescription. In a system with single dynamics, where there is only a single dispersion relation $\omega \sim k^z$, the rescaling is done as

$$\vec{k} \rightarrow b \vec{k} \quad \text{and} \quad \omega \rightarrow b^z \omega . \quad (5.66)$$

For a more detailed introduction to the standard renormalization group approach, see appendix A. In systems with multiple dynamics and thus several dynamical exponents, it is not clear which exponent should be used to rescale frequencies. Fundamentally even worse, a rescaling scheme such as Eq. (5.66) defines in what way physics at some length scale ξ are resummed with physics at what time scale τ (namely precisely regrouping the physics at a length scales ξ with the physics at time scales $\tau \sim \xi^z$). The choice of a given dynamical exponent thus corresponds to choosing a precise resummation scheme. Consequently, different dynamical exponents yield different resummations, and thus in general inconsistent results.

In order not to favor one of the two dynamics, we will in the following rescale frequencies with a dynamical exponent z of arbitrary value. This unphysical dynamical exponent will in the end drop out of physical observables. In order to obtain a renormalizable theory, we introduce the before mentioned kinetic coefficients η_i into the bare propagators,

$$g_i(\vec{k}, \omega) = \left(r + |\vec{k}|^{1/\nu_0} + \frac{|\omega|^{y_i}}{|\vec{k}|^{y_i z_i - 1/\nu_0}} \right)^{-1} \rightarrow \left(r + |\vec{k}|^{1/\nu_0} + \frac{|\eta_i \omega|^{y_i}}{|\vec{k}|^{y_i z_i - 1/\nu_0}} \right)^{-1} . \quad (5.67)$$

These kinetic coefficients absorb the difference in scaling dimension between the RG scaling $\omega \stackrel{\text{RG}}{\sim} k^z$ and the dispersion $\omega \stackrel{\text{dispersion}}{\sim} k^{z_i}$, and obey in a one-loop approximation the RG equations

$$\frac{\partial \eta_i}{\partial \ln(b)} = (z_i - z) \eta_i(b) . \quad (5.68)$$

The technique of absorbing additional scaling dimensions into kinetic coefficients has been introduced in the context of quantum phase transitions with multiple dynamics by Zacharias et al. in Ref. [53], but similar considerations have independently existed in the context of dynamic critical phenomena at classical phase transitions.^{77,84}

5.7 Pomeranchuk instability

A particularly interesting example of coexisting multiple dynamics can be found at the quantum critical point of a d -wave Pomeranchuk instability in a two-dimensional metal. A Pomeranchuk instability is a spontaneous deformation of a Fermi surface.⁸⁵ During the instability, the original symmetry of the Fermi surface, usually set by the lattice symmetries, is spontaneously broken. The deformation can best be classified according to the related angular momentum channel. The best-known example for a spontaneous deformation of a Fermi surface is probably the Stoner instability in a ferromagnet. At the latter, the Fermi surface of one spin species is uniformly enlarged, while the Fermi surface of the other species shrinks. The Stoner instability is thus of s -wave type. Fig. 5.8a depicts the for us more relevant example of a d -wave deformation of an initially circularly symmetric Fermi surface in two dimensions. A d -wave Pomeranchuk instability in the charge sector of a two-dimensional system was first discussed in the context of Hubbard

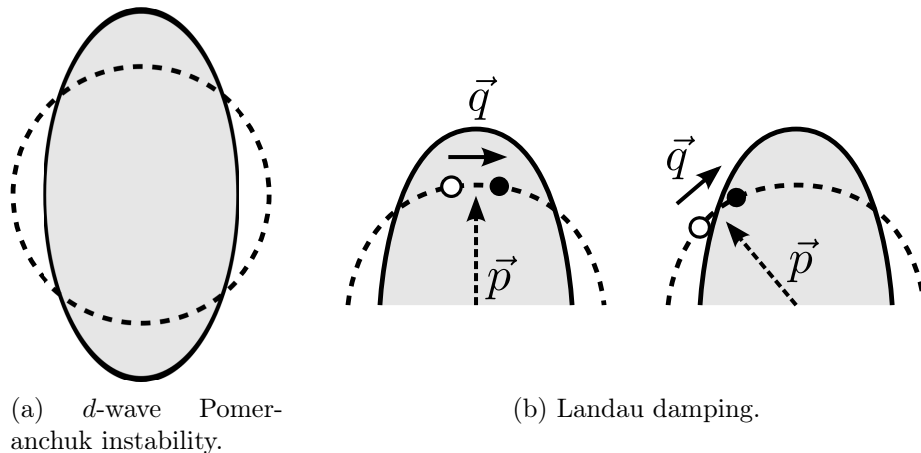


Figure 5.8: The d -wave deformation of a two-dimensional Fermi surface due to a Pomeranchuk instability. Subfigure (a) shows the deformed Fermi surface (solid lines) and the initial isotropic one (dashed line). Upon approaching the quantum critical point from the disordered side, the isotropic Fermi surface coexists with fluctuations of the collective deformation. Close to the anti-nodal points, see left part of subfigure (b), the fluctuations associated with the collective deformation are Landau damped, but not close to the nodal points (right part), see main text. Figure adapted from Ref. [53].

models motivated by high-temperature superconductors.^{86–88} For isotropic systems, the action of the critical Pomeranchuk model was established by Oganessian et al.,⁷⁰ and different aspects of the Pomeranchuk instability have been analyzed in a number of papers.^{89–100} Being a collective deformation of the entire Fermi surface with a given angular symmetry, Pomeranchuk instabilities are described by bosonic tensor order parameters. The tensor type is determined by the associated angular momentum channel, and the tensor has in general several independent entries. For a d -wave instability, the order parameter is a traceless quadrupolar tensor with two independent entries. The latter corresponds to the operator⁷⁰

$$Q(\vec{r}, t) = \Psi^\dagger(\vec{r}, t) \frac{1}{k_F^2} \begin{pmatrix} \partial_x^2 - \partial_y^2 & 2\partial_x\partial_y \\ 2\partial_x\partial_y & \partial_y^2 - \partial_x^2 \end{pmatrix} \Psi(\vec{r}, t), \quad (5.69)$$

where Ψ is a fermionic annihilation operator. Being a traceless, symmetric and two-dimensional tensor, the order parameter Q has two independent components, and a d -wave Pomeranchuk instability in two dimensions is thus described by two independent modes of bosonic quasiparticles. The latter can physically be interpreted as the longitudinal and transversal shear modes of the Fermi surface.⁷⁰ Because of the elongated shape of the Fermi surface after the transition, the d -wave Pomeranchuk instability is also known as a nematic transition.

At the transition, a Pomeranchuk unstable system can be understood as being composed of fermionic quasiparticles with a given, initial Fermi surface coupled to bosonic excitations describing the collective deformation of the Fermi surface. The coupling between the fermionic quasiparticles and the collective bosonic low energy degrees of freedom gives rise to the so-called Landau damping of the collective modes.¹⁰¹ Consider a bosonic mode of frequency ω and momentum \vec{q} . Being coupled to the fermionic degrees of freedom, the latter can decay into the creation of a particle-hole pair. If the electrons in

the system have an energy $E(\vec{p}) = \vec{v}_{\vec{p}} \cdot \vec{p}$ for a momentum $|\vec{p}| \approx p_F$ close to the Fermi surface, the bosonic mode can decay into a particle-hole pair if $\omega = E(\vec{p} + \vec{q}) - E(\vec{p}) \approx \vec{v}_{\vec{p}} \cdot \vec{q}$, provided that $|\vec{q}| \ll p_F$. Close to criticality, where $\omega \rightarrow 0$, Landau damping is thus most efficient if $\vec{v}_{\vec{p}} \perp \vec{q}$. For the d -wave Pomeranchuk instability in two dimensions, Landau damping however primarily acts close to the anti-nodal points shown in Fig. 5.8b, where the Fermi surface is substantially deformed. Close to the nodal points, the Fermi surface oscillates only very weakly (and not at all exactly at the normal points), and the interaction between the collective mode and particle-hole pairs is suppressed. Therefore, only the former mode is Landau damped, resulting in distinct dynamical exponents $z_{<} = 2$ and $z_{>} = 3$ for the two bosonic modes describing the transition. The details of the derivation of the effective action for the Pomeranchuk model can be found in Refs. [53,70].

Although it has not yet been realized experimentally, the d -wave Pomeranchuk instability in two dimensions is interesting for our following discussions because of mainly two reasons. Firstly, it involves two modes of different dynamics that are critical at the same time. Their distance to the critical point r is identical since they both derive from the same deformation of a Fermi surface.⁷⁰ This does not only apply to the bare value of r , but also holds true during a renormalization group analysis.⁵³ We can thus study a quantum critical point naturally involving multiple dynamics without any need for fine tuning or coupling between competing orders. Secondly, a two-dimensional Pomeranchuk unstable metal is in fact a system exactly at its upper critical dimension. As usual in this situation, Zacharias et al. have found that the critical scaling laws exhibit logarithmic corrections to the naive expectations. As an example, the correlation length at zero temperature was found to behave as⁵³

$$\xi \sim r^{-\nu} (\ln(\Lambda/\sqrt{r}))^{4\nu/9} \quad (5.70)$$

with $\nu = 1/2$ and where Λ is some constant related to the cutoff of the theory. This differs from the naive scaling expectation $\xi \sim r^\nu$ valid above the upper critical dimension. Since the system is at its upper critical dimension, this is not surprising. One might however speculate that the logarithms are promoted to power laws when the system is pushed below its upper critical dimension. This would result in unusual new scaling exponents. In the following, we will therefore generalize the model of a d -wave Pomeranchuk instability in a metal below its upper critical dimension and analyze the resulting critical scaling properties of thermodynamics.

Chapter 6

Emergent unusual exponents: the case of the generalized Pomeranchuk model

In the following sections, we will generalize the Pomeranchuk model discussed in Sec. 5.7 and define the related action. Thereafter, we will derive and discuss the system's renormalization group (RG) equations in a perturbative expansion of the interactions and show that they lead to unusual scaling laws and the emergence of new exponents. We furthermore discuss the behavior of different thermodynamic quantities, which can also exhibit novel scaling.

6.1 Generalized Pomeranchuk model

In the model of a d -wave Pomeranchuk instability in a two-dimensional metal, the scaling of thermodynamic observables followed the naive scaling expectations to logarithmic accuracy. In a careful analysis, it has been shown that various quantities exhibit logarithmic scaling corrections, which could be traced back to the fact that the mode with the smaller dynamical exponent (and thus the whole system) was exactly at the upper critical dimension.⁵³ Naturally, this leads to logarithmic corrections in a renormalization group analysis and thus to the critical scaling. If one of the modes lived below the upper critical dimension, these logarithmic corrections could be promoted to power law corrections modifying the scaling of thermodynamics. A d -wave Pomeranchuk unstable metal hence constitutes a promising candidate for unusual scaling as described in Sec. 5.5.1. In order to study the effect of multiple dynamics on thermodynamic scaling in a concrete toy model, we now generalize the d -wave Pomeranchuk model such that the mode with the smaller dynamical exponent lives below the upper critical dimension (and consequently so the full system). This implies the condition $d + z_c < 2/\nu_0$, where d denotes the number of space dimensions and z and ν_0 are the bare values of the dynamical exponent and the correlation length exponent, respectively. Generalizing the model of Ref. [70], we obtain the action

$$\mathcal{S} = \frac{1}{2} \sum_k \vec{n}_{-k}^T \mathcal{G}_0(k)^{-1} \vec{n}_k + \frac{u}{4! \beta V} \sum_{k_i} (\vec{n}_{k_1}^T \vec{n}_{k_2}) (\vec{n}_{k_3}^T \vec{n}_{k_4}) \delta_{k_1+k_2, k_3+k_4} , \quad (6.1)$$

where k abbreviates $k = (\omega_n, \vec{k})$, β is the inverse temperature, V denotes the volume in $d = 2$ spatial dimension, and u is the bare interaction of the modes. The vector \vec{n}_q is

the order parameter field and embraces the longitudinal and transverse mode. The bare inverse propagator $\mathcal{G}_0^{-1}(q)$ is a (2×2) -matrix that is diagonal in the frame of reference where \vec{k} is parallel to the x -axis and reads

$$\mathcal{G}_0(k)^{-1} = U(k)^{-1} \begin{pmatrix} g_>(k) & 0 \\ 0 & g_<(k) \end{pmatrix} U(k), \quad (6.2)$$

with $U(k)$ performing the necessary rotation of 2θ in order to diagonalize the Green's function matrix (θ is the angle between \vec{k} and the x -axis),

$$U(k) = \begin{pmatrix} \cos(2\theta) & \sin(2\theta) \\ -\sin(2\theta) & \cos(2\theta) \end{pmatrix}. \quad (6.3)$$

Different to earlier studies, we use the generalized propagators

$$g_<(\vec{k}, \omega_n) = r + |\vec{k}|^2 + \frac{(\eta_< \omega_n)^2}{|\vec{k}|^{2z_<-2}}, \quad (6.4)$$

$$g_>(\vec{k}, \omega_n) = r + |\vec{k}|^2 + \frac{|\eta_> \omega_n|}{|\vec{k}|^{z_>-2}}, \quad (6.5)$$

where the kinetic coefficients η_i are parameters that absorb the difference between the scaling dimension z_i and z . The previously studied model of a d -wave Pomeranchuk instability in a two-dimensional metal is obtained for $d = z_< = 2$ and $z_> = 3$. We note similarly to Sec. 5.5, both modes are characterized by the same bare correlation length exponent $\nu_0 = 1/2$. In order to keep the following discussions as general as possible, we will not only leave the dynamical exponents $z_>$ and $z_<$, but also the spatial dimensionality d of the system undefined. With these definitions, the system is below its upper critical dimension if the condition

$$d + z_< < 4 = \frac{2}{\nu_0} = D_c^+, \quad (6.6)$$

is fulfilled, and the distance to the upper critical dimension can freely be distributed between d and $z_<$.

6.2 Extended quantum to classical crossover

The concepts of universality and scaling allow to express the lowest energy physics close to a second order phase transition in terms of a few relevant length scales that diverge when the phase transition is approached. As discussed in Sec. 5.1, these relevant length scales derive from the physical tuning parameters that drive (quantum) phase transitions, such as pressure or doping, and the temperature T . The temperature is translated into a length scale by virtue of the dynamical exponent z , which generally relates energies and inverse lengths. It is usually set by the dispersion of the critical degrees of freedom, $\omega \sim k^z$.

The length scale related to the temperature, $\xi_T = T^{-1/z}$, marks the so-called quantum to classical crossover of the critical degrees of freedom, see Sec. 5.2.2. For momenta higher than the inverse thermal length, only quantum fluctuations at zero temperature of the critical mode are important, and the critical properties of these fluctuations can be described in terms of zero temperature physics. For momenta smaller than the thermal

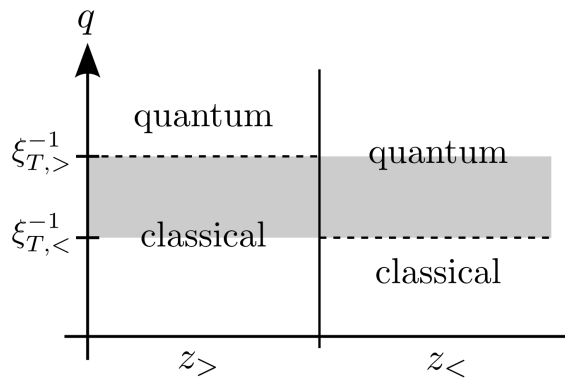


Figure 6.1: Character of the critical fluctuations of the two modes with respective dynamical exponents $z_<$ and $z_>$ (with $z_< < z_>$). At finite temperature T , the inverse thermal length scale $\xi_T^{i-1} = T^{1/z_i}$ marks a quantum to classical crossover for the respective mode $i = <, >$ as a function of the momentum $q = |\vec{q}|$. Since the two thermal momenta are parametrically different, there exists an intermediate regime where quantum fluctuations of the $z_<$ -mode coexists with classical fluctuations of the $z_>$ mode. This regime is the extended quantum to classical crossover and here shown in grey. Figure adapted from Ref. [53].

momentum ξ_T^{-1} , the critical degrees of freedom realize that the system is at a finite temperature, and thermal corrections need to be taken into account as well. Therefore, the momentum regime $|q| > \xi_T^{-1}$ is called the quantum regime, while the range of small momenta $|q| < \xi_T^{-1}$ is known as the classical momentum range. The latter name derives from the fact that for systems above their classical critical dimension, this momentum range can effectively be described by a classical theory for the Matsubara zero mode only, while all other modes are gapped by the finite temperature, see Sec. 5.3.⁸¹

In systems with multiple dynamics, and concretely in a system with two different dynamical exponents $z_<$ and $z_>$, the temperature T can be related to two distinct thermal length scales,

$$\xi_T^< = (\eta_< T)^{-1/z_<} \quad \text{and} \quad \xi_T^> = (\eta_> T)^{-1/z_>} . \quad (6.7)$$

These length scales give rise to two thermal momenta $\xi_T^{>-1}$ and $\xi_T^{<-1}$, each of which marks the quantum to classical crossover for one of the modes. Since $\xi_T^{>-1}$ is parametrically larger than $\xi_T^{<-1}$, there exists an intermediate momentum range in which the mode with the smaller dynamical exponent $z_<$ is still “quantum”, while the mode with the larger dynamical exponent $z_>$ is already “classical”. This regime has first been discussed in Ref. [53], where it was dubbed the *extended quantum to classical crossover regime*, and is shown in Fig. 6.1. As we will discuss in the remainder of this chapter, it is the unusual interplay of quantum fluctuations and thermal fluctuations in precisely this extended quantum to classical crossover regime that can potentially generate unusual scaling exponents.

6.3 Renormalization group equations up to $\xi_T^{\leq -1}$

In the next sections, we want to analyze the generalized Pomeranchuk system by a thermal renormalization group (RG) analysis with multiple dynamics. As explained in Sec. 5.6 and appendix C.6, the presence of multiple dynamics requires a generalization of the usual RG scheme, in which frequencies are rescaled using an arbitrary dynamical exponent z . This in turn requires the introduction of kinetic coefficients η_i that relate the arbitrary dynamical exponent z to the physical exponents $z_<$ and $z_>$. Using this generalized RG scheme, we can derive the renormalization group equations as usual by subsequently integrating out high energy modes. As can be seen by inspection of Fig. 6.1, the first stages of the RG will be governed by a purely quantum flow. Only when the running cutoff reaches the larger thermal scale $\xi_T^{\geq -1}$, i.e. when the RG enters the extended quantum to classical crossover regime, additional thermal corrections stemming from the mode with the larger dynamical exponent $z_>$ arise. Since we integrate out modes between Λ and Λ/b at each RG step (where Λ is the momentum UV cutoff and $b > 1$), the running cutoff reaches this thermal scale at an RG stage $b_T^{\leq} = \Lambda/\xi_T^{\leq -1}$. Thermal fluctuations of the mode with the smaller dynamical exponent $z_<$ would be important at RG stages $b > b_T^{\leq} = \Lambda/\xi_T^{\leq -1}$. We will however see that this regime is never reached since the RG is always stopped before or exactly at b_T^{\leq} (we stop the flow when the running mass r reaches the cutoff, since all modes are fully gapped beyond the point).

In the purely classical regime, i.e. for RG stages $1 < b < b_T^{\geq}$, quantum fluctuations of both modes can in principle lead to singular corrections to the mass r and the interaction u . To one-loop order, the renormalizations of the mass and the interaction are given by the diagrams

$$\delta r \sim \frac{\text{diagram } z_<}{u} + \frac{\text{diagram } z_>}{u} , \quad (6.8)$$

$$\delta u \sim \text{diagram } z_< + \text{diagram } z_> + \text{diagram } z_> z_< . \quad (6.9)$$

These quantum corrections can be further simplified by simple dimensional arguments. The mode with the smaller dynamical exponent $z_<$ is by construction below the upper critical dimension, $d + z_< < D_c^+$, and its fluctuations therefore importantly affect the state of the system. The second mode, on the other hand, has a higher quantum dimension $d + z_>$. Its fluctuations are less singular than the ones of the $z_<$ -mode, and the quantum part of the RG equations will asymptotically be fully governed by the mode with the smaller dynamical exponent $z_<$. Technically, this follows from the fact that a diagram involving the $z_>$ mode is asymptotically suppressed by a factor of

$$\frac{\eta_<(b)}{\eta_>(b)} \sim b^{-(z_>-z_<)} \rightarrow 0 , \quad (6.10)$$

with respect to a diagram involving only the $z_<$ -mode, see appendix C.6. These sub-leading terms will thus only be active at the initial stages of the RG. Their effect can be absorbed into a redefinition of the bare values of the mass r and coupling constant u , and we will drop them in our RG analysis.

When the RG enters the extended quantum to classical crossover regime in Fig. 6.1, i.e. for RG stages $b > b_T^>$, also thermal fluctuations of the mode with the larger dynamical exponent $z_>$ yield potentially singular corrections that modify the RG flow. As we discuss in appendix C.1, these thermal corrections are however only relevant for the correction to the mass r : close to the quantum critical point, where r is small, the quantum fluctuations give rise to singular corrections proportional to r itself,

$$\delta r|_{\text{quantum}} = A u r , \quad (6.11)$$

where A is an appropriate constant. Terms like $\delta r \sim A' u$ exist, but are not singular (see appendix C.1). In comparison, the thermal corrections typically have the form

$$\delta r|_{\text{thermal}} = B u T \quad (6.12)$$

(B again denotes some constant). This characteristic form proportional to $u T$ reflects the fact that for systems above the classical critical dimension, only the Matsubara zero mode contributes to the singular renormalization of the mass,

$$\delta r \sim u \frac{1}{\beta V} \sum_{\vec{k}} \sum_{\omega_n} (\dots) \delta_{\omega_n, 0} \rightarrow u \frac{T}{V} \sum_{\vec{k}} (\dots) . \quad (6.13)$$

The characteristic form however also holds if non-zero Matsubara modes have important fluctuations, see appendix C.1. In the quantum critical region, the thermal correction to the mass is larger than its quantum correction, and should therefore be retained in the RG equations. This is different for the interaction, where quantum fluctuations yield corrections of the form (C again denotes a constant)

$$\delta u|_{\text{quantum}} = C u^2 \quad (6.14)$$

outside the Ginzburg regime which we do not consider here. Since the interaction has a finite value, a thermal correction $\sim u^2 T$ is comparably negligibly small close enough to the quantum critical point. In conclusion, thermal fluctuations (if present) only affect the correction to the mass as

$$\delta r \sim \frac{\text{blue circle } z_<}{u} + \frac{\text{red circle } z_>}{u} , \quad (6.15)$$

while the RG equation for the interaction remains unchanged,

$$\delta u \sim \frac{\text{blue loop } z_<}{u} . \quad (6.16)$$

As in Eq. (6.9), blue lines denote quantum fluctuations, while red lines stand for thermal fluctuations. Note that we have already dropped the quantum correction due to the mode with the larger dynamical exponent $z_>$, as discussed in the last paragraph. The full set of RG equations for RG stages $b < \Lambda/\xi_T^{\leq -1}$ can thus be written as

$$\frac{\partial r}{\partial \ln(b)} = 2r(b) - \frac{K_{d,z<,2,1/2}}{36} \Lambda^{d+z-4} \frac{u(b)r(b)}{\eta_{<}(b)} + \frac{\Omega_d}{(2\pi)^{(d+1)}} \frac{2\pi}{3} u(b) T(b) \Lambda^{d-2} \Theta(b - b_T^>) , \quad (6.17a)$$

$$\frac{\partial u}{\partial \ln(b)} = (4 - d - z) u(b) - \frac{3}{48} K_{d,z<,2,1/2} \Lambda^{d+z-4} \frac{u^2(b)}{\eta_{<}(b)} , \quad (6.17b)$$

$$\frac{\partial T}{\partial \ln(b)} = z T(b) , \quad (6.17c)$$

$$\frac{\partial \eta_{<}}{\partial \ln(b)} = (z_{<} - z) \eta_{<}(b) , \quad (6.17d)$$

$$\frac{\partial \eta_{>}}{\partial \ln(b)} = (z_{>} - z) \eta_{>}(b) , \quad (6.17e)$$

where $K_{d,z<,2,1/2}$ is a constant of order one, see Eq. (C.133). Note that this constant is independent of the arbitrarily chosen z . For the derivation of these RG equations, see appendices C.1, C.5 and C.6.

6.4 Analysis of the RG equations

We will now proceed to the analysis of the RG equations (6.17). First discussing the limiting cases of zero temperature $T = 0$ and finite mass $r > 0$ (i.e. low temperatures in the disordered phase), and then $r = 0$ at finite T (i.e. the quantum critical region), we will be able to identify all important RG scales in the problem. We then turn to the full solution of the RG equations for arbitrary values of r and T . In the RG analysis, we again want to use the *distance to the upper critical dimension* Δ_q and the *distance to the classical critical dimension* Δ_c defined in Sec. 5.3. Since quantum fluctuations are dominated by the smaller dynamical exponent $z_{<}$, the quantum distance Δ_q is defined via latter (quantum fluctuations of $z_{>}$ are subleading, and the arbitrary exponent z is unphysical). For the generalized Pomeranchuk model, the distances to the upper critical dimension and classical critical dimension are thus given by

$$\Delta_q = 4 - d - z_{<} \quad \text{and} \quad \Delta_c = 2 - d , \quad (6.18)$$

such that quantum or classical fluctuations are singular if the distance to the respective critical dimension is positive, $\Delta_q > 0$ or $\Delta_c > 0$. By construction, the generalized Pomeranchuk model is below its upper critical dimension, $\Delta_q > 0$. The RG equations for the temperature and kinetic coefficients can easily be integrated to

$$T(b) = T b^z \quad , \quad \eta_{<}(b) = \eta_{<,0} b^{z_{<} - z} \quad , \quad \eta_{>}(b) = \eta_{>,0} b^{z_{>} - z} \quad , \quad (6.19)$$

where T equals the physical temperature, and the bare values of the kinetic coefficients $\eta_{i,0}$ are some constants of order one. The RG equations for the mass r and the interaction u are more complicated and will be discussed in detail in the following.

6.4.1 Zero temperature, finite mass

In the limit of zero temperature $T = 0$ and finite mass $r > 0$, the RG equations are particularly simple. The system is then governed by quantum fluctuations only, which in turn are dominated by the mode with the smaller dynamical exponent $z_<$. Since both thermal momenta $\xi_T^{(i)-1} = (\eta_i T)^{1/z_i}$ vanish at $T = 0$, the interesting extended quantum to classical crossover regime does not exist in the limit of zero temperature. The integration of the RG equations is detailed in appendix C.7 and can be divided into two stages.

Initial flow away from the Gaussian fixed point: $1 \leq b < b_{\text{WF}}$

The bare value of the interaction $u = u_0$ is assumed to be perturbatively small, and the system is thus initially close to a (repulsive) Gaussian fixed point. In the early stages of the RG flow, the quantum fluctuations drive the system to an interacting Wilson-Fisher fixed point. Since this flow is driven by the mode with the smaller dynamical exponent $z_<$, we find that it is the effective interaction

$$U(b) = \frac{u(b)}{\eta_<(b)} \quad (6.20)$$

that acquires the Wilson-Fisher fixed point value. Integrating the RG equation for $U(b)$, we obtain

$$U(b) = U_{\text{WF}} \frac{1}{1 + (b_{\text{WF}}/b)^{\Delta_q}} , \quad (6.21a)$$

$$U_{\text{WF}} = \frac{\Delta_q}{\frac{3}{48} K_{d,z_<,2,1/2} \Lambda^{-\Delta_q}} , \quad (6.21b)$$

$$b_{\text{WF}} = \left(\frac{U_{\text{WF}}}{U_0} - 1 \right)^{1/\Delta_q} . \quad (6.21c)$$

We note that the one-loop approximation made here is only appropriate if the Wilson-Fisher fixed point interaction U_{WF} is still small. This implies that

$$\Delta_q \ll 1 . \quad (6.22)$$

Flow dominated by the Wilson-Fisher fixed point: $b_{\text{WF}} \leq b$

After the Wilson-Fisher fixed point has been reached, one may approximate $u(b)/\eta_<(b) \approx U_{\text{WF}}$ in the RG equation for the mass r ,

$$\frac{\partial r}{\partial \ln(b)} \approx \frac{1}{\nu_{\text{WF}}} r(b) \quad \text{with} \quad \frac{1}{\nu_{\text{WF}}} = 2 - \frac{4}{9} \Delta_q , \quad (6.23)$$

where we have introduced the Wilson-Fisher fixed point value of the correlation length exponent ν_{WF} . The RG flow has to be stopped when the flowing mass equals the high momentum cutoff Λ^2 , since all modes are fully gapped beyond this scale. This defines the RG stage b^* as $r(b^*) = \Lambda^2$. The final mass in turn sets the correlation length ξ according to the engineering dimension of the mass term as

$$r(b^*) = \xi^{-2} b^{*2} , \quad (6.24)$$

which implies $b^* = \Lambda \xi$. We furthermore assume that the Wilson-Fisher fixed point describes a strongly interacting system

$$U_{\text{WF}} \stackrel{!}{\gg} U_0, \quad (6.25)$$

and that the latter fixed point is responsible for the low energy behavior of the system, implying that there is an extended RG regime governed by the Wilson-Fisher fixed point,

$$b^* \stackrel{!}{\gg} b_{\text{WF}}. \quad (6.26)$$

With these assumptions, we find that the correlation length at low temperatures ξ_{LT} is given by

$$\xi_{\text{LT}} = r^{-\nu_{\text{WF}}} \left(\frac{\frac{3}{48} K_{d,z<,2,1/2}}{\Delta_q} U_0 \right)^{\frac{4}{9} \nu_{\text{WF}}}. \quad (6.27)$$

For the details of the calculation, the reader is referred to appendix C.7. As expected, the correlation length ξ_{LT} is independent of the arbitrary z . At zero temperature, the correlation length is thus proportional to $r^{-\nu_{\text{WF}}}$. Since we have constructed the model such that there is only this single length scale deriving from the mass r at $T = 0$, this is not a surprising result. Furthermore, the anomalous scaling dimension of the mass, $[r]_{\text{anom.}} = \frac{1}{\nu_{\text{WF}}} - \frac{1}{\nu} = -4\Delta_q/9$, reflects the fact that the system is at a strongly interacting Wilson-Fisher fixed point.

6.4.2 Zero mass, finite temperature

In the opposite limit of vanishing mass $r = 0$ and finite temperature T , i.e. right above the quantum critical point, the system has two distinct thermal scales set by the two dynamical exponents, $\xi_T^{(i)-1} = (\eta_i T)^{1/z_i}$. As we will show in the next paragraphs, the resulting extended quantum to classical crossover regime will be responsible for the behavior of the correlation length and thermodynamical observables. Again, the flow can be divided into (now three) characteristic stages.

Quantum flow away from the Gaussian fixed point: $1 \leq b < b_{\text{WF}}$

The very early stages of the RG are again responsible for driving the system away from vicinity of the weakly interacting Gaussian fixed point and towards the Wilson-Fisher fixed point discussed in Sec. 6.4.1. The effective interaction $U = u/\eta_{<}$ approaches the fixed point value U_{WF} just as for the zero temperature case (see Eq. (6.21)),

$$U(b) = U_{\text{WF}} \frac{1}{1 + (b_{\text{WF}}/b)^{\Delta_q}}. \quad (6.28a)$$

Since the mass initially vanishes, $r = 0$, it does at first not flow. If we assume to be close enough to the quantum critical point, one can always ensure that $b_{\text{WF}} \ll b_T^> = \Lambda/T^{z>}$, such that thermal fluctuations get activated long after the Wilson-Fisher fixed point has been reached. In this case, $r(b) = 0$ holds in the entire regime $1 \leq b < b_{\text{WF}}$ (and until the larger thermal RG scale $b_T^>$ is reached).

Figure 6.2: Renormalizations of the mass in the extended quantum to classical crossover regime due to quantum fluctuations of the mode with the smaller dynamical exponent $z_<$ (blue) and thermal fluctuations of the mode with the larger dynamical exponent $z_>$ (red). The interaction vertex is given by the Wilson-Fisher fixed point value U_{WF} , which is set by quantum fluctuations of the $z_<$ -mode.

Quantum flow dominated by the Wilson-Fisher fixed point: $b_{\text{WF}} \leq b < b_T^>$

Beyond the Wilson-Fisher RG scale b_{WF} , the interaction can be approximated by $u(b)/\eta_<(b) \approx U_{\text{WF}}$. As long as the thermal scale $b_T^>$ has not been reached, the mass does however still not flow.

Flow in the extended quantum to classical crossover regime: $b_T^> \leq b < b_T^<$

The RG enters the extended quantum to classical crossover regime of Fig. 6.1 when it reaches the thermal scale $b \geq b_T^>$ with $b_T^> = \Lambda/\xi_T^>$. Since the system is already at the Wilson-Fisher fixed point, we can approximate the RG equation for the mass as

$$\frac{\partial r}{\partial \ln(b)} = \frac{1}{\nu_{\text{WF}}} r(b) + \frac{\Omega_d}{(2\pi)^{(d+1)}} \frac{2\pi}{3} U_{\text{WF}} \eta_<(b) T(b) \Lambda^{d-2} \Theta(b - b_T^>) . \quad (6.29)$$

This equation is one of the central formulas of this chapter. The corresponding diagrams are shown in Fig. 6.2. Equation (6.29) encodes in a nutshell how quantum fluctuations of the mode with the smaller dynamical exponent $z_<$ and thermal fluctuations of the mode with the larger dynamical exponent $z_>$ coexist and interact in the extended quantum to classical crossover regime. We note that the thermal fluctuations of the mode with the larger dynamical exponent $z_>$ modify the mass by virtue of the Wilson-Fisher fixed point interaction. Since the latter is set by the mode with the smaller dynamical exponent $z_<$, the temperature effectively scales with the latter exponent, $\eta_<(b) T(b) = t_<(b) = \eta_{<,0} T b^{z_<}$. If this seems a bit surprising at first glance, we recall that thermal fluctuations are classical, and therefore do not know about the quantum dynamics of the mode they derive from (except for the scale $b_T^>$ where they get activated).

Both quantum and thermal fluctuations disorder the system and consequently increase the mass. The physical behavior of the system crucially depends on which of the two disordering mechanism is the more powerful one. This in turn depends on whether the quantum term or the thermal term in Eq. (6.29) grows asymptotically faster. Since the quantum term has a scaling $\sim b^{1/\nu_{\text{WF}}}$, while the thermal term scales as $b^{z_<}$, we can distinguish two scenarios. For

$$\frac{1}{\nu_{\text{WF}}} > z_< \quad \text{or equivalently} \quad \frac{5}{9} \Delta_q > \Delta_c , \quad (6.30)$$

quantum fluctuations are most singular and therefore govern the asymptotic flow. In the opposite case, thermal fluctuations of the mode with the larger dynamical exponent $z_>$

dominate over quantum fluctuations of the mode with the smaller dynamical exponent $z_<$.

Thermal fluctuations are dominant: $\frac{5}{9} \Delta_q < \Delta_c$

Let us first turn to the less interesting case that thermal fluctuations are asymptotically the most dominant ones, $z > \frac{1}{\nu_{\text{WF}}}$. The RG equation for the mass can then be integrated as shown in appendix C.7. We find that the thermal fluctuations generate a finite mass r similarly to the case of single dynamics, see Sec. 5.4. This mass continues to flow due to thermal fluctuations up to the scale b^* with $r(b^*) = \Lambda^2$ (and $b^* = \Lambda \xi$ as before). Up to numerical prefactors of order one, the correlation length $\xi_{\text{QC,thermal}}$ in the quantum critical regime for a flow dominated by thermal fluctuations is given by

$$\xi_{\text{QC,thermal}} \sim (\eta_< T)^{-1/z_<} \left(\frac{\Delta_c - \frac{5}{9} \Delta_q}{\Delta_q} \right)^{1/z_<} . \quad (6.31)$$

We thus find that since the thermal fluctuations are coupled with an interaction set by the Wilson-Fisher fixed point, and thus set by the mode with the smaller dynamical exponent $z_<$, also the temperature scaling of the correlation length is set by the smaller dynamical exponent $z_<$. Compared to the thermal length $\xi_T^<$ related to this mode, the correlation length is however suppressed by a factor of $\sim ((\Delta_c - \frac{5}{9} \Delta_q)/\Delta_q)^{1/z_<}$ due the interplay of classical and thermal fluctuations. However, no new scaling exponents emerge. We also note that the flow stops at the scale $b^* = \Lambda \xi \sim \Lambda/T^{-1/z_<} = b_T^<$, i.e. at the scale $b_T^<$. The purely thermal regime at later RG stages does thus not contribute to the RG flow.

Quantum fluctuations are dominant: $\frac{5}{9} \Delta_q > \Delta_c$

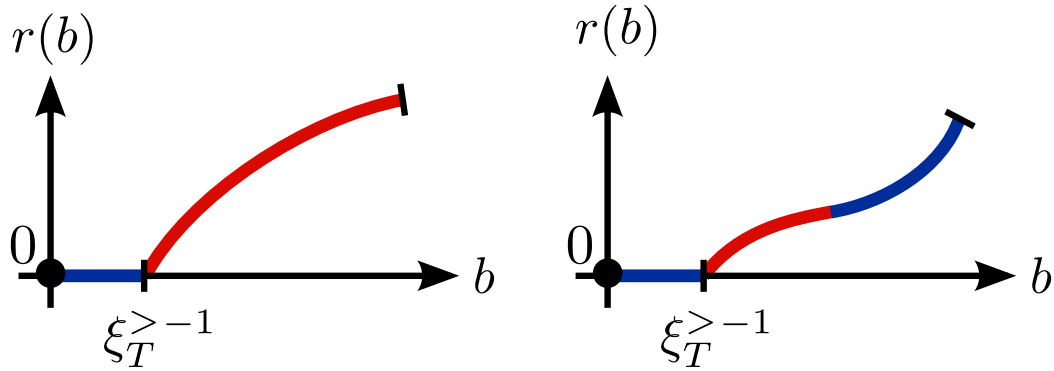
If quantum fluctuations dominate the asymptotic flow of the RG equations, the situation is far less standard. This happens if the distance to the upper critical dimension is more important than the distance to the classical critical dimension, $\frac{5}{9} \Delta_q > \Delta_c$. Although in this case the first term on the right-hand side of Eq. (6.29) is asymptotically much larger than the second one, the former depends on $r(b)$, and consequently vanishes close to the thermal scale $b \approx b_T^>$, i.e. when the RG enters the extended quantum to classical crossover regime in Fig. 6.1. The RG flow is thus first due to thermal fluctuations only

$$\left. \frac{\partial r}{\partial \ln(b)} \right|_{b \approx b_T^>} \approx \frac{\Omega_d}{(2\pi)^{(d+1)}} \frac{2\pi}{3} U_{\text{WF}} \eta_<(b) T(b) \Lambda^{d-2} . \quad (6.32)$$

When thermal fluctuations have generated a finite mass $r(b) \sim U_{\text{WF}} \eta_<(b) T(b) \Lambda^{d-2}$, quantum fluctuations take over the flow, which however happens very quickly (in particular still at the RG scale $b \approx b_T^>$). The initial ‘‘thermal mass’’ is then boosted by quantum fluctuations and described by the flow equation

$$\left. \frac{\partial r}{\partial \ln(b)} \right|_{b > b_T^>} \approx \frac{1}{\nu_{\text{WF}}} r(b) . \quad (6.33)$$

The flow ends again at a scale b^* when $r(b^*) = \Lambda^2$. Since the mass now grows faster than it did in the case $\frac{5}{9} \Delta_q < \Delta_c$, the scale b^* is parametrically smaller than $b_T^<$, and the purely



(a) Thermal fluctuations dominate.

(b) Quantum boosted thermal flow.

Figure 6.3: Typical RG trajectories of the mass $r(b)$ as a function of the RG scale b if the physical mass (quantum detuning from the quantum critical point) vanishes, $r = 0$. Subfigure (a) depicts the case that thermal fluctuations are more singular than quantum fluctuations, in which case the mass is generated and flows according due to thermal fluctuations. Subfigure (b) shows the scenario that quantum fluctuations are asymptotically dominant, when thermal fluctuations generate a finite starting value for the mass (red part of the RG trajectory), which is then boosted by quantum fluctuations (blue part of the RG trajectory). The black bar denotes the end of the RG scale. The diagrams corresponding to this RG flow are depicted in Fig. 6.2.

thermal RG regime beyond this scale is again not important (note that this scale b^* does *not* coincide with b^* from the last paragraph). This unusual *quantum boosted thermal flow* is depicted in Fig. 6.3b. The end of the RG flow allows to define the correlation length in the quantum critical regime as before via $r(\Lambda\xi) = \Lambda^2$ (now set by quantum boosted thermal fluctuations). Again dropping numerical prefactors of order one, we obtain

$$\xi_{\text{QC,boosted}} \sim T^{-1/z_e} \left(\frac{\frac{5}{9}\Delta_q - \Delta_c}{\Delta_q} \right)^{\nu_{\text{WF}}}, \quad (6.34)$$

where a new dynamical exponent

$$z_e = \frac{z_>}{1 + \nu_{\text{WF}}(z_> - z_<)} \quad (6.35)$$

has emerged. It depends on the larger dynamical exponent $z_>$ (because thermal fluctuations at the scale $b_T^>$ generate the classical starting value for the mass), on the effective correlation length exponent ν_{WF} (since the latter characterizes the asymptotic flow due to quantum fluctuations), and the smaller dynamical exponent $z_<$ (since the Wilson-Fisher fixed point setting the interaction has been reached due to quantum fluctuations of the $z_<$ -mode). It does however *not* depend on the number of space dimensions d , and neither on the microscopic interaction u . The simplicity of Eq. (6.35) suggests that the emergent dynamical exponent z_e is valid not only in the precise problem under discussion, but might generically occur in systems with multiple dynamics.

6.5 Scaling with the multiple dynamics and diagonalized RG equations

As we have seen in the last paragraph, the interaction between coexisting thermal and quantum fluctuations generates a new emergent exponent z_e , see Eq. (6.35). From a scaling perspective, the mixing of thermal and quantum fluctuations also mixes the initially independent scaling field $r(b)$ and $T(b)$. We can thus gain further insight into the scaling and subsequently the resulting thermodynamics by re-diagonalizing the RG equations in the extended quantum to classical crossover regime, which yields the emergent scaling fields of the problem. These new scaling fields will then allow to define the characteristic length scales of the problem. Firstly, the relevant interaction is given by

$$U(b) = \frac{u(b)}{\eta_{<}(b)}, \quad (6.36)$$

since it is always this combination that appears in the RG equations (6.17). Physically, this is due to the fact that the mode with the smaller dynamical exponent $z_{<}$ drives all renormalizations of the interaction and thus all scale dependencies of the latter. Secondly, as discussed in Sec. 5.5, the temperature can be related to different length scales $\xi_T^{(i)} = (\eta_i T)^{-1/z_i}$ by virtue of the two different dynamical exponents. It is thus reasonable to introduce the scaling fields

$$t_{<}(b) = \eta_{<}(b) T(b) \quad \text{and} \quad t_{>}(b) = \eta_{>}(b) T(b), \quad (6.37)$$

which replace $\eta_{<}(b)$, $\eta_{>}(b)$, and $T(b)$ and have the physically relevant scaling dimensions. The mixing of r and T can be diagonalized using the emergent scaling field

$$R(b) = r(b) + \frac{\Omega_d}{(2\pi)^{(d+1)}} \frac{2\pi}{3} \frac{U_{\text{WF}} \Lambda^{d-2}}{1/\nu_{\text{WF}} - z_{<}} t_{<}(b). \quad (6.38)$$

With these fields, the RG equations take the simple form

$$\frac{\partial R}{\partial \ln(b)} = \frac{1}{\nu_{\text{WF}}} R(b), \quad (6.39a)$$

$$\frac{\partial U}{\partial \ln(b)} = U_{\text{WF}} U(b) - U(b)^2, \quad (6.39b)$$

$$\frac{\partial t_{<}}{\partial \ln(b)} = z_{<} t_{<}(b), \quad (6.39c)$$

$$\frac{\partial t_{>}}{\partial \ln(b)} = z_{>} t_{>}(b). \quad (6.39d)$$

These equations are valid for RG stages beyond the thermal scale $b_T^> = \Lambda/t_{>}^{1/z_{>}} = \Lambda/(\eta_{>} T^{1/z_{>}})$ and come with the initial condition

$$R(b_T^>) = r(b_T^>) + \frac{\Omega_d}{(2\pi)^{(d+1)}} \frac{2\pi}{3} \frac{U_{\text{WF}} \Lambda^{d-2}}{1/\nu_{\text{WF}} - z_{<}} t_{<}(b_T^>) \quad (6.40a)$$

$$= \left(\frac{1}{\xi_{\text{LT}}^{1/\nu_{\text{WF}}}} + \frac{1}{\xi_{\text{QC,boosted}}^{1/\nu_{\text{WF}}}} \right) \Lambda^{2-1/\nu_{\text{WF}}} b_T^>^{1/\nu_{\text{WF}}}, \quad (6.40b)$$

where we have used expressions (6.27) for the correlation length in the low temperature regime ξ_{LT} and (6.34) for the correlation length in the quantum critical regime for quantum boosted thermal fluctuations, $\xi_{\text{QC,boosted}}$. The characteristic length scales of the system can now be defined as the RG scales where the different flowing quantities equal the cutoff (to the respective engineering dimension),

$$t_{<}(\Lambda \xi_{t_{<}}) = \Lambda^{z_{<}} \quad , \quad t_{>}(\Lambda \xi_{t_{>}}) = \Lambda^{z_{>}} \quad \text{and} \quad R(\Lambda \xi_R) = \Lambda^2 \quad . \quad (6.41)$$

These three length scales thus evaluate to

$$\xi_{t_{<}} = (\eta_{<} T)^{-1/z_{<}} \quad , \quad (6.42)$$

$$\xi_{t_{>}} = (\eta_{>} T)^{-1/z_{>}} \quad , \quad (6.43)$$

$$\xi_R = \left(\frac{1}{\xi_{\text{LT}}^{1/\nu_{\text{WF}}}} + \frac{1}{\xi_{\text{QC,boosted}}^{1/\nu_{\text{WF}}}} \right)^{-\nu_{\text{WF}}} \quad . \quad (6.44)$$

While the two thermal scales $\xi_{t_{<}}$ and $\xi_{t_{>}}$ are naturally given by the thermal length scales $\xi_T^{(i)}$ that we have already used before, the third length scale ξ_R replaces the usual length scale $\xi_r = r^{-\nu}$ related to the quantum tuning parameter r . The mixing of thermal and quantum fluctuations does thus not only lead to the emergence of a new dynamical exponent, but also generated a new length scale. The latter is non-zero even directly above the quantum critical point $r = 0$. Thermodynamics therefore derive from the comparison of the three characteristic length scales $\xi_{t_{<}}$, $\xi_{t_{>}}$ and ξ_R .

6.6 Solution to the RG equations at arbitrary values of r and T

Having understood the behavior of the RG equations in different limiting cases, we can summarize our findings by stating the general results for arbitrary values of the physical temperature T and the quantum tuning parameter r . As detailed in appendix C.7.4, we find that the RG equations have three characteristic stages, which are depicted in Fig. 6.4.

Flow to the Wilson-Fisher fixed point: $1 \leq b < b_{\text{WF}}$

The very initial flow stems from integrating out the highest energy quantum modes and is thus dominated by the mode with the smaller dynamical exponent $z_{<}$. It pushes the system away from the vicinity of a weakly interacting Gaussian fixed point towards a strongly interacting Wilson-Fisher fixed point. The latter is reached at a scale b_{WF} , when the interaction $U = u/\eta_{<}$ reaches the Wilson-Fisher value $U_{\text{WF}} \sim \Delta_q = 4 - d - z$. The fact that the interaction has to be rescaled with the kinetic coefficient $\eta_{<}$ reflects the fact that the Wilson-Fisher fixed point is reached due to quantum fluctuations of the mode with the smaller dynamical exponent $z_{<}$. We note that the scale $b_{\text{WF}} = (U_{\text{WF}}/U_0 - 1)^{1/\Delta_q}$ is generically the first characteristic RG scale close enough to the quantum critical point.

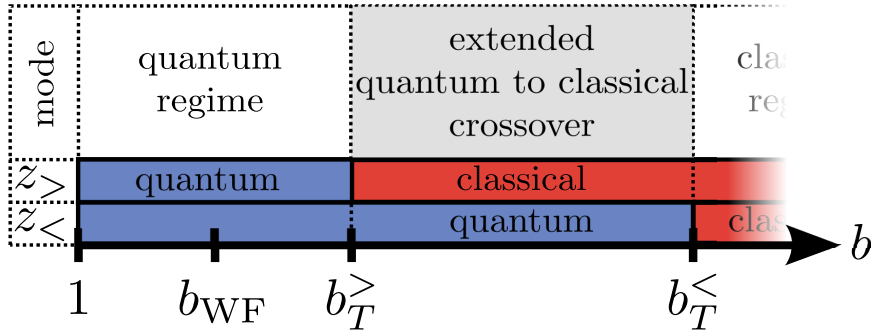


Figure 6.4: Different RG scales and stages as a function of the cutoff reduction factor b (the RG step involves $\Lambda \rightarrow \Lambda/b$). The characteristic stages are $b_{\text{WF}} = (U_{\text{WF}}/U_0 - 1)^{1/\Delta_q}$, the scale when the Wilson-Fisher fixed point is reached, and the scales when either of the two modes $z_>$ and $z_<$ changes its character from quantum to classical, $b_T^> = \Lambda \xi_T^>$ and $b_T^< = \Lambda \xi_T^<$. The entirely classical regime for $b > b_T^<$ is never reached. This RG scale mode corresponds to subsequently integration out the high energy modes diagram in Fig. 6.1.

Further quantum flow: $b_{\text{WF}} \leq b < b_T^>$

Once the Wilson-Fisher fixed point has been reached, the interaction stops flowing. The mass and temperature however keep on flowing with their respective zero temperature quantum flow until the thermal RG scale $b_T^> = \Lambda \xi_T^>$ related to the mode with the larger dynamical exponent $z_>$ is reached.

Flow in the extended quantum to classical crossover regime: $b_T^> \leq b < b_T^<$

In the extended quantum to classical crossover regime, both thermal fluctuations of the mode with the larger dynamical exponent $z_>$ and quantum fluctuations of the mode with the smaller dynamical exponent $z_<$ renormalize the mass, see Fig. 6.2. This coexistence leads to a mixing of the scaling fields $r(b)$ and $t_<(b)$. The fact that the rescaled temperature $t_<(b) = \eta_<(b)T(b)$ is defined with respect to the smaller dynamical exponent $z_<$ is again related to the Wilson-Fisher fixed point (which in turn is set by the $z_<$ -mode). The mixing leads to the emergence of a new scaling field $R(b) = r(b) + \alpha t_<(b)$, see Eq. (6.38) (with $\alpha = \text{const.}$). This field replaces the flowing mass $r(b)$ and gives rise to the emergence of a new length scale

$$\xi_R \sim (r + \tilde{\alpha} T^{1/(\nu_{\text{WF}} z_e)})^{-\nu_{\text{WF}}}, \quad (6.45)$$

where $\tilde{\alpha}$ is an appropriate constant, see Eq. (6.44). This emergent length scale depends on an emergent dynamical exponent

$$z_e = \frac{z_>}{1 + \nu_{\text{WF}}(z_> - z_<)}. \quad (6.46)$$

The latter encodes that thermal fluctuations at the scale $b_T^>$ (which is set by the larger dynamical exponent $z_>$) generate a classical starting mass which is then boosted by quantum fluctuations. The *quantum boost of thermal fluctuations* corresponds to a secondary flow with the exponent ν_{WF} set by the Wilson-Fisher fixed point. The end of the RG flow is reached when the mass generated by interacting thermal and quantum fluctuations

reaches the cutoff Λ^2 , since all fluctuations are fully gapped beyond this scale. This happens either at or before the smaller thermal RG scale $b_T^<$, such that the purely classical momentum range can never influence the RG flow. The correlation length ξ of the system can be obtained from the implicit equation

$$\xi \approx \begin{cases} \frac{\xi_R}{\left(1 + \left(\frac{\xi_R}{\xi}\right)^{1/\nu_{\text{WF}}}\left(\frac{\xi}{\xi_{\text{QC,thermal}}}\right)^{z_<}\right)^{\nu_{\text{WF}}}} & , \quad \xi > \xi_T^> \\ \xi_r & , \quad \xi < \xi_T^> \end{cases}, \quad (6.47)$$

see appendix C.7.4, where $\xi_{\text{QC,thermal}} \sim \xi_T^< = (\eta_< T)^{-1/z_<}$ is detailed in Eq. (6.31) and with $\xi_r = r^{-\nu_{\text{WF}}}$. Physical observables are however only affected if the new length scale ξ_R is smaller than the length scale $\xi_{\text{QC,thermal}}$ in the quantum critical region. This implies that the condition

$$z_e > z_< \quad \text{or equivalently} \quad \frac{1}{\nu_{\text{WF}}} > z_< \quad \text{or equivalently} \quad \frac{5}{9}\Delta_q > \Delta_c \quad (6.48)$$

is fulfilled, i.e. quantum fluctuations are more singular than thermal fluctuations. In this case, the quantum boosted thermal fluctuations dominate over pure thermal fluctuations, which in turn results in the unusual scaling of the correlation length. We find that if the conditions (6.48) are fulfilled, the correlation length ξ is given by

$$\xi \sim \begin{cases} r^{-\nu_{\text{WF}}} & \text{if } T < r^{\nu_{\text{WF}}z_e} \\ T^{-1/z_e} & \text{if } T > r^{\nu_{\text{WF}}z_e} \end{cases}, \quad (6.49)$$

while the more standard scaling

$$\xi \sim \begin{cases} r^{-\nu_{\text{WF}}} & \text{if } T < r^{\nu_{\text{WF}}z_<} \\ T^{-1/z_<} & \text{if } T > r^{\nu_{\text{WF}}z_<} \end{cases} \quad (6.50)$$

is obtained otherwise. In the next sections, we will show how the unusual scaling due to the emergent dynamical exponent also affects other thermodynamical observables if the conditions (6.48) are respected.

6.7 Thermodynamics

Thermodynamic properties of the generalized Pomeranchuk model can be derived from the critical part of the free energy density $\mathcal{F} = F_{\text{crit.}}/V$ via derivatives with respect to the temperature T or the quantum tuning parameter r , see Secs. 5.1.2 and 5.5. As usual, the interaction prohibits an exact calculation of the free energy. We therefore calculate the latter in a standard crossover theory following the work of Nelson¹⁰² and Millis¹⁰³. As detailed in appendix C.8, this approach allows to calculate the free energy density as the integration over a perturbative RG trajectory. We obtain the physically transparent equation

$$\mathcal{F} = \mathcal{F}_< + \mathcal{F}_> , \quad (6.51)$$

$$\mathcal{F}_< = \int_0^\Lambda dq \int \frac{d\Omega_d}{(2\pi)^d} q^{d-1} T \ln \left(2 \sinh \left(\frac{\sqrt{q^{2z_<-2}(\tilde{r}(\Lambda/q) + q^2)}}{2\eta_{<,0} T} \right) \right) , \quad (6.52)$$

$$\mathcal{F}_> = \int_0^\Lambda dq \int \frac{d\Omega_d}{(2\pi)^d} q^{d-1} \int_0^\infty \frac{d\omega}{2\pi} \coth \left(\frac{\omega}{2T} \right) \arctan \left(\frac{\eta_> \omega}{q^{z_>-2}(\tilde{r}(\Lambda/q) + q^2)} \right) . \quad (6.53)$$

where we used the definition

$$\tilde{r}(b) = b^{-2} r(b) . \quad (6.54)$$

Up to the flowing expression of the mass, $\tilde{r}(b)$, the free energy densities are thus identical to the ones obtained for the non-interacting system (for details, see appendix C.8). The rescaled mass $\tilde{r}(b)$ only flows with the anomalous dimension of r , and therefore corresponds to the scale dependence of $r(b)$ due to interaction effects. In order to make the connection to the emergent scaling field R defined in Eq. (6.38) and the scaling form (5.63) defined in Sec. 5.5, it is also instructive to first let the integrals go from 0 to ∞ and then redefine $q = (\eta_< T)^{1/z_<} e^{-l}$ for $\mathcal{F}_<$, and $q = (\eta_> T)^{1/z_>} e^{-l}$ and $\omega = T \epsilon$ for $\mathcal{F}_>$, which yields

$$\mathcal{F}_< = \frac{(\eta_< T)^{(d+z_<)/z_<}}{\eta_<} \int_{-\infty}^\infty dl \int \frac{d\Omega_d}{(2\pi)^d} e^{-dl} \ln \left(2 \sinh \left(\frac{\sqrt{r(e^l \Lambda (\eta_< T)^{-1/z_<})/\Lambda^2 + 1}}{2e^{z_<l}} \right) \right) , \quad (6.55a)$$

$$\mathcal{F}_> = \frac{(\eta_> T)^{(d+z_>)/z_>}}{\eta_>} \int_{-\infty}^\infty dl \int \frac{d\Omega_d}{(2\pi)^d} \int_0^\infty \frac{d\epsilon}{2\pi} e^{-dl} \coth \left(\frac{\epsilon}{2} \right) \arctan \left(\frac{\epsilon e^{z_>l}}{r(e^l \Lambda (\eta_> T)^{-1/z_>})/\Lambda^2 + 1} \right) . \quad (6.55b)$$

Note that these expressions are manifestly independent of the unphysical and arbitrary dynamical exponent z , as expected.

In the low temperature regime and for RG stages $b \gg b_{\text{WF}} \gg 1$, the flowing mass yields

$$r(e^l \Lambda t_<^{-1/z_<})/\Lambda^2 = r t_<^{-1/(\nu_{\text{WF}} z_<)} e^{l/\nu_{\text{WF}}} (U_{\text{WF}}/U_0)^{4/9} \Lambda^{1/\nu_{\text{WF}}-2} \quad (6.56)$$

with $t_< = \eta_< T$. As could have been expected, the scaling function $f_<$ thus only depends on the combination $r t_<^{-1/(\nu_{\text{WF}} z_<)}$ at low temperatures. In the high temperature regime, the asymptotic flow of the mass is described by the new scaling field $R(b)$ defined in Eq. (6.38). Denoting $R(b) = R b^{1/\nu_{\text{WF}}}$, we find that the free energy density of the mode with the smaller dynamical exponent only depends on

$$r(e^l \Lambda t_<^{-1/z_<})/\Lambda^2 = R t_<^{-1/(\nu_{\text{WF}} z_<)} \Lambda^{1/\nu_{\text{WF}}-2} e^{l/\nu_{\text{WF}}} - \frac{\Omega_d}{(2\pi)^{(d+1)}} \frac{2\pi}{3} \frac{\Delta_q}{\frac{5}{9}\Delta_q - \Delta_c} e^{z_<l} , \quad (6.57)$$

and thus only on the combination $R t_<^{-1/(\nu_{\text{WF}} z_<)}$. Similar considerations show that the free energy density of the mode with the larger dynamical exponent depends on $R t_>^{-1/(\nu_{\text{WF}} z_>)}$

(or $r t_{>}^{-1/(\nu_{\text{WF}} z_{>})}$ at low temperatures) and $t_{<} t_{>}^{-z_{<}/z_{>}}$. In the high temperature regime, where the interesting quantum boost of thermal fluctuations is visible, the free energy densities can thus be described by the scaling forms

$$\mathcal{F}_{<} = b^{-(d+z_{<})} \frac{1}{\eta_{<}} \tilde{f}_{<}(b^{1/\nu_{\text{WF}}} R, b^{z_{<}} t_{<}), \quad (6.58)$$

$$\mathcal{F}_{>} = b^{-(d+z_{>})} \frac{1}{\eta_{>}} \tilde{f}_{>}(b^{1/\nu_{\text{WF}}} R, b^{z_{<}} t_{<}, b^{z_{>}} t_{>}), \quad (6.59)$$

where $t_i = \eta_i T$. Whereas the contribution to the free energy from the mode with the smaller dynamical exponent $z_{<}$ is set by the interplay of the length scales ξ_R and $\xi_T^{<}$, the mode with the larger dynamical exponent has a contribution to the free energy that derives from the comparison of all three length scales ξ_R , $\xi_T^{<}$ and $\xi_T^{>}$. Finally, in order to make the connection to the scaling expectations of Sec. 5.5.1, it is useful to recall from Eq. (6.45) that

$$R = \Lambda^{2-1/\nu_{\text{WF}}} \xi_R^{1/\nu_{\text{WF}}} \sim r + \tilde{\alpha} T^{1/(\nu_{\text{WF}} z_e)} = r + \tilde{\alpha} T^{1/(\nu_{\text{WF}} z_{>})} (T T^{-z_{<}/z_{>}}). \quad (6.60)$$

Therefore, the scaling of the free energy density $\mathcal{F}_{<}$ in the quantum critical region directly above the quantum critical point is in agreement with the result found in Sec. 5.5.1,

$$\mathcal{F}_{<} = t_{<}^{(d+z_{<})/z_{<}} f_{<}(t_{<}^{-1/(\nu_{\text{WF}} z_{<})} r, 1, t_{>} t_{<}^{-z_{>}/z_{<}}). \quad (6.61)$$

More precisely, we find that this scaling form collapses as

$$f_{<}(x_1, 1, x_3) = \frac{1}{\eta_{<}} \tilde{f}_{<}(x_1 + \tilde{\alpha} x_3^{\frac{1-\nu_{\text{WF}} z_{<}}{\nu_{\text{WF}} z_{>}}}, 1). \quad (6.62)$$

In conclusion, we find that the free energy densities scale as

$$\mathcal{F}_{<} \sim \min \{\xi, \xi_T^{<}\}^{-(d+z_{<})} = \xi^{-(d+z_{<})}, \quad (6.63)$$

$$\mathcal{F}_{>} \sim \min \{\xi, \xi_T^{>}\}^{-(d+z_{>})}, \quad (6.64)$$

where we used that $\xi_T^{>} \ll \xi_T^{<}$ and replaced ξ_r and ξ_R by the correlation length. This result can also be more formally obtained by integrating the RG trajectories (6.55), which is exemplified for $\mathcal{F}_{<}$ in appendix C.9.

6.7.1 Coupling exponents

In order to calculate thermodynamic observables, we do of course need to know the full expressions of the free energy densities, rather than just the leading scaling behavior. This especially includes the coupling exponents ψ_n defined in Sec. 5.5.1. Using Eq. (6.47), we find that the leading temperature scaling of $\partial_r^n \mathcal{F}_{<}$ directly above the quantum critical point is given by

$$\frac{\partial^n \mathcal{F}_{<}}{\partial r^n} \sim \begin{cases} T^{(d+z_{<} - n/\nu_{\text{WF}})/z_{<}} & \text{if } z_e < z_{<} \\ T^{(d+z_{<} - n/\nu_{\text{WF}})/z_e} & \text{if } z_e > z_{<} \end{cases}. \quad (6.65)$$

The coupling exponents ψ_n have in Sec. 5.5.1 been defined as the unusual scaling dimension resulting from the divergence of the third argument free energy scaling form

$$\frac{\partial^n \mathcal{F}_<}{\partial r^n} = T^{\frac{d+z_<-n/\nu_{\text{WF}}}{z_<}} f_<^{(n),0,0}(0, 1, T T^{-z_>/z_<}) \sim T^{\frac{d+z_<-n/\nu_{\text{WF}}}{z_<}} (T T^{-z_>/z_<})^{\psi_n} . \quad (6.66)$$

They are thus given by

$$\psi_n = \begin{cases} 0 & \text{if } z_e < z_< \\ (\nu_{\text{WF}}(d + z_<) - n) \frac{1/\nu_{\text{WF}} - z_<}{z_>} & \text{if } z_e > z_< \end{cases} . \quad (6.67)$$

We also recall that unusual scaling for a thermodynamic observable involving n derivatives with respect to r is expected if

$$\psi_n > (d - n/\nu_{\text{WF}})/z_> \quad \text{and} \quad \psi_n \neq 0 , \quad (6.68)$$

see Sec. 5.5.1. This implies that we obtain unusual scaling whenever

$$n > \frac{2 - \frac{5}{9}\Delta_q}{2 - \frac{4}{9}\Delta_q} . \quad (6.69)$$

where we used the values $1/\nu_{\text{WF}} = 2 - (4/9)\Delta_q$, and $\Delta_q = 4 - d - z_<$ specific to our model. For the generalized Pomeranchuk model, we thus obtain unusual scaling in the quantum critical region for any thermodynamic observable that involves at least one derivative with respect to r if the principal criterion $\frac{5}{9}\Delta_q > \Delta_c$ (or $z_e > z_<$ or $1/\nu_{\text{WF}} > z_<$) is fulfilled. The free energy itself and the specific heat $c \sim T \partial_T^2 \mathcal{F}$ would only exhibit unusual scaling if the system was very far below its quantum critical dimension, namely if $\Delta_q = 4 - d - z_< > 3.6$, which seems unphysical.

6.7.2 Scaling of thermodynamic observables

We want to close this section with the explicit calculation of the scaling of the most interesting physical observables using the RG trajectories for the free energy densities (6.55) and demonstrate that the emerging exponent also alters the scaling of thermodynamic observables. This leads to new crossover scales in the phase diagram. The calculation is in principle straightforward. We however note that subtleties arise when derivatives are taken, e.g. with respect to the quantum tuning parameter r . The latter enters the RG trajectories via the combination

$$\tilde{r}(b) = b^{-2} r(b) , \quad (6.70)$$

which is explicitly given in Eq. (C.178). From there, we find that in all regimes

$$\frac{\partial \tilde{r} \left(\frac{\Lambda}{q} \right)}{\partial r} = b_{\text{WF}}^{4\Delta_q/9} \left(\frac{\Lambda}{q} \right)^{1/\nu_{\text{WF}}-2} \approx \left(\frac{48 \Delta_q}{3 K_{d,z_<,2,1/2} U_0} \right)^{4/9} q^{2-1/\nu_{\text{WF}}} . \quad (6.71)$$

It is now only a matter of solving integrals to obtain the leading scaling behavior of different thermodynamic observables in the different regions of the phase diagram. The

explicit calculation of the thermal expansion $\alpha = \partial_T \partial_r \mathcal{F}$ is given in appendix C.9, the other quantities are calculated in a similar fashion. Since the free energy densities scale as

$$\mathcal{F}_< \sim \xi^{-(d+z_<)} , \quad (6.72)$$

$$\mathcal{F}_> \sim \min \{ \xi, \xi_T^> \}^{-(d+z_>)} , \quad (6.73)$$

$$(6.74)$$

the contribution of each of the modes changes its scaling behavior whenever the free energy density itself does so. We find that the free energy density of the mode with the larger dynamical exponent $z_<$ behaves as

$$\mathcal{F}_< \sim \begin{cases} r^{\nu_{\text{WF}}(d+z_>)} & \text{if } T < r^{\nu_{\text{WF}}z_>} \\ T^{(d+z_>)/z_>} & \text{if } T > r^{\nu_{\text{WF}}z_>} \end{cases} . \quad (6.75)$$

Similarly, the free energy density of the mode with the smaller dynamical exponent $z_<$ scales as

$$\mathcal{F}_< \sim \begin{cases} r^{\nu_{\text{WF}}(d+z_<)} & \text{if } T < r^{\nu_{\text{WF}}z_{(\cdot)}} \\ T^{(d+z_>)/z_{(\cdot)}} & \text{if } T > r^{\nu_{\text{WF}}z_{(\cdot)}} \end{cases} , \quad (6.76)$$

where $z_{(\cdot)}$ is given by $\max\{z_e, z_<\}$. These crossovers from low temperature scaling to quantum critical scaling are naturally reflected in the scaling of the contribution of the respective mode to thermodynamic observables. Since the two crossovers do not coincide, we can generically divide the disordered side of the phase diagram into three regions. In the low temperature region (LT), both modes are in their low temperature regime. In the intermediate regime (IR), the mode with the larger dynamical exponent $z_>$ already exhibits finite temperature scaling, while the mode with the smaller dynamical exponent is still in its low temperature regime. In the high temperature or quantum critical region (QC), both modes are in their high temperature regimes. For a better orientation, we refer to the final phase diagrams as given in Fig. 6.5.

Specific heat

The specific heat is defined as

$$c_r = -T \frac{\partial^2 \mathcal{F}}{\partial T^2} . \quad (6.77)$$

The contributions of the two modes can be evaluated by applying the derivatives to the RG trajectories (6.55) and then integrating them, similarly to appendix C.10. We find that the contribution of the mode with the smaller dynamical exponent behaves as

$$c_{r,<} \sim \begin{cases} T^{y_0} \xi^{-(d-y_0z_<)} & , \quad T \ll r^{\nu_{\text{WF}}z_>} \\ T \xi^{-(d-z_<)} & , \quad T \gg r^{\nu_{\text{WF}}z_>} \text{ and } z_e < z_< , \\ T^{2/(\nu_{\text{WF}}z_e)-1} \xi^{-(d+z_<-2/\nu_{\text{WF}})} & , \quad T \gg r^{\nu_{\text{WF}}z_>} \text{ and } z_e > z_< \end{cases} , \quad (6.78)$$

with

$$y_0 = \frac{d}{z_{<} - \frac{1}{2\nu_{\text{WF}}}} . \quad (6.79)$$

The crossover at $T \sim r^{\nu_{\text{WF}}z_{>}}$ is not fully resolved by our calculation, probably because we do not take into account the generation of the temperature dependence of the running mass due to thermal fluctuations of the mode with the larger dynamical exponent $z_{>}$ exactly. The integration of the RG trajectory using the full expression of the running mass is in progress and will be published in future work. However, this mismatch is a subleading effect for the overall compressibility $c_r = c_{r,<} + c_{r,>}$ (see below) and can thus be disregarded for our purposes (i.e. precisely the derivation of the leading scaling of c_r). In any case, since the correlation length has a crossover at $T \sim r^{\nu_{\text{WF}}z_{(\cdot)}}$ with $z_{(\cdot)} = \max\{z_e, z_{<}\}$, the contribution $c_{r,<}$ is actually sensitive to both crossovers at $T \sim r^{\nu_{\text{WF}}z_{>}}$ and $T \sim r^{\nu_{\text{WF}}z_{(\cdot)}}$. Note furthermore that in the quantum critical region, we can also express this result via the coupling exponents defined in Eq. (6.67) as

$$c_{r,<} \sim T^{d/z_{<} + \psi_0(z_{<} - z_{>})/z_{<}} . \quad (6.80)$$

The contribution of the mode with the larger dynamical exponent, on the other hand, reads

$$c_{r,>} \sim \begin{cases} T \xi^{-(d-z_{>})} & , \quad T \ll r^{\nu_{\text{WF}}z_{>}} \\ \xi_T^{>-d} & , \quad T \gg r^{\nu_{\text{WF}}z_{>}} \end{cases} . \quad (6.81)$$

We thus find that if no unusual scaling is obtained, i.e. if $z_e < z_{<}$, the contributions of both modes in the low temperature regime $T \ll r^{\nu_{\text{WF}}z_{>}}$ and the quantum critical regime $T \gg r^{\nu_{\text{WF}}z_{>}}$ can be understood within the naive scaling expectations of two decoupled modes, see Sec. 5.1.2. In the intermediate regime, the mode with the smaller dynamical exponent feels the presence of thermal fluctuations of the mode with the larger dynamical exponent, which modifies its scaling. The usual scaling for the specific heat of the mode with the smaller dynamical exponent also breaks down in the quantum critical regime if the quantum fluctuations are strong enough to boost the thermally generated mass during the RG flow, i.e. if $z_e > z_{<}$. We can then understand the scaling of the specific heat with the coupling exponent ψ_0 defined in Eq. (6.67). The overall scaling of the specific heat, however, is always dominated by the mode with the larger dynamical exponent (unless the system is very far below its upper critical dimension, $4 - d - z_{<} \geq 3.6$, which seems unphysical and is beyond the scope of our one-loop calculation, see Sec. 6.7.1). We thus find that the specific heat scales as

$$c_r \sim \begin{cases} T r^{\nu_{\text{WF}}(d-z_{>})} & , \quad T \ll r^{\nu_{\text{WF}}z_{>}} \quad (\text{LT}) \\ T^{d/z_{>}} & , \quad T \gg r^{\nu_{\text{WF}}z_{>}} \quad (\text{IR}) \text{ and } (\text{QC}) \end{cases} . \quad (6.82)$$

Thermal expansion

The mixed second order derivative

$$\alpha = \frac{\partial^2 \mathcal{F}}{\partial T \partial r} \quad (6.83)$$

determines the thermal expansion in the case of pressure induced quantum criticality. The contributions of the different modes to the thermal expansion are explicitly calculated in appendix C.10. The contribution of the mode with the smaller dynamical exponent scales as

$$\alpha_{<} \sim \begin{cases} T^{y_0} \xi^{-(d-y_0 z_{<} - 1/\nu_{\text{WF}})} & , \quad T \ll r^{\nu_{\text{WF}} z_{>}} \\ \xi^{-(d-1/\nu_{\text{WF}})} & , \quad T \gg r^{\nu_{\text{WF}} z_{>}} \quad \text{and } z_e < z_{<} \quad , \\ T^{1/(\nu_{\text{WF}} z_e) - 1} \xi^{-(d+z_{<} - 2/\nu_{\text{WF}})} & , \quad T \gg r^{\nu_{\text{WF}} z_{>}} \quad \text{and } z_e > z_{<} \end{cases} \quad (6.84)$$

with

$$y_0 = \frac{d}{z_{<} - \frac{1}{2\nu_{\text{WF}}}} \quad , \quad (6.85)$$

Again, the scaling of $\alpha_{<}$ close to $T \sim r^{\nu_{\text{WF}} z_{>}}$ could not be fully resolved by our analysis, but the leading behavior of $\alpha = \alpha_{<} + \alpha_{>}$ turns out to be obtained correctly (see below). Note again that since the correlation length has a crossover at $T \sim r^{\nu_{\text{WF}} z_{(\cdot)}}$ with $z_{(\cdot)} = \max\{z_e, z_{<}\}$, the contribution $\alpha_{<}$ is sensitive to both crossovers at $T \sim r^{\nu_{\text{WF}} z_{>}}$ and $T \sim r^{\nu_{\text{WF}} z_{(\cdot)}}$. We thus find that when no unusual scaling is obtained, i.e. $z_e < z_{<}$, the contribution of the mode with the smaller dynamical exponent satisfies the naivest scaling expectations of Sec. 5.1.2 at lowest temperature and in the quantum critical region. In the intermediate regime $r^{\nu_{\text{WF}} z_{>}} \ll T \ll r^{\nu_{\text{WF}} z_{(\cdot)}}$, however, the thermal expansion is already given by the high-temperature expression (when written in terms of the correlation length), since thermal fluctuations already exist. The correlation length, on the other hand, is still given by its low-temperature expression, which leads to a non-trivial scaling in this intermediate region. For $z_e > z_{<}$, the emergent unusual scaling of the correlation length is also reflected in the scaling of $\alpha_{<}$, both in the intermediate and quantum critical regions. We note that expression (6.84) can in the high temperature regime also be written as

$$\alpha_{<} \sim T^{(d-1/\nu_{\text{WF}})/z_{<} + \psi_1(z_{<} - z_{>})/z_{<}} \quad (6.86)$$

with the coupling exponent ψ_1 defined in Eq. (6.67), and the scaling is thus in agreement with our more elaborate expectation of Sec. 5.5.1. The contribution of the mode with the larger dynamical exponent $z_{>}$, on the other hand, has the scaling

$$\alpha_{>} \sim \begin{cases} T \xi^{z_{>} - d + 1/\nu_{\text{WF}}} & , \quad T \ll r^{\nu_{\text{WF}} z_{>}} \\ \max\{\xi_T^{> - (d-1/\nu_{\text{WF}})}, \xi^{-(d-1/\nu_{\text{WF}})}\} & , \quad T \gg r^{\nu_{\text{WF}} z_{>}} \quad . \end{cases} \quad (6.87)$$

In the intermediate and quantum critical regimes, where $\xi_T^{>} \ll \xi$, the scaling of $\alpha_{>}$ depends on the sign of $d - 1/\nu_{\text{WF}} = \frac{4}{9} \Delta_q - \Delta_c$. For $\Delta_c > \frac{4}{9} \Delta_q$, the mode with the larger dynamical exponent $z_{>}$ has a thermal expansion that neither agrees with the naive expectations for high nor for low temperatures. This is due to the fact that in a system with multiple dynamics, the correlation length and the thermal length of the mode with the larger dynamical exponent $z_{>}$ do *not* coincide in the high temperature regime of this mode, i.e. for $T > r^{\nu_{\text{WF}} z_{>}}$. The unusual scaling then stems from the Matsubara zero mode. The latter is associated with a free energy given by

$$\mathcal{F}_> \sim T \int_0^{T^{1/z_>}} d^d q \ln(\beta(\xi^{-2} + q^2)) \sim T \xi^{-d} \int_0^{\xi T^{1/z_>}} d^d \tilde{q} \ln(\beta \xi^{-1} (1 + \tilde{q}^2)) \quad (6.88)$$

$$\Rightarrow \mathcal{F}_> \sim T \xi^{-d} .$$

The thermal expansion due to the Matsubara zero mode is thus indeed given by $\xi^{-(d-1/\nu_{\text{WF}})}$. In terms of the scaling functions defined in Sec. 5.5, this means that the derivative with respect to r of the free energy scaling function $f_>$ does not go to a constant but rather vanishes upon approaching the quantum critical point. In agreement with the discussion of Sec. 5.5.1, we thus find that the mode with the smaller dynamical exponent $z_<$ dominates the scaling in the quantum critical region for $1 > d\nu_{\text{WF}}$, i.e. for $\Delta_c > \frac{4}{9}\Delta_q$. This also holds true for $\Delta_c < \frac{4}{9}\Delta_q$, now however because then criterion $\frac{5}{9}\Delta_q > \Delta_c$ for unusual scaling due to the emergent exponent z_e is met. In conclusion, the scaling of α in the quantum critical region and the intermediate temperature regime $r^{\nu_{\text{WF}}z_>} < T < r^{\nu_{\text{WF}}z_(<)} ,$ with $z_(<) = \max\{z_e, z_<\}$, is always dominated by the mode with the smaller dynamical exponent (for $\Delta_c > \frac{5}{9}\Delta_q$, the scaling behavior of the two contributions coincides). The thermal expansion is thus sensitive to the crossover at $T \sim r^{\nu_{\text{WF}}z_(<)}$. The low temperature regime $T \ll r^{\nu_{\text{WF}}z_>}$ is however always dominated by the mode with the larger dynamical exponent. Hence, the thermal expansion is also sensitive to the lower crossover at $T \sim r^{\nu_{\text{WF}}z_>}$. The scaling of $\alpha = \alpha_> + \alpha_<$ is thus given by

$$\alpha \sim \begin{cases} T r^{-\nu_{\text{WF}}(z_>-d+1/\nu_{\text{WF}})} & , T \ll r^{\nu_{\text{WF}}z_>} \\ r^{\nu_{\text{WF}}(d-\frac{1}{\nu_{\text{WF}}})} & , r^{\nu_{\text{WF}}z_>} \ll T \ll r^{\nu_{\text{WF}}z_<} , \\ T^{(d-1/\nu_{\text{WF}})/z_<} & , T \gg r^{\nu_{\text{WF}}z_<} \end{cases} \quad (6.89)$$

for $z_e < z_>$ and by

$$\alpha \sim \begin{cases} T r^{-\nu_{\text{WF}}(z_>-d+1/\nu_{\text{WF}})} & , T \ll r^{\nu_{\text{WF}}z_>} \\ T^{\frac{1}{\nu_{\text{WF}}z_e}-1} r^{\nu_{\text{WF}}(d+z_<-\frac{2}{\nu_{\text{WF}}})} & , r^{\nu_{\text{WF}}z_>} \ll T \ll r^{\nu_{\text{WF}}z_e} , \\ T^{-1} T^{(d+z_<-1/\nu_{\text{WF}})/z_e} & , T \gg r^{\nu_{\text{WF}}z_e} \end{cases} \quad (6.90)$$

for $z_e < z_>$. Using the explicit definition of z_e , one can easily check that the overall scaling of the thermal expansion matches at the lower crossover $T \sim r^{\nu_{\text{WF}}z_>}$. Most importantly, the thermal expansion is always sensitive to the quantum to classical crossovers of both modes. The analogue of the latter behavior has already been found for the regular, two-dimensional Pomeranchuk instability discussed in Ref. [53].

Compressibility

The susceptibility of the system with respect to the quantum tuning parameter r , which is the compressibility for pressure-induced quantum criticality, is defined as

$$\kappa = \frac{\partial^2 \mathcal{F}}{\partial r^2} . \quad (6.91)$$

Since the latter involves two derivatives with respect to the quantum tuning parameter r , it is naturally much more sensitive to fluctuations associated with r , i.e. quantum fluctuations. Since already the thermal expansion was importantly influenced by the mode with the smaller dynamical exponent, it is natural to expect that the compressibility is even more sensitive to the latter mode. The contributions can be obtained by integration of the respective RG trajectories, or by direct differentiation of expressions (6.64) for the free energy densities. We find that the two modes have contributions

$$\kappa_{<} = \xi^{-(d+z_{<} - 2/\nu_{\text{WF}})} \quad \forall T \text{ and } r, \quad (6.92)$$

and

$$\kappa_{>} \sim \begin{cases} \xi^{-(d+z_{>} - 2/\nu_{\text{WF}})} & , \quad T \ll r^{\nu_{\text{WF}} z_{>}} \\ \max \{ T \xi_T^{>-(d-2/\nu_{\text{WF}})}, T \xi^{-(d-2/\nu_{\text{WF}})} \} & , \quad T \gg r^{\nu_{\text{WF}} z_{>}} \end{cases}. \quad (6.93)$$

In the intermediate and high temperature regimes, we thus find that the contribution of the mode with the larger dynamical exponent $\kappa_{>}$ is dominated by the Matsubara zero mode and set by the correlation length for $\Delta_c > \frac{8}{9}\Delta_q - 2$, while it is set by the thermal length $\xi_T^{>}$ otherwise (where we used that $d - 2/\nu_{\text{WF}} = \frac{8}{9}\Delta_q - 2 - \Delta_c$). However, we find that the overall scaling of the total compressibility $\kappa = \kappa_{>} + \kappa_{<}$ is always determined by the mode with the smaller dynamical exponent and behaves as

$$\kappa \sim \xi^{-(d+z_{<} - 2/\nu_{\text{WF}})} \sim \begin{cases} r^{\nu_{\text{WF}}(d+z_{<} - 2)} & , \quad T \ll r^{\nu_{\text{WF}} z_{(\cdot)}} \quad (\text{LT and IR}) \\ T^{(d+z_{<} - 2/\nu_{\text{WF}})/z_{(\cdot)}} & , \quad T \gg r^{\nu_{\text{WF}} z_{(\cdot)}} \quad (\text{QC}) \end{cases}, \quad (6.94)$$

with $z_{(\cdot)} = \max\{z_e, z_{<}\}$. It thus has a single crossover at the scale $T \sim r^{\nu_{\text{WF}} z_{(\cdot)}}$.

6.8 Summary

Let us now summarize our findings in the phase diagram of the generalized Pomeranchuk model. The latter describes a system with two coupled degrees of freedom characterized by different dynamics, $\omega_{<} \sim k^{z_{<}}$ and $\omega_{>} \sim k^{z_{>}}$ with $z_{<}$ smaller than $z_{>}$. The system has a quantum critical point as a function of a quantum tuning parameter r , at which both modes perform a quantum phase transition from a disordered to an ordered state. This model, inspired by the d -wave Pomeranchuk instability of two-dimensional metals, was however kept fairly general. As such, we worked in a general spatial dimension d and with arbitrary dynamical exponents $z_{<}$ and $z_{>}$. The only requirement was to have the system below its upper critical dimension, which implies $d + z_{<} < 4$.

Analyzing the system with a generalized renormalization group (RG) analysis appropriate for systems with multiple dynamics, we found that the RG flow of the system can be divided into three stages. At first, when modes of momenta higher than the larger inverse thermal length $\xi_T^{>} \sim T^{1/z_{>}}$ are integrated out, the flow is dominantly driven by quantum fluctuations of the mode with the smaller dynamical exponent $z_{<}$ because the latter has the smallest quantum dimension $D_i = d + z_i$. Since the system is below its upper critical dimension, it first flows from the vicinity of an initial Gaussian fixed point towards a strongly interacting Wilson-Fisher fixed point.

When the running cutoff reaches the scale $\xi_T^{>-1}$, the RG enters the so-called extended quantum to classical crossover regime.⁵³ In the latter, the RG flow is driven not only by quantum fluctuations of the mode with the smaller dynamical exponent $z_<$, but also by thermal fluctuations of the mode with the larger dynamical exponent $z_>$ (note that the latter mode only feels the finite temperature below the scale $\xi_T^{>-1} = T^{1/z_>}$, while it does not for larger momenta). The interplay of thermal fluctuations of the mode with the larger dynamical exponent $z_>$ and quantum fluctuations of the mode with the smaller dynamical exponent $z_<$ in the extended quantum to classical crossover regime can potentially give rise to unusual scaling laws at finite temperature. We find that this happens when quantum fluctuations are sufficiently more singular than thermal fluctuations, in which case a *quantum boost of thermal fluctuations* generates a new length scale

$$\xi_R \sim (r + \tilde{\alpha} T^{\nu_{\text{WF}} z_e})^{-\nu_{\text{WF}}} , \quad (6.95)$$

see Sec. 6.5. This *emergent length scale* basically replaces the usual zero temperature length scale $\xi_r = r^{-\nu_{\text{WF}}}$, and most importantly depends on an *emergent dynamical exponent*

$$z_e = \frac{1}{1 + \nu_{\text{WF}}(z_> - z_<)} . \quad (6.96)$$

The emergent exponent z_e has a rather simple and universal form, and does in particular not depend on the (bare) value of the interaction u , and neither on the spatial dimensionality d . We therefore conjecture that the mechanism leading to the emergence of this new dynamical exponent is rather general and *not* limited to the precise model studied here. We would however like to stress that we have worked in a one-loop approximation, and that our results can not be expected to generally hold in higher loop orders. The quantum boost of thermal fluctuations is however only sufficiently strong if the system is further below its upper critical dimension (the distance to the latter is $\Delta_q = 4 - d - z_<$) than it is below its classical critical dimension (characterized by the distance $\Delta_c = 2 - d$). More precisely, the quantum boost of thermal fluctuations can determine the asymptotic flow of the RG equations describing our model if

$$z_e > z_< \quad \text{or equivalently} \quad \frac{1}{\nu_{\text{WF}}} > z_< \quad \text{or equivalently} \quad \frac{5}{9}\Delta_q > \Delta_c . \quad (6.97)$$

If the condition (6.97) is fulfilled, the emergent length scale naturally affects scaling behaviors of the system at finite temperatures when $T \gg r^{\nu_{\text{WF}} z_e}$. We find that it not only modifies the scaling of the correlation length ξ , but also sets the scaling of the thermal expansion α and the compressibility κ of the system. If on the contrary condition (6.97) is not met, the scaling of thermodynamic observables follows the naive scaling laws expected for two decoupled modes. We therefore refer to the latter situation as *decoupled multiple dynamic scaling*, while the unusual scaling obtained otherwise is denoted as *coupled multiple dynamic scaling*. In any case, the phase diagram exhibits two crossovers. At the scale

$$T \sim r^{\nu_{\text{WF}} z_>} , \quad (6.98)$$

the fluctuations of the mode with the larger dynamical exponent $z_>$ change their behavior from quantum to thermal. All physical observables that dominantly probe thermal

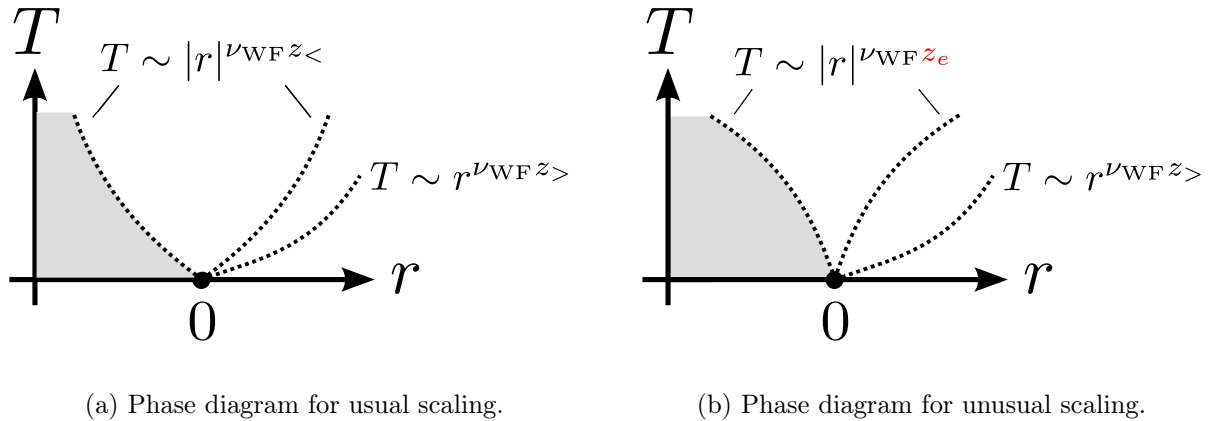


Figure 6.5: The phase diagram of the generalized Pomeranchuk model exhibits always two crossovers. Depending on whether a given thermodynamic observable rather probes the thermal or quantum fluctuations, it is sensitive to either the one or the other crossover (or possibly even to both). If no unusual scaling is obtained, the two crossovers are set by the Wilson-Fisher fixed point value correlation length exponent ν_{WF} and the two dynamical exponents $z_{<}$ and $z_{>}$ of the two modes. If unusual scaling is obtained, the higher crossover is set by the emergent exponent z_e , and so are the scaling laws of various observables directly above the quantum critical point ($r = 0$). We note that the cases of coupled and decoupled dynamic scaling can easily be distinguished by the slope of the upper crossover line, which is $\nu_{WF} z_{<} > 1$ for decoupled scaling and $\nu_{WF} z_e < 1$ for coupled scaling. At negative r , the gray shaded area is delimited by the Ginzburg line.

fluctuations and thus the mode with the larger dynamical exponent (for which thermal fluctuations have a larger phase space) are sensitive to this crossover and change their critical scaling at this scale. For our case, these were the specific heat and the thermal expansion. Other thermodynamic quantities, such as the compressibility, are less sensitive to thermal fluctuations and rather probe quantum fluctuations. The latter are in turn dominated by the mode with the smaller dynamical exponent $z_{<}$ because of the smaller quantum dimension $D_{<} = d + z_{<}$, and potentially boost thermal fluctuations. These observables therefore feel a crossover at

$$T \sim r^{\nu_{WF} z_{(\cdot)}}, \quad (6.99)$$

where $z_{(\cdot)} = \max\{z_e, z_{<}\}$. If the quantum thermal boost is active, i.e. if condition (6.97) is met, these quantities thus exhibit unusual scaling set by z_e in the quantum critical regime above the quantum critical point. The most interesting scaling behavior was obtained for the thermal expansion, which is defined as the mixed derivative $\partial_T \partial_r \mathcal{F}$ of the free energy density, and is thus sensitive to both quantum and thermal fluctuations. We found that the thermal expansion is sensitive to the quantum-to-classical crossovers of both modes, and that it is also sensitive to the emergent dynamical exponent z_e .

Conclusion

In conclusion, we found that the naive scaling expectations of two decoupled subsystems only hold if quantum fluctuations are not too singular. When quantum fluctuations become sufficiently important, a quantum boost of thermal fluctuations leads to unusual

scaling above the quantum critical point. The latter is due to the emergence of a new dynamical exponent z_e . This exponent has a rather universal form, and we believe that the coexistence of multiple dynamics is a *generic new mechanism for the breakdown of usual scaling*. Instead, the scaling of the free energy density \mathcal{F} in the quantum critical region follows from the new scaling forms

$$\begin{aligned} \mathcal{F} &= \mathcal{F}_< + \mathcal{F}_> \\ &= b_1^{-(d+z_<)} f_<(b_1^{1/\nu} r, b_1^{z_<} t_<, b_1^{z_>} t_>) + b_2^{-(d+z_<)} f_>(b_2^{1/\nu} r, b_2^{z_<} t_<, b_2^{z_>} t_>) , \end{aligned} \quad (6.100)$$

with $t_i = \eta_i T$. Importantly, the third argument of the function $f_<$ diverges upon approaching the quantum critical point in the quantum critical region. If unusual scaling is obtained due to the quantum thermal boost, the scaling of thermodynamics of the mode with the smaller dynamical exponent in the quantum critical region is set by *coupling exponents* ψ_n that characterize the behavior of the scaling function $f_<$ and its derivative with respect to the divergent third argument. As an example, the scaling of the free energy density above the quantum critical point reads

$$f_<(1, 0, x_3) \stackrel{x_3 \rightarrow \infty}{\sim} x_3^{\psi_0} . \quad (6.101)$$

Depending on the values of the coupling exponents, the scaling exponents can in principle take any value. While the precise exponents of the unusual scaling due to the coexistence of multiple dynamics are model dependent, they are probably generically generated by the quantum boost of thermal fluctuations and thus a function of the emergent exponent z_e . Finally, the phase diagram of a system with multiple dynamics is always characterized by two crossover scales on the disordered side, one of which is set by z_e if unusual scaling is obtained. The phase diagram is shown in Fig. 6.5. As we have discussed in the last section, different physical quantities see either only the lower crossover (this is the case for the specific heat), only the upper crossover (the compressibility), or may even be sensitive to both crossovers (the thermal expansion). On the ordered side for $r < 0$, we expect a phase transition at sufficiently negative values of the quantum tuning parameter r . The extension of the latter is however beyond the scope of this calculation. We can only state that it will appear within the gray shaded area delimited by the Ginzburg line. The latter is also set by the emergent exponent (if it emerges at all) and marks the crossover from the quantum Wilson-Fisher fixed point to a secondary, classical fixed point describing the thermally disordered state. Finally, we note that the cases of coupled and decoupled multiple dynamics can relatively easily be distinguished in the phase diagram. For *decoupled* multiple dynamic scaling, its exponent is

$$\nu_{\text{WF}} z_< > 1 . \quad (6.102)$$

For *coupled* multiple dynamic scaling, where $\nu_{\text{WF}} z_< < 1$, we use that $\nu_{\text{WF}} z_e - 1 = (\nu_{\text{WF}} z_< - 1)/(1 + \nu_{\text{WF}}(z_> - z_<)) < 0$, which implies that the upper crossover line has an exponent

$$\nu_{\text{WF}} z_e < 1 . \quad (6.103)$$

The slope of the upper crossover line can thus be used as a convenient criterion for the distinction between coupled and decoupled multiple dynamic scaling.

Outlook

From a theoretical perspective, it would firstly be desirable to apply our formalism to more realistic models than the generalized d -wave Pomeranchuk instability in a two-dimensional metal. This might include the study of systems with competing orders, where different degrees of freedom have a multicritical critical point. Also the extension of the present work to higher loop orders is an important future objective, since e.g. self-energy corrections become frequency and momentum dependent in that case. It would not be surprising if one would then also need to take into account the full scale dependence of the vortices, or at least explicitly keep track of the physics in the different energy momentum shells $\omega \sim k^{z_>}$, $\omega \sim k^{z_<}$ and $\omega \sim k^{z_e}$ (if a single emergent dynamical exponent z_e can still be defined). Furthermore, quantum critical systems involving fermionic degrees of freedom could be studied. On the experimental side, we hope that our findings are helpful in the interpretation of certain experiments where the usual scaling expectations are not respected, at least if these systems involve multiple time scale close to the quantum critical point.

Part III

Weyl superconductors

Chapter 7

Introduction to Weyl semimetals

In band structure theory, a semimetal is a material that has a very small overlap between conduction and valence band, as opposed to a true metal (that has partially filled bands), a semiconductor (that has a small gap) or an insulator (with a large band gap). Although this definition is a little vague, a system where conduction and valence band touch only in a manifold of measure zero is certainly a prime example of a semimetal. This includes for instance three-dimensional systems whose conduction and valence bands touch in isolated points or lines. In the following, we will in particular be concerned with three-dimensional systems that have band touchings in a set of discrete points. Although such materials have been known since a long time in condensed matter physics,¹⁰⁴ it has only been understood very recently that they have a topologically non-trivial character, starting with pioneering work of Volovik (and others) on the A-phase of ³Helium.^{105,106} As such, it has been demonstrated that topological semimetals phases can arise due to the interplay of strong spin-orbit interactions and electronic correlations in solid state systems.¹⁰⁷ Since the relevant low energy physics are described by a relativistic Weyl equation, these topological semimetals have been named “Weyl semimetals”.

Within one year since their identification, the solid Weyl semimetals have generated a fair amount of scientific interest. By now, several materials have been proposed to be Weyl semimetals, such as the pyrochlore iridates,^{107,108} Bi_2Se_3 ,¹⁰⁹ HgCr_2Se_4 ,¹¹⁰ or heterostructures of topological and normal insulators.^{111–113} Their relation to the most prominent example of topological band structures (namely topological insulators) has been addressed,¹¹⁴ and a number of interesting effects have been predicted, including an anomalous Quantum Hall effect (which in some materials is pressure dependent) or possible magnetic field induced charge density.^{111,115} Furthermore, the effects of interactions and disorder on transport have at least partially been addressed.^{107,108,115–117} Last but not least, a superconducting variant of Weyl semimetals has been proposed to exist in ferromagnetic spin-triplet superconductors and non-centrosymmetric superconductors, with related phenomena in superconducting helical magnets.^{118–122}

Nevertheless, a systematic analysis of the physics of Weyl superconductors is missing to date. Also in view of the flourishing field of topological superconductors and their promising application to topological quantum computation proposals, we want to devote the next two chapters to a systematic study of Weyl superconductors. There is however also a proper fundamental interest in the study of Weyl superconductors. A first important question would be if, and under which conditions, the gaplessness of normal Weyl semimetals may survive in the presence superconductivity. Secondly, one may ex-

pect gapless Majorana-like states on the surface of a Weyl superconductor in analogy to other topological superconductors. In the following, we want to quantify the presence or absence of gapless bulk points, surface Majorana modes and Majorana Fermi arcs and classify the possible phases of Weyl superconductors in a phase diagram. Related to the expected surface states, the physics of vortices in Weyl superconductors is of special interest. We will more specifically discuss if Weyl superconductors can bind unique Majorana fermion zero modes at vortices, and if they are suitable for quantum computation. We will finally address possible experiments, both in view of observable signatures of Majorana physics and of experimental systems which could possibly be used for these experiments.

Finally, we note that Weyl semimetals and Weyl superconductors can more generally also be understood as exotic quantum critical states. Firstly, Weyl phases appear as intermediate phases between a topological and a normal insulator (or superconductor) when the respective quantum phase transition between the two is perturbed with a time reversal symmetry breaking or an inversion symmetry breaking term. Secondly, Weyl semimetals and superconductors have gapless points in their three-dimensional Brillouin zone. At these Weyl nodes or Bogoliubov Weyl nodes, respectively, a single conduction band and a single valence band touch. As we will see, these points can be understood as a quantum critical point of a quantum Hall system (for the semimetals) or a $p_x + ip_y$ -superconductor (for the Weyl superconductors), i.e. critical points where the respective system would transit between a topologically trivial and topologically non-trivial state. A Weyl superconductor can therefore be understood as an exotic quantum critical state of matter.

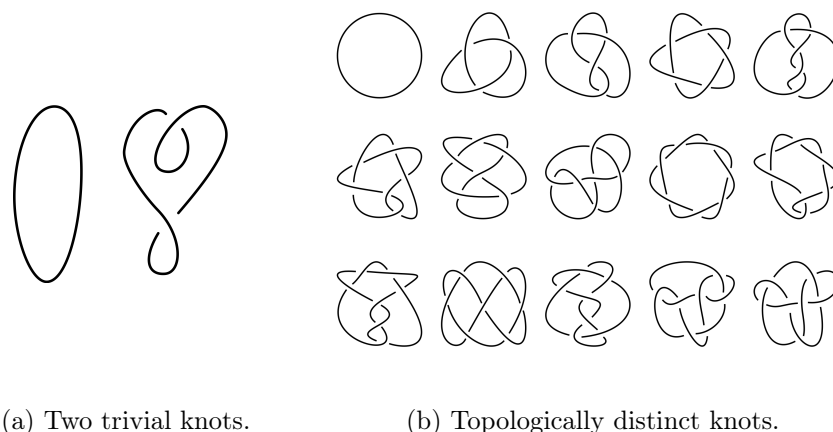
Plan of the next two chapters

We begin with an introductory chapter containing four sections. After briefly mentioning a few concepts of topology, some basic aspects of the relativistic Dirac equation are reviewed, especially focusing on Weyl and Majorana fermions. We then elaborate a bit further on Weyl fermions in solid state systems, and show in what way Weyl semimetals are related to topological insulators. We close the introduction with a short review of the physics of Weyl semimetals. We explain how Weyl semimetals are related to quantum Hall systems and especially highlighting their (potentially present) surface states and Fermi arcs in the surface Brillouin zones.

The next chapter will then introduce and analyze a toy model for Weyl superconductors. Based thereon, a phase diagram will classify different phases of Weyl superconductors. We will investigate the physics of vortices and finally conclude with some proposals for experiments.

7.1 Topology and solid state physics

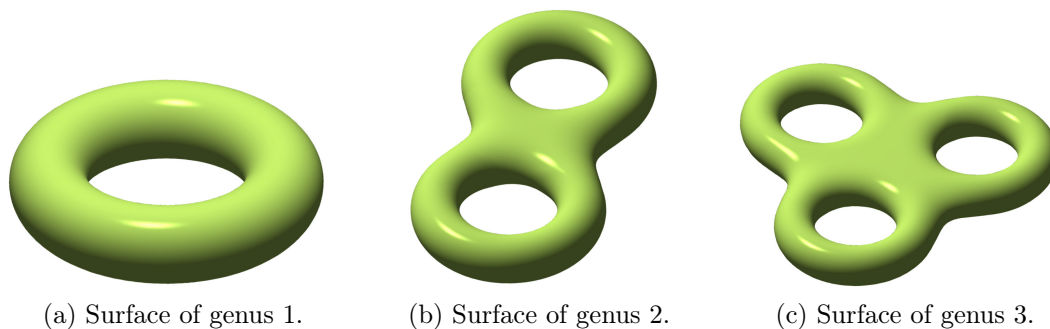
We begin with a very short introduction to some of the concepts of topology and motivate their relation to (solid state) physics. We then turn to the subject of topological insulators, the probably most prominent example of topological systems in today's research.



(a) Two trivial knots.

(b) Topologically distinct knots.

Figure 7.1: The lefthand-side shows two topologically trivial knots which can be deformed into one another by smooth deformations. The right-hand side shows some of the simplest topologically distinct knots.¹²³



(a) Surface of genus 1.

(b) Surface of genus 2.

(c) Surface of genus 3.

Figure 7.2: Surfaces of different genus.¹²⁴

7.1.1 A very short introduction to topology

Topology is a subdiscipline of mathematics studying properties of mathematical objects that are conserved under continuous deformations. Possible deformations include for instance stretching, rotations or shearing. Put in a more pictorial way, any re-shaping one can do to a piece of dough without dividing it into different pieces or punching a hole into it constitutes a continuous deformation. One famous example is the deformation of a doughnut into a coffee mug, which are equivalent from a topological point of view.

The emergence of topology in the mid 19th century has been stimulated by a number of mathematical research areas, one of which being the knot theory. Mathematically, a knot in a closed loop is a topologically non-trivial embedding of a circle in three-dimensional space. While some knots can be continuously deformed into one another (see Fig. 7.1a for two topologically equivalent trivial knots), there exists an enormous number of topologically nonequivalent knots. Fig. 7.1b depicts some of the simplest topologically distinct knots. By virtue of Seifert surfaces, knots are closely related to another topological concept, the genus of a surface. The latter corresponds to the number of holes in a connected and orientable surface. Examples for surfaces of different genus are shown in Fig. 7.2. Obviously, punching a hole into a surface is a rather drastic process, and turns out to be a discontinuous transformation in the mathematical sense. Therefore, surfaces with different numbers of holes are topologically distinct.

In conclusion, two mathematical objects are topologically equivalent if there is a sufficiently smooth transformation (the before-mentioned continuous mapping) that transforms the two objects into one another. This concept can not only be applied to knots or holes in surfaces, but also to more abstract mathematical objects. Consider for instance a family of mappings ϕ_i ($i = 1, 2, \dots$) from some base manifold M to a target space T ,

$$\phi_i : M \rightarrow T , \quad (7.1)$$

$$z \mapsto \phi_i(z) . \quad (7.2)$$

In a physical context, such mappings may for instance correspond to band structure functions that map momenta to energies. Two such mappings ϕ_1 and ϕ_2 are topologically equivalent if they can be transformed into one another by a continuous transformation, and the continuous transformation that takes $\phi_1 \rightarrow \phi_2$ is called a homotopy. For a more detailed introduction to the mathematical foundations of topology and homotopies, the reader is referred to textbooks.¹²⁵

7.1.2 Topology in physics

In physics, the concepts of topology have been known and used since a long time, most commonly in order to classify defects in ordered media (consider for instance a review article from 1979, Ref. [126]). One well-known example are vortices in a model as simple as the classical, two-dimensional XY-model. The latter describes classical two-dimensional spins $\vec{s}_i = (s_{i,x}, s_{i,y})^T$ arranged on a two-dimensional square lattice. The spins are supposed to be coupled ferromagnetically. In nearest neighbor approximation, the respective classical Hamiltonian reads

$$H = - \sum_{\langle i,j \rangle} J \vec{s}_i \cdot \vec{s}_j . \quad (7.3)$$

This model has two phases as a function of temperature. At high temperatures, the system is in a totally disordered phase, and spin-spin correlations decay exponentially in the distance. At low temperatures, the system undergoes a Kosterlitz-Thouless transition to a quasi-long range ordered state, in which the spin-spin correlations only decay as a power law with distance. This transition has been understood as the formation of vortices, the topological defects of the spin state depicted in Fig. 7.3. The topological character is defined by the winding number, that measures how often the spins wind around the vortex on a path encircling the vortex core once. The winding number is indeed an integer (just like the number of holes in a surface) and can not be changed by a deformation of the spin structure that does not remove the vortex (i.e. continuous transformations of the spin structure). A vortex is associated with an energy that grows logarithmically with system size since it distorts all spins of the system. At lowest temperature, the ground state will therefore have no vortices at all. Once a vortex has nevertheless been created, it can be placed anywhere in the system, which corresponds to an entropy that also depends logarithmically on the system size. Above some critical temperature, the entropy gain outweighs the energy cost for vortex creation, and the system spontaneously generates vortices that disorder the system entirely.

The winding number of a vortex is also called its “topological charge” by analogy to electrostatics. A single vortex, as depicted in Fig. 7.3, is visible at any distance,

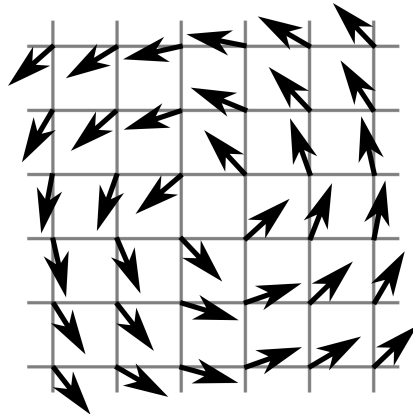


Figure 7.3: A vortex in the classical XY spin model. The spins wind once on any path encircling the vortex core once, this vortex has thus an associated winding number of 1.

similarly to a single electric charge. Two vortices of opposite topological charge, i.e. opposite winding, screen each other just like two opposite electric charges would do. Fig. 7.4 illustrates the canceling of long-distance effects far from the defect pair. A vortex-antivortex pair can also annihilate, leaving the spin system entirely unperturbed. Consequently, only the total topological charge (here corresponding to the sum of all winding numbers of all vortices and antivortices in the system) is conserved by continuous transformations, and is therefore called a “topological invariant”. In conclusion, only system configurations of different net topological charge are topologically distinct, while configurations with the same total global topological charge are topologically equivalent.

Aharonov-Bohm phase

Topology does of course not only enter classical physics, but also plays an important role in quantum theories. A first example is the Aharonov-Bohm phase of an electron encircling a magnetic flux along some path \mathcal{C} outside the area threaded by the field, see Fig. 7.5. The total phase is composed of a geometrical part

$$\varphi_{\text{geo}} = \oint_{\mathcal{C}} d\vec{r} \cdot \vec{k}(\vec{r}) , \quad (7.4)$$

which depends on the momentum \vec{k} and the length of the path. In addition, the particle picks up an “Aharonov-Bohm phase”

$$\varphi_{\text{AB}} = -e \oint_{\mathcal{C}} d\vec{r} \cdot \vec{A} . \quad (7.5)$$

Using the Kelvin-Stokes theorem, this phase can be rewritten as

$$\varphi_{\text{AB}} = -e \int_{S(\mathcal{C})} d\vec{S} \cdot \nabla \times \vec{A} = -e \int_{S(\vec{B})} d\vec{S} \cdot \vec{B} = -e \Phi , \quad (7.6)$$

where $S(\mathcal{C})$ is the area bordered by the path \mathcal{C} and $S(\vec{B})$ denotes the area threaded by the magnetic field. The Aharonov-Bohm phase thus only depends on the flux Φ encircled by the electron, and not on the precise path, as long as the different paths are smoothly connected without crossing the field-threaded region. Mathematically, this is equivalent

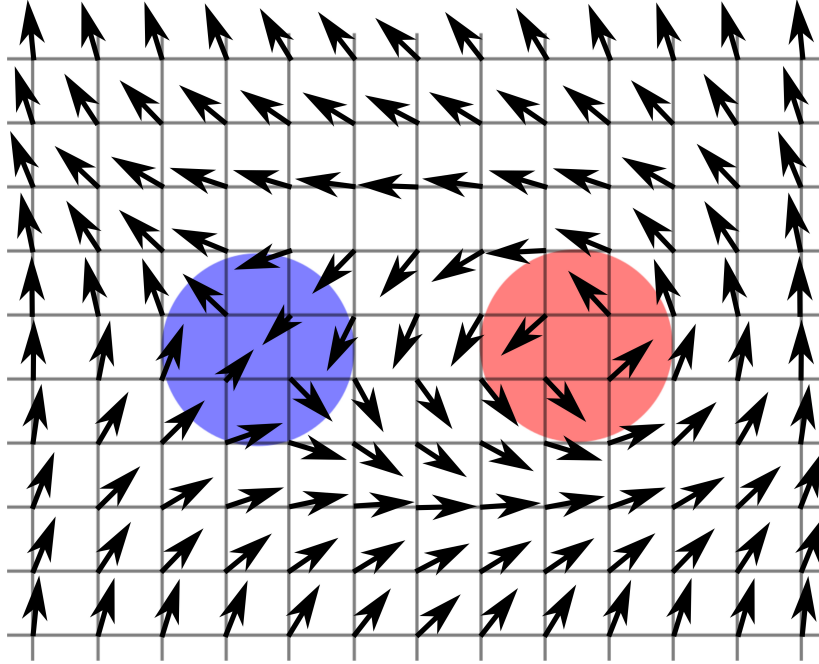


Figure 7.4: A vortex-antivortex pair. The vortex (red) has a winding number of 1, the antivortex (blue) has a winding number of -1 . Sufficiently far away from the two defects of opposite winding number (i.e. opposite topological charge), the defect pair does not distort the spins anymore.

to saying that they can be deformed into one another by a continuous deformation. The Aharonov-Bohm is thus a topological quantum phase.

Berry phase, Berry curvature and Berry connection

Topological phases occur quite generally when quantum mechanical systems undergo adiabatic cycles, as has been pioneered by Berry in a seminal paper.¹²⁷ This section recalls the main results of this work. Consider a general Hamiltonian with eigenstates $|n\rangle$ of energy E_n . The Hamiltonian is further supposed to depend on a vector of parameters $\vec{x}(t)$ that are changed in an adiabatic cycle, $\vec{x}(0) = \vec{x}(1)$. In the context of the Aharonov-Bohm effect, the adiabatic cycle corresponded to taking the electron around the magnetic

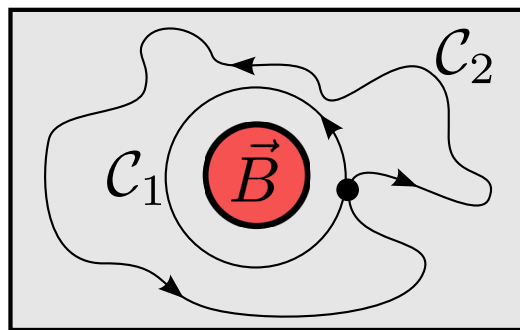


Figure 7.5: Sketch of two topologically equivalent paths C_1 and C_2 on which an electron could encircle a region threaded by a magnetic field \vec{B} (the latter is shown in red, the black dot depicts the electron).

field. Due to the assumption of adiabaticity, a state $|\Psi(t)\rangle$ that has been prepared in an initial eigenstate, $|\Psi(0)\rangle = |n(\vec{x}(0))\rangle$, evolves during the cycle as the parameter-dependent eigenstate $|n(\vec{x}(t))\rangle$, up to a phase. At an intermediate time t , it can be written as

$$|\Psi(t)\rangle = e^{i\gamma_n(\vec{x}(t))} e^{-i \int_0^t dt' E_n(\vec{x}(t'))} |n(\vec{x}(t))\rangle , \quad (7.7)$$

where the second exponential is the usual time evolution of the state $|n(x(t))\rangle$ (for the Aharonov-Bohm effect discussed above this would simply be the geometrical phase). The first term is an extra phase that accommodates for all effects beyond dynamical phases, such as the Aharonov-Bohm phase. Using the Schrödinger equation for the state $|\Psi(t)\rangle$, one obtains

$$\gamma_n(\vec{x}(t)) = i \int_0^t dt' \langle n(\vec{x}(t')) | \frac{d}{dt'} |n(\vec{x}(t'))\rangle = i \int_{\vec{x}(0)}^{\vec{x}(t)} d\vec{x} \langle n(\vec{x}) | \nabla_{\vec{x}} |n(\vec{x})\rangle . \quad (7.8)$$

For a full cycle \mathcal{C} in the parameter space, we get

$$\gamma_n = i \oint_{\mathcal{C}} d\vec{x} \langle n(\vec{x}) | \nabla_{\vec{x}} |n(\vec{x})\rangle . \quad (7.9)$$

The phase γ_n is known as the ‘‘Berry phase’’. Using the Kelvin-Stokes theorem, it can be written as

$$\gamma_n = \oint_{\mathcal{C}} d\vec{x} \cdot \vec{A}_n(\vec{x}) . \quad (7.10)$$

where we have introduced the ‘‘Berry connection’’

$$\vec{A}_n(\vec{x}) = i \langle n(\vec{x}) | \nabla_{\vec{x}} |n(\vec{x})\rangle . \quad (7.11)$$

Comparing Eqs. (7.11) and (7.5), we find that the Berry connection plays the role of an effective vector potential in an effective Aharonov-Bohm problem. Being a generalized magnetic vector potential, the Berry curvature is not invariant under gauge transformations:

$$|n(\vec{x})\rangle \rightarrow e^{i\varphi_n(\vec{x})} |n(\vec{x})\rangle \quad \Rightarrow \quad \vec{A}_n(\vec{x}) \rightarrow \vec{A}_n(\vec{x}) - \nabla_{\vec{x}} \varphi_n(\vec{x}) . \quad (7.12)$$

Since physical quantities can not be gauge dependent, it is often useful to consider the so-called ‘‘Berry curvature’’

$$\vec{B}_n(\vec{x}) = \nabla_{\vec{x}} \times \vec{A}_n(\vec{x}) \quad (7.13)$$

that corresponds to an effective magnetic field and which is thus gauge independent.

Berry phase of a spin in a magnetic field

One common example of a Berry phase is the one of a rotating spin.¹²⁷ Let us thus consider the Hamiltonian of a spin in a magnetic field

$$H = -\mu \vec{\sigma} \cdot \vec{B} , \quad (7.14)$$

where μ is the magnetic moment, $\vec{\sigma}$ are the Pauli matrices and \vec{B} is the magnetic field. The Hamiltonian has two eigenstates $|\pm\rangle$ of eigenenergies $E_{\pm} = \pm\mu |\vec{B}|$ that read

$$|-\rangle = \begin{pmatrix} \sin\left(\frac{\theta}{2}\right) e^{-i\phi} \\ -\cos\left(\frac{\theta}{2}\right) \end{pmatrix}, \quad (7.15a)$$

$$|+\rangle = \begin{pmatrix} \cos\left(\frac{\theta}{2}\right) e^{-i\phi} \\ \sin\left(\frac{\theta}{2}\right) \end{pmatrix}, \quad (7.15b)$$

where θ and ϕ denote the direction of the magnetic field. Since the eigenstates are (anti-)parallel to \vec{B} , the spin can be rotated by adiabatically changing the magnetic field. For concreteness, we suppose that \vec{B} is rotated n times within the (x, y) -plane,

$$\vec{B} = B \begin{pmatrix} \cos(\phi(t)) \\ \sin(\phi(t)) \\ 0 \end{pmatrix}, \quad \phi(t) = 2\pi n t, \quad t: 0 \rightarrow 1. \quad (7.16)$$

According to our general definition in Eq. (7.9), a spin in the state $|-\rangle$ acquires a Berry phase

$$\gamma_- = i \oint_0^{2\pi n} d\phi \langle - | \frac{d}{d\phi} | - \rangle \quad (7.17)$$

$$= i \oint_0^{2\pi n} d\phi \frac{1}{\sqrt{2}} (e^{i\phi}, -1) \frac{d}{d\phi} \frac{1}{\sqrt{2}} \begin{pmatrix} e^{-i\phi} \\ -1 \end{pmatrix} \quad (7.18)$$

$$= i \oint_0^{2\pi n} d\phi \frac{1}{2} (e^{i\phi}, -1) \begin{pmatrix} -i e^{-i\phi} \\ 0 \end{pmatrix} = n\pi, \quad (7.19)$$

and a similar reasoning can be made for the state $|+\rangle$. Since the Berry phase is of topological origin, it only depends on how often the magnetic field, and consequently the spin, is rotated, but not on further details. In particular, only situations with different net winding numbers are topologically different. Rotating for instance the spin five times in one direction and then two times in the opposite direction is equivalent to rotating it three times in the initial direction as both yield a net phase of $(5 - 2)\pi = 3\pi$. We conclude in particular that rotating a spin once by an angle of 2π yields Berry phase of π for the wave function, a fundamental result that we will encounter again later on.

7.1.3 Topological insulators

One of the goals of solid state physics is to understand the properties of different materials and to classify them accordingly. An important example for such a characteristic is the ability to conduct electric currents. Materials that do conduct electric currents are referred to as metals, while the ones that do not are called insulators (for simplicity, this section neglects the intermediate cases of semiconductors and semimetals, despite the fact that the latter are at the heart of the following discussion). This simple classification scheme is of course only a very first step, since different metals or insulators show a vast variety of entirely different behaviors in diverse (other) physical properties. In addition, the fact that a material is metallic or insulating is influenced by a whole set of factors. A metal can become insulating either because repulsive interactions localize the electrons, leading to a strongly correlated Mott insulator. Alternatively, a very disordered system may also be an insulator because, roughly speaking, the electrons are just back-scattered

too much. This mechanism is known as Anderson localization. But one does not even need to resort to disorder or strong correlations: the material could be also a simple band insulator, in which a number of filled valence bands just happen to be separated by an energy gap from the empty conduction bands.

Since different insulating states are in general very distinct, we can not hope that all of them are smoothly connected in the topological sense. To make this point a little more precise, we note that any insulator is in general described by a multi-band Hamiltonian. As usual, two Hamiltonians are considered to be topologically equivalent if they can be deformed into one another by a continuous transformation. In the context of insulators, this means that the transformation is not allowed to close the gap, which would turn the insulator into a (semi-)metal. We however note that a transition between topologically distinct states is possible even without the closing of the gap if the symmetries protecting the topological state are broken during the transformation, or if interacting systems are considered¹²⁸. The topological character of a given Hamiltonian will also be handed on to its eigenstates. For an insulator, the latter are the crystal momentum dependent bands $|n(\vec{k})\rangle$. According to the last section, an electron in a topologically non-trivial band should acquire a Berry phase when some parameter of the Hamiltonian is taken through some adiabatic cycle. By analogy to the general discussion of Berry phase, Berry curvature and Berry connection above, one can already guess that this parameter will be given by the crystal momentum \vec{k} .

Let us thus consider the evolution of a state $|n(\vec{k})\rangle$ as the crystal momentum is changed in an adiabatic cycle \mathcal{C} through the Brillouin zone, the final state has to be identical to in the initial one modulo a phase. This phase can be divided into a non-topological part and the topological Berry phase. According to our previous discussions, the Berry phase depends on the topological character of the encircled parameter space, since

$$\gamma_n = \oint_{\mathcal{C}} d\vec{k} \cdot \vec{A}_n(\vec{k}) = \int_{S(\mathcal{C})} d\vec{S} \cdot \vec{B}_n(\vec{k}) , \quad (7.20)$$

where the Berry connection of the n^{th} band

$$\vec{A}_n(\vec{k}) = i \langle n(\vec{k}) | \nabla_{\vec{k}} | n(\vec{k}) \rangle \quad (7.21)$$

defines the corresponding Berry curvature as $\vec{B}_n(\vec{k}) = \nabla_{\vec{k}} \times \vec{A}_n(\vec{k})$ and $S(\mathcal{C})$ is the surface encircled by the cycle \mathcal{C} through the Brillouin zone. If we are considering a two-dimensional system, it is intuitive to assume that the full topological character of the band is only captured if the full Brillouin zone is encircled. Indeed, as has been shown by Thouless, Kohmoto, Nightingale and den Nijs in the context of the quantum Hall effect the topological character of a band is related to the integral of the respective Berry curvature over the full Brillouin zone. The latter yields a number known as TKNN invariant or chern number,¹²⁹

$$\gamma_n^{\text{TKNN}} = \int_{\text{BZ}} dk_x dk_y B_{n,z}(\vec{k}) . \quad (7.22)$$

On general grounds, it can be shown that the TKNN invariant needs to be quantized in units of 2π . The sum of all TKNN invariants over all bands, $\sum_n \gamma_n^{\text{TKNN}}$, is the topological invariant of the total system, and remains unchanged for any continuous deformation of the Hamiltonian. This can be shown to remain true even in the presence of band degeneracies, provided that the gap between occupied and empty bands stays

finite and that symmetries remain intact (for non-interacting systems,¹²⁸ since interactions might for instance spontaneously break symmetries). In three-dimensional systems, a (one-dimensional) path \mathcal{C} can of course not encircle the Brillouin zone, but adequate generalizations have been established.^{2,4,5,130} Whatever the dimension, every insulating system with non-trivial global topological invariant (or adequate generalization thereof) is called a “topological insulator”, as opposed to “non-topological” or “normal” insulators. Since the vacuum is surely of trivial topology, we note that all topologically trivial insulators are equivalent to vacuum (at least from the point of view of topology). Although first contributions to the field have already been made in the mid-eighties by Pankratov and collaborators,¹ topological insulators have received a tremendous amount of interest starting with their experimental detection in 2007.³ Besides the fundamental interest in materials with topological order, fascinating ideas for applications of the edge states (see next section) have made topological insulators one of the most active fields in condensed matter physics. As an example, the well-defined spin orientation of the edge states in quantum Hall samples and the related quantum spin Hall samples can hopefully be used in spintronics. Furthermore, superconducting topological materials (see below) can under certain conditions trap isolated Majorana modes at vortices, which could be useful for quantum computation. In addition, the theoretically proposed Majorana modes in topological superconductors are amongst the most promising candidates for the first experimental detection of a Majorana fermion. More extensive introductions to the field of topological insulators can be found the review articles and references therein.^{5,130}

Edge states and the quantum Hall effect

One important statement of the last section is that two topologically distinct insulating Hamiltonians can not be connected without closing the gap (provided that the symmetries protecting the topological order remain unbroken and if non-interacting systems are considered). On the other hand, we know that a real world system with an interface between two different subsystems is described by one global Hamiltonian that (more or less smoothly) interpolates between the two sub-Hamiltonians. Consider for instance a piece of topological insulator in vacuum, and assume the insulator to be described by a non-interacting theory with the relevant symmetries being unbroken. The total system, i.e. the topological insulator in a vacuum, is described by one single Hamiltonian. Deep in the topological insulator, this total Hamiltonian will be equal to the Hamiltonian of the topological insulator, while it will be equal to the Hamiltonian of vacuum far outside the topological insulator. The surface of the topological insulator, however, is described by the interpolation between the two limiting Hamiltonians. Since this interpolation can not happen without closing the gap, a gapless state must exist at the surface. The same reasoning can be made for any interface between topologically nonequivalent materials. We can thus conclude that an interface between topologically distinct materials must have gapless states, provided that the symmetries protecting the topological order are unbroken (and in the absence of interactions, which can e.g. break symmetries spontaneously). Nevertheless, we note that interfaces generically do break symmetries such as inversion or translation symmetry, which in turn might kill the edge states.

Let us illustrate this with the example of the quantum Hall effect. As is well known, a quantum Hall sample has a gapless state running around the edge of the two-dimensional system. This is not surprising, since the quantum Hall effect has a non-trivial chern number (see above) and therefore a non-trivial topological character. The edge of a

quantum Hall sample is thus an interface between the topologically trivial vacuum and a topological system, and therefore has to carry a gapless edge state. It is furthermore instructive to consider the effective Hamiltonian for quantum Hall systems derived by Ludwig and collaborators.¹³¹ They showed that a quantum Hall sample is at low energies described by an effective Dirac Hamiltonian. The latter contains two pairs of bands, one of which has a large gap. The bands have Hamiltonians

$$H_i = v_F (\sigma^x k_x + \sigma^y k_y) + m_i \sigma_z , \quad (7.23)$$

where v_F is the Fermi velocity, σ^i are Pauli matrices, k_i denotes the two-dimensional momentum and m_i is the effective band mass in band i . Ludwig et al. argued that the TKKN invariant for the full Hamiltonian (including the second pair of bands) depends on whether the two masses have the same or opposite signs. Suppose that the first band has a large positive mass $m_1 \gg |m_2|$. For $m_2 < 0$, the system has a trivial TKKN invariant, and is thus equivalent to vacuum. For $m_2 > 0$, however, the TKKN invariant becomes a unit quantum, and the system is a quantum Hall insulator. The interface between a quantum Hall sample and vacuum can thus be modeled by a spatially depended mass m_2 . If the sample has an edge at $y = 0$, as depicted in Fig. 7.6, we can for instance assume that

$$m_2(y) = -m_{2,0} \arctan(y) . \quad (7.24)$$

We immediately see that the mass vanishes at the edge, such that it can indeed host a gapless state. To find this state, we have to identify an eigenstate of the Hamiltonian

$$H(x) = v_F \left(\sigma^x k_x - i\sigma^y \frac{\partial}{\partial y} \right) + m_2(y) \sigma_z , \quad (7.25)$$

that is localized at the edge (note that we had to replace the $k_y \rightarrow -i\partial_y$ since the system is not translational invariant in y -direction anymore). The appropriate wavefunction reads

$$\Psi(x, y) = e^{i k_x x} e^{\int_0^y dy' m_2(y')/v_F} \begin{pmatrix} 1 \\ 1 \end{pmatrix} . \quad (7.26)$$

As expected, $\Psi(x, y)$ is exponentially localized at the edge around $y = 0$. It has an energy $E = v_F k_x$ and therefore travels with a velocity v_F in positive x -direction along the edge, as it should. From the spinor structure we find that the spin of the edge state is in the $\sigma^x = +1/2$ -state, and thus points into the direction of motion.

Topology and superconductivity

A special class of gapped systems are superconductors. In the BCS picture, electrons at the Fermi surface of a metal are unstable towards the formation of a condensate of Cooper pairs, which leads to a gap for single-particle excitations. Like any other gapped system, superconductors can potentially have a topologically non-trivial band structure.¹³² In a seminal paper, Fu and Kane considered a heterostructure of a topological insulator and an s-wave BCS superconductor.¹³³ This heterostructure turns out to be one example of a topological superconductor, which basically inherits superconductivity and a topologically non-trivial character from its respective constituents, while other materials are

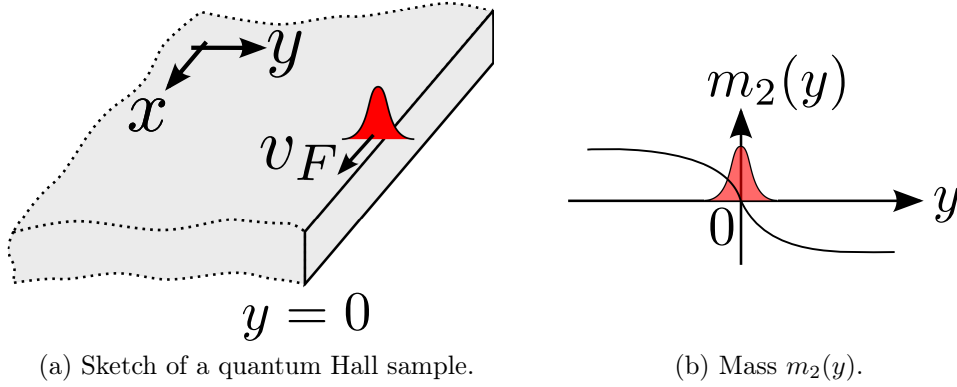


Figure 7.6: Subfigure (a) shows a quantum Hall sample with an edge at $y = 0$, which supports a gapless state that runs with a velocity v_F in positive x -direction along the edge of the sample. This state (shown in red) is exponentially localized around the edge. Subfigure (b) shows the associated mass $m_2(y)$ that has to change sign between the topologically non-trivial quantum Hall sample and the vacuum and thus vanishes at the edge. This explains the gaplessness of the edge state.

intrinsically both topological and superconducting. As Fu and Kane argued, the two-dimensional surface states of the topological insulator are gapped out by the proximity induced superconductivity, and can then be understood as a two-dimensional topological superconductor. If a magnetic field is applied, vortices appear at the interface, which can be thought of as closed edges of the topological superconductor. By analogy to $p_x + ip_y$ -superconductors, these vortices trap zero energy Majorana modes which are known to have non-abelian statistics and could thus be used for braiding processes in quantum computation.^{134,135}

7.2 Dirac, Weyl and Majorana

Before giving a detailed introduction to Weyl fermions and Weyl nodes, this section is supposed to classify them in the larger framework of the Dirac equation, where they historically originated from. We first give some background information on the Dirac equation itself, before turning to two special kinds of solutions that we will be concerned with in the following, namely Majorana fermions and Weyl fermions.

7.2.1 The Dirac equation

Quantum mechanics is founded on Schrödinger's equation that describes the time evolution of a state $|\Psi\rangle$ in a system described by a Hamiltonian H as

$$i\hbar \frac{\partial}{\partial t} |\Psi\rangle = H |\Psi\rangle. \quad (7.27)$$

For a free particle, the Hamiltonian is simply given by the operator corresponding to its kinetic energy, and the Schrödinger equation reads

$$i\hbar \frac{\partial}{\partial t} |\Psi\rangle = \frac{p^2}{2m} |\Psi\rangle \quad (7.28)$$

(where the electron mass m has been introduced). Although quantum mechanics successfully explains a large number of intriguing experiments, Schrödinger's equation is in disagreement with the second big theoretical breakthrough of the early 20th century, namely the theory of relativity. Whereas the latter treats time and space on equal footing, or rather even as a single entity called space-time, quantum mechanics does not. In a quantum theory, time is a mere parameter, while position is an observable. Really dramatic, however, is the fact the Schrödinger's equation is not Lorentz-invariant since it treats time with a linear derivative, but space with a double derivative.

Based on the relativistic energy of a free particle,

$$E = \sqrt{p^2 c^2 + m^2 c^4} , \quad (7.29)$$

two generalizations of Schrödinger's equation have been proposed. The first one, known as the Klein-Gordon equation, treats both time and space with a double derivative,

$$\left(i\hbar \frac{\partial}{\partial t} \right)^2 \Psi = (c^2 p^2 + m^2 c^4) \Psi . \quad (7.30)$$

It took however the seminal insight of Paul Dirac to realize that one could also find a linear differential equation with first order derivatives in both time and space that generalizes Schrödinger's equation to a Lorentz covariant form.¹³⁶ His famous "Dirac equation" turned out to describe spin-1/2 fermions, in contrast to the Klein-Gordon equation that describes spin-0 mesons, i.e. bosons. Starting from an equation of the form

$$i\hbar \frac{\partial}{\partial t} \Psi = \left(\sum_{k=1,2,3} \frac{\hbar c}{i} \alpha^k \frac{\partial}{\partial x^k} + \beta m c^2 \right) \Psi , \quad (7.31)$$

where α^k and β are some general ($n \times n$)-matrices and Ψ is an n -vector, Dirac showed that one can satisfy

$$\left(i\hbar \frac{\partial}{\partial t} \right)^2 \Psi = \left(\sum_{k=1,2,3} -\hbar^2 c^2 \left(\frac{\partial^2}{\partial x^k} \right)^2 + m^2 c^4 \right) \Psi \quad (7.32)$$

by choosing α^k and β as anticommuting matrices that square to $\mathbf{1}$. While for $n = 2$, this algebraic structure is realized by the three Pauli matrices σ^i (but no other matrix), $n = 4$ is the smallest dimension that yields 4 such matrices. The precise form of these matrices can be altered by basis rotations, but one possible and commonly used choice is

$$\alpha^i = \begin{pmatrix} 0 & \sigma^i \\ \sigma^i & 0 \end{pmatrix} , \quad \beta = \begin{pmatrix} \mathbf{1}_{2 \times 2} & 0 \\ 0 & -\mathbf{1}_{2 \times 2} \end{pmatrix} . \quad (7.33)$$

A more compact writing of the Dirac equation is achieved by defining the Dirac- or γ -matrices

$$\gamma^0 = \beta = \begin{pmatrix} \mathbf{1}_{2 \times 2} & 0 \\ 0 & -\mathbf{1}_{2 \times 2} \end{pmatrix} , \quad \gamma^i = \beta \alpha^i = \begin{pmatrix} 0 & \sigma^i \\ -\sigma^i & 0 \end{pmatrix} . \quad (7.34)$$

Making use of these matrices and the Einstein sum convention, Dirac's equation reads

$$\left(i \gamma^\mu \partial_\mu - \frac{mc}{\hbar} \right) \Psi = 0 . \quad (7.35)$$

7.2.2 Weyl fermions: special massless Dirac fermions

A second possible choice for the Dirac matrices is known as the chiral representation. It basically corresponds to changing γ^0 to

$$\gamma_{ch}^0 = \begin{pmatrix} 0 & \mathbb{1}_{2 \times 2} \\ \mathbb{1}_{2 \times 2} & 0 \end{pmatrix}. \quad (7.36)$$

In this representation, the Dirac equation explicitly reads

$$\begin{pmatrix} -\frac{mc}{\hbar} & i(\partial_0 + \vec{\sigma} \cdot \nabla) \\ i(\partial_0 - \vec{\sigma} \cdot \nabla) & -\frac{mc}{\hbar} \end{pmatrix} \Psi_{ch} = 0 \quad (7.37)$$

(where Ψ_{ch} is the Dirac spinor in the chiral representation). If one is interested in massless fermions, $m \rightarrow 0$, the Dirac equation decomposes into two decoupled sectors. Instead of one (4×4) -Dirac equation, one can thus consider two independent (2×2) equations that are known as the Weyl equations differing only by a minus sign,

$$i(\partial_0 - \vec{\sigma} \cdot \nabla) \Psi_L = 0 \quad , \quad i(\partial_0 + \vec{\sigma} \cdot \nabla) \Psi_R = 0 \quad , \quad (7.38)$$

where we introduced the left- and right-handed Weyl spinors Ψ_L and Ψ_R as a decomposition of the Dirac spinor, $\Psi_{ch} = (\Psi_L, \Psi_R)^T$. The chirality is measured by the action of

$$\gamma^5 = \begin{pmatrix} 0 & \mathbb{1}_{2 \times 2} \\ \mathbb{1}_{2 \times 2} & 0 \end{pmatrix} \quad \text{or} \quad \gamma_{ch}^5 = \begin{pmatrix} -\mathbb{1}_{2 \times 2} & 0 \\ 0 & \mathbb{1}_{2 \times 2} \end{pmatrix} \quad (7.39)$$

on the Dirac spinors, depending on whether one works in the standard or chiral representation. Since we are dealing with massless particles, the chirality also coincides with the helicity (the projection of the spin onto the momentum), which is probably the physically most transparent definition. Note that from a more mathematical point of view, the chirality is the handedness of the transformation behavior of a particle with respect to the Poincaré group. Finally, using $c\partial_0 = \partial_t$, the Weyl equations can also be interpreted as two Schrödinger equations with chiral Weyl Hamiltonians

$$H_L = c\vec{\sigma} \cdot \vec{p} \quad , \quad H_R = -c\vec{\sigma} \cdot \vec{p} \quad . \quad (7.40)$$

Summing up, Weyl fermions (i.e. the objects described by the Weyl spinors) are nothing but particular massless Dirac fermions, namely ones of definite chirality. They do not only satisfy the massless (4×4) -Dirac equation, but can in addition be interpreted as eigenstates of one of the (2×2) Weyl Hamiltonians. In the following, ‘‘Weyl’’ will thus denote (2×2) -matrices and 2-spinors, whereas ‘‘Dirac’’ will refer to (4×4) -matrices and 4-spinors.

7.2.3 Majorana fermions: particles being their own antiparticles

The solutions of the Dirac equation are fermionic particles (such as electrons) which are in general different from their anti-particles (such as positrons or holes). In 1937, Ettore Majorana however showed that it is possible to find solutions of the Dirac equation that are their own antiparticles.¹³⁷ This is most conveniently understood if one rewrites the Dirac equation in the Majorana representation in which all γ -matrices are purely imaginary,

$$\gamma_M^0 = \begin{pmatrix} 0 & \sigma^2 \\ \sigma^2 & 0 \end{pmatrix}, \quad \gamma_M^1 = i \begin{pmatrix} 0 & \sigma^1 \\ \sigma^1 & 0 \end{pmatrix}, \quad \gamma_M^2 = i \begin{pmatrix} 0 & \mathbb{1}_{2 \times 2} \\ \mathbb{1}_{2 \times 2} & 0 \end{pmatrix}, \quad \gamma_M^3 = i \begin{pmatrix} 0 & \sigma^3 \\ \sigma^3 & 0 \end{pmatrix}. \quad (7.41)$$

In this representation, the Dirac equation

$$\left(i \gamma_M^\mu \partial_\mu - \frac{mc}{\hbar} \right) \Psi_M = 0 \quad (7.42)$$

is a purely real differential equation for Ψ_M , the Dirac-spinor in Majorana representation (note that the matrices γ_M^i are purely imaginary in the Majorana representation). Complex conjugation of Eq. (7.42) furthermore implies that if the spinor Ψ_M is a solution of this equation, so is its complex conjugate Ψ_M^* . The latter complex conjugate spinor is however known to be the antiparticle of Ψ_M . A real solution $\Psi_M^* = \Psi_M$ is therefore its own antiparticle, and has been dubbed a Majorana fermion after its proposer. Since Majorana fermions are their own anti-particles, they have to be uncharged, but do carry a (four-)momentum and spin.

For the subsequent discussions, it is useful to also understand Majorana fermions in terms of operators. As an example, consider some “regular” (i.e. non-Majorana) fermions that are created by the second-quantized operators c_i^\dagger . Being fermions, these operators satisfy the anticommutator $\{c_i^\dagger, c_j\} = \delta_{i,j}$. From every such operator, two independent Majorana Fermions can be constructed. One possible choice is

$$\Psi_{i,1} = \frac{c_i^\dagger + c_i}{\sqrt{2}}, \quad \Psi_{i,2} = \frac{c_i^\dagger - c_i}{\sqrt{2}i}. \quad (7.43)$$

These new operators obey the relations

$$\Psi_{i,n}^\dagger = \Psi_{i,n} \quad (7.44a)$$

$$\{\Psi_{i,n}^\dagger, \Psi_{i,m}\} = \delta_{i,j} \delta_{n,m}, \quad (7.44b)$$

and thus describe fermionic particles that are their own antiparticles, as promised. In addition, Eqs. (7.44a) and (7.44b) imply

$$\{\Psi_{i,n}^\dagger, \Psi_{i,m}^\dagger\} = \{\Psi_{i,n}, \Psi_{i,m}\} = \delta_{i,j} \delta_{n,m} \quad (7.45)$$

and

$$\Psi_{i,n} \Psi_{i,n} = \Psi_{i,n}^\dagger \Psi_{i,n} = \Psi_{i,n} \Psi_{i,n}^\dagger = \Psi_{i,n}^\dagger \Psi_{i,n}^\dagger = \frac{1}{2}. \quad (7.46)$$

In conclusion, every regular fermion can be decomposed into two Majorana fermions. Vice versa, two Majorana fermions can be combined into one regular fermion. In case the initial fermion is charged, such as an electron, its charge must be absorbed into some other degrees of freedom as one goes from electronic operators to Majorana operators. Superconductors, where particle number and charge are not conserved, are thus natural candidates for hosting Majorana fermions, as charge can simply be absorbed into the superconducting condensate. As discussed, this applies especially for the edge states of topological superconductors. Nevertheless, and despite the intense search of generations of physicists, the experimental detection of Majorana fermions remained elusive for a long time. This goes partially along with the statement that none of the elementary particle

of the standard model is currently supposed to be a Majorana fermion. At this point, many two possible experimental detections are under debate. Firstly, there is an ongoing dispute about the nature of the neutrino, see for instance Ref. [138] and references therein. In case the neutrino was a (massful) Majorana fermion, the neutrinoless double beta decay would be possible. Experiments are currently testing this hypothesis. Secondly, solid state experiments involving topological superconductors have very recently detected zero bias conduction peaks as well single charge Shapiro steps,^{139–143} which could potentially be due to Majorana fermions. It remains to be confirmed that these experiments have really detected Majorana physics, but the experimental progress in this field is in any case rapid, impressive and promising.

7.3 Weyl fermions and Weyl nodes

Following the definition of the last section, a Weyl fermion is a massless Dirac fermion of definite chirality. The neutrino, presented in the last section as a candidate for a massful Majorana fermion, has also been believed a long time to be such a massless chiral particle. These hypotheses are obviously in competition, and today's perspective seems to favor the Majorana character over the Weyl character. Weyl fermions can however also emerge as effective degrees of freedom in more complex systems, one such example being Helium-3 in its A-phase.¹⁰⁵ In this section, we shall thus first discuss how Weyl fermions can arise as low-energy degrees of freedoms in solids, before investigating their properties in some more detail. In particular, we will present a no-go theorem for the minimum number of Weyl nodes, analyze their topological character and discuss the implications of the for us most relevant symmetries, time-reversal and inversion symmetry.

7.3.1 Weyl fermions at band touchings: Weyl nodes

At first, we shall demonstrate how and under which conditions a Weyl Hamiltonian can arise as a low-energy theory for parts of the Brillouin zone of a solid. To that end, we study a system that is supposed to have two (and only two) bands touching at some momentum \vec{k}_0 . All other possibly present bands are supposed to be sufficiently gapped and can thus be neglected, such that a (2×2) -Hamiltonian describes the relevant low energy physics. Using the Pauli matrices σ^i , this general (2×2) -Hamiltonian can be decomposed as

$$H = a(\vec{k}) + \vec{\sigma} \cdot \vec{b}(\vec{k}) . \quad (7.47)$$

Close to the band touching at $\vec{k} = \vec{k}_0$, the effective low energy theory reads

$$H(\vec{k} \approx \vec{k}_0) \approx E(\vec{k}_0) \mathbb{1}_{2 \times 2} + \vec{\sigma} \cdot \vec{b}(\vec{k}_0) + \vec{\sigma} \cdot \left(\frac{\partial b_i}{\partial k_j} \right)_{\vec{k}=\vec{k}_0} (\vec{k} - \vec{k}_0) . \quad (7.48)$$

This is nothing but a Weyl Hamiltonian, albeit potentially distorted, anisotropic and with offsets in energy and momentum. In the remainder, a touching point of two bands will therefore also be called a ‘‘Weyl node’’. It seems worthwhile to stress that the Pauli matrices $\vec{\sigma}$ in Eq. (7.48) label the pseudospin associated with the two bands. This pseudospin may be the physical spin like in Sec. 7.2.2, or could alternatively denote any other two-level degree of freedom. We note that our short analysis is in agreement with the

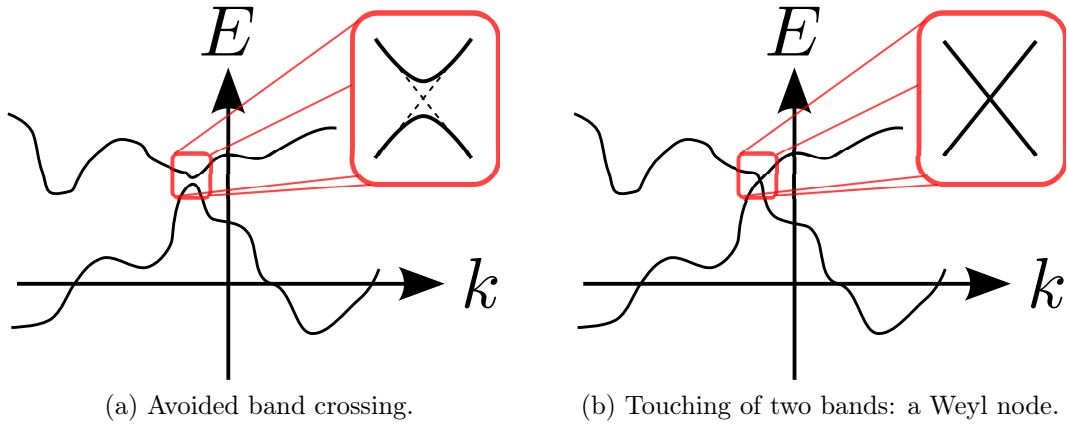


Figure 7.7: When two bands approach each other at some point in the Brillouin-zone of a one- or two-dimensional system without special symmetries, they generically have an avoided crossing as sketched in subfigure (a). In a three-dimensional system, however, a true band crossing or touching is possible, see subfigure (b). In both subfigures, E is the energy and k parametrizes a path through the Brillouin zone containing the (potential) Weyl node.

general fact that the energy has to vanish linearly in the momentum upon approaching a band touching in a crystal without special symmetries. This has already been established in 1937 by Herring.¹⁰⁴

The presence of such a band touching may at first glance seem unlikely for a generic Hamiltonian without special symmetries. The phenomenon of level repulsion should lead to an avoided crossing rather than a band touching, as depicted in Fig. 7.7a. Indeed, as has been discussed by Wigner and von Neumann in 1929, one has to adjust three real parameters in a quantum mechanical system in order to have two levels cross.¹⁴⁴ Since its Hamiltonian is a hermitian (2×2) -matrix, the band touching corresponds to

$$H = \begin{pmatrix} a & b \\ b^* & c \end{pmatrix} \stackrel{!}{=} \begin{pmatrix} a & 0 \\ 0 & a \end{pmatrix}, \quad (7.49)$$

which imposes the three real conditions

$$a = c \quad , \quad \text{Re}\{b\} = 0 \quad , \quad \text{Im}\{b\} = 0 . \quad (7.50)$$

In a three-dimensional system, the satisfaction of these three conditions is however nothing extraordinary, since the three components of the momentum \vec{k} can serve as the tuning parameters, shown in Fig. 7.7b. Therefore, a band touching can generically occur at some point in the Brillouin zone of a three-dimensional system. The situation is different in one and two dimensions, where less tuning parameters are available and band touchings have a probability of measure zero. If the Hamiltonian respects some given symmetries, the number of constraints can be reduced, such that more symmetric systems can exhibit band touchings also in lower dimensions. One can finally also consider the case that more than two bands touch. For a touching of n bands, the low energy description is given by an $(n \times n)$ -matrix. Because the latter has in the most general case n^2 independent real parameters, the number of constraints is dramatically increased, namely up to a maximum number of $n^2 - 1$ for systems without symmetries. Again, symmetries can reduce the number of constraints.

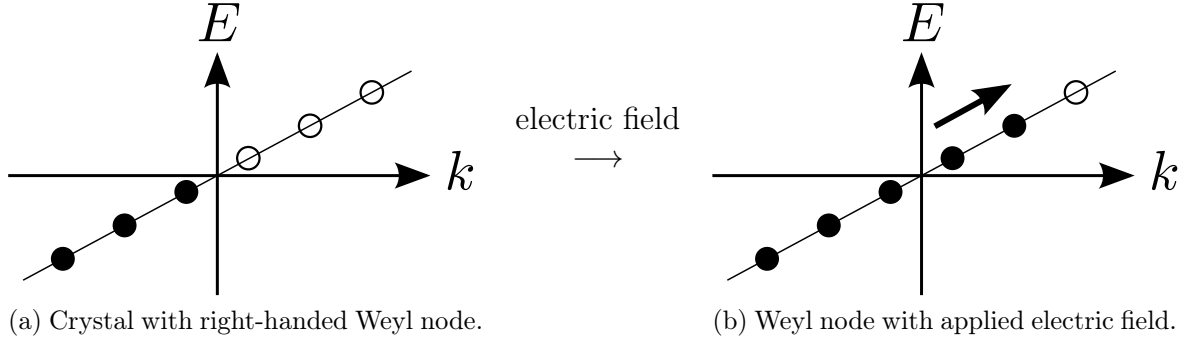


Figure 7.8: In a crystal with one single Weyl node, for instance a right-handed Weyl node as shown in subfigure (a), the application of an electric field would shift the electrons up or down the dispersion, thus generating or annihilating electrons, see subfigure (b). Full black dots correspond to occupied states, while empty circles are unoccupied states. Figure adapted from Ref. [147].

7.3.2 The Nielsen-Ninomiya fermion doubling theorem

In a system of chiral fermions, a chiral symmetry is a transformation that leaves the Dirac Lagrangian invariant and acts independently on right- and left-handed particles. One distinguishes between vector symmetries and axial symmetries. The symmetry operation related to the prior one acts similarly on the two sectors of the Hamiltonian describing the two handednesses, while the ones related to axial symmetries act in opposite ways onto left- and right-handed fermions. As an example, the transformation

$$\Psi_{ch} \rightarrow \left[\frac{1}{2}(\mathbb{1}_{4 \times 4} + \gamma_{ch}^5) e^{i\theta} + \frac{1}{2}(\mathbb{1}_{4 \times 4} - \gamma_{ch}^5) e^{-i\theta} \right] \Psi_{ch} \quad (7.51)$$

would imply the presence of a vector symmetry if it leaves the Hamiltonian invariant, whereas an invariance under

$$\Psi_{ch} \rightarrow \left[\frac{1}{2}(\mathbb{1}_{4 \times 4} + \gamma_{ch}^5) e^{i\theta} + \frac{1}{2}(\mathbb{1}_{4 \times 4} - \gamma_{ch}^5) e^{-i\theta} \right] \Psi_{ch} \quad (7.52)$$

would correspond to the presence of an axial symmetry. If a given chiral symmetry is broken, the associated charge and current are not conserved, as usual for symmetry breaking. An example of an anomalous non-conservation of a chiral current is the Adler-Bell-Jackiw anomaly, abbreviated ABJ-anomaly, and has been known since the late 1960's in particle physics.^{145,146}

In 1983, Nielsen and Ninomiya studied the ABJ-anomaly and a related no-go theorem (also known as the fermion doubling theorem) derived in their earlier work in order to give it an interpretation in terms of solid state systems, specifically analyzing the behavior of Weyl fermions in a crystal.¹⁴⁷⁻¹⁵⁰ Their line of argument is most easily understood in one dimension, where the Weyl Hamiltonians are $H = \pm v_F k$. More specifically, they considered a system with one single right-handed Weyl node as depicted in Fig. 7.8a,

$$H = +v_F k . \quad (7.53)$$

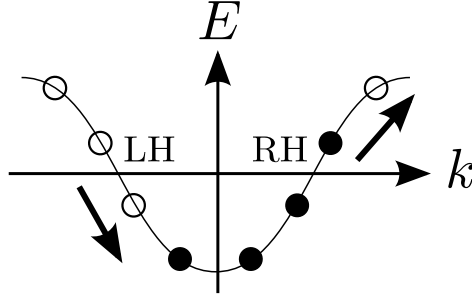


Figure 7.9: If a crystal has as many right-handed Weyl nodes (RH) as left-handed ones (LH), the application of an electric field pumps electrons from one Weyl node to the other. In the figure, full black dots correspond to occupied states, while empty circles are unoccupied states. This increases the number of, for instance, right-handed electrons at the expense of the left-handed ones, but does not create or annihilate physical electrons. Figure adapted from Ref. [147].

Since there is no left-handed Weyl node, the system is obviously not symmetric in the two chiralities. The non-conserved charge associated with this symmetry breaking turns out to be the number of Weyl fermions. To see that, Nielsen and Ninomiya considered the effect of an electric field on the system. The latter simply accelerates the Weyl fermions, thus pushing them “up the dispersion” in Fig. 7.8b. This obviously enlarges the occupied momentum range and therefore corresponds to a creation of Weyl fermions. One could also have done a similar reasoning with left-handed Weyl fermions (or reversed the electric field), which would have led to an annihilation of Weyl fermions.

In a real solid state system, even if the electrons have a Weyl node somewhere in their Brillouin zone, an electric field can obviously never create or annihilate electrons, but only move them around. Nielsen and Ninomiya concluded that a solid state system must therefore always have an equal number of left- and right-handed Weyl nodes. As shown in Fig. 7.9, the application of an electric field will at lowest energies indeed seemingly destroy electrons of the one handedness and create electrons of the other, but the paradox is resolved once the full bandstructure is taken into account. The electric field simply pumps electrons from one Weyl node to the other, passing through a region of the Brillouin zone connecting the two nodes which is not described by a Weyl Hamiltonian. We can summarize the findings of Nielsen and Ninomiya in the following version of the fermion doubling theorem:

Weyl nodes in a crystal always come in pairs of opposite chirality.

7.3.3 Topological character of Weyl nodes

The discussion of Sec. 7.3.1 already suggests that a single Weyl node should be extremely stable, since it seems to be allowed for a general 2 band system. Let us thus consider a general perturbation to a Weyl Hamiltonian,

$$H = \pm v_F \vec{\sigma} \cdot \vec{k} + H_{\text{pert}} , \quad (7.54a)$$

$$H_{\text{pert}} = a_{\text{pert}}(\vec{k}) \mathbb{1}_{2 \times 2} + \vec{b}_{\text{pert}}(\vec{k}) \cdot \vec{\sigma} . \quad (7.54b)$$

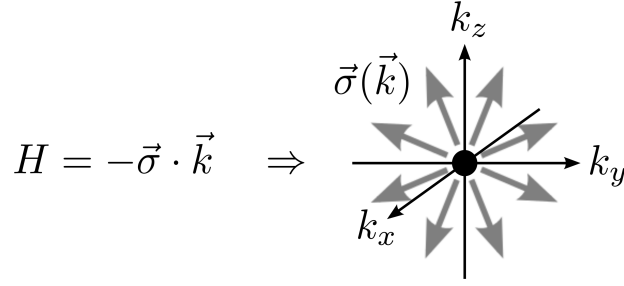


Figure 7.10: At a right-handed Weyl node, the (pseudo-)spins align parallel to the momentum measured relative to the Weyl node. The Weyl node is thus a (pseudo-)spin hedgehog in momentum space. The black dot depicts the Weyl node, the grey arrows show the (pseudo-)spins.

Expanding the perturbation close to the Weyl node, we obtain

$$H \approx \pm v_F \vec{\sigma} \cdot \vec{k} + a_{\text{pert}}(\vec{k}) \mathbb{1}_{2 \times 2} + \vec{\sigma} \cdot \vec{b}_{\text{pert}}(0) + \vec{\sigma} \cdot \left(\frac{\partial \vec{b}_{\text{pert},i}}{\partial k_j} \right)_{\vec{k}=0} \vec{k}. \quad (7.55)$$

Here, the second term acts like a momentum-dependent chemical potential, while the third term shifts the Weyl node to some non-zero momentum. The last term can change the velocity associated with the Weyl node, possibly in an anisotropic way. None of the terms can however remove the Weyl node from the system. Therefore, a single Weyl node is perturbatively absolutely stable.

This absolute stability gives a hint that Weyl nodes can be understood in analogy to topological defects. To see this, we first recall that Weyl fermions are characterized by their chirality (which is identical to their helicity). Therefore, the electrons associated with a right-handed Weyl node have their (pseudo-)spin pointing parallel to their momentum, while left-handed Weyl electrons have their (pseudo-)spin pointing antiparallel to their momentum. A Weyl node is thus a (pseudo-)spin hedgehog in momentum-space, one of the prototypes of a topological defect, see Fig. 7.10.

Weyl nodes as sources of Berry flux

The topological character of a Weyl node is mathematically proven by showing that it is a quantized source of Berry flux, as has first been done by Volovik in the context of $^3\text{He-A}$, but in general already foreseen by Berry in his original paper on the Berry phase.^{105,127,151} To this end, we recall the concepts of Berry connection and Berry curvature in the case of a Weyl semimetal (a more general discussion can be found in Sec. 7.1.2). For a Weyl semimetal, which in general is a multi-band system out of which some levels touch in Weyl nodes, the electrons in the n^{th} band are described by wavefunctions

$$\Psi_{n,\vec{k}}(\vec{r}) = \langle \vec{r} | n(\vec{k}) \rangle. \quad (7.56)$$

The Berry connection of the n^{th} band,

$$\vec{A}_n(\vec{k}) = i \langle n(\vec{k}) | \nabla_{\vec{k}} | n(\vec{k}) \rangle, \quad (7.57)$$

is by definition related to the respective Berry curvature by

$$\vec{B}_n(\vec{k}) = \nabla_{\vec{k}} \times \vec{A}_n(\vec{k}). \quad (7.58)$$

Since the Berry curvature is the curl of the Berry connection, it should itself be divergence free,

$$\nabla_{\vec{k}} \cdot \vec{B}_n(\vec{k}) \stackrel{!}{=} 0 . \quad (7.59)$$

This is however only true as long as all the above steps are well-defined. In particular, Eq. (7.59) is only true as long as the n bands are non-degenerate. At a Weyl point, where (at least) two bands are degenerate, any linear combination of the two bands is equivalent. Consequently, the Berry connection and Berry curvature turn out to be ill-defined at a Weyl node. For a Hamiltonian of the form

$$H = a(\vec{k}) \mathbb{1}_{2 \times 2} + \vec{b}(\vec{k}) \cdot \vec{\sigma} , \quad (7.60)$$

i.e. a Hamiltonian that topologically equivalent to a spin in a magnetic field, it is well known¹²⁵ that the general expression of the i^{th} component of the (appropriately normalized) Berry curvature is given by

$$B_i(\vec{k}) = -\frac{1}{8\pi} \frac{1}{|\vec{b}(\vec{k})|^3} \epsilon_{ijm} \vec{b}(\vec{k}) \cdot \frac{\partial \vec{b}}{\partial k_j} \times \frac{\partial \vec{b}}{\partial k_m} . \quad (7.61)$$

For right- and left-handed Weyl Hamiltonians, where $\vec{b}(\vec{k}) = \pm v_F \vec{k}$, the Berry curvature thus reads

$$\vec{B}_{\text{RH}}(\vec{k}) = \frac{1}{4\pi} \frac{\vec{k}}{|\vec{k}|^3} \quad \text{and} \quad \vec{B}_{\text{LH}}(\vec{k}) = -\frac{1}{4\pi} \frac{\vec{k}}{|\vec{k}|^3} . \quad (7.62)$$

By analogy to Coulomb's law, one can now easily conclude that a Weyl node is a quantized source of Berry flux,

$$\nabla_{\vec{k}} \cdot \vec{B}_{\text{RH}}(\vec{k}) = \delta(\vec{k}) \quad \text{and} \quad \nabla_{\vec{k}} \cdot \vec{B}_{\text{LH}}(\vec{k}) = -\delta(\vec{k}) . \quad (7.63)$$

7.3.4 Weyl nodes with and without symmetries

In a solid, one often has symmetries constraining the form of the Hamiltonian. We will especially be concerned with time-reversal symmetry (TRS) and inversion symmetry (IS). Let us first consider a system that respects time-reversal symmetry and has a Weyl node of a given handedness at \vec{k}_0 ,

$$H(\vec{k} \approx \vec{k}_0) \approx \pm v_F \vec{\sigma} \cdot (\vec{k} - \vec{k}_0) . \quad (7.64)$$

As the total Hamiltonian of the system is invariant under time reversal by assumption, it remains identical if we take $\vec{k} \leftrightarrow -\vec{k}$ and $\vec{\sigma} \leftrightarrow -\vec{\sigma}$ (note that in case $\vec{\sigma}$ does not denote the physical spin, the notion of time-reversal symmetry is understood to be generalized to the given pseudospin $\vec{\sigma}$). Close to the Weyl node, we obtain

$$\begin{aligned} H(\vec{k} \approx \vec{k}_0) \approx \pm v_F \vec{\sigma} \cdot (\vec{k} - \vec{k}_0) & \xleftrightarrow{\text{TRS}} H(-\vec{k} \approx \vec{k}_0) \approx \pm v_F (-\vec{\sigma}) \cdot (-\vec{k} - \vec{k}_0) \\ & = \pm v_F \vec{\sigma} \cdot (\vec{k} + \vec{k}_0) . \end{aligned} \quad (7.65)$$

The presence of time reversal symmetry thus implies that every Weyl node at a momentum \vec{k}_0 has a partner Weyl node of the same chirality and same energy at $-\vec{k}_0$. Since in addition there must be an equal number of right- and left-handed Weyl nodes,

| TRS | IS | Implications | Min. number |
|-----|----|---|-------------|
| × | × | Weyl nodes can be at any \vec{k} and may have different energies. ¹¹³ | 2 |
| ✓ | × | Weyl node at $\vec{k}_0 \Leftrightarrow$ Weyl node of <i>same</i> chirality at $-\vec{k}_0$. | 4 |
| × | ✓ | Weyl node at $\vec{k}_0 \Leftrightarrow$ Weyl node of <i>opposite</i> chirality at $-\vec{k}_0$. | 2 |
| ✓ | ✓ | No stable, individually separated Weyl nodes possible. | none |

Table 7.1: The implications of presence or absence of time-reversal symmetry (TRS) and inversion symmetry (IS) for Weyl nodes, along with the minimum number of Weyl nodes (if they are present at all).

a time reversal symmetric Weyl system must have at least four Weyl nodes (two of each chirality).

A similar reasoning can be made in the presence of inversion symmetry, which only takes $\vec{k} \leftrightarrow -\vec{k}$. There, the presence of a Weyl node of a given chirality at \vec{k}_0 implies a Weyl node of opposite chirality but same energy at $-\vec{k}_0$:

$$H(\vec{k} \approx \vec{k}_0) \approx \pm v_F \vec{\sigma} \cdot (\vec{k} - \vec{k}_0) \xleftrightarrow{IS} H(-\vec{k} \approx \vec{k}_0) \approx \pm v_F \vec{\sigma} \cdot (-\vec{k} - \vec{k}_0) = (-1)(\pm) v_F \vec{\sigma} \cdot (\vec{k} + \vec{k}_0). \quad (7.66)$$

The minimum number of Weyl nodes for an inversion symmetric system is therefore 2 (on of each chirality). If a system respects both time reversal and inversion symmetry (as unlikely as it may seem according to Sec. 7.3.1), each Weyl node would have to be superimposed with a Weyl node of opposite chirality. Being topological defects of opposite charge, the two Weyl nodes would annihilate immediately, leaving the system in a trivial insulating state. We can thus make the statement of Sec. 7.3.1 even stronger by saying that the presence of time-reversal and inversion symmetry forbids the existence of Weyl nodes symmetry-wise. For systems with neither time-reversal nor inversion symmetry, the Weyl nodes are in principle totally independent in their location and energy.¹¹³ These results are summarized in Tab. 7.1.

7.4 Weyl semimetals as a perturbed transition between topological and normal insulators

In Sec. 7.3, we have shown that a three-dimensional solid can in general exhibit Weyl nodes, at least as long as either time reversal and/or inversion symmetry is broken. If the bandstructure has an energy range where only the Weyl nodes matter, and if these are energetically degenerate, the system is a proper semimetal: conduction and valence band(s) touch only in a few points, namely the Weyl nodes. Consequently, such systems have been dubbed “Weyl semimetals”.

As discussed in Sec. 7.3.3, a Weyl node carries a topological charge, which makes the band structure of a Weyl semimetal a topological one. The general connection between Weyl semimetals and topological insulators, the most prominent example of topological band structures, has been established by Burkov, Hook and Balents in Ref. [114]. In addition, Balents et al. showed in Refs. [111] and [112] how Weyl semimetal phases can be engineered within heterostructures of topological and normal insulators. This section shortly reviews some of their results, which are related to earlier work by Murakami who

studied the transition between a topologically non-trivial quantum spin Hall state (QSH) and a trivial insulator in three dimensions.¹⁰⁶ Like Balents et al., he also concluded that a topological semimetal could exist as an intermediate phase between the QSH state and a trivial insulator if inversion symmetry was broken.

7.4.1 Transition between topological and normal insulators

Balents et al. started from a generic model for a topological insulator that respects both time reversal and inversion symmetry. The corresponding effective model has been established in Ref. [152]. The model takes into account only one pair of conduction bands and one pair of valence bands (note that the bands are doubly Kramers degenerate due to symmetries), and is thus a (4×4) -Hamiltonian. In $\vec{k} \cdot \vec{p}$ expansion around the Γ -point, the model reads

$$H_0 = \sum_{i=1}^3 k_i \gamma^i + m \gamma^0 \quad (7.67)$$

in terms of the Dirac-matrices defined in Eq. (7.34). It is well-known that this model has a transition from a topologically trivial to a topologically non-trivial state as the sign of the Dirac-mass m changes, see Sec. 7.1.3. Since Weyl nodes can only appear if either time reversal (TRS) or inversion symmetry (IS) are broken, Balents et al. investigated the effect of perturbations to the Hamiltonian (7.67) that precisely break either of the two. As an example, let us consider the perturbation

$$H_{pert} = u \gamma_{23} \quad , \quad \gamma^{23} = -\frac{i}{2} [\gamma^2, \gamma^3] . \quad (7.68)$$

Since the original Hamiltonian (7.67) respects both time reversal and inversion symmetry, and since the momentum is odd under both, the Dirac-matrices γ^1 , γ^2 and γ^3 also have to be odd under time reversal and inversion. The commutator $[\gamma^2, \gamma^3]$ is therefore even under both, such that the matrix γ^{23} is even under inversion symmetry, but odd under time reversal symmetry (note that the latter corresponds to an anti-unitary operator). H_{pert} thus breaks time reversal symmetry, but conserves inversion symmetry. The eigenvalues of the perturbed Hamiltonian are simply obtained by direct diagonalization. Balents et al. found that two Weyl nodes appear whenever

$$|u| > |m| . \quad (7.69)$$

This extended Weyl phase is shown in the phase diagram of Fig. 7.11. As advertised, it appears as an intermediate phase between a topological and normal insulator upon perturbing the system with a time reversal breaking term. As will be discussed in Sec. 7.4.2, the Weyl semimetal inherits properties from both the normal and the topological insulator, while its gaplessness can be interpreted as a heritage of the transition itself. A similar reasoning can be made for inversion symmetry breaking terms, which (if properly dealt with) also lead to a Weyl phase intermediate between a topological and a normal insulator.^{112,114}

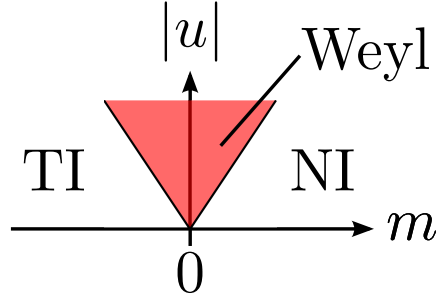


Figure 7.11: The phase diagram of a gapped Dirac insulator shows a transition from a topological insulator state (TI) to a normal insulator state (NI) as a function of the Dirac mass m . If time reversal symmetry is broken by a term $\sim u$, an extended Weyl semimetal phase appears as a function of $|u|$ between the topological and the normal insulator. This phase diagram is based on the results of Ref. [114].

7.4.2 Weyl semimetals in heterostructures

When trying to analyze the fundamental properties of Weyl semimetals, it is desirable to have at hand a well-defined and fully-understood toy system that is easily tunable between different phases. This concerns not only experiments, but also applies to theory, for example when it comes to complicated band structures such as in the pyrochlore iridates.¹⁰⁷ To make life particularly easy, one would further like to have the minimum number of two Weyl nodes, as opposed to, for instance, 24 Weyl nodes suggested the pyrochlore iridates¹⁰⁷. Therefore, only systems with broken time reversal symmetry should be considered. On the quest for an appropriate model system, Burkov and Balents analyzed a heterostructure of topological (TI) and normal insulators (NI), shown in Fig. 7.12a. Both top and bottom surfaces of each topological insulator slab constitute a layer of Dirac surface electrons. The different surfaces are tunnel coupled across the thin layers. The tunneling amplitude between the two Dirac surfaces of the same topological insulator is t_S , the coupling between different layers is t_D . This heterostructure has a quantum phase transition between a topological and a trivial state as a function of the ratio t_S/t_D . If $t_S \gg t_D$, the two surfaces of each of the topological insulator slabs will hybridize and be gapped out, such that no gapless Dirac surfaces are left. The heterostructure is then a normal insulator as shown in the upper part of Fig. 7.12b.

If on the other hand $t_S \ll t_D$, the top and bottom surfaces of neighboring layers of topological insulator will hybridize and be gapped out. This is however not possible for the top surface of the uppermost and the bottom surface of the lowermost TI layer, since they simply do not have a neighboring layer. There will thus be two layers of Dirac electrons on the very top and the very bottom surfaces of the heterostructure, which is equivalent to having one big topological insulator, see the lower part of Fig. 7.12b.

In conclusion, the heterostructure can be tuned from a topologically non-trivial to a topologically trivial insulating state as a function of t_S/t_D . To obtain a Weyl semimetal, Burkov and Balents introduced magnetic impurities that are supposed to order ferromagnetically along the stacking axis of the heterostructure, see Fig. 7.13. This leads to a Zeeman field for the surface states, which are thus gapped, but does not induce a vector potential. Although every individual layer of surface Dirac electrons is now gapped, the total system becomes a gapless Weyl semimetal. As Burkov and Balents showed, the relevant physics are described by the Hamiltonian

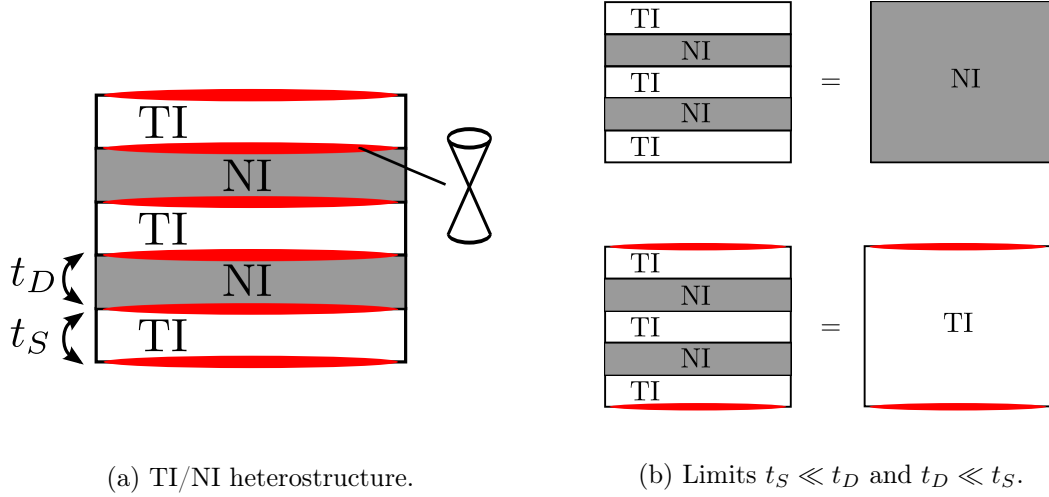


Figure 7.12: Heterostructure made from stacked layers of topological insulator (TI) and normal insulator (NI). Subfigure (a) depicts the general structure, with t_S being the tunnel coupling between Dirac fermions at the top and bottom surface of the same TI slab, t_D denotes the coupling between neighboring Dirac layers in different TI slabs. The layers of Dirac fermions are shown in red. Subfigure (b) depicts the limits $t_S \ll t_D$ (upper part) and $t_S \ll t_D$ (lower part).

$$H = \sum_{\vec{k}} (c_{\vec{k}\uparrow}^\dagger, c_{\vec{k}\downarrow}^\dagger) \left[v_F (\hat{z} \times \vec{\sigma}) \cdot \vec{k} + M(k_z) \sigma_z \right] \begin{pmatrix} c_{\vec{k}\uparrow} \\ c_{\vec{k}\downarrow} \end{pmatrix}, \quad (7.70a)$$

$$M(k_z) = m - \sqrt{t_S^2 + t_D^2 + 2t_S t_D \cos(k_z d)} \quad (7.70b)$$

As we shall see in the next section, the Hamiltonian (7.70a) indeed describes a Weyl semimetal. The derivation of Eqs. (7.70) and the physical discussion are similar to the ones of the Weyl superconductor in Sec. 8.1.1, and the interested reader is referred to this section and the original paper in Ref. [111] for further details.

Weyl semimetal as stacked quantum Hall layers

If there is a $k_z = k_0$ with $M(k_0) = 0$, the Hamiltonian (7.70a) has two inversion symmetric gapless points at $\vec{k} = (0, 0, \pm k_0)$. These gapless points are of course nothing but the expected Weyl nodes of opposite chirality. Burkov and Balents demonstrated that Weyl nodes exist for an intermediate strength of time reversal symmetry breaking, namely for $(t_S - t_D)^2 \leq m^2 \leq (t_S + t_D)^2$.¹¹¹ To understand this, we recall that the heterostructure is a trivial insulator for the time reversal symmetric limit $m = 0$ (note that inversion symmetry is not broken in the heterostructure), see Sec. 7.3.4. When m is increased to $|t_S - t_D|$, a node-antinode pair is generated at $\vec{k} = (0, 0, \pi)$. Upon further increase of m , the two nodes move in opposite directions along the k_z -axis. They finally meet again at $\vec{k} = 0$ for $m = |t_S + t_D|$, and annihilate.

For fixed k_z , it is useful to reinterpret the Weyl semimetal Hamiltonian (7.70a) as a gapped two-dimensional Dirac Hamiltonian of given mass $M(k_z)$. The latter is well-known to describe an integer quantum Hall system that has a quantum Hall transition

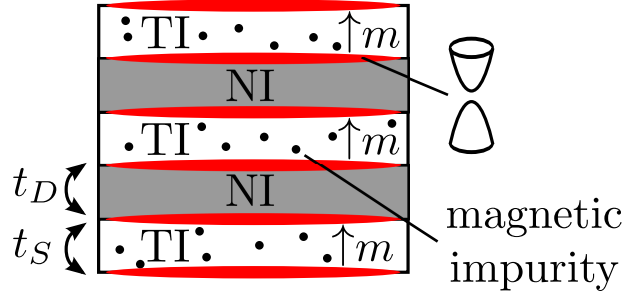


Figure 7.13: In a heterostructure made from layers of topological (TI) and normal insulators (NI), which in addition contains magnetic impurities, a Weyl semimetal can be realized (see text). In the figure, t_S is the tunnel coupling between Dirac fermions (shown in red) at the top and bottom surface of the same TI slab, t_D denotes the coupling between neighboring Dirac layers in different TI slabs. The magnetic impurities m are supposed to order ferromagnetically along the stacking axis of the heterostructure. Note that although each individual layer of Dirac electrons is gapped due to the magnetic impurities, the global heterostructure is a gapless topological Weyl semimetal.

when the Dirac mass changes sign, see again Sec. 7.1.3 or Ref. [131]. A Weyl semimetal may thus also be understood as layers of quantum Hall systems that have been stacked in momentum space, see Fig. 7.14. Each value of k_z corresponds to a different quantum Hall layer and the sign of the corresponding effective mass $M(k_z)$ defines whether the given layer is topologically trivial or not. Since the Weyl nodes mark the sign change of the Dirac mass and thus a quantum Hall transition, all quantum Hall layers between the two nodes are topologically non-trivial, while all other layers are topologically trivial. It is in this sense that the Weyl semimetals inherit features from both topological and normal insulators, as advertised in Sec. 7.4.1. If the Weyl nodes have annihilated upon increasing m to $m \geq |t_S + t_D|$, the entire Brillouin zone is left in a topologically non-trivial state, and the system is a quantum Hall insulator.

Just like the bulk physics, the surface properties of Weyl semimetals are best understood in momentum space. Each of the quantum Hall layers that are in the topologically non-trivial range of k_z contributes one quantum Hall surface state on the surfaces parallel to \hat{z} . A Weyl semimetal thus has topologically protected surface states on the 4 side surfaces. As usual for quantum Hall edge states, the surface states are chiral and propagate unidirectionally around the sample. The direction of propagation is set by the time reversal symmetry breaking (reversing the moments of the magnetic impurities in the heterostructure would thus invert the propagation). The top and bottom surface, however, are trivial insulators.

To become a little more technical, the surface Brillouin zones essentially correspond to the projection of the bulk Brillouin zone onto the planes defining the surfaces and are shown in Fig. 7.15. On the top and bottom surfaces, the projection of the bulk Brillouin zone superimposes the positive and negative Weyl node, such that these two surfaces see no topological charge at all. Consequently, they are trivially insulating state. The side surface Brillouin zones, however, have topological edge states. These states exist for all two-dimensional surface momenta that have a k_z in the topological momentum range (“between the Weyl nodes”, again indicated by a red line in Fig. 7.15). The surface states are half-filled, just like the bulk states. The surface Fermi line lays on the k_z -axis and

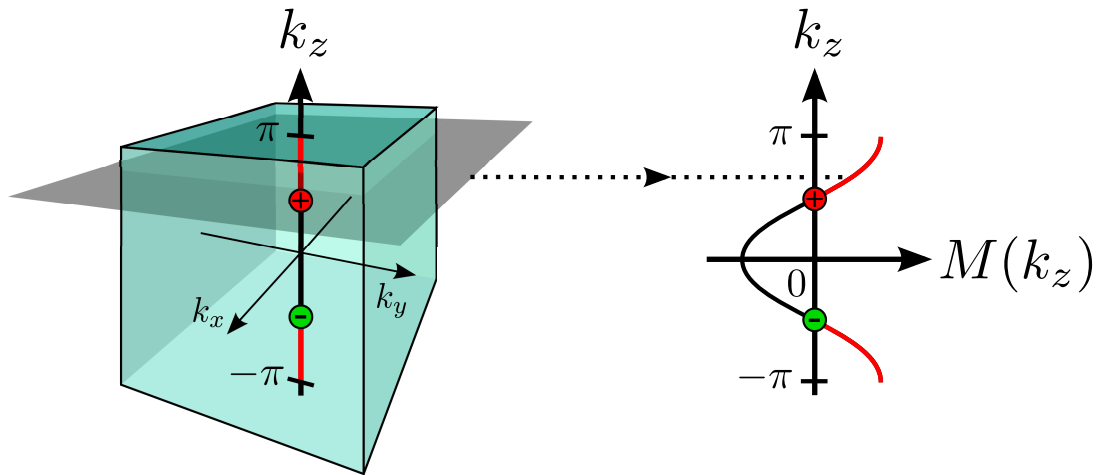


Figure 7.14: On the left, the bulk Brillouin zone of a Weyl semimetal is shown. Two Weyl nodes of positive and negative chirality separate the topologically non-trivial momentum range from the topologically trivial momenta. The topologically non-trivial momentum range is colored in red and corresponds to positive values of the effective mass function $M(k_z)$, see right-hand side. For a fixed value of k_z , the (k_x, k_y) -cut through the bulk Brillouin zone can be understood as the Brillouin zone of a quantum Hall system in either a topologically trivial or non-trivial state. The exemplary cut shown by the gray plane on the left-hand side thus corresponds to a topologically non-trivial quantum Hall state.

thus coincides with the red line in the lower right subfigure of Fig. 7.15. Interestingly, the surface Fermi line is not closed but forms a so-called Fermi arc. It therefore seems like one could go from occupied to the unoccupied states without ever crossing a Fermi line by following the curved path indicated by the arrow. This apparent contradiction is resolved when we recall that we are dealing with the surface of a three-dimensional system, and that surface electrons can be delocalized into the bulk. When the momentum is changed along the path, the states indeed initially correspond to occupied surface states. When however the dotted line in Fig. 7.15 denoting the end of the topological surface momentum range is crossed, the states detach from the surface into the bulk, where the transition from occupied to unoccupied occurs. Since the transition happens in the bulk, it is not reflected in the surface Brillouin zone. As we continue along the path, the unoccupied bulk states finally comes back to the surface when k_z reenters the topological range. In other words, the crossing of the surface Fermi line can only be circumvented by choosing to cross the bulk Fermi surface instead.

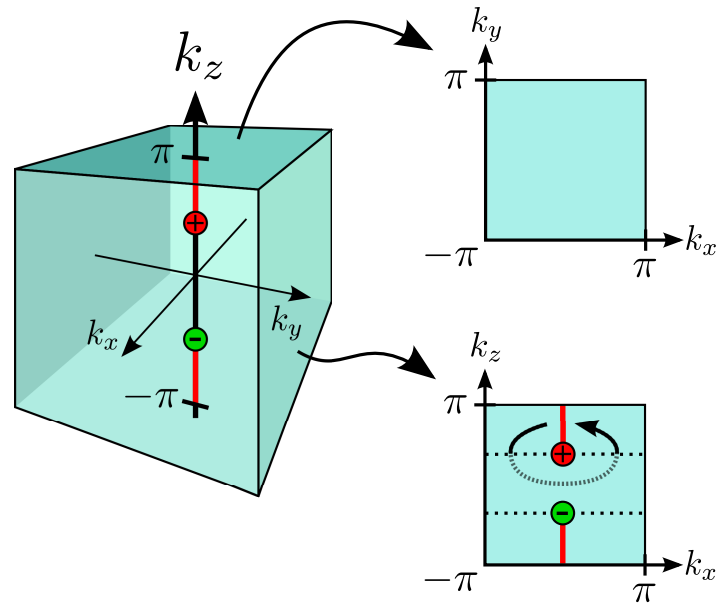


Figure 7.15: Bulk Brillouin zone of a Weyl semimetal (left) along with the corresponding surface Brillouin zones. The top right figure shows the Brillouin zone of a surface perpendicular to the \hat{z} -axis, the lower right figure depicts a Brillouin zone of a surface parallel to \hat{z} . In general, a surface Brillouin zone can be understood as the respective projection of the bulk Brillouin zone. On surfaces parallel to \hat{z} , a Fermi arc forms in the topological range of k_z (both depicted by the red line, the dotted line further illustrates the limits of the topological momentum range). The arrow depicts a special path through the surface Brillouin zone, see the main text. Only the solid part of the arrow lives at the surface, while the dashed part lives in the bulk. The Weyl nodes on the lower right figure are to be understood as the projection of the bulk Weyl nodes, and have no special meaning in the surface Brillouin zone.

Chapter 8

Weyl superconductors

8.1 Weyl superconductors in heterostructures

As we have discussed in the last sections, a Weyl semimetal is an interesting topological system that can be understood as being in between a topological insulator and a normal insulator. It can only exist if time reversal and/or inversion symmetry are broken, and has an even number of gapless Weyl nodes in the band structure. The minimum number of two Weyl nodes can only be achieved if time reversal symmetry is broken. We further argued that superconducting systems can have topological band structures just as regular insulators may, and that particularly interesting Majorana states can be associated with their boundaries. It therefore seems natural to ask if also Weyl semimetals can somehow be brought into a superconducting state, and what this state would look like. In particular, we wanted to analyze the behavior of the bulk band structure (“Does the latter have a superconducting gap and what happens to the Weyl nodes?”) and the potentially associated surface states (“Do they exist, and if so, what happens to the Fermi arcs of normal Weyl semimetals?”).

8.1.1 Physical model and Hamiltonian

In the following, we want to answer these questions using a well-controlled toy model. Since we want things to be particularly simple, we would like to have only two Weyl nodes, but keep inversion symmetry. In generalization of the normal Weyl semimetal,¹¹¹ we consider a heterostructure of layers of a topological insulator and a standard s-wave BCS superconductor as shown in Fig. 8.1. Time reversal symmetry is broken by magnetic impurities within the layers of topological insulator, and superconductivity enters the game through the proximity effect of each superconducting layer on the surface states of the neighboring layers of topological insulator. We would like to advertise that the breaking of time reversal symmetry will turn out to be a crucial ingredient for topologically non-trivial physics, see Sec. 8.1.3 and appendix D.2, and that time reversal symmetric Weyl superconductors are consequently topologically trivial.

For our model Hamiltonian, we focus only on the effectively relevant low-energy degrees of freedom and therefore only take into account the magnetically gapped surface states of each layer of topological insulator along with their proximity induced BCS mean field superconducting correlations. The individual layers are assumed to be thin, such that each surface is tunnel coupled to its neighbors. The magnetic impurities are considered

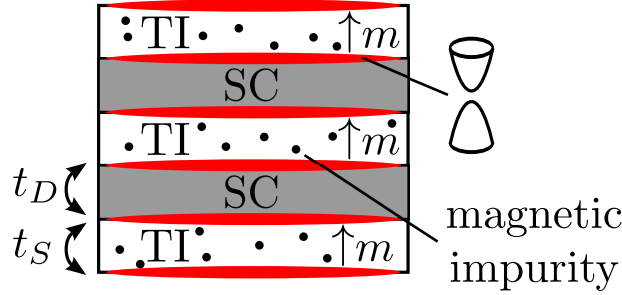


Figure 8.1: A weyl superconductor can be realized in a heterostructure composed of layers of topological insulator (TI) and standard s-wave BCS superconductor (SC). The topological insulator layers are assumed to be doped with magnetic impurities that order ferromagnetically throughout the sample, leading to a homogenous magnetization m seen by the (therefore gapped) surface states of the TI layers (the latter are shown in red). Both the layers of TI and SC are assumed to be thin, such that the different surface state layers are tunnel coupled. The coupling between the surfaces of the same TI layer is t_S , while t_D denotes the coupling surface states of between neighboring layers.

to order ferromagnetically along the stacking axis of the heterostructure. We furthermore assume that each surface layer sees the same average magnetization. Since the individual layers are thin, we also assume superconductivity to be globally phase-coherent. We note that the two surfaces are related by inversion symmetry, and that each surface can effectively be described by a magnetically gapped two-dimensional "Dirac" Hamiltonian.¹⁵³ Working in units of $\hbar = 1$, our model Hamiltonian reads

$$H = \sum_{\vec{k}_\perp, i, j} c_{\vec{k}_\perp i}^\dagger \mathcal{H}_{ij} c_{\vec{k}_\perp j} + H_{SC} , \quad (8.1)$$

$$\begin{aligned} \mathcal{H}_{ij} = & v_F \tau^z (\hat{z} \times \vec{\sigma}) \cdot \vec{k}_\perp \delta_{i,j} + m \sigma^z \delta_{i,j} \\ & + t_S \tau^x \delta_{i,j} + \frac{1}{2} t_D \tau^+ \delta_{i,j+1} + \frac{1}{2} t_D \tau^- \delta_{i,j-1} \end{aligned} \quad (8.2)$$

$$H_{SC} = \sum_{\vec{k}_\perp, i} \Delta \left(c_{\vec{k}_\perp \uparrow i}^{\text{top}} \dagger c_{-\vec{k}_\perp \downarrow i}^{\text{top}} \dagger + c_{\vec{k}_\perp \uparrow i}^{\text{bot.}} \dagger c_{-\vec{k}_\perp \downarrow i}^{\text{bot.}} \dagger \right) + \text{h.c.} , \quad (8.3)$$

where $c_{\vec{k}_\perp i} = (c_{\vec{k}_\perp \uparrow i}^{\text{top}}, c_{\vec{k}_\perp \downarrow i}^{\text{top}}, c_{\vec{k}_\perp \uparrow i}^{\text{bot.}}, c_{\vec{k}_\perp \downarrow i}^{\text{bot.}})^T$ comprises annihilation operators for electrons of spin up and down in the top and bottom surfaces of layer i with in-plane momentum \vec{k}_\perp . The unit vector along the perpendicular axis is \hat{z} . The Fermi velocity of the Dirac nodes is v_F , for simplicity considered to be the same on each surface, and Pauli matrices $\vec{\sigma}$ act on the real spin. The additional pseudo spin for the top/bottom surface degree of freedom is denoted by the Pauli matrices $\vec{\tau}$. The Zeeman mass of the Dirac nodes is given by the average magnetization m (we consider $m \geq 0$ without loss of generality), the tunneling between top and bottom surface of the same TI layer is denoted by t_S , and the tunneling between different TI layers is t_D (both tunneling amplitudes are assumed to be positive without loss of generality). The proximity induced superconductivity is characterized by $\Delta = |\Delta|e^{i\varphi}$, with φ being the globally coherent superconducting phase.

The Hamiltonian can be recast into a more convenient form by a couple of lengthy transformations which are detailed in the appendix D.1. At first, we Fourier transform

along the \hat{z} -axis and diagonalize the hopping part of the Hamiltonian. This yields two independent superconducting (2×2) -Hamiltonians. The matrix structure is still due to spin up and down, but the eigenstates rather correspond to electrons of definite chirality. Next, we perform a Bogoliubov transformation in order to take into account the superconducting correlations for both sub-Hamiltonians. The resulting eigenstates (the Bogoliubov quasiparticles) can be understood as the decomposition of electrons and holes into particle-hole symmetric and particle-hole anti-symmetric quasiparticles. To understand this, we note that the Hamiltonian (8.1) is from the beginning on invariant under the superconducting particle hole symmetry

$$c_{\vec{k}_\perp \sigma i}^{(\cdot)} \leftrightarrow c_{-\vec{k}_\perp \bar{\sigma} i}^{(\cdot) \dagger} e^{i\varphi} , \quad (8.4)$$

but that the particle-hole symmetric and anti-symmetric states of the Hamiltonian are energetically degenerate in the non-superconducting case. It was therefore sensible to interpret the Hamiltonian in terms of particles and holes (which are only eigenstates of the Hamiltonian, but not the particle-hole symmetry). If however superconductivity is turned on, particle-hole symmetric and anti-symmetric states are energetically split by $\sim 2|\Delta|$, and the Hamiltonian itself is only diagonal in terms of Bogoliubov quasiparticles. In summary, the Hamiltonian is transformed as

$$\begin{aligned} & \text{(top \& bottom surface)} \quad \otimes \quad \text{(spin } \uparrow \text{ \& } \downarrow) \quad + \quad \text{superconductivity} \\ \rightarrow & \text{(2 hopping diagonal parts)} \quad \otimes \quad \text{(spin } \uparrow \text{ \& } \downarrow) \quad + \quad \text{superconductivity} \\ \rightarrow & \text{(2 hopping diagonal parts)} \quad \otimes \quad \text{(spin } \uparrow \text{ \& } \downarrow) \quad \otimes \quad \text{(2 particle-hole symmetries)} \\ \equiv & \text{(2 hopping diagonal parts)} \quad \otimes \quad \text{(2 chiralities)} \quad \otimes \quad \text{(2 particle-hole symmetries)} . \end{aligned}$$

We can thus recast (8.1) into 4 decoupled (2×2) blocks. Each block corresponds to a definite particle-hole symmetry and hopping eigenstate, while the matrix structure encodes the two chiralities. Remarkably, all of the blocks have exactly the form of a Weyl semimetal as presented Sec. 7.4.2, although they describe Bogoliubov quasiparticles rather than electrons. Our final Hamiltonian thus reads

$$H = H_+ + H_- \quad (8.5)$$

with H_\pm being the two hopping diagonal sectors. They are given by

$$H_\alpha = \frac{1}{2} \sum_{\vec{k}, i=\pm} \Phi_{\vec{k}, i, \alpha}^\dagger \mathcal{H}_\alpha^{i\Delta}(\vec{k}) \Phi_{\vec{k}, i, \alpha} , \quad (8.6)$$

where the index i labels the particle-hole symmetry, and (with $\alpha = \pm$)

$$\mathcal{H}_\alpha^{\pm\Delta}(\vec{k}) = v_F (\hat{z} \times \vec{\sigma}) \cdot \vec{k} + M_\alpha^{\pm\Delta}(k_z) \sigma^z , \quad (8.7)$$

$$M_\alpha^{\pm\Delta}(k_z) = (m \pm |\Delta|) + \alpha \sqrt{t_S^2 + t_D^2 + 2t_S t_D \cos(k_z d)} . \quad (8.8)$$

Here d is the superlattice period along \hat{z} and \vec{k} denotes the three-dimensional momentum.

The new degrees of freedom $\Phi_{\vec{k},i,\alpha}$ are the appropriate Bogoliubov quasiparticles and read

$$\Phi_{\vec{k},+,\alpha} = \left(d_{\vec{k}\alpha}, d_{-\vec{k}\alpha}^\dagger \right)^T, \quad \Phi_{\vec{k},-,\alpha} = \left(f_{\vec{k}\alpha}, f_{-\vec{k}\alpha}^\dagger \right)^T, \quad (8.9a)$$

$$d_{\vec{k}\alpha} = \frac{1}{\sqrt{2}} \left(e^{-i\varphi/2} c_{\vec{k}\uparrow\alpha} + e^{+i\varphi/2} c_{-\vec{k}\downarrow\alpha}^\dagger \right), \quad (8.9b)$$

$$f_{\vec{k}\alpha} = \frac{1}{\sqrt{2}i} \left(e^{-i\varphi/2} c_{\vec{k}\uparrow\alpha} - e^{+i\varphi/2} c_{-\vec{k}\downarrow\alpha}^\dagger \right). \quad (8.9c)$$

As usual, the Bogoliubov quasiparticles are independent, anticommuting fermionic excitations. The operators $c_{\vec{k}\sigma\alpha}$ appearing in Eqs. (8.9) are the hopping diagonal quasiparticles of Eq. 8.1 before the Bogoliubov transformation. They are related by essentially a rotation in the top/bottom pseudospin to $c_{\vec{k}\sigma}^{\text{top}}$ and $c_{\vec{k}\sigma}^{\text{bot.}}$, the Fourier transforms along \hat{z} of $c_{\vec{k}\perp\sigma}^{\text{top}}$ and $c_{\vec{k}\perp\sigma}^{\text{bot.}}$.

8.1.2 Existence of Bogoliubov Weyl nodes

In the following, we want to discuss the behavior of the Hamiltonian in terms of the four decoupled (2×2) sub-Hamiltonians $\mathcal{H}_\alpha^{i\Delta}(\vec{k})$ (with $\alpha, i = \pm$). Since each of them has the form of a non-superconducting Weyl semimetal, the following discussion is similar to the Sec. 7.4.2 and Ref. [111] (both treating the normal Weyl semimetal in a heterostructure).

For fixed k_z , the Hamiltonians $\mathcal{H}_\alpha^{i\Delta}(\vec{k})$ have the form of two-dimensional quantum Hall Hamiltonians of given masses $M_\alpha^{i\Delta}(k_z)$ similar to the non-superconducting case. Since the associated quasiparticles are however of Bogoliubov type, one should rather interpret them as spinless $p_x + ip_y$ -superconductor Hamiltonians. Just as quantum Hall systems, the latter are known to have both a topologically trivial and non-trivial phase.¹³⁴ A Weyl superconductor in a heterostructure can thus be understood as four independent sets of two-dimensional $p_x + ip_y$ -superconductor layers stacked in momentum space along k_z , as illustrated in Fig. 8.2 (with at most two of the four sets of stacked layers being topologically non-trivial). Put differently, a Weyl superconductor realizes a three-dimensional $p_x + ip_y$ superconductor. A sign change in one of the masses $M_\alpha^{i\Delta}(k_z)$ signals a topological transition in the respective subsector. In addition, we know from Sec. 7.3.4 that the non-superconducting, inversion and time-reversal symmetric limit $|\Delta|, m \rightarrow 0$ corresponds to an entirely topologically trivial system. This allows to identify which sign of each mass corresponds to the topologically trivial or non-trivial regime, namely

$$M_+^{\pm\Delta} : \begin{cases} M_+^{\pm\Delta}(k_z) > 0 & \equiv \text{topologically trivial} \\ M_+^{\pm\Delta}(k_z) < 0 & \equiv \text{topologically non-trivial} \end{cases},$$

and

$$M_-^{\pm\Delta} : \begin{cases} M_-^{\pm\Delta}(k_z) > 0 & \equiv \text{topologically non-trivial} \\ M_-^{\pm\Delta}(k_z) < 0 & \equiv \text{topologically trivial} \end{cases}.$$

If one of the masses changes sign at some momentum $k_z = k_0$, inversion symmetry guarantees a second sign change at $k_z = -k_0$. The two gapless points at $\pm k_0$ are the analogs of Weyl nodes for Bogoliubov quasiparticles, and we shall therefore call them

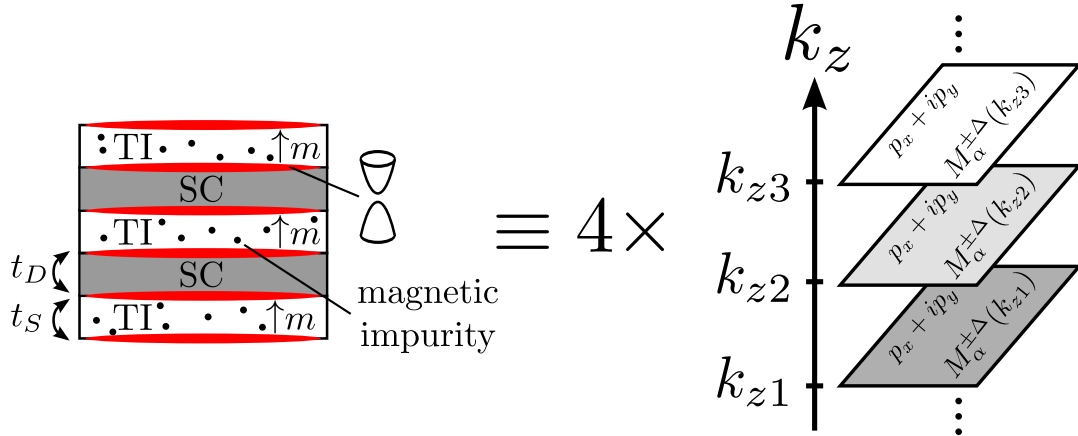


Figure 8.2: The Hamiltonian of a Weyl superconductor heterostructure has four independent sectors. For fixed k_z , each of the sectors can be interpreted as a two-dimensional $p_x + ip_y$ -superconductor layer (denoted by $p_x + ip_y$). The Weyl superconductor can thus be viewed as four sets of $p_x + ip_y$ -superconductor systems stacked in momentum space.

“Bogoliubov Weyl nodes”. Since they are inversion symmetric partner, they must be of opposite chirality.

However, Bogoliubov Weyl nodes do not always exist. Mathematically, each of the mass functions $M_\alpha^{i\Delta}(k_z)$ in Eq. (8.8) can only have a sign change as a function of k_z within some window of m and $|\Delta|$. This can physically be understood based on the interpretation of a Weyl superconductor as stacked $p_x + ip_y$ -superconductor layers. Since the non-superconducting, inversion and time-reversal symmetric limit corresponds to a topologically trivial gapped state, both m and $|\Delta|$ can be viewed as driving the system towards a topologically non-trivial state. If initially both m and $|\Delta|$ are small, the system remains in a topologically trivial state since it is still too close to the trivial limit. When m and $|\Delta|$ are increased above some threshold, parts of the system, i.e. some but not all of the $p_x + ip_y$ -superconductor layers, become topologically non-trivial, while the others still remain in the trivial phase. At the boundary values of k_z separating the topologically trivial and non-trivial $p_x + ip_y$ -superconductor layers, gapless states exist as usual for an interface between topologically distinct systems. These gapless points are of course the Bogoliubov Weyl nodes. If finally m and/or $|\Delta|$ are large, all of the $p_x + ip_y$ -superconductor layers may be in a topologically non-trivial state. Since there is no boundary between $p_x + ip_y$ -superconductor layers of different topological character anymore, no gapless state (i.e. no Bogoliubov Weyl node) exist.

By analyzing the roots of the mass functions $M_\alpha^{i\Delta}(k_z)$, one can quantify the presence or absence of Bogoliubov Weyl nodes in the different subsectors. We recall that we consider $m > 0$ for concreteness, but a similar analysis can be made for $m < 0$. Firstly, the mass $M_+^{+\Delta}$ is always positive. The associated sub-Hamiltonian $\mathcal{H}_+^{+\Delta}(\vec{k})$ is therefore always in a topologically trivial gapped state and can thus be neglected in the subsequent low-energy description. Secondly, the mass $M_-^{+\Delta}$ can have Weyl nodes in the parameter range

$$m_{c1} < m + |\Delta| < m_{c2} , \quad (8.10)$$

where we introduced

$$m_{c1} = |t_S - t_D| \quad , \quad m_{c1} = t_S + t_D \quad (8.11)$$

(note that we considered $t_S, t_D > 0$, but a similar analysis can again be made for the other cases). In this regime, two Bogoliubov Weyl nodes of opposite chirality exist at the momenta $\vec{k} = (0, 0, \pi/d \pm k_1^{\text{Weyl}})^T$ with

$$k_1^{\text{Weyl}} = \frac{1}{d} \arccos \left(1 - \frac{(m + |\Delta|)^2 - (t_S - t_D)^2}{2t_S t_D} \right) . \quad (8.12)$$

The topologically non-trivial momentum range corresponds to momenta “outside the Weyl nodes”, i.e. to $|k_z| > \pi/d - k_{\pm}^{\pm\Delta}$. If $m + |\Delta| < m_{c1}$, the entire sub-Hamiltonian $\mathcal{H}_{-}^{+\Delta}(\vec{k})$ is in a topologically trivially gapped regime, while $m + |\Delta| > m_{c2}$, corresponds to an entirely topologically non-trivial (and gapped) regime.

The remaining sub-Hamiltonians $\mathcal{H}_{\pm}^{-\Delta}(\vec{k})$ can be treated simultaneously. For $m > |\Delta|$, only $\mathcal{H}_{-}^{-\Delta}(\vec{k})$ may be topologically non-trivial, while it is the other way round for $m < |\Delta|$. In any case, the existence of Bogoliubov Weyl nodes in one of the two sectors is tied to the condition

$$m_{c1} < |m - |\Delta|| < m_{c2} . \quad (8.13)$$

If the latter is fulfilled, two Bogoliubov Weyl nodes appear in one of the sectors at the inversion symmetric momenta $\vec{k} = (0, 0, \pi/d \pm k_2^{\text{Weyl}})^T$ with

$$k_2^{\text{Weyl}} = \frac{1}{d} \arccos \left(1 - \frac{(m - |\Delta|)^2 - (t_S - t_D)^2}{2t_S t_D} \right) . \quad (8.14)$$

In conclusion, a Weyl superconductor Hamiltonian may have up to two pairs of Bogoliubov Weyl nodes. The two nodes making up each pair are inversion symmetric partners of opposite chirality. Just as for a normal Weyl semimetal, Bogoliubov Weyl nodes only exist for intermediate values of m and $|\Delta|$. For sufficiently small values of m and $|\Delta|$, the system is adiabatically connected to the topologically trivial limit $m = |\Delta| = 0$, while it is in a topologically non-trivial but fully gapped state for sufficiently high values of m and/or $|\Delta|$, and then corresponds to nontrivial $p_x + ip_y$ -superconductors stacked in momentum space.

8.1.3 Time reversal and inversion symmetry

As we have seen, the (inversion symmetric) Weyl semimetal remains in general gapless even when superconductivity is turned on. This may seem a little surprising at first glance since one would naively expect the formation of a superconducting gap. Even more importantly, the superconducting terms in the Hamiltonian couple Weyl nodes of opposite chirality, which are definitely expected to annihilate under coupling. However, the superconducting correlations more precisely couple electrons on one Weyl node to holes on the other, instead of electrons to electrons like a more standard perturbation would do. This effectively inverts the chirality of the second node. In appendix D.2, we show that a Weyl semimetal indeed remains gapless in the presence of s-wave or p-wave superconductivity as long as the latter only couples Weyl nodes of opposite chiralities. If

the superconductivity however couples Bogoliubov Weyl nodes of the same chirality, the system generically develops a superconducting gap.

This has important consequences for heterostructures that conserve time reversal symmetry but break inversion symmetry. As shown in appendix D.2, such heterostructures are gapped by proximity induced s-wave superconductivity. In addition, the gapped phase is topologically trivial. To understand this, imagine a heterostructure made of layers of topological insulator and s-wave superconductor in which both the strength of the proximity effect and the inversion symmetry breaking can be tuned. We imagine starting from a sample with preserved time reversal and inversion symmetry, which in addition has no superconducting proximity effect. As discussed, this system would be in a trivially gapped phase. As a first step, inversion symmetry is slightly broken such that four Weyl nodes develop. Next, the superconducting proximity effect is turned on, which gaps the system. Now, inversion symmetry is restored. Throughout the restoration of inversion symmetry, the proximity effect ensures the system to be gapped since it couples Weyl nodes of equal chirality. Therefore, time reversal symmetric Weyl superconductors are smoothly connected to a topologically trivial state and thus topologically trivial themselves.

If finally both time reversal and inversion symmetry are broken, the nodes of a non-superconducting Weyl semimetal are shifted to different energies, see Ref. [113]. Instead of Fermi points, the system now has electron and hole pockets. Topological properties are however in general non-trivial, including the existence of surface states. If the proximity effect is efficient at all, the topological state of the superconducting system will depend on the chiralities of the Fermi surfaces coupled by the superconductivity. We note however that a very unsymmetrical system may not exhibit a proximity effect at all.

8.1.4 Bogoliubov Weyl nodes vs. normal Weyl nodes

The physics of Bogoliubov Weyl nodes is most transparent if we follow the evolution of the Hamiltonian while superconductivity is turned on. As discussed in Sec. 7.4.2, a normal Weyl semimetal is essentially described by the electronic Hamiltonian

$$H_{\Delta=0} = \sum_{\vec{k}} (c_{\vec{k}\uparrow}^\dagger, c_{\vec{k}\downarrow}^\dagger) \left[v_F (\hat{z} \times \vec{\sigma}) \cdot \vec{k} + M(k_z) \sigma_z \right] \begin{pmatrix} c_{\vec{k}\uparrow} \\ c_{\vec{k}\downarrow} \end{pmatrix}, \quad (8.15a)$$

$$M(k_z) = m - \sqrt{t_S^2 + t_D^2 + 2t_S t_D \cos(k_z d)}. \quad (8.15b)$$

This Hamiltonian can have two Weyl nodes if the magnetization satisfies $m_{c1} < m < m_{c2}$, which we suppose to be true for the moment. When superconductivity is turned on, the Hamiltonian decomposes into two copies of itself, acting on Bogoliubov quasiparticles rather than electrons. This reflects the fact that superconductivity splits each electronic state into a particle-hole symmetric and particle-hole antisymmetric state with an energy separation $\sim 2|\Delta|$. Indeed, the relevant sub-sectors in this limit $m > |\Delta|$ are

$$H_{\pm} = \frac{1}{2} \sum_{\vec{k}, i=\pm} \Phi_{\vec{k}, i, \pm}^\dagger \left[v_F (\hat{z} \times \vec{\sigma}) \cdot \vec{k} + M_{\pm}^{i\Delta}(k_z) \sigma_z \right] \Phi_{\vec{k}, i, \pm}, \quad (8.16a)$$

$$M_{\pm}^{\pm\Delta}(k_z) = (m \pm |\Delta|) - \sqrt{t_S^2 + t_D^2 + 2t_S t_D \cos(k_z d)}, \quad (8.16b)$$

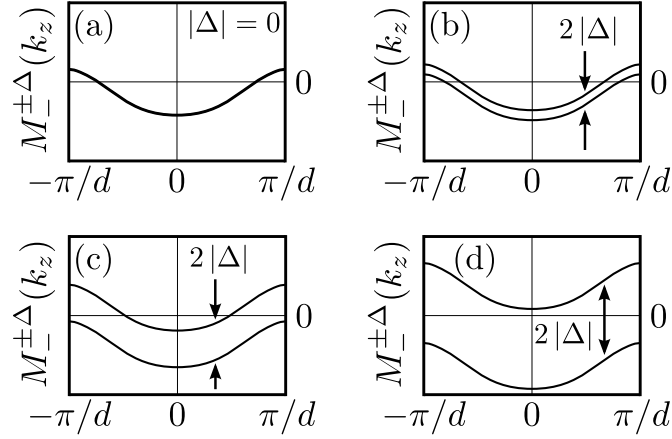


Figure 8.3: Evolution of the masses $M_{-}^{+\Delta}$ (upper curve) and $M_{-}^{-\Delta}$ (lower curve) defined in Eq. (8.8) upon increasing $|\Delta|$. For $|\Delta| = 0$ and $m_{c1} < m < m_{c2}$, the system has two Weyl nodes of chiral electrons, located at the sign changes of $M_{\pm}^{\pm\Delta}$. With superconductivity, each Weyl nodes splits into two Bogoliubov Weyl nodes of equal chirality and opposite particle-hole symmetry. Their separation grows with increasing $|\Delta|$ from subfigures (a) to (d).

where $\Phi_{\vec{k},i,-}$ are the Bogoliubov quasiparticles as defined in Eq. (8.9). For small $|\Delta|$, the latter have Bogoliubov Weyl nodes if the original semimetal had normal Weyl nodes (note that Bogoliubov Weyl nodes exist if $m_{c1} < m \pm |\Delta| < m_{c2}$, which for small enough $|\Delta|$ is equivalent to the condition $m_{c1} < m < m_{c2}$ for the normal Weyl nodes). The superconducting proximity effect thus simply splits the initial electronic system into two Bogoliubov quasiparticle systems, and each normal Weyl node into two Bogoliubov Weyl nodes. Because the normal and superconducting cases are adiabatically connected, both Bogoliubov Weyl nodes inherited their (identical) chirality from the initial electronic Weyl node, and half of the topological charge of the initial Weyl node. The adiabatic evolution from the normal to the superconducting case is illustrated in Fig. 8.3, and the bulk and surface Brillouin zones are shown in Fig. 8.4. A more mathematical discussion of the bisection of Weyl nodes into Bogoliubov Weyl nodes in the presence of superconductivity is given in appendix D.3.

8.1.5 Surface states

Since a Weyl superconductor may be understood as stacked layers of $p_x + ip_y$ -superconductors, one naturally expects edge states for topologically non-trivial momenta. Being the edge states of $p_x + ip_y$ -superconductor layers stacked along k_z , we expect them to run around the side surfaces (the ones which are not perpendicular to \hat{z}). In appendix D.4, the surface physics are explicitly derived for a surface perpendicular to the \hat{y} -direction, but the results can be generalized for an arbitrary surface. They are in full agreement with the $p_x + ip_y$ -superconductor picture.

For each of the four subsectors of the Weyl superconductor Hamiltonian, we find that surface states exist whenever the projection of the three-dimensional bulk Brillouin zone on the surface has a non-trivial momentum range, see Fig. 8.4. They can only be defined for the respective topological range of k_z , and do therefore not exist in the entire surface Brillouin zone if the bulk has Bogoliubov Weyl nodes. In the picture of stacked layers of

$p_x + ip_y$ -superconductors, this would mean that only some of the layers are topologically non-trivial. The surface states are Majorana fermions in real space,

$$\Psi_{\text{surf}}(\vec{r}) = \Psi_{\text{surf}}(\vec{r})^\dagger. \quad (8.17)$$

For a derivation, see appendix D.4. Again, this is similar to the edge state of $p_x + ip_y$ -superconductors.¹³⁴ For a surface of normal vector \hat{n} , they disperse as

$$E = \frac{v_F}{2}(\hat{n} \times \hat{z}) \cdot \vec{k} \quad (8.18)$$

and therefore move into the direction $\hat{n} \times \hat{z}$ (we recall that time reversal symmetry is broken by a magnetization along \hat{z}). The spin points into the direction of motion, such that the surface states are chiral. This is of course to be expected for a Weyl system, and is also in agreement with $p_x + ip_y$ -superconductors. It also agrees with the general idea that superconductivity “splits everything into two halves”, since half a surface electron corresponds to a surface Majorana. As shown in appendix D.4, the superconducting phase then picks “which of the two halves” is used to realize the surface state. For concreteness, we quote the results for surface states of the $\mathcal{H}_-^{+\Delta}$. In terms of the two fundamental Majoranas

$$\gamma_{\vec{\sigma}\parallel\vec{v},-}^{(1)}(\vec{r}) = \frac{c_{\vec{\sigma}\parallel\vec{v},-}(\vec{r}) + c_{\vec{\sigma}\parallel\vec{v},-}^\dagger(\vec{r})}{\sqrt{2}}, \quad \gamma_{\vec{\sigma}\parallel\vec{v},-}^{(2)}(\vec{r}) = \frac{c_{\vec{\sigma}\parallel\vec{v},-}(\vec{r}) - c_{\vec{\sigma}\parallel\vec{v},-}^\dagger(\vec{r})}{\sqrt{2}-} \quad (8.19)$$

that can be constructed from the electron mode $c_{\vec{\sigma}\parallel\vec{v},-}$ at the surface, the surface state of the sector $\mathcal{H}_-^{+\Delta}$ corresponds to

$$\Psi_{\text{surf}}(\vec{r}) \sim \cos\left(\frac{\varphi}{2}\right) \gamma_{\vec{\sigma}\parallel\vec{v},-}^{(1)}(\vec{r}) + \sin\left(\frac{\varphi}{2}\right) \gamma_{\vec{\sigma}\parallel\vec{v},-}^{(2)}(\vec{r}), \quad (8.20)$$

where φ is the superconducting phase.

Majorana Fermi arcs

Just as for normal Weyl semimetals, the side surfaces of a Weyl superconductor can have non-closed Fermi lines which we call “Majorana Fermi arcs”. They exist if the bulk has Bogoliubov Weyl nodes, such that the surface states are not defined within the entire surface Brillouin zone. The Majorana Fermi arcs span the projection of topological momentum range and terminate in the projection of the bulk Bogoliubov Weyl nodes. As explained in Sec. 7.4.2, Majorana Fermi arcs are possible because the surface states can unbind into the bulk when the endpoint of the Majorana Fermi arc is encircled. Since there are up to two topologically non-trivial subsectors, a Weyl superconductor can have up to two Majorana Fermi arcs on a given surface. In an inversion symmetric situation, the Majorana Fermi arcs are superimposed because the Bogoliubov Weyl nodes are pinned to the k_z -axis. This situation is depicted in the lower right picture of Fig. 8.4.

8.1.6 Accessible phases of a Weyl superconductor heterostructure

In a Weyl superconductor heterostructure as we discuss it here, and as it is depicted in Fig. 8.1, the physics entirely depend on five real parameter, namely the average magnetization m , the proximity induced superconducting correlations $\Delta = |\Delta|e^{i\varphi}$ and the

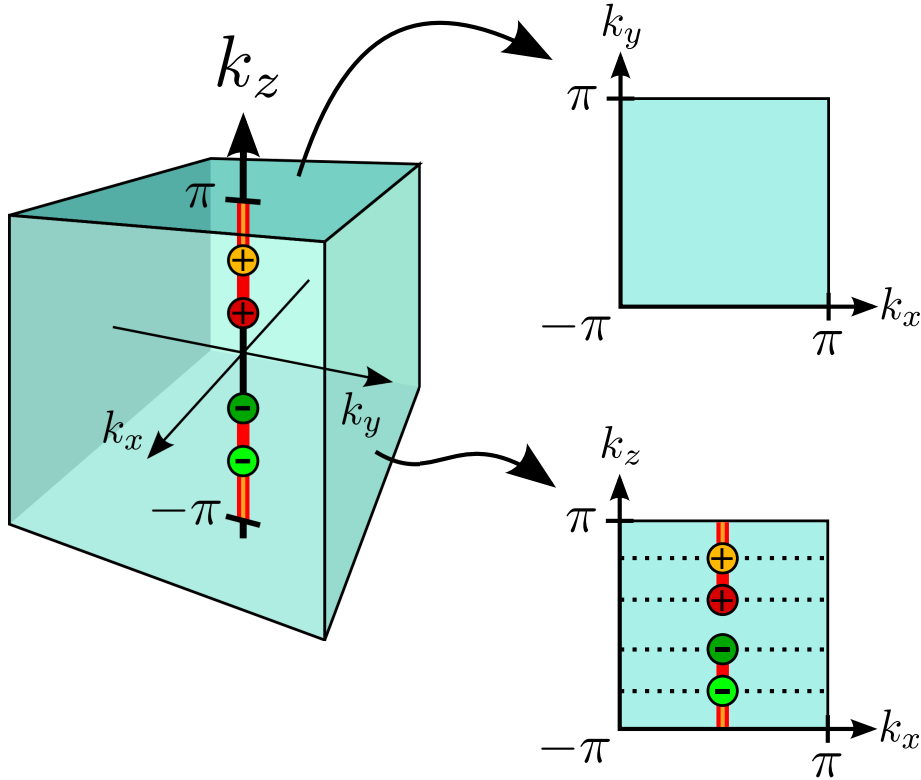


Figure 8.4: Bulk Brillouin zone of a Weyl superconductor (left) along with the corresponding surface Brillouin zones. As compared to the Weyl semimetal (see Fig. 7.15), each Weyl node is split into two Bogoliubov Weyl nodes. The Bogoliubov Weyl nodes inherit the chirality and half of the topological charge of the corresponding normal Weyl node. Every Bogoliubov Weyl node has an inversion symmetric partner of opposite chirality. The inversion symmetric pairs of Bogoliubov Weyl nodes correspond to independent sectors of the Hamiltonian. Although the Hamiltonian contains four subsectors, only two of them may have Weyl nodes at the same time. For a given sector containing Bogoliubov Weyl nodes, the states “outside” the nodes are topologically nontrivial. In the situation depicted here, the system contains the maximum number of two Bogoliubov Weyl nodes, shown as the small circles, the sign indicates their chirality. The respective non-trivial momentum ranges are shown in red and orange. The top right figure shows the Brillouin zone of a surface perpendicular to the \hat{z} -axis, the lower right figure depicts a Brillouin zone of a surface parallel to \hat{z} . In general, a surface Brillouin zones can be understood as the respective projection of the bulk Brillouin zone. Surfaces parallel to \hat{z} contain one set of Majorana surface modes for each topological subsector of the bulk Hamiltonian, which exist for the projection of topological bulk momenta k_z . This leads to the formation of Majorana Fermi arcs (see text), here shown in red and orange, respectively. The Bogoliubov Weyl nodes on the lower right figure are to be understood as the projection of the bulk Bogoliubov Weyl nodes and have no special meaning in the surface Brillouin zone. The dashed lines delimit the momenta for which Majorana surface states exist: the lowest and uppermost lines denote the limit for one of the topologically non-trivial sectors, while the two inner lines denote the limit for the potentially present second non-trivial subsector. In the specific situation depicted here, there are thus two sets of Bogoliubov modes in the uppermost and lowermost “strips”, one set of modes on the middle “strips”, and no modes in the center of the Brillouin zone.

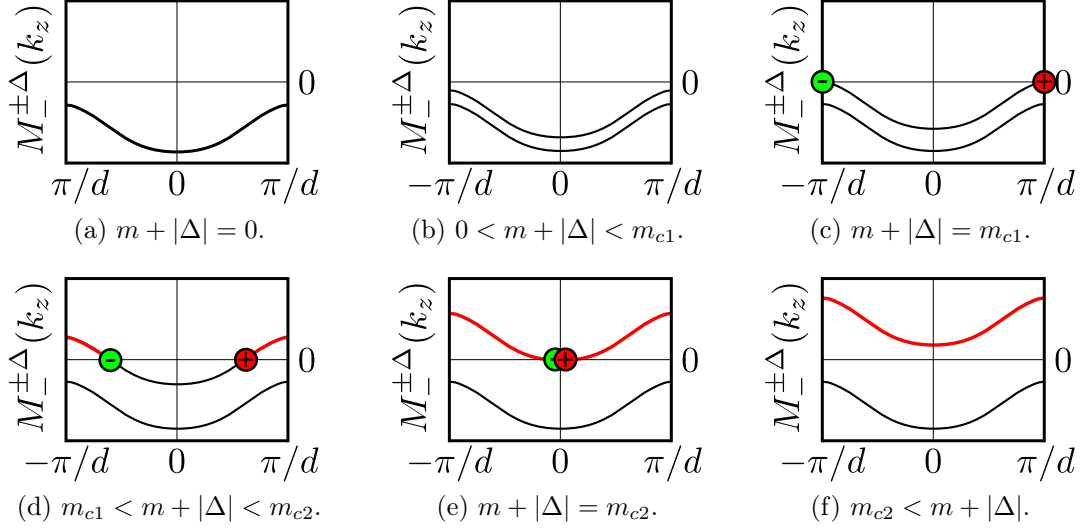


Figure 8.5: Evolution of one of the subsectors (corresponding to $M_-^{+\Delta}$) from topologically trivial to topologically non-trivial as $m + |\Delta|$ is increased from subfigure (a) to (f). The other subsectors (corresponding to $M_-^{-\Delta}$) are kept in the trivial state.

hopping parameters t_S and t_D (we note again that $t_S, t_D > 0$ without loss of generality). Since we are interested in the phase diagram of an isolated Weyl superconductor, the superconducting phase φ is physically irrelevant. As we have seen, we can tune at most two of the four sub-sectors of the Weyl superconductor Hamiltonian into a topologically non-trivial phase by varying m and Δ , or more precisely $|m + |\Delta||$ for one sector and $|m - |\Delta||$ for the other sector. Since these two combinations are independent, we can control each of the (potentially non-trivial) sectors of the Hamiltonian individually. The topological character is then determined by comparing the respective tuning parameter $|m \pm |\Delta||$ to $m_{c1} = |t_S - t_D|$ and $m_{c2} = t_S + t_D$.

In order to illustrate the tunability of Weyl superconductors, we follow the evolution of the system upon increasing $m + |\Delta|$ for fixed $m - |\Delta| = 0$, shown in Fig. 8.5. Consider first the case that both m and $|\Delta|$ vanish, such that system is in a topologically trivial phase. When $m + |\Delta|$ is increased to $m + |\Delta| = m_{c1}$, a pair of Bogoliubov Weyl nodes of opposite chiralities appears at the momentum $(0, 0, \pi/d)^T = (0, 0, -\pi/d)^T$, see Eq. (8.12). Upon further increasing $m + |\Delta|$, the two Bogoliubov Weyl nodes shift symmetrically along the k_z -axis, and a topologically nontrivial momentum range develops “between the nodes” for large k_z . At $m + |\Delta| = m_{c2}$, the Bogoliubov Weyl nodes meet again at the origin, where they annihilate. The entire Brillouin zone is then left in a gapped, but topologically non-trivial state, which can be understood as layers of topologically non-trivial $p_x + ip_y$ superconductors stacked in momentum space along k_z .

It is thus possible to access a number of phases as a function of m and $|\Delta|$. These phases are characterized by the number of pairs of bulk Bogoliubov Weyl nodes (0, 1 or 2) and the number of two-dimensional surface modes (again either 0, 1 or 2). Obviously, the presence of a Weyl nodes implies the existence of a two-dimensional surface mode for the respective subsector, but not the other way round (i.e. a given subsector can be in a topologically nontrivial but entirely bulk gapped phase with surface states). Using the criteria established in Sec. 8.1.2, the phase diagram shown in Fig. 8.6 can be constructed.

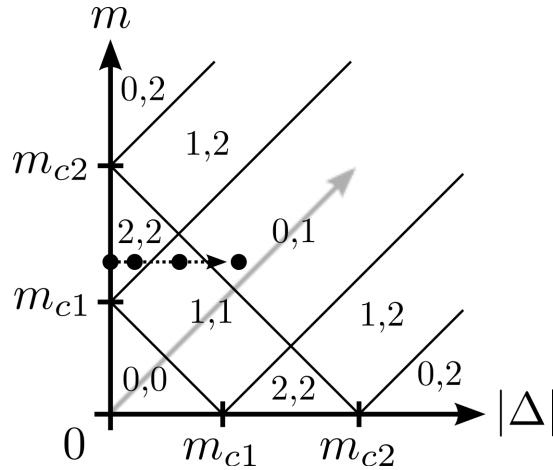


Figure 8.6: Phase diagram of a Weyl superconductor in a TI/SC heterostructure as a function of Zeeman gap m and proximity induced superconducting order parameter $|\Delta|$. The values of m_{c1} and m_{c2} are set by the tunneling amplitudes between the surface Dirac layers of the heterostructure depicted in Fig. 8.1. Each phase is characterized by n_b , the number of pairs of bulk Bogoliubov Weyl nodes, and n_s , the number of two-dimensional Majorana surface modes. The phases are labeled as (n_b, n_s) . The black dots locate the different subfigures of Fig. 8.3, the light grey arrow indicates the evolution the system shown in Fig. 8.5. The phase diagram is mirror symmetric for negative m .

8.2 Vortices in Weyl superconductors

One of the most exciting characteristics of $p_x + ip_y$ -superconductors are their Majorana edge modes.¹³⁴ They are especially interesting because they appear not only at an interface of a $p_x + ip_y$ superconductor with topologically distinct materials, but also at magnetic vortices. This is in itself not surprising, since superconductivity is suppressed in the core of a vortex, making the latter topologically equivalent to vacuum. Putting a vortex into a $p_x + ip_y$ superconductor is thus equivalent to punching a hole into the sample and threading a magnetic flux through the hole. This flux induces a winding of the superconducting order parameter phase, which is essential for the existence of zero energy Majorana modes. Since the vortex has a short circumference, Majorana modes running around the vortex core have quantized wave vectors and energies. If the vortex traps an odd number of superconducting magnetic flux quanta $\Phi_0 = \pi/e$, one of the Majorana modes has zero energy and must be stable against local perturbations.^{134,135} This mode is thus especially robust, and rather easily addressable both because it is well-localized and because it is energetically separated from other modes. Since in addition the trapped Majorana modes at different vortices have non-abelian exchange statistics, they are particularly interesting for quantum computation applications.¹³⁵

Because time reversal symmetry broken Weyl superconductors can be understood as stacked layers of $p_x + ip_y$ superconductors, it is natural to investigate if vortices in Weyl superconductors can also trap Majorana zero modes. This shall now be done for our toy model of an inversion symmetric heterostructure. We must of course expect different physics for vortices along different directions, but we will be able to relate the physics of a vortex along an arbitrary direction to the two limiting cases of vortices along and perpendicular to the intrinsic direction of time reversal symmetry breaking, namely the

\hat{z} -axis. We finally close this section with a discussion of vortices in initially time reversal symmetric Weyl superconductors.

8.2.1 Model of a vortex

Before plunging into the details of vortex physics, let us shortly define how we want to model the latter. In general, a vortex in some ordered material corresponds to a twist in the respective order parameter phase by a multiple of 2π around the vortex core, just as for the magnetic vortices in the classical XY spin model (see Fig. 7.3). In a Weyl superconductor, it is the superconducting phase φ that winds around the vortex. Since the phase can thus not be well-defined in the vortex center, the order parameter $\Delta = |\Delta| e^{i\varphi}$ must be suppressed within the vortex core. In superconductors, where vortices are created by magnetic flux lines penetrating the sample, this is anyways the only possibility allowed by the Meissner effect. As shown in appendix D.5, a magnetic vortex indeed leads to a twist in the order parameter phase. This twist is proportional to the flux inside the vortex. Since the superconducting order parameter must be uniquely defined under rotations by 2π , the magnetic flux must be quantized in units of $\Phi_0 = \pi/e$.

In a real system, the vortex would have a characteristic size set by the coherence length ξ of the superconductor. Within this length scale, the superconducting order parameter is suppressed, but recovers outside. The magnetic field is damped outside the vortex core by the Meissner effect, but can penetrate into the Weyl superconductor on the scale of the magnetic penetration length λ . In order to identify the most important physics associated with vortices in Weyl superconductors, we use an idealized vortex model where the flux is confined to this cylinder. This basically amounts to replacing the exponentially decreasing flux by a step function of radius $R \approx \lambda$. We do however allow for a general spatial variation of the absolute value of the superconducting order parameter. In addition, the magnetic field might affect the average magnetization close to the vortex. From a topological point of view, this model is perfectly appropriate, since the presence or absence of topological bound states is not affected by the details of the vortex core.

For modest field strengths, only few vortices are present, and interactions between vortices can be neglected. We can thus consider the effective problem of a single vortex. The system is naturally described in cylindrical coordinates if the vortex is located at the origin. The suppression of superconductivity inside the vortex puts its core in either the $(0, 2)$, $(2, 2)$ or $(0, 0)$ -phase, see Fig. 8.6. For simplicity, we focus on the case that the vortex core is in the trivial $(0, 0)$ -phase. This can always be realized for an appropriate choice of m and $|\Delta|$. The bulk Weyl superconductor is for simplicity assumed to be in either a $(1, 1)$ or $(1, 0)$ -phase, such that only one of the subsectors of the full Hamiltonian is topologically non-trivial. This situation is sketched in Fig. 8.7.

8.2.2 Vortex along the superlattice axis

By assumption, the vortex core is in a topologically trivial insulating state. The boundary of the vortex is thus equivalent to an interface between a Weyl superconductor and vacuum and has one Majorana edge mode. If the Weyl superconductor is in the $(1, 1)$ -phase, this mode has a restricted range of momenta k_z (it lives “between the Bogoliubov Weyl nodes”). A Weyl superconductor in the $(0, 1)$ -phase has interface modes for any

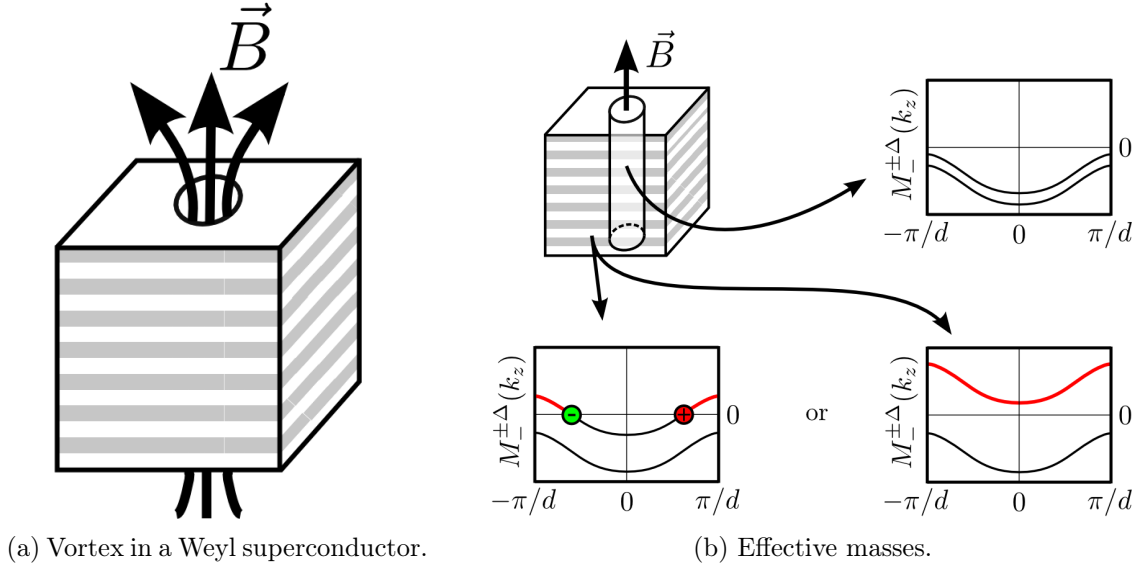


Figure 8.7: Effective description of a vortex. The surrounding Weyl superconductor is supposed assumed to be in a (1, 1) or (0, 1)-phase, such that the suppression of superconductivity puts the vortex core in the trivial (0, 0)-phase (see also the phase diagram in Fig. 8.6). Subfigure (b) depicts the corresponding mass functions $M_{\pm}^{\pm\Delta}$, see text. The red momentum range is topologically nontrivial, the dots mark the Bogoliubov Weyl nodes of opposite chiralities.

momentum k_z . We restrict the discussion to $|\Delta| < m$ far away from the vortex when all relevant physics happens in H_- , but the results can easily be generalized. A more detailed version of the following calculation can be found in appendix D.7.

Exploiting the cylindrical symmetry with respect to the vortex axis, we model the latter by a radially dependent magnetization m and superconducting order parameter $|\Delta|$. The radius of the vortex is considered to be R , and $m(r)$ and $|\Delta(r)|$ are smooth functions interpolating between fixed values m and $|\Delta|$ for $r > R$, and $|m| < m_{c1}$, $|\Delta| = 0$ inside the core of the vortex. The magnetic field is $\vec{B} = B \hat{z}$ inside the vortex and vanishes everywhere else. This gives rise to a vector potential

$$\begin{aligned} \vec{A}(\vec{r}) &= A(r) \hat{e}_\phi, \\ A(r) &= \frac{Br}{2} \Theta(R - r) + \frac{BR^2}{2r} \Theta(r - R) \end{aligned} \quad (8.21)$$

in \hat{e}_ϕ direction, that is taken into account by minimal coupling $\vec{k} \rightarrow \vec{k} - e\vec{A}$ in the Hamiltonian (8.1). The Zeeman effect, i.e. the change in the magnetic mass m due to the magnetic field inside the vortex is taken into account via a radius-dependent $m(r)$ (and consequently the r -dependent $M_-(k_z, r)$). The flux threading the vortex is quantized in units of $\Phi_0 = \pi/e$, as usual for superconductors, and the phase of the superconducting order parameter winds once around the vortex per trapped flux quantum. After a canonical transformation $\sigma^x \rightarrow -\sigma^y$, $\sigma^y \rightarrow \sigma^x$, the relevant Hamiltonian H_- in Eq. (8.6) becomes

$$H_- = \sum_{k_z} \int d^2r \psi_{k_z}^\dagger(\vec{r}) \mathcal{H}_- \psi_{k_z}(\vec{r}) , \quad (8.22a)$$

$$\mathcal{H}_- = \begin{pmatrix} \mathcal{H}_A & |\Delta(r)| e^{i\varphi(\phi)} \sigma^z \\ |\Delta(r)| e^{-i\varphi(\phi)} \sigma^z & \mathcal{H}_{-A} \end{pmatrix} , \quad (8.22b)$$

$$\mathcal{H}_A = M_-(k_z, r) \sigma^z + v_F \begin{pmatrix} 0 & -i e^{-i\phi} \\ -i e^{i\phi} & 0 \end{pmatrix} \frac{\partial}{\partial r} + v_F \begin{pmatrix} 0 & -e^{-i\phi} \\ e^{i\phi} & 0 \end{pmatrix} \left(\frac{1}{r} \frac{\partial}{\partial \phi} + i e A(r) \right) . \quad (8.22c)$$

where $\tilde{\varphi}(\phi) = \varphi - (\Phi/\Phi_0) \phi$ is the twisted phase of the superconducting order parameter. For any given k_z , this Hamiltonian may be interpreted as two copies of a spinless $p_x + ip_y$ superconductor, or alternatively as a topological insulator surface in contact with a superconductor.¹³³ By analogy, the vortex binds one Majorana zero mode per topological value of k_z and per topological subsector if it traps an odd number of flux quanta, and no zero mode for an even number of trapped flux quanta.^{133,134,154} Assuming that there is only a single topologically non-trivial subsector, one can thus define a unique zero energy Majorana mode bound to the vortex. This is explicitly demonstrated for the momentum k_z^0 with $M_-(k_z^0, r) = 0$ in appendix D.7 where the algebra is simplest, but holds of course true as long as the system stays in the same extended topological phase and topological momentum range.

Physically, the Majorana bound state can be understood in terms of an Aharonov-Bohm like phase, a Berry phase and a geometrical phase for the Majorana surface states. Consider the topologically equivalent situation of a Weyl superconductor with a tube-like hole along the \hat{z} axis. Without a magnetic field inside the hole, we know that chiral Majorana surface states exist when k_z is chosen in the range where the 2d superconductor is in the topological phase. Since the spin is locked to the momentum, the surface states pick up a Berry phase of π upon encircling the hole once. This shifts the zero momentum mode away from zero energy and can be interpreted as effectively antiperiodic boundary condition on the geometrical phase in order to counterbalance the Berry phase. If now a unit flux is threaded through the tube-like hole, the surface states pick up an additional phase of π . The latter derives from the winding of the order parameter phase, and is similar to an Aharonov-Bohm effect. It compensates the Berry phase and thus allows for zero energy bound states. Similar effects have also been discussed for confined magnetic flux tubes imposed in 3-dimensional strong topological insulators.^{154,155} For momenta k_z which are in the topologically trivial range, of course, no bound states exist both with and without magnetic flux. Because the magnetic field vanishes outside the vortex, the topological character and especially the existence of surface states is unchanged there. We thus conclude that a vortex with an odd number of flux quanta traps a Majorana zero mode for every topologically non-trivial value of k_z .

8.2.3 Stability of the Majorana zero modes

In a more realistic model, the Majorana bound states will not form totally flat bands as a function of k_z . We will now discuss under which conditions the presence of a zero energy Majorana mode for odd-integer fluxes is at least partially robust. This discussion will follow along the line of a qualitative argument. A quantitative calculation can in

principle be done and would follow the lines of the argument, but will not be given here. As an effective model at lowest energies, we first consider the zero energy band of Majorana modes (thus fixing k_ϕ) as a function of k_z , first for the case that the bulk is in the $(0, 1)$ -phase. A zero energy Majorana mode then exists for all k_z . After transforming to Wannier orbitals, we obtain a set of Majorana bound states at different heights z , as depicted in Fig. 8.8(a). This Hamiltonian can be interpreted as a one-dimensional chain of decoupled sites. Next, we introduce a small hopping of amplitude t along the chain, thus allowing the Majoranas to move up and down the vortex tube. In dimensionless units, their dispersion is given by

$$E = -t \cos(k_z) . \quad (8.23)$$

Applying for instance hard wall boundary conditions, one finds exactly one zero energy Majorana mode if the system has an odd number of superlattice layers, and no zero energy Majorana modes for an even number of layers.

Next, consider the case that the bulk is in a $(1, 1)$ -phase, such that surface Majorana modes exist only for a limited range of momenta k_z (“between the Weyl nodes”). This situation can be mimicked by putting a huge potential $V(k_z)$ to the forbidden range of k_z which gaps these states to infinite energy. Physically, the fact that only some of the states in momentum space are used means that the allowed real space wave functions are highly non-local. This does however not affect the possibility of the real-space states to hop up and down the chain. Rather, the well-defined momentum-space potential $V(k_z)$ even translates to additional non-local hopping terms. If we now add the small hopping along the chain as in the previous case, we will end up with the same cosine dispersion on top of the potential $V(k_z)$. We can therefore conclude that *one single* zero energy Majorana bound states exist if

1. a Majorana bound state can be defined for $\pm\pi/(2d)$, i.e. $M_{\pm}^{\pm\Delta}(\pm\pi/(2d)) > 0$, and if
2. the system has an odd number of superlattice layers,

and *no* zero energy Majorana mode otherwise (note that we have restored the physical units for the momentum in the above conditions). If the single zero energy Majorana mode exists, it is separated by a finite energy gap from all other Majorana modes. This gap is proportional t/N , where t is the hopping along the Majorana chain in real space and N the number of superlattice layers. Since the system is at lowest energies equivalent to a vortex in a $p_x + ip_y$ -superconductor, the zero energy Majorana modes trapped in a vortex in Weyl superconductors also have non-abelian statistics and could thus be used for braiding processes in quantum computation.^{134,135} The non-abelian statistics are possible in this three-dimensional case because the vortex is (infinitely) extended along \hat{z} . The motion of vortices is thus effectively two-dimensional.

8.2.4 Vortex perpendicular to the superlattice axis

According to the phase diagram in Fig. 8.6, also a vortex perpendicular to the \hat{z} -axis should host Majorana surface modes on the side surfaces of the vortex, see Fig. 8.9. For our model, they would run between the front and back surfaces of the heterostructure on the side walls of the vortex. The surface states on right wall are however different particles

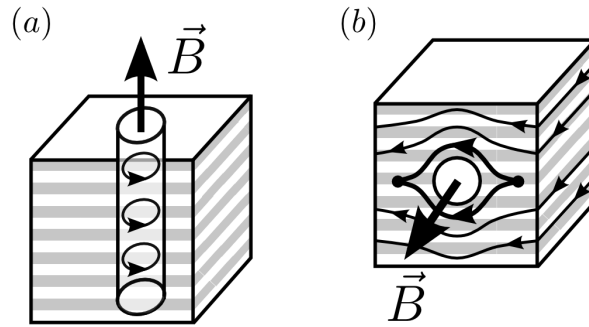


Figure 8.8: The two classes of vortices in Weyl superconductors. Subfigure (a) sketches a vortex along the superlattice axis \hat{z} , with bound states along a tube through the whole sample. Subfigure (b) depicts a vortex perpendicular to \hat{z} . Whereas there are no states bound to the vortex, the surface states can be used for Majorana interferometry (thick line).

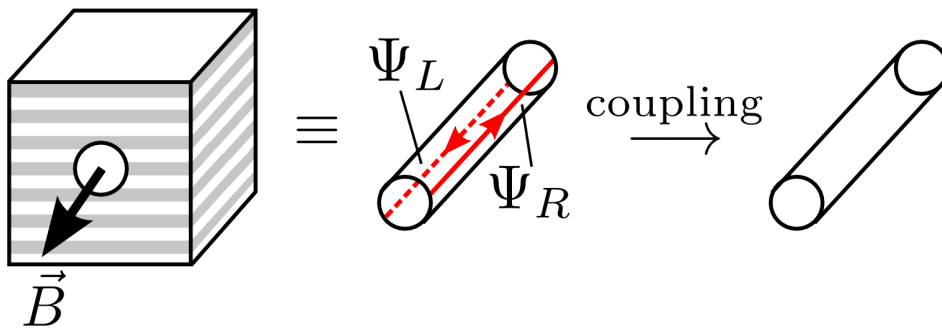


Figure 8.9: Vortices perpendicular to the \hat{z} -axis host two different kinds of gapless Majorana modes Ψ_L and Ψ_R on the right and left side surfaces, respectively. Being two distinct and degenerate particles, any small coupling across the vortex will gap these Majoranas.

than the ones on the left wall, rather than a single delocalized state as for vortices along \hat{z} . For a thin vortex, already a small coupling across the flux line is sufficient to gap out these degenerate states of opposite spin and opposite momentum, and the result of Ref. [156] is recovered.

The vortex can thus be viewed as a hole with enclosed magnetic flux drilled through the Weyl superconductor, and introduces a new edge on the side surface. The nearby surface states will rearrange in order to host the vortex and locally run along this new edge, as depicted in Fig. 8.8(b). While there are no states bound to the vortex, a special class of surface state paths allows for Majorana interferometry, depicted by thick lines in Fig. 8.8(b). Consider the creation of a pair of surface Majorana states at the right hand side of the vortex. When taking the Majoranas to the left, one of them will follow a path above of the vortex, whereas the other one moves below the vortex. The Majoranas are finally annihilated on the left hand side. In the spirit of Ref. [157], the creation and annihilation of these Majorana particles may be due to the injection and extraction of an electron into the surface. Because the two Majoranas encircle the vortex once, they acquire a phase difference of π per flux quantum, similar to a vortex along \hat{z} . This realizes a Majorana interferometer. In contrast, no Berry phase occurs because the spins experience no net rotation. The momentum along the path is not quantized either because no particle returns to its origin, and the geometrical phases for the lower and upper path

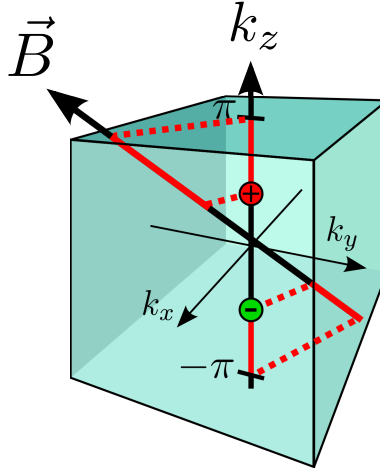


Figure 8.10: Vortices along a general direction bind Majorana modes in the projection of the topologically non-trivial bulk momentum range onto the vortex. The latter is aligned along the direction of the magnetic field \vec{B} . The topologically non-trivial momentum ranges in the bulk and on the vortex are shown in red, the dashed lines are a guide to the eye for the projection.

cancel out. The non-quantization of the momentum implies continuous energies for such interferometer paths.

8.2.5 Vortex along some general direction and vortices in time reversal and inversion symmetry broken Weyl superconductors

The existence of bound states at vortices in Weyl superconductors can in general be understood similarly to the existence of (other) surface modes in terms of the projection of the bulk Bogoliubov Weyl nodes onto the surface defining the vortex, see Sec. 8.1.5. If the topological momentum range “between the Bogoliubov Weyl nodes” has a non-vanishing projection onto the vortex line, the corresponding momentum range supports Majorana (vortex-)surface modes, see Fig. 8.10. This principle has already been applied to vortices in $^3\text{He-A}$ by Volovik in Ref. [156]. By the same reasoning as in Sec. 8.2.3, vortices along some general direction can thus bind a single zero energy Majorana mode if the heterostructure has an odd number of superlattice layers and if the projection of the topological momentum range includes the momentum $\pi/(2d)$. This provides a second, more handwaivy yet maybe more intuitive explanation of why vortices perpendicular to the \hat{z} -axis do not bind Majorana modes.

A similar reasoning should also apply if both time reversal and inversion symmetry are broken. As discussed in Sec. 8.1.3, a Weyl semimetal may be turned into a topologically non-trivial Weyl superconductor even if both of these symmetries are broken. This will in general depend on the chirality of the Fermi surfaces coupled by the superconductivity. If the bulk is topologically non-trivial, the projection of the non-trivial bulk momentum range could then also define a range of existence for Majorana modes at vortices.

8.2.6 Vortices in time reversal symmetric Weyl superconductors

A time-reversal symmetric Weyl superconductor is generally in a topologically trivial phase, see Sec. 8.1.3. Being a superconductor, one can still place a vortex into the system. The magnetic field will now break time reversal symmetry in the vortex core. The latter can thus generally be a non-superconducting Weyl semimetal with both broken inversion and time reversal symmetry. If the inversion symmetry breaking is weak, we expect that the phase diagram of the vortex core looks similar to Fig. 8.6. The vortex boundary is thus an interface between a trivial phase (outside the vortex) and a potentially topologically non-trivial phase inside the vortex. If the vortex core is either a Weyl semimetal (corresponding to the (2,2)-phase in Fig. 8.6) or a Quantum Hall insulator (corresponding to the (0,2)-phase in Fig. 8.6), the vortex boundary will have bound states. The latter are however not Majorana particles, but chiral electrons. A time reversal symmetric Weyl superconductor can thus never bind Majorana modes, including in particular zero energy Majorana bound states.

8.3 Experimental realization and signatures

The construction of a Weyl superconductor heterostructure is experimentally clearly not impossible, but very challenging. It has recently been demonstrated that thin films of topological insulators such as Bi_2Se_3 can be grown using molecular beam epitaxy,^{158–160} while thin films of superconducting materials such as Aluminum or Tin have by now even become a fairly well-controlled tool in nanophysics. The growth of topological insulator (TI)/superconductor (SC) heterostructures with a well-established superconducting proximity effect is however a highly non-trivial experimental task. To date, only a few SC/TI heterostructure devices have been realized, and first signatures of Majorana physics have been claimed to be detected.^{161–167} Nevertheless, further experiments seem to be needed to fully characterize the physics at even a single TI/SC interface. Consequently, the current experiments are far from a three-dimensional, quantum coherent heterostructure device. In addition, at least the zero energy Majorana physics at vortices can much easier be realized with a single TI/SC interface than with a three-dimensional heterostructure.

The experimental relevance of Weyl superconductors is thus mostly founded on materials which naturally are in a Weyl superconducting state (similarly to naturally existing normal Weyl semimetals, e.g. in pyrochlore iridates, Bi_2Se_3 or HgCr_2Se_4 ^{107–110}). A first example for such a material is $^3\text{He-A}$, which however is difficult to conduct experiments with.¹⁰⁵ New hope for comparably easily controllable and solid materials stems from ferromagnetic spin-triplet superconductors. The latter have theoretically been predicted to be in a Weyl superconductor state.¹¹⁸ They are described by a Hamiltonian similar to the one of our toy system heterostructures, see Sec. 8.1.1 and appendix D.1. The main difference is the inversion of the roles of the physical spin $\vec{\sigma}$ and Nambu-pseudospin $\vec{\kappa}$, since it is now the superconductivity that couples to the physical spin rather than the orbital motion. Spin-triplet superconductivity is believed to appear in certain Uranium-based Ising ferromagnetic superconductors, such as UGe_2 , URhGe , and UCoGe .^{168–170} Time reversal symmetry broken non-centrosymmetric superconductors such as $\text{Li}_2\text{Pt}_3\text{B}$ or Y_2C_3 have also been argued to exhibit Weyl superconductor phases.^{119–121} Another potential spin-triplet superconductor is the layered material Sr_2RuO_4 , but its physics may not be three-dimensional enough for our purposes.¹⁷¹

Once a Weyl superconductor device is at hand, whether it is a natural material or a heterostructure, one would long for a smoking-gun experiment that allows to detect, e.g., the Majorana surface states or the bulk Bogoliubov Weyl nodes. Of course, many experiments that have been proposed for $p_x + ip_y$ -superconductors or single TI/SC-interfaces, such as Majorana interferometry,¹⁵⁷ can be transposed to Weyl superconductors, see Sec. 8.2.4. It would nevertheless be most desirable to have an experiment where Weyl superconductors are in some sense “superior” to $p_x + ip_y$ -superconductors or TI/SC-interfaces. An obvious difference to Weyl superconductor surfaces is that the latter two are gapped, except for a single edge mode running around the two-dimensional sample. In Weyl superconductors, on the other hand, Majorana physics could possibly be probed by surface sensitive techniques, leading to the idea of angle-resolved photoemission spectroscopy (ARPES) for Majorana Fermi arcs put forward in Ref. [118]. In addition, Weyl superconductors generally have a large number of Majorana surface modes, which makes surface transport measurements much easier than for the one single edge mode. In the next sections, we present two possible transport experiments that could be conducted with Weyl superconductor surfaces, namely the anomalous thermal Hall effect and unidirectional electronic transport. We assume that these surface transport measurements are performed when the bulk is in a gapped $(0, 1)$ -phase. Although by analogy to topological insulators one may not expect a perfectly insulating bulk, the surface transport should be more prominent than for instance in a $(1, 1)$ -phase. In addition, the bulk and surface contributions to the thermal transport for the anomalous thermal Hall effect should flow along different directions, which may allow for the identification of the surface contribution.

8.3.1 Anomalous thermal Hall effect

Because Majorana particles do not carry electric charge, a natural way to measure surface Majorana states is to detect their thermal transport. The latter should be discernible from bulk heat transport which will not lead to a thermal Hall effect but rather to a standard thermal transport along the thermal gradient, and can thus be disregarded here. As discussed, we focus on a Weyl superconductor in the $(0, 1)$ -phase in order to have only one single Majorana surface mode, and no (or at least few) bulk transport. Nevertheless, also a Weyl superconductor in a $(1, 1)$ -phase should in principle have an anomalous thermal Hall signal, since its bulk transport is perpendicular to the surface transport, see below. This should allow the disentanglement of the two contributions. Since the single Majorana surface mode can be understood as half a regular surface electron mode, we expect only half of the thermal transport of a normal Weyl semimetal in the corresponding regime. For concreteness, we investigate a surface perpendicular to \hat{y} . Thermodynamics can be calculated from the effective Majorana surface partition function. The latter is derived similarly to the bulk Bogoliubov quasiparticle Hamiltonian in appendix D.3, starting from the dispersion relation $E = v_F k_x$ established in appendix D.4. According to Eq. (8.17), the creation operator at $+k_x$ is also the annihilation operator at $-k_x$. We can therefore construct a well-defined path integral for the partition function by restraining the operators to half of the k_x values, which yields

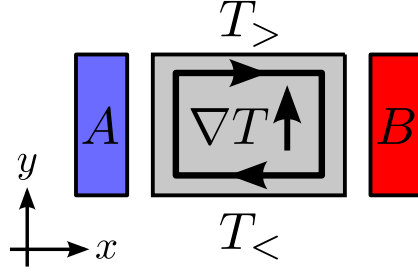


Figure 8.11: Sketch of the anomalous thermal Hall effect in Weyl superconductors. The sample is shown from above. In an experiment, one can envision applying a thermal current from side A (which is at a temperature $T_>$) to the side B (at temperature $T_<$). The Majoranas on the upper surface originating from side A are thus at the temperature $T_>$, while the ones on the lower surface are at the temperature $T_<$. Therefore, a thermal gradient can be measured between top and bottom of the sample. Importantly, this thermal gradient is perpendicular to the applied thermal current between A and B .

$$Z = \int \mathcal{D}(\bar{\Psi}_{\omega_n, k_x, k_z}, \Psi_{\omega_n, k_x, k_z})_{k_x > 0} e^{-\mathcal{S}}, \quad (8.24)$$

$$\mathcal{S} = \sum_{\omega_n, k_z} \sum_{k_x > 0} \bar{\Psi}_{\omega_n, k_x, k_z} (-i\omega_n + v_F k_x) \Psi_{\omega_n, k_x, k_z}, \quad (8.25)$$

where the operators $\Psi_{\omega_n, k_x, k_z}^\dagger = \Psi_{\omega_n, -k_x, k_z}$ create excitations above the Bogoliubov vacuum $|\Omega\rangle$. The latter simply corresponds to occupying all negative energy states,

$$|\Omega\rangle = \prod_{k_x < 0} \Psi_{\omega_n, k_x, k_z}^\dagger |0\rangle = \prod_{k_x > 0} \Psi_{\omega_n, k_x, k_z} |0\rangle, \quad (8.26)$$

where $|0\rangle$ is the electronic vacuum, i.e. the state that is annihilated by all annihilation operators $c_{\vec{k}\sigma\alpha}$.

If a thermal gradient ∇T is applied across the Weyl semimetal, the modes on each surface transport heat only along the respective direction of propagation. Therefore, the thermal gradient leads to a net heat transport perpendicular to ∇T , as depicted in Fig. 8.11. Potential bulk contributions to the thermal transport should be parallel to the gradient and can therefore be separated from the surface contribution. This phenomenon is known as the thermal Hall effect because the heat transport is perpendicular to the temperature gradient. It has been proposed as an experimental signature of various other chiral edge states, for example in the spin Hall effect, the fractional quantum Hall effect or topological superconductors.^{134,172–174}

For small temperature gradients, the net heat current J_Q is in linear response to the perpendicular temperature gradient ∇T ,

$$J_Q = \kappa_{xy} |\nabla T|, \quad (8.27)$$

where κ_{xy} is the thermal Hall conductivity. The latter is defined as $\kappa_{xy} = \partial J_Q / \partial T$, and evaluates to

$$\kappa_{xy} = \sum_{k_z} \int_0^\infty \frac{dk_x}{2\pi} v_F^2 k_x \frac{\partial n_F(v_F k_x)}{\partial T} = \sum_{k_z} \frac{1}{2} \frac{k_B^2 \pi^2 T}{3h} \quad (8.28)$$

with k_z being summed over all topologically non-trivial values for the given phase of the Weyl superconductor ((0, 1) or (1, 1)-phase) and n_F denoting the Fermi-Dirac distribution at the temperature T . For concreteness, we have restored physical unities such as Boltzmann's constant k_B and Planck's constant h . As expected, the surface of a Weyl superconductor has half of the thermal Hall conductance of a quantum Hall edge state per allowed momentum k_z , which is given by $k_B^2 \pi^2 T / (3h)$.¹³⁴ This is not surprising because the thermal Hall coefficient is proportional to the central charge c of the surface modes, $\kappa_{xy} = c \pi^2 k_B^2 T / (3h)$, similar to the heat capacity.^{134,175,176}

Coming back to the Weyl superconductor in the (0, 1) or (1, 1)-phase, the thermal Hall effect has an anomalous coefficient proportional to the distance $2k^{\text{Weyl}}$ between the Weyl nodes defined in Eqs. (8.14) or (8.14), depending on the specific phase the system is in. Concretely, the thermal Hall coefficient per unit length in \hat{z} direction is given by

$$\kappa_{xy} = \frac{1}{2} \frac{k_B^2 \pi^2 T}{3h} \frac{k^{\text{Weyl}}}{\pi}. \quad (8.29)$$

In the (0, 1)-phase, where $k^{\text{Weyl}} = \pi/d$, each topological insulator layer contributes the full Majorana quantum $(1/2) \pi^2 k_B^2 T / (3h)$ to the thermal Hall coefficient. Although thermal surface transport measurements are experimentally demanding, the higher dimensionality of the surface states in a Weyl superconductor as compared to fractional or spin quantum Hall edge states hopefully tends to result in more realistic experiments, since the measured signals are larger by a factor of $\mathcal{O}(N)$, the number of superlattice layers.

8.3.2 Unidirectional electrical transport

As discussed in Sec. 8.1.2, the surface physics of a Weyl superconductor can be understood as layers of spinless $p_x + ip_y$ superconductors stacked in momentum space along k_z . For each value of k_z , there are up to two topologically non-trivial copies of a spinless $p_x + ip_y$ superconductor with associated edge states. If we specialize once more to the (0, 1)-phase, the surface of the Weyl superconductor is equivalent to just one spinless $p_x + ip_y$ superconductor per value of k_z , while the bulk is gapped. In this setup, electric transport experiments that have been proposed for $p_x + ip_y$ superconductors can simply be transferred to Weyl superconductors.

For spinless $p_x + ip_y$ -superconductors, the general idea is to bring two topologically non-trivial samples into contact. Since the interface then has two Majorana modes running into the same direction, electrons can tunnel into the interface by decomposition into the two Majorana particles. These two Majorana particles can then be transported in parallel, giving rise to a one-directional electronic transport channel along the interface.¹⁷⁷ This experiment can relatively easily be transferred to Weyl superconductors. Imagine bringing two Weyl superconductor samples of opposite magnetization into contact. For each value of k_z , there will be one pair of Majorana modes running along the interface, see Fig. 8.12. One can then tunnel electrons of given k_z into the interface, thereby splitting them up into the two states making up the respective Majorana pair.

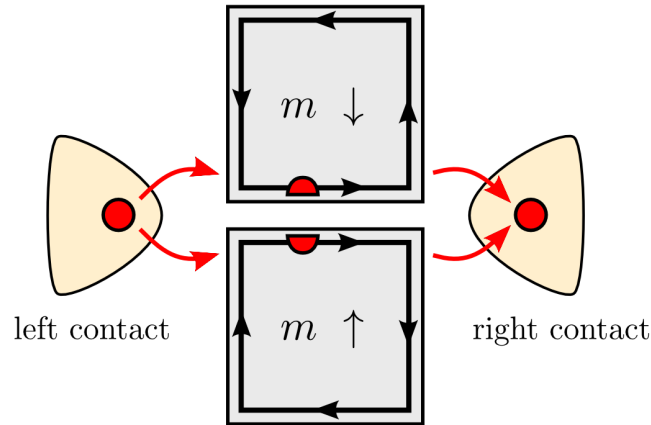


Figure 8.12: Sketch of an experiment for unidirectional electrical transport along the interface of two Weyl superconductors with opposite magnetization m . The samples are shown in grey from above, the black arrows indicate the Majorana surface states. Both Weyl superconductors are supposed to be in the same bulk-gapped 1,0-phase. Electrical transport through the interface can be achieved by tunneling an electron (here shown by the red circles) from a contact into the interface. The electron then splits up into two Majoranas (the red semicircles), which can be recombined and extracted at the other side of the interface. This gives rise to unidirectional electrical transport.¹⁷⁷

At the other side of the interface, the electron can again be extracted from the interface, giving rise to an electrical current. Since the propagation of the Majorana surface states is unidirectional, the electrical current will be only transported into the direction of propagation of the Majorana modes. Note that one might also envision to conduct this experiment with a single Weyl superconductor sample, at the expense of splitting up the electron into two Majorana modes of different k_z .

As an alternative idea, one can also split up several electrons into pairs of Majoranas and recombine them in a different way. For $p_x + ip_y$ -superconductors, this leads to distinct signatures in conductance and noise.¹⁷⁸ The latter experiments are however less appropriate for Weyl superconductors where each surface has a large number of generically coupled Majorana modes at different values of k_z , which might hinder the controlled recombination of specific Majorana particles.

8.4 Conclusions

In the last chapter, we have derived a toy model for inversion symmetric but time reversal symmetry broken Weyl superconductors. While the latter generally have interesting topological phases, we found that time reversal symmetric, but inversion symmetry broken Weyl superconductors are topologically trivial and thus less interesting. Time reversal symmetry broken Weyl superconductors might be realized in ferromagnetic spin triplet superconductors, such as certain Uranium-based Ising ferromagnetic superconductors. We studied their physics using a well-controlled toy system, namely a heterostructure built from alternating layers of topological insulator and s-wave superconductor. Time reversal symmetry is broken by virtue of magnetic impurities in the topological insulator layers.

We found that Weyl superconductors can be interpreted as layers of $p_x + ip_y$ superconductors stacked in momentum space, similar to a normal Weyl semimetal that can be interpreted as stacked Quantum Hall layers. Just like the latter, a Weyl superconductor generally has gapless points in the bulk Brillouin zone. These points have been named Bogoliubov Weyl nodes, and can be interpreted as half a regular Weyl node. Indeed, when superconductivity is switched on in a regular Weyl semimetal, each normal Weyl node splits up into two Bogoliubov Weyl nodes. They carry half the topological charge of a initial Weyl node each, and are characterized by their chirality and behavior under superconducting particle-hole symmetry.

Depending on the strength of the superconducting order parameter and the magnetization resulting from the impurities in the topological insulator layers, Weyl superconductors can be in a number of different phases. Each phase is characterized by the number of bulk Bogoliubov Weyl nodes and surface Majorana modes. The Bogoliubov Weyl nodes always come in pairs of opposite chirality. In our simple toy model, the system could have up to two pairs of nodes present at the same time. Similarly, up to two sets of two-dimensional surface Majorana modes can be present. They live on the side surfaces (parallel to the stacking axis of the heterostructure). In general, the surface modes only exist in parts of the surface Brillouin zone, which gives rise to Majorana Fermi arcs in the surface Brillouin zone.

Inspired by the analogy to spinless $p_x + ip_y$ superconductors, which trap Majorana zero modes at vortices, we studied the physics of vortices in (inversion symmetric) Weyl superconductors. We found that vortices along the stacking axis of the heterostructure can trap zero energy Majorana modes under certain conditions, while vortices perpendicular to the stacking axis do not trap Majorana modes at all. Vortices in general directions can be understood as intermediate between the two latter cases, and can thus in general also trap Majorana zero modes. Just as in $p_x + ip_y$ -superconductors, vortices with Majorana zero modes have non-abelian exchange statistics and could thus be used for quantum computation. Vortices perpendicular to the stacking axis may on the other hand be useful for Majorana interferometry.

We finally concluded by proposing surface transport experiments that could unveil Majorana physics. In complement to existing ideas of ARPES surface measurements, we suggested both thermal and electrical transport measurements, which should best be conducted in a phase with a gapped bulk in order to maximize the surface transport signal. Thermal surface transport yields an anomalous thermal Hall effect that is proportional to the central charge of the Majorana surface modes (which is half the charge of a regular electron). Electrical transport at interfaces of different Weyl superconductor samples, on the other hand, is proposed to be unidirectional.

While our results shed a first light on the physics of Weyl superconductors, a number open questions remain which are certainly worth studying. Amongst the most pressing issues are the effects of disorder and electronic correlations. Both of them might in principle couple the bulk Bogoliubov Weyl nodes and drive the system to a topologically trivial phase. Similar analysis for normal Weyl semimetals however suggest that Weyl superconductors might be stable against modest interaction and disorder strengths.^{107,108,115–117}

Part IV
Appendices

Appendix A

Introduction to the standard renormalization group

The renormalization group is one of the most groundbreaking developments in the toolbox of theoretical physics in the 20th century. It has most influentially been developed by Kenneth G. Wilson, who in 1982 also received the Nobel price for his work.⁸ Early contributions have already been made in the 1950's by Stueckelberg and Petermann, and subsequently by Gell-Mann and Low in the field of quantum electrodynamics.^{179,180} They considered renormalizations of propagators due to interactions, basically describing the physically observed coupling constants as “dressed” or renormalized values, which are then effectively visible at the physically relevant scales.

From a modern solid state theoretical perspective, the basic idea of the renormalization group approach can be related to the universality and self-similarity of physics close to a phase transition. Close to a second order phase transition, physical observables follow simple scaling laws depending only on a few global parameters, such as temperature and (quantum) tuning parameters, e.g. pressure, and a small set of scaling exponents. They are however largely independent of microscopic parameters such as lattice constants. This can be explained by the fact that the physically relevant degrees of freedom fluctuate on macroscopic scales when a phase transition is approached, which washes out microscopic information. Consequently, one should be allowed to somehow get rid of the microscopic details, and obtain the universal physics in a controlled way. This is precisely what is done by the renormalization group.

A.1 Introduction: Kadanoff spin block renormalization group

The probably most pedagogical picture of the renormalization group (RG) is the spin block RG introduced by Kadanoff in 1966.¹⁸¹ It can be classified as a real-space RG, as opposed to momentum-space RGs, see next section. Consider a two-dimensional square lattice of classical Ising spins coupled by a nearest neighbor interaction J , and with linear lattice spacing a . At a temperature T , the system is described by the Hamiltonian $H(J, a)$ and has a partition function

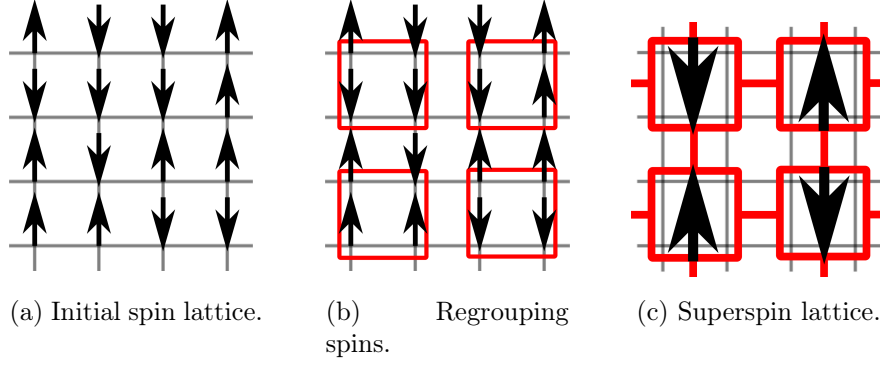


Figure A.1: Idea of the Kadanoff spin block renormalization group. Spins on a square lattice are regrouped into superspins.

$$\mathcal{Z} = \sum_{\{\sigma_{ij}\}} e^{-\beta H(J,a)} , \quad (\text{A.1a})$$

$$H(J, a) = J \sum_{i,j} (\sigma_{ij} \sigma_{i+1,j} + \sigma_{ij} \sigma_{i,j+1}) . \quad (\text{A.1b})$$

One may now proceed by grouping the spins in square blocks of four, which together form a superspin. This superspin points up if the majority of the four original spins was up, while it takes the value down if the majority of the initial spins pointed down. If the initial spins have a vanishing average, the superspin is arbitrarily chosen to be either up or down. This procedure is illustrated in Fig. A.1. The superspins form a two-dimensional square lattice of Ising spins of lattice spacing $2a$, and the initial interaction between the original spins gives rise to an effective interaction between the superspins. The system can thus again be described by the same Hamiltonian as before, where σ now represents the superspins and the initial exchange coupling J needs to be replaced by an effective interaction J' . Since this effective Hamiltonian should describe the same system, the resulting partition functions (and thus total free energy) need to be matched, which can be achieved by appropriately modifying the temperature. The Kadanoff spin block RG thus expresses physics on different scales a and $2a$ by a self-similar Hamiltonian with renormalized parameters,

$$a \rightarrow 2a \quad , \quad J \rightarrow J' \quad , \quad T \rightarrow T' \quad (\text{A.2a})$$

$$\mathcal{Z} = \sum_{\{\sigma_{ij}\}} e^{-\beta H(J,a)} = \sum_{\{\sigma_{ij}\}} e^{-\beta' H(J',2a)} . \quad (\text{A.2b})$$

Technically, the physics at the new scale follow from tracing out the short scale physics. This procedure can be iterated until the physically relevant scale is reached. The renormalization of the coupling J and the temperature T can generally be expressed as scale dependent functions,

$$J \rightarrow J(x) \quad \text{with} \quad J(a) = J, \quad J(2a) = J', \quad \dots \quad (\text{A.3a})$$

$$T \rightarrow T(x) \quad \text{with} \quad T(a) = T, \quad T(2a) = T', \quad \dots \quad (\text{A.3b})$$

As a corollary, we note that there may exist points where the step from scale a to $2a$ does not alter the values of the parameters, $J(a) = J(2a)$ and $T(a) = T(2a)$. These points are called fixed points of the theory, and will be discussed shortly.

A.2 Renormalization group equations

As an alternative to subsequently integrating out short distance physics, as Kadanoff did in his spin block RG, one can subsequently get rid of large momenta. This class of approaches is known as momentum space RGs. Consider a quantum field theory depending on some degrees of freedom living in d dimensions. In Fourier space and using real frequencies, these degrees of freedom correspond to fields $\Psi(\vec{k}, \omega)$, and might be either bosonic or fermionic. For concreteness, we assume that they are described by the action

$$\begin{aligned} \mathcal{S} = & \int d^d k \int d\omega \bar{\Psi}(\vec{k}, \omega) g(\vec{k}, \omega)^{-1} \Psi(\vec{k}, \omega) \\ & + \frac{u}{\beta V} \int \{d^d k\} \int \{d\omega\} \bar{\Psi}(\vec{k}_1, \omega_1) \bar{\Psi}(\vec{k}_2, \omega_2) \Psi(\vec{k}_3, \omega_3) \Psi(\vec{k}_4, \omega_4) \delta_{\vec{k}_1 + \vec{k}_2, \vec{k}_3 + \vec{k}_4} \delta_{\omega_1 + \omega_2, \omega_3 + \omega_4} , \end{aligned} \quad (\text{A.4})$$

where the quadratic part of the action has already been diagonalized, and where additional quantum numbers such as spin have been dropped for simplicity. The interaction between the modes is u , β denotes the inverse temperature and V the d -dimensional volume of the system. The fields $\bar{\Psi}$ are the complex or Grassman conjugate fields of Ψ , and g^{-1} is the inverse propagator. This theory is valid up to some high energy cutoff Λ , i.e. has the restriction $|\vec{k}| \lesssim \Lambda$ and $|\omega| \lesssim \Lambda^z$, where z is the dynamical exponent of the system. The latter is set by the dispersion $\omega \sim k^z$. The action \mathcal{S} can generally be divided into a quadratic part \mathcal{S}_0 and the interaction \mathcal{S}_{int} .

The basic idea of the renormalization group approach is to divide the fields Ψ into high energy/momentum part Ψ_h and a low energy/momentum part Ψ_l , which will subsequently allow to integrate out the high energy/momentum modes. The division can be implemented in various fashions, for instance in a ‘‘circular’’ scheme. The latter treats momentum and frequency as components of an effectively $d + z$ -dimensional vector $K = (\vec{k}^T, \omega)$, and the theory is defined for $|K|^z = \sqrt{\vec{k}^{2z} + |\omega|^2} < \Lambda^z$. The division into high and low energy modes can then be implemented as

$$\Psi(\vec{k}, \omega) = \begin{cases} \Psi_h & \text{if } \sqrt{\vec{k}^{2z} + |\omega|^2} \in [(\Lambda/b)^z, \Lambda^z] \\ \Psi_l & \text{if } \sqrt{\vec{k}^{2z} + |\omega|^2} < (\Lambda/b)^z \end{cases} , \quad (\text{A.5})$$

with $b > 1$. The precise implementation of the cutoff, and deriving from there the division into high- and low energy/momentum modes is also referred to as the ‘‘cutoff scheme’’. Different high-energy cutoff schemes should however naturally yield the same universal low energy physics, such that one is free to choose the most convenient parametrization. With this division, the theory can be written as

$$\mathcal{Z} = \int \mathcal{D}\Psi e^{-\mathcal{S}_0[\Psi_l] - \mathcal{S}_{\text{int}}[\Psi_l, \Psi_l]} e^{-\mathcal{S}_0[\Psi_h] - \mathcal{S}_{\text{int}}[\Psi_h, \Psi_h]} e^{-\mathcal{S}_{\text{int}}[\Psi_l, \Psi_h]} . \quad (\text{A.6})$$

One can now integrate out the high energy modes Ψ_h . The coupling between high energy modes and low energy modes can be evaluated perturbatively to the desired order, which yields new terms depending only on the low energy fields Ψ_l . These corrections are proportional to the momentum range that has been integrated over, i.e. proportional to $b - 1$. The new terms can finally be re-exponentiated and yield corrections to the initial interaction and propagator of the low energy modes. We note that this step may also generate new terms in the Hamiltonian, such as additional interactions. If this is *not* the case, the theory is named “renormalizable”. A commonly used trick to make a theory renormalizable if additional terms are generated is to formally include these terms from the beginning, but to give them an initially vanishing coupling constant. As a last step, one can rescale the remaining low momenta and frequencies as

$$\vec{k} \rightarrow b \vec{k} \quad \text{and} \quad \omega \rightarrow b^z \omega, \quad (\text{A.7})$$

which yields an effective theory that has the same cutoff as before. Additionally, the values of the coupling constants need to be adjusted in order to obtain a theory of the same form than the initial action. This reproduces the self-similarity already encountered in the Kadanoff spin block RG, again with renormalized parameters. As an example, the interaction has the final value

$$u^* = (u + \delta u) b^x, \quad (\text{A.8})$$

where δu is the correction stemming from integrating out high energy modes and b^x is due to the rescaling step. The scaling dimension x is also called the engineering dimension of the respective parameter. This procedure can now be iterated up to a physical scale of interest. The change of the parameters during the repeated renormalization steps can most conveniently be calculated if infinitesimal renormalization steps are considered, i.e. $b = e^\epsilon \approx 1 + \epsilon$ with $\epsilon \ll 1$. In this case, the renormalized parameters of Eq. (A.8) can be expanded as

$$u(b = 1 + \epsilon) \approx u(b = 1) + \epsilon x u(b = 1) + \delta u, \quad (\text{A.9})$$

where we have used that $\delta u \sim (b - 1) \sim \epsilon$. In the limit $\epsilon \rightarrow 0$, one can then define the RG equation

$$\left. \frac{\partial u(b)}{\partial \ln(b)} \right|_{b=1} = \lim_{\epsilon \rightarrow 0} \frac{u(1 + \epsilon) - u(1)}{\epsilon} = x u(b = 1) + \frac{\delta u}{\epsilon}. \quad (\text{A.10})$$

Since the theory has by assumption a self-similar form on all scales, also the RG equation will not change its form during the flow, and the condition $b = 1$ in the above equation can be relaxed. At the end of the day, one ends up with a set of RG equations $\partial_{\ln(b)} g_i = \beta(\{g\})$, one per parameter g_i (where we have introduced the so-called β -function, which simply corresponds to the right-hand side of the RG equation).

A.3 RG fixed points

Especially important in a renormalization group analysis are points where the flow of all parameters $g_i(b)$ stops,

$$\frac{\partial g_i}{\partial \ln(b)} = \beta_i(\{g\}) = 0 \quad \forall i. \quad (\text{A.11})$$

The set of values $\{g^*\}$ for which this happens is called a “fixed point” in the parameters space $\{g\}$. A fixed point corresponds to a situation where the physics has an identical description on all scales. Pictorially, one can zoom out and obtains the exact same image on all zoom scales. On the other hand, every physical system has an intrinsic length scale ξ corresponding to the characteristic length of the low energy fluctuations. These two statements can only agree if ξ either vanishes or becomes infinite. An RG fixed point therefore naturally describes an entirely disordered phase (corresponding to $\xi = 0$), an entirely ordered phase ($\xi \rightarrow \infty$), or phase transition of second order (also $\xi \rightarrow \infty$). If the system is close, but not exactly at a fixed point, each of the couplings g_i can have three types of behaviors. If a given coupling approaches its fixed point value under RG, $g_i(b) - g_i^* \rightarrow 0$, the coupling is said to be irrelevant under RG with respect to the given fixed point. Relevant couplings are the ones that are driven away from their fixed point value, and $|g_i(b) - g_i^*|$ grows. Finally, if to leading order in the interactions the coupling does not change close to a fixed point, $g_i(b) - g_i^* = \text{const.}$, it is called marginal. The subleading orders then decide whether the coupling is marginally irrelevant or marginally relevant with respect to the given fixed point.

The character of the fixed point itself can be deduced from the character of the couplings g_i with respect to this fixed point. If all couplings are (marginally) irrelevant with respect to a given fixed point, the system flows to this fixed point if it is only close enough. Such fixed point are called attractive or stable fixed points, and correspond to stable phases of matter. If at least one coupling is (marginally) relevant, any displacement in the relevant coupling off the fixed point value will push the system away from the latter, and the fixed point is dubbed unstable. Phase transitions are thus described by unstable fixed points. The boundary between two extended phases, i.e. a phase transition line (or surface), corresponds to an unstable fixed point that has at least one (or two) irrelevant operator(s), and the extension of the line (or surface) corresponds to the irrelevant operator(s). The concept of fixed points is illustrated in Fig. A.2.

To conclude, we note that the framework of stable fixed points also explains the universality of long range physics. Consider the entire world as an enormous parameter space with a bunch of stable and unstable fixed points. Different physical systems correspond to different specific values in this huge parameter space. If two systems are both close to the same, stable fixed point, their lowest energy physics is given by the same parameter values $\{g^*\}$ corresponding to the fixed point values. They can thus be described by the same universal low-energy theory, which naturally gives rise to the concept of universality and universality classes (i.e. the class of all systems that are asymptotically described by the same fixed point). As an exception to the rule, we note that there exist as well so-called “dangerously irrelevant operators”. These correspond to operators which are irrelevant under RG but do affect the low energy physics of a system. Consequently, if one of the two parameters g_1 and g_2 in Fig. A.2 was dangerously irrelevant, the two systems indicated by the red crosses would in general not exhibit the same low-energy physics. Finally, we note that the name “renormalization group” is actually a little misleading, since the RG is a semigroup in the mathematical sense. During an RG step, information about high energy degrees of freedom is continuously lost (as only the physics relevant for low energies is retained). There is thus no inverse transformation that allows to re-obtain

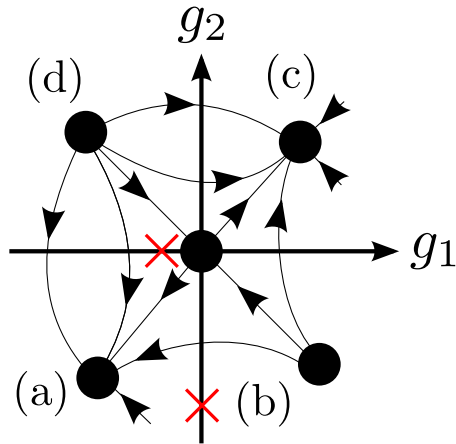


Figure A.2: Generic RG flow diagram for a world with two parameters g_1 and g_2 and five fixed points (black dots). The fixed points (a) and (c) are stable, the fixed points (b) and (d) are unstable. The flow diagram thus describes a world with two stable phases of matter, corresponding to (a) and (c). The fixed point $g_1 = g_2 = 0$ is also an unstable fixed point, but has both relevant and irrelevant perturbations. It describes the transition between the two stable phases (a) and (c). Since the fixed point is non-interacting, $g_1 = g_2 = 0$, it is described by a quadratic, or gaussian, action. This fixed is thus called the “gaussian fixed point”. The red crosses denote two different physical systems that could exist in the world given by the parameter space $\{g_1, g_2\}$. Although they seem very different (one has only the coupling g_1 , which in addition is small, while the other one has only the coupling g_2 , which is large), they correspond to the same universal low energy physics described by the fixed point (a).

the full initial Hamiltonian from a given low energy Hamiltonian (in agreement with the concept of universality), and the RG is thus a semigroup. For more detailed introductions to the formalism of renormalization group, the reader is referred to textbooks, see for instance Ref. [125].

Appendix B

Quantum phase transitions in quantum wires

B.1 Derivation of the Wigner crystal action

In this appendix, we want to explicitly derive the action for the Wigner crystal. We start from the Hamiltonian in Eq. (2.1) describing the harmonically confined two-dimensional electron gas,

$$H_{2\text{DEG}} = T + V_{\text{int}} + V_{\text{conf}} , \quad (\text{B.1})$$

where, as before,

$$T = \sum_i \frac{\vec{p}_i^2}{2m} , \quad (\text{B.2a})$$

$$V_{\text{int}} = \frac{1}{2} \sum_{i \neq j} U(|\vec{r}_i - \vec{r}_j|) , \quad (\text{B.2b})$$

$$V_{\text{conf}} = \frac{1}{2} m \Omega^2 \sum_i \vec{y}_i^2 . \quad (\text{B.2c})$$

Note that we treat this Hamiltonian as a classical Hamilton function for now and perform the canonical quantization at the very end. The interaction energy V_{int} describes the screened Coulomb interaction,

$$U(|\vec{r}|) = \frac{e^2}{\epsilon_r} \left[\frac{1}{|\vec{r}|} - \frac{1}{\sqrt{r^2 + (2d)^2}} \right] . \quad (\text{B.3})$$

The screening is due to mirror charges in the nearby gates, which are positioned at a distance d , and decays as a dipole at large distances, $U(r) \stackrel{r \gg d}{\approx} d^2/r^3$. Although one can straight-forwardly take the finite-range interactions into account, we want to approximate the screened Coulomb interactions by an interaction between neighboring sites of the Wigner crystal in order to simplify the discussion (we recall that we expand the action for small displacements around the Wigner crystal sites). The full finite range interaction

corresponds to logarithmic corrections to the subsequent formulas.¹⁶ We will thus work with the effective interaction

$$V_{\text{int}}^{\text{eff}} = \frac{e^2}{\epsilon_r} \sum_i \left[\frac{1}{|\vec{r}_{i+1} - \vec{r}_i|} - \frac{1}{\sqrt{(\vec{r}_{i+1} - \vec{r}_i)^2 + (2d)^2}} \right]. \quad (\text{B.4})$$

The positions of the electrons are defined by their (dimensionless) displacements \vec{u} with respect to the equilibrium positions,

$$\vec{x}_i = \begin{pmatrix} i a + a u_{x,i} \\ a u_{y,i} \end{pmatrix}, \quad (\text{B.5})$$

where $a = n^{-1}$ is the inverse density. We thus start from the Hamiltonian

$$\begin{aligned} H^{\text{eff}} &= T + V_{\text{int}}^{\text{eff}} + V_{\text{conf}} \\ &= \sum_i \frac{\vec{p}_i^2}{2m} + \frac{1}{2} m \Omega^2 a^2 \sum_i u_{y,i}^2 \\ &\quad + \frac{e^2}{\epsilon_r a} \sum_i \left[\frac{1}{\sqrt{(1 + u_{x,i+1} - u_{x,i})^2 + (u_{y,i+1} - u_{y,i})^2}} \right] \\ &\quad - \frac{e^2}{\epsilon_r a} \sum_i \left[\frac{1}{\sqrt{(1 + u_{x,i+1} - u_{x,i})^2 + (u_{y,i+1} - u_{y,i})^2 + (2d/a)^2}} \right]. \end{aligned} \quad (\text{B.6})$$

As a next step, we expand this Hamiltonian in the small displacements up to fourth order. We furthermore do this in the limit $d^{-1} \ll n \ll a_B^{-1}$, which implies $d/a \gg 1$. For even smaller densities, the screening will eventually lead to a melting of the Wigner crystal, which is not considered here. Using $\delta u_{x,i} = u_{x,i+1} - u_{x,i}$, $\delta u_{x,i} = u_{y,i+1} - u_{y,i}$, $x_0 = 1/\sqrt{m\Omega}$, $a_B = \epsilon/(e^2 m)$ and $a = n^{-1}$ yields,

$$\begin{aligned} H^{\text{eff}} &\approx \sum_i \frac{p_{x,i}^2}{2m} + \frac{e^2}{\epsilon_r a} \sum_i \left[-\delta u_{x,i} + \delta u_{x,i}^2 - \delta u_{x,i}^3 + \delta u_{x,i}^4 \right] \\ &\quad + \sum_i \frac{p_{y,i}^2}{2m} + \frac{e^2}{\epsilon_r a} \sum_i \left[\frac{a_B}{x_0^4 n^3} u_{y,i}^2 - \frac{1}{2} \delta u_{y,i}^2 + \frac{3}{8} \delta u_{y,i}^4 \right] \\ &\quad + \frac{e^2}{\epsilon_r a} \sum_i \left[\frac{3}{2} \delta u_{x,i} \delta u_{y,i}^2 - 3 \delta u_{x,i}^2 \delta u_{y,i}^2 \right] + \frac{e^2}{\epsilon_r a} \sum_i 1. \end{aligned} \quad (\text{B.7})$$

Next, we use that $\sum_i \delta u_{x,i} = \sum_i (u_{x,i+1} - u_{x,i}) = 0$, and retain only the leading order terms. For the first line in Eq. (B.7), the leading contribution is thus of order $\delta u_{x,i}^2$. For the second line, we have to keep all terms, since the interplay between the confining energy $\sim u_{y,i}^2$ and the second order interaction term $\sim \delta u_{x,i}^2$ drives a phase transition. In the ordered phase, the second order term only would thus describe an unstable system. In addition, we drop the last term, since it can be absorbed into a shift of the energy

measure. This yields

$$\begin{aligned}
H^{\text{eff}} \approx & \sum_i \frac{p_{x,i}^2}{2m} + \frac{e^2}{\epsilon_r a} \sum_i \delta u_{x,i}^2 \\
& + \sum_i \frac{p_{y,i}^2}{2m} + \frac{e^2}{\epsilon_r a} \sum_i \left[\frac{a_B}{x_0^4 n^3} u_{y,i}^2 - \frac{1}{2} \delta u_{y,i}^2 + \frac{3}{8} \delta u_{y,i}^4 \right] \\
& + \frac{e^2}{\epsilon_r a} \sum_i \left[\frac{3}{2} \delta u_{x,i} \delta u_{y,i}^2 - 3 \delta u_{x,i}^2 \delta u_{y,i}^2 \right].
\end{aligned} \tag{B.8}$$

Next, we go to Fourier space in order to identify the energies the most relevant Fourier modes, namely the in and out-of phase modes parallel and perpendicular to the wire. We use the convention

$$u_{(\cdot)}(k) = \frac{1}{\sqrt{N}} \sum_{n=1}^N e^{-ik(na)} u_{(\cdot),n} \quad \text{and} \quad u_{(\cdot),n} = \frac{1}{\sqrt{N}} \sum_{k=1}^N e^{ik(na)} u_{(\cdot)}(k), \tag{B.9}$$

which yields for the quadratic terms

$$\begin{aligned}
H^{\text{eff}} \approx & \sum_i \frac{p_{x,i}^2}{2m} + \frac{e^2}{\epsilon_r a N} \sum_k u_x(k) u_x(-k) [2 - 2e^{ika}] \\
& + \sum_i \frac{p_{y,i}^2}{2m} + \frac{e^2}{\epsilon_r a N} \sum_k u_y(k) u_y(-k) \left[\frac{a_B}{x_0^4 n^3} - \frac{1}{2} [2 - 2e^{ika}] \right] \\
& + \sum_i \left[\frac{3}{8} \delta u_{y,i}^4 \right] + \frac{e^2}{\epsilon_r a} \sum_i \left[\frac{3}{2} \delta u_{x,i} \delta u_{y,i}^2 - 3 \delta u_{x,i}^2 \delta u_{y,i}^2 \right].
\end{aligned} \tag{B.10}$$

For the relevant modes we use the notation

$$u_0^{\parallel}(q) = u_x(0+q) \quad , \quad \text{thus corresponding to } k \approx 0, \tag{B.11a}$$

$$u_{\pi}^{\parallel}(q) = u_x(\pi/a+q) \quad , \quad \text{thus corresponding to } k \approx \pi/a, \tag{B.11b}$$

$$u_0^{\perp}(q) = u_y(0+q) \quad , \quad \text{thus corresponding to } k \approx 0, \tag{B.11c}$$

$$u_{\pi}^{\perp}(q) = u_y(\pi/a+q) \quad , \quad \text{thus corresponding to } k \approx \pi/a, \tag{B.11d}$$

where $q \ll \pi/a$ is the momentum of the respective modes. Also splitting the momenta, and only retaining the necessary leading orders in the small displacements and wave

vectors q , we find

$$\begin{aligned}
H^{\text{eff}} \approx & \sum_i \frac{p_{0,i}^{\parallel 2}}{2m} + \frac{e^2}{\epsilon_r a N} \sum_q u_0^{\parallel}(q) (qa)^2 u_0^{\parallel}(-q) \\
& + \sum_i \frac{p_{\pi,i}^{\parallel 2}}{2m} + \frac{e^2}{\epsilon_r a N} \sum_q 4 u_{\pi}^{\parallel}(q) u_{\pi}^{\parallel}(-q) \\
& + \sum_i \frac{p_{0,i}^{\perp 2}}{2m} + \frac{e^2}{\epsilon_r a N} \sum_q u_0^{\perp}(q) u_0^{\perp}(-q) \frac{a_B}{x_0^4 n^3} \\
& + \sum_i \frac{p_{\pi,i}^{\perp 2}}{2m} + \frac{e^2}{\epsilon_r a N} \sum_k u_{\pi}^{\perp}(q) u_{\pi}^{\perp}(-q) \left[\frac{a_B}{x_0^4 n^3} - 2 + \frac{(qa)^2}{2} \right] \\
& + \sum_{q_1, q_2, q_3, q_4} 3 u_{\pi}^{\perp}(q_1) u_{\pi}^{\perp}(q_2) u_{\pi}^{\perp}(q_3) u_{\pi}^{\perp}(q_4) \delta_{q_1+q_2+q_3+q_4, 0} \\
& + \frac{e^2}{\epsilon_r a} \sum_i \left[\frac{3}{2} \delta u_{x,i} \delta u_{y,i}^2 - 3 \delta u_{x,i}^2 \delta u_{y,i}^2 \right].
\end{aligned} \tag{B.12}$$

We thus find that the mode u_0^{\parallel} , i.e. the uniform displacement of all electrons in the Wigner crystal along the axis of the wire, is always gapless. This is not surprising since it is the Goldstone mode related to the spontaneous breaking of translation symmetry. The mode u_{π}^{\perp} , which is responsible for the zigzag transition, becomes gapless if $a_B/(x_0^4 n^3) = 2$. The mode u_{π}^{\parallel} is always gapped, and has a gap of the order of the average Coulomb interaction, while the mode u_0^{\perp} has a gap set by the confining potential. At the zigzag transition, these two gaps are obviously of the same order. We thus only have to take into account the interaction between the modes u_0^{\parallel} and u_{π}^{\perp} , whose most relevant term is a cubic one. In addition, we keep the quartic term for the u_{π}^{\perp} -mode in order to stabilize the theory in the ordered phase. Going back to real space, we find the low energy Hamiltonian

$$\begin{aligned}
H^{\text{eff}} \approx & \sum_i \frac{p_{0,i}^{\parallel 2}}{2m} + \frac{e^2 a}{\epsilon_r} \sum_i \left(\partial_{x_i} u_0^{\parallel}(x_i) \right)^2 \\
& + \sum_i \frac{p_{\pi,i}^{\perp 2}}{2m} + \frac{e^2}{\epsilon_r a} \sum_i \left(\left[\frac{a_B}{x_0^4 n^3} - 2 \right] u_{\pi}^{\perp}(x_i)^2 + \frac{a^2}{2} \left(\partial_{x_i} u_{\pi}^{\perp}(x_i) \right)^2 + 3 u_{\pi}^{\perp}(x_i)^4 \right) \\
& + \frac{e^2}{\epsilon_r a} \sum_i 6a \left(\partial_{x_i} u_0^{\parallel}(x_i) \right) u_{\pi}^{\perp}(x_i)^2.
\end{aligned}$$

In order to quantize this Hamiltonian, we first perform the canonical transformation to the classical Lagrangians, followed the canonical quantization. Taking finally the continuum limit $\sum_i \rightarrow \int dx/a$, we find the action

$$\mathcal{S} = \int d\tau \int dx \left(\mathcal{L}_{\parallel 0} + \mathcal{L}_{\perp \pi} + \mathcal{L}_{\text{int}} \right) \tag{B.13}$$

where the Lagrangian densities read

$$\mathcal{L}_{\parallel 0} = \frac{m}{2n} \left[(\partial_\tau u_0^\parallel)^2 + v_{\parallel 0}^2 (\partial_x u_0^\parallel)^2 \right], \quad (\text{B.14a})$$

$$\mathcal{L}_{\perp \pi} = \frac{m}{2n} \left[(\partial_\tau u_\pi^\perp)^2 + v_{\perp \pi}^2 (\partial_x u_\pi^\perp)^2 + r (u_\pi^\perp)^2 + s (u_\pi^\perp)^4 \right], \quad (\text{B.14b})$$

$$\mathcal{L}_{\text{int}} = \lambda (\partial_x u_0^\parallel) u_\pi^\perp{}^2, \quad (\text{B.14c})$$

where τ is the imaginary time and where the longitudinal velocity $v_{\parallel 0}$ evaluates to $v_{\parallel 0}^2 = 2n/(m^2 a_B)$, the transversal velocity is $v_{\perp \pi}^2 = n/(m^2 a_B)$, the control parameter is $r = (2/m) (x_0^{-4} - x_{0c}^{-4})$ with $x_{0c} = (a_B/(2n^3))^{1/4}$, and $s = 6n^3/(m^2 a_B)$. The interaction between the modes finally evaluates to $\lambda = 6n/(a_B m)$. If we had used the full expression of the interaction, and not just nearest neighbor repulsions, we would get essentially the same expressions up to logarithmic corrections. In the limit $d^{-1} \ll n \ll a_B^{-1}$, one finds $v_{\parallel 0}^2 = 2n/(m^2 a_B) \ln(8nd)$, $x_{0c} = (2a_B/(7\zeta(3)n^3))^{1/4}$, $v_{\perp \pi}^2 = n/(m^2 a_B) \ln(2)$, $s = 93\zeta(5)n^3/(8m^2 a_B)$, and $\lambda = 21\zeta(3)n/(4a_B m)$.^{13,16}

B.2 Two-particle Green's function in the second band and its ladder resummation

The bare retarded two-particle Green's function in the second band is defined as

$$\mathcal{D}_2^0(x - x', t - t') = -i\theta(t - t') \langle [c_{2\uparrow}(x, t)c_{2\downarrow}(x, t), c_{2\downarrow}^\dagger(x', t')c_{2\uparrow}^\dagger(x', t')] \rangle_0, \quad (\text{B.15})$$

where the expectation value is taken with respect to the non-interacting Hamiltonian in the second band. It is most conveniently calculated in imaginary time,

$$\mathcal{D}_2^0(x - x', \tau - \tau') = -\langle \mathcal{T}_\tau c_{2\uparrow}(x, \tau)c_{2\downarrow}(x, \tau), c_{2\downarrow}^\dagger(x', \tau')c_{2\uparrow}^\dagger(x', \tau') \rangle_0, \quad (\text{B.16})$$

where τ and τ' are imaginary times and \mathcal{T}_τ is the imaginary time ordering operator. Its Fourier transform is given by the Matsubara frequency and momentum dependent form

$$\mathcal{D}_2^0(q, \omega_n) = \beta L \int_{-\infty}^{\infty} dx \int_0^\beta d\tau e^{i(\omega_n(\tau - \tau') - q(x - x'))} \mathcal{D}_2^0(x - x', \tau - \tau') \quad (\text{B.17})$$

We note that ω_n is here a bosonic Matsubara frequency since $\mathcal{D}_2^0(q, \omega_n)$ is a two-particle Green's function. Next, we Fourier transform this expression using the conventions

$$c_\sigma(x, \tau) = \frac{1}{\sqrt{\beta L}} \sum_{\omega_n, q} e^{-i(\omega_n \tau - qx)} c_\sigma(q, \omega_n), \quad (\text{B.18a})$$

$$c_\sigma(q, \omega_n) = \frac{1}{\sqrt{\beta L}} \int_{-\infty}^{\infty} dx \int_0^\beta d\tau e^{i(\omega_n \tau - qx)} c_\sigma(x, \tau) \quad (\text{B.18b})$$

and perform the average, which yields

$$\mathcal{D}_2^0(q, \omega_n) = -\frac{1}{\beta L} \sum_{\omega_{n1}, k_1} \mathcal{G}_\uparrow^0(\omega_{n1}, k_1) \mathcal{G}_\downarrow^0(\omega_n - \omega_{n1}, q - k_1), \quad (\text{B.19})$$

where the bare single particle Green's function is independent of the spin and given by

$$\mathcal{G}_\sigma^0(\omega_n, q) = \frac{1}{i\omega_n - \epsilon(k)}, \quad (\text{B.20})$$

with the dispersion is given by $\epsilon(k) = k^2/(2m) - \mu_2$, and where the Matsubara frequencies of the single particle Green's functions are of course fermionic. This yields

$$\mathcal{D}_2^0(q, \omega_n) = -\frac{1}{\beta L} \sum_{\omega_{n1}, k_1} \frac{1}{(i\omega_{n1} - \epsilon(k_1)) (i\omega_n - i\omega_{n1} - \epsilon(q - k_1))}. \quad (\text{B.21})$$

We can now perform the standard trick of rewriting the sum over Matsubara frequencies as a contour integral around the poles of the Fermi function n_F and deform the integral at infinity, which then yields (by virtue of the residue theorem)

$$\mathcal{D}_2^0(q, \omega_n) = -\frac{1}{L} \sum_{k_1} \frac{n_F(\epsilon(k_1)) - n_F(i\omega_n - \epsilon(q - k_1))}{i\omega_n - \epsilon(k_1) - \epsilon(q - k_1)}, \quad (\text{B.22})$$

Next, we exploit that for bosonic frequencies ω_n , the Fermi function obeys

$$n_F(\epsilon \pm i\omega_n) = n_F(\epsilon), \quad (\text{B.23})$$

and take the continuum limit in real space. This yields

$$\mathcal{D}_2^0(q, \omega_n) = -\int_{-\infty}^{\infty} \frac{dk_1}{2\pi} \frac{n_F(\epsilon(k_1)) - n_F(-\epsilon(q - k_1))}{i\omega_n - \epsilon(k_1) - \epsilon(q - k_1)}, \quad (\text{B.24})$$

We note that this expression coincides with the generic formula for a particle-particle bubble, see Eq. (3.31). For the case $\mu_2 < 0$ under consideration here, this integral simplifies to

$$\begin{aligned} \mathcal{D}_2^0(q, \omega_n) &= \int_{-\infty}^{\infty} \frac{dk_1}{2\pi} \frac{1}{i\omega_n - \epsilon(k_1) - \epsilon(q - k_1)} \\ &= -\int_{-\infty}^{\infty} \frac{dk_1}{2\pi} m \frac{1}{(k_1 - K)(k_1 + K)}, \end{aligned} \quad (\text{B.25})$$

where we introduced $K = \sqrt{i\omega_n m + 2m\mu_2 - q^2/4}$. This integrals has poles at complex values $k_1 = \pm K$. By closing the integral at complex infinity and then using the residue theorem, we obtain

$$\mathcal{D}_2^0(q, \omega_n) = \frac{m}{2\pi} \left(-\frac{2\pi i}{2K} \right) = -i \frac{\sqrt{m}}{\sqrt{i\omega_n - \frac{q^2}{4m} + 2\mu_2}}. \quad (\text{B.26})$$

The retarded two-particle Green's function is then given by the analytical continuation $i\omega_n \rightarrow \omega + i0^+$,

$$\mathcal{D}_2^0(q, \omega) = -i \frac{\sqrt{m}}{\sqrt{\omega - \frac{q^2}{4m} + 2\mu_2 + i0^+}}. \quad (\text{B.27})$$

B.2.1 Resummation of the interacting two-particle Green's function

If interactions are taken into account, two particle Green's function gets promoted to its interacting version,

$$\mathcal{D}_2(x - x', t - t') = -i\theta(t - t') \langle [c_{2\uparrow}(x, t)c_{2\downarrow}(x, t), c_{2\downarrow}^\dagger(x', t')c_{2\uparrow}^\dagger(x', t')] \rangle, \quad (\text{B.28})$$

where now the expectation value is taken with respect to the interacting Hamiltonian,

$$\mathcal{H}_2 = \int dx \left[\sum_\sigma c_{2\sigma}^\dagger(x) \left(-\frac{\partial_x^2}{2m} - \mu_2 \right) c_{2\sigma}(x) + V c_{2\uparrow}^\dagger(x)c_{2\downarrow}^\dagger(x)c_{2\downarrow}(x)c_{2\uparrow}(x) \right]. \quad (\text{B.29})$$

The perturbative analysis is most conveniently done in a quantum field theoretical approach. There, the full two particle Green's function can readily be expressed in imaginary time as

$$\mathcal{D}_2(x - x', \tau - \tau') = -\langle \mathcal{T}_\tau c_{2\uparrow}(x, \tau)c_{2\downarrow}(x, \tau)c_{2\downarrow}^\dagger(x', \tau')c_{2\uparrow}^\dagger(x', \tau') \rangle_{\mathcal{S}}, \quad (\text{B.30})$$

where $\mathcal{S} = \mathcal{S}_0 + \mathcal{S}_{\text{int}}$ is the action corresponding to the interacting Hamiltonian \mathcal{H}_2 . In n^{th} order perturbation theory, the interaction terms yields the contribution

$$\begin{aligned} & -\frac{(-1)^n}{n!} \int dx_1 \dots \int dx_n \int d\tau_1 \dots \int d\tau_n \\ & \langle \mathcal{T}_\tau c_{2\uparrow}(x, \tau)c_{2\downarrow}(x, \tau) \times c_{2\uparrow}(x_1, \tau_1)c_{2\downarrow}(x_1, \tau_1)c_{2\downarrow}^\dagger(x_1, \tau_1)c_{2\uparrow}^\dagger(x', \tau_1) \times \\ & \dots \times c_{2\uparrow}(x_n, \tau_n)c_{2\downarrow}(x_n, \tau_n)c_{2\downarrow}^\dagger(x_n, \tau_n)c_{2\uparrow}^\dagger(x', \tau_n) \times c_{2\downarrow}^\dagger(x', \tau')c_{2\uparrow}^\dagger(x', \tau') \rangle_{\mathcal{S}_0}. \end{aligned} \quad (\text{B.31})$$

Since in the case $\mu_2 < 0$, no hole-like diagrams are allowed, the only way to perform the above average is to combine it into $n + 1$ particle-particle bubbles. One is then left with a geometrical series of particle-particle bubbles, which can readily be summed up as

$$\mathcal{D}_2 = \mathcal{D}_2^0 \sum_{n=0}^{\infty} (-1)^n V^n \text{bubble}^n = \frac{\mathcal{D}_2^0}{1 - V \text{bubble}}. \quad (\text{B.32})$$

Since the particle hole bubble exactly corresponds to the bare Green's function (times the interaction vertex), see last section, we find

$$\mathcal{D}_2 = \mathcal{D}_2^0 \sum_{n=0}^{\infty} (-V \mathcal{D}_2^0)^n = \frac{\mathcal{D}_2^0}{1 - V \mathcal{D}_2^0}, \quad (\text{B.33})$$

which of course can also be understood as the solution to Dyson's equation for the two particle Green's function,

$$\mathcal{D}_2^{-1}(k, \omega) = \mathcal{D}_2^{(0)-1}(k, \omega) - V . \quad (\text{B.34})$$

B.3 Particle-particle and particle-hole bubble involving the first subband

In order to calculate the perturbative corrections due to diagrams living at least partially in the first band, we have to evaluate the corresponding particle-particle and particle hole bubbles. The particle-particle bubble requires the evaluation of

$$I_{pp}^{a,b}(\omega_n, k) = \frac{1}{L} \sum_q \frac{n_F(-\epsilon_b(k-q)) - n_F(\epsilon_a(q))}{\epsilon_a(q) + \epsilon_b(k-q) - \omega} ,$$

see Eq. (3.31), where ω_n is the small incoming energy and k the small incoming momentum. The particle-hole bubble, on the other hand, is given by

$$I_{ph}^{a,b}(\omega_n, k) = \frac{1}{L} \sum_q \frac{n_F(\epsilon_a(q)) - n_F(\epsilon_b(k+q))}{\epsilon_a(q) - \epsilon_b(k+q) - \omega_n} ,$$

If at least one of the particles lives in the first subband, here without loss of generality taken to be the particle b , we have $\epsilon_b(-k+q) = -\epsilon_b(k-q)$, which implies that

$$I_{pp}^{a,b}(\omega_n, k) = -I_{ph}^{a,b}(\omega_n, -k) .$$

It is thus sufficient to only evaluate the particle-particle diagrams. In addition, various particle-particle and particle-hole diagrams will cancel.

B.3.1 Bubbles involving both bands, $\mu_2 < 0$

The particle-particle bubble involving particles from bands is particularly simple if we choose the particle in the second band to be particle a . We then find

$$\begin{aligned} \text{Re} \{ I_{pp}^{2,L/R}(\omega + i0^+, k) \} &= \frac{1}{L} \mathcal{P} \sum_q \frac{n_F(-\epsilon_{L/R}(k-q)) - n_F(\epsilon_2(q))}{\epsilon_2(q) + \epsilon_{L/R}(k-q) - \omega} \\ &= \frac{1}{L} \mathcal{P} \sum_q \frac{n_F(-\epsilon_{L/R}(k-q))}{\epsilon_2(q) + \epsilon_{L/R}(k-q) - \omega} \\ &= \mathcal{P} \frac{1}{2\pi} \int_{-\infty}^{\infty} \frac{n_F(-\epsilon_{L/R}(k-q))}{\epsilon_2(q) + \epsilon_{L/R}(k-q) - \omega} . \end{aligned} \quad (\text{B.35})$$

As a next step, we introduce a high-energy cut-off $\mu_2 \ll E_0 \ll E_{F1}$ and shift the integration variable. For right-movers, we then find

$$\begin{aligned}
\operatorname{Re} \{I_{pp}^{2,R}(\omega + i0^+, k)\} &= \mathcal{P} \frac{1}{2\pi} \int_{-E_0/v_{F1}}^{E_0/v_{F1}} \frac{n_F(-v_{F1}(-q))}{\frac{(q+k)^2}{2m} - \mu_2 + v_{F1}(-q) - \omega} \\
&= \mathcal{P} \frac{1}{2\pi} \int_{-E_0/v_{F1}}^0 \frac{1}{\frac{(q+k)^2}{2m} - \mu_2 - v_{F1}q - \omega} \\
&= \mathcal{P} \frac{1}{2\pi} \int_0^{E_0/v_{F1}} \frac{1}{\frac{(q-k)^2}{2m} - \mu_2 + v_{F1}q - \omega}.
\end{aligned} \tag{B.36}$$

Similarly, we find that $I_{pp}^{2,R}(\omega, k) = I_{pp}^{2,L}(\omega, -k)$, and thus only proceed with the right-movers. For these, we can rewrite the integral as

$$\operatorname{Re} \{I_{pp}^{2,R}\} = \mathcal{P} \frac{1}{2\pi} \int_0^{E_0/v_{F1}} \frac{2m}{(q - (k - mv_{F1}))^2 + k^2 - (k - mv_{F1})^2 - 2m\mu_2 - 2m\omega} \tag{B.37}$$

$$= \mathcal{P} \frac{1}{2\pi} \int_{-(k-mv_{F1})}^{E_0/v_{F1}-(k-mv_{F1})} \frac{2m}{q^2 - Q^2} \tag{B.38}$$

with $Q = \sqrt{(k - mv_{F1})^2 + 2m\mu_2 + 2m\omega - k^2} \approx mv_{F1}$. This can easily be integrated and yields

$$\begin{aligned}
\operatorname{Re} \{I_{pp}^{2,R}\} &= \frac{m}{\pi 2Q} \left[\ln \left(\left| \frac{E_0/v_{F1} - (k - mv_{F1}) - Q}{E_0/v_{F1} - (k - mv_{F1}) + Q} \right| \right) - \ln \left(\left| \frac{-(k - mv_{F1}) - Q}{-(k - mv_{F1}) + Q} \right| \right) \right] \\
&\approx \frac{1}{2\pi v_{F1}} \ln \left(\left| \frac{E_0/v_{F1}}{-k + mv_{F1} - Q} \right| \right),
\end{aligned} \tag{B.39}$$

where we used that $m\omega, k^2 \ll m^2 v_{F1}^2$. Finally, we expand Q as

$$Q \approx mv_{F1} + \frac{\mu_2 + \omega - v_{F1}k}{v_{F1}} \tag{B.40}$$

and obtain

$$\operatorname{Re} \{I_{pp}^{2,R}(\omega + i0^+, k)\} \approx \frac{1}{2\pi v_{F1}} \ln \left(\frac{E_0}{|\mu_2 + \omega|} \right). \tag{B.41}$$

B.3.2 Both particles in the first subband

If both particles are in the first subband, only diagrams involving one right- and one left-mover are logarithmically divergent. To demonstrate this, we consider a particle-particle bubble involving only right-movers, which is given by

$$\begin{aligned}
\operatorname{Re} \{I_{pp}^{R,R}(\omega + i0^+, k)\} &= \frac{1}{L} \mathcal{P} \sum_q \frac{n_F(-\epsilon_R(k-q)) - n_F(\epsilon_R(q))}{\epsilon_R(q) + \epsilon_R(k-q) - \omega} \\
&= \frac{1}{L} \mathcal{P} \sum_q \frac{n_F(-\epsilon_R(k-q)) - n_F(\epsilon_R(q))}{v_{F1}q + v_{F1}(k-q) - \omega} \\
&= \frac{1}{L} \mathcal{P} \sum_q \frac{n_F(-\epsilon_R(k-q)) - n_F(\epsilon_R(q))}{v_{F1}k - \omega},
\end{aligned} \tag{B.42}$$

which is simply the integral of a constant and thus not singular. We therefore only need to consider diagrams involving one right- and one left-mover,

$$\begin{aligned} \text{Re} \{ I_{pp}^{R,L}(\omega + i0^+, k) \} &= \frac{1}{L} \mathcal{P} \sum_q \frac{n_F(-\epsilon_L(k-q)) - n_F(\epsilon_R(q))}{\epsilon_R(q) + \epsilon_L(k-q) - \omega} \\ &= \frac{1}{L} \mathcal{P} \sum_q \frac{n_F(-\epsilon_L(k-q)) - n_F(\epsilon_R(q))}{v_{F1}q - v_{F1}(k-q) - \omega}. \end{aligned} \quad (\text{B.43})$$

Using that $n_F(-\epsilon_L) = n_F(\epsilon_R)$, taking the continuum limit and denoting $\epsilon = v_{F1}q$, we obtain

$$\text{Re} \{ I_{pp}^{R,L}(\omega + i0^+, k) \} = \mathcal{P} \int_{-\infty}^{\infty} \frac{d\epsilon}{2\pi v_{F1}} \frac{n_F(v_{F1}k - \epsilon) - n_F(\epsilon)}{2\epsilon - v_{F1}k - \omega}. \quad (\text{B.44})$$

Next, we introduce the high energy cutoff $E_0 \ll E_{F1}$ and obtain

$$\begin{aligned} \text{Re} \{ I_{pp}^{R,L}(\omega + i0^+, k) \} &= \mathcal{P} \int_{v_{F1}k}^{E_0} \frac{d\epsilon}{2\pi v_{F1}} \frac{1}{2\epsilon - v_{F1}k - \omega} \\ &\quad - \mathcal{P} \int_{-E_0}^0 \frac{d\epsilon}{2\pi v_{F1}} \frac{1}{2\epsilon - v_{F1}k - \omega}. \end{aligned} \quad (\text{B.45})$$

This can simply be integrated and yields

$$\begin{aligned} \text{Re} \{ I_{pp}^{R,L} \} &= \frac{1}{4\pi v_{F1}} \left[\ln \left(\left| \frac{2E_0 - v_{F1}k - \omega}{2v_{F1}k - v_{F1}k - \omega} \right| \right) - \ln \left(\left| \frac{-v_{F1}k - \omega}{-2E_0 - v_{F1}k - \omega} \right| \right) \right] \\ &\approx \frac{1}{2\pi v_{F1}} \ln \left(\frac{2E_0}{\sqrt{|\omega^2 - v_{F1}^2 k^2|}} \right), \end{aligned} \quad (\text{B.46})$$

which is the usual logarithmic divergence of perturbative processes in a Luttinger liquid.

B.4 Solution of the RG equations in the limit of large negative μ_2

In the limit of large negative μ_2 , scattering processes in the first, Luttinger liquid type band, yield logarithmically divergent diagrams. These divergencies can be summed up by a conventional perturbative RG, and the resulting RG equations have been found in Sec. 3.4 as

$$\frac{\partial g_{1s}}{\partial \ln b} = -\frac{g_{1s}^2}{2\pi v_{F1}}, \quad (\text{B.47a})$$

$$\frac{\partial V}{\partial \ln b} = -\frac{u_t^2}{\pi v_{F1}}, \quad (\text{B.47b})$$

$$\frac{\partial u_t}{\partial \ln b} = -\frac{(g_{1c} + 3g_{1s}/4)u_t}{2\pi v_{F1}}. \quad (\text{B.47c})$$

We will now integrate these equations. Firstly, spin the interaction within the first band, g_{1s} , integrates to

$$g_{1s}(b) = \frac{g_{1s}^0}{1 + g_{1s}^0/(2\pi v_{F1}) \ln(b)}, \quad (\text{B.48})$$

where g_{1s}^0 is the initial value of g_{1s} . This interaction thus goes logarithmically to weak coupling. It contributes initially to the flow of the pair tunneling, u_t , the scaling dimension of which however asymptotically approaches $(g_{1c}/(2\pi v_{F1}))$. The pair tunneling thus goes to zero as a power law with logarithmic corrections,

$$u_t(b) = u_t^0 b^{-g_{1c}/(2\pi v_{F1})} \left[1 + \frac{g_{1s}^0}{2\pi v_{F1}} \ln(b) \right]^{3/4}, \quad (\text{B.49})$$

where again u_s^0 is the initial value. This can now be plugged into the RG equation for the interaction in the second subband, V . Since u_t goes rapidly to zero, the flow of V is rather short. We find that it asymptotically only gets a finite renormalization, which reads

$$V_{\text{eff}} = V - \frac{(u_t^0)^2}{g_{1c}} \phi\left(\frac{g_{1s}^0}{g_{1c}}\right), \quad (\text{B.50})$$

where the function ϕ is asymptotically given by

$$\phi(x) = \frac{4}{x} + 4 e^{2/x} x^{-3/2} \sqrt{2\pi} \left(\text{Erf}\left(\sqrt{2/x}\right) - 1 \right) \quad (\text{B.51})$$

and has the limits $\phi(0) = 1$ and $\phi(x) \approx 4/x$ for $x \rightarrow \infty$. We finally note that we have dropped the superscripts $X^0 \rightarrow X$ for the coupling X in the main text for improved readability.

B.5 RG at $\mu_2 = 0$

At criticality, i.e. for $\mu_2 = 0$, Balents and Fisher have derived the RG equations

$$\frac{\partial g_{1c}}{\partial \ln b} = -\frac{u_t^2}{4\pi v}, \quad (\text{B.52a})$$

$$\frac{\partial g_{1s}}{\partial \ln b} = -\frac{g_{1s}^2}{2\pi v_{F1}} - \frac{u_t^2}{\pi v}, \quad (\text{B.52b})$$

$$\frac{\partial V}{\partial \ln b} = \epsilon V - \frac{V^2}{2\pi v} - \frac{u_t^2}{\pi v_{F1}}, \quad (\text{B.52c})$$

$$\frac{\partial u_c}{\partial \ln b} = \frac{u_t^2}{2\pi(v_{F1} + v)}, \quad (\text{B.52d})$$

$$\frac{\partial u_s}{\partial \ln b} = -\frac{u_s^2}{2\pi(v_{F1} + v)}, \quad (\text{B.52e})$$

$$\frac{\partial u_t}{\partial \ln b} = \left(\frac{\epsilon}{2} - \frac{V}{2\pi v} + \frac{2u_c}{\pi(v_{F1} + v)} - \frac{g_{1c} + \frac{3}{4}g_{1s}}{2\pi v_{F1}} \right) u_t. \quad (\text{B.52f})$$

using an ϵ -expansion in the dispersion of the second subband, which they approximated by $\varepsilon(k) = |k|^{1+\epsilon} v^{1-\epsilon}/(2m)^\epsilon$. The details of this calculation and the derivation of the RG equations can be found in Ref. [33]. The flow of Eqs. (B.52) can be divided into

several stages. To this end, it is useful to recall that $\epsilon \rightarrow 1$ in the physical system, such that terms linear in ϵ are to be considered as much larger than terms linear in the initial values of the coupling constants. The very initial RG flow is thus driven by the two terms linear in ϵ , which initially make the couplings V and u_t grow very rapidly. The initially important terms of the RG flow are thus given by

$$\frac{\partial g_{1c}}{\partial \ln b} = -\frac{u_t^2}{4\pi v}, \quad (\text{B.53a})$$

$$\frac{\partial g_{1s}}{\partial \ln b} = -\frac{u_t^2}{\pi v}, \quad (\text{B.53b})$$

$$\frac{\partial V}{\partial \ln b} = \epsilon V - \frac{V^2}{2\pi v} - \frac{u_t^2}{\pi v_{F1}}, \quad (\text{B.53c})$$

$$\frac{\partial u_c}{\partial \ln b} = \frac{u_t^2}{2\pi(v_{F1} + v)}, \quad (\text{B.53d})$$

$$\frac{\partial u_t}{\partial \ln b} = \left(\frac{\epsilon}{2} - \frac{V}{2\pi v} \right) u_t. \quad (\text{B.53e})$$

These equations have a non-trivial fixed point at $V/(2\pi v) = \epsilon$, $u_t = 0$. We can thus conclude that after a first rapid rise, the pair tunneling coupling u_t is suppressed again and flows to weak coupling. This fixed point naturally corresponds to the impenetrable electron gas fixed point: the interaction in the second subband is strong, while the pair tunneling is suppressed. The initial flow thus corresponds to summing up all square-root divergences in the perturbation theory, which indeed are the most divergent terms. Only once the system has reached the impenetrable electron gas fixed point, the additional terms of Eqs. (B.52) become important and yield the same secondary flow as obtained in Sec. 3.5.

B.5.1 Intermediate stationary point

On the flow towards this fixed point, V grows more or less continuously with a scaling dimension that is of order ϵ . The pair tunneling u_t , on the other hand, first increases, but then slows down rapidly, until it reaches an approximate fixed point when V is close to $V/(2\pi v) \approx \epsilon/2$. Since this intermediate stationary point corresponds to the maximal value of u_t , and since it is a stationary point, we expect that the biggest part of all renormalization due to u_t stem from this intermediate RG stage $b = b_{\max}$. Since at this scale the coupling V is already much bigger than the pair tunneling, $V(b_{\max}) \gg u_t(b_{\max})$, we can analyze the intermediate stationary point by approximating the flow of V by

$$\left. \frac{\partial V}{\partial \ln b} \right|_{b \approx b_{\max}} = \epsilon V - \frac{V^2}{2\pi v}, \quad (\text{B.54})$$

$$V(b_{\max}) = \frac{\epsilon}{2}, \quad (\text{B.55})$$

which yields

$$V(b \approx b_{\max}) \approx 2\pi v \left[\frac{\epsilon}{2} + \frac{\epsilon^2}{4} \ln(b/b_{\max}) \right]. \quad (\text{B.56})$$

Plugging this into the equation for the pair tunneling, we find

$$u_t(b \approx b_{\max}) \approx u_t(b_{\max}) e^{-\epsilon^2/8 \ln^2(b/b_{\max})} \quad (\text{B.57})$$

The maximal value of the pair-tunneling, $u_{t\max}$, is obtained from the approximate RG invariant of the initial flow. Considering the coupled equations (B.52c) and (B.52f), and keeping only the dominant first two terms in Eq. (B.52f), one finds the approximate RG invariant $\mathcal{I} = (\epsilon V - V^2/(2\pi v))\pi v_{F1}/u_t^2 + 2 \ln u_t$ with $\partial\mathcal{I}/\partial \ln b = 0$. With $V(b_m)/(2\pi v) = \epsilon/2$, the maximal pair tunneling is then given by the implicit formula

$$\left(\epsilon V^0 - \frac{(V^0)^2}{2\pi v} \right) \frac{\pi v_{F1}}{(u_t^0)^2} + 2 \ln(u_t^0) = \left(\epsilon V(b_{\max}) - \frac{V(b_{\max})^2}{2\pi v} \right) \frac{\pi v_{F1}}{u_t(b_{\max})^2} + 2 \ln(u_t(b_{\max})) , \quad (\text{B.58})$$

where the superscript 0 indicates the initial values of the respective coupling constants. Dropping the logarithms (which are slowly varying functions) and neglecting the V^2 -term with respect to $\epsilon V \gg V^2$, one finds

$$u_{t\max} \approx u_t^0 \sqrt{\pi v \epsilon / (2V^0)} \quad (\text{B.59})$$

i.e., the pair-tunneling close to b_{\max} is enhanced by the large factor $\sqrt{\pi v \epsilon / (2V^0)}$ with respect to its initial value.

B.5.2 Contribution of the stationary point to the total flow

The contribution of the stationary point to the initial flow can be estimated by plugging

$$u_t(b) \approx u_t^0 \sqrt{\pi v \epsilon / (2V^0)} e^{-\epsilon^2/8 \ln^2(b/b_{\max})} \quad (\text{B.60a})$$

into the approximate RG equations of g_{1c} and g_{1s} close to this approximate fixed point, which read

$$\frac{\partial g_{1x}}{\partial \ln b} = -C_x \frac{(u_t^0)^2}{2\pi v} , \quad (\text{B.61})$$

where $C_c = 1/2$ and $C_s = 2$ like in Eq. (3.52). Integrating these equations yields the asymptotic value

$$g_{1x}^{\text{eff}} = g_{1x}^0 - C_x \frac{\sqrt{\pi}}{4} \frac{(u_t^0)^2}{V^0} , \quad (\text{B.62})$$

where again g_{1x}^0 denotes the initial value of g_{1x} . The stationary point of the RG flow thus accounts already for a reduction of the coupling constant with a prefactor $\sqrt{\pi}/4$ as compared to the full reduction obtained in section 3.5.

B.5.3 Full initial flow

We can also try to find an approximate solution for the full initial of the RG flow. To do this, we realize that u_t is generally much smaller than V , except for the very initial RG

flow, which however is governed by ϵ . The full first stage of the RG is thus described by the equations

$$\frac{\partial g_{1x}}{\partial \ln b} = -C_x \frac{u_t^2}{2\pi v}, \quad (\text{B.63a})$$

$$\frac{\partial V}{\partial \ln b} = \epsilon V - \frac{V^2}{2\pi v}, \quad (\text{B.63b})$$

$$\frac{\partial u_t}{\partial \ln b} = \left(\frac{\epsilon}{2} - \frac{V}{2\pi v} \right) u_t, \quad (\text{B.63c})$$

again using $C_c = 1/2$ and $C_s = 2$. These equations can simply be integrated. At the end of the first stage, we exactly recover the expressions of Sec. 3.5 for the couplings in the first band, namely

$$g_{1x}^{\text{eff}} = g_{1x}^0 - C_x \frac{(u_t^0)^2}{V^0}. \quad (\text{B.64})$$

We finally note that we have dropped the superscripts $X^0 \rightarrow X$ for the coupling X in the main text for improved readability.

B.6 Analytical evaluation of the coupling strengths

The magnitude of the coupling constants follows from the microscopic model (2.1) as the matrix elements of the interaction, calculated for the wavefunctions of the first and second subband. The corresponding oscillator eigenfunctions are

$$\phi_1(y) = \left(\frac{m\Omega}{\pi} \right)^{1/4} e^{-\frac{1}{2}m\Omega y^2}, \quad (\text{B.65a})$$

$$\phi_2(y) = \sqrt{2m\Omega} \left(\frac{m\Omega}{\pi} \right)^{1/4} y e^{-\frac{1}{2}m\Omega y^2}. \quad (\text{B.65b})$$

These wave functions yield

$$\Gamma_{1111}(q_y) = e^{-q_y^2/(2m\Omega)}, \quad (\text{B.66})$$

$$\Gamma_{2222}(q_y) = e^{-q_y^2/(2m\Omega)} \left(\frac{2m\Omega - q_y^2}{2m\Omega} \right)^2, \quad (\text{B.67})$$

$$\Gamma_{1221}(q_y) = e^{-q_y^2/(2m\Omega)} \frac{2m\Omega - q_y^2}{2m\Omega}, \quad (\text{B.68})$$

$$\Gamma_{1122}(q_y) = e^{-q_y^2/(2m\Omega)} \frac{q_y^2}{2m\Omega} = \Gamma_{1212}(q_y). \quad (\text{B.69})$$

While the integrals resulting from Eq. (3.5) are rather complicated, one can calculate them analytically using some simplifications. As a first step, the exponentials in $\Gamma_{n_1 n_2 n_3 n_4}$ may be approximated by Heaviside step functions,

$$e^{-q_y^2/(2m\Omega)} = e^{-q_y^2 x_0^2/2} \approx \theta(q_y x_0 + 1) - \theta(q_y x_0 - 1). \quad (\text{B.70})$$

All transverse momenta thus have to be compared with the inverse oscillator length x_0^{-1} , which is of course the natural momentum scale for the transverse confinement. In the case of a quantum wire close to the activation of the second subband, where $x_0 n \sim 1$ and $n > 1/d$, one can furthermore take the limit $x_0 \ll d$. The integral then decomposes in two parts. The very long range part, corresponding to small momenta $q_x < d^{-1}$, is screened. At larger momenta, the interaction is only weakly screened, and one can set $\exp(-2d\sqrt{q_x^2 + q_y^2}) \rightarrow 0$. With these approximations and to leading order, the relevant interaction matrix elements have the form

$$U_{1111}(0) = \frac{2e^2}{\epsilon} \ln \left(\frac{d}{x_0} \right), \quad (\text{B.71})$$

$$U_{1111}(2k_{F1}) = \frac{2e^2}{\epsilon} \ln \left(\frac{1 + \sqrt{1 + (2k_{F1}x_0)^2}}{2k_{F1}x_0} \right), \quad (\text{B.72})$$

$$U_{2222}(0) = \frac{2e^2}{\epsilon} \ln \left(\frac{d}{x_0} \right), \quad (\text{B.73})$$

$$U_{1221}(0) = \frac{2e^2}{\epsilon} \ln \left(\frac{d}{x_0} \right), \quad (\text{B.74})$$

$$U_{1221}(k_{F1}) = \frac{2e^2}{\epsilon} \left(\frac{1}{4} \ln \left(\frac{1 + \sqrt{1 + k_{F1}^2 x_0^2}}{k_{F1} x_0} \right) (4 + k_{F1}^2 x_0^2) - \frac{1}{4} \sqrt{1 + k_{F1}^2 x_0^2} \right), \quad (\text{B.75})$$

$$U_{1122}(k_{F1}) = \frac{2e^2}{\epsilon} \frac{1}{4} \left(\sqrt{1 + k_{F1}^2 x_0^2} + k_{F1}^2 x_0^2 \ln \left(\frac{k_{F1} x_0}{1 + \sqrt{1 + k_{F1}^2 x_0^2}} \right) \right), \quad (\text{B.76})$$

where $k_{F1} = \sqrt{2m\mu_1} \sim n$. Note that, when the Wigner crystal regime is approached, $na_B \rightarrow 1$, the dimensionless couplings $\nu_1 U_{n_1 n_2 n_3 n_4}$ become of order one (apart from the logarithmic enhancement⁵⁹), as expected. In the multiband quantum wire regime, however, the interactions are small and can be treated perturbatively. Using the density of states in the filled lower subband, $\nu_1 = (2/\pi)\sqrt{m/(2\mu_1)}$, and exploiting $k_{F1}x_0 \sim 1$ close to the transition, the effective interactions in the multiband quantum wire model are

$$g_{1s}, u_s, u_t \sim \frac{1}{\nu_1 na_B}, \quad (\text{B.77a})$$

$$g_{1c}, V, u_c \sim \frac{1}{\nu_1 na_B} \ln \frac{d}{x_0}, \quad (\text{B.77b})$$

such that in particular the pair tunneling is logarithmically smaller than the intraband interactions V and g_{1c} .

B.7 Canonical transformation to polarons

Our starting point is the following Hamiltonian, that already describes the first band in terms of a Luttinger liquid, but leaving the second band in a generic fermionic description. It reads

$$\mathcal{H} = \mathcal{H}_1 + \mathcal{H}_2 + \mathcal{H}_{12, \text{marg}} + \mathcal{H}'_{12} \quad (\text{B.78})$$

with

$$\begin{aligned} \mathcal{H}_1 = & \frac{1}{2\pi} \int dx \left(u_\rho^{(1)} K_\rho^{(1)} (\partial_x \theta_\rho^{(1)}(x))^2 + \frac{u_\rho^{(1)}}{K_\rho^{(1)}} (\partial_x \phi_\rho^{(1)}(x))^2 \right) \\ & + \frac{1}{2\pi} \int dx \left(u_\sigma^{(1)} K_\sigma^{(1)} (\partial_x \theta_\sigma^{(1)}(x))^2 + \frac{u_\sigma^{(1)}}{K_\sigma^{(1)}} (\partial_x \phi_\sigma^{(1)}(x))^2 \right) \\ & + \frac{g_{1\perp(1)}}{(2\pi\alpha_1)^2} \int dx \left(F_{1L\uparrow}^\dagger F_{1R\downarrow}^\dagger F_{1L\downarrow} F_{1R\uparrow} e^{-i\sqrt{8}\phi_\sigma^{(1)}} + \text{h.c.} \right), \end{aligned} \quad (\text{B.79})$$

$$\begin{aligned} \mathcal{H}_2 = & \sum_{s=\uparrow,\downarrow} \int dx \Psi_{2s}^\dagger(x) \left(-\frac{1}{2m_2} \partial_x^2 - \frac{k_{F2}}{2m_2} \right) \Psi_{2s}(x) \\ & + \sum_{s1,s2,s3,s4} \frac{1}{2} \int dx \int dx' V_{s1,s2,s3,s4}(x-x') \Psi_{2s1}^\dagger(x) \Psi_{2s2}^\dagger(x') \Psi_{2s3}(x') \Psi_{2s4}(x), \end{aligned} \quad (\text{B.80})$$

$$\mathcal{H}_{12,marg} = u_c \int dx \left(-\frac{\sqrt{2}}{\pi} \right) (\partial_x \phi_\rho^{(1)}) (\rho_{2\uparrow} + \rho_{2\downarrow}) - \frac{u_s}{2} \int dx \left(-\frac{\sqrt{2}}{\pi} \right) (\partial_x \phi_\sigma^{(1)}) (\rho_{2\uparrow} - \rho_{2\downarrow}) \quad (\text{B.81})$$

and

$$\begin{aligned} \mathcal{H}'_{12} = & -\frac{u_s}{2} \int dx \left(\left(F_{R1\uparrow}^\dagger F_{R1\downarrow} e^{i\sqrt{2}(\phi_\sigma^{(1)} - \theta_\sigma^{(1)})} + F_{L1\uparrow}^\dagger F_{L1\downarrow} e^{-i\sqrt{2}(\phi_\sigma^{(1)} + \theta_\sigma^{(1)})} \right) \Psi_{2\downarrow}^\dagger \Psi_{2\uparrow} + \text{h.c.} \right) \\ & + \mathcal{H}_{12t}. \end{aligned} \quad (\text{B.82})$$

In these equations, $\mathcal{H}_{12,marg}$ are the RG marginal interactions responsible for the unphysical divergence in a straightforward bosonization (i.e. without transforming to polaronic degrees of freedom), while \mathcal{H}_{12t} still describes pair tunneling between the two bands. The commutation relations for the bosonic fields are taken to be

$$[\phi_\mu^{(1)}(x), \theta_\nu^{(1)}(x')] = i\pi \delta_{\mu\nu} \theta(x' - x), \quad (\text{B.83})$$

with $\mu, \nu \in \{\sigma, \rho\}$. As this implies

$$[\phi_\mu^{(1)}(\infty), \theta_\nu^{(1)}(x')] = 0, \quad (\text{B.84})$$

we will furthermore assign the value

$$\phi_\mu^{(1)}(\infty) = 0 \quad (\text{B.85})$$

to the ϕ -fields at $+\infty$. As a technical side remark, note that one may also specify the equal point commutator a bit more. Using the commutation relation between the original chiral fermionic operators in the first band,

$$\{\Psi_{L1s}(x), \Psi_{R1s}(x)\} = 0 \text{ with } s = \uparrow, \downarrow, \quad (\text{B.86})$$

one can show that also the bosonic equal point commutator reads

$$[\phi_\mu^{(1)}(x), \theta_\nu^{(1)}(x)] = i\pi \delta_{\mu\nu} m \text{ with } m \in \mathbb{Z}. \quad (\text{B.87})$$

We will now get rid of the marginal interactions by transforming the fields to polaronic excitations. In order to do so, we rewrite

$$\begin{aligned}
 \mathcal{H} &= (\mathcal{H}_1 + \mathcal{H}_{12,marg}) + \mathcal{H}_2 + \mathcal{H}'_{12} \\
 &= \frac{1}{2\pi} \int dx \left(u_\rho^{(1)} K_\rho^{(1)} (\partial_x \theta_\rho^{(1)}(x))^2 + \frac{u_\rho^{(1)}}{K_\rho^{(1)}} \left[\partial_x \phi_\rho^{(1)}(x) + \frac{K_\rho^{(1)}}{u_\rho^{(1)}} (-\sqrt{2}) u_c (\rho_{2\uparrow} + \rho_{2\downarrow}) \right]^2 \right) \\
 &+ \frac{1}{2\pi} \int dx \left(u_\sigma^{(1)} K_\sigma^{(1)} (\partial_x \theta_\sigma^{(1)}(x))^2 + \frac{u_\sigma^{(1)}}{K_\sigma^{(1)}} \left[\partial_x \phi_\sigma^{(1)}(x) - \frac{K_\sigma^{(1)}}{u_\sigma^{(1)}} (-\sqrt{2}) \frac{u_s}{4} (\rho_{2\uparrow} - \rho_{2\downarrow}) \right]^2 \right) \\
 &+ \frac{g_{1\perp(1)}}{(2\pi\alpha_1)^2} \int dx \left(F_{1L\uparrow}^\dagger F_{1R\downarrow}^\dagger F_{1L\downarrow} F_{1R\uparrow} e^{-i\sqrt{8}\phi_\sigma^{(1)}} + \text{h.c.} \right) \tag{B.88} \\
 &- \frac{1}{2\pi} \int dx \frac{K_\rho^{(1)}}{u_\rho^{(1)}} 2 u_c^2 (\rho_{2\uparrow} + \rho_{2\downarrow})^2 + \frac{1}{2\pi} \int dx \frac{K_\sigma^{(1)}}{u_\sigma^{(1)}} 2 \left(\frac{u_s}{4} \right)^2 (\rho_{2\uparrow} - \rho_{2\downarrow})^2 \\
 &+ \mathcal{H}_2 + \mathcal{H}'_{12}
 \end{aligned}$$

The transformation for the fields in the first band is now rather obvious and reads:

$$\phi_\rho^{(1)'}(x) = \phi_\rho^{(1)} + \sqrt{2} \frac{K_\rho^{(1)}}{u_\rho^{(1)}} u_c \int_x^\infty dx' (\rho_{2\uparrow}(x') + \rho_{2\downarrow}(x')) , \tag{B.89}$$

$$\theta_\rho^{(1)'}(x) = \theta_\rho^{(1)}(x) , \tag{B.90}$$

$$\phi_\sigma^{(1)'}(x) = \phi_\sigma^{(1)}(x) - \sqrt{2} \frac{K_\sigma^{(1)}}{u_\sigma^{(1)}} \frac{u_s}{4} \int_x^\infty dx' (\rho_{2\uparrow}(x') - \rho_{2\downarrow}(x')) , \tag{B.91}$$

$$\theta_\sigma^{(1)'}(x) = \theta_\sigma^{(1)}(x) . \tag{B.92}$$

In order to conserve also the commutation relations with the operators in the second band, these have to transform according to

$$c'_{2\uparrow}(x) = e^{i\frac{1}{\pi}(\gamma_\rho\theta_\rho(x) + \gamma_\sigma\theta_\sigma(x))} c_{2\uparrow}(x) , \tag{B.93}$$

$$c'_{2\downarrow}(x) = e^{i\frac{1}{\pi}(\gamma_\rho\theta_\rho(x) - \gamma_\sigma\theta_\sigma(x))} c_{2\downarrow}(x) , \tag{B.94}$$

with

$$\gamma_\rho = -\sqrt{2} \frac{K_\rho^{(1)}}{u_\rho^{(1)}} u_c \quad \text{and} \quad \gamma_\sigma = \sqrt{2} \frac{K_\sigma^{(1)}}{u_\sigma^{(1)}} \frac{u_s}{4} . \tag{B.95}$$

Plugging these transformations into the Hamiltonian removes the RG marginal interactions and generates a residual interaction (see Eq. (B.100)). This interaction contains quadratic terms, which can be diagonalized by a simple rotation, and higher order terms, which are irrelevant in the RG sense.

B.8 Second bosonization and final form of the Hamiltonian

After having switched to the physically relevant degrees of freedom, we may now proceed to the bosonization of the second subband, now containing polarons. This is done in

complete analogy to the first band's bosonization, leading to e.g. the same commutation relations. For the sake of readability, we drop all primes on the transformed fields. Focusing on the most important interaction terms coupling right- and left-movers (and dropping for instance terms that couple left-movers to left-movers), the Hamiltonian reads:

$$\mathcal{H} = \mathcal{H}_0 + \mathcal{H}_{int,1} + \mathcal{H}_{int,2} + \tilde{\mathcal{H}}_{int,res} + \mathcal{H}_{int,12} \quad (\text{B.96})$$

with

$$\begin{aligned} \mathcal{H}_0 = & \frac{1}{2\pi} \int dx \left(u_\rho^{(1)} K_\rho^{(1)} (\partial_x \theta_\rho^{(1)}(x))^2 + \frac{u_\rho^{(1)}}{K_\rho^{(1)}} (\partial_x \phi_\rho^{(1)}(x))^2 \right) \\ & + \frac{1}{2\pi} \int dx \left(u_\sigma^{(1)} K_\sigma^{(1)} (\partial_x \theta_\sigma^{(1)}(x))^2 + \frac{u_\sigma^{(1)}}{K_\sigma^{(1)}} (\partial_x \phi_\sigma^{(1)}(x))^2 \right) \\ & + \frac{1}{2\pi} \int dx \left(u_\rho^{(2)} K_\rho^{(2)} (\partial_x \theta_\rho^{(2)}(x))^2 + \frac{u_\rho^{(2)}}{K_\rho^{(2)}} (\partial_x \phi_\rho^{(2)}(x))^2 \right) \\ & + \frac{1}{2\pi} \int dx \left(u_\sigma^{(2)} K_\sigma^{(2)} (\partial_x \theta_\sigma^{(2)}(x))^2 + \frac{u_\sigma^{(2)}}{K_\sigma^{(2)}} (\partial_x \phi_\sigma^{(2)}(x))^2 \right), \end{aligned} \quad (\text{B.97})$$

$$\mathcal{H}_{int,1} = \frac{g_{1\perp(1)}}{(2\pi\alpha_1)^2} \int dx \left(F_{1L\uparrow}^\dagger F_{1R\downarrow}^\dagger F_{1L\downarrow} F_{1R\uparrow} e^{-i\sqrt{8}(\phi_\sigma^{(1)} - \frac{K_\sigma^{(1)}}{u_\sigma^{(1)}} \frac{2J}{4\pi} \phi_\sigma^{(2)})} + \text{h.c.} \right), \quad (\text{B.98})$$

$$\mathcal{H}_{int,2} = \frac{g_{2\perp(1)}}{(2\pi\alpha_2)^2} \int dx \left(F_{2L\uparrow}^\dagger F_{2R\downarrow}^\dagger F_{2L\downarrow} F_{2R\uparrow} e^{-i\sqrt{8}\phi_\sigma^{(2)}} + \text{h.c.} \right), \quad (\text{B.99})$$

$$\begin{aligned} \tilde{\mathcal{H}}_{int,res} = & \frac{1}{2\pi} \int dx \left(-\frac{\sqrt{2}}{m_2} \left[\left(\frac{\gamma_\rho}{\pi} \partial_x \theta_\rho^{(1)} \right)^2 + \left(\frac{\gamma_\sigma}{\pi} \partial_x \theta_\sigma^{(1)} \right)^2 \right] (\partial_x \phi_\rho^{(2)}) \right. \\ & \left. - \frac{\sqrt{2}}{m_2} 2 \left(\frac{\gamma_\rho}{\pi} \partial_x \theta_\rho^{(1)} \right) \left(\frac{\gamma_\sigma}{\pi} \partial_x \theta_\sigma^{(1)} \right) (\partial_x \phi_\sigma^{(2)}) \right) \\ & + \frac{1}{2\pi} \int dx \left(-2 \frac{\sqrt{2}}{\pi} \gamma_\rho u_\rho^{(2)} K_\rho^{(2)} (\partial_x \theta_\rho^{(1)}) (\partial_x \theta_\rho^{(2)}) - 2 \frac{\sqrt{2}}{\pi} \gamma_\sigma u_\sigma^{(2)} K_\sigma^{(2)} (\partial_x \theta_\sigma^{(1)}) (\partial_x \theta_\sigma^{(2)}) \right), \end{aligned} \quad (\text{B.100})$$

where m_2 is the mass in the second band, and finally

$$\begin{aligned}
 \mathcal{H}_{int,12} = & \frac{g_{t\parallel}}{(2\pi)^2 \alpha_1 \alpha_2} \int \left\{ dx F_{1R\uparrow}^\dagger F_{1L\uparrow}^\dagger F_{2L\uparrow} F_{2R\uparrow} e^{-i\sqrt{2} \left(\left[1 - \frac{K_\rho^{(1)}}{u_\rho^{(1)}} \frac{2u_c}{\pi} \right] \theta_\rho^{(1)} + \left[1 - \frac{K_\sigma^{(1)}}{u_\sigma^{(1)}} \frac{2J}{4\pi} \right] \theta_\sigma^{(1)} - \theta_\rho^{(2)} - \theta_\sigma^{(2)} \right)} \right. \\
 & + F_{1R\downarrow}^\dagger F_{1L\downarrow}^\dagger F_{2L\downarrow} F_{2R\downarrow} e^{-i\sqrt{2} \left(\left[1 - \frac{K_\rho^{(1)}}{u_\rho^{(1)}} \frac{2U_{12}}{\pi} \right] \theta_\rho^{(1)} - \left[1 - \frac{K_\sigma^{(1)}}{u_\sigma^{(1)}} \frac{2J}{4\pi} \right] \theta_\sigma^{(1)} + \theta_\sigma^{(2)} - \theta_\rho^{(2)} \right)} \\
 & \left. + \text{h.c.} \right\} \tag{B.101} \\
 & + \frac{g_{t\perp(2)}}{(2\pi)^2 \alpha_1 \alpha_2} \int \left\{ dx F_{1R\uparrow}^\dagger F_{1L\downarrow}^\dagger F_{2L\downarrow} F_{2R\uparrow} e^{i\sqrt{2} \left(\phi_{\sigma^{(1)}} - \left[1 - \frac{K_\rho^{(1)}}{u_\rho^{(1)}} \frac{2U_{12}}{\pi} \right] \theta_\rho^{(1)} - \left[1 + \frac{K_\sigma^{(1)}}{u_\sigma^{(1)}} \frac{2J}{4\pi} \right] \phi_\sigma^{(2)} + \theta_\rho^{(2)} \right)} \right. \\
 & + F_{1R\downarrow}^\dagger F_{1L\uparrow}^\dagger F_{2L\uparrow} F_{2R\downarrow} e^{-i\sqrt{2} \left(\phi_\sigma^{(1)} + \left[1 - \frac{K_\rho^{(1)}}{u_\rho^{(1)}} \frac{2U_{12}}{\pi} \right] \theta_\rho^{(1)} - \left[1 + \frac{K_\sigma^{(1)}}{u_\sigma^{(1)}} \frac{2J}{4\pi} \right] \phi_\sigma^{(2)} - \theta_\rho^{(2)} \right)} \\
 & \left. + \text{h.c.} \right\} \\
 & + \frac{g_{t\perp(1)}}{(2\pi)^2 \alpha_1 \alpha_2} \int \left\{ dx F_{1R\downarrow}^\dagger F_{1L\uparrow}^\dagger F_{2R\uparrow} F_{2L\downarrow} e^{-i\sqrt{2} \left(\phi_{\sigma^{(1)}} + \left[1 - \frac{K_\rho^{(1)}}{u_\rho^{(1)}} \frac{2U_{12}}{\pi} \right] \theta_\rho^{(1)} + \left[1 - \frac{K_\sigma^{(1)}}{u_\sigma^{(1)}} \frac{2J}{4\pi} \right] \phi_\sigma^{(2)} - \theta_\rho^{(2)} \right)} \right. \\
 & + F_{1R\uparrow}^\dagger F_{1L\downarrow}^\dagger F_{2R\downarrow} F_{2L\uparrow} e^{i\sqrt{2} \left(\phi_\sigma^{(1)} - \left[1 - \frac{K_\rho^{(1)}}{u_\rho^{(1)}} \frac{2U_{12}}{\pi} \right] \theta_\rho^{(1)} + \left[1 - \frac{K_\sigma^{(1)}}{u_\sigma^{(1)}} \frac{2J}{4\pi} \right] \phi_\sigma^{(2)} + \theta_\rho^{(2)} \right)} \\
 & \left. + \text{h.c.} \right\} \\
 & + \frac{u_s^\perp}{2} \frac{1}{(2\pi)^2 \alpha_1 \alpha_2} \int dx \left\{ F_{1R\uparrow}^\dagger F_{2L\downarrow}^\dagger F_{1R\downarrow} F_{2L\uparrow} e^{i\sqrt{2} \left(\phi_\sigma^{(1)} - \left[1 - \frac{K_\rho^{(1)}}{u_\rho^{(1)}} \frac{2J}{4\pi} \right] \theta_\sigma^{(1)} + \left[1 - \frac{K_\sigma^{(1)}}{u_\sigma^{(1)}} \frac{2J}{4\pi} \right] \phi_\sigma^{(2)} + \theta_\sigma^{(2)} \right)} \right. \\
 & + F_{1L\uparrow}^\dagger F_{2R\downarrow}^\dagger F_{1L\downarrow} F_{2R\uparrow} e^{-i\sqrt{2} \left(\phi_\sigma^{(1)} + \left[1 - \frac{K_\rho^{(1)}}{u_\rho^{(1)}} \frac{2J}{4\pi} \right] \theta_\sigma^{(1)} + \left[1 - \frac{K_\sigma^{(1)}}{u_\sigma^{(1)}} \frac{2J}{4\pi} \right] \phi_\sigma^{(2)} - \theta_\sigma^{(2)} \right)} \\
 & \left. + \text{h.c.} \right\} .
 \end{aligned}$$

Thereby, $g_{t\parallel}$ is the coupling constant for pair tunneling of electrons with parallel spin, $g_{t\perp(2)}$ describes pair tunneling of electrons with opposite spin without spin flip (i.e. forward scattering tunneling), and $g_{t\perp(1)}$ describes pair tunneling with spin flip (backward scattering tunneling). In the limit of $E_{F2} \rightarrow 0$, these coupling constants can be expressed in terms of the pair tunneling u_t used in chapter as

$$g_{t\parallel} \rightarrow 0 , \tag{B.102}$$

$$g_{t\perp(1)}, g_{t\perp(2)} \rightarrow u_t . \tag{B.103}$$

We recall that there, the tunneling of a pair of equal spin was suppressed by powers of k_{F2} , a consequence of the Pauli principle forbidding a truly local pair tunneling since a distinction between right- and left-movers was impossible in the upper band for $k_{F2} \rightarrow 0$. This of course different for finite μ_2 . In addition, spin rotation invariance implies that

$$g_{t\parallel} = g_{t\perp(2)} - g_{t\perp(1)} , \quad (\text{B.104})$$

similarly to Eq. (4.20). Finally, we find that the pair tunneling terms break spin-charge separation because they transfer both the charge and the spin of an electron from one of the subbands to the other subband. Furthermore, the interband spin-flip coupling, u_s has been renamed into u_s^\perp for later convenience. Indeed, the coupling u_s shows up not only as the prefactor of a cosine-term in Eq. (B.101), but also in the Luttinger parameters. When we will derive the renormalization group equations, the coupling u_s^\perp will flow explicitly. The coupling u_s , on the contrary, has no explicit flow. It is rather the entire Luttinger parameter that flows, and the flow of the latter contains all flows of all couplings constants included into the Luttinger parameter. It is thus necessary to distinguish between u_s^\perp and u_s . The Luttinger parameters and velocities are defined as

$$K_\rho^{(1)} = \sqrt{\frac{\pi v_{F1} - \frac{g_{1\parallel} + g_{1\perp(2)}}{2}}{\pi v_{F1} + \frac{g_{1\parallel} + g_{1\perp(2)}}{2}}} , \quad K_\sigma^{(1)} = \sqrt{\frac{\pi v_{F1} - \frac{g_{1\parallel} - g_{1\perp(2)}}{2}}{\pi v_{F1} + \frac{g_{1\parallel} - g_{1\perp(2)}}{2}}} , \quad (\text{B.105})$$

$$K_\rho^{(2)} = \sqrt{\frac{\pi v_{F2} - \frac{g_{2\parallel}^{eff} + g_{2\perp(2)}^{eff}}{2}}{\pi v_{F2} + \frac{g_{2\parallel}^{eff} + g_{2\perp(2)}^{eff}}{2}}} , \quad K_\sigma^{(2)} = \sqrt{\frac{\pi v_{F2} - \frac{g_{2\parallel}^{eff} - g_{2\perp(2)}^{eff}}{2}}{\pi v_{F2} + \frac{g_{2\parallel}^{eff} - g_{2\perp(2)}^{eff}}{2}}} , \quad (\text{B.106})$$

$$u_\rho^{(1)} = v_{F1} \sqrt{1 - \left(\frac{g_{1\parallel} + g_{1\perp(2)}}{2\pi v_{F1}}\right)^2} , \quad u_\sigma^{(1)} = v_{F1} \sqrt{1 - \left(\frac{g_{1\parallel} - g_{1\perp(2)}}{2\pi v_{F1}}\right)^2} , \quad (\text{B.107})$$

$$u_\rho^{(2)} = v_{F2} \sqrt{1 - \left(\frac{g_{2\parallel}^{eff} + g_{2\perp(2)}^{eff}}{2\pi v_{F2}}\right)^2} , \quad u_\sigma^{(2)} = v_{F2} \sqrt{1 - \left(\frac{g_{2\parallel}^{eff} - g_{2\perp(2)}^{eff}}{2\pi v_{F2}}\right)^2} , \quad (\text{B.108})$$

with

$$g_{2\parallel}^{eff} = g_{2\parallel} - 4 \left(\frac{K_\rho^{(1)}}{u_{\rho(1)}} u_c^2 + \frac{K_\sigma^{(1)}}{u_{\sigma(1)}} \left(\frac{u_s}{4}\right)^2 \right) , \quad (\text{B.109})$$

$$g_{2\perp(2)}^{eff} = g_{2\parallel} - 4 \left(\frac{K_\rho^{(1)}}{u_{\rho(1)}} u_c^2 - \frac{K_\sigma^{(1)}}{u_{\sigma(1)}} \left(\frac{u_s}{4}\right)^2 \right) . \quad (\text{B.110})$$

B.8.1 Diagonalization of the remaining quadratic Hamiltonian

We now diagonalize the quadratic part of the Hamiltonian by a rotation and thereby absorb the quadratic terms in $\mathcal{H}_{int,res}$ into the velocities and Luttinger parameters. To this end, we introduce new fields defined by

$$\phi_\mu^+ = \sqrt{\frac{K_\mu^+}{u_\mu^+}} \left(\frac{1}{\sqrt{1+a_\mu^2}} \sqrt{\frac{u_\mu^{(1)}}{K_\mu^{(1)}}} \phi_\mu^{(1)} + \frac{a_\mu}{\sqrt{1+a_\mu^2}} \sqrt{\frac{u_\mu^{(2)}}{K_\mu^{(2)}}} \phi_\mu^{(2)} \right), \quad (\text{B.111})$$

$$\phi_\mu^- = \sqrt{\frac{K_\mu^-}{u_\mu^-}} \left(\frac{a_\mu}{\sqrt{1+a_\mu^2}} \sqrt{\frac{u_\mu^{(1)}}{K_\mu^{(1)}}} \phi_\mu^{(1)} - \frac{1}{\sqrt{1+a_\mu^2}} \sqrt{\frac{u_\mu^{(2)}}{K_\mu^{(2)}}} \phi_\mu^{(2)} \right), \quad (\text{B.112})$$

$$\theta_\mu^+ = \sqrt{\frac{u_\mu^+}{K_\mu^+}} \left(\frac{1}{\sqrt{1+a_\mu^2}} \sqrt{\frac{K_\mu^{(1)}}{u_\mu^{(1)}}} \theta_\mu^{(1)} + \frac{a_\mu}{\sqrt{1+a_\mu^2}} \sqrt{\frac{K_\mu^{(2)}}{u_\mu^{(2)}}} \theta_\mu^{(2)} \right), \quad (\text{B.113})$$

$$\theta_\mu^- = \sqrt{\frac{u_\mu^-}{K_\mu^-}} \left(\frac{a_\mu}{\sqrt{1+a_\mu^2}} \sqrt{\frac{K_\mu^{(1)}}{u_\mu^{(1)}}} \theta_\mu^{(1)} - \frac{1}{\sqrt{1+a_\mu^2}} \sqrt{\frac{K_\mu^{(2)}}{u_\mu^{(2)}}} \theta_\mu^{(2)} \right), \quad (\text{B.114})$$

with $\mu = \rho, \sigma$. The rotations are parametrized by

$$a_\rho = \frac{-\frac{\sqrt{2}}{\pi} \gamma_\rho u_\rho^{(2)2} \sqrt{\frac{u_\rho^{(1)} K_\rho^{(2)}}{u_\rho^{(2)} K_\rho^{(1)}}}}{\sqrt{\left(\frac{u_\rho^{(1)2} - u_\rho^{(2)2}}{2}\right)^2 + \left(\frac{\sqrt{2}}{\pi} \gamma_\rho u_\rho^{(2)2} \sqrt{\frac{u_\rho^{(1)} K_\rho^{(2)}}{u_\rho^{(2)} K_\rho^{(1)}}}\right)^2} + \frac{u_\rho^{(1)2} - u_\rho^{(2)2}}{2}}, \quad (\text{B.115})$$

$$a_\sigma = \frac{-\frac{\sqrt{2}}{\pi} \gamma_\sigma u_\sigma^{(2)2} \sqrt{\frac{u_\sigma^{(1)} K_\sigma^{(2)}}{u_\sigma^{(2)} K_\sigma^{(1)}}}}{\sqrt{\left(\frac{u_\sigma^{(1)2} - u_\sigma^{(2)2}}{2}\right)^2 + \left(\frac{\sqrt{2}}{\pi} \gamma_\sigma u_\sigma^{(2)2} \sqrt{\frac{u_\sigma^{(1)} K_\sigma^{(2)}}{u_\sigma^{(2)} K_\sigma^{(1)}}}\right)^2} + \frac{u_\sigma^{(1)2} - u_\sigma^{(2)2}}{2}}, \quad (\text{B.116})$$

$$(\text{B.117})$$

the new velocities are given by

$$u_\rho^\pm = \sqrt{\frac{u_\rho^{(1)2} + u_\rho^{(2)2}}{2} \pm \sqrt{\left(\frac{u_\rho^{(1)2} - u_\rho^{(2)2}}{2}\right)^2 + \left(\frac{\sqrt{2}}{\pi} \gamma_\rho u_\rho^{(2)2} \sqrt{\frac{u_\rho^{(1)} K_\rho^{(2)}}{u_\rho^{(2)} K_\rho^{(1)}}}\right)^2}}, \quad (\text{B.118})$$

$$u_\sigma^\pm = \sqrt{\frac{u_\sigma^{(1)2} + u_\sigma^{(2)2}}{2} \pm \sqrt{\left(\frac{u_\sigma^{(1)2} - u_\sigma^{(2)2}}{2}\right)^2 + \left(\frac{\sqrt{2}}{\pi} \gamma_\sigma u_\sigma^{(2)2} \sqrt{\frac{u_\sigma^{(1)} K_\sigma^{(2)}}{u_\sigma^{(2)} K_\sigma^{(1)}}}\right)^2}}, \quad (\text{B.119})$$

and the new Luttinger parameters are taken to have a bare value of 1,

$$K_\rho^+ = K_\rho^- = K_\sigma^+ = K_\sigma^- = 1. \quad (\text{B.120})$$

The Hamiltonian now reads

$$\mathcal{H} = \mathcal{H}_0 + \mathcal{H}_{int} \quad (\text{B.121})$$

with

$$\begin{aligned}
\mathcal{H}_0 = & \frac{1}{2\pi} \int dx \left(u_\rho^+ K_\rho^+ (\partial_x \theta_\rho^+(x))^2 + \frac{u_\rho^+}{K_\rho^+} (\partial_x \phi_\rho^+(x))^2 \right) \\
& + \frac{1}{2\pi} \int dx \left(u_\sigma^+ K_\sigma^+ (\partial_x \theta_\sigma^+(x))^2 + \frac{u_\sigma^+}{K_\sigma^+} (\partial_x \phi_\sigma^+(x))^2 \right) \\
& + \frac{1}{2\pi} \int dx \left(u_\rho^- K_\rho^- (\partial_x \theta_\rho^-(x))^2 + \frac{u_\rho^-}{K_\rho^-} (\partial_x \phi_\rho^-(x))^2 \right) \\
& + \frac{1}{2\pi} \int dx \left(u_\sigma^- K_\sigma^- (\partial_x \theta_\sigma^-(x))^2 + \frac{u_\sigma^-}{K_\sigma^-} (\partial_x \phi_\sigma^-(x))^2 \right),
\end{aligned} \tag{B.122}$$

while the interaction is given by

$$\mathcal{H}_{int} = \mathcal{H}_{res} + \mathcal{H}_{int,1} + \mathcal{H}_{int,2} + \mathcal{H}_{int,12}, \tag{B.123}$$

where \mathcal{H}_{res} is the cubic part of $\tilde{\mathcal{H}}_{int,res}$ in equation (B.100), and the other interactions are defined like in equations (B.98), (B.99) and (B.101). For the sake of readability, we don't give the explicit expressions of the interactions in terms of the new fields here.

B.8.2 Comment on the singularity encountered without polaronic degrees of freedom

Before proceeding to the diagonalization of the of the Hamiltonian, we note that the canonical transformation yielded a quadratic current-current interaction and a term cubic in the fields. Still, we've managed to qualitatively improve the situation. The quadratic interaction is now smaller by a factor $u_\rho^{(2)}$ ($u_\sigma^{(2)}$) than the initial one. Especially, one can show that this avoids the unphysical singularity we encountered before. Without the transformation to polaronic degrees of freedom, the singularity could not be avoided upon approaching the Lifshitz transition from above as the spin and charge velocities have to be smaller than some critical values eventually, see Sec. 4.2.3. After the transformation to polaronic degrees of freedom and diagonalization of the Hamiltonian, the singularity would be encountered for new critical velocities given by

$$u_{\sigma,2}^c{}' = \frac{u_{\sigma,1}^3}{K_{\sigma,1} K_{\sigma,2} (u_s / (2\pi))^2} \tag{B.124}$$

$$u_{\rho,2}^c{}' = \frac{u_{\rho,1}^3}{K_{\rho,1} K_{\rho,2} (2u_c / \pi)^2}. \tag{B.125}$$

As these velocities are much larger than $u_{\rho,1}, u_{\sigma,1}$, the singularity is avoided as advertised.

It is interesting to note that this singularity is reminiscent of the so-called Wentzel-Bardeen singularity encountered in one-dimensional electronic systems coupled to low momentum phonons, see for instance Refs. [182–184]). It has initially been investigated by Wentzel and Bardeen when they studied conventional superconductivity. There, the singularity marked a superconducting instability of the electronic degrees of freedom. It occurred when the coupling between the electrons and phonons exceeded a critical value essentially equivalent to Eqs. (4.44).

B.9 Derivation of the RG equations

The renormalization group (RG) equations for the coupling constants are derived following Ref. [22] by analyzing the renormalization of the free energy upon integrating out high energy shells. To this end, we divide the action into the quadratic part \mathcal{S}_0 and the interactions,

$$\mathcal{S} = \mathcal{S}_0 + \mathcal{S}_{int} . \quad (\text{B.126})$$

The free energy is defined as

$$F = -T \ln(Z) \quad \text{with} \quad Z = \int d\Phi d\theta e^{-\mathcal{S}} , \quad (\text{B.127})$$

where T is the temperature of the system. The partition function is expanded perturbatively as

$$Z = \int d\Phi d\theta e^{-\mathcal{S}} \quad (\text{B.128})$$

$$\approx \int d\Phi d\theta e^{-\mathcal{S}_0} \left(1 - \mathcal{S}_{int} + \frac{1}{2} \mathcal{S}_{int}^2 \right) . \quad (\text{B.129})$$

The easiest way to derive the leading RG equations for the coupling constants is now to integrate out high energy shells and to identify the renormalizations of the action. The leading renormalization of the coupling constants can be found from the linear term in the perturbative expansion. Denoting the bare partition function by $Z_0 = \int d\Phi d\theta e^{-\mathcal{S}_0}$ and introducing

$$\langle (\cdot) \rangle_0 = \int d\Phi d\theta e^{-\mathcal{S}_0} (\cdot) , \quad (\text{B.130})$$

we have

$$\frac{Z}{Z_0} \approx 1 - \frac{1}{Z_0} \int \int d\Phi d\theta e^{-\mathcal{S}_0} \langle \mathcal{S}_{int} \rangle_0 . \quad (\text{B.131})$$

The averages of the interaction terms can easily be calculated. For a general term, one finds

$$\begin{aligned} & \langle \exp \left(i \sum_j [A_j \phi_j(x) + B \theta_j(x)] \right) \rangle_0 = \\ & \exp \left(-\frac{1}{2\beta L} \sum_{\vec{q}} \sum_j (B_j(-\vec{q}), A_j(-\vec{q})) M_j(\vec{q}) (B_j(\vec{q}), A_j(\vec{q}))^T \right) \end{aligned} \quad (\text{B.132})$$

with $\beta = T^{-1}$ and L being the length of the system and j comprises $(+, -)$ and (σ, ρ) , and $\vec{q} = (q, \omega_n)$. The propagator matrix is defined via its inverse

$$M_j^{-1}(\vec{q}) = \begin{pmatrix} \frac{q^2 u_j K_j}{\pi} & \frac{ik\omega_n}{\pi} \\ \frac{iq\omega_n}{\pi} & \frac{k^2 u_j}{K_j \pi} \end{pmatrix} . \quad (\text{B.133})$$

The next step is to introduce a circular high energy cutoff in momentum-frequency space and to integrate out high energy shells. Being linear in momentum and frequency, the off-diagonal terms in the above matrices vanish, and only diagonal terms are left. The latter only depend on the radius in the momentum-frequency plane, and the integrals over some small high energy shell can easily be evaluated. One is then left with a theory defined on smaller momentum scales. The final step is a rescaling of energy and momentum in order to obtain a theory with the initial form and cut-offs. As momentum and energy are the Fourier transforms of space and time, the rescaling has to be performed simultaneously for inverse and real space (a peculiarity of this calculation where real space and Fourier space appear at the same time). This yields a new effective coupling constant which depends on the reduction of the momentum cutoff, and its logarithmic derivative finally yields the RG equations.

B.10 Complete 1st order RG equations

The first order RG equations can now readily be calculated. We do not present intermediate steps of the calculation here which are far too lengthy to be of great use here, but the results follow straight-forwardly from the recipe in appendix B.9.

$$\begin{aligned} \frac{dg_{1\perp(1)}}{d \ln b} = g_{1\perp(1)} & \left(2 - 2 \left[\left(\sqrt{\frac{u_{\sigma}^{+} K_{\sigma}^{(1)}}{u_{\sigma}^{(1)}}} \frac{1}{\sqrt{1+a_{\sigma}^2}} - \frac{K_{\sigma}^{(1)} 2u_s}{u_{\sigma}^{(1)} 4\pi} \sqrt{\frac{u_{\sigma}^{+} K_{\sigma}^{(2)}}{u_{\sigma}^{(2)}}} \frac{a_{\sigma}}{\sqrt{1+a_{\sigma}^2}} \right)^2 \right. \right. \\ & \left. \left. + \left(\sqrt{\frac{u_{\sigma}^{-} K_{\sigma}^{(1)}}{u_{\sigma}^{(1)}}} \frac{a_{\sigma}}{\sqrt{1+a_{\sigma}^2}} + \frac{K_{\sigma}^{(1)} 2u_s}{u_{\sigma}^{(1)} 4\pi} \sqrt{\frac{u_{\sigma}^{-} K_{\sigma}^{(2)}}{u_{\sigma}^{(2)}}} \frac{1}{\sqrt{1+a_{\sigma}^2}} \right)^2 \right] \right), \end{aligned} \quad (\text{B.134a})$$

$$\frac{dg_{2\perp(1)}}{d \ln b} = g_{2\perp(1)} \left(2 - 2 \left[\left(\sqrt{\frac{u_{\sigma}^{+} K_{\sigma}^{(2)}}{u_{\sigma}^{(2)}}} \frac{a_{\sigma}}{\sqrt{1+a_{\sigma}^2}} \right)^2 + \left(\sqrt{\frac{u_{\sigma}^{-} K_{\sigma}^{(2)}}{u_{\sigma}^{(2)}}} \frac{1}{\sqrt{1+a_{\sigma}^2}} \right)^2 \right] \right), \quad (\text{B.134b})$$

$$\begin{aligned}
\frac{dg_{t\parallel}}{d\ln b} = g_{t\parallel} & \left(2 - \frac{1}{2} \left[\left(\left[1 - \frac{K_\sigma^{(1)} 2u_s}{u_\sigma^{(1)} 4\pi} \right] \sqrt{\frac{u_\sigma^{(1)}}{u_\sigma^+ K_\sigma^{(1)}} \frac{1}{\sqrt{1+a_\sigma^2}}} - \sqrt{\frac{u_\sigma^{(2)}}{u_\sigma^+ K_\sigma^{(2)}} \frac{a_\sigma}{\sqrt{1+a_\sigma^2}}} \right)^2 \right. \right. \\
& + \left(\left[1 - \frac{K_\sigma^{(1)} 2u_s}{u_\sigma^{(1)} 4\pi} \right] \sqrt{\frac{u_\sigma^{(1)}}{u_\sigma^- K_\sigma^{(1)}} \frac{a_\sigma}{\sqrt{1+a_\sigma^2}}} + \sqrt{\frac{u_\sigma^{(2)}}{u_\sigma^- K_\sigma^{(2)}} \frac{1}{\sqrt{1+a_\sigma^2}}} \right)^2 \\
& + \left(\left[1 - \frac{K_\rho^{(1)} 2u_c}{u_\rho^{(1)} \pi} \right] \sqrt{\frac{u_\rho^{(1)}}{u_\rho^+ K_\rho^{(1)}} \frac{1}{\sqrt{1+a_\rho^2}}} - \sqrt{\frac{u_\rho^{(2)}}{u_\rho^+ K_\rho^{(2)}} \frac{a_\rho}{\sqrt{1+a_\rho^2}}} \right)^2 \\
& \left. \left. + \left(\left[1 - \frac{K_\rho^{(1)} 2u_c}{u_\rho^{(1)} \pi} \right] \sqrt{\frac{u_\rho^{(1)}}{u_\rho^- K_\rho^{(1)}} \frac{a_\rho}{\sqrt{1+a_\rho^2}}} + \sqrt{\frac{u_\rho^{(2)}}{u_\rho^- K_\rho^{(2)}} \frac{1}{\sqrt{1+a_\rho^2}}} \right)^2 \right] \right) , \tag{B.134c}
\end{aligned}$$

$$\begin{aligned}
\frac{dg_{t\perp(2)}}{d\ln b} = g_{t\perp(2)} & \left(2 - \frac{1}{2} \left[\left(\sqrt{\frac{u_\sigma^+ K_\sigma^{(1)}}{u_\sigma^{(1)}} \frac{1}{\sqrt{1+a_\sigma^2}}} - \left[1 + \frac{K_\sigma^{(1)} 2u_s}{u_\sigma^{(1)} 4\pi} \right] \sqrt{\frac{u_\sigma^+ K_\sigma^{(2)}}{u_\sigma^{(2)}} \frac{a_\sigma}{\sqrt{1+a_\sigma^2}}} \right)^2 \right. \right. \\
& + \left(\sqrt{\frac{u_\sigma^- K_\sigma^{(1)}}{u_\sigma^{(1)}} \frac{a_\sigma}{\sqrt{1+a_\sigma^2}}} + \left[1 + \frac{K_\sigma^{(1)} 2u_s}{u_\sigma^{(1)} 4\pi} \right] \sqrt{\frac{u_\sigma^- K_\sigma^{(2)}}{u_\sigma^{(2)}} \frac{1}{\sqrt{1+a_\sigma^2}}} \right)^2 \\
& + \left(\left[1 - \frac{K_\rho^{(1)} 2u_c}{u_\rho^{(1)} \pi} \right] \sqrt{\frac{u_\rho^{(1)}}{u_\rho^+ K_\rho^{(1)}} \frac{1}{\sqrt{1+a_\rho^2}}} - \sqrt{\frac{u_\rho^{(2)}}{u_\rho^+ K_\rho^{(2)}} \frac{a_\rho}{\sqrt{1+a_\rho^2}}} \right)^2 \\
& \left. \left. + \left(\left[1 - \frac{K_\rho^{(1)} 2u_c}{u_\rho^{(1)} \pi} \right] \sqrt{\frac{u_\rho^{(1)}}{u_\rho^- K_\rho^{(1)}} \frac{a_\rho}{\sqrt{1+a_\rho^2}}} + \sqrt{\frac{u_\rho^{(2)}}{u_\rho^- K_\rho^{(2)}} \frac{1}{\sqrt{1+a_\rho^2}}} \right)^2 \right] \right) , \tag{B.134d}
\end{aligned}$$

$$\begin{aligned}
\frac{dg_{t\perp(1)}}{d\ln b} = g_{t\perp(1)} & \left(2 - \frac{1}{2} \left[\left(\sqrt{\frac{u_\sigma^+ K_\sigma^{(1)}}{u_\sigma^{(1)}} \frac{1}{\sqrt{1+a_\sigma^2}}} + \left[1 - \frac{K_\sigma^{(1)} 2u_s}{u_\sigma^{(1)} 4\pi} \right] \sqrt{\frac{u_\sigma^+ K_\sigma^{(2)}}{u_\sigma^{(2)}} \frac{a_\sigma}{\sqrt{1+a_\sigma^2}}} \right)^2 \right. \right. \\
& + \left(\sqrt{\frac{u_\sigma^- K_\sigma^{(1)}}{u_\sigma^{(1)}} \frac{a_\sigma}{\sqrt{1+a_\sigma^2}}} - \left[1 - \frac{K_\sigma^{(1)} 2u_s}{u_\sigma^{(1)} 4\pi} \right] \sqrt{\frac{u_\sigma^- K_\sigma^{(2)}}{u_\sigma^{(2)}} \frac{1}{\sqrt{1+a_\sigma^2}}} \right)^2 \\
& + \left(\left[1 - \frac{K_\rho^{(1)} 2u_c}{u_\rho^{(1)} \pi} \right] \sqrt{\frac{u_\rho^{(1)}}{u_\rho^+ K_\rho^{(1)}} \frac{1}{\sqrt{1+a_\rho^2}}} - \sqrt{\frac{u_\rho^{(2)}}{u_\rho^+ K_\rho^{(2)}} \frac{a_\rho}{\sqrt{1+a_\rho^2}}} \right)^2 \\
& \left. \left. + \left(\left[1 - \frac{K_\rho^{(1)} 2u_c}{u_\rho^{(1)} \pi} \right] \sqrt{\frac{u_\rho^{(1)}}{u_\rho^- K_\rho^{(1)}} \frac{a_\rho}{\sqrt{1+a_\rho^2}}} + \sqrt{\frac{u_\rho^{(2)}}{u_\rho^- K_\rho^{(2)}} \frac{1}{\sqrt{1+a_\rho^2}}} \right)^2 \right] \right) , \tag{B.134e}
\end{aligned}$$

$$\begin{aligned}
\frac{du_s^\perp}{d \ln b} = u_s^\perp & \left(2 - \frac{1}{2} \left[\left(\sqrt{\frac{u_\sigma^+ K_\sigma^{(1)}}{u_\sigma^{(1)}}} \frac{1}{\sqrt{1+a_\sigma^2}} + \left[1 - \frac{K_\sigma^{(1)} 2u_s}{u_\sigma^{(1)} 4\pi} \right] \sqrt{\frac{u_\sigma^+ K_\sigma^{(2)}}{u_\sigma^{(2)}}} \frac{a_\sigma}{\sqrt{1+a_\sigma^2}} \right)^2 \right. \right. \\
& + \left. \left(\sqrt{\frac{u_\sigma^- K_\sigma^{(1)}}{u_\sigma^{(1)}}} \frac{a_\sigma}{\sqrt{1+a_\sigma^2}} - \left[1 - \frac{K_\sigma^{(1)} 2u_s}{u_\sigma^{(1)} 4\pi} \right] \sqrt{\frac{u_\sigma^- K_\sigma^{(2)}}{u_\sigma^{(2)}}} \frac{1}{\sqrt{1+a_\sigma^2}} \right)^2 \right. \\
& + \left. \left(\left[1 - \frac{K_\sigma^{(1)} 2u_s}{u_\sigma^{(1)} 4\pi} \right] \sqrt{\frac{u_\sigma^{(1)}}{u_\sigma^+ K_\sigma^{(1)}}} \frac{1}{\sqrt{1+a_\sigma^2}} - \sqrt{\frac{u_\sigma^{(2)}}{u_\sigma^+ K_\sigma^{(2)}}} \frac{a_\sigma}{\sqrt{1+a_\sigma^2}} \right)^2 \right. \\
& \left. + \left(\left[1 - \frac{K_\sigma^{(1)} 2u_s}{u_\sigma^{(1)} 4\pi} \right] \sqrt{\frac{u_\sigma^{(1)}}{u_\sigma^- K_\sigma^{(1)}}} \frac{a_\sigma}{\sqrt{1+a_\sigma^2}} + \sqrt{\frac{u_\sigma^{(2)}}{u_\sigma^- K_\sigma^{(2)}}} \frac{1}{\sqrt{1+a_\sigma^2}} \right)^2 \right] \right). \tag{B.134f}
\end{aligned}$$

B.11 Limiting cases

We now compare the full RG equations given in appendix B.10 to the corresponding equations of the fermionic analysis in Ref. [30]. Since these do not treat the density-density interactions exactly and do not work with polaronic degrees of freedom, the fermionic RG equations are much simpler, and in particular only contain terms up to second order in the interactions. We thus expand our RG equations (including the Luttinger parameters and effective velocities) up to second order in the coupling strengths. However, we note that our RG equations can not fully reproduce the results of Ref. [30], simply because we did not do a full second order calculation. For a given coupling g_i , we can thus only find terms of the form

$$\frac{dg_i}{dl} \sim g_i g_j, \tag{B.135}$$

where g_j denotes any coupling. Terms of the form

$$\frac{dg_i}{dl} \sim g_j g_k \quad , \quad j, k \neq i \tag{B.136}$$

however result from higher orders in perturbation theory when the Hamiltonian is bosonized, and are thus not obtained here. As a final remark, we introduce the parameter

$$\beta = \frac{v_{F2}}{v_{F1}} \ll 1 \tag{B.137}$$

which will be used to extract the most relevant terms of the RG equations.

B.11.1 Pair tunneling of parallel spins: $g_{t\parallel}$

The RG equation for $g_{t\parallel}$ yields, upon expanding,

$$\frac{dg_{t\parallel}}{d \ln b} \approx -\frac{1}{2\pi v_{F1}} \left(g_{1\parallel} + \frac{1}{\beta} g_{2\parallel} \right) g_{t\parallel} + \frac{2/(\pi v_{F1})}{1+\beta} (u_c - \frac{1}{4} u_s) g_{t\parallel}. \tag{B.138}$$

Varma and Zawadowski's calculation³⁰ lead to

$$\frac{dg_{t\parallel}}{d \ln b} = -\frac{1}{2\pi v_{F1}} \left(g_{1\parallel} + \frac{1}{\beta} g_{2\parallel} \right) g_{t\parallel} + \frac{2/(\pi v_{F1})}{1+\beta} (u_c - \frac{1}{4} u_s) g_{t\parallel} + \frac{1}{\pi v_{F1}} \frac{1}{1+\beta} u_s^\perp g_{t\perp(1)} . \quad (\text{B.139})$$

Up to the last terms, which are not proportional to $g_{t\parallel}$, we exactly reproduce the result of Varma and Zawadowski.

B.11.2 Pair tunneling of opposite spins without spin flip: $g_{t\perp(2)}$

The RG equation for $g_{t\perp(2)}$ yields

$$\frac{dg_{t\perp(2)}}{d \ln b} \approx -\frac{1}{2\pi v_{F1}} \left(g_{1\perp(2)} + \frac{1}{\beta} g_{2\perp(2)} \right) g_{t\perp(2)} + \frac{2/(\pi v_{F1})}{1+\beta} (u_c + \frac{1}{4} u_s) g_{t\perp(2)} . \quad (\text{B.140})$$

Varma and Zawadowski's calculation yields

$$\begin{aligned} \frac{dg_{t\perp(2)}}{d \ln b} = & -\frac{1}{2\pi v_{F1}} \left(g_{1\perp(2)} + \frac{1}{\beta} g_{2\perp(2)} \right) g_{t\perp(2)} - \frac{1}{2\pi v_{F1}} \left(g_{1\perp(1)} + \frac{1}{\beta} g_{2\perp(1)} \right) g_{t\perp(1)} \\ & + \frac{2/(\pi v_{F1})}{1+\beta} (u_c + \frac{1}{4} u_s) g_{t\perp(2)} . \end{aligned} \quad (\text{B.141})$$

Again, we reproduce the result as far as we can expect.

B.11.3 Pair tunneling of opposite spins without spin flip: $g_{t\perp(1)}$

Expanding our RG equations, we find

$$\frac{dg_{t\perp(1)}}{d \ln b} \approx -\frac{1}{2\pi v_{F1}} \left(g_{1\perp(2)} + \frac{1}{\beta} g_{2\perp(2)} \right) g_{t\perp(1)} + \frac{2/(\pi v_{F1})}{1+\beta} (u_c + \frac{1}{4} u_s) g_{t\perp(1)} . \quad (\text{B.142})$$

Varma and Zawadowski's result was

$$\begin{aligned} \frac{dg_{t\perp(1)}}{d \ln b} = & -\frac{1}{2\pi v_{F1}} \left(g_{1\perp(2)} + \frac{1}{\beta} g_{2\perp(2)} \right) g_{t\perp(1)} - \frac{1}{2\pi v_{F1}} \left(g_{1\perp(1)} + \frac{1}{\beta} g_{2\perp(1)} \right) g_{t\perp(2)} \\ & + \frac{2/(\pi v_{F1})}{1+\beta} \left((u_c + \frac{1}{4} u_s) g_{t\perp(1)} + \frac{1}{2} u_s^\perp g_{t\parallel} \right) . \end{aligned} \quad (\text{B.143})$$

Hence, we have again consistent results.

B.11.4 The spin exchange interaction with spin flip: u_s^\perp

We find that u_s^\perp flows according to

$$\frac{du_s^\perp}{d \ln b} \approx -\frac{1/(\pi v_{F1})}{1+\beta} u_s^{\perp 2} . \quad (\text{B.144})$$

This is once more in agreement with Varma and Zawadowski's result, that reads:

$$\frac{du_s^\perp}{d \ln b} = -\frac{1/(\pi v_{F1})}{1+\beta} u_s^{\perp 2} . \quad (\text{B.145})$$

B.11.5 Intraband coupling with spin flip in the first band: $g_{1\perp(1)}$

Here, the RG equations simplifies to

$$\frac{dg_{1\perp(1)}}{d \ln b} \approx -\frac{1}{\pi v_{F1}} g_{1\perp(1)} (g_{1\perp(2)} - g_{1\parallel}) , \quad (\text{B.146})$$

again in agreement with the Varma/Zawadowksi result given by

$$\frac{dg_{1\perp(1)}}{d \ln b} = -\frac{1}{\pi v_{F1}} g_{1\perp(1)} (g_{1\perp(2)} - g_{1\parallel}) - \frac{1}{\pi v_{F1}} \frac{1}{\beta} g_{t\perp(2)} g_{t\perp(1)} . \quad (\text{B.147})$$

B.11.6 Intraband coupling with spin flip in the second band:

$g_{2\perp(1)}$

We can obviously play the same game in the second band and find:

$$\frac{dg_{2\perp(1)}}{d \ln b} \approx -\frac{1}{\pi v_{F1}} \frac{1}{\beta} g_{2\perp(1)} (g_{2\perp(2)} - g_{2\parallel}) . \quad (\text{B.148})$$

This agrees again with Varma/Zawadowksi, who found

$$\frac{dg_{2\perp(1)}}{d \ln b} = -\frac{1}{\pi v_{F1}} \frac{1}{\beta} g_{2\perp(1)} (g_{2\perp(2)} - g_{2\parallel}) - \frac{1}{\pi v_{F1}} g_{t\perp(2)} g_{t\perp(1)} . \quad (\text{B.149})$$

B.12 Solution of the leading order RG equations

Our results for the full RG equations to first order perturbation, see appendix B.10, are in perfect agreement with the results of Varma and Zawadowksi, see Ref. [30]. In order to make contact to our calculations in chapter 2, we want to analyze the leading terms in the RG equations small fillings in the second subband, $v_{F2} \ll v_{F1}$. In this limit, the leading terms in the RG analysis are enhanced by a factor of v_{F1}/v_{F2} with respect to all other terms. Using the identifications (see Eq. (4.18))

$$g_{n\perp(1)} = g_{ns}/2 , \quad (\text{B.150})$$

$$g_{n\perp(2)} = g_{nc} + g_{ns}/4 , \quad (\text{B.151})$$

and the fact that spin-rotation invariance implies $g_{t\parallel} = g_{t\perp(2)} - g_{t\perp(1)}$ (which also remains true under RG), see Eq. (B.104), we can extract the leading order RG terms from appendix B.11. We stress that we use the equations derived by Varma and Zawadowksi in Ref. [30] rather than the bosonized equations, since the latter has to miss some terms of the full second order perturbation theory in fermionic language, see appendix B.11. In the limit $v_{F2} \ll v_{F1}$, we find

$$\frac{dg_{1s}}{d \ln b} = -\frac{2}{\pi v_{F_2}} g_{t\perp(2)} g_{t\perp(1)} , \quad (\text{B.152a})$$

$$\frac{dg_{2s}}{d \ln b} = -\frac{1}{2\pi v_{F_2}} g_{2s}^2 , \quad (\text{B.152b})$$

$$\frac{dg_{t\perp(1)}}{d \ln b} = -\frac{1}{2\pi v_{F_2}} \left(g_{2c} + \frac{1}{4} g_{2s} \right) g_{t\perp(1)} - \frac{1}{4\pi v_{F_2}} g_{2s} g_{t\perp(2)} , \quad (\text{B.152c})$$

$$\frac{dg_{t\perp(2)}}{d \ln b} = -\frac{1}{2\pi v_{F_2}} \left(g_{2c} + \frac{1}{4} g_{2s} \right) g_{t\perp(2)} - \frac{1}{4\pi v_{F_2}} g_{2s} g_{t\perp(1)} . \quad (\text{B.152d})$$

The perturbative treatment is controlled as long as all the terms on the right hand side of Eqs. (B.152) are smaller than the coupling constants they renormalize. For the parameters of our model, Eqs. (3.30), the largest term is $\sim g_{2s}^2/v_{F_2}$ in Eq. (B.152b). Thus, we obtain the condition $g_{2s}/v_{F_2} \ll 1$ or, equivalently, $\mu_2 \gg E_p$ with the strong-coupling energy scale $E_p = mV^2$ of Eq. (3.22), which precisely coincides with the definition of the regime we are analyzing. We thus proceed to the solution of the RG equations (B.152). Since these are very similar to the equations in appendix B.4, the solution is also very similar. It turns out convenient to first define new tunneling couplings

$$g_{t+} = \frac{g_{t\perp(1)} + g_{t\perp(2)}}{2} \quad \text{and} \quad g_{t-} = \frac{g_{t\perp(1)} - g_{t\perp(2)}}{2} , \quad (\text{B.153})$$

which obey the RG equations

$$\frac{dg_{t+}}{d \ln b} = -\frac{1}{2\pi v_{F_2}} \left(g_{2c} + \frac{3}{4} g_{2s} \right) g_{t+} , \quad (\text{B.154a})$$

$$\frac{dg_{t-}}{d \ln b} = -\frac{1}{2\pi v_{F_2}} \left(g_{2c} - \frac{1}{4} g_{2s} \right) g_{t-} . \quad (\text{B.154b})$$

These RG equations can now simply be integrated. The flow if g_{2s} is totally decoupled, and yields

$$g_{2s}(b) = \frac{g_{2s}^0}{1 + g_{2s}^0/(2\pi v_{F_2}) \ln(b)} , \quad (\text{B.155})$$

where g_{2s}^0 is the initial value of the coupling g_{2s} , such that the spin coupling in the second subband flows to weak coupling. Consequently, the flow of the tunnel couplings is essentially governed by the constant g_{2c} , and thus goes to weak coupling as a power law (with logarithmic corrections),

$$g_{t+}(b) = b^{-g_{2c}/(2\pi v_{F_2})} g_{t+}^0 \left[1 + g_{2s}^0/(2\pi v_{F_2}) \ln(b) \right]^{-3/4} , \quad (\text{B.156})$$

$$g_{t-}(b) = b^{-g_{2c}/(2\pi v_{F_2})} g_{t-}^0 \left[1 + g_{2s}^0/(2\pi v_{F_2}) \ln(b) \right]^{1/4} . \quad (\text{B.157})$$

We note that close to the limit $\mu_2 \rightarrow 0$, where $g_{t\perp(1)} = g_{t\perp(2)} = u_t$ we have $g_{t+}^0 \approx u_t$, while $g_{t-}^0 \approx 0$. The flow of g_{1s} , governed by the equation

$$\frac{dg_{1s}}{d \ln b} = -\frac{2}{\pi v_{F_2}} (g_{t+}^2 - g_{t-}^2) \quad (\text{B.158})$$

is thus short and only renormalizes the starting value of the coupling. For $\mu_2 > E_p$, where $g_{2c}^0 = V/2$ and $g_{2s}^0 = 2V$, we can for simplicity drop the logarithmic corrections due to g_{2s} in the flow of g_{1s} . Going back to the original notation of the tunnel couplings, we obtain

$$g_{1s}(b) \approx g_{1s}^0 - 2 \frac{g_{t\perp(1)}^0 g_{t\perp(2)}^0}{g_{2c}} [1 - b^{-g_{2c}/(\pi v_{F2})}] , \quad (\text{B.159})$$

which asymptotically leads to

$$g_{1s}^{\text{eff}} \approx g_{1s}^0 - 2 \frac{g_{t\perp(1)}^0 g_{t\perp(2)}^0}{g_{2c}} . \quad (\text{B.160})$$

We finally again note that we have dropped the superscripts $X^0 \rightarrow X$ for the coupling X in the main text for improved readability.

Appendix C

Quantum phase transitions with multiple dynamics

C.1 Evaluation of the one-loop diagrams

In this appendix, we want to give the general results for the one-loop corrections to the mass and interaction. Starting point is the following action

$$\mathcal{S} = \int d^d x \int d\tau \Psi(\vec{x}, \tau) \frac{g^{-1}}{2} \Psi(\vec{x}, \tau) + u \int d^d x \int d\tau \Psi(\vec{x}, \tau) \Psi(\vec{x}, \tau) \Psi(\vec{x}, \tau) \Psi(\vec{x}, \tau), \quad (\text{C.1})$$

where the bare propagator reads, as a function of momentum k and imaginary time ω_n ,

$$g(\omega_n, \vec{k})^{-1} = r + k^{1/\nu_0} + \frac{|\omega_n|^y}{k^{yz-1/\nu_0}}. \quad (\text{C.2})$$

This general action defines a bosonic mode Ψ characterized by a dynamical exponent z and a bare correlation length exponent ν_0 . It lives in d spatial dimensions and is assumed to be rotationally symmetric (it thus only depends on $k = |\vec{k}|$). The exponent y is for now left undefined. The one-loop corrections to the mass and interaction are depicted in Fig. C.1, and we shall now calculate the corresponding diagrams at finite temperature T .

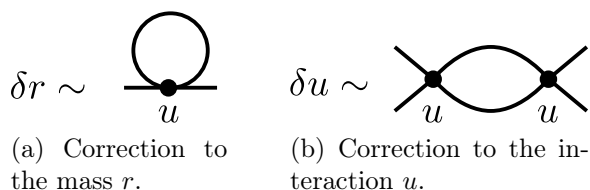


Figure C.1: One-loop corrections to the mass r and the interaction u .

C.1.1 Mass correction

The one-loop mass correction is depicted in Fig. C.1a. It is most conveniently calculated in the imaginary time formalism, where the action (C.1) reads

$$\begin{aligned} \mathcal{S} &= \sum_{\vec{k}, \omega_n} \Psi(-\vec{k}, -\omega_n) \frac{g(\vec{k}, \omega_n)^{-1}}{2} \Psi(\vec{k}, \omega_n) \\ &+ \frac{u}{\beta V} \sum_{\{\omega_{ni}\}} \sum_{\{\vec{k}_i\}} \Psi(\vec{k}_1, \omega_{n1}) \Psi(\vec{k}_2, \omega_{n2}) \Psi(\vec{k}_3, \omega_{n3}) \Psi(\vec{k}_4, \omega_{n4}) \delta_{\omega_{n1}+\omega_{n2}+\omega_{n3}+\omega_{n4}, 0} \delta_{\vec{k}_1+\vec{k}_2+\vec{k}_3+\vec{k}_4, 0}, \end{aligned} \quad (\text{C.3})$$

$$(\text{C.4})$$

where the inverse propagator is given in Eq. (C.2). $\beta = 1/T$ denotes the inverse temperature, and V is the d -dimensional volume. The correction to the mass term can now be found by a standard perturbative expansion of the action. Collecting all combinatorial factors, we find

$$\begin{aligned} \delta r &= 2 \binom{4}{2} \frac{u}{\beta V} \sum_{\omega_n, \vec{k}} \langle \Psi(-\vec{k}, -\omega_n) \Psi(\vec{k}, \omega_n) \rangle \\ &= 12 \frac{u}{\beta V} \sum_{\omega_n, \vec{k}} \frac{1}{r + k^{1/\nu_0} + \frac{|\omega_n|^y}{k^{yz-1/\nu_0}}}. \end{aligned} \quad (\text{C.5})$$

C.1.2 Analysis at zero temperature

At zero temperature, the spacing of the Matsubara modes goes to zero, and we can exchange the sums for integrations. This yields

$$\delta r = 12 \frac{u}{(2\pi)^{d+1}} \int_0^\infty dk k^{d-1} \int d\Omega_d \int_{-\infty}^\infty d\omega \frac{1}{r + k^{1/\nu_0} + \frac{|\omega|^y}{k^{yz-1/\nu_0}}},$$

where $d\Omega_d$ is the differential of the d -dimensional solid angle Ω_d . We thus find

$$\delta r = \frac{24 \Omega_d}{(2\pi)^{d+1}} u \int_0^\infty dk \int_0^\infty d\omega \frac{k^{d-1}}{r + k^{1/\nu_0} + \frac{\omega^y}{k^{yz-1/\nu_0}}},$$

Next, we introduce some high energy cutoffs Λ for the momenta and Γ for the frequencies, which relate as $\Gamma \sim \Lambda^z$. This regularizes the integral in Eq. (C.6) at high energies. Since we are furthermore interested in the physics close to the quantum critical point, where $r \rightarrow 0$, we can furthermore expand the above integral to first order in r . This yields

$$\delta r \approx \delta r^{(0)} + \delta r^{(1)}, \quad (\text{C.6})$$

$$\delta r^{(0)} = \frac{24 \Omega_d}{(2\pi)^{d+1}} u \int_0^\Lambda dk \int_0^\Gamma d\omega \frac{k^{d-1}}{k^{1/\nu_0} + \frac{\omega^y}{k^{yz-1/\nu_0}}} \quad (\text{C.7})$$

$$\delta r^{(1)} = \frac{24 \Omega_d}{(2\pi)^{d+1}} u \int_0^\Lambda dk \int_0^\Gamma d\omega \frac{(-r) k^{d-1}}{\left(k^{1/\nu_0} + \frac{\omega^y}{k^{yz-1/\nu_0}}\right)^2}.$$

The term $\delta r^{(0)}$ scales as k^{d+z-1/ν_0} . Assuming that

$$d + z - \frac{1}{\nu_0} > 0, \quad (\text{C.8})$$

which is surely a realistic assumption for the models we are dealing with, this term leads to a non-divergent correction that can be absorbed into a redefinition of the initial $r \rightarrow r^{\text{eff}} = r + \delta r^{(0)}$. Alternatively, one could also retain the term $\delta r^{(0)}$ along with $\delta r^{(1)}$ in an RG analysis. Since the latter however grows as r , while the prior does not, $\delta r^{(0)}$ is indeed only important in the very first RG stages. In conclusion, the quantum critical point corresponds to $r^{\text{eff}} = r + \delta r^{(0)} = 0$, such that the correction $\delta r^{(1)}$ is small but non-zero, and definitely much larger than r^{eff} .

Term $\delta r^{(0)}$: non-singular high-energy correction

To be explicit, we find that $\delta r^{(0)}$ can be evaluated as follows:

$$\delta r^{(0)} = \frac{24 \Omega_d}{(2\pi)^{d+1}} u \int_0^\Lambda dk \int_0^\Gamma d\omega \frac{k^{d-1}}{k^{1/\nu_0} + \frac{\omega^y}{k^{yz-1/\nu_0}}} \quad (\text{C.9})$$

$$= \frac{24 \Omega_d}{(2\pi)^{d+1}} u \int_0^\Lambda dk \int_0^\Gamma d\omega \frac{k^{d+yz-1/\nu_0-1}}{k^{yz} + \omega^y}. \quad (\text{C.10})$$

Now performing the redefinition

$$k \rightarrow q_1 \quad \text{and} \quad \omega \rightarrow q_2^z, \quad (\text{C.11})$$

we can write this integral as

$$\delta r^{(0)} = \frac{24 \Omega_d}{(2\pi)^{d+1}} u \int_0^\Lambda dq_1 \int_0^\Lambda dq_2 \frac{q_1^{d+yz-1/\nu_0-1} q_2^{z-1}}{q_2^{zy} + q_2^{zy}}. \quad (\text{C.12})$$

We can now go to spherical coordinates by replacing $q_1 \rightarrow q \cos(\phi)$ and $q_2 \rightarrow q \sin(\phi)$ and obtain

$$\delta r^{(0)} = \frac{24 \Omega_d}{(2\pi)^{d+1}} u \int_0^\Lambda dq \int_0^{\pi/2} d\phi \frac{q^{d+yz-1/\nu_0} \cos^{d+yz-1/\nu_0-1}(\phi) q^{z-1} \sin^{z-1}(\phi)}{q^{yz} (\cos^{yz}(\phi) + \sin^{yz}(\phi))} \quad (\text{C.13})$$

(note that we replace the rectangular integration boundaries by a quarter circle, which does however not affect the low energy physics). This yields

$$\delta r^{(0)} = \frac{24 \Omega_d}{(2\pi)^{d+1}} \mathcal{A} u \int_0^\Lambda dq q^{d+z-1/\nu_0-1}, \quad (\text{C.14})$$

where the integration over the angular part yields some constant number of order one,

$$\mathcal{A} = \int_0^{\pi/2} d\phi \frac{\cos^{d+yz-1/\nu_0-1}(\phi) \sin^{z-1}(\phi)}{\cos^y(\phi) + \sin^y(\phi)} \quad (\text{C.15})$$

Note that $\cos^{yz}(\phi) + \sin^{yz}(\phi)$ can never vanish. In addition, the exponent of the cosine fulfills $d + yz - 1/\nu_0 - 1 > (y-1)z - 1 > -1$ (since $d + z - 1/\nu_0 > 0$ by assumption, and $y \geq 1$ for the models that we will consider), such that it is non-singular. We furthermore assume $z > 1$, which also renders the sine-term well-defined. In conclusion, the correction $\delta r^{(0)}$ yields some non-divergent correction, as promised. It does thus only affect the high-energy behavior, but not the universal low-energy physics (compare also Sec. 5.1.1).

Term $\delta r^{(1)}$: leading low energy divergence

The term $\delta r^{(1)}$ scales as k^{d+z-2/ν_0} . Importantly, this scaling dimension $d+z-2/\nu_0$ is also the engineering dimension of the interaction u (as follows from a simple power counting for the action (C.1)), and therefore corresponds to the upper critical dimension of the system. If the system is above its upper critical dimension, fluctuations are anyways not important, while they are for systems below the upper critical dimension. The term $\delta r^{(1)}$ therefore constitutes the leading divergence. It is given by

$$\delta r^{(1)} = \frac{24 \Omega_d}{(2\pi)^{d+1}} u \int_0^\Lambda dk \int_0^\Gamma d\omega \frac{(-r) k^{d-1}}{\left(k^{1/\nu_0} + \frac{\omega^y}{k^{yz-1/\nu_0}}\right)^2}, \quad (\text{C.16})$$

and best analyzed by a renormalization group (RG) approach. The RG step corresponds to integrating out a high-energy, high-momentum shell, and renormalizing momenta as $k \rightarrow bk$ and frequencies as $\omega \rightarrow b^z \omega$. We choose a rectangular cutoff scheme, which yields the high-energy, high-momentum shell as

$$\Delta \delta r^{(1)} = \frac{24 \Omega_d}{(2\pi)^{d+1}} u \left[\int_{\Lambda/b}^\Lambda dk \int_0^\Gamma d\omega \frac{(-r) k^{d-1}}{\left(k^{1/\nu_0} + \frac{\omega^y}{k^{yz-1/\nu_0}}\right)^2} + \int_0^\Lambda dk \int_{\Gamma/b^z}^\Gamma d\omega \frac{(-r) k^{d-1}}{\left(k^{1/\nu_0} + \frac{\omega^y}{k^{yz-1/\nu_0}}\right)^2} \right]. \quad (\text{C.17})$$

The interaction contribution of the RG equation for the flowing $r(b)$ is now obtained by differentiation of (C.17) with respect to $\ln(b)$ at $b = 1$, and reads

$$\frac{\partial r(b)}{\partial \ln(b)} = \left. \frac{\partial \Delta \delta r^{(1)}}{\partial \ln(b)} \right|_{b=1} \quad (\text{C.18})$$

$$= \frac{24 \Omega_d}{(2\pi)^{d+1}} u \left[\Lambda \int_0^\Gamma d\omega \frac{(-r) \Lambda^{d-1}}{\left(\Lambda^{1/\nu_0} + \frac{\omega^y}{\Lambda^{yz-1/\nu_0}}\right)^2} + z \Gamma \int_0^\Lambda dk \frac{(-r) k^{d-1}}{\left(k^{1/\nu_0} + \frac{\Gamma^y}{k^{yz-1/\nu_0}}\right)^2} \right] \quad (\text{C.19})$$

$$= \frac{24 \Omega_d}{(2\pi)^{d+1}} u \left[\int_0^\Gamma d\omega \frac{(-r) \Lambda^{d+2yz-2/\nu_0}}{(\Lambda^{yz} + \omega^y)^2} + z \Gamma \int_0^\Lambda dk \frac{(-r) k^{d+2yz-2/\nu_0-1}}{(k^{yz} + \Gamma^y)^2} \right]. \quad (\text{C.20})$$

Note that this term is not the full RG equation, since the effect of thermal fluctuations as well as the engineering dimensions have to be added in the end. This equation can be brought to a more convenient form by defining $\omega = k^z$ in the second term, and using $\Gamma = \Lambda^z$, which yields

$$\frac{\partial r(b)}{\partial \ln(b)} = \frac{24 \Omega_d}{(2\pi)^{d+1}} u \left[\int_0^\Gamma d\omega \frac{(-r) \Gamma^{(d+2yz-2/\nu_0)/z}}{(\Gamma^y + \omega^y)^2} + \Gamma \int_0^\Gamma d\omega \frac{(-r) \omega^{(d+2yz-2/\nu_0-z)/z}}{(\omega^y + \Gamma^y)^2} \right]. \quad (\text{C.21})$$

Next, it is useful to go to dimensionless variables $\tilde{\omega} = \omega/\Gamma$, which leads to

$$\frac{\partial r(b)}{\partial \ln(b)} = \frac{24 \Omega_d}{(2\pi)^{d+1}} u (-r) \Gamma^{(d+z-2/\nu_0)/z} \int_0^1 d\tilde{\omega} \frac{1 + \tilde{\omega}^{(d+2yz-2/\nu_0-z)/z}}{(1 + \tilde{\omega}^y)^2}. \quad (\text{C.22})$$

We can thus write the final RG equation as

$$\frac{\partial r(b)}{\partial \ln(b)} = -K_{d,z,y,\nu_0} \Lambda^{d+z-2/\nu_0} u(b) r(b) , \quad (\text{C.23})$$

where

$$K_{d,z,y,\nu_0} = \frac{24 \Omega_d}{(2\pi)^{d+1}} \int_0^1 d\tilde{\omega} \frac{1 + \tilde{\omega}^{(d+2yz-2/\nu_0-z)/z}}{(1 + \tilde{\omega}^y)^2} \quad (\text{C.24})$$

is some constant number (with Ω_d being the d -dimensional solid angle). We finally note that for our purposes, the combination $(d + 2z - 2\nu_0 - z)/z > -1$, see below.

C.1.3 Analysis at finite temperature, case $y = 1$

At finite temperature, thermal fluctuations will contribute an additional renormalization of the mass r . We specialize to the case $y = 1$, which turns out to be the relevant one for our discussion. This additional contribution can be obtained by writing the full finite temperature renormalization as the zero temperature one plus “something”, where the “something” then naturally corresponds to the effects of finite temperature,

$$\delta r|_T = \delta r|_{T=0} + [\delta r|_T - \delta r|_{T=0}] . \quad (\text{C.25})$$

We can thus represent the effect of thermal fluctuations as an additional contribution to the RG equations, and obtain it as

$$\delta r|_T - \delta r|_{T=0} = 12 \frac{u}{\beta V} \left(\left[\sum_{\omega_n, \vec{k}} \frac{1}{r + k^{1/\nu_0} + \frac{|\omega_n|}{k^{yz-1/\nu_0}}} \right]_T - \left[\sum_{\omega_n, \vec{k}} \frac{1}{r + k^{1/\nu_0} + \frac{|\omega_n|}{k^{yz-1/\nu_0}}} \right]_{T \rightarrow 0} \right) . \quad (\text{C.26})$$

This expression can now be evaluated by first separating the sum into the Matsubara zero mode and all other modes, and then rewriting the remaining sum over (bosonic) Matsubara frequencies as a contour integral enclosing the poles of the hyperbolic cotangent, since

$$\frac{1}{\beta} \sum_{\omega_n} \frac{1}{r + k^{1/\nu_0} + \frac{|\omega_n|}{k^{yz-1/\nu_0}}} = \frac{1}{\beta} \frac{1}{r + k^{1/\nu_0}} + \frac{2}{\beta} \sum_{\omega_n > 0} \frac{1}{r + k^{1/\nu_0} + \frac{\omega_n}{k^{z-1/\nu_0}}} \quad (\text{C.27})$$

$$= \frac{1}{\beta} \frac{1}{r + k^{1/\nu_0}} + \frac{1}{2\pi i} \int_{\mathcal{C}_>} dz \coth\left(\frac{\beta z}{2}\right) \frac{1}{r + k^{1/\nu_0} + \frac{-iz}{k^{z-1/\nu_0}}} . \quad (\text{C.28})$$

This can now be used to evaluate, very generally, the difference of two thermal terms,

$$\frac{1}{\beta} \left(\left[\sum_{\omega_n} \frac{1}{r + k^{1/\nu_0} + \frac{|\omega_n|}{k^{z-1/\nu_0}}} \right]_{T_1} - \left[\sum_{\omega_n} \frac{1}{r + k^{1/\nu_0} + \frac{|\omega_n|}{k^{z-1/\nu_0}}} \right]_{T_2} \right) \quad (\text{C.29})$$

$$= \frac{1}{\beta_1} \frac{1}{r + k^{1/\nu_0}} - \frac{1}{\beta_2} \frac{1}{r + k^{1/\nu_0}} \quad (\text{C.30})$$

$$+ \frac{1}{2\pi i} \int_{\mathcal{C}_>} dz \left(\coth\left(\frac{\beta_1 z}{2}\right) - \coth\left(\frac{\beta_2 z}{2}\right) \right) \frac{1}{r + k^{1/\nu_0} + \frac{-iz}{k^{z-1/\nu_0}}} . \quad (\text{C.31})$$

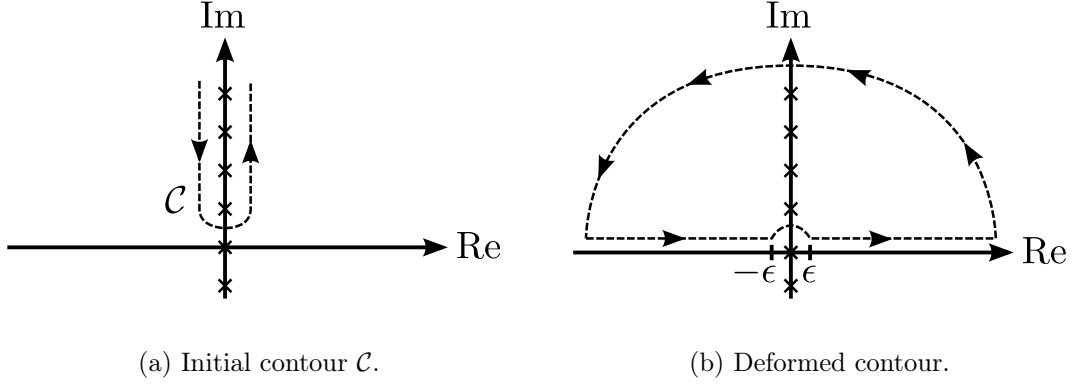


Figure C.2: Deformation of the contour \mathcal{C} , see main text. The contour \mathcal{C} encloses the bosonic Matsubara frequencies, which can be interpreted as poles of the hyperbolic cotangent. They are indicated by the crosses. The deformation can be done since there is no pole encountered in the upper hemisphere or on the real axis, except for the pole corresponding to $\omega_n = 0$. This pole needs to be encircled on a semicircle of radius ϵ . The deformed contour in subfigure (b) can be evaluated as a line integral, which vanishes on the big semicircle at $|z| \rightarrow \infty$. One is thus left with two integrals in the positive and negative parts of the real axis, plus the semicircle around the origin.

The difference of the two hyperbolic cotangents is exponentially suppressed at large $|z|$,

$$\left(\coth\left(\frac{\beta_1 z}{2}\right) - \coth\left(\frac{\beta_2 z}{2}\right) \right) \xrightarrow{|z| \rightarrow \infty} 2(e^{-\beta_1 z} - e^{-\beta_2 z}) \rightarrow 0, \quad (\text{C.32})$$

It is thus permissible to deform the contour integral as depicted in Fig. C.2: firstly, the integrand vanishes faster than $1/|z|$ on the semicircle $|z| \rightarrow \infty$, and secondly the pole of

$$\frac{1}{r + k^{1/\nu_0} + \frac{-iz}{k^{z-1/\nu_0}}} \quad (\text{C.33})$$

is on the imaginary axis in the lower hemisphere and thus not enclosed by the integration contour. After changing the integration contour, the semicircle at infinity can be dropped (since the corresponding contour integral vanishes due to the exponential suppression),

and one obtains

$$\frac{1}{\beta} \left(\left[\sum_{\omega_n} \frac{1}{r + k^{1/\nu_0} + \frac{|\omega_n|}{k^{yz-1/\nu_0}}} \right]_{T_1} - \left[\sum_{\omega_n} \frac{1}{r + k^{1/\nu_0} + \frac{|\omega_n|}{k^{yz-1/\nu_0}}} \right]_{T_2} \right) \quad (\text{C.34})$$

$$\begin{aligned} &= \frac{1}{\beta_1} \frac{1}{r + k^{1/\nu_0}} - \frac{1}{\beta_2} \frac{1}{r + k^{1/\nu_0}} \\ &+ \frac{1}{2\pi i} \int_{-\infty}^{-\epsilon} d\mathcal{E} \left(\coth \left(\frac{\beta_1 \mathcal{E}}{2} \right) - \coth \left(\frac{\beta_2 \mathcal{E}}{2} \right) \right) \frac{1}{r + k^{1/\nu_0} + \frac{-i\mathcal{E}}{k^{z-1/\nu_0}}} \\ &+ \frac{1}{2\pi i} \int_{\epsilon}^{\infty} d\mathcal{E} \left(\coth \left(\frac{\beta_1 \mathcal{E}}{2} \right) - \coth \left(\frac{\beta_2 \mathcal{E}}{2} \right) \right) \frac{1}{r + k^{1/\nu_0} + \frac{-i\mathcal{E}}{k^{z-1/\nu_0}}} \\ &+ \frac{1}{2\pi i} \int_{\pi}^0 d\phi i \epsilon e^{i\phi} \left(\coth \left(\frac{\beta_1 \epsilon e^{i\phi}}{2} \right) - \coth \left(\frac{\beta_2 \epsilon e^{i\phi}}{2} \right) \right) \frac{1}{r + k^{1/\nu_0} + \frac{-i \epsilon e^{i\phi}}{k^{yz-1/\nu_0}}} \end{aligned} \quad (\text{C.35})$$

$$\begin{aligned} &= \frac{1}{\beta_1} \frac{1}{r + k^{1/\nu_0}} - \frac{1}{\beta_2} \frac{1}{r + k^{1/\nu_0}} \\ &+ \frac{1}{2\pi i} \int_{\epsilon}^{\infty} d\mathcal{E} \left(\coth \left(\frac{\beta_1 \mathcal{E}}{2} \right) - \coth \left(\frac{\beta_2 \mathcal{E}}{2} \right) \right) \left(\frac{1}{r + k^{1/\nu_0} + \frac{-i\mathcal{E}}{k^{z-1/\nu_0}}} - \frac{1}{r + k^{1/\nu_0} + \frac{i\mathcal{E}}{k^{z-1/\nu_0}}} \right) \\ &+ \frac{1}{2\pi i} \int_0^{\pi} d\phi i \epsilon e^{i\phi} \left(\coth \left(\frac{\beta_1 \epsilon e^{i\phi}}{2} \right) - \coth \left(\frac{\beta_2 \epsilon e^{i\phi}}{2} \right) \right) \frac{1}{r + k^{1/\nu_0} + \frac{-i \epsilon e^{i\phi}}{k^{z-1/\nu_0}}} \end{aligned} \quad (\text{C.36})$$

$$\begin{aligned} &\approx \frac{1}{\beta_1} \frac{1}{r + k^{1/\nu_0}} - \frac{1}{\beta_2} \frac{1}{r + k^{1/\nu_0}} \\ &+ \frac{1}{2\pi i} \int_{\epsilon}^{\infty} d\mathcal{E} \left(\coth \left(\frac{\beta_1 \mathcal{E}}{2} \right) - \coth \left(\frac{\beta_2 \mathcal{E}}{2} \right) \right) \left(\frac{1}{r + k^{1/\nu_0} + \frac{-i\mathcal{E}}{k^{z-1/\nu_0}}} - \frac{1}{r + k^{1/\nu_0} + \frac{i\mathcal{E}}{k^{z-1/\nu_0}}} \right) \\ &+ \frac{1}{2\pi i} \int_0^{\pi} d\phi i \epsilon e^{i\phi} \left(\coth \left(\frac{\beta_1 \epsilon e^{i\phi}}{2} \right) - \coth \left(\frac{\beta_2 \epsilon e^{i\phi}}{2} \right) \right) \frac{1}{r + k^{1/\nu_0} + \frac{-i \epsilon e^{i\phi}}{k^{z-1/\nu_0}}} \end{aligned} \quad (\text{C.37})$$

$$\begin{aligned} &+ \frac{1}{2\pi i} \int_{\epsilon}^{\infty} d\mathcal{E} \left(\coth \left(\frac{\beta_1 \mathcal{E}}{2} \right) - \coth \left(\frac{\beta_2 \mathcal{E}}{2} \right) \right) \left(\frac{1}{r + k^{1/\nu_0} + \frac{-i\mathcal{E}}{k^{z-1/\nu_0}}} - \frac{1}{r + k^{1/\nu_0} + \frac{i\mathcal{E}}{k^{z-1/\nu_0}}} \right) \\ &+ \frac{1}{2\pi i} \int_{\pi}^0 d\phi i \epsilon e^{i\phi} \left(\frac{2}{\beta_1 \epsilon e^{i\phi}} - \frac{2}{\beta_2 \epsilon e^{i\phi}} \right) \frac{1}{r + k^{1/\nu_0}} , \end{aligned}$$

where in the last step we have used $\epsilon \rightarrow 0$ and $\coth(x) \rightarrow 1/x$ for $x \rightarrow 0$ at the small semicircle close to the origin. Performing the angular integral in the last line finally cancels the contribution of the Matsubara zero modes, and we are left with

$$\frac{1}{\beta} \left(\left[\sum_{\omega_n} \frac{1}{r + k^{1/\nu_0} + \frac{|\omega_n|}{k^{z-1/\nu_0}}} \right]_{T_1} - \left[\sum_{\omega_n} \frac{1}{r + k^{1/\nu_0} + \frac{|\omega_n|}{k^{z-1/\nu_0}}} \right]_{T_2} \right) \quad (\text{C.38})$$

$$\approx \frac{1}{2\pi i} \int_{\epsilon}^{\infty} d\mathcal{E} \left(\coth \left(\frac{\beta_1 \mathcal{E}}{2} \right) - \coth \left(\frac{\beta_2 \mathcal{E}}{2} \right) \right) \left(\frac{1}{r + k^{1/\nu_0} + \frac{-i\mathcal{E}}{k^{z-1/\nu_0}}} - \frac{1}{r + k^{1/\nu_0} + \frac{i\mathcal{E}}{k^{z-1/\nu_0}}} \right) . \quad (\text{C.39})$$

Finally, we can now take the limit $\epsilon \rightarrow 0$, which is not singular in the above expression, and plug this result back into the thermal correction to the mass term. We find

$$\delta r|_T - \delta r|_{T=0} = 12 \frac{u}{V} \sum_{\vec{k}} \frac{1}{2\pi i} \int_0^\infty d\mathcal{E} \left(\coth\left(\frac{\beta\mathcal{E}}{2}\right) - 1 \right) \left(\frac{1}{r + k^{1/\nu_0} + \frac{-i\mathcal{E}}{k^{z-1/\nu_0}}} - \frac{1}{r + k^{1/\nu_0} + \frac{i\mathcal{E}}{k^{z-1/\nu_0}}} \right) \quad (\text{C.40})$$

$$= 12 \frac{u}{V} \sum_{\vec{k}} \frac{1}{2\pi i} \int_0^\infty d\mathcal{E} \left(\coth\left(\frac{\beta\mathcal{E}}{2}\right) - 1 \right) \frac{\frac{i\mathcal{E}}{k^{z-1/\nu_0}} - \frac{-i\mathcal{E}}{k^{z-1/\nu_0}}}{(r + k^{1/\nu_0})^2 + \left(\frac{\mathcal{E}}{k^{z-1/\nu_0}}\right)^2}. \quad (\text{C.41})$$

Next, we approximate the hyperbolic cotangent as

$$\coth(x) \approx \begin{cases} \frac{1}{x} & , \quad x \ll 1 \\ 1 & , \quad x \gg 1 \end{cases}, \quad (\text{C.42})$$

and obtain

$$\delta r|_T - \delta r|_{T=0} = 24 \frac{uT}{V} \sum_{\vec{k}} \frac{1}{2\pi i} \int_0^{2T} d\mathcal{E} \frac{1}{\mathcal{E}} \frac{\frac{i\mathcal{E}}{k^{z-1/\nu_0}} - \frac{-i\mathcal{E}}{k^{z-1/\nu_0}}}{(r + k^{1/\nu_0})^2 + \left(\frac{\mathcal{E}}{k^{z-1/\nu_0}}\right)^2}. \quad (\text{C.43})$$

Now taking the continuum limit in real space and introducing the high-momentum cutoff Λ , we find

$$\delta r|_T - \delta r|_{T=0} = 24 u T \int_0^\Lambda \frac{dk}{(2\pi)^d} k^{d-1} \int d\Omega_d \frac{1}{2\pi i} \int_0^{2T} d\mathcal{E} \frac{1}{\mathcal{E}} \frac{\frac{i\mathcal{E}}{k^{z-1/\nu_0}} - \frac{-i\mathcal{E}}{k^{z-1/\nu_0}}}{(r + k^{1/\nu_0})^2 + \left(\frac{\mathcal{E}}{k^{z-1/\nu_0}}\right)^2} \quad (\text{C.44})$$

$$= \frac{24 \Omega_d}{(2\pi)^{(d+1)}} u T \int_0^\Lambda dk k^{d-1} \frac{1}{i} \int_0^{2T} d\mathcal{E} \frac{1}{\mathcal{E}} \frac{\frac{i\mathcal{E}}{k^{z-1/\nu_0}} - \frac{-i\mathcal{E}}{k^{z-1/\nu_0}}}{(r + k^{1/\nu_0})^2 + \left(\frac{\mathcal{E}}{k^{z-1/\nu_0}}\right)^2} \quad (\text{C.45})$$

$$= \frac{24 \Omega_d}{(2\pi)^{(d+1)}} u T \int_0^\Lambda dk \int_0^{2T} d\mathcal{E} k^{d-1+z-1/\nu_0} \frac{1 - (-1)}{(k^{z-1/\nu_0}(r + k^{1/\nu_0}))^2 + \mathcal{E}^2}. \quad (\text{C.46})$$

The RG equation is then defined in the last section as the logarithmic derivative of the high-momentum shell, which yields

$$\left. \frac{\partial r}{\partial \ln(b)} \right|_{T-T=0} = \frac{24 \Omega_d}{(2\pi)^{(d+1)}} u(b) T(b) \Lambda \int_0^{2T(b)} d\mathcal{E} \Lambda^{d-1+z-1/\nu_0} \frac{2}{(\Lambda^{z-1/\nu_0}(r + \Lambda^{1/\nu_0}))^2 + \mathcal{E}^2}. \quad (\text{C.47})$$

Close to the quantum critical point, where $\Lambda^{1/\nu_0} \gg r$, we thus obtain

$$\left. \frac{\partial r}{\partial \ln(b)} \right|_{T-T=0} = \frac{24 \Omega_d}{(2\pi)^{(d+1)}} u(b) T(b) \Lambda \int_0^{2T(b)} d\mathcal{E} \Lambda^{d-1+z-1/\nu_0} \frac{2}{\Lambda^{2z} + \mathcal{E}^2}. \quad (\text{C.48})$$

In dimensionless variables $\epsilon = \mathcal{E}/\Lambda^z$, we finally obtain

$$\left. \frac{\partial r}{\partial \ln(b)} \right|_{T=T=0} = \frac{24 \Omega_d}{(2\pi)^{(d+1)}} u(b) T(b) \Lambda^{d-1/\nu_0} \int_0^{2T(b)/\Lambda^z} d\epsilon \frac{2}{1+\epsilon^2} \quad (\text{C.49})$$

$$= \frac{24 \Omega_d}{(2\pi)^{(d+1)}} u T \Lambda^{d-1/\nu_0} 2 \arctan \left(\frac{2T(b)}{\Lambda^z} \right) . \quad (\text{C.50})$$

This term is very small compared to the zero temperature term, unless the inverse tangent has an argument of order $\mathcal{O}(1)$ or larger (which might happen at some point during the RG flow). We can thus approximate

$$\left. \frac{\partial r}{\partial \ln(b)} \right|_{T=T=0} \approx \frac{24 \Omega_d}{(2\pi)^{(d+1)}} \pi u(b) T(b) \Lambda^{d-1/\nu_0} \Theta \left(\frac{T(b)}{\Lambda^z} - 1 \right) , \quad (\text{C.51})$$

where $\Theta(x)$ denotes the Heaviside step function.

Full RG equation for the mass for $y = 1$

We can now put all pieces together and obtain the RG equation for the mass by adding the engineering dimension of r to the zero temperature and finite temperature RG contributions. The engineering dimension can be found to be $1/\nu_0$ by power counting of the action (C.1), and we obtain the full RG equation

$$\frac{\partial r}{\partial \ln(b)} = \frac{1}{\nu_0} r(b) - K_{d,z,y=1,\nu_0} \Lambda^{d+z-2/\nu_0} u(b) r(b) + \frac{24 \Omega_d}{(2\pi)^{(d+1)}} \pi u(b) T(b) \Lambda^{d-1/\nu_0} \Theta \left(\frac{T(b)}{\Lambda^z} - 1 \right) , \quad (\text{C.52})$$

$$K_{d,z,y,\nu_0} = \frac{24 \Omega_d}{(2\pi)^{d+1}} \int_0^1 d\tilde{\omega} \frac{1 + \tilde{\omega}^{(d+2yz-2/\nu_0-z)/z}}{(1 + \tilde{\omega}^y)^2} , \quad (\text{C.53})$$

where again Ω_d is the d -dimensional solid angle.

C.1.4 Correction to the interaction

To one-loop order, the interaction is renormalized by the bubble shown in Fig. C.1b. Again expanding the action and collecting all combinatorial factors, we obtain

$$\begin{aligned} \delta u &= -\frac{1}{2} \frac{4 \cdot 3 \cdot 4 \cdot 3}{2} \frac{u^2}{\beta V} \sum_{\omega_n, \vec{k}} \langle \Psi(-\vec{k}, -\omega_n) \Psi(\vec{k}, \omega_n) \rangle \langle \Psi(-\vec{k}, -\omega_n) \Psi(\vec{k}, \omega_n) \rangle \quad (\text{C.54}) \\ &= -36 \frac{u^2}{\beta V} \sum_{\omega_n, \vec{k}} \left(\frac{1}{r + k^{1/\nu_0} + \frac{|\omega_n|^y}{k^{yz-1/\nu_0}}} \right)^2 . \end{aligned}$$

Different to the mass, already the zero order term in r is low energy divergent and in fact exactly coincides with (three times) the correction $\delta r^{(1)}$ discussed in the last section. By analogy, the RG equation for the interaction reads

$$\frac{\partial u}{\partial \ln(b)} = \left(\frac{2}{\nu_0} - d - z \right) u(b) - 3 K_{d,z,y,\nu_0} \Lambda^{d+z-2/\nu_0} u^2(b) , \quad (\text{C.55})$$

where the engineering dimension again follows from power counting of the action (C.1), and with the same constant K_{d,z,y,ν_0} as in Eq. (C.53). Note that we only considered the zero temperature correction, since all other terms will turn out to be irrelevant (the interaction either flows to a Wilson-Fisher fixed point if the theory is at the upper critical dimension, or to a Gaussian fixed point if the theory is above the upper critical dimension). If the system reaches the Wilson-Fisher fixed point (which will happen due to quantum fluctuations only well before thermal fluctuations become important), the interaction is already large. The effective, renormalized interaction

$$u^{\text{eff}} = u + A u^2 + B u^2 T \approx u + A u^2 , \quad (\text{C.56})$$

can thus be approximated by the zero temperature corrections only (A and B are the appropriate constants and left undefined for this qualitative discussion). This is qualitatively different for the mass, where at the quantum critical point $r \rightarrow 0$ the effective mass is given by

$$r^{\text{eff}} = r + A' u r + B' u T \approx B' u T , \quad (\text{C.57})$$

such that the finite temperature correction is crucial.

C.2 RG equations for single dynamics above the thermal scale

For a system with single dynamics, governed by the action (5.31), the zero temperature RG equations read

$$\frac{\partial r}{\partial \ln(b)} = \frac{1}{\nu_0} r(b) - K_{d,z,1,\nu_0} \Lambda^{d+z-2/\nu_0} u(b) r(b) , \quad (\text{C.58a})$$

$$\frac{\partial u}{\partial \ln(b)} = \left(\frac{2}{\nu_0} - d - z \right) u(b) - 3 K_{d,z,1,\nu_0} \Lambda^{d+z-2/\nu_0} u^2(b) , \quad (\text{C.58b})$$

$$\frac{\partial T}{\partial \ln(b)} = z T(b) . \quad (\text{C.58c})$$

The RG equations express how the mass r and temperature T are renormalized at low energies, both by the mere effect of “zooming into smaller energies”, which gives rise to the engineering dimensions, and the additional corrections due to interactions, also known as “anomalous scaling dimension”. The engineering dimensions follow from simple power counting of the action (5.31), while the anomalous dimensions have been discussed in appendix C.1 (see for instance Eq. (C.53) for the constant $K_{d,z,1,\nu_0}$). The starting values of the RG flow, $r(b=1)$, $u(b=1)$ and $T(b=1)$ are set by the physical values of r , u and T . We relabel them as $r(b=1) = r = r_0$, $u(b=1) = u = u_0$ and $T(b=1) = T = T_0$ for better distinction with the running values. These initial values are often referred to as “bare” values.

Above the quantum critical point, $r = r_0 = 0$, the RG equations can trivially be integrated as

$$r(b) = 0 , \quad (\text{C.59a})$$

$$u(b) = u_0 b^{\frac{2}{\nu_0} - d - z} \frac{\frac{2}{\nu_0} - d - z}{\frac{2}{\nu_0} - d - z + 3 K_{d,z,y,\nu_0} \Lambda^{d+z-2/\nu_0} u_0 (1 - b^{\frac{2}{\nu_0} - d - z})} , \quad (\text{C.59b})$$

$$T(b) = T_0 b^z . \quad (\text{C.59c})$$

While the mass is not renormalized at all above the quantum critical point, the fate of the interaction depends on the dimensionality of the system. If the system is above its upper critical dimension, $d + z > D_c^+ = 2/\nu_0$, the interaction rapidly flows to zero, $u(b) \rightarrow 0$. If the system is below its upper critical value, the interaction goes to a finite value,

$$u(b) = u_{\text{WF}} \frac{1}{1 + (b_{\text{WF}}/b)^{2\nu_0 - d - z}} \quad (\text{C.60a})$$

$$u_{\text{WF}} = \frac{\frac{2}{\nu_0} - d - z}{3 K_{d,z,1,\nu_0} \Lambda^{d+z-2/\nu_0}} \quad (\text{C.60b})$$

$$b_{\text{WF}} = \left(\frac{u_{\text{WF}}}{u_0} - 1 \right)^{1/(2\nu_0) - d - z} . \quad (\text{C.60c})$$

This Wilson-Fisher fixed point value is reached at the scale $b \approx b_{\text{WF}}$, which happens long before the thermal scale where the flowing temperature equals the cutoff,

$$T(b_T) = \Lambda \quad \Rightarrow \quad b_T = \frac{\Lambda}{\xi_T^{-1}} = \frac{\Lambda}{T^{1/z}} \quad (\text{C.61})$$

for low enough temperatures.

C.3 Integrating out the non-zero Matsubara modes

After having reached the thermal scale, the non-zero Matsubara modes can be integrated out perturbatively if they are sufficiently gapped. The integration over the non-zero Matsubara modes then yields an effective mass for the Matsubara zero mode. This mass should be much smaller than the temperature, which sets the gap for the non-zero Matsubara modes. We thus start with the action

$$\begin{aligned} \mathcal{S}_{eff} = & \sum_{k \leq \xi_T^{-1}} \sum_{\omega_n} \Psi(-\vec{k}, -\omega_n) \frac{1}{2} \left[r^* + k^{1/\nu_0} + \frac{|\omega_n|^y}{k^{yz-1/\nu_0}} \right] \Psi(\vec{k}, \omega_n) \quad (\text{C.62}) \\ & + u^* \int d^d x \int d\tau \Psi(\vec{x}, \tau) \Psi(\vec{x}, \tau) \Psi(\vec{x}, \tau) \Psi(\vec{x}, \tau) . \end{aligned}$$

The effective mass r^* and effective interaction u^* are obtained as the result of the high-energy RG up to the thermal scale $b_T = \Lambda/T^{1/z}$. One can now adopt two perspectives. Either, we use the RG-renormalized values $u(b_T)$, $T(b_T) = \Lambda$ and $r(b_T) = 0$ as starting values for a theory of cutoff Λ , or we rescale everything with the inverse engineering

dimension to obtain a theory of cutoff $|\vec{k}| \leq T_0^{1/z}$, which is physically more transparent, and the scheme discussed in Secs. 5.2.2 and 5.3. We then obtain

$$r^* = r(b_T) \left(\frac{T^{1/z}}{\Lambda} \right)^{1/\nu_0} = 0, \quad (\text{C.63a})$$

$$u^* = u(b_T) \left(\frac{T^{1/z}}{\Lambda} \right)^{2/\nu_0 - d - z}, \quad (\text{C.63b})$$

$$T = T(b_T) \left(\frac{T^{1/z}}{\Lambda} \right)^z = T. \quad (\text{C.63c})$$

If the system is below its upper critical dimension and thus governed by a Wilson-Fisher fixed point, the effective interaction thus reads

$$u^* = u_{\text{WF}} \left(\frac{T^{1/z}}{\Lambda} \right)^{2/\nu_0 - d - z}, \quad (\text{C.64})$$

where u_{WF} is given in Eq. (C.60a). For a system above its upper critical dimension we find from Eq. (C.59b), and with the assumption that $\Lambda^{d+z-2/\nu_0} u_0 \ll 1$, that the interaction is essentially unrenormalized,

$$u^* = u_0. \quad (\text{C.65})$$

This is not surprising: if the system is above its upper critical dimension, quantum fluctuations do not yield significant corrections, including corrections to the interaction. Assuming that the non-zero Matsubara modes are sufficiently gapped, we integrate them out perturbatively. The resulting effective mass for the zero mode,

$$r_0^* = 12 \frac{u^*}{V} \sum_{|\vec{k}| \leq \xi_T^{-1}} \frac{1}{\beta} \left(\left[\sum_{\omega_n \neq 0} \frac{1}{r + k^{1/\nu_0} + \frac{|\omega_n|}{k^{z-1/\nu_0}}} \right]_T - \left[\sum_{\omega_n \neq 0} \frac{1}{r + k^{1/\nu_0} + \frac{|\omega_n|}{k^{z-1/\nu_0}}} \right]_{T \rightarrow 0} \right) \quad (\text{C.66})$$

$$\approx \frac{24 \Omega_d}{(2\pi)^{(d+1)}} u^* T \int_0^{T^{1/z}} dk \int_0^{2T} d\mathcal{E} k^{d-1+z-1/\nu_0} \frac{2}{k^{2z} + \mathcal{E}^2} \quad (\text{C.67})$$

is calculated by subtracting the corresponding sums at zero temperature (note that we have used the results of appendix C.1 to rewrite the sums, and Ω_d is the d -dimensional solid angle). This is necessary to avoid unphysical divergencies and double counting of zero temperature physics, as the latter have already been captured by the RG performed in the first step.⁸¹ We now define the dimensionless variables

$$q_1 = \frac{k^z}{T} \quad \text{and} \quad q_2 = \frac{\mathcal{E}}{2T}, \quad (\text{C.68})$$

which yields

$$r_0^* = \frac{24 \Omega_d}{(2\pi)^{(d+1)}} u^* T T^{(d-1/\nu_0)/z} \int_0^1 dq_1 \int_0^1 dq_2 q_1^{(d-1/\nu_0)/z} \frac{1}{q_1^2 + 4q_2^2}. \quad (\text{C.69})$$

Now transforming to polar coordinates, $q_1 = q \cos(\phi)$ and $q_2 = q \sin(\phi)$, we obtain

$$r_0^* \approx \frac{24 \Omega_d}{(2\pi)^{(d+1)}} u^* T^{(d+z-1/\nu_0)/z} \int_0^1 dq \int_0^{\pi/4} d\phi q^{(d-1/\nu_0)/z-1} \frac{\cos^{(d-1/\nu_0)/z}(\phi)}{\cos^2(\phi) + 4 \sin^2(\phi)}. \quad (\text{C.70})$$

This integral has two kinds of behaviors. If

$$d > \frac{1}{\nu_0}, \quad (\text{C.71})$$

it is well-behaved and can be evaluated as

$$r_0^* \approx \frac{24 \Omega_d}{(2\pi)^{(d+1)}} u^* T^{(d+z-2/\nu_0)/z} T^{1/(\nu_0 z)} \frac{z}{d-1/\nu_0} \int_0^{\pi/4} d\phi \frac{\cos^{(d-1/\nu_0)/z}(\phi)}{\cos^2(\phi) + 4 \sin^2(\phi)} \quad (\text{C.72})$$

$$\sim u^* T^{(d-1/\nu_0)/z} = u^* T^{(d+z-2/\nu_0)/z} T^{1/(\nu_0 z)}. \quad (\text{C.73})$$

The effective mass of the Matsubara zero mode is then much smaller than gap of the other modes, $T^{1/\nu_0 z}$. For a system below its upper critical dimension, we obtain

$$\frac{r_0^*}{T^{1/(\nu_0 z)}} \sim u_{\text{WF}} \left(\frac{T}{\Lambda} \right)^{2/\nu_0 - d - z} T^{(d+z-2/\nu_0)/z} = \frac{u_{\text{WF}}}{\Lambda^{2/\nu_0 - d - z}} = \frac{\frac{2}{\nu_0} - d - z}{3 K_{d,z,1,\nu_0}} \sim \frac{2}{\nu_0} - d - z. \quad (\text{C.74})$$

For a system above its upper critical dimension (implying $d + z > 2/\nu_0$), the mass reads

$$\frac{r_0^*}{T^{1/(\nu_0 z)}} \sim u_0 T^{d+z-2/\nu_0} T^{1/(\nu_0 z)} \quad (\text{C.75})$$

and is even much smaller. In conclusion, if the system is above the classical lower critical dimension, $d > 1/\nu_0$, the integration over the non-zero Matsubara modes was well-defined and our calculation was consistent. If on the other hand

$$d < \frac{1}{\nu_0}, \quad (\text{C.76})$$

the integral is singular at low q , and the effective mass of the Matsubara zero mode is not small, and the non-zero Matsubara modes can not be considered as being effectively gapped by the temperature.

C.4 Full finite temperature RG equations for single dynamics for $r = 0$

Alternatively to a two step procedure involving a zero temperature RG and subsequent perturbative integration over non-zero Matsubara modes, a critical field theory involving only a single dynamics can be alternatively be treated in a finite temperature RG scheme. We derive the latter for the action defined in Eq. (5.31), and the calculation is done in appendix C.1. We find the RG equation to read

$$\frac{\partial r}{\partial \ln(b)} = \frac{1}{\nu_0} r(b) - K_{d,z,y=1,\nu_0} \Lambda^{d+z-2/\nu_0} u(b) r(b) + \frac{24 \Omega_d}{(2\pi)^{(d+1)}} \pi u(b) T(b) \Lambda^{d-1/\nu_0} \Theta \left(\frac{T(b)}{\Lambda^z} - 1 \right) , \quad (\text{C.77a})$$

$$\frac{\partial u}{\partial \ln(b)} = \left(\frac{2}{\nu_0} - d - z \right) u(b) - 3 K_{d,z,1,\nu_0} \Lambda^{d+z-2/\nu_0} u^2(b) , \quad (\text{C.77b})$$

$$\frac{\partial T}{\partial \ln(b)} = z T(b) . \quad (\text{C.77c})$$

where the constant $K_{d,z,y=1,\nu_0}$ is given by

$$K_{d,z,y,\nu_0} = \frac{24 \Omega_d}{(2\pi)^{d+1}} \int_0^1 d\tilde{\omega} \frac{1 + \tilde{\omega}^{(d+2yz-2/\nu_0-z)/z}}{(1 + \tilde{\omega}^y)^2} , \quad (\text{C.78})$$

and Ω_d is the d -dimensional solid angle. Since we assume the system to be below its upper critical dimension,

$$d + z < \frac{2}{\nu_0} , \quad (\text{C.79})$$

the interaction flows to the Wilson Fisher fixed point. The integration of the RG equation (C.77b) yields, just as in appendix C.2,

$$u(b) = u_{\text{WF}} \frac{1}{1 + (b_{\text{WF}}/b)^{2\nu_0-d-z}} , \quad (\text{C.80a})$$

$$u_{\text{WF}} = \frac{\frac{2}{\nu_0} - d - z}{3 K_{d,z,1,\nu_0} \Lambda^{d+z-2/\nu_0}} , \quad (\text{C.80b})$$

$$b_{\text{WF}} = \left(\frac{u_{\text{WF}}}{u_0} - 1 \right)^{1/(2\nu_0-d-z)} , \quad (\text{C.80c})$$

where u_0 is the initial, bare value of the coupling u . The RG equation for the temperature integrates to

$$T(b) = T_0 b^z , \quad (\text{C.81})$$

where T_0 is the physical temperature in the system. Close enough to the quantum critical point, such that $b_{\text{WF}} \ll b_T = \Lambda/T^{1/z}$, the Wilson-Fisher fixed point is reached well before the thermal term in the RG equation for r gets activated. Since the initial value of the mass is assumed to vanish, $r_0 = r(b=1) = r = 0$, it can be treated by the effective Wilson-Fisher fixed point RG equation, where we replaced $u(b) \rightarrow u_{\text{WF}}$,

$$\frac{\partial r}{\partial \ln(b)} = \frac{1}{\nu_{\text{WF}}} r(b) + \kappa_{d,z,1,\nu_0} \frac{\frac{2}{\nu_0} - d - z}{\Lambda^{d+z-2/\nu_0}} T(b) \Lambda^{d-1/\nu_0} \Theta(b - b_T) , \quad (\text{C.82})$$

with the Wilson-Fisher fixed point value of ν_{WF} being

$$\frac{1}{\nu_{\text{WF}}} = \frac{1}{\nu_0} - \frac{\frac{2}{\nu_0} - d - z}{3} \quad (\text{C.83})$$

and where the flowing interaction and temperature obey

$$u(b) = u_{\text{WF}} \quad \text{and} \quad T(b) = T_0 b^z . \quad (\text{C.84})$$

The new constant $\kappa_{d,z,1,\nu_0}$ is of order one and given by

$$\kappa_{d,z,1,\nu_0} = \frac{\pi}{3} \left(\int_0^1 d\tilde{\omega} \frac{1 + \tilde{\omega}^{(d+2yz-2/\nu_0-z)/z}}{(1 + \tilde{\omega}^y)^2} \right)^{-1} . \quad (\text{C.85})$$

These equations are valid for RG stages $b > b_{\text{WF}}$ (note that we have used $b_T = \Lambda/T^{1/z}$). The RG equation for $r(b)$ is now most conveniently solved by defining

$$\tilde{r}(b) = b^{-1/\nu_{\text{WF}}} r(b) , \quad (\text{C.86})$$

which obeys the RG equation

$$\frac{\partial \tilde{r}}{\partial \ln(b)} = \kappa_{d,z,1,\nu_0} \frac{\frac{2}{\nu_0} - d - z}{\Lambda^{d+z-2/\nu_0}} T(b) b^{-1/\nu_{\text{WF}}} \Lambda^{d-1/\nu_0} \Theta(b - b_T) . \quad (\text{C.87})$$

This equation integrates to

$$\tilde{r}(b) = \kappa_{d,z,1,\nu_0} \frac{\frac{2}{\nu_0} - d - z}{\Lambda^{z-1/\nu_0}} T_0 \int_{b_T}^b db b^{z-1/\nu_{\text{WF}}-1} \quad (\text{C.88})$$

$$= \kappa_{d,z,1,\nu_0} \frac{\frac{2}{\nu_0} - d - z}{\Lambda^{z-1/\nu_0}} T_0 \frac{1}{z - 1/\nu_{\text{WF}}} \left(b^{z-1/\nu_{\text{WF}}} - b_T^{z-1/\nu_{\text{WF}}} \right) . \quad (\text{C.89})$$

We note that if $1/\nu_{\text{WF}} = z$, there are logarithmic corrections to this expression similar to Ref. [53], see appendix C.7.2. We will however specialize to the case $1/\nu_{\text{WF}} \neq z$ only for the sake of readability, since $1/\nu_{\text{WF}} = z$ can be treated in a perfectly way. From Eq. (C.89), we directly obtain

$$r(b) = \kappa_{d,z,1,\nu_0} \frac{\frac{2}{\nu_0} - d - z}{\Lambda^{z-1/\nu_0}} \frac{1}{z - 1/\nu_{\text{WF}}} T_0 b^z \left(1 - \left(\frac{b_T}{b} \right)^{z-1/\nu_{\text{WF}}} \right) . \quad (\text{C.90})$$

The asymptotic scaling of the mass $r(b)$ thus depends on the comparison of z and $1/\nu_{\text{WF}}$. First, we want to recover the perturbative result obtained in Sec. C.3, which was obtained for a system below the upper critical dimension, $d + z < 2/\nu_0$, but above the classical lower critical dimension, $d > 1/\nu_0$. We find it useful to define

$$\Delta_q = \frac{2}{\nu_0} - d - z \quad \text{and} \quad \Delta_c = \frac{1}{\nu_0} - d , \quad (\text{C.91})$$

such that the system is below the (quantum) upper critical dimension or classical lower critical dimension if $\Delta_q > 0$ or $\Delta_c > 0$, respectively. To compare the results obtained by integrating out the non-zero Matsubara modes with the finite temperature RG, it is most convenient to discuss the behavior of the correlation length. Using the prior analysis, we have obtained a theory for the Matsubara zero mode characterized by the an effective propagator

$$g(\omega_n = 0, \vec{k})^{-1} = r_0^* + k^{1/\nu_0} . \quad (\text{C.92})$$

Fourier transformation of this propagator yields a correlation length of

$$\xi = (r_0^*)^{-\nu_0} \sim \Delta_q^{-\nu_0} T^{-1/z} . \quad (\text{C.93})$$

In order to evaluate the correlation length with the finite temperature RG, we rewrite the combination $z - 1/\nu_{\text{WF}}$ as

$$z - \frac{1}{\nu_{\text{WF}}} = z - \frac{1}{\nu_0} + \frac{\Delta_q}{3} = d + z - \frac{2}{\nu_0} - \left(d - \frac{1}{\nu_0}\right) + \frac{\Delta_q}{3} = -\frac{2}{3}\Delta_q + \Delta_c < 0 . \quad (\text{C.94})$$

The asymptotic scaling of the mass $r(b)$ is thus given by

$$r(b) = \kappa_{d,z,1,\nu_0} \frac{1}{\Lambda^{z-1/\nu_0}} \frac{\Delta_q}{\frac{2}{3}\Delta_q - \Delta_c} T_0 b^{1/\nu_{\text{WF}}} b_T^{z-1/\nu_{\text{WF}}} . \quad (\text{C.95})$$

We recall that in the case $z = 1/\nu_{\text{WF}}$, implying that $(2/3)\Delta_q = \Delta_c$, logarithmic corrections arise that render the expression of $r(b)$ well-defined. The correlation length can now be defined by understanding that the flow of Eq. (C.95) stems from integrating out fluctuating high energy modes. These modes do however only fluctuate if their momentum is higher than the mass. If $r(b) \geq \Lambda^{1/\nu_0}$, the mass cuts off the diagrams and the flow stops. We can thus determine the scale b^* corresponding to the end of the RG flow as

$$r(b^*) = \Lambda^{1/\nu_0} . \quad (\text{C.96})$$

The physical correlation length can then be defined as above by Fourier transform of the propagator, after undoing the rescaling of the length using the engineering dimension. We thus obtain

$$\xi^{-1/\nu_0} = r(b^*) b^{*-1/\nu_0} \Rightarrow r(b^*) = \Lambda^{1/\nu_0} = \xi^{-1/\nu_0} b^{*1/\nu_0} \Rightarrow b^* = \Lambda \xi . \quad (\text{C.97})$$

From there, we can simply obtain the correlation length as

$$\Lambda^{1/\nu_0} = \kappa_{d,z,1,\nu_0} \frac{1}{\Lambda^{z-1/\nu_0}} \frac{\Delta_q}{\frac{2}{3}\Delta_q - \Delta_c} T_0 (\Lambda \xi)^{1/\nu_{\text{WF}}} b_T^{z-1/\nu_{\text{WF}}} \quad (\text{C.98})$$

$$= \kappa_{d,z,1,\nu_0} \frac{1}{\Lambda^{z-1/\nu_0}} \frac{\Delta_q}{\frac{2}{3}\Delta_q - \Delta_c} T_0 (\Lambda \xi)^{1/\nu_{\text{WF}}} \left(\Lambda/T_0^{1/z}\right)^{z-1/\nu_{\text{WF}}} \quad (\text{C.99})$$

$$= \kappa_{d,z,1,\nu_0} \frac{1}{\Lambda^{z-1/\nu_0}} \frac{\Delta_q}{\frac{2}{3}\Delta_q - \Delta_c} T_0^{1/(z\nu_{\text{WF}})} \xi^{1/\nu_{\text{WF}}} \Lambda^z , \quad (\text{C.100})$$

and therefore obtain

$$\xi^{-1/\nu_{\text{WF}}} = \kappa_{d,z,1,\nu_0} \frac{\Delta_q}{\frac{2}{3}\Delta_q - \Delta_c} T_0^{1/(z\nu_{\text{WF}})} \quad (\text{C.101})$$

$$\Rightarrow \xi = \left(\kappa_{d,z,1,\nu_0} \frac{\Delta_q}{\frac{2}{3}\Delta_q - \Delta_c} \right)^{-\nu_{\text{WF}}} T_0^{-1/z} \sim \left(\frac{\Delta_q}{\frac{2}{3}\Delta_q - \Delta_c} \right)^{-\nu_{\text{WF}}} T_0^{-1/z} . \quad (\text{C.102})$$

We thus find that if $z < \frac{1}{\nu_0}$, and in particular if the theory is above its classical lower critical dimension, $\Delta_c < 0$, the thermal RG reproduces the result of the perturbative

analysis, at least as long as the system is not too close to the classical lower critical dimension, $|\Delta_c| \sim \mathcal{O}(1)$. When the system is in addition far below its upper critical dimension, $\Delta_q \sim \mathcal{O}(1)$, the prefactor is of order one and does therefore not matter for scaling. When Δ_q is small, the prefactor leads to an additional suppression of the correlation length. Since small Δ_q implies $1/\nu_{\text{WF}} = 1/\nu_0 - \Delta_q/3 \sim \mathcal{O}(1/\nu_0)$, we essentially obtain the same small prefactor as before.

If on the other hand the system approaches its classical lower critical dimension, $\Delta_c \rightarrow 0$, the correlation length is even further suppressed by a factor $\Delta_q^{-\nu_{\text{WF}}}$, which signals the fact that thermal fluctuations become important and also disorder the system. When finally the system is below the classical lower critical dimension, $\Delta_c < 0$, the correlation length further decreases until the the RG flow changes its scaling dimension when $\Delta_c \geq 2\Delta_q/3$, or equivalently $z \geq 1/\nu_{\text{WF}}$. In this case, the mass flows as

$$r(b) = \kappa_{d,z,1,\nu_0} \frac{1}{\Lambda^{z-1/\nu_0}} \frac{\Delta_q}{\Delta_c - \frac{2}{3}\Delta_q} T_0 b^z . \quad (\text{C.103})$$

The correlation length, still set by $r(\Lambda\xi) = \Lambda^{1/\nu_0}$, then becomes

$$\xi = \left(\kappa_{d,z,1,\nu_0} \frac{\Delta_q}{\Delta_c - \frac{2}{3}\Delta_q} \right)^{-1/z} T_0^{-1/z} \sim \left(\frac{\Delta_q}{\Delta_c - \frac{2}{3}\Delta_q} \right)^{-1/z} T_0^{-1/z} . \quad (\text{C.104})$$

The correlation length thus has the same temperature scaling, but a different prefactor. This is however not a surprising result. At criticality $r = 0$, the temperature is the only relevant scale, and the correlation length thus has to scale as $T^{-1/z}$ only the prefactor of this scaling can depend on whether the system is above or below the classical lower critical dimension. To conclude, we note that the correlation length can generically be written as

$$\xi = \left(\frac{|\frac{2}{3}\Delta_q - \Delta_c|}{\kappa_{d,z,1,\nu_0} \Delta_q} \right)^{\frac{1}{\max\{1/\nu_{\text{WF}}, z\}}} T_0^{-1/z} . \quad (\text{C.105})$$

C.5 RG equations for the generalized Pommeranchuk model

Different to our previous discussions, the (generalized) Pommeranchuk model has a (2×2) matrix structure, and its order parameter \vec{n} is a 2-component vector. The propagator contains rotation matrices, which modifies the RG equations due to angular averages. In order to derive the modification of the RG equations, we recall that the generalized Pommeranchuk model is described by the action

$$\mathcal{S} = \frac{1}{2} \sum_q \vec{n}_{-q}^T \mathcal{G}_0(q)^{-1} \vec{n}_q + \frac{u_0}{4! \beta V} \sum_{\{q_i\}} (\vec{n}_{q_1}^T \vec{n}_{q_2}) (\vec{n}_{q_3}^T \vec{n}_{q_4}) \delta_{q_1+q_2, q_3+q_4} \quad (\text{C.106})$$

$$= \frac{1}{2} \sum_q \vec{n}_{-q}^T \mathcal{G}_0(q)^{-1} \vec{n}_q + \frac{u_0}{4! \beta V} \sum_{\{q_i\}, j, k} (n_{q_1}^{(j)} n_{q_2}^{(j)}) (n_{q_3}^{(k)} n_{q_4}^{(k)}) \delta_{q_1+q_2, q_3+q_4} , \quad (\text{C.107})$$

where q abbreviates $q = (\omega_n, \vec{q})$, β is the inverse temperature, V denotes the volume in $d = 2$ spatial dimension, and u_0 is the bare interaction of the modes. The vector \vec{n}_q is

the order parameter field and embraces the longitudinal and transversal mode. Its bare inverse propagator $\mathcal{G}_0^{-1}(q)$ is a 2×2 matrix that is diagonal in the frame of reference where \vec{q} is parallel to the x -axis and reads

$$\mathcal{G}_0(q)^{-1} = U(q)^{-1} \begin{pmatrix} g_>(q)^{-1} & 0 \\ 0 & g_<(q)^{-1} \end{pmatrix} U(q) , \quad (\text{C.108})$$

with $U(q)$ performing the necessary rotation of 2θ in order to diagonalize the Green's function matrix (θ is the angle between \vec{q} and the x -axis),

$$U(q) = \begin{pmatrix} \cos(2\theta) & \sin(2\theta) \\ -\sin(2\theta) & \cos(2\theta) \end{pmatrix} . \quad (\text{C.109})$$

The generalized propagators read

$$g_<(\vec{q}, \omega_n)^{-1} = r_0 + q^{1/\nu_0} + \frac{(\eta_< \omega_n)^2}{q^{2z_<-1/\nu_0}} , \quad (\text{C.110})$$

$$g_>(\vec{q}, \omega_n)^{-1} = r_0 + q^{1/\nu_0} + \eta_> \frac{|\omega_n|}{q^{z_>-1/\nu_0}} , \quad (\text{C.111})$$

where η_i are the kinetic coefficients. The propagator is thus given by

$$\mathcal{G}_0(q) = U(q)^{-1} \begin{pmatrix} g_>(q) & 0 \\ 0 & g_<(q) \end{pmatrix} U(q) \quad (\text{C.112})$$

$$= \begin{pmatrix} g_>(q) \cos^2(2\theta) + g_<(q) \sin^2(2\theta) & (g_>(q) - g_<(q)) \cos(2\theta) \sin(2\theta) \\ (g_>(q) - g_<(q)) \cos(2\theta) \sin(2\theta) & g_>(q) \sin^2(2\theta) + g_<(q) \cos^2(2\theta) \end{pmatrix} . \quad (\text{C.113})$$

The interaction then gives rise to a matrix self energy Σ that has the diagonal components

$$\Sigma_{11} = \frac{u_0}{4!} \frac{1}{\beta V} \sum_{q_1} \left(6 \langle n_{q_1}^{(1)} n_{-q_1}^{(1)} \rangle + 2 \langle n_{q_1}^{(2)} n_{-q_1}^{(2)} \rangle \right) , \quad (\text{C.114})$$

$$\Sigma_{22} = \frac{u_0}{4!} \frac{1}{\beta V} \sum_{q_1} \left(6 \langle n_{q_1}^{(2)} n_{-q_1}^{(2)} \rangle + 2 \langle n_{q_1}^{(1)} n_{-q_1}^{(1)} \rangle \right) , \quad (\text{C.115})$$

$$\Sigma_{12} = \frac{u_0}{4!} \frac{1}{\beta V} \sum_{q_1} 4 \langle n_{q_1}^{(1)} n_{-q_1}^{(2)} \rangle , \quad (\text{C.116})$$

$$\Sigma_{21} = \frac{u_0}{4!} \frac{1}{\beta V} \sum_{q_1} 4 \langle n_{q_1}^{(2)} n_{-q_1}^{(1)} \rangle . \quad (\text{C.117})$$

The average over the angular coordinate θ yield

$$\left(6 \langle n_{q_1}^{(1)} n_{-q_1}^{(1)} \rangle + 2 \langle n_{q_1}^{(2)} n_{-q_1}^{(2)} \rangle \right) = \left(6 \langle n_{q_1}^{(1)} n_{-q_1}^{(1)} \rangle + 2 \langle n_{q_1}^{(2)} n_{-q_1}^{(2)} \rangle \right) = 4 (\langle g_< \rangle + \langle g_> \rangle) , \quad (\text{C.118})$$

$$\langle n_{q_1}^{(1)} n_{-q_1}^{(2)} \rangle = \langle n_{q_1}^{(2)} n_{-q_1}^{(1)} \rangle = 0 , \quad (\text{C.119})$$

since the propagators $g_<$ and $g_>$ do not depend on θ . These averages can now be performed just as in appendix C.1. The self energy can than be split between the two modes as

$$\Sigma_{ii} = \Sigma_{ii} \cos^2(\theta) + \Sigma_{ii} \sin^2(\theta) , \quad (\text{C.120})$$

which finally both obtain the same mass renormalization $\delta r = 2\Sigma_{11} = 2\Sigma_{22}$ (the factor of 2 is due to the fact that the propagator contains a factor $1/2$). The RG equation of the mass r is thus given by the contributions of the two modes as we have calculated them before, multiplied with a prefactor of

$$\frac{2 \cdot 4}{12} \frac{1}{4!} = \frac{1}{36} . \quad (\text{C.121})$$

For the interaction, a similar analysis can be made. The expansion of of action to second order yields the one-loop correction to the interaction as

$$\delta u = -\frac{1}{2} \frac{u^2}{4!} 36 \frac{1}{\beta V} \sum_{\omega_n \vec{k}} (\langle g_{<}^2 \rangle + \langle g_{>}^2 \rangle + 2\langle g_{<} g_{>} \rangle) , \quad (\text{C.122})$$

where the factor $1/2$ appears since we analyze a second order expansion, and the factor of 36 enters because of the sum over various contributions and the averages over $\cos^4(2\theta)$, $\sin^4(2\theta)$, $\sin^2(2\theta) \cos^2(2\theta)$ and so on. Compared to the initial calculation, this leads to an *additional* prefactor of

$$\frac{1}{36} \frac{1}{2} \frac{1}{4!} 36 = \frac{1}{2 \cdot 4!} = \frac{1}{48} , \quad (\text{C.123})$$

and the appearance of mixed terms.

C.6 Modification of the RG equations due to kinetic coefficients

In a system with multiple dynamics, the propagators have to be generalized by the introduction of kinetic coefficients $\eta_i > 0$, see Sec. 5.6. The generalized action is then of the form

$$\mathcal{S} = \int d^d x \int d\tau \Psi(\vec{x}, \tau) \frac{g_i^{-1}}{2} \Psi(\vec{x}, \tau) + u \int d^d x \int d\tau \Psi(\vec{x}, \tau) \Psi(\vec{x}, \tau) \Psi(\vec{x}, \tau) \Psi(\vec{x}, \tau) , \quad (\text{C.124})$$

where the generalized propagator reads, as a function of momentum k and imaginary time ω_n ,

$$g_i(\omega_n, \vec{k})^{-1} = r + k^{1/\nu_0} + \frac{|\eta_i \omega_n|^y}{k^{y z_i - 1/\nu_0}} . \quad (\text{C.125})$$

This does of course also affect the RG equations.

Zero temperature RG

The zero temperature RG equations can be derived from the generalized zero temperature correction

$$\delta r^{(1)} = \frac{24 \Omega_d}{(2\pi)^{d+1}} u \int_0^\Lambda dk \int_0^\Gamma d\omega \frac{(-r) k^{d-1}}{\left(k^{1/\nu_0} + \frac{(\eta_i \omega)^y}{k^{y z_i - 1/\nu_0}}\right)^2}. \quad (\text{C.126})$$

As a first step, we redefine $\eta_i \omega \rightarrow \omega$ and obtain

$$\delta r^{(1)} = \frac{24 \Omega_d}{(2\pi)^{d+1}} \frac{u}{\eta_i} \int_0^\Lambda dk \int_0^{\eta_i \Gamma} d\omega \frac{(-r) k^{d-1}}{\left(k^{1/\nu_0} + \frac{\omega^y}{k^{y z_i - 1/\nu_0}}\right)^2}. \quad (\text{C.127})$$

The RG step still consists of integrating out a shell of momenta $[\Lambda/b, \Lambda]$ and frequencies $[\eta_i \Gamma/b^{z_i}, \eta_i \Gamma]$, where $\eta_i \Gamma \sim \Lambda^{z_i}$. Importantly, due to our redefinition $\eta_i \omega \rightarrow \omega$, the RG step does now involve the dynamical exponent z_i , and not the arbitrary exponent z . We find

$$\Delta \delta r^{(1)} = \frac{24 \Omega_d}{(2\pi)^{d+1}} \frac{u}{\eta_i} \left[\int_{\Lambda/b}^\Lambda dk \int_0^{\eta_i \Gamma} d\omega \frac{(-r) k^{d-1}}{\left(k^{1/\nu_0} + \frac{\omega^y}{k^{y z_i - 1/\nu_0}}\right)^2} + \int_0^\Lambda dk \int_{\eta_i \Gamma/b^{z_i}}^{\eta_i \Gamma} d\omega \frac{(-r) k^{d-1}}{\left(k^{1/\nu_0} + \frac{\omega^y}{k^{y z_i - 1/\nu_0}}\right)^2} \right]. \quad (\text{C.128})$$

The RG equation thus becomes

$$\frac{\partial r(b)}{\partial \ln(b)} = \frac{24 \Omega_d}{(2\pi)^{d+1}} \frac{u}{\eta_i} \left[\int_0^{\eta_i \Gamma} d\omega \frac{(-r) \Lambda^{d+2y z_i - 2/\nu_0}}{(\Lambda^{y z_i} + \omega^y)^2} + z_i \eta_i \Gamma \int_0^\Lambda dk \frac{(-r) k^{d+2y z_i - 2/\nu_0 - 1}}{(k^{y z_i} + (\eta_i \Gamma)^y)^2} \right]. \quad (\text{C.129})$$

Now defining $k^{z_i} = \omega$ in the second term, we find

$$\frac{\partial r(b)}{\partial \ln(b)} = \frac{24 \Omega_d}{(2\pi)^{d+1}} \frac{u}{\eta_i} \left[\int_0^{\eta_i \Gamma} d\omega \frac{(-r) \Lambda^{d+2y z_i - 2/\nu_0}}{(\Lambda^{y z_i} + \omega^y)^2} + \eta_i \Gamma \int_0^{\Lambda^{z_i}} d\omega \frac{(-r) \omega^{(d+2y z_i - 2/\nu_0 - z_i)/z_i}}{(\omega^y + \Lambda^{y z_i})^2} \right], \quad (\text{C.130})$$

and with $\eta_i \Gamma = \Lambda^{z_i}$ and $\tilde{\omega} = \omega/\Lambda^{z_i}$, we finally obtain

$$\frac{\partial r(b)}{\partial \ln(b)} = \frac{24 \Omega_d}{(2\pi)^{d+1}} \frac{u}{\eta_i} (-r) \Lambda^{(d+z_i-2/\nu_0)} \int_0^1 d\tilde{\omega} \frac{1 + \tilde{\omega}^{(d+2y z_i - 2/\nu_0 - z_i)/z_i}}{(1 + \tilde{\omega}^y)^2}. \quad (\text{C.131})$$

We can thus write the final RG equation as

$$\frac{\partial r(b)}{\partial \ln(b)} = -K_{d, z_i, y, \nu_0} \Lambda^{d+z_i-2/\nu_0} \frac{u(b) r(b)}{\eta_i(b)}, \quad (\text{C.132})$$

where

$$K_{d, z_i, y, \nu_0} = \frac{24 \Omega_d}{(2\pi)^{d+1}} \int_0^1 d\tilde{\omega} \frac{1 + \tilde{\omega}^{(d+2y z_i - 2/\nu_0 - z_i)/z_i}}{(1 + \tilde{\omega}^y)^2} \quad (\text{C.133})$$

Finite temperatures correction for $y = 1$

For the finite temperature correction, we stick to the case $y = 1$. Equation (C.43) then becomes

$$\delta r|_T - \delta r|_{T=0} = 24 \frac{uT}{V} \sum_{\vec{k}} \frac{1}{2\pi i} \int_0^{2T} d\mathcal{E} \frac{1}{\mathcal{E}} \frac{\frac{i\eta_i \mathcal{E}}{k^{z_i-1/\nu_0}} - \frac{-i\eta_i \mathcal{E}}{k^{z_i-1/\nu_0}}}{(r + k^{1/\nu_0})^2 + \left(\frac{\eta_i \mathcal{E}}{k^{z_i-1/\nu_0}}\right)^2} \quad (\text{C.134})$$

$$= 24 \frac{uT}{V} \sum_{\vec{k}} \frac{1}{2\pi i} \int_0^{2\eta_i T} d\mathcal{E}' \frac{1}{\mathcal{E}'} \frac{\frac{i\mathcal{E}'}{k^{z_i-1/\nu_0}} - \frac{-i\mathcal{E}'}{k^{z_i-1/\nu_0}}}{(r + k^{1/\nu_0})^2 + \left(\frac{\mathcal{E}'}{k^{z_i-1/\nu_0}}\right)^2}, \quad (\text{C.135})$$

where we have defined $\mathcal{E}' = \eta_i \mathcal{E}$. From there, it is easy to obtain the finite temperature contribution to the RG equation as

$$\left. \frac{\partial r}{\partial \ln(b)} \right|_{T-T=0} \approx \frac{24 \Omega_d}{(2\pi)^{(d+1)}} \pi u(b) T(b) \Lambda^{d-1/\nu_0} \Theta \left(\frac{\eta_i(b) T(b)}{\Lambda^{z_i}} - 1 \right). \quad (\text{C.136})$$

C.6.1 Additional mixed diagrams

In addition to the diagrams involving only the one or the other mode, additional mixed diagrams will appear for the renormalization of the interaction. The mixing modes have dynamical exponents z_1 and z_2 with $z_1 < z_2$. Dropping numerical prefactors, these have the form

$$\delta u_{\text{mixed}} \sim u^2 \int_0^\Lambda dk \int_0^\Gamma d\omega \frac{(-r) k^{d-1}}{\left(k^{1/\nu_0} + \frac{(\eta_1 \omega)^{y_1}}{k^{y_1 z_1 - 1/\nu_0}}\right) \left(k^{1/\nu_0} + \frac{(\eta_2 \omega)^{y_2}}{k^{y_2 z_2 - 1/\nu_0}}\right)} \quad (\text{C.137})$$

$$= u^2 \int_0^\Lambda dk \int_0^\Gamma d\omega \frac{(-r) k^{d+y_1 z_1 + y_2 z_2 - 2/\nu_0 - 1}}{(k^{y_1 z_1} + (\eta_1 \omega)^{y_1}) (k^{y_2 z_2} + (\eta_2 \omega)^{y_2})} \quad (\text{C.138})$$

$$= \frac{u^2}{\eta_2} \int_0^\Lambda dk \int_0^{\Lambda^{z_2}} d\omega' \frac{(-r) k^{d+y_1 z_1 + y_2 z_2 - 2/\nu_0 - 1}}{(k^{y_1 z_1} + ((\eta_1/\eta_2) \omega')^{y_1}) (k^{y_2 z_2} + \omega'^{y_2})}, \quad (\text{C.139})$$

where $\omega' = \eta_2 \omega$ and using $\eta_i \Gamma = \Lambda^{z_i}$. In an RG analysis where frequencies are rescaled with an arbitrary dynamical exponent z , the kinetic coefficients flow as

$$\frac{\partial \eta_i}{\ln(b)} = (z_i - z) \eta_i(b), \quad (\text{C.140})$$

see Sec. 5.6. In this case, the ratio η_1/η_2 is suppressed, $\eta_1(b)/\eta_2(b) \sim b^{z_1 - z_2}$. Asymptotically, the correction to the interaction stemming from mixed terms is thus of the form

$$\delta u_{\text{mixed}} \rightarrow \frac{u^2}{\eta_2} \int_0^\Lambda dk \int_0^{\Lambda^{z_2}} d\omega' \frac{(-r) k^{d+y_1 z_1 + y_2 z_2 - 2/\nu_0 - 1}}{(k^{y_1 z_1}) (k^{y_2 z_2} + \omega'^{y_2})}, \quad (\text{C.141})$$

and thus suppressed with a prefactor of $1/\eta_2$.

C.7 Integration of the RG equations for the generalized Pomeranchuk model

The full RG equations for the generalized Pomeranchuk model are given by

$$\frac{\partial r}{\partial \ln(b)} = 2r(b) - \frac{K_{d,z<,2,1/2}}{36} \Lambda^{d+z-4} \frac{u(b)r(b)}{\eta_{<}(b)} + \frac{\Omega_d}{(2\pi)^{(d+1)}} \frac{2\pi}{3} u(b) T(b) \Lambda^{d-2} \Theta(b - b_T^>) , \quad (\text{C.142a})$$

$$\frac{\partial u}{\partial \ln(b)} = (4 - d - z) u(b) - \frac{3}{48} K_{d,z<,2,1/2} \Lambda^{d+z-4} \frac{u^2(b)}{\eta_{<}(b)} , \quad (\text{C.142b})$$

$$\frac{\partial T}{\partial \ln(b)} = z T(b) , \quad (\text{C.142c})$$

$$\frac{\partial \eta_{<}}{\partial \ln(b)} = (z_{<} - z) \eta_{<}(b) , \quad (\text{C.142d})$$

$$\frac{\partial \eta_{>}}{\partial \ln(b)} = (z_{>} - z) \eta_{>}(b) \quad (\text{C.142e})$$

where $K_{d,z<,2,1/2}$ is a constant of order one, see Eq. (C.133) and appendices C.1, C.6 and C.5. In the RG analysis, we again want to use the distances from the upper critical dimension Δ_q and the distance to classical lower critical dimension Δ_c defined in Sec. 5.3. For the generalized Pomeranchuk model, they are given by

$$\Delta_q = 4 - d - z_{<} \quad \text{and} \quad \Delta_c = 2 - d , \quad (\text{C.143})$$

such that quantum or classical fluctuations are singular if the distance to the respective critical dimension is positive, $\Delta_q > 0$ or $\Delta_c > 0$. By construction, the generalized Pomeranchuk model is below its upper critical dimension, $\Delta_q > 0$.

C.7.1 Zero temperature flow

At zero temperature, the integration of the above RG equations is straight forward. The temperature and kinetic coefficients flow as

$$T(b) = T_0 b^z , \quad \eta_{<}(b) = \eta_{<,0} b^{z_{<} - z} , \quad \eta_{>}(b) = \eta_{>,0} b^{z_{>} - z} , \quad (\text{C.144})$$

where T_0 , $\eta_{<,0}$ and $\eta_{>,0}$ are the initial values of T , $\eta_{<}$ and $\eta_{>}$. The initial temperature T_0 equals the physical temperature $T = 0$, such that also the flowing temperature always vanishes,

$$T(b) = 0 . \quad (\text{C.145})$$

The quantum fluctuations of the mode with the smaller dynamical exponent $z_{<}$ drive a flow of the rescaled interaction

$$U(b) = \frac{u(b)}{\eta_{<}(b)} , \quad (\text{C.146})$$

which integrates to

$$U(b) = U_{\text{WF}} \frac{1}{1 + (b_{\text{WF}}/b)^{\Delta_q}} , \quad (\text{C.147a})$$

$$U_{\text{WF}} = \frac{\Delta_q}{\frac{3}{48} K_{d,z<,2,1/2} \Lambda^{d+z-4}} , \quad (\text{C.147b})$$

$$b_{\text{WF}} = \left(\frac{U_{\text{WF}}}{U_0} - 1 \right)^{1/\Delta_q} , \quad (\text{C.147c})$$

with initial condition $U_0 = u_0/\eta_{<,0}$. The fact that the relevant effective interaction is given by $U = u/\eta_{<}$ reflects the fact that quantum fluctuations are governed by the mode with the smaller dynamical exponent $z_{<}$, which is thus responsible for reaching the Wilson-Fisher fixed point. This can now be plugged into the RG equations for r , which as a function of the effective interaction U reads at zero temperature

$$\frac{\partial r}{\partial \ln(b)} = 2r(b) - \frac{4}{9} \frac{\Delta_q}{U_{\text{WF}}} U(b) r(b) , \quad (\text{C.148})$$

which yields

$$r(b) = r_0 b^{2 - \frac{4}{9} \Delta_q} \left(\frac{1 + b_{\text{WF}}^{\Delta_q}}{1 + (b_{\text{WF}}/b)^{\Delta_q}} \right)^{4/9} . \quad (\text{C.149})$$

The initial value of the flowing mass is given the physical value, $r_0 = r$. We note that RG stages $b \gg b_{\text{WF}}$, the flow of $r(b)$ can be approximated by

$$\frac{\partial r}{\partial \ln(b)} = \frac{1}{\nu_{\text{WF}}} r(b) , \quad (\text{C.150})$$

where we have introduced the Wilson-Fisher value of the correlation length exponent

$$\frac{1}{\nu_{\text{WF}}} = 2 - \frac{4}{9} \Delta_q . \quad (\text{C.151})$$

The RG flow has to be stopped when the flowing mass equals the high momentum cutoff Λ^2 , since all modes are fully gapped beyond this scale. This defines the RG stage b^* as

$$r(b^*) = \Lambda^2 . \quad (\text{C.152})$$

This final mass sets the correlation length ξ according to the engineering dimension of the mass term as

$$r(b^*) = \xi^{-2} b^{*2} , \quad (\text{C.153})$$

which implies $b^* = \Lambda \xi$. Assuming that $b^* \gg b_{\text{WF}}$, i.e. assuming that the Wilson-Fisher fixed point is the relevant fixed point for the system, we find that

$$\Lambda^2 = r_0 (\Lambda \xi)^{1/\nu_{\text{WF}}} \left(1 + b_{\text{WF}}^{\frac{4}{9} \Delta_q} \right) \quad (\text{C.154})$$

$$\Rightarrow \quad \xi = r_0^{-\nu_{\text{WF}}} \left(\frac{\Lambda^{\frac{4}{9} \Delta_q}}{\left(1 + b_{\text{WF}}^{\frac{4}{9} \Delta_q} \right)} \right)^{\nu_{\text{WF}}} . \quad (\text{C.155})$$

If we furthermore assume that $U_0 \ll U_{\text{WF}}$, or equivalently $b_{\text{WF}} \gg 1$, the correlation length is given

$$\xi = r_0^{-\nu_{\text{WF}}} \left(\frac{\frac{3}{48} K_{d,z_<,2,1/2}}{\Delta_q} U_0 \right)^{\frac{4}{9} \nu_{\text{WF}}} . \quad (\text{C.156})$$

C.7.2 Finite temperature flow: $\frac{1}{\nu_{\text{WF}}} < z_<$

At finite temperature T above the quantum critical point and for $1/\nu_{\text{WF}} < z_<$ the flow beyond the scale $b_T^>$ is driven by thermal fluctuations. The RG equation for r ,

$$\frac{\partial r}{\partial \ln(b)} = \frac{1}{\nu_{\text{WF}}} r(b) + \frac{\Omega_d}{(2\pi)^{(d+1)}} \frac{2\pi}{3} U_{\text{WF}} \eta_{<,0}(b) T(b) \Lambda^{d-2} \Theta(b - b_T^>) , \quad (\text{C.157})$$

$$(\text{C.158})$$

can be integrated as

$$r(b) = \frac{\Omega_d}{(2\pi)^{(d+1)}} \frac{2\pi}{3} \frac{U_{\text{WF}}}{z_< - 1/\nu_{\text{WF}}} \eta_{<,0} T_0 \Lambda^{d-2} (b^{z_<} - b^{1/\nu_{\text{WF}}} b_T^{> z_< - 1/\nu_{\text{WF}}}) \quad (\text{C.159})$$

$$\approx \frac{\Omega_d}{(2\pi)^{(d+1)}} \frac{2\pi}{3} \frac{U_{\text{WF}}}{z_< - 1/\nu_{\text{WF}}} \eta_{<,0} T_0 \Lambda^{d-2} b^{z_<} . \quad (\text{C.160})$$

Again, logarithmic corrections arise in the special case $z_< = 1/\nu_{\text{WF}}$, which render the expression of $r(b)$ well-defined in this case. We obtain

$$r(b) \stackrel{z_< = \frac{1}{\nu_{\text{WF}}}}{=} \frac{\Omega_d}{(2\pi)^{(d+1)}} \frac{2\pi}{3} U_{\text{WF}} \eta_{<,0} T_0 \Lambda^{d-2} b^{z_<} \ln \left(\frac{b}{b_T^>} \right) . \quad (\text{C.161})$$

For the sake of readability, we will however from now on specialize to the case $z_< \neq 1/\nu_{\text{WF}}$. The case $z_< = 1/\nu_{\text{WF}}$ can however be discussed in a perfectly analogous way. The correlation length ξ is then found as before using $r(\Lambda\xi) = \Lambda^2$, see Eq. (C.153). We obtain

$$\xi = T_0^{-1/z_<} \left(\frac{\Omega_d}{(2\pi)^{(d+1)}} \frac{2\pi}{3} \frac{U_{\text{WF}} \Lambda^{d+z_<-4}}{z_< - 1/\nu_{\text{WF}}} \eta_{<,0} \right)^{-1/z_<} \quad (\text{C.162})$$

$$= T_0^{-1/z_<} \left(\frac{\Omega_d}{(2\pi)^{(d+1)}} \frac{2\pi}{3} \frac{\Delta_q}{z_< - 1/\nu_{\text{WF}}} \frac{48}{3 K_{d,z_<,2,1/2}} \eta_{<,0} \right)^{-1/z_<} , \quad (\text{C.163})$$

$$= T_0^{-1/z_<} \left(\frac{\Delta_c - \frac{5}{9} \Delta_q}{\Delta_q} \right)^{1/z_<} \left(\frac{\Omega_d}{(2\pi)^{(d+1)}} \frac{2\pi}{3} \frac{48}{3 K_{d,z_<,2,1/2}} \eta_{<,0} \right)^{-1/z_<} . \quad (\text{C.164})$$

C.7.3 Finite temperature flow: $\frac{1}{\nu_{\text{WF}}} > z_{<}$

If quantum fluctuations dominate the asymptotic flow, i.e. for $\frac{1}{\nu_{\text{WF}}} > z_{<}$, the mass integrates to

$$r(b) = \frac{\Omega_d}{(2\pi)^{(d+1)}} \frac{2\pi}{3} \frac{U_{\text{WF}}}{1/\nu_{\text{WF}} - z_{<}} \eta_{<,0} T_0 \Lambda^{d-2} (b^{1/\nu_{\text{WF}}} b_T^{>z_{<-1/\nu_{\text{WF}}} - b^{z_{<}}) \quad (\text{C.165})$$

$$\approx \frac{\Omega_d}{(2\pi)^{(d+1)}} \frac{2\pi}{3} \frac{U_{\text{WF}}}{1/\nu_{\text{WF}} - z_{<}} \eta_{<,0} T_0 \Lambda^{d-2} b^{1/\nu_{\text{WF}}} b_T^{>z_{<-1/\nu_{\text{WF}}}. \quad (\text{C.166})$$

The flow of $r(b)$ is driven by thermal fluctuations for $r(b) < T(b)$, which thus yield a classical starting value for the mass. Quantum fluctuations boost this initial thermal mass when $r(b) \geq T(b)$, which happens for RG stages

$$b \geq b_T^{>} \left(1 + \frac{1}{\frac{\Omega_d}{(2\pi)^{(d+1)}} \frac{2\pi}{3} \frac{U_{\text{WF}}}{1/\nu_{\text{WF}} - z_{<}} \eta_{<,0} \Lambda^{d-2}} \right)^{1/\nu_{\text{WF}} - z_{<}} \approx b_T^{>} \quad (\text{C.167})$$

Thermal fluctuations are thus really only active at the scale $b_T^{>}$. The correlation length, defined by $r(\Lambda\xi) = \Lambda^2$ is then given by

$$\xi = \left(\frac{\Omega_d}{(2\pi)^{(d+1)}} \frac{2\pi}{3} \frac{U_{\text{WF}}}{1/\nu_{\text{WF}} - z_{<}} \eta_{<,0} T_0 \Lambda^{d-4} \Lambda^{1/\nu_{\text{WF}}} b_T^{>z_{<-1/\nu_{\text{WF}}} \right)^{-\nu_{\text{WF}}} \quad (\text{C.168})$$

$$= \left(\frac{\Omega_d}{(2\pi)^{(d+1)}} \frac{2\pi}{3} \frac{U_{\text{WF}} \Lambda^{d+z_{<-4}}}{1/\nu_{\text{WF}} - z_{<}} \eta_{<,0} T_0 (\eta_{>,0} T_0)^{-z_{<+1/\nu_{\text{WF}}}} \right)^{-\nu_{\text{WF}}} \quad (\text{C.169})$$

$$= T_0^{-1/z_e} \left(\frac{\Omega_d}{(2\pi)^{(d+1)}} \frac{2\pi}{3} \frac{U_{\text{WF}} \Lambda^{d+z_{<-4}}}{1/\nu_{\text{WF}} - z_{<}} \eta_{<,0} \eta_{>,0}^{(1/\nu_{\text{WF}} - z_{<})/z_{>}} \right)^{-\nu_{\text{WF}}} \quad (\text{C.170})$$

$$= T_0^{-1/z_e} \left(\frac{\frac{5}{9}\Delta_q - \Delta_c}{\Delta_q} \right)^{\nu_{\text{WF}}} \left(\frac{\Omega_d}{(2\pi)^{(d+1)}} \frac{2\pi}{3} \frac{48}{3K_{d,z_{<},2,1/2}} \eta_{<,0} \eta_{>,0}^{(1/\nu_{\text{WF}} - z_{<})/z_{>}} \right)^{-\nu_{\text{WF}}}, \quad (\text{C.171})$$

where a new dynamical exponent

$$z_e = \frac{z_{>}}{1 + \nu_{\text{WF}}(z_{>} - z_{<})} \quad (\text{C.172})$$

has emerged.

C.7.4 General expression of the correlation length

The correlation length can of course also be calculated for arbitrary starting values of mass and temperature. In this case, we integrate the full RG equation for the mass,

$$\frac{\partial r}{\partial \ln(b)} = 2r(b) - \frac{4}{9} \frac{\Delta_q}{U_{\text{WF}}} U(b) r(b) + \frac{\Omega_d}{(2\pi)^{(d+1)}} \frac{2\pi}{3} U(b) \eta_{<}(b) T(b) \Lambda^{d-2} \Theta(b - b_T^{>}), \quad (\text{C.173})$$

$$(\text{C.174})$$

where the interaction flows as

$$U(b) = U_{\text{WF}} \frac{1}{1 + (b_{\text{WF}}/b)^{\Delta_q}}, \quad (\text{C.175a})$$

$$U_{\text{WF}} = \frac{\Delta_q}{\frac{3}{48} K_{d,z<,2,1/2} \Lambda^{d+z-4}}, \quad (\text{C.175b})$$

$$b_{\text{WF}} = \left(\frac{U_{\text{WF}}}{U_0} - 1 \right)^{1/\Delta_q}, \quad (\text{C.175c})$$

with initial condition $U_0 = u_0/\eta_{<,0}$. In the pure quantum regime $b < b_T^>$, the mass integrates to the same expression already found in Eq. (C.149),

$$r(b) = r_0 b^{1/\nu_{\text{WF}}} \left(\frac{1 + b_{\text{WF}}^{\Delta_q}}{1 + (b_{\text{WF}}/b)^{\Delta_q}} \right)^{4/9}. \quad (\text{C.176})$$

This yields a starting value of

$$r(b_T^>) = r_0 b_T^{>1/\nu_{\text{WF}}} \left(\frac{1 + b_{\text{WF}}^{\Delta_q}}{1 + (b_{\text{WF}}/b_T^>)^{\Delta_q}} \right)^{4/9}. \quad (\text{C.177})$$

for the flow in the extended quantum to classical crossover regime. Further integration yields

$$r(b) = r(b_T^>) \left(\frac{b}{b_T^>} \right)^{1/\nu_{\text{WF}}} + \frac{\Omega_d}{(2\pi)^{(d+1)}} \frac{2\pi}{3} \frac{U_{\text{WF}}}{1/\nu_{\text{WF}} - z_<} \eta_{<,0} T_0 \Lambda^{d-2} (b^{1/\nu_{\text{WF}}} b_T^{>z_<-1/\nu_{\text{WF}}} - b^{z_<}), \quad (\text{C.178})$$

where we have used the fact that the interaction in the extended quantum to classical crossover regime is entirely given by the Wilson-Fisher fixed point value of U_{WF} if the system is considered close enough to the quantum critical point. For arbitrary r and T , the running mass is thus essentially simply the sum of the two limiting cases $r = 0$, finite T and $T = 0$, finite r . Using the symbols ξ_{LT} for the correlation length at low temperatures, $\xi_{\text{QC,thermal}}$ for the correlation length in the quantum critical regime set by thermal fluctuations (if $z_< > 1/\nu_{\text{WF}}$) and $\xi_{\text{QC,boosted}}$ for the correlation length in the quantum critical regime after for quantum boosted thermal fluctuations,

$$\xi_{\text{LT}} = r_0^{-\nu_{\text{WF}}} \left(\frac{\frac{3}{48} K_{d,z<,2,1/2} U_0}{\Delta_q} \right)^{\frac{4}{9} \nu_{\text{WF}}} \quad (\text{C.179})$$

$$\xi_{\text{QC,thermal}} = (\eta_{<,0} T_0)^{-1/z_<} \left(\frac{\Delta_c - \frac{5}{9} \Delta_q}{\Delta_q} \right)^{1/z_<} \left(\frac{\Omega_d}{(2\pi)^{(d+1)}} \frac{2\pi}{3} \frac{48}{3 K_{d,z<,2,1/2}} \right)^{-1/z_<} \quad (\text{C.180})$$

$$\xi_{\text{QC,boosted}} = T_0^{-1/z_e} \left(\frac{\frac{5}{9} \Delta_q - \Delta_c}{\Delta_q} \right)^{\nu_{\text{WF}}} \left(\frac{\Omega_d}{(2\pi)^{(d+1)}} \frac{2\pi}{3} \frac{48}{3 K_{d,z<,2,1/2}} \eta_{<,0} \eta_{>,0}^{(1/\nu_{\text{WF}} - z_<)/z_>} \right)^{-\nu_{\text{WF}}}, \quad (\text{C.181})$$

the flow of the mass can be written as

$$r(b) = \Lambda^2 \left(\frac{b}{\Lambda \xi_{\text{LT}}} \right)^{1/\nu_{\text{WF}}} + \Lambda^2 \left(\left(\frac{b}{\Lambda \xi_{\text{QC,thermal}}} \right)^{z_{<}} + \left(\frac{b}{\Lambda \xi_{\text{QC,boosted}}} \right)^{1/\nu_{\text{WF}}} \right) \Theta(b - b_T^>). \quad (\text{C.182})$$

The correlation length is then given as the solution of the implicit equation $r(\Lambda\xi) = \Lambda^2$, and thus

$$1 = \left(\frac{\xi}{\xi_{\text{LT}}} \right)^{1/\nu_{\text{WF}}} + \left(\left(\frac{\xi}{\xi_{\text{QC,thermal}}} \right)^{z_{<}} + \left(\frac{\xi}{\xi_{\text{QC,boosted}}} \right)^{1/\nu_{\text{WF}}} \right) \Theta(\xi - \xi_T^>) \quad (\text{C.183})$$

$$\Rightarrow \xi^{1/\nu_{\text{WF}}} = \frac{1}{\left(\frac{1}{\xi_{\text{LT}}} \right)^{1/\nu_{\text{WF}}} + \left[\left(\frac{1}{\xi_{\text{QC,thermal}}} \right)^{1/\nu_{\text{WF}}} \left(\frac{\xi}{\xi_{\text{QC,thermal}}} \right)^{z_{<-1/\nu_{\text{WF}}}} + \left(\frac{1}{\xi_{\text{QC,boosted}}} \right)^{1/\nu_{\text{WF}}} \right] \Theta(\xi - \xi_T^>)}. \quad (\text{C.184})$$

Since furthermore $\xi_T^>$ is always smaller than $\xi_{\text{QC,thermal}}$ and $\xi_{\text{QC,boosted}}$, we can drop the Heaviside function and express the correlation length as the minimum of the three length scales ξ_{LT} , $\xi_{\text{QC,thermal}}$ and $\xi_{\text{QC,boosted}}$,

$$\xi = \min \{ \xi_{\text{LT}}, \xi_{\text{QC,thermal}}, \xi_{\text{QC,boosted}} \}. \quad (\text{C.185})$$

We can thus reasonably approximate the solution to the implicit equation (C.184) as

$$\begin{aligned} \xi &\approx \left[\frac{1}{\left(\frac{1}{\xi_{\text{LT}}} \right)^{1/\nu_{\text{WF}}} + \left(\frac{1}{\xi_{\text{QC,boosted}}} \right)^{1/\nu_{\text{WF}}} + \left(\frac{1}{\xi_{\text{QC,thermal}}} \right)^{1/\nu_{\text{WF}}} \left(\frac{\xi}{\xi_{\text{QC,thermal}}} \right)^{z_{<-1/\nu_{\text{WF}}}}} \right]^{\nu_{\text{WF}}} \\ &= \frac{\xi_R}{\left(1 + \left(\frac{\xi_R}{\xi} \right)^{1/\nu_{\text{WF}}} \left(\frac{\xi}{\xi_{\text{QC,thermal}}} \right)^{z_{<}} \right)^{\nu_{\text{WF}}}}. \end{aligned} \quad (\text{C.186})$$

C.8 RG equation for the free energy

Since the presence of the interaction u_0 in the generalized Pomeranchuk problem prohibits an exact calculation of the free energy, the latter is most conveniently calculated in a perturbative RG approach around the Gaussian fixed point. We will now derive the corresponding RG equations, following work of Nelson and Millis.^{102,103} Starting point is the action of the generalized Pomeranchuk model

$$\mathcal{S} = \frac{1}{2} \sum_k \vec{n}_{-k}^T \mathcal{G}_0(k)^{-1} \vec{n}_k + \frac{u_0}{4! \beta V} \sum_{k_i} (\vec{n}_{k_1}^T \vec{n}_{k_2}) (\vec{n}_{k_3}^T \vec{n}_{k_4}) \delta_{k_1+k_2, k_3+k_4}, \quad (\text{C.187})$$

$$\mathcal{G}_0(k)^{-1} = \begin{pmatrix} \cos(2\theta) & -\sin(2\theta) \\ \sin(2\theta) & \cos(2\theta) \end{pmatrix} \begin{pmatrix} g_>(k) & 0 \\ 0 & g_<(k) \end{pmatrix} \begin{pmatrix} \cos(2\theta) & \sin(2\theta) \\ -\sin(2\theta) & \cos(2\theta) \end{pmatrix}, \quad (\text{C.188})$$

$$g_<(\vec{k}, \omega_n) = r + |\vec{k}|^2 + \frac{(\eta_< \omega_n)^2}{|\vec{k}|^{2z_<-2}} \quad \text{and} \quad g_>(\vec{k}, \omega_n) = r + |\vec{k}|^2 + \frac{|\eta_> \omega_n|}{|\vec{k}|^{z_>-2}}. \quad (\text{C.189})$$

The latter defines the free energy as

$$F = -T \ln(\mathcal{Z}) \quad (\text{C.190})$$

where the partition function is given by functional integral

$$\mathcal{Z} = \int \mathcal{D}(\vec{n}) e^{-\mathcal{S}}. \quad (\text{C.191})$$

In the non-interacting case, $u_0 = 0$, the critical part of free energy density $\mathcal{F}_0 = (F_{\text{crit.}}/V)_{u_0 \rightarrow 0}$ can straightforwardly be evaluated. Performing the functional integral, we obtain

$$\begin{aligned} \mathcal{F}_0[r, T, \eta_<, \eta_>, \Lambda] &= \frac{1}{2} \frac{1}{\beta} \sum_{\omega_n} \int d^d q \left[\ln \left(\beta(r + q^2 + \frac{(\eta_< \omega_n)^2}{q^{2z_<-2}}) \right) \right. \\ &\quad \left. + \ln \left(\beta(r + q^2 + \frac{|\eta_> \omega_n|}{q^{z_>-2}}) \right) \right] \\ &= \int_0^\Lambda dq \int \frac{d\Omega_d}{(2\pi)^d} q^{d-1} T \ln \left(2 \sinh \left(\frac{\sqrt{q^{2z_<-2}(r + q^2)}}{2\eta_< T} \right) \right) \\ &\quad + \int_0^\Lambda dq \int \frac{d\Omega_d}{(2\pi)^d} q^{d-1} \int_0^\infty \frac{d\omega}{2\pi} \coth \left(\frac{\omega}{2T} \right) \arctan \left(\frac{\eta_> \omega}{q^{z_>-2}(r + q^2)} \right), \end{aligned} \quad (\text{C.192})$$

where we have already introduced the high momentum cutoff, $|\vec{k}| \leq \Lambda$ and detailed on the lefthand-side the various parameters entering the free energy density. The renormalizations of the free energy due to interactions is now captured by a perturbative RG. To this end, we divide the full action into its free part and the interactions,

$$\mathcal{S}_\Lambda = \mathcal{S}_0[r, T, \eta_<, \eta_>, \Lambda] + \mathcal{S}_{\text{int}}[u_0, T, \Lambda], \quad (\text{C.193})$$

where the dependence of the various parameters and the cutoff has been detailed. We can now proceed to integrating out high energy shells as discussed in appendix C.1. Performing the integral over the high momentum shell $|\vec{k}| \in [\Lambda/b, \Lambda]$ perturbatively to one-loop order and proceeding with the rescaling of all lengths, frequencies and parameters, we are left with an action that has the same form as before, but effectively renormalized parameters,

$$\mathcal{S}_{\Lambda/b} = \mathcal{S}_0[r(b), T(b), \eta_{<}(b), \eta_{>}(b), \Lambda] + \mathcal{S}_{\text{int}}[u(b), T(b), \Lambda] . \quad (\text{C.194})$$

This action only describes the degrees of freedom living below the reduced cutoff Λ/b , while the renormalization of the various parameters takes into account the interactions with the high energy degrees of freedom. The latter have disappeared from the effective low energy action. They do, however, yields a contribution to the free energy, which reads

$$\delta\mathcal{F} = -\frac{T}{V} \ln(\mathcal{Z}_\Lambda) + \frac{T}{V} \ln(\mathcal{Z}_{\Lambda/b}) , \quad (\text{C.195})$$

where

$$\mathcal{Z}_\Lambda = \int \mathcal{D}(\vec{n}) e^{-\mathcal{S}_\Lambda} . \quad (\text{C.196})$$

For an infinitesimal small RG step, $b \rightarrow 1^+$, and because we are doing a one-loop perturbation theory around the non-interacting limit where interactions are considered as renormalizations of the other parameters in the system, the correction to the free energy due to the high momentum shell $|\vec{k}| \in [\Lambda/b, \Lambda]$ is calculated as

$$\delta\mathcal{F} = \mathcal{F}_0[r, T, \eta_{<}, \eta_{>}, \Lambda] - \mathcal{F}_0[r, T, \eta_{<}, \eta_{>}, \Lambda/b] , \quad (\text{C.197})$$

where \mathcal{F}_0 is the non-interacting form of the free energy, see Eq. (C.192). The effect of interactions is captured by the rescaling $r \rightarrow r(b)$, $T \rightarrow T(b)$ and $\eta_i \rightarrow \eta_i(b)$ for the next RG step. The continuous RG equation for the free energy can thus be defined as

$$\frac{\partial\mathcal{F}}{\partial \ln(b)} = \lim_{b \rightarrow 1^+} \frac{\delta\mathcal{F}}{\ln(b)} \Big|_{b=1} , \quad (\text{C.198})$$

and we obtain

$$\begin{aligned} \frac{\partial\mathcal{F}}{\partial \ln(b)} &= b^{-(d+z)} \int \frac{d\Omega_d}{(2\pi)^d} \Lambda^{d-1} T(b) \ln \left(2 \sinh \left(\frac{\sqrt{\Lambda^{2z < -2}(r(b) + \Lambda^2)}}{2\eta_{<}(b) T(b)} \right) \right) \\ &+ b^{-(d+z)} \int \frac{d\Omega_d}{(2\pi)^d} \Lambda^{d-1} \int_0^\infty \frac{d\omega}{2\pi} \coth \left(\frac{\omega}{2T(b)} \right) \arctan \left(\frac{\eta_{>}(b) \omega}{\Lambda^{z > -2}(r(b) + \Lambda^2)} \right) , \end{aligned} \quad (\text{C.199})$$

where, as usual, the bare values of the different parameters have been replaced by the flowing ones, e.g. $T \rightarrow T(b)$. In addition, a global scaling factor of b^{-d+z} has to be taken into account since the free energy density is a dimensional quantity (this is different in the RG for an action, since actions are dimensionless). The physical free energy density is then obtained when the RG equation (C.199) is integrated,

$$\begin{aligned} \mathcal{F} &= \int_0^\infty d \ln(b) \frac{\partial\mathcal{F}}{\partial \ln(b)} \\ &= \int_0^\infty d \ln(b) b^{-(d+z)} \int \frac{d\Omega_d}{(2\pi)^d} \Lambda^{d-1} T(b) \ln \left(2 \sinh \left(\frac{\sqrt{\Lambda^{2z < -2}(r(b) + \Lambda^2)}}{2\eta_{<}(b) T(b)} \right) \right) \\ &+ \int_0^\infty d \ln(b) b^{-(d+z)} \int \frac{d\Omega_d}{(2\pi)^d} \Lambda^{d-1} \int_0^\infty \frac{d\omega}{2\pi} \coth \left(\frac{\omega}{2T(b)} \right) \arctan \left(\frac{\eta_{>}(b) \omega}{\Lambda^{z > -2}(r(b) + \Lambda^2)} \right) , \end{aligned} \quad (\text{C.200})$$

This equation can be brought into a more physical form by defining

$$q = \frac{\Lambda}{b} \quad (\text{C.201})$$

and introducing

$$\epsilon = b^{z>} \omega , \quad (\text{C.202a})$$

$$\tilde{r}(b) = b^{-2} r(b) , \quad (\text{C.202b})$$

$$\tilde{u}(b) = b^{-(d+z-4)} u(b) , \quad (\text{C.202c})$$

$$\tilde{T}(b) = b^{-z} T(b) = T_0 , \quad (\text{C.202d})$$

$$\tilde{\eta}_{<}(b) = b^{z-z_{<}} \eta_{<}(b) = \eta_{<,0} , \quad (\text{C.202e})$$

$$\tilde{\eta}_{>}(b) = b^{z-z_{>}} \eta_{>}(b) = \eta_{>,0} . \quad (\text{C.202f})$$

$$(\text{C.202g})$$

With these definitions, we find that

$$\mathcal{F} = \mathcal{F}_{<} + \mathcal{F}_{>} , \quad (\text{C.203})$$

$$\mathcal{F}_{<} = \int_0^\Lambda dq \int \frac{d\Omega_d}{(2\pi)^d} q^{d-1} T_0 \ln \left(2 \sinh \left(\frac{\sqrt{q^{2z_{<}-2}(\tilde{r}(\Lambda/q) + q^2)}}{2\eta_{<,0} T_0} \right) \right) , \quad (\text{C.204})$$

$$\mathcal{F}_{>} = \int_0^\Lambda dq \int \frac{d\Omega_d}{(2\pi)^d} q^{d-1} \int_0^\infty \frac{d\epsilon}{2\pi} \coth \left(\frac{\epsilon}{2T_0} \right) \arctan \left(\frac{\eta_{>,0} \epsilon}{q^{z_{>}-2}(\tilde{r}(\Lambda/q) + q^2)} \right) . \quad (\text{C.205})$$

This formula almost coincides with the expression of the free energy without interactions in Eq. (C.192), but shows how the interactions renormalize the mass. In the perturbative RG approach, the effect of interactions can thus be understood as scale-dependent parameters, where the scale dependence is only given by the anomalous scaling dimension.

C.9 Calculation of $\mathcal{F}_{<}$ via RG

We will now calculate the free energy and derivatives thereof in order to derive the leading scaling behavior of various thermodynamic observables. We note that the universal, critical part of the free energy has to vanish in the limit of $r \rightarrow 0, T \rightarrow 0$. In order to extract the scaling of the universal part of the critical free energy density, we will thus always subtract the limit $r \rightarrow 0, T \rightarrow 0$ from expressions (C.203), which removes the leading non-universal part.⁵³ We show here explicitly how the calculation can be done for the free energy density of the mode with the smaller dynamical exponent $\mathcal{F}_{<}$, and are only interested in the leading critical scaling behavior of $\mathcal{F}_{<}$ as a function of r and T close to the quantum critical point. This will allow to perform a number of convenient simplifications, the price for which is that the prefactors of the critical scaling will not be accessible in this calculation. The RG trajectory for the free energy density of the mode with the smaller dynamical exponent $z_{<}$ reads

$$\mathcal{F}_{<} = \int_0^\Lambda dq \int \frac{d\Omega_d}{(2\pi)^d} q^{d-1} T_0 \ln \left(2 \sinh \left(\frac{\sqrt{q^{2z_{<}-2}(\tilde{r}(\Lambda/q) + q^2)}}{2\eta_{<,0} T_0} \right) \right) . \quad (\text{C.206})$$

where $\tilde{r}(b) = b^{-2} r(b)$. It is useful to express the latter combination in terms of the correlation length, which reads

$$\xi = \min \{ \xi_R, \xi_{\text{QC,thermal}} \} = \begin{cases} \xi_R & z_e > z_< \quad \text{or} \quad T < r^{\nu_{\text{WF}} z_<} \\ \xi_{\text{QC,thermal}} & z_e < z_< \quad \text{and} \quad T > r^{\nu_{\text{WF}} z_<} \end{cases}, \quad (\text{C.207})$$

see Eq. (C.184). We can treat these two cases in one go using that

$$\tilde{r}(b) = b^{-2} r(b) = \xi^{-x} \left(\frac{b}{\Lambda} \right)^{x-2}, \quad (\text{C.208})$$

where $x = z_<$ if $\xi = \xi_{\text{QC,thermal}}$ and $x = 1/\nu_{\text{WF}}$ if $\xi = \xi_R$. In addition, we note that $\xi T_0^{1/z_<} \sim \xi/\xi_{\text{QC,thermal}} \leq 1$. The free energy density $\mathcal{F}_<$ can then be written as

$$\mathcal{F}_< \approx \int_0^{\xi^{-1}} dq \int \frac{d\Omega_d}{(2\pi)^d} q^{d-1} T_0 \ln \left(2 \sinh \left(\frac{q^{z_<} \sqrt{\xi^{-x} q^{-x}}}{2\eta_{<,0} T_0} \right) \right) \quad (\text{C.209})$$

$$+ \int_{\xi^{-1}}^{\Lambda} dq \int \frac{d\Omega_d}{(2\pi)^d} q^{d-1} T_0 \ln \left(2 \sinh \left(\frac{q^{z_<}}{2\eta_{<,0} T_0} \right) \right)$$

$$\approx \int_0^{\xi^{-1}} dq \int \frac{d\Omega_d}{(2\pi)^d} q^{d-1} T_0 \ln \left(2 \frac{q^{z_<} \sqrt{\xi^{-x} q^{-x}}}{2\eta_{<,0} T_0} \right) \quad (\text{C.210})$$

$$+ \int_{\xi^{-1}}^{\Lambda} dq \int \frac{d\Omega_d}{(2\pi)^d} q^{d-1} T_0 \frac{q^{z_<}}{2\eta_{<,0} T_0},$$

where we used

$$\ln(2 \sinh(x)) \approx \begin{cases} \ln(2x) & , \quad x \ll 1 \\ x & , \quad x \gg 1 \end{cases}. \quad (\text{C.211})$$

Now defining $x = q \xi$, we obtain

$$\mathcal{F}_< \approx \xi^{-d} T_0 \int_0^1 dx \int \frac{d\Omega_d}{(2\pi)^d} x^{d-1} \ln \left(2 \frac{\xi^{-z_<} x^{z_<-x/2}}{2\eta_{<,0} T_0} \right) \quad (\text{C.212})$$

$$+ \xi^{-(d+z_<)} \int_1^{\Lambda \xi} dx \int \frac{d\Omega_d}{(2\pi)^d} x^{d-1} \frac{x^{z_<}}{2\eta_{<,0}},$$

Next, we calculate the non-universal background. In the limit $r_0 \rightarrow 0$, $T_0 \rightarrow 0$, we obtain (using Eq. (C.211) and that $\tilde{r}(b) \rightarrow 0$ in this limit)

$$\mathcal{F}_<^{\text{non-univ.}} = \int_0^{\Lambda} dq \int \frac{d\Omega_d}{(2\pi)^d} q^{d-1} \frac{q^{z_<}}{2\eta_{<,0}} = \xi^{-(d+z_<)} \int_0^{\xi \Lambda} dx \int \frac{d\Omega_d}{(2\pi)^d} x^{d-1} \frac{x^{z_<}}{2\eta_{<,0}}. \quad (\text{C.213})$$

Performing the integral over the logarithm and subtracting the non-universal part, we find that the free energy density dominantly scales as

$$\mathcal{F}_< \sim \xi^{-(d+z_<)}, \quad (\text{C.214})$$

where we used the fact that $\xi^{-z_<} \gtrsim T_0$.

C.10 Calculation of the thermal expansion using RG trajectories

We want to calculate the two contributions to the thermal expansion deriving from the two modes using their expression an an RG trajectory. The thermal expansion α corresponds to the mixed derivative

$$\alpha = \frac{\partial^2 \mathcal{F}}{\partial T \partial r} = \alpha_{<} + \alpha_{>} , \quad (\text{C.215})$$

$$\alpha_{(\cdot)} = \frac{\partial^2 \mathcal{F}_{(\cdot)}}{\partial T \partial r} . \quad (\text{C.216})$$

We recall from the discussion in Sec. 6.7.2 that a derivative with respect to r acts on \tilde{r} as

$$\frac{\partial \tilde{r} \left(\frac{\Lambda}{q} \right)}{\partial r} \approx c q^{2-1/\nu_{\text{WF}}} , \quad (\text{C.217})$$

$$c = \left(\frac{48 \Delta_q}{3 K_{d,z_{<},2,1/2} U_0} \right)^{4/9} . \quad (\text{C.218})$$

For RG stages $b > b_T^>$, which matter in the $T > r_0^{\nu_{\text{WF}} z_{>}}$ -part of the phase diagram, also the derivative with respect to the temperature T is non-zero. Depending on the ratio of $z_e/z_{<}$, the derivative takes the form

$$\frac{\partial \tilde{r} \left(\frac{\Lambda}{q} \right)}{\partial T} \sim \begin{cases} b^{2-z_{<}} & , \quad z_{<} > z_e \\ T^{1/(\nu_{\text{WF}} z_e)-1} b^{2-1/\nu_{\text{WF}}} & , \quad z_{<} < z_e \end{cases} . \quad (\text{C.219})$$

We will now perform the calculation of the thermal expansion by an integration of the RG trajectories in detail, thereby only trying to extract the scaling behavior with respect to r and T close to the quantum critical point. Like in appendix C.9, our analysis will however *not* attempt to calculate the precise prefactors of the leading scaling behavior, which allows for some convenient approximations.

C.10.1 Contribution of the mode with the smaller dynamical exponent

The contribution of the mode with the smaller dynamical exponent is given by

$$\alpha_{<} = \frac{\partial^2 \mathcal{F}_{<}}{\partial T \partial r} . \quad (\text{C.220})$$

In the high temperature regime, where

$$\xi \approx \left[\frac{1}{\xi_R^{-1/\nu_{\text{WF}}} + \xi_{\text{QC,thermal}}^{-1/\nu_{\text{WF}}}} \right]^{-(d+z_{<})} , \quad (\text{C.221})$$

we can most easily obtain $\alpha_{<}$ from Eq. (C.214),

$$\alpha_{<} = T^{-1} \xi^{-(d+z-1/\nu_0)} . \quad (\text{C.222})$$

This is not possible in the low temperature and intermediate regimes, i.e. for $T < r^{\nu_{\text{WF}} z_{(\cdot)}}$ with $z_{(\cdot)} = \max\{z_{<}, z_e\}$, since the correlation length is then given by

$$\xi = r^{-\nu_{\text{WF}}} . \quad (\text{C.223})$$

and does not depend on temperature anymore. The derivative with respect to r would then vanish. Instead, one has to integrate the full RG trajectory.

Low temperatures: $T < r_0^{\nu_{\text{WF}} z_{>}}$

At lowest temperatures, $T < r_0^{\nu_{\text{WF}} z_{>}}$, the flowing mass has no temperature dependence since its flow is cut off before the thermal scale $b_T^{\>}$ is reached. In this case, the derivation with respect to temperature does only act on the terms explicitly depending on T_0 in Eq. (C.203). We thus find that

$$\alpha_{<} = \int_0^\Lambda dq \int \frac{d\Omega_d}{(2\pi)^d} q^{d+2z_{<}-3} \frac{1}{8 T_0^2 \eta_{<,0}^2} \sinh^{-2} \left(\frac{\sqrt{q^{2z_{<}-2} (\tilde{r}(\Lambda/q) + q^2)}}{2\eta_{<,0} T_0} \right) c q^{2-1/\nu_{\text{WF}}} , \quad (\text{C.224})$$

with

$$\tilde{r}(\Lambda/q) = b^{-2} r(\Lambda/q) = \xi^{-1/\nu_{\text{WF}}} q^{2-1/\nu_{\text{WF}}} . \quad (\text{C.225})$$

This leads us to

$$\alpha_{<} = \int_0^\Lambda dq \int \frac{d\Omega_d}{(2\pi)^d} q^{d+2z_{<}-1-1/\nu_{\text{WF}}} \frac{1}{8 T_0^2 \eta_{<,0}^2} \sinh^{-2} \left(\frac{q^{z_{<}} \sqrt{(\xi^{-1/\nu_{\text{WF}}} q^{-1/\nu_{\text{WF}}} + 1)}}{2\eta_{<,0} T_0} \right) c \quad (\text{C.226})$$

$$\begin{aligned} &\approx \int_0^{\xi^{-1}} dq \frac{\Omega_d}{(2\pi)^d} q^{d+2z_{<}-1-1/\nu_{\text{WF}}} \frac{1}{8 T_0^2 \eta_{<,0}^2} \sinh^{-2} \left(\frac{q^{z_{<}} \sqrt{\xi^{-1/\nu_{\text{WF}}} q^{-1/\nu_{\text{WF}}}}}{2\eta_{<,0} T_0} \right) c \\ &+ \int_{\xi^{-1}}^\Lambda dq \frac{\Omega_d}{(2\pi)^d} q^{d+2z_{<}-1-1/\nu_{\text{WF}}} \frac{1}{8 T_0^2 \eta_{<,0}^2} \sinh^{-2} \left(\frac{q^{z_{<}}}{2\eta_{<,0} T_0} \right) c , \end{aligned} \quad (\text{C.227})$$

where we assumed that $z_{<} > 1/(2\nu_{\text{WF}})$. This is however not a strict requirement, since the condition $d + z_{<} < 4$ implies that $z_{<} < 1/2(\nu_{\text{WF}})$ is only possible for $z_{<} < 1$ in three dimensions and smaller $z_{<}$ in smaller dimensions. Next, we use that for $q \geq \xi^{-1}$, the argument of the sinh is larger than one. Since furthermore the sinh can be approximated as

$$\sinh^{-2}(x) \approx \begin{cases} x^{-2} & , \quad x \ll 1 \\ 4 e^{-2x} & , \quad x \gg 1 \end{cases} , \quad (\text{C.228})$$

we obtain

$$\alpha_{<} \approx c \int_0^{\xi^{-1}} dq \frac{\Omega_d}{(2\pi)^d} q^{d+2z_{<}-1-1/\nu_{\text{WF}}} \frac{1}{8T_0^2 \eta_{<,0}^2} \sinh^{-2} \left(\frac{q^{z_{<}} \sqrt{\xi^{-1/\nu_{\text{WF}}} q^{-1/\nu_{\text{WF}}}}}{2\eta_{<,0} T_0} \right) \quad (\text{C.229})$$

$$\approx c \xi^{-(d-1/\nu_{\text{WF}})} \frac{1}{2(2T_0 \eta_{<,0} \xi^{z_{<}})^2} \int_0^1 dk \frac{\Omega_d}{(2\pi)^d} k^{d+2z_{<}-1-1/\nu_{\text{WF}}} \sinh^{-2} \left(\frac{k^{z_{<}-1/(2\nu_{\text{WF}})}}{2\eta_{<,0} T_0 \xi^{z_{<}}} \right) \quad (\text{C.230})$$

Now defining $q = k^{z_{<}-1/(2\nu_{\text{WF}})}$, we obtain

$$\alpha_{<} \approx c \xi^{-(d-1/\nu_{\text{WF}})} \frac{1}{2(2T_0 \eta_{<,0} \xi^{z_{<}})^2} \int_0^1 dq \frac{\Omega_d}{(2\pi)^d} q^{\frac{d+z_{<}-1/(2\nu_{\text{WF}})}{z_{<}-1/(2\nu_{\text{WF}})}} \sinh^{-2} \left(\frac{q}{2\eta_{<,0} T_0 \xi^{z_{<}}} \right) \quad (\text{C.231})$$

with $k = q\xi$. Since the sinh cuts off the integral in an exponential fashion when its argument reaches one, and since $\xi < T^{-1/z_{<}}$, which implies that this cutoff is reached before $k = 1$, we find

$$\begin{aligned} \alpha_{<} &\approx c \xi^{-(d-1/\nu_{\text{WF}})} \frac{1}{2(2T_0 \eta_{<,0} \xi^{z_{<}})^2} \int_0^{2\eta_{<,0} T_0 \xi^{z_{<}}} dq \frac{\Omega_d}{(2\pi)^d} q^{\frac{d+z_{<}-1/(2\nu_{\text{WF}})}{z_{<}-1/(2\nu_{\text{WF}})}} \left(\frac{q}{2\eta_{<,0} T_0 \xi^{z_{<}}} \right)^{-2} \\ &\sim \xi^{-(d-1/\nu_{\text{WF}})} (T_0 \xi^{z_{<}})^{\frac{d}{z_{<}-1/(2\nu_{\text{WF}})}}. \end{aligned} \quad (\text{C.232})$$

This is exactly the result one would have obtained from a scaling analysis in the spirit of Sec. 5.1.2.. In particular, the fact that the entropy has to vanish at zero temperature implies that $y_0 > 0$, see Sec. 5.1.2, where now

$$y_0 = \frac{d}{z_{<} - \frac{1}{2\nu_{\text{WF}}}}. \quad (\text{C.233})$$

High temperatures

Although we already know the scaling of $\alpha_{<}$ for highest temperatures $T > r^{\nu_{\text{WF}} z_{(\cdot)}}$ with $z_{(\cdot)} = \max\{z_e, z_{<}\}$, let us shortly illustrate how it can be obtained by integrating the RG trajectory. Furthermore, the intermediate temperature regime is also not fully described by the calculation of the last section, since the running mass now also has a temperature dependence. Consequently, the basic definition of the thermal expansion now translates to

$$\alpha_{<} = \frac{\partial^2 \mathcal{F}_{<}}{\partial T \partial r} = \frac{\partial^2 \mathcal{F}_{<}}{\partial T \partial \tilde{r}} \frac{\partial \tilde{r}}{\partial r} + \frac{\partial^2 \mathcal{F}_{<}}{\partial \tilde{r}^2} \frac{\partial \tilde{r}}{\partial r} \frac{\partial \tilde{r}}{\partial T}. \quad (\text{C.234})$$

This is most conveniently calculated by first calculating $\partial_r \mathcal{F}_{<}$ and then differentiating this result with respect to T (although of course the same result obtains if the second order derivative is taken from the very beginning). We obtain, directly subtracting the leading non-universal background,

$$\frac{\partial \mathcal{F}_<}{\partial r_0} = c \int_0^\Lambda dq \int \frac{d\Omega_d}{(2\pi)^d} \frac{q^{d+2z_- - 1/\nu_{\text{WF}} - 1}}{4\eta_{<,0} \sqrt{q^{2z_- - 2}(\tilde{r}(\Lambda/q) + q^2)}} \coth \left(\frac{\sqrt{q^{2z_- - 2}(\tilde{r}(\Lambda/q) + q^2)}}{2\eta_{<,0} T_0} \right) \quad (\text{C.235})$$

$$- c \int_0^\Lambda dq \int \frac{d\Omega_d}{(2\pi)^d} \frac{q^{d+2z_- - 1/\nu_{\text{WF}} - 1}}{4\eta_{<,0} q^{z_-}}. \quad (\text{C.236})$$

Again using $\tilde{r}(\Lambda/q) = b^{-2} r(\Lambda/q) = \xi^{-x} q^{2-x}$, we find

$$\frac{\partial \mathcal{F}_<}{\partial r_0} = c \int_0^\Lambda dq \int \frac{d\Omega_d}{(2\pi)^d} \frac{q^{d+2z_- - 1/\nu_{\text{WF}} - 1}}{4\eta_{<,0} \sqrt{q^{2z_-}(\xi^{-x} q^{-x} + 1)}} \coth \left(\frac{\sqrt{q^{2z_-}(\xi^{-x} q^{-x} + 1)}}{2\eta_{<,0} T_0} \right) \quad (\text{C.237})$$

$$- c \int_0^\Lambda dq \int \frac{d\Omega_d}{(2\pi)^d} \frac{q^{d+2z_- - 1/\nu_{\text{WF}} - 1}}{4\eta_{<,0} q^{z_-}} \quad (\text{C.238})$$

$$\approx c \int_0^{\xi^{-1}} dq \int \frac{d\Omega_d}{(2\pi)^d} \frac{q^{d+2z_- - 1/\nu_{\text{WF}} - 1}}{4\eta_{<,0} q^{z_- - x/2} \xi^{-x/2}} \coth \left(\frac{q^{z_- - x/2} \xi^{-x/2}}{2\eta_{<,0} T_0} \right) \quad (\text{C.239})$$

$$+ c \int_{\xi^{-1}}^\Lambda dq \int \frac{d\Omega_d}{(2\pi)^d} \frac{q^{d+2z_- - 1/\nu_{\text{WF}} - 1}}{4\eta_{<,0} q^{z_-}} \coth \left(\frac{q^{z_-}}{2\eta_{<,0} T_0} \right) \quad (\text{C.240})$$

$$- c \int_0^\Lambda dq \int \frac{d\Omega_d}{(2\pi)^d} \frac{q^{d+2z_- - 1/\nu_{\text{WF}} - 1}}{4\eta_{<,0} q^{z_-}}. \quad (\text{C.241})$$

Next, we expand the coth as

$$\coth(x) \approx \begin{cases} x^{-1} & , \quad x \ll 1 \\ 1 & , \quad x \gg 1 \end{cases}, \quad (\text{C.242})$$

and obtain

$$\begin{aligned} \frac{\partial \mathcal{F}_<}{\partial r_0} &\approx c \int_0^{\xi^{-1}} dq \int \frac{d\Omega_d}{(2\pi)^d} \frac{q^{d+2z_- - 1/\nu_{\text{WF}} - 1}}{4\eta_{<,0} q^{z_- - x/2} \xi^{-x/2}} \coth \left(\frac{q^{z_- - x/2} \xi^{-x/2}}{2\eta_{<,0} T_0} \right) \\ &- c \int_0^{\xi^{-1}} dq \int \frac{d\Omega_d}{(2\pi)^d} \frac{q^{d+2z_- - 1/\nu_{\text{WF}} - 1}}{4\eta_{<,0} q^{z_-}}. \end{aligned} \quad (\text{C.243})$$

Next, we again introduce $k = q \xi$ and find

$$\begin{aligned} \frac{\partial \mathcal{F}_<}{\partial r_0} &\approx \xi^{-(d+z_- - 1/\nu_{\text{WF}})} c \int_0^1 dk \int \frac{d\Omega_d}{(2\pi)^d} \frac{k^{d+z_- - 1/\nu_{\text{WF}} + x/2 - 1}}{4\eta_{<,0}} \coth \left(\frac{k^{z_- - x/2}}{2\eta_{<,0} T_0 \xi^{z_-}} \right) \\ &- \xi^{-(d+z_- - 1/\nu_{\text{WF}})} c \int_0^1 dk \int \frac{d\Omega_d}{(2\pi)^d} \frac{k^{d+z_- - 1/\nu_{\text{WF}} - 1}}{4\eta_{<,0}}. \end{aligned} \quad (\text{C.244})$$

Again expanding the coth, we obtain for the first term

$$\begin{aligned} \frac{\partial \mathcal{F}_<^{(1)}}{\partial r_0} &\approx T_0 \xi^{-(d-1/\nu_{\text{WF}})} c \int_0^{(2\eta_{<,0} T_0 \xi^{z_-})^{1/(z_- - x/2)}} dk \int \frac{d\Omega_d}{(2\pi)^d} \frac{k^{d-1/\nu_{\text{WF}} + x - 1}}{2} \\ &+ \xi^{-(d+z_- - 1/\nu_{\text{WF}})} c \int_0^1 dk \int \frac{d\Omega_d}{(2\pi)^d} \frac{k^{d+z_- - 1/\nu_{\text{WF}} + x/2 - 1}}{4\eta_{<,0}}. \end{aligned} \quad (\text{C.245})$$

Therefore, the scaling behavior of $\partial_r \mathcal{F}_<$ is given by

$$\begin{aligned} \frac{\partial \mathcal{F}_<}{\partial r_0} &\sim A \xi^{-(d+z_<-1/\nu_{\text{WF}})} + B T_0 \xi^{-(d-1/\nu_{\text{WF}})} (T_0 \xi^{z_<})^{(d-1/\nu_{\text{WF}}+x)/(z_<-x/2)} \\ &\sim \xi^{-(d+z_<-1/\nu_{\text{WF}})} (1 + (B/A) (T \xi^{z_<})^{(d+z_<-1/\nu_{\text{WF}}+x/2)/(z_<-x/2)}) , \end{aligned} \quad (\text{C.246})$$

where A and B are some constants. This expression is in fact valid whatever the value of T_0 is. In the low temperature regime $T_0 < r_0^{\nu_{\text{WF}} z_>}$, where ξ has no T -dependence, we obtain the same scaling result as before. In the quantum critical region $T_0 > r_0^{\nu_{\text{WF}} z_{(\cdot)}}$ with $z_{(\cdot)} = \max\{z_e, z_<\}$, where $\xi \sim T^{-1/z_{(\cdot)}}$, we find the leading scaling behavior of the thermal expansion to be

$$\frac{\partial^2 \mathcal{F}_<}{\partial T_0 \partial r_0} \sim T_0^{-1} \xi^{-(d+z_<-1/\nu_{\text{WF}})} . \quad (\text{C.247})$$

In the intermediate temperature regime $r_0^{\nu_{\text{WF}} z_>} < T_0 < r_0^{\nu_{\text{WF}} z_{(\cdot)}}$, the calculation is a little more involved. It is helpful to start from the definition of the correlation length as $r(\Lambda \xi) = \Lambda^2$ given in Eq. (C.184) and derive this equation with respect to the temperature T . For RG states $b = \Lambda \xi > b_T^>$, the derivation of the latter equation yields, with the appropriate prefactors A and B ,

$$0 = \xi^{-1} \frac{\partial \xi}{\partial T} + A T^{1/(\nu_{\text{WF}} z_e)-1} \xi^{1/\nu_{\text{WF}}} + B \xi^{z_<} . \quad (\text{C.248})$$

This implies that

$$\frac{\partial \xi}{\partial T} \sim \xi \max \left\{ T^{1/(\nu_{\text{WF}} z_e)-1} \xi^{1/\nu_{\text{WF}}}, \xi^{z_<} \right\} , \quad (\text{C.249})$$

which can also be written as

$$\frac{\partial \xi}{\partial T} \sim \xi (\xi_T^>)^{z_>} \max \left\{ (\xi/\xi_T^>)^{1/\nu_{\text{WF}}}, (\xi/\xi_T^>)^{z_<} \right\} . \quad (\text{C.250})$$

We thus find that the contribution of the mode with the smaller dynamical exponent $z_<$ to the specific heat behaves for $T > r_0^{\nu_{\text{WF}} z_>}$ as

$$\alpha_< \sim \frac{\partial^2 \mathcal{F}_<}{\partial T_0 \partial r_0} \sim \begin{cases} T_0^{1/(\nu_{\text{WF}} z_e)-1} \xi^{-(d+z_<-2/\nu_{\text{WF}})} & , \quad \frac{1}{\nu_{\text{WF}}} > z_< \\ \xi^{-(d-1/\nu_{\text{WF}})} & , \quad \frac{1}{\nu_{\text{WF}}} < z_< \end{cases} . \quad (\text{C.251})$$

This expression has a crossover at $T \sim r^{\nu_{\text{WF}} z_{(\cdot)}}$ with $z_{(\cdot)} = \max\{z_e, z_<\}$ since the correlation length changes from $\xi \sim r^{\nu_{\text{WF}}} \rightarrow \xi \sim T^{1/z_{(\cdot)}}$. Although Eq. (C.251) does not match the low temperature scaling derived in the last subsection and given in Eq. (C.232) at $T \sim r^{\nu_{\text{WF}} z_>}$, the leading behavior of the overall thermal expansion turns out to be consistently explained by this simple calculation. In order to resolve the full crossover behavior of the contribution $\alpha_<$ to the thermal expansion at $T \sim r^{\nu_{\text{WF}} z_>}$, one would need to take into account the full flow of the mass $r(b)$, and especially the onset of thermal fluctuations, which is not done here (the calculation would be straight forward, but the leading behavior of α would not be modified).

C.10.2 Contribution of the mode with the larger dynamical exponent

The contribution of the mode with the larger dynamical exponent is given by

$$\alpha_{>} = c \int_0^\Lambda dq \int \frac{d\Omega_d}{(2\pi)^d} \int_0^\infty \frac{d\omega}{2\pi} \frac{\eta_{>,0} \omega^2}{2T_0^2} \frac{q^{d+z_{>}-1-1/\nu_{\text{WF}}}}{q^{2z_{>}} (\xi^{-x} q^{-x} + 1)^2 + \eta_{>,0}^2 \omega^2} \sinh^{-2} \left(\frac{\omega}{2T_0} \right) \quad (\text{C.252})$$

where we again used $\tilde{r}(\Lambda/q) = b^{-2} r(\Lambda/q) = \xi^{-x} q^{2-x}$. This can be approximated as

$$\alpha_{>} = c \int_0^\Lambda dq \int \frac{d\Omega_d}{(2\pi)^d} \int_0^{2T_0} \frac{d\omega}{2\pi} 2\eta_{>,0} \frac{q^{d+z_{>}-1-1/\nu_{\text{WF}}}}{q^{2z_{>}} (\xi^{-x} q^{-x} + 1)^2 + \eta_{>,0}^2 \omega^2} \quad (\text{C.253})$$

$$\begin{aligned} &\approx c \int_0^{\xi^{-1}} dq \int \frac{d\Omega_d}{(2\pi)^d} \int_0^{2T_0} \frac{d\omega}{2\pi} 2\eta_{>,0} \frac{q^{d+z_{>}-1-1/\nu_{\text{WF}}}}{q^{2z_{>}-2x} \xi^{-2x} + \eta_{>,0}^2 \omega^2} \\ &+ c \int_{\xi^{-1}}^\Lambda dq \int \frac{d\Omega_d}{(2\pi)^d} \int_0^{2T_0} \frac{d\omega}{2\pi} 2\eta_{>,0} \frac{q^{d+z_{>}-1-1/\nu_{\text{WF}}}}{q^{2z_{>}} + \eta_{>,0}^2 \omega^2} \end{aligned} \quad (\text{C.254})$$

In order to proceed, we now distinguish the cases $\xi > (\eta_{>,0} T_0)^{-1/z_{>}}$ and $\xi < (\eta_{>,0} T_0)^{-1/z_{>}}$. We also note that the leading non-universal background, obtained in the limit $T_0, \tilde{r} \rightarrow 0$, vanishes. There is, however, other non-universal background, which will be discussed later.

Case $\xi < T_0^{-1/z_{>}}$: low temperature regime

In the low temperature regime, the integral can be approximated as

$$\alpha_{>} \approx c \int_0^{2T_0} \frac{d\omega}{2\pi} \int_0^{(\eta_{>,0} \omega \xi^x)^{1/(z_{>}-x)}} dq \int \frac{d\Omega_d}{(2\pi)^d} 2\pi 2\eta_{>,0} \frac{q^{d+z_{>}-1-1/\nu_{\text{WF}}}}{\eta_{>,0}^2 \omega^2} \quad (\text{C.255})$$

$$\begin{aligned} &+ c \int_0^{2T_0} \frac{d\omega}{2\pi} \int_{(\eta_{>,0} \omega \xi^x)^{1/(z_{>}-x)}}^{\xi^{-1}} dq \int \frac{d\Omega_d}{(2\pi)^d} 2\eta_{>,0} q^{d-z_{>}-1+2x-1/\nu_{\text{WF}}} \xi^{2x} \\ &+ c \int_{\xi^{-1}}^\Lambda dq \int \frac{d\Omega_d}{(2\pi)^d} \int_0^{2T_0} \frac{d\omega}{2\pi} 2\eta_{>,0} q^{d-z_{>}-1-1/\nu_{\text{WF}}} \end{aligned} \quad (\text{C.256})$$

Therefore, the contribution $\alpha_{>}$ scales as

$$\alpha_{>} \sim T_0 \xi^{2x} (\mathcal{A}' \xi^{-(d-z_{>}+2x-1/\nu_{\text{WF}})} + \mathcal{B}' (T_0^{-1} \xi^{-x})^{-(d-z_{>}+2x-1/\nu_{\text{WF}})/(z_{>}-x)}) , \quad (\text{C.257})$$

where \mathcal{A}' and \mathcal{B}' are some constants and we have dropped cutoff dependent terms. Notice that this corresponds to the subtraction of the non-universal background to the free energy, see appendix C.9. We thus find that the contribution of the mode with the larger dynamical exponent behaves as

$$\alpha_{>} \sim T_0 \xi^{z_{>}-d+1/\nu_{\text{WF}}} \sim T_0 r_0^{\nu_{\text{WF}}(d-z_{>})-1} \quad (\text{C.258})$$

in the low temperature regime. As a final remark, the cutoff-dependent term can be disregarded since it corresponds to some non-universal background.

Case $\xi > T_0^{-1/z_>}$: quantum critical region and intermediate regime

In the high temperature regime of the mode with the larger dynamical exponent $z_>$, corresponding to the quantum critical region and the intermediate region of the overall phase diagram, we can most conveniently calculate the thermal expansion by again first calculation $\partial_r \mathcal{F}_>$ and then deriving the result with respect to T . We obtain that

$$\frac{\partial \mathcal{F}_>}{\partial r} = c \int_0^\Lambda dq \int \frac{d\Omega_d}{(2\pi)^d} \int_0^\infty \frac{d\omega}{2\pi} \frac{\eta_{>,0} \omega q^{d+z_>-1-1/\nu_{\text{WF}}}}{q^{2z_>} (\xi^{-x} q^{-x} + 1)^2 + \eta_{>,0}^2 \omega^2} \coth\left(\frac{\omega}{2T_0}\right). \quad (\text{C.259})$$

Next, we approximate the cosh as in Eq. (C.242) and obtain

$$\frac{\partial \mathcal{F}_>}{\partial r} \approx c \int_0^\Lambda dq \int \frac{d\Omega_d}{(2\pi)^d} \int_0^{2T_0} \frac{d\omega}{2\pi} \frac{\eta_{>,0} 2T_0 q^{d+z_>-1-1/\nu_{\text{WF}}}}{q^{2z_>} (\xi^{-x} q^{-x} + 1)^2 + \eta_{>,0}^2 \omega^2} \quad (\text{C.260})$$

$$+ c \int_0^\Lambda dq \int \frac{d\Omega_d}{(2\pi)^d} \int_{2T_0}^\infty \frac{d\omega}{2\pi} \frac{\eta_{>,0} \omega q^{d+z_>-1-1/\nu_{\text{WF}}}}{q^{2z_>} (\xi^{-x} q^{-x} + 1)^2 + \eta_{>,0}^2 \omega^2} \\ \approx c \int_0^{\xi^{-1}} dq \int \frac{d\Omega_d}{(2\pi)^d} \int_0^{2T_0} \frac{d\omega}{2\pi} \frac{\eta_{>,0} 2T_0 q^{d+z_>-1-1/\nu_{\text{WF}}}}{q^{2z_>} \xi^{-2x} q^{-2x} + \eta_{>,0}^2 \omega^2} \quad (\text{C.261})$$

$$+ c \int_{\xi^{-1}}^\Lambda dq \int \frac{d\Omega_d}{(2\pi)^d} \int_0^{2T_0} \frac{d\omega}{2\pi} \frac{\eta_{>,0} 2T_0 q^{d+z_>-1-1/\nu_{\text{WF}}}}{q^{2z_>} + \eta_{>,0}^2 \omega^2} \\ + c \int_0^{\xi^{-1}} dq \int \frac{d\Omega_d}{(2\pi)^d} \int_{2T_0}^\infty \frac{d\omega}{2\pi} \frac{\eta_{>,0} \omega q^{d+z_>-1-1/\nu_{\text{WF}}}}{q^{2z_>} \xi^{-2x} q^{-2x} + \eta_{>,0}^2 \omega^2} \\ + c \int_{\xi^{-1}}^\Lambda dq \int \frac{d\Omega_d}{(2\pi)^d} \int_{2T_0}^\infty \frac{d\omega}{2\pi} \frac{\eta_{>,0} \omega q^{d+z_>-1-1/\nu_{\text{WF}}}}{q^{2z_>} + \eta_{>,0}^2 \omega^2}.$$

Since furthermore $\xi^{-z_>} < \eta_{>,0} T_0$, we find

$$\frac{\partial \mathcal{F}_>}{\partial r} \approx c \int_0^{\xi^{-1}} dq \int \frac{d\Omega_d}{(2\pi)^d} \int_0^{q^{z_>-x} \xi^{-x} \eta_{>,0}^{-1}} \frac{d\omega}{2\pi} \eta_{>,0} 2T_0 q^{d-z_>+2x-1-1/\nu_{\text{WF}}} \xi^{2x} \quad (\text{C.262}) \\ + c \int_0^{\xi^{-1}} dq \int \frac{d\Omega_d}{(2\pi)^d} \int_{q^{z_>-x} \xi^{-x} \eta_{>,0}^{-1}}^{2T_0} \frac{d\omega}{2\pi} \frac{\eta_{>,0} 2T_0 q^{d+z_>-1-1/\nu_{\text{WF}}}}{\eta_{>,0}^2 \omega^2} \\ + c \int_{\xi^{-1}}^{(2\eta_{>,0} T_0)^{1/z_>}} dq \int \frac{d\Omega_d}{(2\pi)^d} \int_0^{q^{z_>} \eta_{>,0}^{-1}} \frac{d\omega}{2\pi} \eta_{>,0} 2T_0 q^{d-z_>-1-1/\nu_{\text{WF}}} \\ + c \int_{\xi^{-1}}^{(2\eta_{>,0} T_0)^{1/z_>}} dq \int \frac{d\Omega_d}{(2\pi)^d} \int_{q^{z_>} \eta_{>,0}^{-1}}^{2T_0} \frac{d\omega}{2\pi} \frac{\eta_{>,0} 2T_0 q^{d+z_>-1-1/\nu_{\text{WF}}}}{\eta_{>,0}^2 \omega^2} \\ + c \int_{(2\eta_{>,0} T_0)^{1/z_>}}^\Lambda dq \int \frac{d\Omega_d}{(2\pi)^d} \int_0^{2T_0} \frac{d\omega}{2\pi} \eta_{>,0} 2T_0 q^{d-z_>-1-1/\nu_{\text{WF}}} \\ + c \int_0^{\xi^{-1}} dq \int \frac{d\Omega_d}{(2\pi)^d} \int_{2T_0}^\infty \frac{d\omega}{2\pi} \frac{\eta_{>,0} \omega q^{d+z_>-1-1/\nu_{\text{WF}}}}{\eta_{>,0}^2 \omega^2} \\ + c \int_{\xi^{-1}}^\Lambda dq \int \frac{d\Omega_d}{(2\pi)^d} \int_{2T_0}^\infty \frac{d\omega}{2\pi} \frac{\eta_{>,0} \omega q^{d+z_>-1-1/\nu_{\text{WF}}}}{q^{2z_>} + \eta_{>,0}^2 \omega^2}.$$

Again using that $\xi^{-z} < \eta_{>,0} T_0$, we can approximate the last two terms as

$$\begin{aligned}
\frac{\partial \mathcal{F}_>}{\partial r} &\approx c \int_0^{\xi^{-1}} dq \int \frac{d\Omega_d}{(2\pi)^d} \int_0^{q^{z>-x}\xi^{-x}\eta_{>,0}^{-1}} \frac{d\omega}{2\pi} \eta_{>,0} 2 T_0 q^{d-z>+2x-1-1/\nu_{\text{WF}}} \xi^{2x} \quad (\text{C.263}) \\
&+ c \int_0^{\xi^{-1}} dq \int \frac{d\Omega_d}{(2\pi)^d} \int_{q^{z>-x}\xi^{-x}\eta_{>,0}^{-1}}^{2T_0} \frac{d\omega}{2\pi} \frac{\eta_{>,0} 2 T_0 q^{d+z>-1-1/\nu_{\text{WF}}}}{\eta_{>,0}^2 \omega^2} \\
&+ c \int_{\xi^{-1}}^{(2\eta_{>,0} T_0)^{1/z>}} dq \int \frac{d\Omega_d}{(2\pi)^d} \int_0^{q^{z>}\eta_{>,0}^{-1}} \frac{d\omega}{2\pi} \eta_{>,0} 2 T_0 q^{d-z>-1-1/\nu_{\text{WF}}} \\
&+ c \int_{\xi^{-1}}^{(2\eta_{>,0} T_0)^{1/z>}} dq \int \frac{d\Omega_d}{(2\pi)^d} \int_{q^{z>}\eta_{>,0}^{-1}}^{2T_0} \frac{d\omega}{2\pi} \frac{\eta_{>,0} 2 T_0 q^{d+z>-1-1/\nu_{\text{WF}}}}{\eta_{>,0}^2 \omega^2} \\
&+ c \int_{(2\eta_{>,0} T_0)^{1/z>}}^{\Lambda} dq \int \frac{d\Omega_d}{(2\pi)^d} \int_0^{2T_0} \frac{d\omega}{2\pi} \eta_{>,0} 2 T_0 q^{d-z>-1-1/\nu_{\text{WF}}} \\
&+ c \int_0^{\Lambda} dq \int \frac{d\Omega_d}{(2\pi)^d} \int_{2T_0}^{\infty} \frac{d\omega}{2\pi} \frac{\eta_{>,0} \omega q^{d+z>-1-1/\nu_{\text{WF}}}}{q^{2z>} + \eta_{>,0}^2 \omega^2} .
\end{aligned}$$

It is now useful to subtract the non-universal background one obtains in the limit $r_0, T_0 \rightarrow 0$, which implies $\xi^{-1} \rightarrow 0$, which yields

$$\begin{aligned}
\frac{\partial \mathcal{F}_>}{\partial r} &\approx c \int_0^{\xi^{-1}} dq \int \frac{d\Omega_d}{(2\pi)^d} \int_0^{q^{z>-x}\xi^{-x}\eta_{>,0}^{-1}} \frac{d\omega}{2\pi} \eta_{>,0} 2 T_0 q^{d-z>+2x-1-1/\nu_{\text{WF}}} \xi^{2x} \quad (\text{C.264}) \\
&+ c \int_0^{\xi^{-1}} dq \int \frac{d\Omega_d}{(2\pi)^d} \int_{q^{z>-x}\xi^{-x}\eta_{>,0}^{-1}}^{2T_0} \frac{d\omega}{2\pi} \frac{\eta_{>,0} 2 T_0 q^{d+z>-1-1/\nu_{\text{WF}}}}{\eta_{>,0}^2 \omega^2} \\
&+ c \int_{\xi^{-1}}^{(2\eta_{>,0} T_0)^{1/z>}} dq \int \frac{d\Omega_d}{(2\pi)^d} \int_0^{q^{z>}\eta_{>,0}^{-1}} \frac{d\omega}{2\pi} \eta_{>,0} 2 T_0 q^{d-z>-1-1/\nu_{\text{WF}}} \\
&+ c \int_{\xi^{-1}}^{(2\eta_{>,0} T_0)^{1/z>}} dq \int \frac{d\Omega_d}{(2\pi)^d} \int_{q^{z>}\eta_{>,0}^{-1}}^{2T_0} \frac{d\omega}{2\pi} \frac{\eta_{>,0} 2 T_0 q^{d+z>-1-1/\nu_{\text{WF}}}}{\eta_{>,0}^2 \omega^2} \\
&+ c \int_{(2\eta_{>,0} T_0)^{1/z>}}^{\Lambda} dq \int \frac{d\Omega_d}{(2\pi)^d} \int_0^{2T_0} \frac{d\omega}{2\pi} \eta_{>,0} 2 T_0 q^{d-z>-1-1/\nu_{\text{WF}}} \\
&- c \int_0^{\Lambda} dq \int \frac{d\Omega_d}{(2\pi)^d} \int_0^{2T_0} \frac{d\omega}{2\pi} \frac{\eta_{>,0} \omega q^{d+z>-1-1/\nu_{\text{WF}}}}{q^{2z>} + \eta_{>,0}^2 \omega^2} ,
\end{aligned}$$

and thus

$$\begin{aligned}
\frac{\partial \mathcal{F}_{>}}{\partial r} &\approx c \int_0^{\xi^{-1}} dq \int \frac{d\Omega_d}{(2\pi)^d} \int_0^{q^{z>-x}\xi^{-x}\eta_{>,0}^{-1}} \frac{d\omega}{2\pi} \eta_{>,0} 2 T_0 q^{d-z>+2x-1-1/\nu_{\text{WF}}} \xi^{2x} \quad (\text{C.265}) \\
&+ c \int_0^{\xi^{-1}} dq \int \frac{d\Omega_d}{(2\pi)^d} \int_{q^{z>-x}\xi^{-x}\eta_{>,0}^{-1}}^{2T_0} \frac{d\omega}{2\pi} \frac{\eta_{>,0} 2 T_0 q^{d+z>-1-1/\nu_{\text{WF}}}}{\eta_{>,0}^2 \omega^2} \\
&+ c \int_{\xi^{-1}}^{(2\eta_{>,0} T_0)^{1/z>}} dq \int \frac{d\Omega_d}{(2\pi)^d} \int_0^{q^{z>}\eta_{>,0}^{-1}} \frac{d\omega}{2\pi} \eta_{>,0} 2 T_0 q^{d-z>-1-1/\nu_{\text{WF}}} \\
&+ c \int_{\xi^{-1}}^{(2\eta_{>,0} T_0)^{1/z>}} dq \int \frac{d\Omega_d}{(2\pi)^d} \int_{q^{z>}\eta_{>,0}^{-1}}^{2T_0} \frac{d\omega}{2\pi} \frac{\eta_{>,0} 2 T_0 q^{d+z>-1-1/\nu_{\text{WF}}}}{\eta_{>,0}^2 \omega^2} \\
&+ c \int_{(2\eta_{>,0} T_0)^{1/z>}}^{\Lambda} dq \int \frac{d\Omega_d}{(2\pi)^d} \int_0^{2T_0} \frac{d\omega}{2\pi} \eta_{>,0} 2 T_0 q^{d-z>-1-1/\nu_{\text{WF}}} \\
&- c \int_0^{\Lambda} dq \int \frac{d\Omega_d}{(2\pi)^d} \int_0^{2T_0} \frac{d\omega}{2\pi} \frac{\eta_{>,0} \omega q^{d+z>-1-1/\nu_{\text{WF}}}}{q^{2z>} + \eta_{>,0}^2 \omega^2}.
\end{aligned}$$

From there, we obtain with $k = T_0^{-1/z>} q$ and $\epsilon = T_0 \omega$

$$\begin{aligned}
\frac{\partial \mathcal{F}_{>}}{\partial r} &\approx c \int_0^{\xi^{-1}} dq \int \frac{d\Omega_d}{(2\pi)^d} \int_0^{q^{z>-x}\xi^{-x}\eta_{>,0}^{-1}} \frac{d\omega}{2\pi} \eta_{>,0} 2 T_0 q^{d-z>+2x-1-1/\nu_{\text{WF}}} \xi^{2x} \quad (\text{C.266}) \\
&+ c \int_0^{\xi^{-1}} dq \int \frac{d\Omega_d}{(2\pi)^d} \int_{q^{z>-x}\xi^{-x}\eta_{>,0}^{-1}}^{2T_0} \frac{d\omega}{2\pi} \frac{\eta_{>,0} 2 T_0 q^{d+z>-1-1/\nu_{\text{WF}}}}{\eta_{>,0}^2 \omega^2} \\
&+ c \int_{\xi^{-1}}^{(2\eta_{>,0} T_0)^{1/z>}} dq \int \frac{d\Omega_d}{(2\pi)^d} \int_0^{q^{z>}\eta_{>,0}^{-1}} \frac{d\omega}{2\pi} \eta_{>,0} 2 T_0 q^{d-z>-1-1/\nu_{\text{WF}}} \\
&+ c \int_{\xi^{-1}}^{(2\eta_{>,0} T_0)^{1/z>}} dq \int \frac{d\Omega_d}{(2\pi)^d} \int_{q^{z>}\eta_{>,0}^{-1}}^{2T_0} \frac{d\omega}{2\pi} \frac{\eta_{>,0} 2 T_0 q^{d+z>-1-1/\nu_{\text{WF}}}}{\eta_{>,0}^2 \omega^2} \\
&+ T_0 T_0^{(d-1/\nu_{\text{WF}})/z>} c \int_{(2\eta_{>,0})^{1/z>}}^{T_0^{-1/z>} \Lambda} dk \int \frac{d\Omega_d}{(2\pi)^{d+1}} 4 \eta_{>,0} k^{d-z>-1-1/\nu_{\text{WF}}} \\
&- T_0 T_0^{(d-1/\nu_{\text{WF}})/z>} c \int_0^{T_0^{-1/z>} \Lambda} dk \int \frac{d\Omega_d}{(2\pi)^{d+1}} \int_0^2 d\epsilon \frac{\eta_{>,0} \epsilon k^{d+z>-1-1/\nu_{\text{WF}}}}{k^{2z>} + \eta_{>,0}^2 \epsilon^2}.
\end{aligned}$$

The last two terms scale as $T_0 T_0^{(d-1/\nu_{\text{WF}})/z>}$, up to cutoff-dependent terms. We now realize that the effective theory described by the above equations is only valid beyond the RG scale $b_T >$, namely beyond the scale where thermal fluctuations start to be important. One possible choice for the effective cutoff is thus $\Lambda = T_0^{-1/z>}$, and the integrals in the last two terms are thus dimensionless. The first four terms can now be further analyzed, and we obtain

$$\begin{aligned}
\frac{\partial \mathcal{F}_{>}^{1-4}}{\partial r} &\approx c \int_0^{\xi^{-1}} dq \int \frac{d\Omega_d}{(2\pi)^{d+1}} 4 T_0 q^{d+x-1-1/\nu_{\text{WF}}} \xi^x \quad (\text{C.267}) \\
&- c \int_0^{(2\eta_{>,0} T_0)^{1/z>}} dq \int \frac{d\Omega_d}{(2\pi)^{d+1}} \frac{q^{d+z>-1-1/\nu_{\text{WF}}}}{\eta_{>,0}} \\
&+ c \int_{\xi^{-1}}^{(2\eta_{>,0} T_0)^{1/z>}} dq \int \frac{d\Omega_d}{(2\pi)^{d+1}} 4 T_0 q^{d-1-1/\nu_{\text{WF}}}.
\end{aligned}$$

Performing these last integrals, we find in total that the derivative of $\mathcal{F}_>$ with respect to r scales as

$$\frac{\partial \mathcal{F}_>}{\partial r} = T_0 \mathcal{A}'' T_0^{(d-1/\nu_{\text{WF}})/z_>} + T_0 \mathcal{B}'' \xi^{-(d-1/\nu_{\text{WF}})} , \quad (\text{C.268})$$

where \mathcal{A}'' and \mathcal{B}'' are appropriate constants. The contribution of the mode with the larger dynamical exponent to the thermal expansion in the high temperature regime, which is simply the derivative with respect to T_0 of Eq. (C.268), thus scales as

$$\alpha_> = a'' T_0^{(d-1/\nu_{\text{WF}})/z_>} + b'' \xi^{-(d-1/\nu_{\text{WF}})} , \quad (\text{C.269})$$

where a'' and b'' are again the appropriate constants. The scaling of $\alpha_>$ thus depends on the sign of

$$d - \frac{1}{\nu_{\text{WF}}} = 2 - \left(2 - \frac{4}{9}(4 - d - z_<)\right) = \frac{5d - 4z_< - 2}{9} = \frac{4}{9} \Delta_q - \Delta_c , \quad (\text{C.270})$$

and can be written as

$$\alpha_> \sim \max \left\{ T_0^{(d-1/\nu_{\text{WF}})/z_>} , \xi^{-(d-1/\nu_{\text{WF}})} \right\} = \max \left\{ \xi_T^{>1/\nu_{\text{WF}}-d} , \xi^{1/\nu_{\text{WF}}-d} \right\} . \quad (\text{C.271})$$

Appendix D

Weyl superconductors

D.1 Derivation of the Weyl superconductor Hamiltonian

The Weyl superconductor Hamiltonian, as it has been motivated in Sec. 8.1.1, reads

$$H = \sum_{\vec{k}_\perp, i, j} c_{\vec{k}_\perp i}^\dagger \mathcal{H}_{ij} c_{\vec{k}_\perp j} + H_{SC} , \quad (\text{D.1})$$

$$\begin{aligned} \mathcal{H}_{ij} = & v_F \tau^z (\hat{z} \times \vec{\sigma}) \cdot \vec{k}_\perp \delta_{i,j} + m \sigma^z \delta_{i,j} \\ & + t_S \tau^x \delta_{i,j} + \frac{1}{2} t_D \tau^+ \delta_{i,j+1} + \frac{1}{2} t_D \tau^- \delta_{i,j-1} \end{aligned} \quad (\text{D.2})$$

$$H_{SC} = \sum_{\vec{k}_\perp, i} \Delta \left(c_{\vec{k}_\perp \uparrow i}^{\text{top} \dagger} c_{-\vec{k}_\perp \downarrow i}^{\text{top} \dagger} + c_{\vec{k}_\perp \uparrow i}^{\text{bot.} \dagger} c_{-\vec{k}_\perp \downarrow i}^{\text{bot.} \dagger} \right) + \text{h.c.} , \quad (\text{D.3})$$

where $c_{\vec{k}_\perp i} = (c_{\vec{k}_\perp \uparrow i}^{\text{top}}, c_{\vec{k}_\perp \downarrow i}^{\text{top}}, c_{\vec{k}_\perp \uparrow i}^{\text{bot.}}, c_{\vec{k}_\perp \downarrow i}^{\text{bot.}})^T$ comprises annihilation operators for electrons of spin up and down in the top and bottom surfaces of layer i with in-plane momentum \vec{k}_\perp . The unit vector along the perpendicular axis is \hat{z} . The Fermi velocity of the Dirac nodes is v_F , for simplicity considered to be the same on each surface, and Pauli matrices $\vec{\sigma}$ act on the real spin. The additional pseudo spin for the top/bottom surface degree of freedom denoted by the Pauli matrices $\vec{\tau}$. The Zeeman mass of the Dirac nodes is given by the magnetization m , the tunneling between top and bottom surface of the same TI layer is denoted by t_S , and the tunneling between different TI layers is t_D . The proximity induced superconductivity is characterized by $\Delta = |\Delta| e^{i\varphi}$, with φ being the globally coherent superconducting phase.

In order to recast this Hamiltonian into a more transparent form, we first rewrite it in Nambu space. The associated pseudospin is denoted by $\vec{\kappa}$, a third vector of Pauli matrices. In addition, we Fourier transform the Hamiltonian long \hat{z} , where the superlattice constant is d . The Hamiltonian can then be written as

$$H = \sum_{\vec{k}_\perp, i, j} \zeta_{\vec{k}}^\dagger \frac{\mathbb{1}_\kappa + \kappa^z}{2} \mathcal{H}_{\vec{k}} \zeta_{\vec{k}} + H_{SC}, \quad (\text{D.4})$$

$$\begin{aligned} \mathcal{H}_{\vec{k}} &= v_F \tau^z (\hat{z} \times \vec{\sigma}) \cdot \vec{k} + m \sigma^z \\ &+ t_S \tau^x + \frac{1}{2} t_D \tau^+ e^{-ik_z d} + \frac{1}{2} t_D \tau^- e^{+ik_z d} \end{aligned} \quad (\text{D.5})$$

$$H_{SC} = \sum_{\vec{k}} \zeta_{\vec{k}}^\dagger \frac{\mathbb{1}_\tau \sigma^z}{4} (\Delta \kappa^+ + \Delta^* \kappa^-) \zeta_{\vec{k}}, \quad (\text{D.6})$$

where \vec{k} is now the three-dimensional momentum and

$$\zeta_{\vec{k}} = (c_{\vec{k}\uparrow}^{\text{top}}, c_{\vec{k}\downarrow}^{\text{top}}, c_{\vec{k}\uparrow}^{\text{bot.}}, c_{\vec{k}\downarrow}^{\text{bot.}}, c_{-\vec{k}\downarrow}^{\text{top}\dagger}, c_{-\vec{k}\uparrow}^{\text{top}\dagger}, c_{-\vec{k}\downarrow}^{\text{bot.}\dagger}, c_{-\vec{k}\uparrow}^{\text{bot.}\dagger})^T \quad (\text{D.7})$$

is the Nambu spinor, with $c_{k\sigma}^{(\cdot)}$ denoting the Fourier transform of $c_{\vec{k}_\perp \sigma i}^{(\cdot)}$ along \hat{z} . After a canonical transformation

$$\sigma^\pm \rightarrow \tau^z \sigma^\pm, \quad \tau^\pm \rightarrow \sigma^z \tau^\pm, \quad (\text{D.8})$$

and the subsequent diagonalization in the $\vec{\tau}$ subspace, the Hamiltonian reads

$$H = \sum_{\vec{k}, l=\pm} \zeta_{\vec{k}l}^\dagger \left[\frac{\mathbb{1}_\kappa + \kappa^z}{2} \mathcal{H}_l(\vec{k}) + \frac{\sigma^z}{4} (\Delta \kappa^+ + \Delta^* \kappa^-) \right] \zeta_{\vec{k}l}, \quad (\text{D.9})$$

$$\mathcal{H}_\pm(\vec{k}) = v_F (\hat{z} \times \vec{\sigma}) \cdot \vec{k} + M_\pm(k_z) \sigma^z, \quad (\text{D.10})$$

$$M_\pm(k_z) = m \pm \sqrt{t_S^2 + t_D^2 + 2 t_S t_D \cos(k_z d)}, \quad (\text{D.11})$$

where $\zeta_{\vec{k}\pm}^\dagger = (c_{\vec{k}\uparrow\pm}^\dagger, c_{\vec{k}\downarrow\pm}^\dagger, c_{-\vec{k}\downarrow\pm}^\dagger, c_{-\vec{k}\uparrow\pm}^\dagger)^T$ is now composed of the appropriate eigenoperators resulting from the diagonalization in the $\vec{\tau}$ -subspace. In order to proceed to the diagonalization of the \vec{k} subspace, we note that the non-superconducting hopping-diagonal part of the Hamiltonian can be recast as

$$\begin{aligned} H_\pm^0 &= \sum_{\vec{k}} (c_{\vec{k}\uparrow\pm}, c_{\vec{k}\downarrow\pm}) \left[v_F (\hat{z} \times \vec{\sigma}) \cdot \vec{k} + M_\pm(k_z) \sigma^z \right] \begin{pmatrix} c_{\vec{k}\uparrow\pm}^\dagger \\ c_{\vec{k}\downarrow\pm}^\dagger \end{pmatrix} \\ &= \sum_{\vec{k}} (c_{\vec{k}\downarrow\pm}^\dagger, c_{\vec{k}\uparrow\pm}^\dagger) \left[-v_F (\hat{z} \times \vec{\sigma}) \cdot \vec{k} + M_\pm(k_z) \sigma^z \right] \begin{pmatrix} c_{\vec{k}\downarrow\pm} \\ c_{\vec{k}\uparrow\pm} \end{pmatrix}. \end{aligned} \quad (\text{D.12})$$

Since furthermore $M_\pm(k_z)$ is an even function of k_z , the total Hamiltonian can be written as

$$H = \sum_{\vec{k}, l=\pm} \zeta_{\vec{k}l}^\dagger \frac{1}{2} \left[\mathbb{1}_\kappa \mathcal{H}_l(\vec{k}) + \frac{\sigma^z}{2} (\Delta \kappa^+ + \Delta^* \kappa^-) \right] \zeta_{\vec{k}l}, \quad (\text{D.13})$$

$$\mathcal{H}_\pm(\vec{k}) = v_F (\hat{z} \times \vec{\sigma}) \cdot \vec{k} + M_\pm(k_z) \sigma^z, \quad (\text{D.14})$$

$$M_\pm(k_z) = m \pm \sqrt{t_S^2 + t_D^2 + 2 t_S t_D \cos(k_z d)}. \quad (\text{D.15})$$

It is now easy to diagonalize the \vec{k} subspace, which yields Bogoliubov quasiparticles of definite particle-hole symmetry. We obtain

$$H = H_+ + H_- \quad (\text{D.16})$$

with

$$H_\alpha = \frac{1}{2} \sum_{\vec{k}, i=\pm} \Phi_{\vec{k}, i, \alpha}^\dagger \mathcal{H}_\alpha^{i\Delta}(\vec{k}) \Phi_{\vec{k}, i, \alpha}, \quad (\text{D.17})$$

where

$$\mathcal{H}_\alpha^{\pm\Delta}(\vec{k}) = v_F (\hat{z} \times \vec{\sigma}) \cdot \vec{k} + M_\alpha^{\pm\Delta}(k_z) \sigma^z, \quad (\text{D.18})$$

$$M_\alpha^{\pm\Delta}(k_z) = (m \pm |\Delta|) + \alpha \sqrt{t_S^2 + t_D^2 + 2t_S t_D \cos(k_z d)}, \quad (\text{D.19})$$

and

$$\Phi_{\vec{k}, +, \alpha} = (d_{\vec{k}\alpha}, d_{-\vec{k}\alpha}^\dagger)^T, \quad \Phi_{\vec{k}, -, \alpha} = (f_{\vec{k}\alpha}, f_{-\vec{k}\alpha}^\dagger)^T, \quad (\text{D.20a})$$

$$d_{\vec{k}\alpha} = \frac{1}{\sqrt{2}} \left(e^{-i\varphi/2} c_{\vec{k}\uparrow\alpha} + e^{+i\varphi/2} c_{-\vec{k}\downarrow\alpha}^\dagger \right), \quad (\text{D.20b})$$

$$f_{\vec{k}\alpha} = \frac{1}{\sqrt{2}i} \left(e^{-i\varphi/2} c_{\vec{k}\uparrow\alpha} - e^{+i\varphi/2} c_{-\vec{k}\downarrow\alpha}^\dagger \right). \quad (\text{D.20c})$$

D.2 Stability of Weyl nodes against superconductivity

In this section, we want to analyze under which conditions a Weyl semimetal remains gapless if either s-wave or p-wave superconductivity is added to the Hamiltonian. To this end, we assume that superconductivity couples electrons in the vicinity of two Weyl nodes. The electrons on one node correspond to operators $c_{1, \vec{k}, \sigma}$, the ones on the other node to $c_{2, \vec{k}, \sigma}$. Our result will only depend on whether the two Weyl nodes have the same or opposite chirality. We therefore assume one Weyl node to have positive chirality, $H_1 \sim \vec{\sigma} \cdot \vec{k}$, while the second node is so far keep in a general notation, $H_2 \sim \pm \vec{\sigma} \cdot \vec{k}$. We furthermore focus on the effective low energy theory and measure the momenta relative to the respective Weyl nodes, such that our starting Hamiltonian reads

$$H_0 = \sum_{\vec{k}} (c_{1, \vec{k}, \uparrow}^\dagger, c_{1, \vec{k}, \downarrow}^\dagger) (v_F \vec{\sigma} \cdot \vec{k}) \begin{pmatrix} c_{1, \vec{k}, \uparrow} \\ c_{1, \vec{k}, \downarrow} \end{pmatrix} + \sum_{\vec{k}} (c_{2, \vec{k}, \uparrow}^\dagger, c_{2, \vec{k}, \downarrow}^\dagger) (\pm v_F \vec{\sigma} \cdot \vec{k}) \begin{pmatrix} c_{2, \vec{k}, \uparrow} \\ c_{2, \vec{k}, \downarrow} \end{pmatrix} \quad (\text{D.21})$$

$$= \sum_{\vec{k}} (c_{1, \vec{k}, \uparrow}^\dagger, c_{1, \vec{k}, \downarrow}^\dagger, c_{2, \vec{k}, \uparrow}^\dagger, c_{2, \vec{k}, \downarrow}^\dagger) \begin{pmatrix} v_F \vec{\sigma} \cdot \vec{k} & 0 \\ 0 & \pm v_F \vec{\sigma} \cdot \vec{k} \end{pmatrix} \begin{pmatrix} c_{1, \vec{k}, \uparrow} \\ c_{1, \vec{k}, \downarrow} \\ c_{2, \vec{k}, \uparrow} \\ c_{2, \vec{k}, \downarrow} \end{pmatrix}.$$

We assume that the superconducting part of the Hamiltonian then only contains terms of the form

$$H_{SC} \sim c_{1,\vec{k},\sigma}^\dagger c_{2,-\vec{k},\sigma'}^\dagger + \text{h.c.}, \quad (\text{D.22})$$

which in particular includes s-wave and p-wave pairing. It is now useful to rewrite the non-superconducting part of the Hamiltonian as

$$H_0 = \sum_{\vec{k}} (c_{1,\vec{k},\uparrow}^\dagger, c_{1,\vec{k},\downarrow}^\dagger, c_{2,-\vec{k},\downarrow}, -c_{2,-\vec{k},\uparrow}) \begin{pmatrix} v_F \vec{\sigma} \cdot \vec{k} & 0 \\ 0 & \mp v_F \vec{\sigma} \cdot \vec{k} \end{pmatrix} \begin{pmatrix} c_{1,\vec{k},\uparrow} \\ c_{1,\vec{k},\downarrow} \\ c_{2,-\vec{k},\downarrow}^\dagger \\ -c_{2,-\vec{k},\uparrow}^\dagger \end{pmatrix}, \quad (\text{D.23})$$

where the sign of the second Weyl node in the Hamiltonian had to be reversed due to the inversion of creation and annihilation operators. Including the general superconducting term, the full Hamiltonian $H = H_0 + H_{SC}$ can be written as

$$H = \sum_{\vec{k}} (c_{1,\vec{k},\uparrow}^\dagger, c_{1,\vec{k},\downarrow}^\dagger, c_{2,-\vec{k},\downarrow}, -c_{2,-\vec{k},\uparrow}) \begin{pmatrix} v_F \vec{\sigma} \cdot \vec{k} & [\alpha(\vec{k}) \mathbb{1}_\sigma + \vec{\beta}(\vec{k}) \cdot \vec{\sigma}] \\ [\alpha(\vec{k})^* \mathbb{1}_\sigma + \vec{\beta}(\vec{k})^* \cdot \vec{\sigma}] & \mp v_F \vec{\sigma} \cdot \vec{k} \end{pmatrix} \begin{pmatrix} c_{1,\vec{k},\uparrow} \\ c_{1,\vec{k},\downarrow} \\ c_{2,-\vec{k},\downarrow}^\dagger \\ -c_{2,-\vec{k},\uparrow}^\dagger \end{pmatrix}. \quad (\text{D.24})$$

In case the two Weyl nodes are of opposite chirality and the lower (plus) sign applies, the diagonal is proportional to the unit matrix in Nambu space. Superconductivity can therefore never open up a gap, but only shift the Bogoliubov Weyl nodes around. For two Weyl nodes of equal chirality, the Hamiltonian should in general be gapped. As an example, we consider s-wave superconductivity. The latter corresponds to

$$H_{\text{s-wave}} = \sum_{\vec{k}} \Delta c_{1,\vec{k},\uparrow}^\dagger c_{2,-\vec{k},\downarrow}^\dagger + \text{h.c.} = \sum_{\vec{k}} \frac{\Delta}{2} (c_{1,\vec{k},\uparrow}^\dagger c_{2,-\vec{k},\downarrow}^\dagger - c_{2,-\vec{k},\downarrow}^\dagger c_{1,-\vec{k},\uparrow}^\dagger) + \text{h.c.}, \quad (\text{D.25})$$

where we neglect the superconducting phase for simplicity, i.e. $\Delta = |\Delta|$. The total Hamiltonian then reads

$$H = \sum_{\vec{k}} (c_{1,\vec{k},\uparrow}^\dagger, c_{1,\vec{k},\downarrow}^\dagger, c_{2,-\vec{k},\downarrow}, -c_{2,-\vec{k},\uparrow}) \begin{pmatrix} v_F \vec{\sigma} \cdot \vec{k} & \frac{\Delta}{2} \mathbb{1}_\sigma \\ \frac{\Delta}{2} \mathbb{1}_\sigma & -v_F \vec{\sigma} \cdot \vec{k} \end{pmatrix} \begin{pmatrix} c_{1,\vec{k},\uparrow} \\ c_{1,\vec{k},\downarrow} \\ c_{2,-\vec{k},\downarrow}^\dagger \\ -c_{2,-\vec{k},\uparrow}^\dagger \end{pmatrix}. \quad (\text{D.26})$$

The eigenvalues of this Hamiltonian are easily found to be

$$E = \pm \sqrt{(v_F \vec{\sigma} \cdot \vec{k})^2 + \frac{|\Delta|^2}{4}}, \quad (\text{D.27})$$

and the system is gapped as expected.

D.3 Bogoliubov Weyl nodes as halves of regular Weyl nodes

The topological charge of a Bogoliubov Weyl node can be calculated very analogously to the case of a normal Weyl node. We start from a general Weyl superconductor Hamiltonian

$$H = \sum_{\vec{k}} (d_{\vec{k}}^\dagger, d_{-\vec{k}}) \frac{1}{2} [v_F (\sigma^x k_x + \sigma^y k_y) + \sigma^z M_\Delta(k_z)] \begin{pmatrix} d_{\vec{k}} \\ d_{-\vec{k}}^\dagger \end{pmatrix}, \quad (\text{D.28})$$

where $d_{\vec{k}}$ are the Bogoliubov quasiparticles. For simplicity, we specialize to the inversion symmetric case $M_\Delta(k_z) = M_\Delta(-k_z)$, but the argument holds true on general grounds. We furthermore require that the parameters are such that the Hamiltonian has two Bogoliubov Weyl nodes of opposite chiralities at $\vec{k} = (0, 0, \pm k_0)$. This Hamiltonian is in a way redundant since all operators appear twice. A commonly used trick to get rid of this redundancy is to restrict the sum over half the Brillouin zone only, say to positive k_x . This is achieved by first rewriting

$$\begin{aligned} H = & \sum_{\vec{k}, k_x > 0} (d_{\vec{k}}^\dagger, d_{-\vec{k}}) \frac{1}{2} [v_F (\sigma^x k_x + \sigma^y k_y) + \sigma^z M_\Delta(k_z)] \begin{pmatrix} d_{\vec{k}} \\ d_{-\vec{k}}^\dagger \end{pmatrix} \\ & + \sum_{\vec{k}, k_x = 0} (d_{\vec{k}}^\dagger, d_{-\vec{k}}) \frac{1}{4} [v_F (\sigma^x 0 + \sigma^y k_y) + \sigma^z M_\Delta(k_z)] \begin{pmatrix} d_{\vec{k}} \\ d_{-\vec{k}}^\dagger \end{pmatrix} \\ & + \sum_{\vec{k}, k_x < 0} (d_{\vec{k}}^\dagger, d_{-\vec{k}}) \frac{1}{2} [v_F (\sigma^x k_x + \sigma^y k_y) + \sigma^z M_\Delta(k_z)] \begin{pmatrix} d_{\vec{k}} \\ d_{-\vec{k}}^\dagger \end{pmatrix} \\ & + \sum_{\vec{k}, k_x = 0} (d_{\vec{k}}^\dagger, d_{-\vec{k}}) \frac{1}{4} [v_F (\sigma^x 0 + \sigma^y k_y) + \sigma^z M_\Delta(k_z)] \begin{pmatrix} d_{\vec{k}} \\ d_{-\vec{k}}^\dagger \end{pmatrix}. \end{aligned} \quad (\text{D.29})$$

Inverting the momenta in the last two terms yields

$$\begin{aligned} H = & \sum_{\vec{k}, k_x > 0} (d_{\vec{k}}^\dagger, d_{-\vec{k}}) \frac{1}{2} [v_F (\sigma^x k_x + \sigma^y k_y) + \sigma^z M_\Delta(k_z)] \begin{pmatrix} d_{\vec{k}} \\ d_{-\vec{k}}^\dagger \end{pmatrix} \\ & + \sum_{\vec{k}, k_x = 0} (d_{\vec{k}}^\dagger, d_{-\vec{k}}) \frac{1}{4} [v_F (\sigma^x 0 + \sigma^y k_y) + \sigma^z M_\Delta(k_z)] \begin{pmatrix} d_{\vec{k}} \\ d_{-\vec{k}}^\dagger \end{pmatrix} \\ & + \sum_{\vec{k}, k_x > 0} (d_{-\vec{k}}^\dagger, d_{\vec{k}}) \frac{1}{2} [v_F (\sigma^x (-k_x) + \sigma^y (-k_y)) + \sigma^z M(-k_z)] \begin{pmatrix} d_{-\vec{k}} \\ d_{\vec{k}}^\dagger \end{pmatrix} \\ & + \sum_{\vec{k}, k_x = 0} (d_{-\vec{k}}^\dagger, d_{\vec{k}}) \frac{1}{4} [v_F (\sigma^x 0 + \sigma^y (-k_y)) + \sigma^z M(-k_z)] \begin{pmatrix} d_{-\vec{k}} \\ d_{\vec{k}}^\dagger \end{pmatrix} \end{aligned} \quad (\text{D.30})$$

One can now unambiguously define

$$d_{\vec{k}} = \begin{cases} d_{\vec{k}, \uparrow} & \text{if } k_x > 0, \\ d_{-\vec{k}, \downarrow}^\dagger & \text{if } k_x < 0, \end{cases} \quad (\text{D.31})$$

which yields (together with $M_\Delta(k_z) = M(-k_z)$)

$$H = \sum_{\vec{k}, k_x > 0} (d_{\vec{k}, \uparrow}^\dagger, d_{\vec{k}, \downarrow}^\dagger) \frac{1}{2} [v_F (\sigma^x k_x + \sigma^y k_y) + \sigma^z M_\Delta(k_z)] \begin{pmatrix} d_{\vec{k}, \uparrow} \\ d_{\vec{k}, \downarrow} \end{pmatrix} \quad (\text{D.32})$$

$$+ \sum_{\vec{k}, k_x = 0} (d_{\vec{k}, \uparrow}^\dagger, d_{\vec{k}, \downarrow}^\dagger) \frac{1}{4} [v_F (\sigma^x 0 + \sigma^y k_y) + \sigma^z M_\Delta(k_z)] \begin{pmatrix} d_{\vec{k}, \uparrow} \\ d_{\vec{k}, \downarrow} \end{pmatrix} \quad (\text{D.33})$$

$$+ \sum_{\vec{k}, k_x > 0} (d_{\vec{k}, \downarrow}^\dagger, d_{\vec{k}, \uparrow}^\dagger) \frac{1}{2} [-v_F (\sigma^x k_x + \sigma^y k_y) + \sigma^z M_\Delta(k_z)] \begin{pmatrix} d_{\vec{k}, \downarrow}^\dagger \\ d_{\vec{k}, \uparrow}^\dagger \end{pmatrix} \quad (\text{D.34})$$

$$+ \sum_{\vec{k}, k_x = 0} (d_{\vec{k}, \downarrow}^\dagger, d_{\vec{k}, \uparrow}^\dagger) \frac{1}{4} [-v_F (\sigma^x 0 + \sigma^y k_y) + \sigma^z M_\Delta(k_z)] \begin{pmatrix} d_{\vec{k}, \downarrow}^\dagger \\ d_{\vec{k}, \uparrow}^\dagger \end{pmatrix}. \quad (\text{D.35})$$

Reordering the operators yields

$$H = \sum_{\vec{k}, k_x > 0} (d_{\vec{k}, \uparrow}^\dagger, d_{\vec{k}, \downarrow}^\dagger) 2 \times \frac{1}{2} [v_F (\sigma^x k_x + \sigma^y k_y) + \sigma^z M_\Delta(k_z)] \begin{pmatrix} d_{\vec{k}, \uparrow} \\ d_{\vec{k}, \downarrow} \end{pmatrix} \quad (\text{D.36})$$

$$+ \sum_{\vec{k}, k_x = 0} (d_{\vec{k}, \uparrow}^\dagger, d_{\vec{k}, \downarrow}^\dagger) 2 \times \frac{1}{4} [v_F (\sigma^x 0 + \sigma^y k_y) + \sigma^z M_\Delta(k_z)] \begin{pmatrix} d_{\vec{k}, \uparrow} \\ d_{\vec{k}, \downarrow} \end{pmatrix}. \quad (\text{D.37})$$

This Hamiltonian has by assumption two gapless points at $\vec{k} = (0, 0, \pm k_0)$. Close to these points, we get two halved regular Weyl nodes (namely the $k_x > 0$ -halves plus half of the contribution of $k_x = 0$ for each node in the partitioning chosen here). A Bogoliubov Weyl node can thus be interpreted as the exact half of a normal Weyl node.

In order to calculate the topological charge of the Bogoliubov Weyl nodes, we expand the Hamiltonian close one of the Bogoliubov nodes. Denoting the relative momentum by \vec{q} , we obtain

$$H \approx \frac{1}{2} \sum_{\vec{q}, q_z > 0} (d_{\vec{q}, \uparrow}^\dagger, d_{\vec{q}, \downarrow}^\dagger) [\pm \vec{\sigma} \cdot \vec{q}] \begin{pmatrix} d_{\vec{q}, \uparrow} \\ d_{\vec{q}, \downarrow} \end{pmatrix} + \frac{1}{2} \sum_{\vec{q}, q_z \geq 0} (d_{\vec{q}, \uparrow}^\dagger, d_{\vec{q}, \downarrow}^\dagger) [\pm \vec{\sigma} \cdot \vec{q}] \begin{pmatrix} d_{\vec{q}, \uparrow} \\ d_{\vec{q}, \downarrow} \end{pmatrix}. \quad (\text{D.38})$$

A Bogoliubov Weyl node can thus be understood as the average of a system containing a Weyl node and a system that does not contain a Weyl node. Since a Weyl node is a topological defect of unit charge (see Sec. 7.3.3), a Bogoliubov Weyl node carries a topological charge of $1/2(1 + 0) = 1/2$.

D.4 A Weyl superconductor with a surface at $y = 0$

We analyze the surface physics for a semi-infinite sample with a surface at $y = 0$, and exemplarily illustrate and characterize the edge states in the sub-Hamiltonian $\mathcal{H}_-^{\pm\Delta}$. The other sectors can be treated analogously. We model the vacuum outside the sample (for $y > 0$) as a ‘‘Weyl superconductor’’ in the trivially gapped limit $m \rightarrow 0, |\Delta| \rightarrow 0$. Inside the sample (for $y < 0$), m and $|\Delta|$ are considered to take some finite values

$m_0, |\Delta_0| > 0$. The surface can thus be taken into account by smooth functions $m(y)$ and $|\Delta|(y)$ interpolating between these two limits. After a canonical transformation $\sigma^x \rightarrow \sigma^y$, $\sigma^y \rightarrow -\sigma^x$, the $\mathcal{H}_-^{+\Delta}$ -subsector in the presence of a surface at $y = 0$ has the Hamiltonian

$$H_-^{+\Delta} = \frac{1}{2} \sum_{k_x, y, k_z} \Phi_{k_x, k_y, +, -}^\dagger(y) \mathcal{H}_-^{+\Delta}(k_x, y, k_z) \Phi_{k_x, k_z, +, -}(y), \quad (\text{D.39})$$

where $\Phi_{k_x, k_y, +, -}(y)$ is the Fourier transform of $\Phi_{\vec{k}, +, -}$ along k_y . The matrix Hamiltonian reads

$$\mathcal{H}_-^{+\Delta}(k_x, y, k_z) = \begin{pmatrix} M_-^\Delta(k_z, y) & v_F \left(k_x - \frac{\partial}{\partial y} \right) \\ v_F \left(k_x + \frac{\partial}{\partial y} \right) & -M_-^\Delta(k_z, y) \end{pmatrix}, \quad (\text{D.40})$$

where we had to replace $k_y \rightarrow -i\partial_y$ because the surface breaks translation invariance in \hat{y} -direction. The y -dependent effective mass $M_-^{+\Delta}(k_z, y)$ is defined as

$$M_-^{+\Delta}(k_z, y) = m(y) + |\Delta|(y) - \sqrt{t_S^2 + t_D^2 + 2t_S t_D \cos(k_z d)}, \quad (\text{D.41a})$$

$$m(y) + |\Delta|(y) = \begin{cases} m_0 + |\Delta_0| > 0 & \text{for } y \rightarrow -\infty \\ 0 & \text{for } y \rightarrow +\infty \end{cases} \approx [m_0 + |\Delta_0|] \theta(-y). \quad (\text{D.41b})$$

As discussed in Sec. 8.1.2, a positive effective mass $M_-^{+\Delta}(k_z, y) > 0$ corresponds to a topologically non-trivial situation, while negative effective masses signal a trivial state that is adiabatically connected to the vacuum (note that indeed $M_-^{+\Delta}(k_z, y) < 0$ outside the sample). In the spinor notation, the surface states are particular solutions of the Schrödinger equation

$$\mathcal{H}_-^{+\Delta}(k_x, y, k_z) \Psi_{\text{surf}}(k_x, k_z, y) = E \Psi_{\text{surf}}(k_x, k_z, y) \quad (\text{D.42})$$

that live on the surface. One can easily check that they are given by

$$\Psi_{\text{surf}}(k_x, k_z, y) = \frac{1}{\mathcal{N}} e^{\int_0^y dy' M_-^{+\Delta}(k_z, y')/v_F} \begin{pmatrix} 1 \\ 1 \end{pmatrix} \quad (\text{D.43})$$

which are normalizable and exponentially localized at the surface only for momenta k_z with $M_-^{+\Delta}(k_z, y) > 0$ (\mathcal{N} is the corresponding normalization factor). This confirms that there exists one edge state per non-trivial momentum k_z , as could be expected based on the picture of a Weyl superconductor as layers of $p_x + ip_y$ -superconductor stacked in momentum space. The dispersion of the surface state is linear and reads

$$E = \frac{1}{2} v_F k_x. \quad (\text{D.44})$$

The surface states are thus moving in positive \hat{x} -direction with a velocity $v_F/2$. Using the definition of the spinor from Eq. (8.9), we can express the surface state annihilation operator in terms of electronic operators as

$$\begin{aligned}
\Psi_{\text{surf}}(k_x, k_z) &\sim \int dy' \Psi_{\text{surf}}(k_x, k_z, y') \left[\frac{1}{\sqrt{2}} \left(e^{-i\varphi/2} c_{k_x, k_z, \uparrow, -}(y') + e^{+i\varphi/2} c_{-k_x, -k_z, \downarrow, -}^\dagger(y') \right) \right. \\
&\quad \left. + \frac{1}{\sqrt{2}} \left(e^{+i\varphi/2} c_{-k_x, -k_z, \uparrow, -}^\dagger(y') + e^{-i\varphi/2} c_{k_x, k_z, \downarrow, -}(y') \right) \right] \\
&= \int dy' \Psi_{\text{surf}}(k_x, k_z, y') \left[e^{-i\varphi/2} \frac{c_{k_x, k_z, \uparrow, -}(y') + c_{k_x, k_z, \downarrow, -}(y')}{\sqrt{2}} \right. \\
&\quad \left. + e^{+i\varphi/2} \frac{c_{-k_x, -k_z, \uparrow, -}^\dagger(y') + c_{-k_x, -k_z, \downarrow, -}^\dagger(y')}{\sqrt{2}} \right] \\
&= \int dy' \Psi_{\text{surf}}(k_x, k_z, y') \left[e^{-i\varphi/2} c_{k_x, k_z, \sigma^x=+1, -}(y') + e^{+i\varphi/2} c_{-k_x, -k_z, \sigma^x=+1, -}^\dagger(y') \right].
\end{aligned} \tag{D.45}$$

Firstly, this means that the spin of the surface states points into the direction of motion. Secondly, the surface states are Majorana fermion in real space. This is best seen in the case that all momenta k_z support topological surface states, in which case we can straight-forwardly define the Fourier transformation of Eq. (D.45) along k_x and k_z as

$$\begin{aligned}
\Psi_{\text{surf}}(\vec{r}) &\sim \int dy' \Psi_{\text{surf}}(x, z, y') \left[e^{-i\varphi/2} c_{\sigma^x=+1, -}(\vec{r}) + e^{+i\varphi/2} c_{\sigma^x=+1, -}^\dagger(\vec{r}) \right] \\
&= \sqrt{2} \int dy' \Psi_{\text{surf}}(x, z, y') \left[\cos\left(\frac{\varphi}{2}\right) \frac{c_{\sigma^x=+1, -}(\vec{r}) + c_{\sigma^x=+1, -}^\dagger(\vec{r})}{\sqrt{2}} \right. \\
&\quad \left. + \sin\left(\frac{\varphi}{2}\right) \frac{c_{\sigma^x=+1, -}(\vec{r}) - c_{\sigma^x=+1, -}^\dagger(\vec{r})}{\sqrt{2}i} \right].
\end{aligned} \tag{D.46}$$

In terms of the two fundamental real space Majorana modes with spin in \hat{x} -direction that can be constructed out of the electrons $c_{\sigma, -}$,

$$\gamma_{\sigma^x=+1, -}^{(1)} = \frac{c_{\sigma^x=+1, -}(\vec{r}) + c_{\sigma^x=+1, -}^\dagger(\vec{r})}{\sqrt{2}}, \quad \gamma_{\sigma^x=+1, -}^{(2)} = \frac{c_{\sigma^x=+1, -}(\vec{r}) - c_{\sigma^x=+1, -}^\dagger(\vec{r})}{\sqrt{2}i} \tag{D.47}$$

the surface state thus corresponds to the operator

$$\Psi_{\text{surf}}(\vec{r}) \sim \int dy' \Psi_{\text{surf}}(x, z, y') \left[\cos\left(\frac{\varphi}{2}\right) \gamma_{\sigma^x=+1, -}^{(1)}(\vec{r}) + \sin\left(\frac{\varphi}{2}\right) \gamma_{\sigma^x=+1, -}^{(2)}(\vec{r}) \right]. \tag{D.48}$$

The surface state is thus in general a linear superposition of the two fundamental Majorana modes, and the superconducting phase ‘‘picks’’ the precise realization.

D.5 A reminder on vortices in superconductors

Consider a bulk s-wave BCS superconductor with a vortex localized at $\vec{r} = 0$. Since we are not interested in the detailed physics close to the vortex yet, we may simply model the vortex as a cylinder of radius R where superconductivity is suppressed. This cylinder

traps a magnetic flux. Neglecting the finite penetration depth of the field and modeling it to be entirely confined to the vortex core, the magnetic field inside the vortex

$$\vec{B} = B \hat{z} \theta(r - R) . \quad (\text{D.49})$$

gives rise to the vector potential

$$\vec{A} = \left[\frac{B r}{2} \theta(R - r) + \frac{B R^2}{2r} \theta(r - R) \right] \hat{e}_\phi . \quad (\text{D.50})$$

The magnetic field (D.49) affects the Hamiltonian in two ways. Firstly, it changes the canonical momentum as $\vec{p} \rightarrow \vec{p} + e\vec{A}$. Secondly, it introduces a winding for the superconducting order parameter. To understand this, we have to self-consistently solve for the latter in the presence of a vortex. Let us thus consider the full electronic Hamiltonian with an attractive interaction V leading to the formation of superconductivity, first in the absence of vortices. The Hamiltonian is then described by

$$H = \int d^d r \sum_{i,j} c_i^\dagger(\vec{r}) \mathcal{H}_{ij}(-i\nabla) c_j(\vec{r}) + \sum_{i,j,k,l} \int d^d r V_{ijkl} c_i^\dagger(\vec{r}) c_j^\dagger(\vec{r}) c_k(\vec{r}) c_l(\vec{r}) , \quad (\text{D.51})$$

where the index of the fermionic operators c_i comprises all implicit quantum number (such as spin). By assumption, this Hamiltonian describes an s-wave BCS superconductor with a self-consistent BCS mean field order parameter

$$\Delta_{ij} = |\Delta|_{ij} e^{i\varphi} = \left\langle \sum_{kl} V_{ijkl} c_k(\vec{r}) c_l(\vec{r}) \right\rangle . \quad (\text{D.52})$$

In this mean field approximation, the Hamiltonian reads

$$H = \int d^d r \sum_{i,j} c_i^\dagger(\vec{r}) \mathcal{H}_{ij}(-i\nabla) c_j(\vec{r}) + \sum_{i,j} \int d^d r \left(\Delta_{ij} c_i^\dagger(\vec{r}) c_j^\dagger(\vec{r}) + \text{h.c.} \right) . \quad (\text{D.53})$$

As a next step, we introduce a vortex at the origin. Outside the vortex core, the Hamiltonian then reads

$$H = \int_{r>R} d^d x \sum_{i,j} c_i^\dagger(\vec{r}) \mathcal{H}_{ij}(-i\nabla + e\vec{A}) c_j(\vec{r}) + \sum_{i,j,k,l} \int_{r>R} d^d r V_{ijkl} c_i^\dagger(\vec{r}) c_j^\dagger(\vec{r}) c_k(\vec{r}) c_l(\vec{r}) . \quad (\text{D.54})$$

Outside the vortex, where $\vec{B} = \nabla \times \vec{A} = 0$, it is furthermore always possible to find a scalar function $\vartheta(\vec{r})$ such that

$$\vec{A}(\vec{r}) = \nabla \vartheta(\vec{r}) . \quad (\text{D.55})$$

One possible choice is

$$\vartheta(\vec{r})|_{r>R} = \frac{BR^2}{2} \phi . \quad (\text{D.56})$$

The vector potential can then be gauged away using

$$\tilde{c}_{i,\sigma}(\vec{r}) = c_{i,\sigma}(\vec{r}) e^{+ie\vartheta(\vec{r})} . \quad (\text{D.57})$$

This brings the Hamiltonian into the form

$$H = \int_{r>R} d^d x \sum_{i,j} \tilde{c}_i^\dagger(\vec{r}) \mathcal{H}_{ij}(-i\nabla) \tilde{c}_j(\vec{r}) + \sum_{i,j,k,l} \int_{r>R} d^d r V_{ijkl} \tilde{c}_i^\dagger(\vec{r}) \tilde{c}_j^\dagger(\vec{r}) \tilde{c}_k(\vec{r}) \tilde{c}_l(\vec{r}) , \quad (\text{D.58})$$

where the vector potential is now reflected in the boundary conditions of the gauge-transformed fermionic operators,

$$\tilde{c}_{i,\sigma}(\phi + 2\pi) = \tilde{c}_{i,\sigma}(\phi) e^{+ie\vartheta(\phi+2\pi)} \quad (\text{D.59})$$

(where we used the angular coordinate ϕ only instead of the full coordinate \vec{r} for simplicity). Since the Hamiltonians (D.51) and (D.58) have the same form, we can perform the same mean field analysis as before. We will thus find the same mean field

$$\Delta_{ij} = |\Delta|_{ij} e^{i\varphi} = \left\langle \sum_{kl} V_{ijkl} \tilde{c}_k(\vec{r}) \tilde{c}_l(\vec{r}) \right\rangle \quad (\text{D.60})$$

for the gauge transformed operators (a note on the well-definiteness of this expression follows below). The mean field Hamiltonian thus reads

$$H = \int d^d r \sum_{i,j} \tilde{c}_i^\dagger(\vec{r}) \mathcal{H}_{ij}(-i\nabla) \tilde{c}_j(\vec{r}) + \sum_{i,j} \int d^d r \left(\Delta_{ij} \tilde{c}_i^\dagger(\vec{r}) \tilde{c}_j^\dagger(\vec{r}) + \text{h.c.} \right) . \quad (\text{D.61})$$

Undoing the gauge transformation yield finally the mean field Hamiltonian

$$H = \int d^d r \sum_{i,j} c_i^\dagger(\vec{r}) \mathcal{H}_{ij}(-i\nabla + e\vec{A}) c_j(\vec{r}) + \sum_{i,j} \int d^d r \left(\Delta_{ij} e^{-i2e\vartheta(\vec{r})} c_i^\dagger(\vec{r}) c_j^\dagger(\vec{r}) + \text{h.c.} \right) . \quad (\text{D.62})$$

Therefore, the self-consistent mean field Hamiltonian of a superconductor threaded by a flux takes the form

$$\Delta_{ij}^{\text{flux}}(\vec{r}) = \Delta_{ij} e^{-i2e\vartheta(\vec{r})} = |\Delta_{ij}| e^{i\tilde{\varphi}(\vec{r})} , \quad (\text{D.63})$$

where we have introduced the winding order parameter

$$\tilde{\varphi}(\vec{r}) = \varphi - 2e\vartheta(\vec{r}) . \quad (\text{D.64})$$

Since the order parameter must be well-defined under rotations by 2π , the function $\vartheta(\vec{r})$ must be such that

$$2e\vartheta(\phi + 2\pi) = 2e\vartheta(\phi) + n2\pi , \quad n \in \mathbb{Z} . \quad (\text{D.65})$$

This however implies

$$B\pi R^2 = n \frac{\pi}{e} , \quad n \in \mathbb{Z} . \quad (\text{D.66})$$

The flux $\Phi = B\pi R^2$ through a vortex in a superconductor is thus quantized in units of the so-called superconducting flux quantum $\Phi_0 = \pi/e$ (note that we work in units of $\hbar = 1$, and that $\Phi_0 = h/(2e)$ if all physical units are restored), and the phase of the order parameter phase winds by 2π for every flux quantum. We note that the flux quantization also renders Eq. (D.60) well defined.

D.6 Symmetries of the Hamiltonian for magnetic fields parallel to \hat{z}

Besides time reversal and inversion symmetry, a Weyl superconductor has two more important symmetries that we shall shortly discuss here. We allow for breaking of translation invariance along \hat{x} and \hat{y} , but consider only inversion symmetric situations. In order to tackle vortex physics, magnetic fields along the \hat{z} axis are allowed within a limited region around the origin such that the vector potential \vec{A} is confined to the $x-y$ -plane. We then perform the gauge transformation Eq. D.57, and are able to rewrite the Hamiltonian as discussed in Sec. 8.1.1. It decouples into four independent sectors and reads

$$H = \frac{1}{2} \sum_{i=\pm, \alpha=\pm} \int d^2 r_{\perp} \Phi_{k_z, i, \alpha}^{\dagger}(\vec{r}_{\perp}) \mathcal{H}_{\alpha}^{i\Delta}(x, y, k_z) \Phi_{k_z, i, \alpha}(\vec{r}_{\perp}) , \quad (\text{D.67})$$

where

$$\mathcal{H}_{\alpha}^{\pm\Delta}(x, y, k_z) = v_F \left(-i \frac{\partial}{\partial x} \sigma^x - i \frac{\partial}{\partial y} \sigma^y \right) + M_{\alpha}^{\pm\Delta}(x, y, k_z) \sigma^z , \quad (\text{D.68})$$

$$M_{\alpha}^{\pm\Delta}(x, y, k_z) = M_{\alpha}^{\pm\Delta}(x, y, -k_z) . \quad (\text{D.69})$$

The quasiparticle spinors $\Phi_{k_z, i, \alpha}(\vec{r}_{\perp})$ are the Fourier transforms along \hat{x} and \hat{y} of $\Phi_{\vec{k}, i, \alpha}$ as defined in Eq. (8.9), although the superconducting phase entering definition is now space dependent due to the gauge transformation,

$$\varphi \rightarrow \tilde{\varphi}(\vec{r}_{\perp}) = \varphi + 2e \vartheta(\vec{r}) , \quad A_i(\vec{r}_{\perp}) = \partial_{x_i} \vartheta(\vec{r}_{\perp}) . \quad (\text{D.70})$$

D.6.1 Superconducting particle-hole symmetry

The first important symmetry is the superconducting particle-hole symmetry. The latter is obviously respected, since the quasiparticles $\Phi_{\vec{k}, i, \alpha}$ were defined such that they respect this symmetry. We state it for the sake of completeness and in order to contrast it with the second symmetry, namely charge conjugation symmetry, that is sometimes also called particle-hole symmetry. In terms of electron operators, the superconducting particle-hole symmetry corresponds to

$$c_{k_z \sigma i}(\vec{r}_{\perp}) e^{-i\tilde{\varphi}(\vec{r}_{\perp})/2} \leftrightarrow c_{-k_z \bar{\sigma} i}^{\dagger}(\vec{r}_{\perp}) e^{i\tilde{\varphi}(\vec{r}_{\perp})/2} , \quad (\text{D.71})$$

which yields for the quasiparticle spinors

$$\Phi_{k_z, i, \alpha}(\vec{r}_{\perp}) \leftrightarrow (-1)^i \Phi_{k_z, i, \alpha}(\vec{r}_{\perp}) . \quad (\text{D.72})$$

The Hamiltonian thus trivially transforms as

$$H \leftrightarrow H . \quad (\text{D.73})$$

D.6.2 Charge conjugation symmetry

The second symmetry is commonly referred to as charge conjugation symmetry, or alternatively particle-hole symmetry since it generally connects electron-like states with

hole-like states of opposite energy. We stress that the corresponding symmetry operation is similar, but different to the superconducting particle-hole symmetry. In terms of the original electrons, it corresponds to the transformation

$$c_{k_z \sigma i}(\vec{r}_\perp) e^{-i\tilde{\varphi}(\vec{r}_\perp)/2} \leftrightarrow c_{k_z \sigma i}^\dagger(-\vec{r}_\perp) e^{i\tilde{\varphi}(\vec{r}_\perp)/2}, \quad (\text{D.74})$$

which yields

$$\Phi_{k_z, i, \alpha}(\vec{r}_\perp) \leftrightarrow (-1)^i \left(\Phi_{k_z, i, \alpha}^\dagger(-\vec{r}_\perp) \right)^T. \quad (\text{D.75})$$

for the quasiparticle spinors. We exemplarily discuss the subsequent steps for the sector $\mathcal{H}_-^{+\Delta}$, which initially reads

$$\begin{aligned} H_-^{+\Delta} = & \frac{1}{2} \sum_{k_z} \int d^2 r_\perp \left(M_-^{+\Delta}(x, y, k_z) \left[d_{k_z, i}^\dagger(\vec{r}_\perp) d_{k_z, i}(\vec{r}_\perp) - d_{-k_z, i}(\vec{r}_\perp) d_{-k_z, i}^\dagger(\vec{r}_\perp) \right] \right. \\ & \left. + d_{k_z, i}^\dagger(\vec{r}_\perp) \left[-i \frac{\partial}{\partial x} - \frac{\partial}{\partial y} \right] d_{-k_z, i}^\dagger(\vec{r}_\perp) + d_{-k_z, i}(\vec{r}_\perp) \left[-i \frac{\partial}{\partial x} + \frac{\partial}{\partial y} \right] d_{k_z, i}(\vec{r}_\perp) \right) \end{aligned} \quad (\text{D.76})$$

becomes

$$\begin{aligned} H_-^{+\Delta} = & \frac{1}{2} \sum_{k_z} \int d^2 r_\perp \left(M_-^{+\Delta}(x, y, k_z) \left[d_{k_z, i}^\dagger(-\vec{r}_\perp) d_{k_z, i}^\dagger(-\vec{r}_\perp) - d_{-k_z, i}^\dagger(-\vec{r}_\perp) d_{-k_z, i}^\dagger(-\vec{r}_\perp) \right] \right. \\ & \left. + d_{k_z, i}^\dagger(-\vec{r}_\perp) \left[-i \frac{\partial}{\partial x} - \frac{\partial}{\partial y} \right] d_{-k_z, i}^\dagger(-\vec{r}_\perp) + d_{-k_z, i}^\dagger(-\vec{r}_\perp) \left[-i \frac{\partial}{\partial x} + \frac{\partial}{\partial y} \right] d_{k_z, i}^\dagger(-\vec{r}_\perp) \right). \end{aligned} \quad (\text{D.77})$$

Next, we invert the operators in the first line, shift the sum over k_z in the second line as $k_z \rightarrow -k_z$ and invert the integration variable $\vec{r}_\perp \rightarrow -\vec{r}_\perp$, which yields

$$\begin{aligned} H_-^{+\Delta} = & \frac{1}{2} \sum_{k_z} \int d^2 r_\perp \left(M_-^{+\Delta}(-x, -y, k_z) \left[-d_{k_z, i}^\dagger(\vec{r}_\perp) d_{k_z, i}(\vec{r}_\perp) - d_{-k_z, i}(\vec{r}_\perp) d_{-k_z, i}^\dagger(\vec{r}_\perp) \right] \right. \\ & \left. + d_{-k_z, i}(\vec{r}_\perp) \left[i \frac{\partial}{\partial x} + \frac{\partial}{\partial y} \right] d_{k_z, i}(\vec{r}_\perp) + d_{k_z, i}^\dagger(\vec{r}_\perp) \left[i \frac{\partial}{\partial x} - \frac{\partial}{\partial y} \right] d_{-k_z, i}^\dagger(\vec{r}_\perp) \right). \end{aligned} \quad (\text{D.78})$$

Using inversion symmetry in the $x - y$ -plane, i.e. $M_-^{+\Delta}(-x, -y, k_z) = M_-^{+\Delta}(x, y, k_z)$, we finally conclude that the Hamiltonian transforms under charge conjugation as

$$H \leftrightarrow -H^* \quad (\text{D.79})$$

(with the convention that the complex conjugation does not act on many-particle creation/annihilation operators). Denoting the charge conjugation operation \mathcal{C} , we thus find that for any eigenstate of the Hamiltonian, there exists an eigenstate of opposite energy,

$$H \Psi = E \Psi \quad \Rightarrow \quad H (\mathcal{C}\Psi)^* = -E (\mathcal{C}\Psi)^*. \quad (\text{D.80})$$

D.7 Vortices along \hat{z} in Weyl superconductors

As discussed in Sec. 8.2.1, we model a vortex in a Weyl superconductor similarly crudely to appendix D.5 by a cylinder of suppressed superconducting order parameter threaded by a flux. The average magnetization is in general affected by the vortex magnetic field, but for this appendix, we assume possible effects to be restricted to the vortex core. The latter is considered to be in a topologically trivial phase, which implies $|m| < m_{c1}$ there. From a topological point of view, the boundary surface of the vortex is then like a surface to vacuum, and we expect physics similar to Sec. 8.1.5.

Exploiting the cylindrical symmetry with respect to the vortex axis as in appendix D.5, we model the latter by a radially dependent magnetization m and superconducting order parameter $|\Delta|$. The radius of the vortex is considered to be R , and $m(r)$ and $|\Delta(r)|$ are smooth functions interpolating between fixed values m and $|\Delta|$ for $r > R$, and $|m| < m_{c1}$, $|\Delta| = 0$ inside the core of the vortex. The magnetic field is $\vec{B} = B \hat{z}$ inside the vortex and vanishes everywhere else, which leads to a vector potential

$$\begin{aligned} \vec{A}(\vec{r}) &= A(r) \hat{e}_\phi, \\ A(r) &= \frac{Br}{2} \Theta(R-r) + \frac{BR^2}{2r} \Theta(r-R). \end{aligned} \quad (\text{D.81})$$

As motivated in Sec. 8.2.1, we specialize to the case that only one subsector is topologically nontrivial outside the vortex (either fully, if the system is in a (0,1)-phase, or partially if it is in a (1,1)-phase), and that the relevant physics happen in the H_- -part of the Hamiltonian. The results can however readily be generalized. At first, we need to derive the Hamiltonian in cylindrical geometry, which can at least partially be done along the lines of appendix D.1. We start with the non-superconducting Hamiltonian H_- as defined in Eq. (8.5) and rewrite it in cylindrical coordinates for $r > R$. After the canonical transformation $\sigma^x \rightarrow -\sigma^y$, $\sigma^y \rightarrow \sigma^x$, we obtain

$$H_- = \sum_{k_z} d^2r \left(c_{k_z \uparrow -}^\dagger(\vec{r}), c_{k_z \downarrow -}^\dagger(\vec{r}) \right) \mathcal{H}_A \begin{pmatrix} c_{k_z \uparrow -}(\vec{r}) \\ c_{k_z \downarrow -}(\vec{r}) \end{pmatrix}, \quad (\text{D.82})$$

where the matrix Hamiltonian

$$\begin{aligned} \mathcal{H}_A &= M_-(k_z, r) \sigma^z + v_F (\sigma^x [-i\partial_x + eA_x] + \sigma_y [-i\partial_y + eA_y]) \\ &= M_-(k_z, r) \sigma^z + v_F \vec{\sigma} \left(\overleftarrow{e}_x \overrightarrow{e}_x + \overleftarrow{e}_y \overrightarrow{e}_y \right) (-i\nabla + e\vec{A}) \\ &= M_-(k_z, r) \sigma^z + v_F \vec{\sigma} \left(\overleftarrow{e}_r \overrightarrow{e}_r + \overleftarrow{e}_\phi \overrightarrow{e}_\phi \right) (-i\nabla + e\vec{A}) \\ &= M_-(k_z, r) \sigma^z + v_F \begin{pmatrix} 0 & -ie^{-i\phi} \\ -ie^{i\phi} & 0 \end{pmatrix} \frac{\partial}{\partial r} + v_F \begin{pmatrix} 0 & -e^{-i\phi} \\ e^{i\phi} & 0 \end{pmatrix} \left(\frac{1}{r} \frac{\partial}{\partial \phi} + ieA(r) \right) \end{aligned} \quad (\text{D.83})$$

contains the magnetic vector potential \vec{A} defined in Eq. (D.81) and where

$$M_-(k_z, r) = m(r) - \sqrt{t_S^2 + t_D^2 + 2t_S t_D \cos(k_z d)}. \quad (\text{D.84})$$

Note that we neglect the Zeeman effect inside the vortex core, since the latter is assumed to be in a topologically trivially insulating state with a large gap. We can now go

to Nambu space and add the proximity induced superconductivity to the Hamiltonian, which yields

$$H_- = \sum_{k_z} \int d^2r \left(c_{k_z \uparrow -}^\dagger(\vec{r}), c_{k_z \downarrow -}^\dagger(\vec{r}), c_{-k_z \downarrow -}(\vec{r}), c_{-k_z \uparrow -}(\vec{r}) \right) \mathcal{H}_{SC,-} \begin{pmatrix} c_{k_z \uparrow -}(\vec{r}) \\ c_{k_z \downarrow -}(\vec{r}) \\ c_{-k_z \downarrow -}^\dagger(\vec{r}) \\ c_{-k_z \uparrow -}^\dagger(\vec{r}) \end{pmatrix}, \quad (\text{D.85})$$

where

$$\mathcal{H}_{SC,-} = \begin{pmatrix} \mathcal{H}_A & |\Delta(r)| e^{i\tilde{\varphi}(\phi)} & 0 \\ |\Delta(r)| e^{-i\tilde{\varphi}(\phi)} & 0 & -|\Delta(r)| e^{i\tilde{\varphi}(\phi)} \\ 0 & -|\Delta(r)| e^{-i\tilde{\varphi}(\phi)} & \mathcal{H}_{-A} \end{pmatrix}. \quad (\text{D.86})$$

In the above equation, $\tilde{\varphi}(\phi) = \varphi - (\Phi/\Phi_0)\phi$ is the twisted order parameter, see appendix D.5 (ϕ is the angular coordinate, φ is the regular order parameter phase, Φ is the flux in the vortex and Φ_0 the superconducting flux quantum).

D.7.1 Expression of the zero energy Majorana bound state

A vortex in a Weyl superconductor traps a unique zero energy bound state if it contains an odd number of flux quanta. To explicitly show this, let us first discuss the bound state for a simple limiting case where the algebra can be done explicitly, and then turn to the general solution.

The limiting case is defined as follows. We assume that the Zeeman mass m is constant in the entire Weyl superconductor (and in particular takes the same value inside and outside the vortex). Moreover, we assume that $m_{c_1} < m < m_{c_2}$, such that there is one momentum $k_z = k_z^0$ with $M_-(r, k_z^0) = 0$ everywhere. As follows from Fig. 8.6, we are then able to find a $|\Delta| = \Delta_0$ outside the vortex such that only one subsector is topologically non-trivial, and expect a single zero energy Majorana mode bound to the vortex for this choice of $|\Delta|$: the vortex core at this momentum and order parameter has two topological subsectors, while the Weyl superconductors has only one topological subsector (for this momentum), see Fig. 8.6. At the interface, there will thus be a single Majorana mode. In addition, we assume that there is only a single flux quantum inside the vortex. Outside the vortex, the Hamiltonian (8.22) reads for $k_z = k_z^0$

$$H_- = \int_{r>R} d^2r \psi_{k_z^0}^\dagger(\vec{r}) \mathcal{H}_- \psi_{k_z^0}(\vec{r}), \quad (\text{D.87a})$$

$$\mathcal{H}_- = \begin{pmatrix} \mathcal{H}_B & |\Delta(r)| e^{i\varphi(\phi)} \sigma^z \\ |\Delta(r)| e^{-i\varphi(\phi)} \sigma^z & \mathcal{H}_{-B} \end{pmatrix}, \quad (\text{D.87b})$$

$$\mathcal{H}_B = v_F \begin{pmatrix} 0 & -i e^{-i\phi} \\ -i e^{i\phi} & 0 \end{pmatrix} \frac{\partial}{\partial r} + v_F \begin{pmatrix} 0 & -e^{-i\phi} \\ e^{i\phi} & 0 \end{pmatrix} \left(\frac{1}{r} \frac{\partial}{\partial \phi} + i e \frac{BR^2}{2r} \right).$$

The order parameter amplitude $|\Delta(r)|$ goes to zero in the vortex core and takes the value $|\Delta(r)| = \Delta_0$ far away from the vortex. For $k_z = k_z^0$, this Hamiltonian has two linearly independent normalizable zero energy bound state solutions,

$$\Psi_1^{\text{outer}} = \frac{1}{\mathcal{N}''} \frac{1}{\sqrt{r}} e^{-\int_R^r dr' |\Delta(k_z^0, r')|/v_F} \begin{pmatrix} e^{-i\phi} \\ 0 \\ 0 \\ i e^{i\phi} \end{pmatrix}, \quad (\text{D.88})$$

$$\Psi_2^{\text{outer}} = \frac{1}{\mathcal{N}''} \frac{1}{\sqrt{r}} e^{-\int_R^r dr' |\Delta(k_z^0, r')|/v_F} \begin{pmatrix} 0 \\ i \\ 1 \\ 0 \end{pmatrix}. \quad (\text{D.89})$$

Inside the vortex, i.e. for $r < R$, where

$$\mathcal{H}_B = v_F \begin{pmatrix} 0 & -i e^{-i\phi} \\ -i e^{i\phi} & 0 \end{pmatrix} \frac{\partial}{\partial r} + v_F \begin{pmatrix} 0 & -e^{-i\phi} \\ e^{i\phi} & 0 \end{pmatrix} \left(\frac{1}{r} \frac{\partial}{\partial \phi} + i e \frac{Br}{2} \right),$$

only the state

$$\Psi_2^{\text{inner}} = \frac{1}{\mathcal{N}'''} e^{-1/v_F \int_R^r dr' (|\Delta(k_z^0, r')| + eBr'/2)} \begin{pmatrix} 0 \\ i \\ 1 \\ 0 \end{pmatrix} \quad (\text{D.90})$$

is normalizable. The state that would be connected to Ψ_1 is given by

$$\psi_1^{\text{inner}} \sim e^{-1/v_F \int_R^r dr' (|\Delta(k_z^0, r')| + 1/r' - eBr'/2)} \begin{pmatrix} e^{-i\phi} \\ 0 \\ 0 \\ i e^{i\phi} \end{pmatrix}. \quad (\text{D.91})$$

This state however diverges at the origin as $\psi_1^{\text{inner}} \stackrel{r \rightarrow 0}{\sim} 1/r$ and is thus *not normalizable*. Consequently, there is only a single normalizable zero energy state bound to the vortex. Up to the normalization, it is given by

$$\Psi = \Psi_2^{\text{inner}} \Theta(R - r) + \Psi_2^{\text{outer}} \Theta(r - R). \quad (\text{D.92})$$

When we consider a momentum k_z close to k_z^0 or change the Zeeman gap m a little bit, the system will stay in the same extended topological phase. There will thus always be a single zero energy bound state per topological momentum as long as there is no topological phase transition. To be more concrete, we find that the Hamiltonian (8.22) has always two linearly independent zero energy bound states for $r > R$. For $M_-^{+\Delta}(k_z, r) > 0$ and $M_-^{-\Delta}(k_z, r) < 0$ at large r , they are given by

$$\Psi_{+\Delta}^{\text{outer}} = \frac{1}{\mathcal{N}' } \frac{1}{\sqrt{r}} e^{-\int_R^r dr' M_-^{+\Delta}(k_z, r')/v_F} \begin{pmatrix} e^{-i\phi} \\ i \\ 1 \\ i e^{i\phi} \end{pmatrix} \quad (\text{D.93})$$

$$\Psi_{-\Delta}^{\text{outer}} = \frac{1}{\mathcal{N}'''} \frac{1}{\sqrt{r}} e^{+\int_R^r dr' M_-^{-\Delta}(k_z, r')/v_F} \begin{pmatrix} e^{-i\phi} \\ -i \\ -1 \\ i e^{i\phi} \end{pmatrix}. \quad (\text{D.94})$$

The bound state will be a superposition of these two states that connects to the normalizable solution for $r < R$. The special case considered previously corresponds to $M_-^{+\Delta} = -M_-^{-\Delta} = |\Delta(r)|$ and $\Psi_2 \sim \Psi_{+\Delta} - \Psi_{-\Delta}$.

Bibliography

- [1] O. Pankratov, S. Pakhomov, and B. Volkov, *Solid State Communications* **61**, 93 (1987).
- [2] B. A. Bernevig, T. L. Hughes, and S.-C. Zhang, *Science* **314**, 1757 (2006).
- [3] M. König, S. Wiedmann, C. Brüne, A. Roth, H. Buhmann, L. W. Molenkamp, X.-L. Qi, and S.-C. Zhang, *Science* **318**, 766 (2007).
- [4] L. Fu and C. L. Kane, *Phys. Rev. B* **76**, 045302 (2007).
- [5] M. Z. Hasan and C. L. Kane, *Review of Modern Physics* **82**, 3045 (2010).
- [6] L. D. Landau and E. M. Lifshitz, *Statistical Physics*, vol. 5 of *Course of Theoretical Physics* (Butterworth-Heinemann, 1980), 3rd ed.
- [7] S. Sachdev, *Quantum Phase Transitions* (Cambridge University Press, 1999).
- [8] K. G. Wilson, *Rev. Mod. Phys.* **47**, 773 (1975).
- [9] M. Vojta, *Rep. Prog. Phys.* **66**, 2069 (2003).
- [10] J. A. Hertz, *Phys. Rev. B* **14**, 1165 (1976).
- [11] S. L. Sondhi, S. M. Girvin, J. P. Carini, and D. Shahar, *Rev. Mod. Phys.* **69**, 315 (1997).
- [12] P. Coleman and A. J. Schofield, *Nature* p. 226 (2005).
- [13] J. S. Meyer and K. A. Matveev, *J. Phys. Condens. Matter* **21**, 023203 (2009).
- [14] B. J. van Wees, H. van Houten, C. W. J. Beenakker, J. G. Williamson, L. P. Kouwenhoven, D. van der Marel, and C. T. Foxon, *Phys. Rev. Lett.* **60**, 848 (1988).
- [15] A. Y. Kitaev, *Phys.-Usp.* **44**, 131 (2001).
- [16] T. Meng, M. Dixit, M. Garst, and J. S. Meyer, *Phys. Rev. B* **83**, 125323 (2011).
- [17] E. Ising, *Zeitschrift für Physik A* **31**, 253 (1925).
- [18] L. Onsager, *Phys. Rev.* **65**, 117 (1944).
- [19] N. D. Mermin and H. Wagner, *Phys. Rev. Lett.* **17**, 1133 (1966).
- [20] P. C. Hohenberg, *Phys. Rev.* **587**, 383 (1967).

- [21] S. Coleman, *Comm. Math. Phys.* **31**, 259 (1973).
- [22] T. Giamarchi, *Quantum Physics in One Dimension* (Oxford University Press, 2003).
- [23] J. M. Luttinger, *J. Math. Phys.* **4**, 1154 (1963).
- [24] S.-I. Tomonaga, *Prog. Theor. Phys.* **5**, 544 (1950).
- [25] D. C. Mattis and E. H. Lieb, *J. Math. Phys.* **6**, 304 (1965).
- [26] F. D. M. Haldane, *J. Phys. C* **14**, 2585 (1981).
- [27] J. von Delft and H. Schoeller, *Ann. Phys.* **7**, 225 (1998).
- [28] J. Voit, *Rep. Prog. Phys.* **58**, 977 (1995).
- [29] D. Sénéchal (1999), arXiv:cond-mat/9908262.
- [30] C. M. Varma and A. Zawadowski, *Phys. Rev. B* **32**, 7399 (1985).
- [31] K. Penc and J. Sólyom, *Phys. Rev. B* **41**, 704 (1990).
- [32] M. Fabrizio, *Phys. Rev. B* **48**, 15838 (1993).
- [33] L. Balents and M. P. A. Fisher, *Phys. Rev. B* **53**, 12133 (1996).
- [34] K. Louis, J. V. Alvarez, and C. Gros, *Phys. Rev. B* **64**, 113106 (2001).
- [35] G. I. Japaridze, R. M. Noack, D. Baeriswyl, and L. Tincani, *Phys. Rev. B* **76**, 115118 (2007).
- [36] H.-H. Lai and O. I. Motrunich, *Phys. Rev. B* **81**, 045105 (2010).
- [37] J. S. Meyer, K. A. Matveev, and A. I. Larkin, *Phys. Rev. Lett.* **98**, 126404 (2007).
- [38] M. Sitte, A. Rosch, J. S. Meyer, K. A. Matveev, and M. Garst, *Phys. Rev. Lett.* **102**, 176404 (2009).
- [39] E. Wigner, *Phys. Rev.* **46**, 1002 (1934).
- [40] H. J. Schulz, *Phys. Rev. Lett.* **71**, 1864 (1993).
- [41] A. V. Chaplik, *Pisma Zh. Eksp. Teor. Fiz.* **31**, 275 (1980), [*JETP Lett.* **31**, 252 (1980)].
- [42] R. W. Hasse and J. P. Schiffer, *Ann. Phys.* **203**, 419 (1990).
- [43] G. Piacente, I. V. Schweigert, J. J. Betouras, and F. M. Peeters, *Phys. Rev. B* **69**, 045324 (2004).
- [44] R. Cortes-Huerto, M. Paternostro, and P. Ballone, *Phys. Rev. A* **82**, 013623 (2010).
- [45] J. Ruhman, E. G. Dalla Torre, S. D. Huber, and E. Altman, *Phys. Rev. B* **85**, 125121 (2012).

- [46] P. Pfeuty, *Ann. Phys.* **57**, 79 (1970).
- [47] A. D. Klironomos, J. S. Meyer, and K. A. Matveev, *Europhys. Lett.* **74**, 679 (2006).
- [48] A. D. Klironomos, J. S. Meyer, T. Hikihara, and K. A. Matveev, *Phys. Rev. B* **76**, 075302 (2007).
- [49] D. N. Sheng, O. I. Motrunich, and M. P. A. Fisher, *Phys. Rev. B* **79**, 205112 (2009).
- [50] K. A. Matveev, *Phys. Rev. Lett.* **92**, 106801 (2004).
- [51] A. D. Klironomos, R. R. Ramazashvili, and K. A. Matveev, *Phys. Rev. B* **72**, 195343 (2005).
- [52] M. C. Cross and D. S. Fisher, *Phys. Rev. B* **19**, 402 (1979).
- [53] M. Zacharias, P. Wölfle, and M. Garst, *Phys. Rev. B* **80**, 165116 (2009).
- [54] M. Garst and A. V. Chubukov, *Phys. Rev. B* **81**, 235105 (2010).
- [55] M. Ogata and H. Shiba, *Phys. Rev. B* **41**, 2326 (1990).
- [56] F. H. Essler, H. Frahm, F. Göhmann, A. Klümper, and V. E. Korepin, *The One-Dimensional Hubbard Model* (Cambridge University Press, Cambridge, 2005), see chapter 11.
- [57] M. Takahashi, *Prog. Theor. Phys.* **46**, 1388 (1971).
- [58] F. Göhmann, A. G. Izergin, V. E. Korepin, and A. G. Pronko, *Int. J. Mod. Phys. B* **12**, 2409 (1998).
- [59] M. M. Fogler, *Phys. Rev. Lett.* **94**, 056405 (2005).
- [60] P. Nicolíć and S. Sachdev, *Phys. Rev. A* **75**, 033608 (2007).
- [61] L. Balents, *Phys. Rev. B* **61**, 4429 (2000).
- [62] A. Lamacraft, *Phys. Rev. Lett.* **101**, 225301 (2008).
- [63] H. v. Löhneysen, *J. Phys.: Cond. Matter* **8**, 9689 (1996).
- [64] P. Coleman, *Physica B* **259–261**, 353 (1999).
- [65] M. B. Maple, *Journal of Magnetism and Magnetic Materials* **177**, 18 (1998).
- [66] J. Orenstein and A. J. Millis, *Science* **288**, 468 (2000).
- [67] S. Sachdev, *Science* **288**, 475 (2000).
- [68] H. v. Löhneysen, A. Rosch, M. Vojta, and P. Wölfle, *Rev. Mod. Phys.* **79**, 1015 (2007).
- [69] P. Gegenwart, T. Westerkamp, C. Krellner, Y. Tokiwa, S. Paschen, C. Geibel, F. Steglich, E. Abrahams, and Q. Si, *Science* **315**, 969 (2007).

- [70] V. Oganesyan, S. A. Kivelson, and E. Fradkin, *Phys. Rev. B* **64**, 195109 (2001).
- [71] C. Pfleiderer, *J. Phys.: Cond. Matter* **17**, S987 (2005).
- [72] J.-H. She, J. Zaanen, A. R. Bishop, and A. V. Balatsky, *Phys. Rev. B* **82**, 165128 (2010).
- [73] M. A. Metlitski and S. Sachdev, *Phys. Rev. B* **82**, 075127 (2010).
- [74] M. A. Metlitski and S. Sachdev, *Phys. Rev. B* **82**, 075128 (2010).
- [75] B. I. Halperin and P. C. Hohenberg, *Phys. Rev.* **177**, 952 (1969).
- [76] P. C. Hohenberg and B. I. Halperin, *Rev. Mod. Phys.* **49**, 435 (1977).
- [77] R. Folk and G. Moser, *J. Phys. A* **39**, R207 (2006).
- [78] J. Cardy, *Scaling and renormalization in Statistical physics*, vol. 5 of *Cambridge Lecture Notes in Physics* (Cambridge University Press, 1996).
- [79] B. Widom, *J. Chem. Phys.* **43**, 3892 (1965).
- [80] D. Bitko, T. F. Rosenbaum, and G. Aeppli, *Phys. Rev. Lett.* **77**, 940 (1996).
- [81] S. Sachdev, *Phys. Rev. B* **55**, 142 (1997).
- [82] D. Belitz, T. R. Kirkpatrick, M. T. Mercaldo, and S. L. Sessions, *Phys. Rev. B* **63**, 174427 (2001).
- [83] D. Belitz, T. R. Kirkpatrick, M. T. Mercaldo, and S. L. Sessions, *Phys. Rev. B* **63**, 174428 (2001).
- [84] D. Das, A. Basu, M. Barma, and S. Ramaswamy, *Phys. Rev. E* **64**, 021402 (2001).
- [85] I. J. Pomeranchuk, *JETP* **8**, 361 (1958).
- [86] C. J. Halboth and W. Metzner, *Phys. Rev. Lett.* **85**, 5162 (2000).
- [87] H. Yamase and H. Kohno, *J. Phys. Soc. Jpn.* **69**, 332 (2000).
- [88] H. Yamase and H. Kohno, *J. Phys. Soc. Jpn.* **69**, 2151 (2000).
- [89] L. Dell'Anna and W. Metzner, *Phys. Rev. Lett.* **98**, 136402 (2007).
- [90] L. Dell'Anna and W. Metzner, *Phys. Rev. Lett.* **103**, 159904 (2009).
- [91] H.-Y. Kee, E. H. Kim, and C.-H. Chung, *Phys. Rev. B* **68**, 245109 (2003).
- [92] Y. B. Kim and H.-Y. Kee, *J. Phys.: Cond. Matter* **16**, 3139 (2004).
- [93] H.-Y. Kee and Y. B. Kim, *Phys. Rev. B* **71**, 184402 (2005).
- [94] J. Nilsson and A. H. Castro Neto, *Phys. Rev. B* **72**, 195104 (2005).
- [95] J. Quintanilla and A. J. Schofield, *Phys. Rev. B* **74**, 115126 (2006).

- [96] L. Dell'Anna and W. Metzner, Phys. Rev. B **73**, 045127 (2006).
- [97] H. Yamase and W. Metzner, Phys. Rev. B **75**, 155117 (2007).
- [98] J. Quintanilla, M. Haque, and A. J. Schofield, Phys. Rev. B **78**, 035131 (2008).
- [99] P. Wölfle and A. Rosch, Journal of Low Temperature Physics **147**, 165 (2007).
- [100] D. L. Maslov and A. V. Chubukov, Phys. Rev. B **81**, 045110 (2010).
- [101] L. D. Landau, J. Phys. USSR **10**, 25 (1946), reprinted in *Collected Papers of L. D. Landau*, ed. D. Ter Haar, Pergamon Press, 1965.
- [102] D. R. Nelson, Phys. Rev. B **11**, 3504 (1975).
- [103] A. J. Millis, Phys. Rev. B **48**, 7183 (1993).
- [104] C. Herring, Physical Review **52**, 365 (1937).
- [105] G. E. Volovik, *The Universe in a Helium Droplet* (Oxford University Press, 2003).
- [106] S. Murakami, New Journal of Physics **9**, 356 (2007).
- [107] X. Wan, A. M. Turner, A. Vishwanath, and S. Y. Savrasov, Phys. Rev. B **83**, 205101 (2011).
- [108] W. Witczak-Krempa and Y. B. Kim, Phys. Rev. B **85**, 045124 (2012).
- [109] G. Y. Cho (2011), arXiv:1110.1939.
- [110] G. Xu, H. Weng, Z. Wang, X. Dang, and Z. Fang, Phys. Rev. Lett. **107**, 186806 (2011).
- [111] A. A. Burkov and L. Balents, Phys. Rev. Lett. **107**, 127205 (2011).
- [112] G. B. Halász and L. Balents, Phys. Rev. B **85**, 035103 (2012).
- [113] A. A. Zyuzin, S. Wu, and A. A. Burkov, Phys. Rev. B **85**, 165110 (2012).
- [114] A. A. Burkov, M. D. Hook, and L. Balents, Phys. Rev. B **84** (2011).
- [115] K.-Y. Yang, Y.-M. Lu, and Y. Ran, Phys. Rev. B **84**, 075129 (2011).
- [116] P. Hosur, S. A. Parameswaran, and A. Vishwanath, Phys. Rev. Lett. **108**, 046602 (2012).
- [117] A. Go, W. Witczak-Krempa, G. S. Jeon, K. Park, and Y. B. Kim (2012), arXiv:1202.4460.
- [118] J. D. Sau and S. Tewari (2011), arXiv:1110.4110.
- [119] K. Togano, P. Badica, Y. Nakamori, S. Orimo, H. Takeya, and K. Hirata, Phys. Rev. Lett. **93**, 247004 (2004).
- [120] P. Badica, T. Kondo, and K. Togano, J. Phys. Soc. Jpn. **74**, 1014 (2005).

- [121] G. Amano, S. Akutagawa, T. Muranaka, Y. Zenitani, and J. Akimitsu, *J. Phys. Soc. Jpn.* **73**, 530 (2004).
- [122] I. Martin and A. F. Morpurgo, *Phys. Rev. B* **85**, 144505 (2012).
- [123] User:stannered. Two unknots. Digital Image. *Wikipedia*. Web. Taken from http://en.wikipedia.org/wiki/Knot_theory on January 24, 2012. Public domain.
- [124] Oleg Alexandrov. Objects with various genera. Digital Image. *Wikipedia*. Web. Taken from [http://en.wikipedia.org/wiki/Genus_\(mathematics\)](http://en.wikipedia.org/wiki/Genus_(mathematics)) on January 24, 2012. Public domain.
- [125] A. Altland and B. Simons, *Condensed Matter Field Theory* (Cambridge University Press, 2010), 2nd ed.
- [126] N. D. Mermin, *Review of Modern Physics* **51**, 591 (1979).
- [127] M. V. Berry, *Proc. R. Soc. Lond. A* **392**, 45 (1984).
- [128] V. Gurarie, *Phys. Rev. B* **83**, 085426 (2011).
- [129] D. J. Thouless, M. Kohmoto, M. P. Nightingale, and M. den Nijs, *Phys. Rev. Lett.* **49**, 405 (1982).
- [130] X.-L. Qi and S.-C. Zhang, *Review of Modern Physics* **83**, 1057 (2011).
- [131] A. W. W. Ludwig, M. P. A. Fisher, R. Shankar, and G. Grinstein, *Phys. Rev. B* **50**, 7526 (1994).
- [132] A. P. Schnyder, S. Ryu, A. Furusaki, and A. W. W. Ludwig, *Phys. Rev. B* **78**, 195125 (2008).
- [133] L. Fu and C. L. Kane, *Phys. Rev. Lett.* **100**, 096407 (2008).
- [134] N. Read and D. Green, *Phys. Rev. B* **61**, 10267 (2000).
- [135] D. A. Ivanov, *Physics Letters* **86**, 268 (2001).
- [136] P. A. M. Dirac, *Proc. R. Soc. Lond. A* **17**, 610 (1928).
- [137] E. Majorana, *Nuovo Cimento* **14**, 171 (1937).
- [138] H. Klapdor-Kleingrothaus, I. Krivosheina, A. Dietz, and O. Chkvorets, *Physics Letters B* **586**, 198 (2004).
- [139] G. Koren, T. Kirzhner, E. Lahoud, K. B. Chashka, and A. Kanigel, *Phys. Rev. B* **84**, 224521 (2011).
- [140] S. Sasaki, M. Kriener, K. Segawa, K. Yada, Y. Tanaka, M. Sato, and Y. Ando, *Phys. Rev. Lett.* **107**, 217001 (2011).
- [141] V. Mourik, K. Zuo, S. M. Frolov, S. R. Plissard, E. P. A. M. Bakkers, and L. P. Kouwenhoven, *Science* (2012).

- [142] M. T. Deng, C. L. Yu, G. Y. Huang, M. Larsson, P. Caroff, and H. Q. Xu (2012), arXiv:1204.4130.
- [143] L. P. Rokhinson, X. Liu, and J. K. Furdyna (2012), arXiv:1204.4212.
- [144] J. von Neumann and E. P. Wigner, *Physikalische Zeitschrift* **30**, 467 (1929).
- [145] S. L. Adler, *Physical Review* **177**, 2426 (1969).
- [146] J. S. Bell and R. Jackiw, *Nuovo Cimento* **60A**, 47 (1969).
- [147] H. B. Nielsen and M. Ninomiya, *Physics Letters* **130B**, 389 (1983).
- [148] H. B. Nielsen and M. Ninomiya, *Nuclear Physics B* **185**, 20 (1981).
- [149] H. B. Nielsen and M. Ninomiya, *Nuclear Physics B* **193**, 173 (1981).
- [150] H. B. Nielsen and M. Ninomiya, *Physics Letters* **105B**, 219 (1981).
- [151] G. E. Volovik, *Lecture Notes Physics* **718**, 31 (2007).
- [152] H. Zhang, C.-X. Liu, X.-L. Qi, Z. Fang, and S.-C. Zhang, *Nature Physics* **5**, 438 (2009).
- [153] C.-X. Liu, X.-L. Qi, H. Zhang, X. Dai, Z. Fang, and S.-C. Zhang, *Phys. Rev. B* **82**, 045122 (2010).
- [154] C.-K. Chiu, M. J. Gilbert, and T. L. Hughes, *Phys. Rev. B* **84**, 144507 (2011).
- [155] G. Rosenberg, H.-M. Guo, and M. Franz, *Phys. Rev. B* **82**, 041104(R) (2010).
- [156] G. E. Volovik, *JETP Letters* **93**, 66 (2011).
- [157] L. Fu and C. L. Kane, *Phys. Rev. Lett.* **102**, 216403 (2009).
- [158] G. Zhang, H. Qin, J. Teng, J. Guo, Q. Guo, X. Dai, D. Fang, and K. Wu, *Applied Physics Letters* **95**, 053114 (2009).
- [159] H. Peng, K. Lai, D. Kong, S. Meister, Y. Cheng, X.-L. Qi, S.-C. Zhang, Z.-X. Shen, and Y. Cui, *Nature Materials* **9**, 225 (2010).
- [160] Y. Zhang, K. He, C.-Z. Chang, C.-L. Song, L.-L. Wang, X. Chen, J.-F. Jia, Z. Fang, X. Dai, W.-Y. Shan, et al., *Nature Physics* **6**, 584 (2010).
- [161] A. Y. Kasumov, O. V. Kononenko, V. M. Matveev, T. B. Borsenko, V. A. Tulin, E. E. Vdovin, and I. I. Khodos, *Phys. Rev. Lett.* **77**, 3029 (1996).
- [162] B. Sacépé, J. B. Oostinga, J. Li, A. Ubaldini, N. J. G. Couto, E. Giannini, and A. F. Mopurgo, *Nature Communications* **2**, 575 (2011).
- [163] F. Yang, Y. Ding, F. Qu, J. Shen, J. Chen, Z. Wei, Z. Ji, G. Liu, J. Fan, C. Yang, et al., *Phys. Rev. B* **85**, 104508 (2012).
- [164] F. Qu, F. Yang, J. Shen, Y. Ding, J. Chen, Z. Ji, G. Liu, J. Fan, X. Jing, C. Yang, et al., *Scientific Reports* **2**, 339 (2012).

- [165] I. Knez, R.-R. Du, and G. Sullivan (2011), arXiv:1106.5819.
- [166] D. Zhang, J. Wang, A. M. DaSilva, J. S. Lee, H. R. Gutierrez, M. H. W. Chan, J. Jain, and N. Samarath, *Phys. Rev. B* **84**, 165120 (2011).
- [167] J. R. Williams, A. B. Beswick, P. Gallagher, S. S. Hong, Y. Cui, A. S. Bleich, J. G. Analytis, I. R. Fisher, and D. Goldhaber-Gordon (2012), arXiv:1202.2323.
- [168] S. S. Saxena, P. Agarwal, K. Ahilan, F. M. Grosche, R. K. W. Haselwimmer, M. J. Steiner, E. Pugh, I. R. Walker, S. R. Julian, P. Monthoux, et al., *Nature* **406**, 587 (2000).
- [169] D. Aoki, A. Huxley, E. Ressouche, D. Braithwaite, J. Flouquet, J.-P. Brison, E. Lhotel, and C. Paulsen, *Nature* **413**, 613 (2001).
- [170] N. T. Huy, A. Gasparini, D. E. de Nijs, Y. Huang, J. C. P. Klaasse, T. Gortenmulder, A. de Visser, A. Hamann, T. Görlach, and H. v. Löhneysen, *Phys. Rev. Lett.* **99**, 067006 (2007).
- [171] Y. Maeno, S. Kittaka, T. Nomura, S. Yonezawa, and K. Ishida, *J. Phys. Soc. Jpn.* **81**, 011009 (2012).
- [172] C. L. Kane and M. P. A. Fisher, *Phys. Rev. B* **55**, 15832 (1997).
- [173] T. Senthil, J. B. Marston, and M. P. A. Fisher, *Phys. Rev. B* **60**, 4245 (1999).
- [174] Z. Wang, X.-L. Qi, and S.-C. Zhang, *Phys. Rev. B* **84**, 014527 (2011).
- [175] H. W. J. Blöte, J. L. Cardy, and M. P. Nightingale, *Phys. Rev. Lett.* **56**, 742 (1986).
- [176] I. Affleck, *Phys. Rev. Lett.* **56**, 746 (1986).
- [177] I. Serban, B. Béri, A. R. Akhmerov, and C. W. J. Beenakker, *Phys. Rev. Lett.* **104**, 147001 (2010).
- [178] S. B. Chung, X.-L. Qi, J. Maciejko, and S.-C. Zhang, *Phys. Rev. B* **83**, 100512(R) (2011).
- [179] E. C. G. Stueckelberg and A. Petermann, *Helv. Phys. Acta* **26**, 499 (1953).
- [180] M. Gell-Mann and F. E. Low, *Phys. Rev.* **95**, 1300 (1954).
- [181] L. P. Kadanoff, *Physics (Long Island City, N.Y.)* **2**, 263 (1966).
- [182] D. Loss and T. Martin, *Phys. Rev. B* **50**, 12160 (1994).
- [183] G. Wentzel, *Phys. Rev.* **83**, 168 (1951).
- [184] J. Bardeen, *Rev. Mod. Phys.* **23**, 261 (1951).

Acknowledgments

First of all, I would like to thank my thesis supervisors PD Dr. Markus Garst and Prof. Dr. Achim Rosch for many invaluable discussions and explanations, for their guidance and support. Working with them was a great pleasure, both scientifically and personally. I am also indebted to Prof. Dr. Matthias Vojta, who co-supervised me during the beginning of my PhD, working with whom I also enjoyed a lot. It has furthermore been a great pleasure to successfully collaborate with Prof. Dr. Julia S. Meyer and Mehul Dixit on the quantum wire project. Similarly, I am very grateful to Prof. Dr. Leon Balents, with whom I had the honor to work on Weyl superconductors, and who welcomed me during three months in Santa Barbara, California. I would also like to acknowledge the great hospitality and very inspiring atmosphere of the Kavli Institute of Theoretical Physics. My time in Santa Barbara was definitely one of the highlights of my PhD, and I believe also an important opportunity for personal development. Related to that, I am also grateful for the financial support of the Bonn-Cologne graduate school of Physics and Astronomy (BCGS), which not only helped financing my stay in Santa Barbara, but also made it possible to attend great workshops, summer schools and the Lindau Nobel Laureate meeting. Similarly, I would like to acknowledge the support of the SFB 608 of the Deutsche Forschungsgemeinschaft.

It has also been a pleasure to share my time in Cologne with great colleagues, with whom it was and will be a pleasure to spend time inside and outside the office. I am grateful to all of them for making my PhD a pleasant and fun time, thanks for listening to my most stupid problems and silliest questions, but also for the administrative staff that helped me to focus on my research. First of all, my thanks go to all of the people I was lucky to share my office with during the last three years. Thank you for a great time, dear Akos, Benjamin, Jonathan, Matthias, Mario and Michael. But of course, I also want to thank Yasemin Tieben and Andreas Sindermann, and all members of our (extended) group, Adel, Alex, Andrew, Carolin, Christoph, David, Eran, Etienne, Heidi, Karen, Koos, Karin, Lars, Lucas, Pascal, Ralf, Ricardo, Simon, Stefan and Stephan. Last but not least, my thanks go to all of my friends, to my family and especially to Vera, who always supported me and made my life in Cologne one of the best times in my life.

Erklärung

Ich versichere, dass ich die von mir vorgelegte Dissertation selbständig angefertigt, die benutzten Quellen und Hilfsmittel vollständig angegeben und die Stellen der Arbeit – einschließlich Tabellen, Karten und Abbildungen –, die anderen Werken im Wortlaut oder dem Sinn nach entnommen sind, in jedem Einzelfall als Entlehnung kenntlich gemacht habe; dass diese Dissertation noch keiner anderen Fakultät oder Universität zur Prüfung vorgelegen hat; dass sie – abgesehen von unten angegebenen Teilpublikationen – noch nicht veröffentlicht worden ist sowie, dass ich eine solche Veröffentlichung vor Abschluss des Promotionsverfahrens nicht vornehmen werde. Die Bestimmungen der Promotionsordnung sind mir bekannt. Die von mir vorgelegte Dissertation ist von Prof. Dr. Achim Rosch betreut worden.

Köln, 9. Juli 2012

Tobias Meng

Teilpublikationen

T. Meng, M. Dixit, M. Garst, and J. S. Meyer,
“Quantum phase transitions in quantum wires controlled by an external gate”,
Phys. Rev. B **83**, 125323 (2011).

In Vorbereitung:

- “Weyl superconductors”, T. Meng und L. Balents (pre-print unter arXiv:1205.5202)
- “Quantum criticality with multiple dynamics”, T. Meng, M. Garst und A. Rosch (pre-print unter arXiv:1205.3400)

CURRICULUM VITAE

TOBIAS PHILIPP MENG, DIPL.-PHYS.

PERSÖNLICHE DATEN

Balthasarstr. 17
50670 Köln
Deutschland

Geburtsdatum und -ort: 11. Dezember 1983 in Mainz
Staatsbürgerschaft: deutsch
Familienstand: ledig

BERUFLICHE ERFAHRUNGEN

09/2011–12/2012 Forschungsaufenthalt am Kavli Institute for Theoretical Physics der University of California, Santa Barbara in der Arbeitsgruppe von Prof. Dr. L. Balents.

- Erforschung von supraleitenden topologischen Weyl-Halbmatalen.

seit April 2009 Dissertation an der Universität zu Köln in der Arbeitsgruppe von Prof. Dr. A. Rosch (Betreuer: Prof. Dr. A. Rosch und PD Dr. M. Garst) zum Thema “Quantenkritische Materie”.

- Erforschung von exotischen Quantenzustände an Lifshitz-Übergängen in stark korrelierten Quantendrähten.
- Erforschung der Quantenkritikalität von Systemen mit multiplen Dynamiken.

04/2008–03/2009 Diplomarbeit am CNRS Grenoble (Betreuer: Dr. S. Florens und Prof. Dr. P. Simon) zum Thema “Andreev bound states in Josephson quantum dot devices”.

- Erforschung der Andreev bound states in einem an supraleitende Elektroden gekoppelten Quantenpunkt.

PUBLIKATIONEN

- “First order $0/\pi$ quantum phase transition in the Kondo regime of a superconducting carbon nanotube quantum dot”, R. Maraud, T. Meng, E. Bonnet, S. Florens, L. Marty und W. Wernsdorfer, Phys. Rev. X **2**, 011009 (2012).
- “Quantum phase transitions in quantum wires controlled by an external gate”, T. Meng, M. Dixit, M. Garst und J. S. Meyer, Phys. Rev. B **83**, 125323 (2011)
- “Self-consistent description of Andreev bound states in Josephson quantum dot devices”, T. Meng, S. Florens und P. Simon, Phys. Rev. B **79**, 224521 (2009).
- “Optical magnetic circular dichroism in threshold photoemission from a magnetic thin film”, K. Hild, J. Maul, T. Meng, M. Kallmeyer, G. Schönhense, H. J. Elmers, R. Ramos, S. K. Arora und I. V. Schvets, J. Phys.: Condens. Matter **20**, 235218 (2008).
- In Vorbereitung:
 - “Weyl superconductors”, T. Meng und L. Balents (pre-print unter arXiv:1205.5202)
 - “Quantum criticality with multiple dynamics”, T. Meng, M. Garst und A. Rosch (pre-print unter arXiv:1205.3400)

STUDIUM UND SCHULBILDUNG

| | |
|-----------------|--|
| März 2009 | Physikdiplom der Universität Karlsruhe (TH), Note: mit Auszeichnung, Schnitt: 1,0. |
| Oktober 2008 | Ingenieursdiplom des Institut National Polytechnique de Grenoble, Note: sehr gut, Schnitt: 17,23/20 Punkte. |
| Juli 2008 | Master 2 recherche der Université Joseph Fourier Grenoble, Note: sehr gut, Schnitt: 18,00/20 Punkte. |
| 10/2007–09/2008 | Studium im Masterstudiengang “Physique de la matière condensée et rayonnement” der Université Joseph Fourier Grenoble (Frankreich). |
| 10/2006–09/2008 | Studium am Institut National Polytechnique de Grenoble (Frankreich) im Rahmen eines Doppeldiplomprogramms der Deutsch-Französischen Hochschule, www.dfh-ufa.org. Spezialisierung: funktionelle Materialien und Nanophysik. |
| Oktober 2005 | Vordiplom (Note: 1,2). Nebenfach: Wirtschaftswissenschaften (BWL, Rechnungswesen). |
| 03/2003–03/2009 | Studium der Physik an der Universität Karlsruhe (TH). |
| Mai 2003 | Allgemeinbildendes Abitur (Note: 1,5) und französisches Baccalauréat scientifique (Note: gut). |
| 1994–2003 | Max-Slevogt-Gymnasium in Landau in der Pfalz, Leistungskurse: Mathematik, Chemie, Französisch (bilingualer Zweig). |
| 1990–1994 | Grundschule Kandel |

AUSZEICHNUNGEN UND STIPENDIEN

| | |
|-------------------|---|
| Juni–Juli 2010 | Einladung zum 60. Treffen der Nobelpreisträger in Lindau als “Young Researcher”. |
| seit Oktober 2009 | Stipendiat der Bonn-Cologne Graduate School of Physics and Astronomy. |
| 2008–2009 | Stipendiat des Deutschen Akademischen Austausch Dienstes (DAAD). |
| 2008–2009 | Bourse sur critères universitaires des französischen Staates (für besondere Studienleistungen). |

SONSTIGES

- Sprachen: Deutsch (Muttersprache), Englisch (fließend in Wort und Schrift), Französisch (fließend in Wort und Schrift), Spanisch (Grundkenntnisse), Niederländisch (Grundkenntnisse).
- Computerkenntnisse: Windows, Linux und OS X, C / C++, L^AT_EX, Mathematica, Word, Excel, Pow-erpoint, HTML, PHP, Grundkenntnisse von Matlab und Femlab/COMSOL.

GESELLSCHAFTLICHES ENGAGEMENT

- Präsident von AEGEE-Köln e.V. (Dezember 2009 - Januar 2011)
 (“Association des Etats Généraux des Etudiants de l’Europe”), www.aegEE-koeln.de.
Management des Vereins (ca. 40 Mitglieder), Alumniarbeit, Planung und Durchführung von thematischen Sommerkursen für europäische Studenten (10-14 Tage, 15-25 Teilnehmer) und eines zweiwöchigen Case Study Trips zu globalen Herausforderungen von 30 Studenten aus Europa, Palästina und Ägypten, Betreuung von Erasmus-Studenten in Köln. Vertreten des Vereins im europaweiten AEGEE-Netzwerk.
- Präsident (2008–2009) und Kassenwart (2007–2008) des deutsch-französischen Studenten-Vereins
 “Association Doubles Diplômes Karlsruhe Grenoble”, <http://adkg.free.fr>.
Management des Vereins (ca. 25 Mitglieder), Alumniarbeit, Organisation von Netzwerk-Events, Informationsveranstaltungen zu deutsch-französischen Austauschprogrammen und Stammtischen von Austauschstudenten. Führen der Konten und Erstellung der Bilanz.